Photon and electron induced desorption from molecular ices

Rémi Dupuy

▶ **To cite this version:**

Rémi Dupuy. Photon and electron induced desorption from molecular ices. Chemical Physics [physics.chem-ph]. Sorbonne Université, 2019. English. NNT : . tel-02354689v1

HAL Id: tel-02354689

https://theses.hal.science/tel-02354689v1

Submitted on 7 Nov 2019 (v1), last revised 16 Oct 2020 (v2)

HAL is a multi-disciplinary open access archive for the deposit and dissemination of scientific research documents, whether they are published or not. The documents may come from teaching and research institutions in France or abroad, or from public or private research centers.

L'archive ouverte pluridisciplinaire **HAL**, est destinée au dépôt et à la diffusion de documents scientifiques de niveau recherche, publiés ou non, émanant des établissements d'enseignement et de recherche français ou étrangers, des laboratoires publics ou privés.

SORBONNE UNIVERSITÉ

CERN

THÈSE DE DOCTORAT
DE SORBONNE UNIVERSITÉ

Spécialité : Physique

École doctorale n°564: Physique en Île-de-France

réalisée

au Laboratoire d'Études du Rayonnement et de la Matière en Astrophysique et Atmosphères

sous la direction de Jean-Hugues Fillion

présentée par

Rémi DUPUY

pour obtenir le grade de :

DOCTEUR DE SORBONNE UNIVERSITÉ

Sujet de la thèse :

Photon and electron induced desorption from molecular ices

soutenue le 10 Octobre 2019

devant le jury composé de :

M.	Marc SIMON	Président
M.	Christian BORDAS	Rapporteur
M.	Martin McCOUSTRA	Rapporteur
Mme	Nathalie CARRASCO	Examinatrice
Mme	Anne LAFOSSE	Examinatrice
M.	Jean-Hugues FILLION	Directeur de thèse
M.	Vincent BAGLIN	Invité

Remerciements

J'ai eu la chance, pendant cette thèse, de pouvoir travailler de près avec plusieurs personnes, que je vais remercier en tout premier lieu pour ces trois années. Je remercie tout d'abord mon directeur de thèse, Jean-Hugues Fillion. Ton regard calme et réfléchi sur les choses m'a souvent aidé à prendre du recul, que ce soit pour les manips ou pour la rédaction des articles ou de ce manuscrit - qui sans toi se serait certainement perdu dans trop de généralités ou de détails par endroit. Malgré les nombreuses charges qui t'incombaient pendant ces trois années (enfin libre!), tu as su être disponible quand c'était nécessaire, que ce soit pour m'expliquer la physique moléculaire, bidouiller les lasers en salle de manip ou prendre les bonnes décisions au bon moment. Je remercie aussi mon encadrant au CERN, Vincent Baglin. Malgré toi aussi tes nombreuses responsabilités dans divers aspects du CERN, tu prends toujours le temps de discuter en face à face, que ce soit avec moi ou avec toute autre personne qui travaille avec toi. Tu fais toujours preuve d'un enthousiasme débordant en parlant de science, et tu es une source inépuisable de connaissances sur des sujets allant de la physique des accélérateurs à la science des surfaces. Une seule de ces discussions suffit en général à faire germer des idées pour plusieurs mois (et encore...) de manips. Un grand merci également à Mathieu Bertin. Tu m'as appris la plupart des techniques expérimentales dont j'ai eu à me servir pendant ma thèse, tu m'as initié à l'utilisation de SPICES et au traitement des données qu'elle génère. Plus généralement, tu as toujours des réponses à mes questions - ou au moins des éléments de réponse, nous menant à disserter longuement sur la nature exacte des excitons dans les solides moléculaires. De plus, tu fais souvent preuve d'une énergie et d'une bonne humeur débordantes, portant par exemple à bout de bras une bonne partie des runs synchrotrons. Je remercie enfin Géraldine Féraud. Nous sommes arrivés presque en même temps au laboratoire, toi en tant que maîtresse de conférences et moi en tant que stagiaire puis doctorant. Nous avons découvert ensemble la manip et les thématiques de l'équipe, et nous avons passé pas mal de temps à discuter de tout ça. Tu m'as beaucoup accompagné en salle de manip la première année, et tu m'as transmis ta ténacité, me poussant à avancer quand les expériences patinent. Ton souci du détail m'a été d'une grande aide. Nous avons aussi vite noué une amitié assez forte pour laquelle je te suis très reconnaissant. Merci pour toutes nos longues discussions tant scientifiques que personnelles.

Je souhaite remercier les membres du jury de cette thèse, pour l'attention et la reconnaissance qu'ils et elles ont portée à mes travaux. Tout d'abord Christian Bordas et Martin McCoustra, qui ont accepté de rapporter ce manuscrit, dont ils ne savaient pas (pas plus que moi à vrai dire) qu'il s'avèrerait aussi long et dense. Je remercie aussi Nathalie Carrasco et Anne Lafosse, examinatrices, et enfin Marc Simon pour avoir présidé ce jury.

J'aimerais remercier les autres personnes sans lesquelles ce travail de recherche n'aurait pas été possible. L'expérimental, c'est finalement beaucoup régler des problèmes techniques (qui ont souvent avoir avec des lasers capricieux, entre autres), et cela n'aurait pas été possible sans l'aide précieuse de Pascal Jeseck, Patrick Marie-Jeanne et Christian Rouillé: merci à vous! Je remercie aussi Nora Roger, qui nous aura sorti de pas mal de galères administratives du début à la fin de ma thèse. Je remercie également toutes les personnes qui ont pu participer aux expériences au synchrotron. En particulier un grand merci à Claire Romanzin qui nous as toujours beaucoup aidés, et merci aussi pour ta sympathie! Merci également à Roberto Cimino, avec qui les discussions scientifiques sont toujours intéressantes. J'en profite aussi pour remercier les équipes des lignes DESIRS et SEXTANTS du synchrotron, qui nous ont aidés à prendre en main la ligne et souvent dépannés. Merci à Yao Té et Marie-Anne Hervé du Penhoat pour avoir fait partie de mon comité de suivi de thèse. Je n'oublie pas non plus les stagiaires avec qui j'ai pu travailler, notamment Maud Hassenfratz, Pauline Muguet, Antoine Roll et Japhar Michoud. Bonne chance à Romain Basalgète qui prend la suite des choses sur SPICES.

Un chaleureux remerciement à celles et ceux que j'ai cotôyés quotidiennement au LERMA pendant ces trois ans. Tout d'abord à Thomas Putaud, avec qui j'ai partagé mon bureau et la galère de doctorant. C'était pas facile tous les jours, mais on s'est bien amusés quand même! Merci aussi à Xavier Michaut, pour sa bonhomie et son énergie, son humour perpétuel - bien que pas toujours de très bon goût hein! - qui animent les couloirs du LERMA (le plus souvent vers 17h). Merci à Laurent Philippe pour sa jovialité - et merci pour les bières avec Mathieu où nous avons discuté si longuement! Merci à Corinne, Yao, Pascal, Christof, Thomas, Hadj, Nora, Patrick, Christian, pour les pauses café toujours animées. Un merci général à tous ceux qui font que notre coin du LERMA Jussieu soit si accueillant et donne envie d'y rester. Je remercie aussi Françoise Pauzat, Yves Ellinger et Alexis Markovits du LCT, que j'ai personnellement plus fréquenté devant une bière qu'en collaboration au labo et qui sont toujours d'agréable compagnie.

Merci aussi aux gens que j'ai pu cotôyer pendant mes séjours au CERN. En particulier un grand merci à Bernard Henrist. Tu m'as beaucoup aidé sur la prise en main de la manip, et tu es toujours d'une bonne humeur et d'une sympathie que j'ai beaucoup appréciées! Merci aussi à Michal Haubner, qui m'a montré les rouages de la manip du CERN et accompagné pendant mon premier séjour. Merci à Patricia, Viktor, Rafael, Victoria, Elena, Anne-Marie, Antoine et tous les autres que j'ai pu croiser.

Je remercie aussi les collègues que j'ai pu croiser en enseignement et qui m'ont guidé et aidé: Christophe Balland, François Mallet, Laurent Coolen, Michel Fioc.

Merci à toute ma famille, mon père, mon frère, ma soeur, et plus particulièrement à ma mère pour tout le soutien qu'elle m'a apporté. Merci à feu papy Jean-Claude, dont j'aurais bien aimé qu'il soit là pour voir la fin de cette thèse, lui qui disait souvent avoir décelé mon appétit de savoir et ma curiosité dès mon plus jeune âge. Merci aux amis. Merci à tous les gens sympathiques que j'ai pu croiser sur les internets.

Ces trois années n'ont pas toujours été faciles, surtout la dernière - pas forcément seulement pour les raisons habituelles - mais elles ont aussi été remplies de sources de joie et resteront inoubliables - une fois de plus, pas forcément que pour les raisons auxquelles je me serais attendu! Le plus difficile n'est cependant certainement pas encore passé, aussi je remercie par avance celles et ceux qui continueront à me donner des raisons d'être moins pessimiste au quotidien.

Contents

List of Figures

List of Tables

List of abbreviations

PID - Photon-Induced Desorption
EID - Electron-Induced Desorption
DIET - Desorption Induced by Electronic Transitions
CR - Cosmic Rays (see I.1.1.4)
DEA - Dissociative Electron Attachment (see II.2.4.4)
FT-RAIRS - Fourier-Transform Reflection-Absorption InfraRed Spectroscopy (see III.1.5)
IP - Ionization Potential (see II.2.2)
ISM - InterStellar Medium (see I.1.1.1)
ISRF - InterStellar Radiation Field (see I.1.1.4)
LHC - Large Hadron Collider (see I.2.2.1)
MGR - Menzel-Gomer-Redhead (model) (see II.3.1)
PDR - Photon-Dominated Region or PhotoDissociation Region (see I.1.1.4)
QMS - Quadrupole Mass Spectrometry/Spectrometer (see III.1.2)
REMPI - Resonance-Enhanced MultiPhoton Ionization (see III.5.2)
RGA - Residual Gas Analysis (see III.1.2)
RGS - Rare-Gas Solid (see II.4)
SDFG - Sum-Difference Frequency Generation (see III.5.1)
SEE - Secondary Electron Emission (see I.2.2.2)
SEM - Secondary Electron Multiplier (see III.1.2)
SEY - Secondary Electron Yield (see I.2.2.2)
TEY - Total Electron Yield (see III.1.6) THG - Triple Harmonic Generation (see III.5.1)
TPD - Temperature-Programmed Desorption (see III.1.4)
UHV - Ultra-High Vacuum (see III.1.1)
VUV - Vacuum UltraViolet (see II.2.3)
XESD - X-ray induced Electron Stimulated Desorption (see VI)

Introduction

> [...] conduit à rejeter à la fois et la vision réaliste naïve selon laquelle le discours scientifique est un reflet direct de la réalité, un pur enregistrement, et la vision constructiviste relativiste, selon laquelle le discours scientifique est le produit d'une construction, orientée par des intérêts et des structures cognitives, qui produirait des visions multiples, sous-déterminées par le monde, de ce monde. La science est une *construction qui fait émerger une découverte* irréductible à la construction et aux conditions sociales qui l'ont rendue possible.
>
> Pierre Bourdieu, *Science de la science et réflexivité*

The fate of electronic excitations in molecules adsorbed on surfaces is a long-standing question that has far-reaching consequences in a variety of fields, from surface chemistry to radiation-induced damage. One of the most basic possible outcomes of energy deposition by energetic radiation (photons, electrons, ions) in adsorbed molecules is the detachment (desorption) of these molecules. Photon and Electron Induced Desorption (PID and EID) are part of this class of phenomena. PID and EID have been studied under very different angles, from fundamental aspects to applications to specific fields, throughout the years. Two of these fields have guided the present work: astrochemistry of icy surfaces, and vacuum dynamics in cryogenic accelerator chambers. These reflect the objectives of the two host institutions of this PhD, which are an astrophysics lab (LERMA) and a vacuum studies group (the vacuum department at CERN).

What do photons, electrons, molecules and surfaces have to do with astrophysics or accelerators? Molecules exist in the not-so-empty space between stars, the interstellar medium, which is made of giant clouds of gas and microscopic dust. This dust provides the surface onto which molecules can stick when the temperature is low enough to allow it - such as in the cold and dense regions where stars and planets are born. Condensed molecules also cover the surface of many bodies of our solar system, from comets to shadowed regions of the Moon. In all of these regions, energetic photons and/or electrons, among other sources of energy, can find their way to the molecule-covered surfaces and play a role in the exchanges happening between the surface and the gas phase. Very similar small molecules constitute the residual gas of vacuum chambers such as those that host the particle beams of accelerators. The walls of these chambers are also covered with these same molecules, all the more when these walls are at cryogenic temperatures like those of the LHC. The beam of energetic particles circulating in accelerators generate

through phenomena like synchrotron radiation photons and electrons that hit the chamber walls and induce desorption, to the detriment of the vacuum that is crucial in keeping the beam stable. It will be the purpose of chapter I to present in much more details the two contexts that have been outlined here.

In addition to astrophysics and vacuum science, PID and EID spark interest across many fields. The first studies of EID originated in the field of vacuum science mainly, but what can be considered as the real start of an independent field of EID and PID studies around 1964 came from a vacuum scientist but also two other scientists with an interest in the fundamentals of surface chemistry. Indeed, (photo)desorption could be said to constitute one of the most basic (photo)chemical reactions on a surface, converting a surface species into a gas phase species. EID and PID were also studied for their consequences in radiation-induced damage, for example. Interest for astrochemistry came comparably later.

Since this work remains, in the end, a work of fundamental research, an emphasis is put on understanding better the fundamental mechanisms of EID and PID, which could be said to constitute the third context of this thesis. It will naturally lead towards investigations that have no real relevance to either astrophysics or vacuum but are interesting by themselves and may have consequences in other contexts. Desorption of molecules is one of the possible outcomes of an electronic excitation at the surface, along with chemistry or energy relaxation for example. PID and EID are therefore linked with how excited states evolve in the systems we study, and constitute in a way a probe of this fundamental process. Chapter II will be devoted to presenting the systems that we study, molecular ices, i.e. solids composed of condensed small molecules (like H_2O, but also CO, CH_4...) bound by weak Van der Waals forces or hydrogen bonds, and their interaction with photons and electrons. I will also review in this chapter what is already known on the mechanisms of EID and PID.

During the course of this PhD, two new systems have been used. The SPICES II (Surface Processes and ICES) chamber at LERMA, an upgrade of a previous set-up, was assembled in 2016 during my master's internship and used for synchrotron experiments to study photon-induced desorption, both in the VUV and the soft X-ray range. I have also carried the development of a new set-up in the laboratory around SPICES II, with the objective of coupling laser desorption and laser spectroscopy of the desorbed molecules. The Multisystem set-up was assembled at CERN in 2017, and I participated in its commissioning and did the first measurements, on electron-induced desorption, that were performed on it. These two set-ups and the experimental techniques that have been used are presented in chapter III.

The last three chapters are devoted to the results obtained. I have chosen to divide them according to the "energy source" used to induce desorption: chapter IV presents results on VUV photon-induced desorption, chapter V results on electron-induced desorption, and chapter VI on soft X-ray photon-induced desorption. The objective of this manuscript is to give some (obviously partial) answers to the following questions: for the VUV, soft X-ray and electron irradiation of the molecular ices we study,

- What are the molecules that desorb? Although we will often focus on the "parent" molecule(s), the one(s) that initially constitute the molecular ice, in their neutral form, we will also look at whether fragments, products of chemistry, cations or

anions may desorb as well, and what this tells us about what is happening in the ice.

- How many molecules desorb? It is crucial for the astrochemical and vacuum context of this work that our data is *quantified*. This means not only making an absolute calibration of the measurements that we do, but also contributing to the bridge between laboratory data and their use by astrophysicists or vacuum engineers, by assessing the limits of our results, trying to identify what is important and what is not, and how the data we obtain can be translated into data that can actually be used.

- How do molecules desorb? As stated previously, we want to find what is the mechanism, at the microscopic scale, that explains how the initial electronic excitation evolves and leads to the desorption of molecules.

The results on VUV-photon induced desorption in chapter IV are a continuation of the work that has been developed in the team at LERMA since 2010. Spectrally-resolved measurements of the desorption of neutral molecules and fragments are done using synchrotron radiation, in the 5-15 eV range where the valence electronic states are excited. Results on several "pure ice" systems (CO, NO, CH_4, H_2O, NH_3 and HCOOH) will be presented first. The results for NO include the first tests of the new lab set-up for laser desorption and spectroscopy. Then the phenomenon of indirect desorption is investigated for model "layered" ices, where one type of molecule is adsorbed in small quantities on a thick ice of another molecule.

In chapter V, first results on electron-induced desorption of neutrals from molecular ices are presented. The range of electron energy investigated (150-2000 eV) is intermediate between two regimes of energy deposition. The EID yield for a number of systems (CO, N_2, Ar, CO_2 and H_2O/D_2O) are measured quantitatively, and the idea that EID can serve as a probe of the transport of energy or particles to the surface will be developed. One objective will be to investigate whether EID can be relevant to astrophysics, where it is not a currently considered process.

The last chapter presents results obtained on photon-induced desorption in the soft X-ray range, when the molecules are core-excited. This domain was new for the team, and we explored neutral but also cation and anion desorption from H_2O ices and CO ices. Synchrotron radiation is again used to obtain spectrally-resolved photodesorption yields. A rich physics is found in the desorption of ions. Here again the question of whether soft X-ray desorption is of importance for astrophysics can be investigated for the first time using our quantified data.

Four papers have been published or will soon be published that are part of this work and where I am first author, and they are therefore reproduced at the end of this manuscript. I will refer to them in the sections where they are relevant.

Chapter I

Context(s)

> Great A'Tuin the star turtle, shell frosted with frozen methane, pitted with meteor craters, and scoured with asteroidal dust.
>
> Terry Pratchett, *The Light Fantastic*

Photon and Electron Induced Desorption (PID and EID) are a class of phenomenon in surface science that have been studied under very different angles for applications to a variety of fields throughout the years. Two of these fields have guided the present work: astrochemistry of icy surfaces, and vacuum dynamics in cryogenic accelerator chambers. The goal of this chapter is to present how the study of the fundamental process of molecules being ejected from surfaces following excitation by photons or electrons is important to these two fields, and how the experimental results are effectively used.

I.1 Astrophysical context

Astrochemistry is the study of molecules in astronomical environments, and of their influence on these environments. It encompasses astronomical observations of molecules in different regions of space in order to understand molecular complexity, the conditions that lead to the formation of molecules, what molecules tell us about the regions they are found in, etc... but also other activities. It also includes astrochemical modelling, which takes a different approach to these problems by trying to simulate the behaviour of the different regions of space, based on a chemical network and a physical model of the region. The third branch of astrochemistry is part of what is called laboratory astrophysics: the experiments and theoretical calculations that bring the knowledge required to understand the observations and give inputs for the models. These three branches complement each others and none can exist without the help of the others. The field of astrochemistry, whether it concerns observations, modelling or laboratory experiments, has been extensively reviewed in recent years, so that it is not difficult to find introductions [1, 2, 3, 4] or more detailed reviews [5, 6, 7, 8, 9, 10, 11, 12, 13] on many different aspects. Most of this part has been written drawing from this material, although I will source in the text some specific affirmations or examples.

I.1.1 Molecules in the universe

Molecules are found on planets, moons, comets and asteroids in planetary systems such as our own, but also in the interstellar medium, which occupies the space between stars and makes up 10% of the matter in a galaxy like ours [4]. In the interstellar medium, molecules are found more particularly in star- and planet-forming regions. The study of molecules in space is interesting from many angles. From an "astrophysical" point of view, the emission and absorption lines of molecules in the spectrum of a given astronomical object is one of the very few information regarding that object that can be obtained from Earth. Molecules are used as tracers of some basic properties like temperature or density, but also more complex ones. But they are not just passive markers of what is happening in a given medium: they also actively participate in the physics of these regions. For example, molecules cool down dense regions by radiatively sending away energy coming from collisional excitations. From a "chemical" point of view, the study of molecules is also extremely interesting because the conditions of density and temperature and the time scales on which reactions occur are extremely different from those on Earth, giving a radically different perspective on chemistry. Explaining how the molecules that are observed can be formed and how far can molecular complexity go in different regions of space is one of the main challenges of astrochemistry. One of the important motivations is

Table I.1: Solar elemental abundances (reproduced from ref. [2])

Element	Abundance	Element	Abundance
H	1	Si	3.2×10^{-5}
He	0.085	Fe	3.2×10^{-5}
O	4.9×10^{-4}	S	1.3×10^{-5}
C	2.7×10^{-4}	Al	2.8×10^{-6}
N	6.8×10^{-5}	Na	1.7×10^{-6}
Mg	4×10^{-5}	P	2.6×10^{-7}

also to figure out how the molecules observed in space traverse the cycle of matter, going from an interstellar cloud to a planet forming disk to comets and planets. What was the inventory of available molecules at the dawn of prebiotic chemistry, and in what way were they delivered to planets like our own, ties the study of molecules in the universe to astrobiology and the question of the origin of life.

Emphasis will be put here on the interstellar medium, in particular regions where the tiny dust grains that are part of the medium are covered with an icy mantle of mainly small condensed molecules. Non-thermal desorption plays a crucial role in the exchanges between these grains and the gas phase. Condensed small molecules also play a role in other regions of space, such as the variety of icy objects of the solar system (comets, moons, dwarf planets and others), and therefore the planetary science aspect of photon and electron irradiation of molecular ices must not be neglected.

I.1.1.1 The interstellar medium

The atomic constitution of the interstellar medium (ISM) is, by mass, 70 % hydrogen, 28 % helium and 2 % other heavier atoms. 99 % of matter is made of gas, and 1 % of dust grains, which will be evoked again later. By number, the constitution becomes 91 % hydrogen, 8.9 % helium and 0.1 % heavier atoms. In table I.1 the (solar) abundances relative to hydrogen of a few relevant atoms is reproduced from ref. [2]. The number density of grains relative to hydrogen depends on the region but in those that are of interest for us, a typical value is 10^{-12}.

By the end of 2018, 204 molecules had been detected in the interstellar medium [14], containing up to 13 atoms (excluding the fullerenes C_{60}, C_{60}^+ and C_{70}). Links to an updated database and a discussion of these detections can be found in the previous reference. These detections are made across the electromagnetic spectrum, either in absorption or emission, from UV-visible (electronic transitions) and near/mid-infrared (vibrational transitions) to radio (mostly rotational transitions), which itself covers a large range going from far-infrared to centimeter wavelengths. Radio-astronomy has been by far the biggest contributor in number of detected molecules, for reasons that will become clear later. These molecules are not evenly distributed in the ISM: in fact, most of the interstellar medium does not contain molecules.

The interstellar medium is composed of regions of very different physical conditions, with most of it being either very hot (10^6 K) and tenuous ($< 10^{-2}$ particles.cm^{-3}) ionized gas, or warmer ($\sim$ 10 000 K) and slightly denser (10^{-1} particles.cm^{-3}) gas that can be

either ionized or neutral. In these regions the conditions of temperature and radiation make it impossible for molecules to be stable. What interests us here is the fraction of the ISM that is denser (> 10 particles.cm^{-3}) and colder (< 300 K), enough that molecules can start forming, the so-called interstellar clouds. This is a small fraction in volume ($< 5\%$) but a significant one in mass (30-60%) of the ISM.

According to the classification of Snow & McCall [15], four types of interstellar clouds can be distinguished: diffuse atomic, diffuse molecular, translucent, or dense, that are placed on a continuum of increasing density (10^1 to $> 10^4$ particles.cm^{-3}), decreasing visual extinction ($A_v = 0$ to 10)[a] and decreasing temperature (100 to 10 K). This classification relies also on a chemical distinction: the transition from diffuse atomic to diffuse molecular is the transition from dominantly atomic H to molecular H_2, the transition from diffuse molecular to translucent is the transition from dominantly C^+ to C, and the transition from translucent to dense is the transition from C to CO.[b]

Diffuse clouds are limited to a relatively simple chemistry because harsh radiations and low densities do not favor the formation of molecules for a long time, but molecules are still detected in these regions (CH, OH, CO, C_3, ArH^+...). In fact, diffuse clouds are among the best understood and constrained regions because the chemistry is simple, and because it is transparent to radiation and UV or IR emission diagnoses give directly access to e.g. the H_2 density, which is a crucial parameter. Grains play an important role in these regions, even when they are too hot for molecules to reside for a significantly long time: they act as catalysts for the formation of H_2 [16]. When dust temperatures are low enough (< 100 K) in these regions, some molecules like water can start forming on grains, so that non-thermal desorption is not irrelevant there. In fact, the irradiation conditions are such that grains are kept bare by photodesorption [17].

In dense regions, observations are less varied: UV spectroscopy is not possible except at the edges, because of too strong dust scattering and molecule absorption. IR spectroscopy in absorption can be done, but only if a background emitter exists behind the cloud or by targeting embedded stellar objects. The main diagnosis for gas phase molecules remains radio-astronomy, with the emission of molecules rotationally excited by collisions or radiation. This has important consequences for what is detected: molecules that lack a dipole moment are invisible for radio-astronomy, while there is a bias towards some types of molecules that have a particularly large one. Important homonuclear diatomic molecules like N_2 or O_2, and even more importantly the main component of the cloud H_2, entirely elude direct detection. The low density and temperature make the gas phase chemistry in these regions driven by kinetics rather than thermodynamic equilibrium, and only barrierless two-body reactions can take place, most notably ion-neutral reactions. The resultant chemistry is particularly exotic, with the observation of very reactive radicals that would be hard to isolate on earth and species that hurt the common sense of someone who only knows undergrad chemistry like myself (e.g. the important H_3^+ molecule).

[a] The visual extinction is the degree of attenuation of light in the visible range by a medium. The A_v number is a log scale: for $A_v = 0$ there is no attenuation and $A_v = 5$ corresponds to a factor of 100 attenuation.

[b] Another more "practical" distinction made by astronomers from an observational point of view is that a line of sight (the solid angle being probed by the telescope) where ices are visible in the infrared is dense, while one where ices are absent is diffuse.

These dense clouds, sometimes also called molecular clouds or dark clouds, are also the hosts of smaller-scale objects that are related to the star and planetary formation processes. This is usually presented in the form of a "cycle of matter" in the ISM. The story goes so: in molecular clouds (whose typical lifetime is of the order of a few My), some denser clumps can appear. These clumps will tend to grow denser and denser by gravitational attraction, forming so-called dense cores or pre-stellar cores, with very high extinctions and very low temperatures (down to 7-8 K). Eventually the gravitational collapse will form a protostellar object at the center and the temperature will start increasing, warming up the surrounding matter which is called a protostellar envelope. Where and when the temperature reaches the point where ice mantles sublimate, we reach a "hot core" (for massive star formation) or "hot corino" (for low mass star formation) phase which is very rich of a new gas phase chemistry, enriched by the ice mantle material and the possibility of neutral-neutral reactions. Matter is ejected from the protostar in the form of jets, creating shocks in the protostellar envelope. For low mass solar type stars, eventually the envelope dissipates, leaving a circumstellar disk, also called protoplanetary disk, surrounding the young star. The process from the start of the collapse into a dense core to the protoplanetary disk surrounding the star takes a total of about a million year. In the protoplanetary disk, future planets will form, along with the other objects we typically find in our solar system (asteroids, comets, moons...), over a time scale of about 10 My. The cycle closes with the end of the life of the star (billions of years later for a solar type star), which expands and leaves a diffuse cloud, redistributing matter once again. Massive stars have much shorter lives and a more complex evolution, and their end leads to much more violent events like supernovae, where elements heavier than Fe are formed.

I.1.1.2 Dust and ice mantles

Dust grains in the ISM lock up a large part of the heavy elements available. They are mostly either silicate grains or carbonated grains, with varied forms of silicates (porous or crystalline, pyroxene and olivine...) and carbon (amorphous, diamondoid, aromatic or aliphatic...). Grains form mostly at the end of the life of a star, in the stellar winds created by the expansion and explosion, which create conditions where stellar material can be accreted in the form of a solid [18]. The carbon abundance in the star will regulate the composition of dust: if the C/O ratio is > 1 mostly carbonaceous grains will be created, while in C/O < 1 conditions carbon is locked up in the formation of CO and silicate grains form. In addition to Si or C, looking at table I.1 these grains should also contain significant amounts of metallic atoms Mg and Fe, along with other refractory material in trace amounts (Al, Na, etc). Only part of these atoms are observed in the gas phase, and the rest is therefore presumed to be locked up in the grains. Models of dust include this material e.g. as nano-inclusions in silicate grains [19]. Grains then evolve with time depending on the conditions they are exposed to: irradiation by UV photons and cosmic rays, or shocks, influence their nature and composition. Models of layered grains are often considered, with for example a core made of amorphous carbon or silicate and a "mantle" of aromatic-rich carbon [19].

The composition of dust can be observed by infrared absorption bands characteristic of either silicates or different types of carbon. Also characteristic of dust is a continuous extinction curve going from the deep UV to the near IR, with a few famous features like

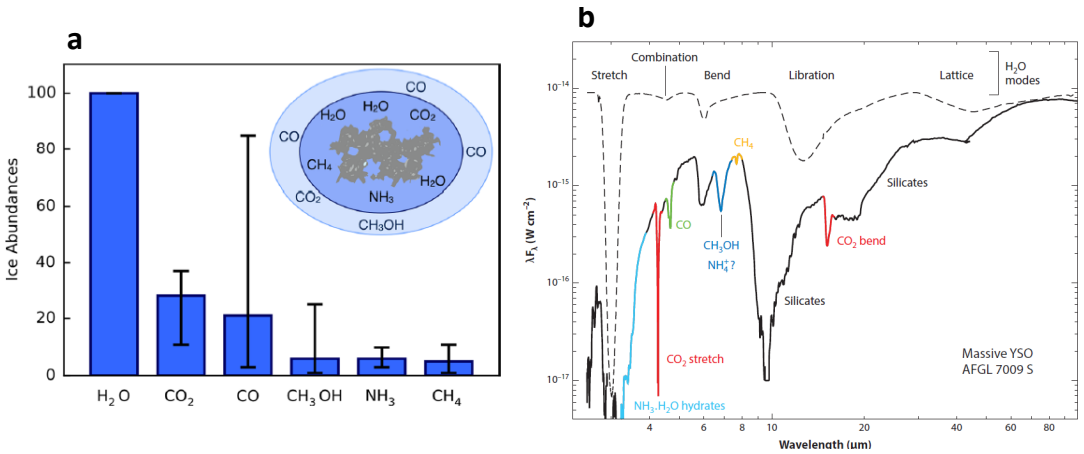

Figure I.1: Molecules detected in the ice mantles of interstellar grains. **a.** Summary of the main observed species composing ice mantles, and their abundances relative to H_2O. The bars represent the variability depending on the sources. A schematics of the two-phase model of grains is shown as well. Taken from Öberg [6]. **b.** Example of an infrared spectrum with ice and dust features, observed towards a massive young stellar object. Taken from Dartois et al. [22] and adapted from Boogert [8].

the 217 nm bump and the diffuse interstellar bands (DIBs) in the visible/near-IR. The counterpart is an emission curve in the mid/far-IR. Models of dust attempt to reproduce correctly the features of these extinction and emission curves, constraining parameters such as the size distribution, shape and composition of the grains. In the ISM grains have sizes varying from about 1 nm to 1 μm, with a peak around 100 nm. The smaller grains are therefore basically macromolecules, with probably big PAHs (polycyclic aromatic hydrocarbons) and fullerenes (C_{60}, C_{70}). Grains are also not particularly spherical: instead evidence from polarization of light by dust grains suggest more asymmetric shapes. In protoplanetary disks, dust grains can start to accrete and grow up to mm sizes. After reaching this size, further growth is difficult and requires other and not yet completely understood mechanisms to explain the formation of planetesimals [20]. See the introduction chapters of [21] for more details on grains.

In the cold regions that are of interest for us, dust grains are covered by an icy mantle of molecules that can go up to a few hundred monolayers in thickness. These molecules either accrete from the gas phase or are formed directly on the grain through surface processes, and stay there when the grain temperature is lower than their sublimation temperature. Only infrared spectroscopy in absorption allows to probe ices, as condensed molecules do not have rotational transitions. As mentioned before, observations are made using either background stars behind the cloud or embedded stellar objects as infrared sources against which absorption features of condensed molecules can be seen. The observations that have been made of icy mantles are reviewed in Boogert [8].

The main species that have been detected in ice mantles are summarized in the graph of fig. I.1a, while an example of dust and ice features in the infrared spectrum of a massive young stellar object is shown in fig. I.1b. Ice mantles are composed mainly of water, with also large amounts of CO_2 and CO. Depending on the line of sights CH_3OH

can be a very abundant molecule or be completely absent. NH_3 and CH_4 are observed at the few percent range. A number of other molecules have been detected in some line of sights, but whether this is representative of a global composition of ice mantles is not clear yet. According to the classification of Boogert [8], H_2CO, OCN^- and OCS are "likely detected" while some other molecules likes HCOOH, SO_2, NH_4^+ or CH_3CHO are "possibly detected". In addition, upper limits for a large number of molecules (including very large upper limits on the abundance of hardly detectable species like N_2 and O_2) have been obtained. Solid phase infrared bands are broad and the sources weak, so that it is difficult to obtain an inventory of molecules as varied and complex as is obtained in the gas phase, although there is undoubtedly numerous other molecules residing in ice mantles, as a result of solid phase (photo)chemistry of the main components mentioned.

The details of the absorption bands also give more information on the exact molecular environment of the molecules. The bands of CO and CO_2 in particular have been used to deduce the existence of different components in the ice. The most common distinction that is made is between polar and apolar ices, with the polar environment being mostly a water matrix and the apolar one a CO environment. This led to a picture of ice mantles as being roughly separated into two phases, linked with the way the mantles build up. At an early stage for the cloud, when grains are still bare and atoms are still available in the gas phase, the accretion of atoms on grains will lead to the formation of molecules like H_2O, CH_4 and NH_3 by hydrogenation, and CO_2. At a later stage when temperature drops so that the abundant gas phase CO freezes out onto the grains, the CO-rich second layer forms, with CO_2 also being present. Hydrogenation of CO leads to CH_3OH, with H_2CO as an intermediate. This picture is coherent with the molecular environment suggested by the shapes of the absorption bands, but also with observations made as a function of extinction (for example CH_3OH appears when extinctions are very high, corresponding to the massive CO freeze-out).

How much is the composition of the ice mantles conserved through the processes of star and planet formation is an important question that is difficult to answer. It seems that an important part of the water is conserved as is from the pre-stellar core to the protoplanetary disk [23], while some portion has been sublimated in the protostellar phase and recondensed afterwards. Objects of the outer stellar system may then inherit this ice.

I.1.1.3 Solar system ices

Many objects in the solar system host molecular ices while being "airless" bodies (with no atmosphere or a very tenuous one), i.e. conditions that are close to the ones we study in the laboratory and in the context of interstellar grains. In the inner solar system (before the asteroid belt), temperatures are usually high, but in some permanently shadowed regions, water ice can exist. Its presence has notably been shown in craters of the Moon [12]. In the outer solar system, there are many more objects of interests: the icy moons of the giant planets, the trans-neptunian objects, and comets.

The well-studied icy moons of Jupiter are Callisto, Europa and Ganymede. Their surfaces are covered with water ice. The surface temperatures are too high to condense more volatile species like CO, N_2 or CH_4 but other molecules such as SO_2 and CO_2 have been detected [12]. Around Saturn, Enceladus is the icy moon that has generated the most interest, and aside from the vast parts of the surface that are covered with nearly

pure water ice, organics and CO_2 have been detected in some places. The other moons, except Titan, are also airless icy bodies for the most part. More details can be found in Bennett et al. [12].

With the Neptunian satellite system, which is mostly its biggest moon Triton, we reach a point where more volatile molecules can be found in icy forms. Thus the surface of Triton is composed of N_2, CH_4, H_2O, CO_2, CO and C_2H_6, with N_2 being a very dominant species. The very volatile N_2, CO and CH_4 are also detected on Pluto. On Charon, only water has been found, although evidence suggests the presence of processed organics at the poles originating from CH_4 photolysis [24].

Comets are the most interesting objects to compare to interstellar grains in terms of ice composition, because they are often believed to have conserved a "primitive" composition, representative of what was found in the circumstellar disk of the our Sun prior to planet formation. Indeed, the composition of cometary ices are well studied and the detailed review of Mumma et al. [13] shows that it is quite similar to the kind of composition found for interstellar ices, with some specific differences [8].

I.1.1.4 Sources of irradiations

Different sources of irradiation prevail in different regions of the ISM, which we will review here. Diffuse clouds, for example, are permeated by the so-called InterStellar Radiation Field (ISRF). The ISRF is a "background" electromagnetic field resultant from the radiation of an average distribution of stars (at least in the IR to UV spectral range: dust emission dominates far IR contributions and the cosmological background radiation even further in the mm range) at a given point that is not too close from any particular star. The star part has two components, one due to low mass stars and peaking around 1 μm, and another more interesting for us due to massive stars peaking around 150 nm (8 eV), both corresponding roughly to black body radiation at different temperatures. The spectrum cuts off at 13.6 eV, the ionization threshold of H, above which radiation is absorbed. A typical (calculated) ISRF spectrum, from Mathis et al. [27], is shown in fig. I.2 (in blue, the scale is not shown). The integrated UV photon flux from the ISRF (from say 5 to 13.6 eV) is of the order of 10^8 photons.s^{-1}.cm^{-2}. The ISRF intensity G_0 is often used as a unit to compare the UV radiation flux of different environments.

The interior of dense clouds is shielded from the ISRF, but the edges are not. The radiation will be progressively attenuated, giving a layered structure to the edge of the cloud. Although the ISRF is not an extremely strong radiation source, and its effects will quickly die out, there can also be stars near the cloud illuminating it with much higher flux. This is common since molecular clouds are precisely the birthplaces of stars. If the nearby star is a massive star, its UV radiation spectrum will be mostly black-body like and resemble that of the ISRF in terms of spectrum. If it is a lower mass star, the UV spectrum will rather be dominated by atomic lines, especially Ly-α (atomic hydrogen line at 121.6 nm/10.2 eV). The star can also be embedded in the cloud: the protostellar envelope of a young star is significantly irradiated. There is a class of regions called Photon-Dominated Regions or PhotoDissociation Regions (PDRs) to qualify, among others, the previously mentioned regions where the UV photon flux is high. They are called thus because their chemical and physical properties are highly controlled by the effects of the UV irradiation, and because they can be (more or less generically) modelled by so-called PDR codes. It

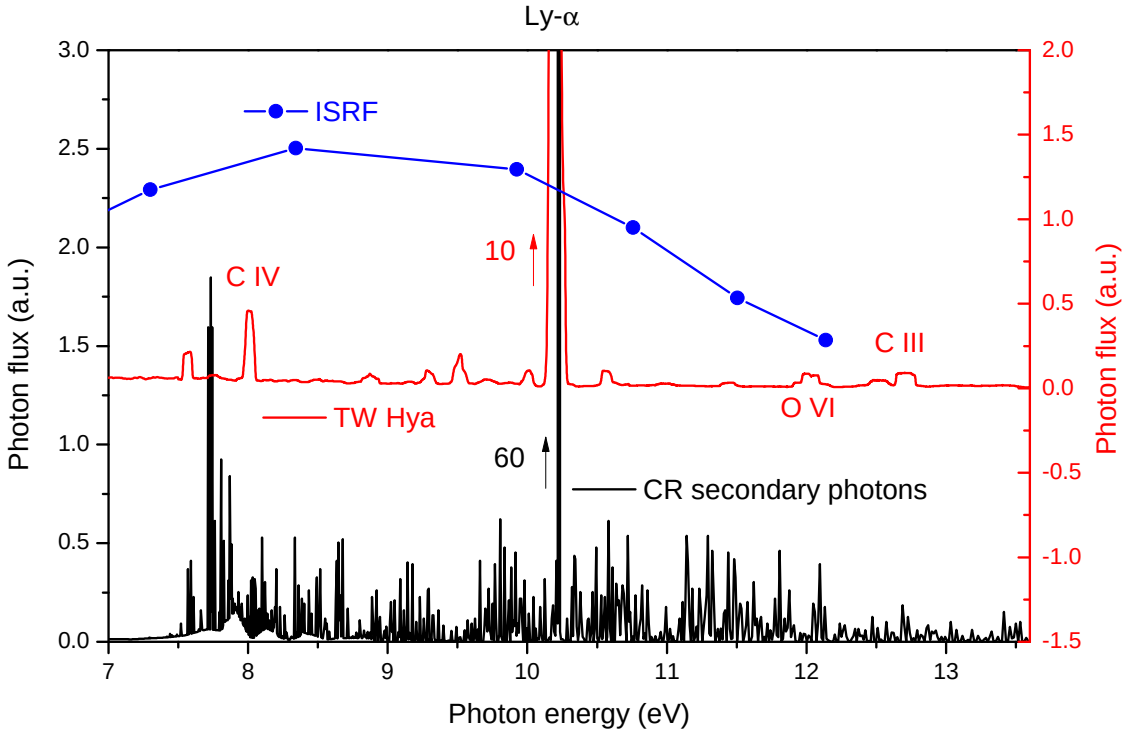

Figure I.2: Different UV spectra in the ISM. In black, left scale: a typical calculated spectrum of the secondary UV photons generated by cosmic rays in interaction with H_2, e.g. in dense clouds, from Gredel et al. [25]. The Ly-α line dominates and has been cut to show the rest of the spectrum. In red, right scale: UV spectrum of the young star TW Hya, reconstituted from observations, from Johns-Krull et al. [26]. Again the Ly-α line dominates and has been cut. Some other atomic lines are visible, and a few are indicated on the figure. In blue: a calculated ISRF spectrum from Mathis et al. [27]. The scale is not indicated, it is arbitrary but the zero is the same as for the black, left scale.

is a class of region transversal to the classification developed in section I.1.1.1 as it covers regions as different as diffuse clouds, the edge of dense clouds, protostellar envelopes or the surface layers of protoplanetary disks. An example of the propagation of a UV flux inside a PDR is shown in fig. I.3. The spectrum of the UV flux for different values of the extinction A_v (0 to 5) has been computed by F. Le Petit using the PDR Meudon code. The starting spectrum is an ISRF spectrum, although the absolute flux is higher ($\sim$ 80 G_0, i.e. 8 $\times 10^9$ photons.s^{-1}.cm^{-2}, typical of the Horsehead nebula PDR). As A_v increases, we see a strong and very structured absorption above 11.2 eV in the Lyman-Werner bands of H_2, and at the Ly-α (10.2 eV) by H. Outside these lines, the absorption is continuous and dominated by dust extinction. We see the 217 nm/5.7 eV extinction bump mentioned earlier. At $A_v = 5$ the total photon flux between 5 and 13.6 eV reaches down to 4 $\times 10^4$ photons.s^{-1}.cm^{-2}.

In the interior of dense clouds, where external photons are completely attenuated, the dominant source of external energy are cosmic rays. Cosmic rays are highly energetic charged particles (positive ions and electrons) that permeate our galaxy. H^+ and He^+

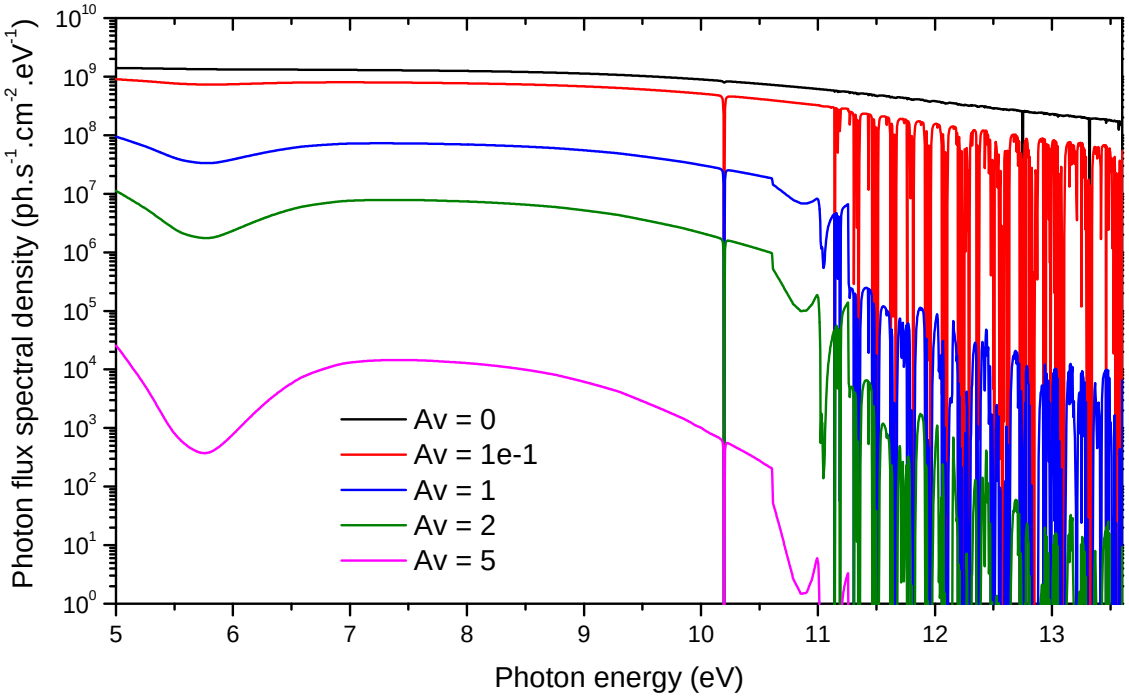

Figure I.3: Photon flux spectral density at different visual extinctions A_v in conditions typical of the Horsehead PDR, calculated by F. Le Petit using the Meudon PDR code. The spectrum evolves as UV irradiation penetrates inside the cloud and is absorbed and diffused by gas and dust.

constitute most of the cosmic rays (90 % and 8 % respectively), with the remaining 2 % being heavier atoms and electrons (electrons are less than 1 % of the cosmic rays). Their origin is not entirely clear: part of them are certainly accelerated in supernovae explosions. The very high energy part of cosmic rays (in our galaxy) has been recently shown to have an extragalactic origin , presumably being accelerated in events that are even more violent than a supernovae explosion. Cosmic rays have high enough energy that they interact little with matter (see chapter II) and can penetrate dense clouds with little attenuation. However, they do interact enough with matter to be an important energy source inside clouds. Cosmic rays excite and ionize gas phase molecules (mostly H_2), and this in turn creates secondary electrons and secondary UV photons that will subsequently have effects. There is therefore still a UV photon flux inside dense clouds. Calculations of this flux give a number of $\sim 10^3$-10^4 photons.s^{-1}.cm^{-2} [28, 29], four orders of magnitude lower than the ISRF. This means that these secondary UV photons dominate the UV flux in a dense cloud when the ISRF is attenuated by a factor of 10^4, which occurs around $A_v = 5$ (depending on the considered region). The secondary electrons created by cosmic rays are quickly thermalized by interaction with H_2 (more will be said on the topic at the end of chapter V). The spectrum of the generated secondary UV photons is very structured since they mostly come from de-excitation of H_2 or H: it consists of many spectral lines between 7 and 13.6 eV, with a strong Ly-α component. The spectrum calculated by Gredel et al. [25] is reproduced in fig. I.2 (in black).

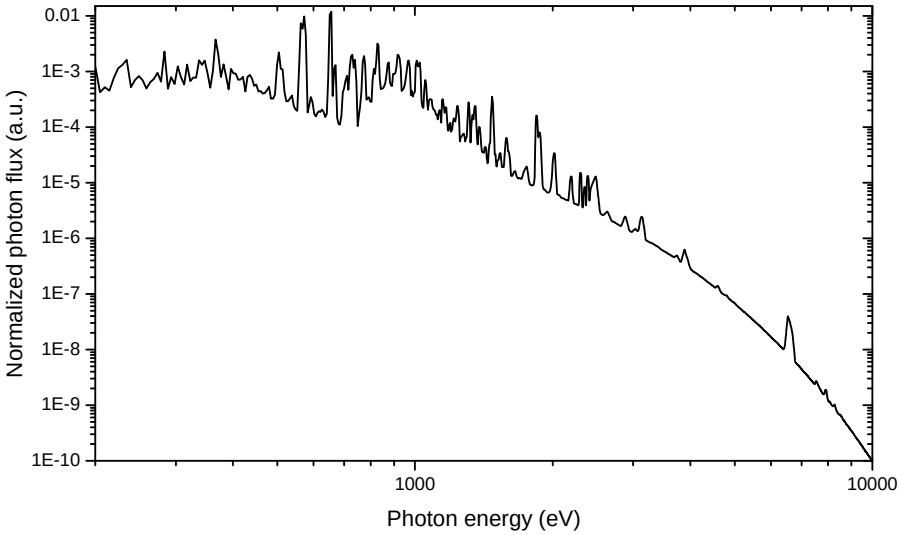

Figure I.4: X-ray spectrum of the young star TW Hya, reconstructed from observations. Taken from Nomura et al. [30].

In protoplanetary disks the sources of irradiation are complex. The disk is close to a young star, which abundantly produces UV and X-rays. The UV spectrum of the young star TW Hya, which hosts a protoplanetary disk that has been very well studied, is shown in fig. I.2 and was taken from [26]. It is dominated by atomic lines. The X-ray spectrum of TW Hya is displayed in fig. I.4, taken from ref. [30]. In the X-ray spectrum, there is a continuum that originates from a hot plasma (here with two components around 2 MK and 8 MK) emission, and atomic lines embedded in the continuum. Although this is not obvious on the log plot, the contribution of atomic lines is important.

The density of the disk is very high, and the irradiation from the star will not be able to penetrate all the way to the disk midplane. Instead in this midplane again cosmic rays should be the main source of energy, with similarly secondary UV photons (and electrons) playing an important role. There is therefore a layered structure which is schematized in fig. I.5. UV photons dominate in the outermost layer, but they are attenuated more quickly than X-rays that will play an important role in an intermediate layer, before being themselves attenuated. The exact structure will depend on various parameters such as the type of disk. Note that propagation through the gas density will change the UV and X-ray spectrum (for attenuation of the X-ray spectrum, see chapter VI). To further complicate the picture, it has been suggested that disks may be shielded from cosmic rays [31] by magnetic effects. If this is the case, then the low flux of X-ray photons that reach the midplane, but also the external UV (ISRF) and X-ray fields (from nearby young stars [32]), which are less attenuated than those from the stars since they come from a different angle and traverse less column density, could become the dominant sources of irradiation instead. Disks are therefore particularly complicated regions.

In the solar system, the solar wind and solar photons play an important role as sources of irradiation. A main-sequence star like our own has a much lower X-ray and deep UV flux than a young star like the ones discussed previously, and therefore the solar X-ray component can be mostly neglected. There is still a significant amount of UV photons,

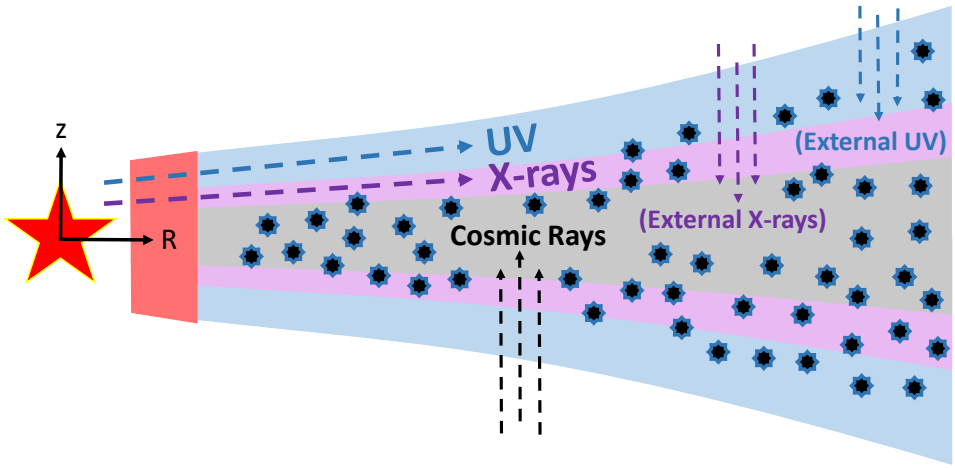

Figure I.5: Sketch of irradiation sources in a protoplanetary disk. To the left is the central star, the R coordinate is the horizontal distance from the star and the z coordinate the vertical distance above the midplane. The red region corresponds to the inner part of the disk that is hot (300 K or more) and dense ($>10^{10}$ particles.cm^{-3}). In the outer part ice mantles can form around grains. The surface layer of the disk (blue) is dominated by UV photons. More penetrating X-rays form an intermediate layer (violet) with the midplane (grey), which is dominated by cosmic rays. External UV and X-rays may also irradiate the disk from different angles.

but the spectrum is largely dominated by infrared and visible light. A much more detailed discussion of the solar photon fluxes can be found in ref. [12]. Surfaces that are exposed directly to sunlight are usually heated to temperatures where thermal desorption is much more important than non-thermal processes (e.g. UV photodesorption). However, these surfaces are not always exposed to sunlight, and other surfaces are never exposed at all. Energetic ions and electrons from the solar wind or from external cosmic rays, as well as UV photons from the interplanetary medium ($\sim 2 \times 10^8$ Ly-α photons.s^{-1}.cm^{-2} [12]), will become important here.

For the icy moons of giant planets with magnetospheres like Jupiter and Saturn, energetic particles are particularly important: the magnetosphere traps solar wind particles and also accelerates other particles originating from the atmospheres of the planets and moons themselves, and sends a shower of energetic particles on the moons. UV photons are not likely to play a role here. It should be noted that the energy of the particles of the solar wind are typically in the keV/amu range, much lower than cosmic rays.

In the outer solar system, for trans-neptunian objects, solar wind and photons are more and more attenuated and external galactic cosmic rays and UV photons can start playing a role. UV photons may irradiate surfaces hidden from the sun by a resonant scattering mechanism: Ly-α photons (from the sun or the interplanetary medium) are resonantly scattered by interplanetary H and illuminate objects like Pluto or Charon with a non-negligible flux (of the order of 10^7 photons.cm^{-2}.s^{-1}) [33].

I.1.2 Role of non-thermal desorption

PID and EID inscribe themselves in the general topic of grain surface processes, one aspect of which is the gas-grain exchanges, as the surface is the interface between these two phases. The question is, what processes regulate gas-grain exchanges, in particular the desorption side? The thermal desorption rate is exponential with temperature: we can basically say that there is a temperature above which thermal desorption will dominate, and below which it is entirely negligible. The intermediate range of temperature is small, although the fact that we are dealing with astronomical time scales (10^4 to 10^6 years) and densities means that it is different from what a surface scientist may be used to in a vacuum chamber.

Wherever the surface temperature is small enough to have more than one monolayer of molecules condensed, thermal desorption is no longer at play and gas-solid exchanges are dominated by non-thermal desorption processes. In the ISM, these non-thermal processes either prevent some molecules from entirely freezing out of the gas phase, or liberate in the gas phase molecules that are formed on grains but should have stayed there. On icy bodies with no atmosphere in the solar system, they may create an "exosphere", a tenuous gas phase density of molecule in equilibrium above the surface, dominated for the larger bodies by gravity rather than gas phase collisions. They can also erode the icy layers and deplete the molecular content if the desorbed molecules are faster than the escape velocity.

I.1.2.1 Different non-thermal desorption processes

There is a variety of non-thermal desorption processes that can been considered in astrophysical environments. A non-thermal desorption process requires bringing energy in some form to the ice to break the physisorption bonds. One source of energy are energetic particles: photons, electrons and ions (cosmic rays, CRs), that all have in common that they excite or ionize the ice, bringing electronic energy (although ions can also transfer momentum by knock-on collisions). This is the class of process that we are interested in in this manuscript, and that will be presented in more detail in the next chapter.

Among these, in the ISM, UV photodesorption is certainly the one that is the most taken into account. Early on, the process was thought to be inefficient [34], but it was realized later with new experimental results that it was in fact orders of magnitude more efficient than reported at first [17]. For the last two decades, UV photodesorption has become an important factor in models to explain a number of observations, as will be detailed in the next section. The ubiquity of UV photons in interstellar media is certainly an important factor of this success, along with the existence of laboratory data to constrain the process. In comparison, processes like electronic desorption by electrons or cosmic rays, despite their presence in all regions as well, are often less considered. Sputtering of molecular ices by energetic ions has been experimentally studied extensively early on (see e.g. [35] and references therein), but these studies were more geared towards a planetary science context, and CR desorption is not always taken into account in models. This could be because calculations suggested that secondary UV photons generated by cosmic rays deposit ten times more energy in ices than cosmic rays directly do [29]. But experimental studies continue still to be made, with an interstellar medium context in mind, for example with heavy ions [36, 37], and they tend to show that in fact, secondary UV photon

desorption and direct CR desorption have comparable effects. To my knowledge, electron-induced desorption is not really taken into account. I will expand on this at the end of chapter V.

X-ray photodesorption is a process that is not taken into account in models yet either. The relevance of X-ray photodesorption is limited to fewer regions: protoplanetary disks, as mentioned earlier, and molecular clouds exposed to the X-ray irradiation of a nearby young star or an object emitting strong X-rays. Relevant experimental data on the process did not exist yet, and providing these is the object of chapter VI.

One type of process that has been taken into account early on is transient heating by cosmic rays or X-rays, which is not to be confused with the desorption by electronic transitions that I just talked about. This is a process where a grain is traversed by a cosmic ray or absorbs an X-ray photon, and the total energy deposited is so large compared with the size of the grain that either the whole grain or a local hot spot is transiently heated to a temperature high enough that molecules from the ice mantle can be evaporated. This process has been formalized e.g. in ref [38, 39]. One advantage is that this process can be understood analytically and is therefore easy to implement in astrochemical models. It works well for particularly volatile species and remains implemented in many models.

Another process that has had a lot of success recently is chemical desorption. In chemical desorption the energy comes from the exothermicity of a chemical reaction: the idea is that a species formed at the surface of the grain may immediately desorb upon formation because of the excess chemical energy that is redistributed. This has been implemented in some models using theoretical estimates [40], but now experimental constraints are starting to exist [41, 42]. In particular a semi-empirical model formula has been proposed by Minissale et al. [43] which allows for easy implementation in astrochemical models. Nonetheless, the process remains poorly constrained for most reactions and, in particular, for reactions occurring on water ice, which is crucial (the process works well on graphite, for example, which allows quantification, but this is not true for water ice).

For the sake of completion, we may also mention shock-induced desorption, which is sometimes included in the lists of non-thermal desorption processes. This term simply corresponds to sputtering of mantle material during collisions between grains. This is a process that is only active in very specific regions (namely, shock regions), and explains observations in these regions (e.g. of methanol [44]) but is not really applicable elsewhere.

I.1.2.2 Astrochemical models

I should explain at this point what the astrochemical models that have been mentioned earlier are, and how data such as what we obtain here are usually implemented in these models. It would be difficult and not particularly relevant to review all the possibilities there are to model the chemistry and physics of different regions of the ISM, but I will try to outline the general idea of "astrochemical models". At the core of an astrochemical model is the conjuction of a database of chemical reactions, up to thousands of them, and of a physical model for the description of the region (importantly: the temperature, the UV flux if necessary, the density...). Some models will put more emphasis on the chemistry and others on the physics: on one extreme we could imagine a model which solves the evolution of chemistry for fixed physical parameters, on the other one that would consider

fixed abundances of molecules and atoms and look at the physical evolution of the region (e.g. by solving a radiative transfer problem to obtain dust and gas temperatures, and the emission of molecular lines).

The details, in particular the number of dimensions of the model, will often depend on the type of region. For example, a PDR model will usually be a 1D model, with the one dimension being equivalently the distance from the edge to the center of the cloud, or the extinction A_v, or the UV photon flux [45]. If the interior of a dense cloud is modeled, a 0D model may be sufficient [46], with for example for a contracting core an extinction increasing with time [47]. The most complex models are often protoplanetary disk models [48, 49], since they require two spatial dimensions (distance from the star in the midplane R and vertical distance z to the midplane, as in fig. I.5) and many different physical ingredients (UV and X-ray flux in two dimensions, very large temperature and density gradients with different types of chemistry depending on the conditions, location and size of dust grains...).

Models may have for purpose to reproduce observations. In this context, sometimes smaller models more focused on a specific problem may be used, using a restricted network and only the relevant parameters, to reduce the variability inherent to very large models. Other more full-blown models may instead be used to gain a more general understanding of the behaviour of a type of region as a function of different input parameters, without necessarily trying to reproduce particular observations, except for "benchmarking" purposes [48, 49].

Most recent models include both gas phase and grain chemistry, although the modelling and understanding of grain chemistry is far less advanced than for the gas phase. Gas phase-only models may be sufficient to answer some specific questions, but grain processes are of course a major part of the overall understanding of all regions. Irradiation-induced chemistry in particular has only started to be taken into account [50].

We arrive then at the question of including non-thermal desorption processes in models. What astrochemists want from laboratory data is a *number*. Typically for UV photodesorption this is an average photodesorption yield Y_i^{avg}, in molecules desorbed per incident photon. Photodesorption is then implemented by considering that there is a flux of photodesorbed molecules going from the solid phase to the gas phase, given by:

$$\frac{dN_i}{dt} = k_i^{PD} N_i = \theta_i \sigma_{gr} n_{gr} Y_i^{avg} F_{UV} N_i$$

where N_i is the density of the considered species i, k_i^{PD} a photodesorption rate for that molecule, θ_i the surface coverage of species i, $\sigma_{gr} n_{gr}$ the effective grain surface and F_{UV} the UV photon flux.

The roughest modelling, that was done in early models, was to consider an equal photodesorption yield for all molecules of 10^{-3} molecules/photon. This remained the case for a relatively long time because the first photodesorption experiments seemed to point towards a value close to 10^{-3} molecules/photon for most molecules, but it rapidly turned out that the yield actually varies over orders of magnitude depending on the molecule (see chapter IV). Now models distinguish a photodesorption yield for each grain species, using published data when available and arbitrary values (still often 10^{-3} molecules/photon) when not (e.g. [51]). Some models go as far as to try to take into account the depth and temperature dependence of photodesorption yields that were modeled in some experiments

[52], but this is less frequent. Recently in Walsh et al. [53] the photodesorption of methanol in the form of fragments (since fragments dominate the desorption yield for this ice [54]) was taken into account and showed some interesting differences with the case where only intact molecule desorption is considered. Despite these best efforts from modellers, it is difficult to fully take into account the information brought by laboratory experiments for one specific process that is part of a much larger and complex model. This is in turn something that us experimentalists should recognize, in order to think about how our data may be put into a form that can be used by modellers. I have attempted to do this for X-ray photodesorption, for example (see chapter VI and ref. [55] / paper III). Another thing worth noting is that in astrochemical modelling, a factor of 2 precision on a number is largely within what is expected. Astrochemical models are extremely complex and their response to a variation in parameter is highly non-linear, often in the sense that an order of magnitude change may have little effect on the final outcomes - although some parameters are much more sensitive, but it is difficult to know which ones a priori.

I.1.2.3 Observations

Let us now look more precisely at how UV photodesorption in particular (since X-ray and electron desorption have not really been considered so far) has been used to explain some astronomical observations.

PDRs are among the obvious regions to look for the effect of photodesorption since they are precisely regions intensely irradiated by UV photons. Indeed, in the PDR model of Hollenbach et al. [56] it is shown that photodesorption keeps water molecules off the grains, preventing the formation of the ice mantle, even when grain temperatures would allow it and maintain a gas phase presence of H_2O down to relatively high extinction A_v depending on the flux. At the initial stage of core contraction, where external UV photons are still present, Kalvans [51] shows that UV photodesorption plays an important role in regulating the build-up of the ice mantle as well. Even in prestellar cores, where only the secondary UV photons generated by cosmic rays exist, a gas phase abundance of water is observed and is explained by UV photodesorption [57].

One important topic at the moment is the question of how organic molecules (in particular the "complex organic molecules" that have more than 6 atoms [7]) end up in the gas phase in different regions such as PDRs and prestellar cores. Gas phase chemistry often fails to produce these molecules (for example CH_3OH) efficiently, and it is therefore assumed that they are formed on grains and some non-thermal desorption process is required. In the case of CH_3OH, it is not entirely clear whether UV photodesorption alone can account for its abundance [58]. In the case of H_2CO, which is an intermediate building block towards COMs, gas-phase chemistry alone cannot account for its abundance in PDRs and photodesorption has been shown to be important [59].

Perhaps the regions where the most examples exist are protoplanetary disks. Protoplanetary disks are a particularly hot topic in astrochemistry, because of their relevance in planet formation and because the challenging observations of such small objects has now become possible. Some of the earliest examples of UV photodesorption being used to explain observations were for observations of gas phase water in protoplanetary disks [60, 61] (although the second study has now been shown to be a non-detection). In protoplanetary disks, cold gas phase water is observed, while water cannot form efficiently in

the gas phase in cold regions. Instead, this water originates from the surface layer of the disk that is illuminated by the central star, where water is photodesorbed from grains. Newer observations and models show this well [62, 63]. In ref. [48] we see clearly that if photodesorption is turned off in the model, there is no way to explain this cold gas phase water. Terada & Tokunaga [64] showed that for Herbig Ae type stars (one of the different types of young stars, which emits a particularly copious amount of UV photons), the water snowline, which is the location in the temperature gradient of the disk where water freezes out on grains, is displaced by photodesorption. The water snowline is particularly important in the context of star formation.

Aside from water, there is a nice result by Öberg et al [65] where spatially resolved ALMA observations allowed to see a double CO snowline in a disk: one which is due to the transition from thermal desorption of CO to freeze out, and one which corresponds to the point where UV photodesorption can no longer maintain a gas phase abundance of CO and everything freezes out onto the grains.

Photodesorption of organics is also a hot topic in protoplanetary disks, where these molecules are starting to be detected. Photodesorption is crucial in explaining the detection of CH_3CN in ref. [66], for example, which is the first detection of a complex organic molecule in disks. The effects of taking into account CH_3OH fragments desorption in the model of Walsh et al. [53] was mentioned earlier. Part of the H_2CO observed also requires photodesorption to be explained [67]. Probing the ice chemistry and the cold midplane of the disk is an important challenge, and the best molecule for this would be CH_3OH, which is currently thought to be the one observable molecule that unambiguously comes from ices - and therefore a precise knowledge of the way it can be non-thermally desorbed is important.

I.2 Vacuum technology context

I.2.1 Non-thermal desorption in vacuum dynamics

The early history of electron-induced desorption (since, at first, electrons were the relevant sources of irradiation) goes hand in hand with the development of vacuum technology from the beginning of the 20th century to the advent of the MGR model around 1964 [68]. The introduction of electron-emitting filaments in vacuum systems for the purposes of mass spectrometry, pressure measurement, etc... inevitably led to problems due to electron-induced desorption, which created anomalous mass signals and limited quantitative measurements of pressure, for example. The earliest example of EID measurement was made with the first mass spectrometer [69]. Progressively, the studies moved from simple observations of the existence of a phenomenon that hindered operation under vacuum to more detailed studies on well characterized surface - the routine development of ultra-high vacuum helping [68]. The first mention of EID originating from electronic excitation of adsorbed molecules dates back to the 40s [70] but a complete formalization of this in the MGR model (which will be presented in chapter II) became possible around the 60s when considerably more studies became available. One of the developers of the MGR model, Redhead, was a vacuum scientist and his interest in the phenomenon of EID came from the development of more and more precise ionization gauges for measuring ultra-high vacuum pressures reliably.

In vacuum science, non-thermal desorption processes like EID are therefore most of the time unwanted phenomena that we would like to avoid if possible. But since this is usually not possible, instead a proper understanding is required to mitigate, or at least quantitatively predict, the impact of these phenomena on vacuum. Only electrons were mentioned here, but sources of UV or X-ray photons, or energetic ions, are all relatively common equipments in vacuum chambers and may all cause non-thermal desorption issues.

I.2.2 Non-thermal desorption in the context of accelerators and the LHC

I.2.2.1 Brief description of the LHC

The Large Hadron Collider (LHC) is the biggest particle accelerator in the world. It is part of the accelerator complex of CERN, and is used for very sophisticated and varied particle physics experiments that I will not attempt to describe here. Operating a machine as large and complex as the LHC requires the cooperation of multiple fields of engineering expertise such as cryogenics, accelerator operation, electrical supply, magnets and superconductors, materials... and vacuum. At the core of an accelerator is a vacuum chamber in which the beam will circulate. Maintaining a good vacuum is essential to stable beam operation, as interactions with the residual gas (elastic collisions and bremsstrahlung energy loss) limit the lifetime.

The LHC is hosted in a tunnel of 27 km circumference. The beam of particles circulates in two parallel vacuum tubes in counter-propagating directions, merging at eight "long straight sections", in four of which collisions occur and detectors are placed. The beam consists of protons or heavy ions (Pb, Xe...) colliding at center of mass energies in the TeV range (14 TeV nominal for protons). The particles circulate in the form of bunches separated by a time that varies depending on the operation (nominally 25 ns) and for protons there are around 10^{11} protons/bunch, and a total of ~ 3000 bunches. Around the vacuum parts are the superconducting magnets used to manipulate the beam, and the cryogenic system, making the total apparatus quite large. The vacuum tubes themselves, however, are only about 5 cm in diameter.

One particularity of the LHC is that large sections ($\sim 80\%$) of the vacuum tubes are operated at cryogenic temperatures. The beam tube is shown in fig. I.6a. The "cold bore" external part is in direct contact with the cold mass of the superconducting magnet at 1.9 K. The "beam screen", made of copper, shields this cold bore from the heat load induced by the particle beam and is maintained at 5 - 20 K. Pumping in operation mode for the LHC is thus achieved directly via the walls of the chamber: at 1.9 K all species but Helium are efficiently cryopumped (pumping speed for H_2: ~ 5 l.s^{-1}.cm^{-2}, see chapter III for a definition of pumping speed). The long straight sections where the pipes are merged are operated at room temperature: there the pumping is achieved by using a NEG coating, a porous material that traps molecules (see chapter III), on the walls of the beam screen. Thus the vacuum tubes are uniformly pumped by the walls of the chamber themselves and the vacuum system is completely isolated during operation.

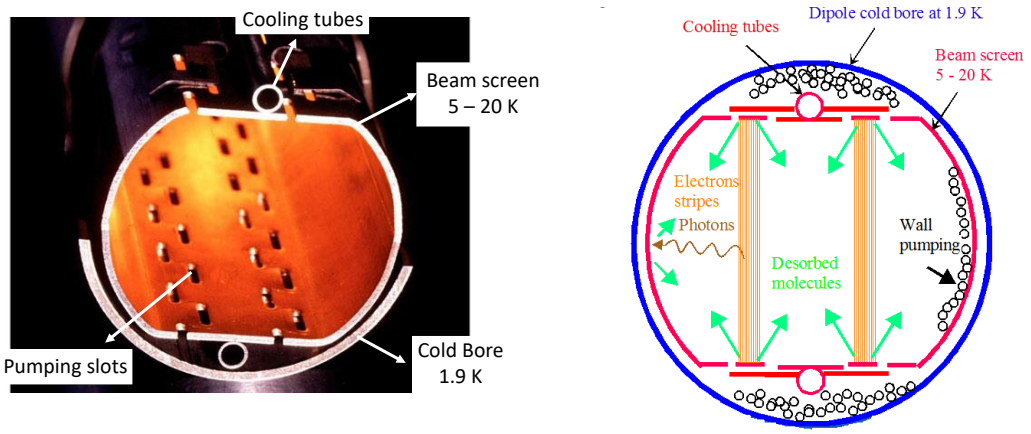

Figure I.6: The vacuum pipe of the LHC, and the non-thermal desorption processes occurring in it. Left: picture of the LHC beam pipe, with the cold bore and the copper beam screen contained inside. Right: cross-section of the beam pipe, including also a schematic of non-thermal desorption processes due to synchrotron radiation and electrons.

I.2.2.2 The different sources of non-thermal desorption in accelerators

The static vacuum (no beam operation) in the LHC vacuum system is below 10^{-11} mbar. This value can increase by orders of magnitude when the beam circulates: this dynamic pressure is due to non-thermal desorption effects, which I will present here.

In the bending parts, the beam loses energy by synchrotron radiation. Any charged particle that is accelerated radially emits synchrotron radiation (cyclotron radiation if it is not relativistic), a highly collimated broadband radiation. The shape of the spectrum of synchrotron radiation is shown in fig. I.7 using electrons of different kinetic energy as an example. A critical photon energy can be defined (the definition is complex and not recalled here) and we see on fig. I.7 that it is an indicator of the photon energy above which the intensity starts becoming low. This critical energy depends on the particle energy but also its mass: for protons, even at the nominal energy of 7 TeV the critical energy is "only" 44.1 eV. But this critical energy is sufficient for photon-induced desorption. The flux is significant for the nominal operation mode of the LHC: 10^{17} ph.s^{-1}.m^{-1} [71].

Scattering of a proton from the beam into the walls may also cause desorption. In addition to these, electrons are created by the photoelectric effect by synchrotron radiation, while ions and electrons are created by interaction of the beam with the residual gas. These charged particles, which do not necessarily have a lot of energy initially, are accelerated by the successive bunches. They may then hit the walls and desorb molecules, but also eject again electrons (and ions), creating a cascade effect.

The cascading effect for electrons is called the "electron cloud effect" and its principle is schematized in fig. I.8. This phenomenon can have major impacts on the vacuum and the heat load of accelerator systems. A crucial element in the electron cloud effect is the secondary electron yield (SEY), which is the number of secondary electrons ejected from the surface per incident electron. The SEY is related to the EID and PID yields, in the sense that the same basic phenomena are at their origin: electrons are part of the particles

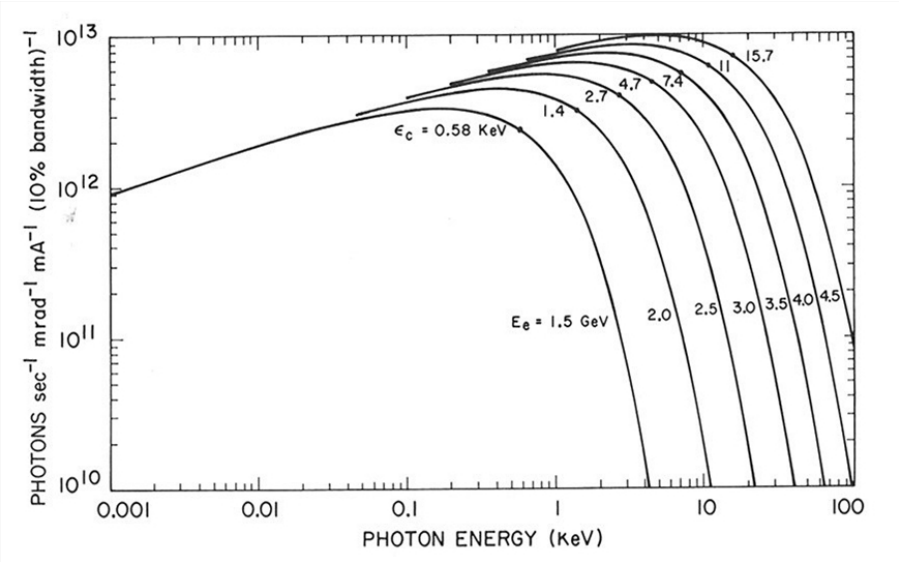

Figure I.7: Spectrum of synchrotron radiation emission for electrons of different energies. By J.D. Jackson - J.D. Jackson, 'Classical Electrodynamics", CC BY 2.5

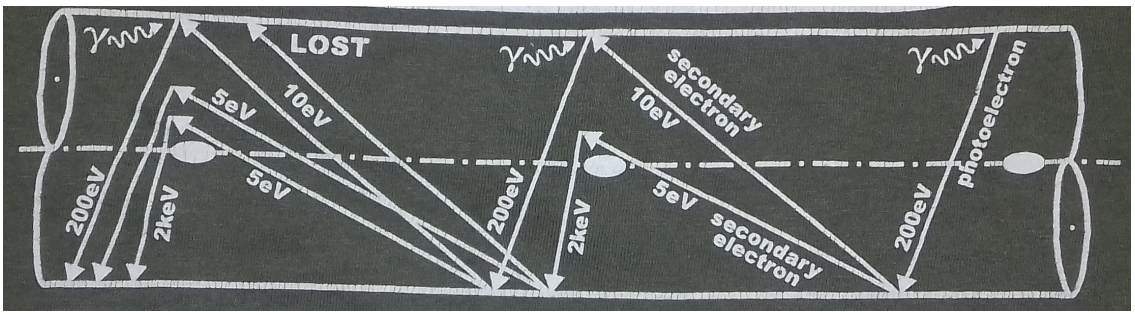

Figure I.8: Principle of the electron cloud effect in accelerators. An initial photon ("γ") from synchrotron radiation ejects a photoelectron (of e.g. 200 eV here), which by hitting the chamber walls eject several secondary electrons with low energies (typically 5-10 eV). These slow electrons can be accelerated by the electric field of a proton bunch to high energies (e.g. 2 keV here) and hit the walls, generating again secondary electrons. Drawing taken from the back of the t-shirts distributed at the e'cloud 18 conference.

ejected from a surface irradiated by electrons or photons (or ions), just like molecules. An electron cloud effect can only occur if at least the average SEY is > 1. In practice, the actual threshold depends on a number of parameters.

Both SEY and PID/EID yields, which are the crucial parameters in understanding the vacuum dynamics of accelerators, have been extensively studied experimentally (e.g. [72, 73, 74, 75]). Aside from a dependence of these yields with the photon/electron energy, there is also a dependence with the initial surface and its evolution with time/photon and electron dose. The surfaces used are not well controlled: they are technical surfaces and their exact surface state is not "clean". It is observed that PID/EID yields and SEY decrease with irradiation time. The diminution of PID/EID yield can be partly explained

by the depletion of the least bound species at the surface. But another important factor is the *chemical* modification of the surface. Electron and photon bombardment modify surface properties, leading to the formation of a layer of carbonaceous non-volatile residue that has a lower SEY, among other things. Therefore there is a so-called "beam scrubbing" strategy used to mitigate the effects of PID/EID and electron clouds: simply circulating the beams will naturally lead towards a better situation.

The non-thermal desorption phenomena in the vacuum pipe are summarized in fig. I.6b. Data obtained from surface science studies of phenomena like PID/EID and SEY can be introduced in the codes that simulate the behaviour of accelerators like the LHC, that have been developed at CERN for example. From this brief description it will however appear that thick molecular ices are not necessarily the most relevant system for accelerators. There is a condensation of molecules like CO, H_2O etc on the cryogenically pumped walls of the accelerator, however thick layers should mostly develop on the cold bore part, which is not supposed to be exposed to irradiation, and not on the beam screen. In fringe cases there could end up being thick layers of condensed molecules: for example, there has been an incident a few years ago in the LHC where an error during initial pumping presumably led to vast quantities of frozen air on the beam screen, which perturbed the operation of the beam as the pressure had a spurious behaviour there. Aside from these fringe cases however, what can be learned from PID/EID of molecular ices is far from useless: transposition of some of the fundamental knowledge gained on the process to systems like physisorbed molecules on technical surfaces (covered with a carbon layer of processed material, for example) is possible.

Chapter II

Fundamental mechanisms of photon and electron-induced desorption

> Strange about learning; the farther I go the more I see that I never knew even existed. A short while ago I thought I could learn everything - all the knowledge in the world. Now I hope only to be able to know of its existence, and to understand one grain of it. Is there time?
>
> Daniel Keyes, *Flowers for Algernon*

In addition to answering the questions asked by the different contexts set out in the previous chapter, we also wish to answer a more fundamental question for the systems we study: what is the microscopic, physical mechanism that explains photon and electron induced desorption? First I will try to clarify what exactly this question means. Then I will lay out the basic physics regarding the systems we study, molecular ices, and their interaction with the UV photons, X-ray photons and electrons that are our source of electronic excitations in this work. Finally, I will present some of the historic models that have been proposed to answer the question of the fundamental mechanism in different systems, present how some of these may transfer to the molecular ice systems, and give an example of a set of systems for which electronically induced desorption mechanisms have more or less been entirely captured through experimental and theoretical investigations: the rare gas solids (RGS).

II.1 Position of the problem

The objective of this section is to try to clarify the range of questions that is covered by the stated goal of "elucidating the fundamental mechanisms of PID/EID". Let us first represent the situation. The most simple system to consider would be an isolated atom, physisorbed on top of an isotropic surface, as represented in fig II.1a. In this case, the only relevant coordinate is the distance to the surface z, and the atom sits in a physisorption well characterizing the surface-adsorbate bond. There is a two-step process: first electronic excitation of the atom, and then subsequent desorption. We can then distinguish three ways to desorb:

1. The atom is excited to an electronic state which is repulsive with respect to the surface-adsorbate coordinate (situation 1 in fig. II.1b). In this case, without further evolution of the system (i.e. decay of the excited state), the atom will desorb, but not in its ground state.

2. In a classical picture, the atom acquires in some way (following relaxation of the electronic excitation) enough kinetic energy to overcome the potential energy of the well and moves away from the surface (situation 2 in fig. II.1b).

3. In a more quantum mechanical picture, the surface-adsorbate bond is vibrationally excited (again, following the electronic relaxation) to the point where it is in a state above its dissociation limit, thus the bond is ruptured and the atom desorbs (situation 3 in fig. II.1b).

Only in the first case we can directly see how electronic excitation leads to desorption, and even then it is left to be shown, from an experimental point of view, that this is indeed how desorption proceeds in some cases and from a theoretical point of view, why is the electronic state repulsive. In the two other cases, "elucidating the mechanism" usually means finding out how the initial electronic excitation is converted in a way or another into either kinetic energy of the atom or excitation of the surface-adsorbate bond.

The representation of the situation becomes more complex as we move towards the actual systems that interest us. First, if we replace the atom by a diatomic molecule, we have two more degrees of freedom added: the internal vibration mode of the molecule (ν),

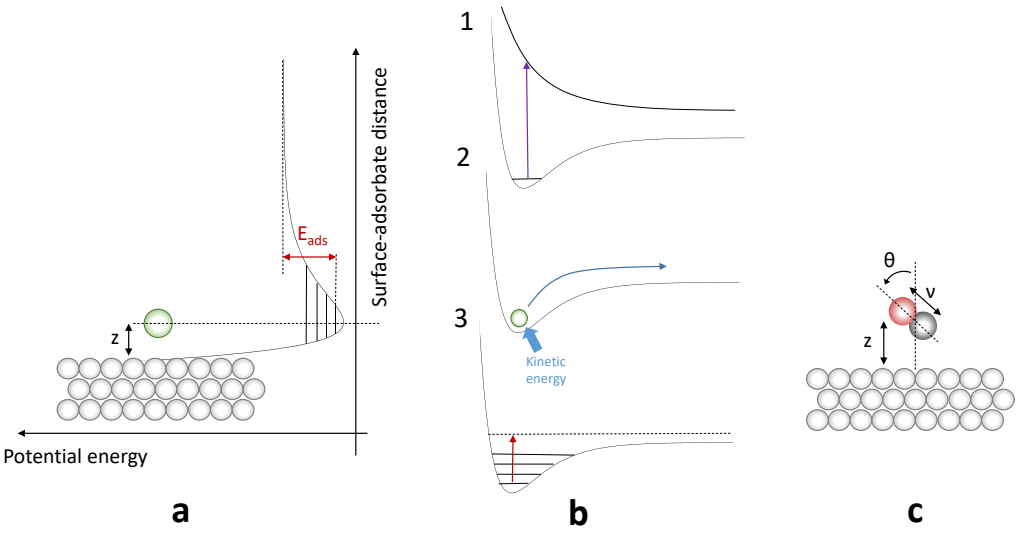

Figure II.1: Sketch of the problem of desorption in a simple case. **a.** An atom adsorbed at a surface, in a physisorption well, and the corresponding potential energy curve. **b.** Three possible ways for the adsorbed atom to desorb (see text for the detail). **c.** A molecule adsorbed at a surface, with the additional degrees of freedom introduced.

and the orientation of the molecule θ with respect to the surface, as sketched in fig. II.1c. This orientation corresponds to the librational degree of freedom, and is a "frustrated" rotation. Note that the interaction of the molecule with the surface should depend on the orientation of the molecule, and therefore the physisorption mode is no longer a simple one-dimensional potential curve but a two-dimensional potential energy surface. This implies that there should be strong coupling between libration and physisorption.

If we move to polyatomic molecules, we have multiple internal vibrational modes, more librational modes as well and all of their combinations, making the problem even more complex. We also need to consider that in most real cases and in particular in molecular solids, we cannot consider an isolated molecule on top of a surface: the molecule interacts with multiple other molecules and is not sitting "on top", making the parametrization complicated. As we will see in the next section, we are not even dealing with perfectly ordered surfaces: ices are polycrystalline with defaults playing an important role, or amorphous.

Let us now look at the problem from an experimental point of view. We have access to two parameters with various degrees of control: the initial excitation, and the final desorbed molecules in the gas phase. We also have sometimes access to (limited) information on the chemistry happening (mostly bulk chemistry) and the ice structure.

The initial excitation is basically what electronic state we are exciting, which also depends on which type of excitation we use. In the VUV range, or even UV-visible for bigger molecules we can excite specific low-lying electronic states (valence excitations). For electrons, we do not have this degree of control, and we can excite many different electronic states, but depending on the electron energy we will change the amount and profile of deposited energy in the ice. For X-ray photons, we excite precisely chosen core

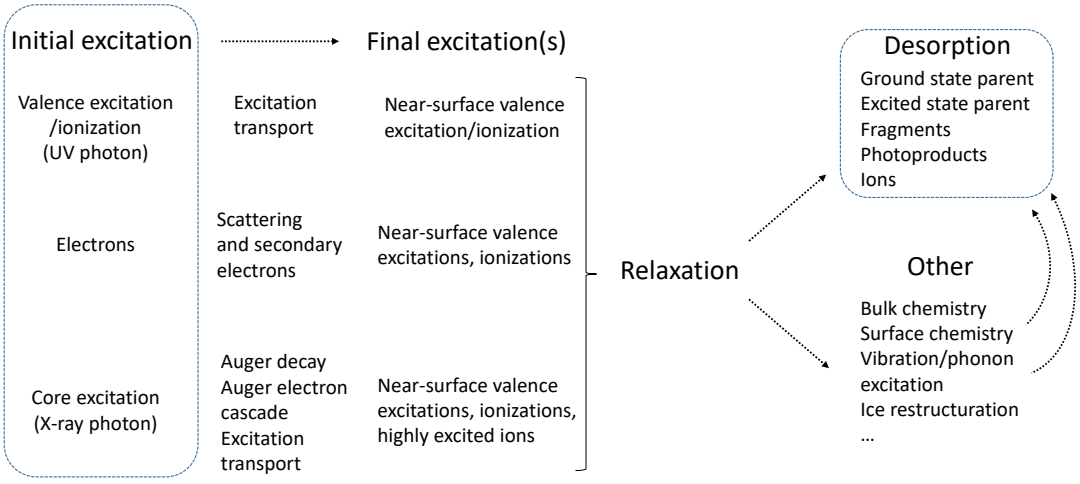

Figure II.2: Overview of the desorption process and the accessible information. In the blue dashed boxes are the initial and final "states", which list what we can have access to. What we are trying to figure out from this is the "relaxation mechanism" for which we have very little a priori insight.

electronic transitions, but these can lead to many different "final excitations". The next section is dedicated to laying out the basics of these different types of initial excitations. In all cases we need to distinguish between initial excitation and final excitation, because there can always be excitation transport in one way or another throughout the molecular ice.

The final desorbed molecules can be characterized in multiple ways, not all of which are explored in this work. We already pointed out that the molecule which we consider can desorb in its ground state, but also in an electronically excited state or ionized state. In addition, molecules can dissociate and therefore fragments, neutral or ionized, can desorb. Surface chemistry can occur, leading to products different from the parent molecules, that can desorb as well. First, information is therefore brought by making the inventory of the desorbing species. Then it is possible to look more finely at these desorbed species. We can characterize their kinetic energy, but also their internal energy state (vibrational and rotational excitation, spin-orbit populations...), their angular distribution, etc. Not all of these techniques will be explored in this manuscript, however. The hope is that by answering to the question, what desorbs, in which state, for which initial excitation, we will gain insights on what happens in between the two steps that we control.

An overview of the situation is summarized in the sketch in fig. II.2. The initial excitation (which we can control) evolves towards final excitations located near the surface. These excitations can relax towards different outcomes, one of which is desorption (which is what we measure). Other outcomes include surface chemistry, vibration and/or phonon excitation (which can in turn lead to desorption), bulk chemistry, ice restructuration... The relaxation part is what we are trying to understand: how the electronic excitation converts to desorption. The details of this figure should become clear after the end of this chapter.

II.2 Interaction of photons and electrons with molecular ices

II.2.1 Ices/molecular solids

The systems studied here correspond to what is often called in the community "ices". Ice here does not refer only to solid water but to any solid composed of small volatile molecules such as CO, N_2, CO_2, CH_4, CH_3OH... to cite a few that will be mentioned extensively in this manuscript[a]. The term overlaps with what can be called elsewhere molecular solids, Van der Waals solids, condensed gas, condensed molecules, etc... These terms point out well that we are considering systems which are a collection of discrete molecules usually found in the form of gas at room temperature and pressure, but here form a solid through weak interactions, i.e. usually Van der Waals interactions, although the stronger hydrogen bond interactions of solid water or ammonia are included. The terms molecular solid or ice or the convenient "molecular ice" of the title of this manuscript will be used indifferently throughout this text, but it should be noted that we are only dealing with a subset of molecular solids here, as the category includes other types of interactions and bigger molecules such as large organics. Some properties of a number of molecular ices that will be encountered here are given in table II.1, including the adsorption energy of molecules.[b] It is clear that we are dealing with weak molecular bonds, as the typical binding energy (excluding water ice) is of the order of 100-200 meV.

Molecules in a molecular solid retain their integrity in the sense that no electron delocalization is involved in the binding of molecules between themselves. Molecular solids therefore stand somewhere between gas phase studies of free molecules and solid-state studies, and the languages of both fields are sometimes used to describe their properties, which can be confusing. One consequence of the fact that there is no electron delocalization is that molecular solids are electrical insulators. For the small molecules considered here, the corresponding solids have large band gaps (from a solid-state point of view) or ionization potentials (from a gas phase point of view), often more than 10 eV. The two notions are not equivalent: while the band gap is the energy gap between the valence band ("ground state") and the conduction band, the ionization potential would correspond to the threshold for photoemission from the solid. In some materials electrons can be promoted to the conduction band and propagate in the solid with a more or less free-electron like behaviour depending on the solid, but cannot escape into the vacuum below a given energy. Ionization potentials for some molecular solids are given in table II.1.

More specifically, the molecular solids we study in the laboratory are nanometre-scale films grown from gas deposition under ultra-high vacuum conditions (see III.1.1) on a substrate cooled down to low temperatures (down to 10 K). Typically we work with ices with thickness' between a single layer of molecule ($\sim$ 3 Å) or less and 100 nm. This is well representative of the kind of ices that are found at the surface of dust grains in the ISM or on the walls of cryogenic parts of vacuum chambers. Because of the difference of scale between the thickness of the film (some nanometres) and the surface onto which

[a] Rare-gas solids (RGS) will also be part of the systems mentioned here. For the sake of not repeating "molecules and atoms" too many times, the rare gases will be treated as honorary molecules.

[b] Adsorption energies for molecular solids can be obtained from, for example, temperature-programmed desorption experiments, see II.1.3. The adsorption energy thus determined can be seen as the dissociation limit D_0 of the physisorption well of the molecule.

Table II.1: Relevant properties of a few molecular solids

Molecules	Density ($g.cm^{-3}$)	ML length (Å)	Surface density ($mols.cm^2$)	Binding energy (meV)	Ionization potential (eV)
CO	1.03^a	3.57	8×10^{14}	79^h	12.5^l
N_2	0.94^b	3.67	7×10^{14}	75^h	14.1^m
NO	1.46^c	3.24	1×10^{15}	200^i	9.6^n
CO_2	1.78^d	3.45	8×10^{14}	232^j	12.3^m
CH_4	0.47^e	3.74	7×10^{14}	103^h	11.3^m
H_2O	0.94^f	3.17	1×10^{15}	500^k	11^o
Ar	1.77^g	3.35	9×10^{14}	77^h	14^p
Kr	3.09^g	3.56	8×10^{14}	116^h	12^p
Xe	3.8^g	3.85	7×10^{14}	151^h	9.9^p

a. For crystalline CO in α phase at 30 K[76] b. For N_2 ice, constant from 10 to 22 K. [77] c. For crystalline $(NO)_2$ dimers (NO forms dimers in the solid phase) at 100 K [78] d. Maximum density of CO_2 ice at 75 K. The density of CO_2 drops with decreasing temperature, down 40% at 10 K. [79] e. For CH_4 ice, constant from 10 to 35 K. [77] f. For compact amorphous water ice (wikipedia) g. For crystalline fcc rare-gas solids [80]. h. TPD data from ref [81] i. Estimated from our TPD experiments j. TPD data from ref [82] k. TPD data from ref [83] l. UPS data from ref [84] m. UPS data from ref [85] n. Gas-phase IP, taken from the NIST database. The solid phase value is not known to my knowledge. o. Ref [86] p. UPS data from ref [87]

it is deposited (typically 1 cm^2), rather than the density of the solid I will mainly refer to two related quantities. The first one is the thickness of the film, given in monolayers (ML), corresponding to the number of layers of molecules. Depending on the molecule, the conversion between monolayer and length is between 3 and 4 Å per monolayer. This conversion is obtained from the density:

$$l_{ML} = 10^8 \times \left(\frac{d \times N_A}{M}\right)^{-1/3}$$

Where l_{ML} is the length of one monolayer in Å, d the density in $g.cm^{-3}$, N_A the Avogadro number and M the molecular weight in $g.mol^{-1}$.

The second quantity is the surface density of molecules. Similarly it is related to the density:

$$s = \left(\frac{d \times N_A}{M}\right)^{2/3}$$

Where s is the surface density of molecules in $molecules.cm^2$. Both these quantities are derived from the density of the molecular solid when it is known in table II.1. The densities for the nanoscale ice films are not always known. A lot of existing density measurements have been done for crystalline solids in equilibrium with their vapour pressure (contrary to our case where the chamber is dynamically pumped), at temperatures where the ice would have sublimated already under UHV conditions. For example, solid CO and N_2 have two distinct crystalline phases, α and β, with quasi-identical properties to the exception that

the transition from α to β occurs at 35.6 K in N_2 and 61.6 K in CO [88]. However, in ultra-high vacuum both CO and N_2 sublimate above 30 K, and no evidence exist that we form α-CO or N_2 when depositing a few tens of monolayers at 15 K. Recently, measurements of the density of astrophysically relevant ices has been undertaken [77, 89], for example for N_2 and CH_4 as indicated in the table. This provides data directly relevant to our conditions. The density obtained by these authors for N_2 [77] (0.94 g.cm^{-3}) is notably different from the one obtained for crystalline α-N_2 at 35 K [90] (1.02 g.cm^{-3}).

The unknown properties of molecular ices do not stop with the density: whether the ice is amorphous or crystalline, its porosity, and other structural details are not always very well known. It is usually assumed instead that the ice is amorphous when the deposition temperature is low enough compared with the sublimation temperature. Evidence of (irreversible) phase transitions exists from infrared spectroscopy measurements (for example around 20 K for CO [91] and 55 K for NO (see IV.1.2) but often nothing tells whether this is a transition between two different amorphous phases or a crystallization. This lack of proper control of the system is one of the difficulties of working on this type of molecular solids: discrepancies between measurements and surprising behaviours could find an explanation in unknown property changes.

One solid that has been extensively studied is water [92, 93, 94, 95] because of its importance. Some studies also exist for CO_2[96, 97]. From these studies, we know that the exact structure of the solid will depend on the growth conditions, most notably the temperature at which the ice is deposited and whether it is annealed later, but also on other parameters such as the deposition angle (background deposition integrating all angles, deposition at a well-defined angle relative to the surface normal with a molecular beam...) or the deposition rate. Still, the exact structure of water ice grown under different conditions is not completely elucidated and remains in fact a topic of heated debate when it is brought up to try to understand the long sought-after structure of liquid water[98].

Some molecular solids also display more exotic properties. This is the case of CO above 20 K, which is presumably crystalline or at least more ordered than below 20 K, and where the alignment of the dipoles of the molecules creates a "spontelectric effect" [99], i.e. a macroscopic scale electric field. This interpretation comes from the changes in the IR spectrum of CO. Such an effect was observed for other materials as well [100]. This spontelectric effect was in turn used to explain changes in the VUV spectrum of solid CO, which will be presented later.

II.2.2 Electronic transitions

The topic of study here are the desorption processes induced by electronic transitions (DIET), so I will make some brief generalities on electronic transitions. Desorption induced by vibrational excitation of molecules, in the infrared range, is also an existing field [101] but will mostly not be brought up. For this section, several textbooks were consulted and the reader is referred to these for more details [102, 103, 104, 105]. A focus is made on diatomic molecules because of their simplicity and because they are an important part of the systems studied in this manuscript.

Electronic transitions are transitions involving the outer electrons of the valence shells of molecules, or their core electrons, inducing a change of electronic state that involves

all degrees of freedom of the molecule (notably also vibrational and rotational). These interactions occur in a domain of wavelengths going from the visible-UV to soft X-rays (or even smaller wavelength for heavier atoms) depending on the types of electrons involved.

Examples of electronic states and configurations are given in fig. II.3 for the CO molecule. In fig. II.3b the ground state electronic configuration of CO is given (the energy spacing between the orbitals is not accurate). In the ground state the orbitals filled are those with the lowest energy. Electronic states are designated with a letter, X for the ground state, their spin multiplicity (2S+1 where S is the total spin) and their symmetry. It also corresponds to the value of an appropriate quantum number, Λ (the projection of the electronic angular momentum along the molecular axis), with the symbol being Σ, Π, Δ etc... for $|\Lambda| = 0, 1, 2...$ (for $\Lambda = 0$ the symmetry can be either Σ^+ or Σ^-). The possible symmetries of electronic states can be deduced from the electronic configuration: here with a closed shell diatomic molecule (all orbitals are completely filled), there is only one possible symmetry which is Σ^+. The closed shell also implies $S = 0$, so that there is only one possible electronic state in this configuration and it is designated as $X^1\Sigma^+$, and its potential energy curve (potential energy as a function of nuclei positions) is represented in fig. II.3a.

Some excited states of CO, the $A^1\Pi$, $a^3\Pi$ and $D^1\Delta$, are also represented, with their potential energy curves in fig. II.3a and their respective electronic configurations in fig. II.3c, d and e. In the context of this manuscript only dipole-allowed transitions will have to be considered, as only intense transitions will be visible in desorption. For CO, for example, the first electronic state that can be reached from the ground state is the $A^1\Pi$ excited state. The lower $a^3\Pi$ state is spin-forbidden, but the $A^1\Pi$ excited state may relax to this state (intersystem crossing). The $D^1\Delta$ state is symmetry-forbidden.

The principle for polyatomic molecules is fairly similar, except the symmetry of the molecule is not necessarily linear and therefore the labelling of molecular orbitals and electronic states is done according to the point group symmetry of the molecule. For example, the H_2O molecule belongs to the C_{2v} symmetry group, which has four possible symmetries labelled A_1, A_2, B_1 and B_2. The first allowed electronic transition for H_2O, from the ground state $\tilde{X}^1A_1$[c] to the excited state $\tilde{A}^1B_1$, involves promotion of an electron from the HOMO (Highest Occupied Molecular Orbital) $1b_1$ (first molecular orbital of B_1 symmetry) to the LUMO (Lowest Unoccupied Molecular Orbital) $4a_1$ (fourth molecular orbital of A_1 symmetry). The electronic structure of water will be detailed in chapter IV.

One important sub-division of electronic transitions for us are those that are dissociative. This is very important in irradiation of ices, because it is a major driver of photon or electron-induced chemistry, and is often tightly linked to the mechanisms of desorption. For bound states, dissociation will only occur if the molecule is excited in a vibrational state sufficiently high that the total energy is greater than the dissociation energy (the asymptotic at infinite interatomic distance of the potential curve). However, some electronic states are dissociative: their potential energy curve has no minimum and the potential energy only decreases with interatomic distance. When the molecule is excited to such a state, the atoms will move away from each others until the molecule is dissociated. An example of dissociative state is represented in fig. II.4a which displays potential energy curves for the ground state and an excited state of $(Ar)_2$: the ground

[c] the tildes are added to avoid confusion between the name of the state and its symmetry

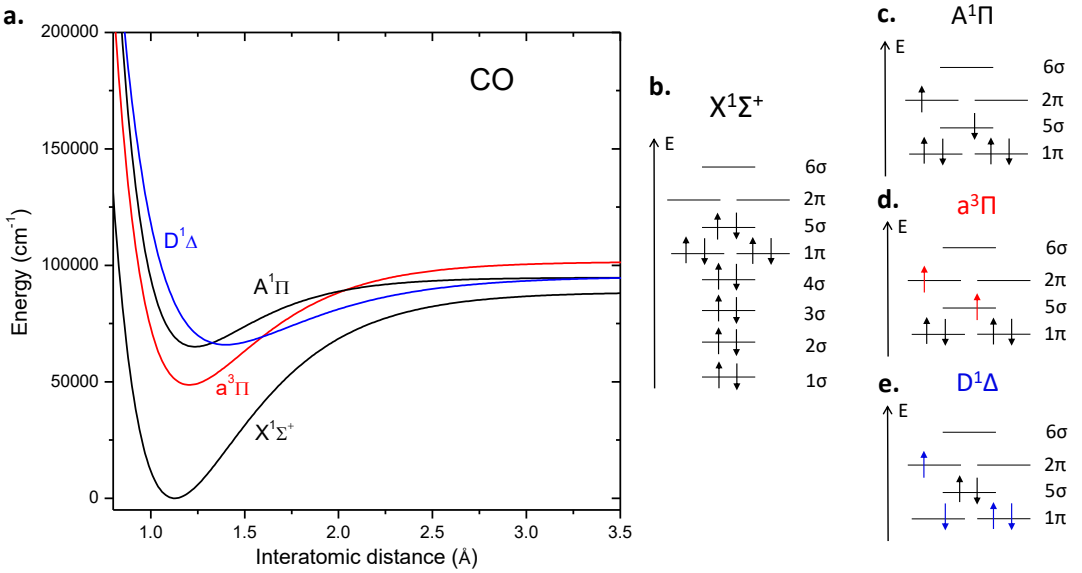

Figure II.3: **a.** Potential energy curves for four electronic states of CO. The parameters for the Morse potential were taken from the NIST database. Note that the expression is approximative, as in reality all of these states converge to the same dissociation limit at infinite interatomic distance. **b.** Electronic configuration corresponding to the ground state ($X^1\Sigma^+$) of CO. **c.** Electronic configuration corresponding to the first allowed electronic state ($A^1\Pi$) of CO **d.** Electronic configuration corresponding to the first triplet electronic state ($a^3\Pi$) of CO. **e.** Electronic configuration of the $D^1\Delta$ electronic state of CO. Note that this electronic configuration can give rise to other electronic states, see text.

state of this dimer is repulsive (it actually has a very shallow well), while several excited states are bound.

Some states are also called predissociated. Such a state is bound, but its potential energy curve is crossed by another, dissociative state. The molecule in such a predissociated state can cross over to the dissociative state and end up dissociated as a result. An exemple of the situation is represented in fig. II.4b in the case of CO. The $B^1\Sigma^+$ bound state of CO has been observed to be predissociated above v = 2 [109], which represents an energy much lower than the depth of the well of this state. However, there is another state close in energy, $D'^1\Sigma^+$, with a very shallow well and a much larger equilibrium distance. The well of this state is so shallow that when a crossing occurs from the $B^1\Sigma^+$ state the energy is above the dissociation limit. It is worth noting that such a situation is not possible within the Born-Oppenheimer approximation: curve crossing of states with the same symmetry is not possible in this case. In reality, non-adiabatic couplings between the states occur, and there is an avoided crossing where the adiabatic curves of the two states cross, so that there is a "$B^1\Sigma^+ + D'^1\Sigma^+$" state with a double well in its potential energy curve[110].

In an electronic transition, the electronic, vibrational and rotational parts of the wavefunction can all be changed. Therefore the vibrational and rotational parts of the en-

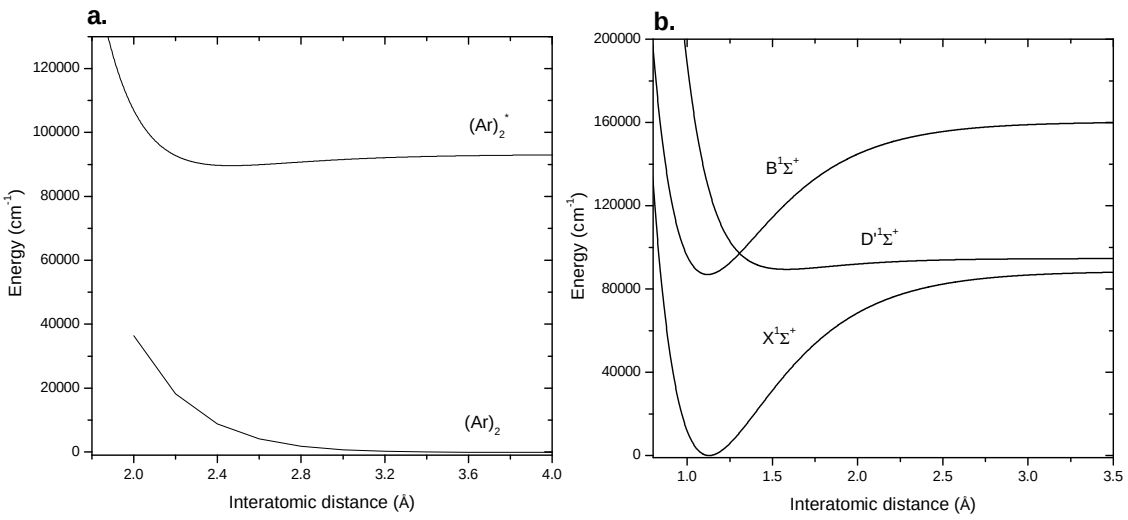

Figure II.4: Examples of dissociative and predissociated electronic states. **a.** Potential energy curves of the argon dimer in its ground state $(Ar)_2$ and in an excited state $(Ar)_2^*$ (called an excimer). The ground state is dissociative, while the excimer is bound. The potential energy curve of the ground state was taken from the calculcations of ref. [106] and the one of the excited state was plotted using a Morse potential with molecular parameters from ref. [107]. **b.** Potential energy curves of the ground state, $B^1\Sigma^+$ and $D'^1\Sigma^+$ states of CO. The B state is predissociated because of curve crossing with the D' state. The curves were plotted using Morse potentials and molecular parameters from the NIST (B and X states) and ref. [108] (D' state).

ergy of the molecule have to be taken into account as well. In the framework of the Born-Oppenheimer approximation, the electronic degree of freedom is decoupled from the vibrational and rotational motion, and $\Delta E_{el} >> \Delta E_{vib}$ and ΔE_{rot}. In addition we generally have $\Delta E_{vib} >> \Delta E_{rot}$, and in a first order approximation, these motions can be decoupled. The structure of vibrational levels is then described by a harmonic oscillator, with the energy levels being of the form $\omega(v + \frac{1}{2})$, and the rotational structure by a rigid rotator, with levels of the form $BJ(J+1)$, where ω and B are respectively vibrational and rotational constants, and v and J quantum numbers. Rotational levels will be discussed in more detail in section III.5.2, but we will not consider them here.

We will exclusively consider here that electronic transitions are governed by the Franck-Condon principle. This principle states that electronic transitions, which are caused by the interaction between the electron and the electromagnetic wave, are much faster than the typical time for vibration (and rotation), and therefore on a potential energy diagram as fig. II.3a the transition is vertical: the nuclear coordinates cannot change during the transition. This means that the intensity of the transition depends on the vertical overlap of the initial and final vibrational levels wavefunctions in the energy diagram. This is illustrated in fig. II.5 with the v" = 0 level of the ground state of CO $X^1\Sigma^+$ and the v' = 1 level of the first allowed excited state $A^1\Pi$. We can see where the two wavefunctions vertically overlap. Quantitatively, the intensity of the transition is

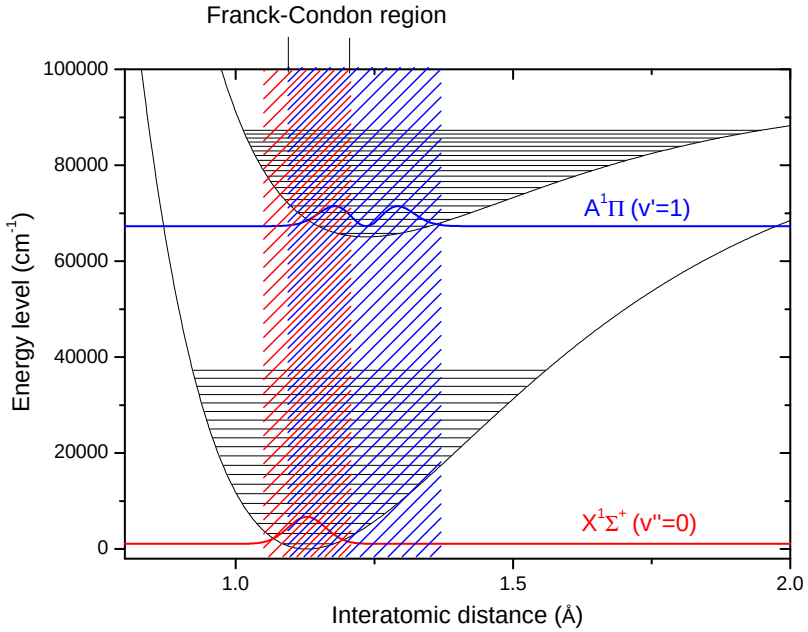

Figure II.5: Illustration of the Franck-Condon principle in the case of CO. The previously presented potential energy curves of the $X^1\Sigma^+$ and $A^1\Pi$ electronic states are represented along with their respective vibrational energy sub-levels. In addition, the vibrational wavefunctions of two of these levels, the v'=1 of the A state and v"=0 of the ground state, have been represented respectively in blue and red. The blue and red hatched regions represent the vertical extent of these wavefunctions, and the Franck-Condon region where a transition is possible corresponds to the overlap of these areas, as indicated on the figure.

proportional to the square of the overlap integral of the two vibrational wavefuntions.

II.2.3 From free molecules to molecular solids

The notions developed previously apply to free molecules. The goal of this section is to see how this translates to the case of molecular solids, which are systems that retain "free" molecular character but are also affected by the condensed state.

In this section, I will focus on the interactions of UV photons with gas phase molecules and molecular solids. Indeed, the valence electronic spectrum of small molecules such as the ones we will be studying here lies deep in the ultraviolet, mostly in the region called vacuum ultraviolet (VUV), between around 6 and 15 eV (200 and 80 nm)[d]. Therefore these photons will cause electronic transitions involving valence electrons. This corresponds to the energy range studied in chapter IV. This will also provide some concrete examples to the notions developed in the previous section. Valence excitations correspond to the promotion of electrons in the highest occupied valence orbitals to empty orbitals.

[d]Vacuum refers here to the fact that light of this wavelength is strongly absorbed by air and therefore requires vacuum to use it. The exact energy span meant by this term varies.

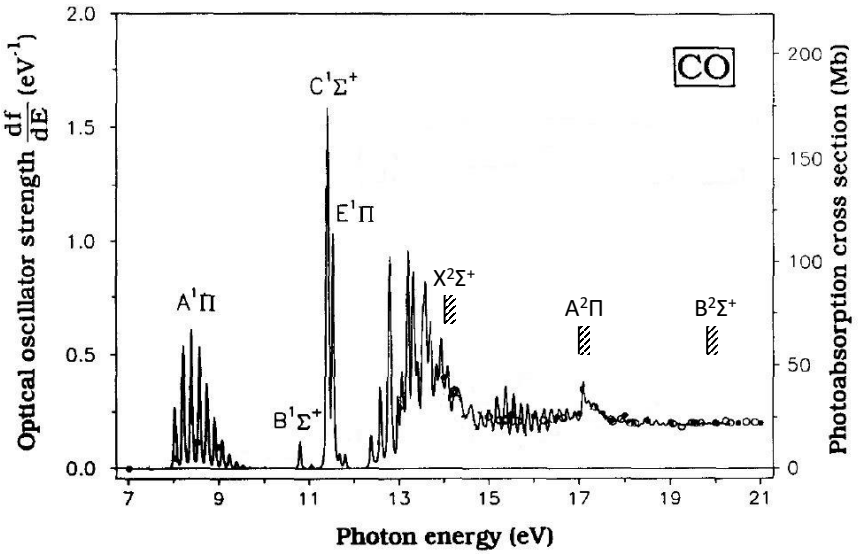

Figure II.6: Gas phase absorption cross section of CO in the VUV region, derived from electron energy loss spectroscopy. Transitions to different electronic states are attributed, as well as ionization potentials (IPs) corresponding to different CO^+ electronic states. Source: Chan et al. [111]

Also in the VUV region of the spectrum, above the first valence excitations in energy, is the ionization threshold of the molecule, which corresponds to the binding energy of electrons in the highest occupied orbital.

A low resolution spectrum of gas phase CO from 7 to 21 eV is reproduced from Chan et al. [111] in fig. II.6. Between 7 and 10 eV is the region where CO is excited to the $A^1\Pi$ electronic state. We see bands corresponding to the vibrational sub-levels of that state, with different relative intensities. This illustrates the Franck-Condon principle, and the intensities of each band give information on the overlap between the initial and final vibrational wavefunctions. If we zoomed on a given vibrational band with sufficient resolution, we would also see the rotational sub-structure. Higher in energy, around 11 - 13 eV, three more electronic states are found, each with their vibrational bands. The fact that the equilibrium distance of the potential curves of these states (contrary to the A state) is very close to the one of the ground state has for consequence that only the first few vibrational levels are seen. As mentioned before, the B state for example is predissociated above v = 2. The dissociation limit of CO, which is the minimal energy required to dissociate the molecule, is 11.1 eV. This is very high compared with other molecules. Indicated on the figure is the ionization threshold of CO, approximately 14 eV. This corresponds to ionization of an electron from the highest occupied molecular orbital (5σ) of CO. Two other thresholds are indicated : they correspond to the thresholds of excited states of the CO^+ ion. It is also worth noting in this figure that above the ionization threshold, structures in the spectrum still exist. Indeed, excited states of the neutral molecules, involving the promotion of electrons from orbitals lower than the HOMO in energy, can be at higher energies than the first ionization energy. However, such excited

states can then decay to an ionic state. This is a process called autoionization.

Let us now consider what happens when we go from gas phase molecules to molecular solids. As mentioned previously, molecular solids are characterized by weak interactions between their constitutive molecules. In particular, no electron delocalization is involved in the bonding, and therefore it still makes sense to speak of exciting or ionizing one particular molecule rather than making collective excitations - even though there can be excitation and charge transfers afterwards. One approach to the understanding of valence excitations in molecular solids is therefore to consider the solid environment as a more or less small perturbation of the free molecule.

In the condensed phase, rotations are no longer possible, therefore the rotational substructure of the spectra disappears. However, frustrated molecular motions (rotations, translations...) called librations exist. Modes related to the movement of the lattice (intermolecular vibrations) appear - they correspond to the solid phase notion of phonons. Phonons couple to the vibronic bands and are responsible for part of their widths. Vibrational modes and frequencies are usually not very modified, but the width of the features in spectra are often broader because of new couplings like those mentioned previously, which can be understood as new energy loss channels that reduce the lifetime of the levels.

For the electronic spectrum, we can distinguish two types of modifications due to the condensed phase environment. The first one is the perturbation of the free molecule state by the environment. How electronic states are perturbed depends quite a lot on their nature, notably on their valence or Rydberg character, as discussed in II.C of Robin [112]. Valence electronic states are usually not very affected. On the other hand, Rydberg states are characterized by large electron radii - equal to or greater than the intermolecular distance in the solid. This means that their spatial extent will overlap with other molecules and consequently they have to be heavily affected by the solid state. I will come back to this afterwards. Another possible perturbation is that the condensed phase can impose deformations on the molecules, but this is mostly relevant for large molecules: organic crystals have been the object of a lot of studies, and there deformations can change the symmetry of molecules and therefore lift degeneracies [113]. Even for much smaller molecules the condensed environment can have an effect: this is not an electronic effect but H_2 adsorbed on water ice becomes slightly infrared-active, for example [114].

Another completely different modification in the spectrum is the possibility of new resonances appearing which are *collective* excitations permitted by the equivalence of molecules in lattice sites of the crystal, and have no counterpart in the free molecule. These collective excitations are either excitons or plasmons, but since plasmons are longitudinal wave excitations, they are not excited by photons and I will not say much on them here. The exciton in solid state theory is usually pictured as a bound electron-hole pair, with tightly bound pairs (radius less than the intermolecular distance) called Frenkel excitons, and weakly bound pairs (radius spanning several intermolecular distances) called Wannier-Mott excitons.

There are excitons of a collective nature in molecular ices, with no counterpart in the gas phase. An example of collective exciton is found in the spectrum of crystalline NH_3 [115] (occuring at 6.4 eV), and disappears when the ice is amorphous, signing a transition which only exists when there is equivalence by translation of the molecules in the crystal. But the term exciton is also used for other electronic excitations below the ionization threshold as well. The analogy between excitons in solid state and electronically excited

states in free molecules is striking: in the end, an electron in an excited state orbiting around the molecular core can be seen as an electron-hole pair. The Frenkel theory of excitons, which makes the approximation of tight-binding, describes in fact the exciton by a free molecule state perturbed by the crystal field. This is a description that is well suited for valence states. While the theory of excitons was originally developed for molecular crystals [116, 117], excitons also exist in amorphous solids and can even be delocalized in these solids [118]. Therefore there is sense in the fact that the term "exciton" is sometimes used to describe *any* electronic state below threshold of a condensed phase molecules: the term does not necessarily imply a collective excitation, a delocalized nature or any useful specificity.

The fate of Rydberg states in condensed phase is more complex and still needs to be discussed. The literature is not entirely clear on this topic. It could be thought that Rydberg states in the condensed phase simply become Wannier excitons because of the analogy between the respective large radii of these states and the fact that they form series converging towards a threshold. This threshold, however, is not the same: the "ionization threshold" in the solid state is usually lower in energy than the ionization threshold in the gas phase. This is because the ionic state is stabilized by interactions with the permanent and induced dipoles (and other multipoles) of the surrounding molecules. In any case, Wannier excitons converge towards the bottom of the conduction band, and if they are purely described by the Wannier model, they bear no parentage to the gas phase Rydberg states.

What becomes of a Rydberg state in the condensed phase can be rationalized following the discussion in Robin [112] based on the work of Rice & Jortner (e.g. [119]). The relevant parameter is the "electron mobility" of the matrix surrounding the molecule, i.e. the scattering mean free path of electrons. Indeed, for a Rydberg state with an electron orbiting on a radius which largely overlaps with other molecules, the lifetime will be severely limited by scattering of the electron, causing spectral broadening. If the scattering mean free path is less than one orbital circumference, the movement of the electron is aperiodic and the Rydberg state is no longer defined. Therefore depending on the environment Rydberg states may be broadened so much as to effectively disappear. In environments like rare-gas matrices where this is not the case, they tend to be blue-shifted for the lower states and red-shifted for the higher ones [120], which leads to an overall compression of Rydberg series - when such series can even be identified. It remains unclear when it can be said that Rydberg states are conserved and when they are replaced by Wannier excitons - and whether that even matters when all we see in the spectrum are broad bumps with no identifiable series.

Let us take a concrete example by looking at the solid phase spectrum of CO. In fig. II.7 the absorption spectrum of solid CO in the VUV region is shown (adapted from ref. [121]). Also displayed for comparison is the spectrum of CO isolated in an Argon matrix in 1:50 proportion, and the CO gas phase spectrum of ref. [111]. In the 7 - 10 eV region we easily recognize the $A^1\Pi - X^1\Sigma^+$ transition, for which the vibrational transition is conserved. The overall level is slightly red-shifted going from gas phase to matrix to solid, and the bands are broader for the solid, but the vibronic progression is still clear. This is therefore typical of a valence state, as mentioned above. Analysis of the vibrational spacing does not yield very significant differences in the vibrational constants [121], however the first few levels are much larger than the rest in the solid.

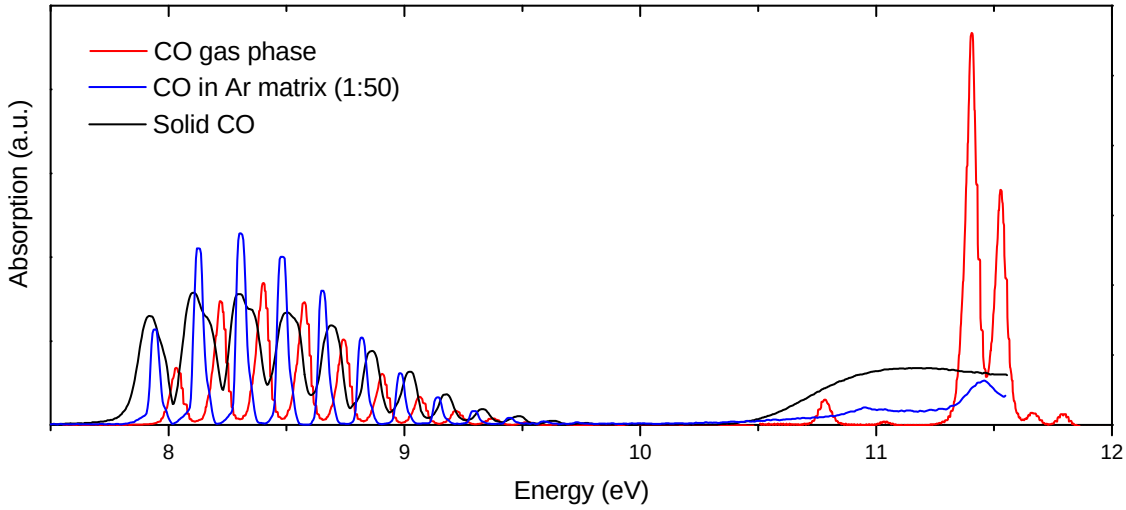

Figure II.7: Photoabsorption spectrum of solid CO (T = 10 K) in the VUV region (black line) and of CO confined in an Argon matrix (T = 10 K) in 1:50 proportion (blue line). Adapted from Lu et al. [121]. Also shown for comparison is the gas phase spectrum of CO (red line) [111].

Their relative intensity is also different compared with the gas phase. An interesting point is that at least the first four levels clearly display a double structure. This is due to a phenomenon specific to molecular crystals called Davydov splitting. It occurs when there is more than one molecule in the unit cell of the crystal, because of dipole interactions between these molecules. When there are two such molecules as for crystalline CO, it can be seen as a splitting between in-phase and out-of-phase vibration of the two molecules. This explains the different widths of the bands, but also possibly the different relative intensities without having to suppose that the Franck-Condon factors are different in the solid phase. Some changes of the VUV spectrum of solid CO in the A-X range were observed above a deposition temperature of 20 K. The spontelectric effect mentioned earlier was suggested to explain these changes. It was shown [122] that the observed shifts could be coherently explained if the A-X electronic state is modeled as a Wannier exciton, i.e. an electron-hole pair with a large radius, that is in interaction with the spontelectric field. But despite this Wannier exciton description, it is clear that the A-X transition retains significant molecular character in the condensed phase.

The situation is very different above 10.5 eV. The B, C and E states are all Rydberg states. In the solid phase none of the gas phase features can be recognized, instead there is only one broad bump (followed by a second one above 11.5 eV, not visible in this spectrum, which could be attributed to the conduction band). Assigning this bump to a Wannier exciton or a broadened Rydberg state is, as mentioned above, not really possible without further information, and it does not change much. The Rydberg states are also strongly modified already in the matrix environment, as expected, although we can still discern two distinct features.

The ionization potential of solid CO is as expected red-shifted with respect to the gas phase, of 1.5 eV in this case, which puts it at 12.5 eV. Although this is not visible in

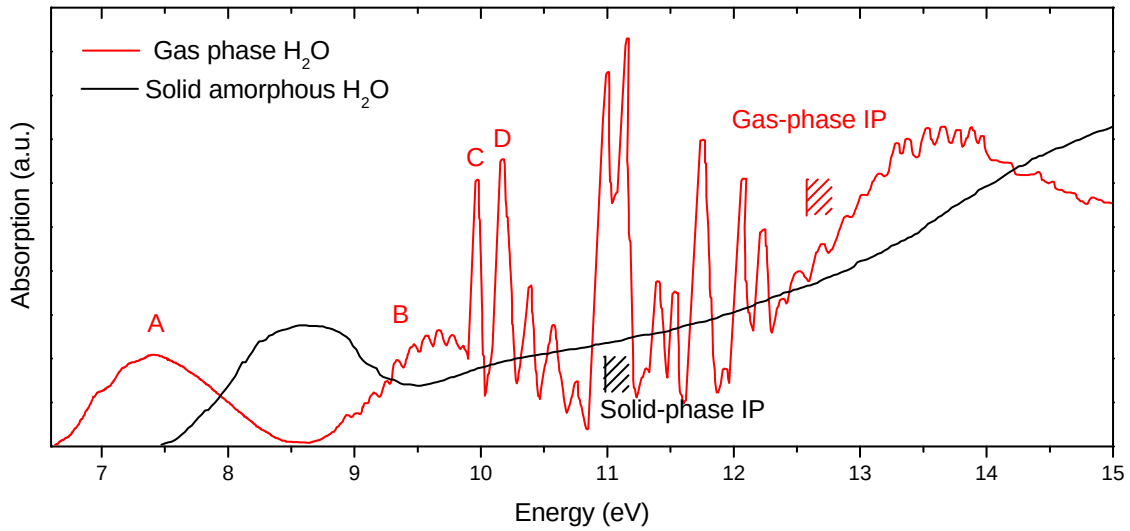

Figure II.8: Photoabsorption spectrum of gas phase H_2O and solid amorphous H_2O in the VUV region. Source: Lee et al. [123] for the gas phase and Kobayashi [86] for the solid phase.

this spectrum (no absorption spectrum is available above 11.5 eV to my knowledge, but we can go beyond that energy on photodesorption spectra), the IP is not marked in the absorption spectrum, which is often the case in the condensed phase.

Another example of gas phase spectrum, the one of H_2O, is given in fig. II.8, adapted from Lee et al. [123]. The first electronic state of H_2O, $\tilde{A}^1B_1$, corresponds to the broad peak between 7 and 8 eV. This state is completely dissociative, and we can see that there is no visible vibrational progression on the spectrum. The second electronic state $\tilde{B}^1A_1$, which corresponds to the promotion of a $3a_1$ electron to the $4a_1$ orbital, occurs between 9 and 10 eV in the spectrum. Although excitation to this state leads to dissociation, the details are more complicated than in the $\tilde{A}$ state [124]. After that we see a series of peaks corresponding to excitations to Rydberg orbitals that converge towards the ionization of a $1b_1$ electron at 12.6 eV. In the same fig. II.8, the spectrum of solid amorphous H_2O from Kobayashi [86] is shown. We see some significant differences, with an important blue-shift of the first state and the disappearance of all structure. The ionization potential is red-shifted by 1.5 eV, down to 11 eV in the solid phase.

II.2.4 Electron-matter interaction

A number of reviews, articles and book chapters were used for the writing of this section and a different presentation as well as more details can be found in these [125, 126, 127, 128, 129, 130].

The interaction of an incident electron with a target depends on its energy - and also on the properties of the target. The primary electrons used in chapter V for EID have energies ranging from 150 eV to 2 keV: they have "medium" energy in the sense that for the molecular ices studied here, electrons need to have a few keV of energy to fully follow the approximations of fast charged particle theory (see below), but they are not low

energy electrons (when the approximations have completely broken down or even when we enter another regime of energy loss channels, i.e. less than 50 or even 20 eV) either. However, low energy electrons are also very much of interest here as secondary electrons of energies ∼5-20 eV will be abundantly produced by electron scattering as well.

Electrons can interact with a molecule or atom through an elastic collision, an inelastic collision or a radiative energy loss. Since we are interested in the way energy is deposited into the ice, elastic collisions are not a concern here - at least not in detail, although they need to be taken into account when discussing the track of an electron in the solid. Radiative energy loss, which is mostly bremsstrahlung (see also section III.), is not of concern either because it only occurs for ultra-relativistic particles (typically 10-100 MeV for an electron). Therefore inelastic collisions are what we are interested in here. In the energy range of interest, interaction of charged particles with molecules occur through the electrostatic interaction with the electrons of the molecules. The incident electron will therefore lose energy by causing electronic excitations and ionizations in the molecules, until it becomes a "sub-excitation" electron, with energy below the first electronic excitation threshold of the molecules of interest. The energy ranges for the different types of energy losses are well separated: radiative loss (bremsstrahlung) does not happen until very high electron energies, while other loss mechanisms which will be discussed later do not kick in until the electron has become sub-excitation. There are therefore similarities between electron-matter and VUV photon-matter interaction: an electron creates several initial events that are similar in nature (electronic transitions) to those that a VUV photon will create, although there are some qualitative and quantitative differences.

When the electron is "sufficiently fast" (relative to the mean orbital velocity of electrons of the molecules or atoms in the target), but not fast enough to be ultra-relativistic, the problem of its interaction with the target is a particular case of the general theory of the inelastic collisions of fast charged particles, first initiated by Bethe [125] and expanded later [126, 127]. The theory is parametrized by momentum. In the case of fast particles, most collisions will involve small momentum changes. In the limit of small momentum transfer, the transitions induced by the particle follow the *optical rule*, in the sense that the allowed transitions are the dipole-allowed ones. Therefore the incident particle can be seen as if emitting radiation of all frequencies at equal amplitudes, up to the maximum energy transfer [130] (which is half of the kinetic energy in the case of an electron). The link between the electron energy loss and the photoabsorption of the molecules is then relatively straightforward to see. For collisions involving non-negligible momentum transfer (which become more and more relevant when the particle is slower), the optical rule is no longer followed and dipole-forbidden transitions have non-zero probabilities. The concept of *generalized oscillator strength* $f_n(K)$ or *generalized dielectric constant* $\epsilon_n(K)$ for solids are then introduced in the theory, where K is the momentum transfer. These quantities tend to the usual optical oscillator strength f_n and dielectric constant ϵ_n when K goes to zero. While these quantities can be experimentally derived [127] or approximated with optical quantities, they are less straightforward than for the simple case of negligible momentum transfer. In ref [127] the generalized oscillator strength for transitions in atomic hydrogen, which can be exactly calculated, are shown. It can be seen that the allowed transition (e.g. 1s-2p) probabilities decrease with increasing momentum, while forbidden transitions (e.g. 1s-2s, 1s-3d...) gain some excitation probability.

The fast charged particle theory allows to derive relatively simple formulas to char-

acterize the energy loss in the target (see below), but it gradually breaks down as the electron energy decreases. It is possible at first to compensate by using appropriate corrections, but at some point no general theory can be used. When the velocity of the electron becomes comparable with that of the bound electrons of the atoms or molecules, they can no longer be distinguished and no simple treatment of the problem can be done (the system incident electron + molecule cannot be "factorized" and in a way the problem becomes the treatment of the dynamics of the excited anion [127]). Exchanges of electrons allow transitions like spin-forbidden transitions.

II.2.4.1 Stopping power

The quantity that is used to capture the electron/ion-matter interaction is the stopping power dE/ds, which is the average energy loss of the particle per unit length when it traverses the target (here the ice). For ions, a distinction can be made between the electronic stopping power (resulting from the interaction of the particle with the electrons) and the nuclear stopping power (resulting from the interaction with the nuclei). Electronic stopping dominates for ions with large energies (e.g. MeV energies for protons), while nuclear stopping dominates for lower energies (e.g. keV energies for protons). For electrons, on the other hand, the mass is so small that there is only an electronic stopping. The stopping power depends, in the fast charged particle theory, only on the velocity of the incident particle, but also on the properties of the target (in a non-trivial way which can, as mentioned previously, be related to the optical properties).

Under the full Born-Bethe approximation (energy of the electron E $\gg$ E_{el} binding energies of the atomic electrons), the stopping power of an electron in an atomic target is given by [126]:

$$\frac{dE}{dx} = \frac{2\pi e^4 N Z}{E} \ln \frac{aE}{I}$$

where e is the electron charge, N the number density (atoms per unit volume) of the target, Z the atomic number of the atoms, I the "mean ionization potential" of the target and a $\simeq$ 1.16 a correction factor due to the undistinguishability of the incident and ionized electrons in the case of ionization. This is the non-relativistic equation: for electron energies $<$ 10 keV, the relativistic formula is not needed. In this equation, the properties of the target appear through the atomic number Z, which occurs because of the sum rule on the oscillator strength:

$$Z = \int_0^{+\infty} f_n(E, K) dE$$

and also by the "mean ionization potential" I, whose physical interpretation is explicit through its name and is defined by:

$$Z \ln I = \int_0^{+\infty} f_n(E) \ln(E) dE$$

This quantity is what is difficult to obtain in the Bethe equation. It requires knowledge of the oscillator strength (or more conveniently for solids, the dielectric constant) over the whole range of energies, although usually values experimentally obtained until a certain

energy are extrapolated to infinity when it is reasonable to think that the spectrum is well-behaved. In practice approximate values are often used such as $I = 11.5Z$ for Z $\leqslant$ 12, or tabulated values exist [128].

The Bethe equation shows that, above a few times the mean ionization potential I, the stopping power for electrons basically only decreases up to the limit where the equation is still valid. However it starts strongly deviating from the correct stopping powers at low energies (in fact it becomes negative at some point), for the reasons mentioned that several issues arise in the approximations made. For example, one issue that is straightforward to see is that at some point when the electron energy decreases, some transitions can become energetically inaccessible. The Bethe equation can be seen as a summation over all possible excitations in the medium traversed by the particle (core excitations, valence excitations, and even plasmon excitations in metals for example). Therefore the problem of energetically inaccessible excitations can be taken into account by applying a "shell correction" [126] or by defining effective Z_{eff} and I_{eff} by truncating the above integrals to the maximum reachable energy instead. This is not sufficient, as the fact that the momentum transfer is not negligible in the collision is also a problem [129]. But some approaches still use approximations to derive correction terms to the Bethe equation [131] that can be calculated if the full optical data is known. There are even codes available for calculating stopping powers at low energies when optical constants are known [132].

Another approach for low energies consists in using a semiempirical formula, where a function with appropriate behaviour at low energies is derived that matches the experimental data, but using some theoretical considerations to justify its form. Such is the case of the formula suggested by Joy & Luo [128]:

$$\frac{dE}{ds} = \frac{2\pi e^4 NZ}{E} \ln \frac{a(E+kI)}{I}$$

where all terms have the same signification as in the Bethe equation and k is an appropriately chosen constant for the given target material (k = 0.77 for carbon and $\sim$ 0.83 for various metals). It is more convenient than the lengthy calculations required for the correction terms of other analytical expressions but in the end chosing the right k for a material with no available experimental data seems difficult, although having a wrong k does not seem to affect the results too much [128].

II.2.4.2 Compounds

The Bethe formula was derived for atoms. When considering molecules and condensed materials, it is sometimes simply assumed that there is additivity of the stopping powers of the different constituting atoms (which is called Bragg's rule). Such an approximation works reasonably well, except in some cases [129]. If we keep in mind that the stopping power is basically a summation of the contribution of the different possible excitations of the target, it is evident that there can be large differences between a molecule and the sum of its constituting atoms, as the electronic structures are quite different. Furthermore, in the condensed phase the electronic structure also changes. The additivity rule, for example, works well for air (considered as a mixture of N_2, O_2 and Ar), but fails in the case of water (and there are also differences between gaseous and solid water because their electronic structure are significantly different, as discussed earlier). Resources and

references on this topic can be found on the SRIM webpage[e], which is a website containing a software to evaluate the stopping power of ions in various media (unfortunately not extended to electrons).

A good approach in general would be to evaluate directly the mean ionization potential of the molecular target using its known optical constants: this is typically what has been done for water ice, where reflectivity data is used to derive the dielectric constant using Kramers-Kronig relations, from which the stopping power can be computed, as mentioned previously.

II.2.4.3 Penetration and energy deposition profiles

Aside from the stopping power, we are also interested in the structure of energy deposition in the solid. To characterize the path of an incident electron in the solid, there are at least three different quantities that need to be distinguished, and naming conventions vary. We can define the length of the path of the electron until it is stopped, the vector distance between the starting point and the final point, and the projection of that distance vector on the axis normal to the surface. All three of these quantities have been called *range* in the literature, the latter two sometimes being called *penetration*. They differ because of the non-forward scattering of the incident particle, which could have been neglected for sufficiently fast and heavy particle but is very important in the case of medium-energy electrons. The quantity that we are the most interested in here is the third one, which I will call penetration throughout this manuscript. Indeed, what is relevant for desorption is the distance between the surface and the location of the deposited energy.

The first quantity, the mean path length of the particle in the ice, can be obtained in first order by assuming the "continuous slow-down approximation" (CSDA, whose name is explicit): the mean path length is then given by the integral of the stopping power between 0 and the initial energy of the particle. The other quantities are related, but they require knowledge of the angular distribution of both elastic and inelastic scattering. Usually they are experimentally determined (e.g. [133, 135]) or calculated using Monte-Carlo simulations (e.g. [134]), and fitted with a simple power law $r = \alpha E^x$, (r being one of the ranges mentioned ealier) with x varying between a bit less than 1 and 2 most of the time.

Another closely related quantity is the *mean energy deposition depth*, which does not exactly correspond to the mean penetration depth and is smaller, because the energy is not equally deposited along the path of the electron. The amount of energy deposited as a function of depth is an energy deposition profile, which is also interesting to know. It has been calculated alongside the other quantities in Monte-Carlo simulations for some solid simple elements (e.g. N_2, Ar...) and 1-10 keV electrons [134]. The energy deposition increases with depth at first then decreases to 0. The shape for all the elements and electron energies of ref [134] were fitted with gaussians, which in practice are truncated on the surface side at around half the maximum.

Some concrete numbers are given for solid N_2 in fig. II.9. In fig. II.9a, the stopping power as a function of electron energy for solid N_2 is shown for the Bethe and modified Bethe equations introduced above (with parameters I = 83 eV and k = 0.8). The measured "effective" stopping power from ref. [133] is also shown, but it should be noted that the

[e] http://www.srim.org/SRIM/Compounds.htm

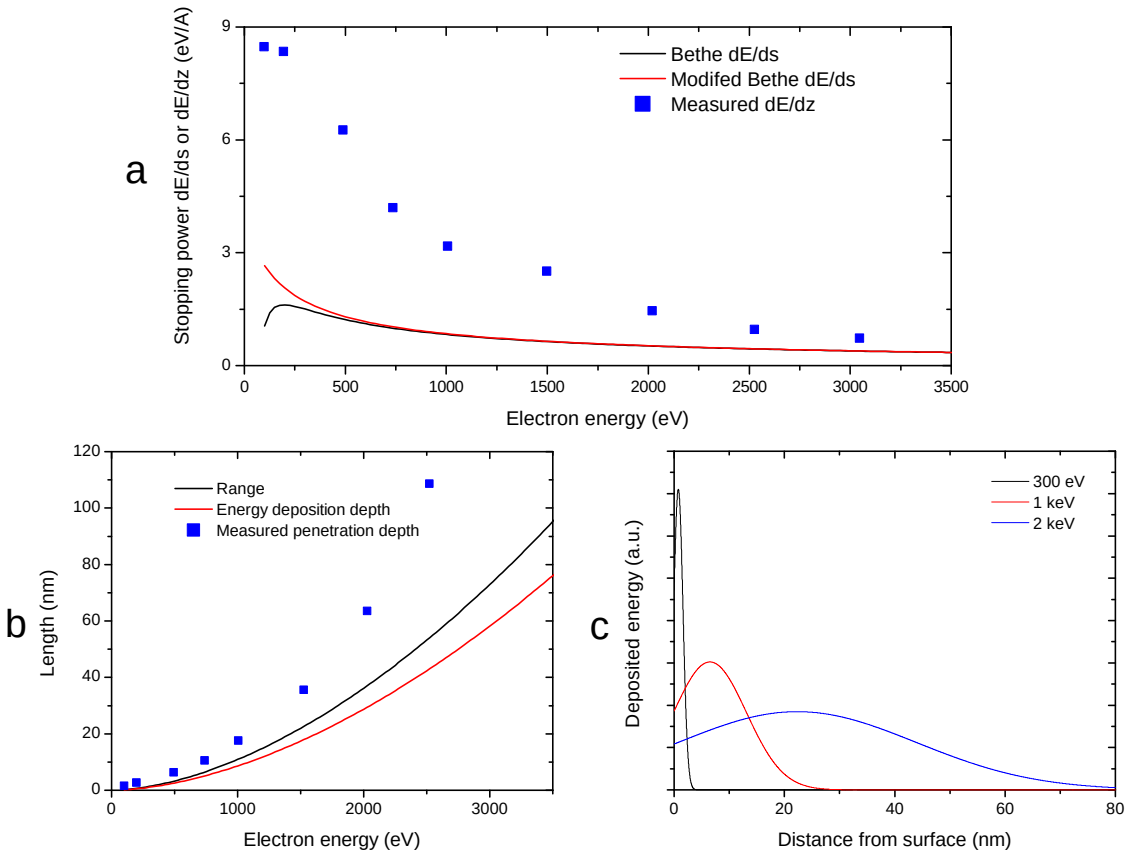

Figure II.9: Stopping power, range and energy deposition profiles of electrons in solid N_2. **a.** Calculated Bethe (black line) and modified Bethe (red line) stopping power dE/ds, for I = 83 eV and k = 0.8. Blue dots: measured stopping power dE/dz from [133]. **b.** Calculated range and mean energy deposition depth using the parameters from [134], and measured penetration depth from [133]. **c.** Energy deposition profile in the ice for 300 eV, 1 keV and 2 keV electrons. Obtained using parameters calculated in ref. [134].

disagreement between this measurement and the theory does not mean the theory is wrong: the quantities are different. The "effective" stopping power is dE/dz, i.e. relative to the penetration of the electron in the ice on the z coordinate. The calculated stopping power on the other hand is dE/ds, with s the coordinate of the path taken by the electron. Considering electrons at these energies do not have straight paths, dE/dz has to be higher than dE/ds. In fig. II.9b, the calculated range and mean energy deposition depth as a function of electron energy are displayed, using the parameters of the Monte-Carlo simulations of ref. [134]. The measured penetration depth of ref. [133] is shown and is once again relative to the z coordinate. In fig. II.9c, the energy deposition profiles for 300 eV, 1 keV and 2 keV electrons are shown, using again the parameters of ref. [134].

II.2.4.4 Low-energy (< 20 eV) electrons

When electrons have a kinetic energy lower than 20 eV, specific processes start coming into play. The electron can still undergo an inelastic collision with a molecule, generating a valence excitation or ionization, but the interaction cross-section as a function of electron energy will be more structured than for higher energy electrons because the energy is close to resonance. But more importantly new interactions arise, such as electron attachment. Electron attachment is a resonant effect, only occurring for specific electron energies, where a transient anion is formed. This transient anion can undergo dissociation: we then speak of Dissociative Electron Attachment (DEA), and both an anion and one or more neutral fragments are formed this way. The transient anion can also undergo autodetachment of an electron and dissociate into neutral fragments or leave a neutral molecule in a highly vibrationally excited state. If dissociation occurrs for molecules on a surface, some of these fragments, whether neutral or anions, can desorb. Desorption induced by low energy electron resonant attachment is a widely explored topic within DIET studies [136].

II.2.5 X-ray photons: core excitations and Auger decay

For this section, the textbook by Stohr [137] and some book chapters in ref. [138], among others, were particularly useful.

Soft X-ray photons interact with molecules much in the same way than UV photons: they cause electronic transitions. However, the electrons involved are different because they are core electrons, the innermost electrons of molecules with binding energies much larger than for valence electrons. Core electrons are mostly atomic in nature: they can be attributed to a specific atom and the electron density of the molecular orbital is almost entirely localized on that atom. For example in the case of CO the innermost 1σ orbital is basically the 1s oxygen atomic orbital, with a binding energy of 542.4 eV typical of the $\sim$ 540 eV binding energy of oxygen in any molecule in any form, while the 2σ orbital is basically the 1s carbon atomic orbital, with a binding energy of 296.2 eV again typical of carbon. Because of their atomic, localized nature the binding energy of core electrons does not vary much from one environment to another, but the few percent of variation ends up being several eVs, which is very well measurable and at the basis of commonly used spectroscopy techniques (in surface science in particular) to characterize molecules, adsorbed molecules, solid surfaces, etc...

Core-holes are short lived: the lifetime of the O 1s core hole is about 4 fs. The decay can be a radiative decay, where the excited electron (in the case of core excitation) or a valence electron fills the core hole and the excess energy is emitted in the form of an X-ray photon, but it is not the dominant decay mechanism in the case of low Z atoms like the ones we are dealing with here. Instead 99% of the decay (for oxygen core holes) occurs through a mechanism called Auger decay. Basically, the principle of Auger decay is that there is an electronic rearrangement with a valence electron filling the core hole, and the excess energy left goes into ionization of another valence electron, which carries away the rest of the energy in the form of kinetic energy. The process is sketched in fig. II.10. Some molecular orbitals of water, used as an example here, are represented. Two cases are considered: core ionization (top of the figure) or core excitation. In the case of core ionization, the decay process is often called "normal" Auger decay: after the photon

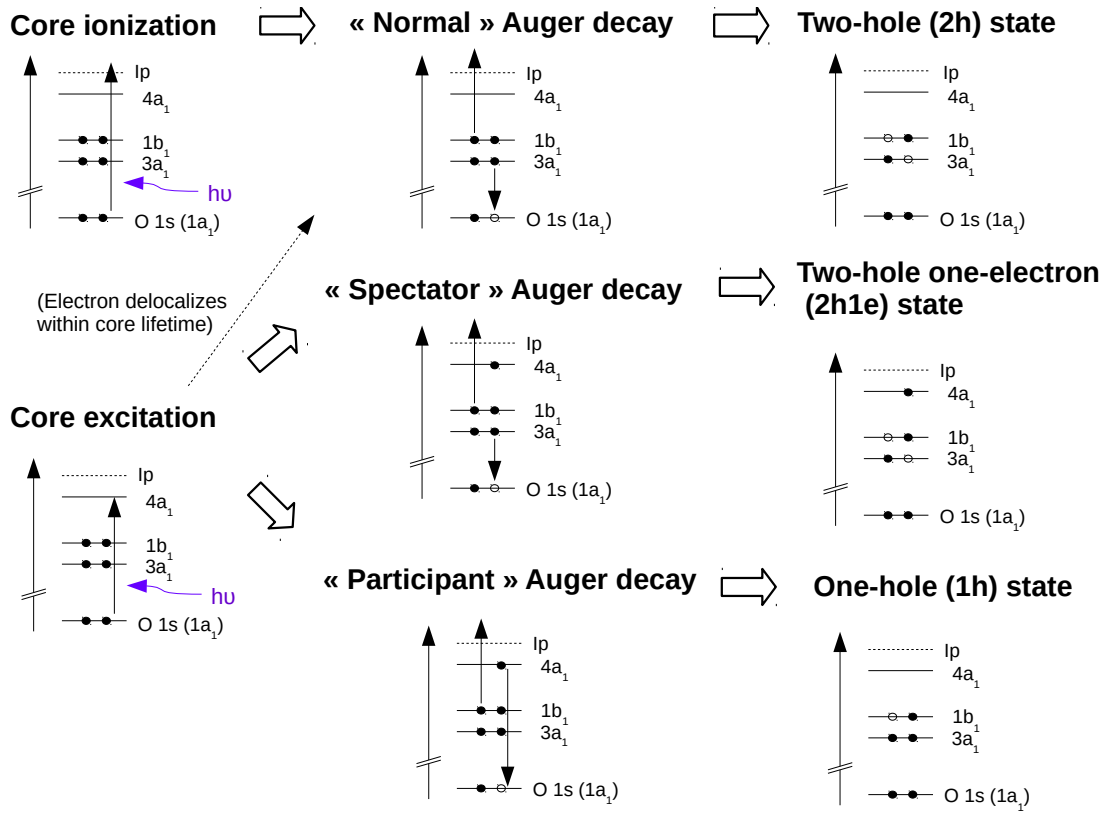

Figure II.10: Schematic representation of the Auger decay process. The example is given using the molecular orbitals of H_2O: the $1a_1$ is the core oxygen orbital, the $1b_1$ and $3a_1$ are occupied valence orbitals and the $4a_1$ is an empty molecular orbital. "Ip" indicates the ionization threshold. Two cases are distinguished, core excitation and core ionization. The valence holes were arbitrarily chosen: other possible final states with different valence holes are possible. See the text for more details.

ionizes an O 1s electron (1st step), an electron from the valence $3a_1$ orbital fills the hole while an electron from the valence $1b_1$ orbital is ejected with $\sim$ 500 eV kinetic energy (2nd step). The ejected electron is called the Auger electron. The final state has two holes in valence orbitals and is therefore called a two-hole (2h) state, or equivalently a doubly-ionized state. The second case is core excitation, where in the figure the core electron has been promoted to the $4a_1$ initially empty molecular orbital. From there, there are two possibilities, which distinguish whether the excited electron in the initially empty orbital is involved in the Auger decay or not. If it does not and two different valence electrons, from initially occupied valence orbitals, respectively fill the hole and are ejected, this is a "spectator" Auger decay. The final state then has two holes in the initially occupied valence orbitals and one electron in an initially empty orbital: it is a two-hole one-electron (2h1e) state, equivalently a satellite state (excited state of the singly charged ion H_2O^+ here). If the excited electron is involved in the Auger decay, then it is a "participant" Auger decay and the final state will simply be a one-hole state (i.e. a simple H_2O^+ ion, although possibly in an excited state as well if the hole is not in the HOMO).

These final states lie typically about 20-70 eV above the ground state (in the case of water). All three types of Auger decay can result in all energetically accessible combinations of valence holes and electrons in respectively 2h, 2h1e and 1h states. The highest energy final state in the case of water would be the $(2a_1)^{-2}$ double ionization of the deep valence $2a_1$ orbital, around 70 eV in direct XUV excitation, which is energetically accessible and still leaves plenty of kinetic energy in the Auger electron. However these decay pathways do not all have the same probability to occur. Each final state corresponds to an Auger electron with a slightly different kinetic energy, which means that kinetic energy analysis of the Auger electrons allows to estimate the relative probabilities of each final states.

In addition to "simple" core ionization and core excitation, more complicated multielectron excitations are possible, just like in the valence regions: we can have doubly excited states (where a core and a valence electron are simultaneously excited), excitation of a valence electron alongside core ionization, ionization of a valence electron alongside core ionization... The latter two processes are sometimes respectively called "shake-up" and "shake-off" processes. These three possibilities, after Auger decay, can respectively yield 3h2e, 3h1e and 3h final states which are even more highly excited states than the previously mentioned ones. Even multielectron excitations involving 3 electrons are possible (e.g. [139]).

In the condensed phase, the release of the Auger electron has important consequences because it will undergo inelastic collisions, just like the primary electrons considered in the previous section - we are thus reduced to the same problem, with the exception that the electron is generated directly inside the ice. The Auger electron carries most of the energy of the initial photon ($\sim$ 500 eV for O 1s), which makes its propagation in the ice and the subsequent cascade of secondary events (ionizations, secondary electrons and valence excitations) important for the problem of subsequent desorption. The net result of a soft X-ray absorption event is therefore one possibly highly excited ion, and the propagation of an energetic electron in the solid creating many secondary events.

II.2.5.1 EXAFS, Shape resonances

The notions of EXAFS and shape resonances will be useful for understanding absorption spectra in the X-ray domain. EXAFS (Extended X-ray Absorption Fine Structure) is a technique for the derivation of structural information from solids exploiting features that are present in some spectra well above (>50 eV) the edge. To understand the principle of EXAFS, we first need to recall that the probability that a molecule/atom absorbs a photon to undergo an electronic transition depends on the transition moment and the wavefunctions of the initial and final electronic states. Well above the edge, when the transition is a core ionization and the photoelectron has a high kinetic energy ($>$ 50 eV), the final state wavefunction is basically a spherical free electron wave when the molecule/atom is isolated. Now, consider the condensed phase where the molecule/atom is surrounded by other molecules/atoms. The spherical wave of the photoelectron is scattered by the surrounding molecules/atoms, and the actual final wavefunction becomes the superposition of the incident and scattered waves. Since the final wavefunction is changed, the transition probability is changed as well. How the probability is affected depends on the wavelength of the free electron wave which depends on the photoelectron kinetic energy,

and therefore on the initial photon energy. In a simple case, this creates in the photon absorption spectrum oscillations around the expected "free molecule" absorption intensity. Scattering also depends on the distance between atoms/molecules in the condensed phase, and therefore these EXAFS oscillations contain information about the intermolecular distances in the solid. A Fourier transform of the oscillations can be used to retrieve these distances. Applied to the case of water ice [140], EXAFS allows to find the O - O distance of 2.76 Å. This will be discussed again in chapter VI. Information can also be extracted from oscillations that occur closer to the threshold, but it requires a more complex theory and multiple scattering is involved.

A shape resonance is the term used to designate some specific broad resonances that appear above ionization thresholds in molecular spectra. There are two conceptual frameworks to understand shape resonances [141]. A perhaps more usual one is to see a shape resonance as a "quasi-bound state" that occurs when there is a barrier in the potential seen by an electron escaping a molecule. Under some conditions, the electron can stay trapped in a state with energy above the ionization energy for a significantly long time before tunnelling out. This gives rise to a resonance peak in the absorption spectrum. Another point of view is linked with the previously described EXAFS phenomenon. If we consider that a free electron wave can be scattered by surrounding molecules, we could also consider that even in a free molecule, a photoelectron wave coming from a given atom (core electrons are well localized on specific atoms) could be scattered by another atom of the same molecule, which could similarly change the transition probability. Of course the problem is much more complicated than the EXAFS problem, especially shape resonances do not occur very high above threshold and simple approximations for higher energy photoelectrons do not apply. Distinguishing actual shape resonances from highly excited electronic states is not trivial [141] and was the object of considerable debate in the literature. A shape resonance is encountered in the CO O 1s edge absorption spectrum, as we will see in chapter VI.

II.3 Historic models of photon- and electron-induced desorption

In this section, I will give an overview of some mechanisms that were proposed to explain EID and PID phenomena when the field of Desorption Induced by Electronic Transitions (DIET) was particularly active. As mentioned in chapter I, EID [68] and PID [142] studies were for a long time scattered and not well defined. The independent field of study and its associated community started growing with the introduction of the first conceptual framework which was the MGR model, backed up by precise experiments. A number of reviews [143] and historical recollections [144, 145, 68] exist on the topic. Additionally, a lot can be found in the first proceedings of the DIET conferences that started taking place in 1983 [146, 147, 148, 149, 150].

II.3.1 The MGR model

The Menzel-Gomer-Redhead model was proposed around 1964, inpendantly by Menzel and Gomer [151, 152] on one side, who were interested in a fundamental understanding of charge transfers on surface, and Redhead [153, 154], who was trying to solve issues related to measurements of pressure in ultra-high vacuum.

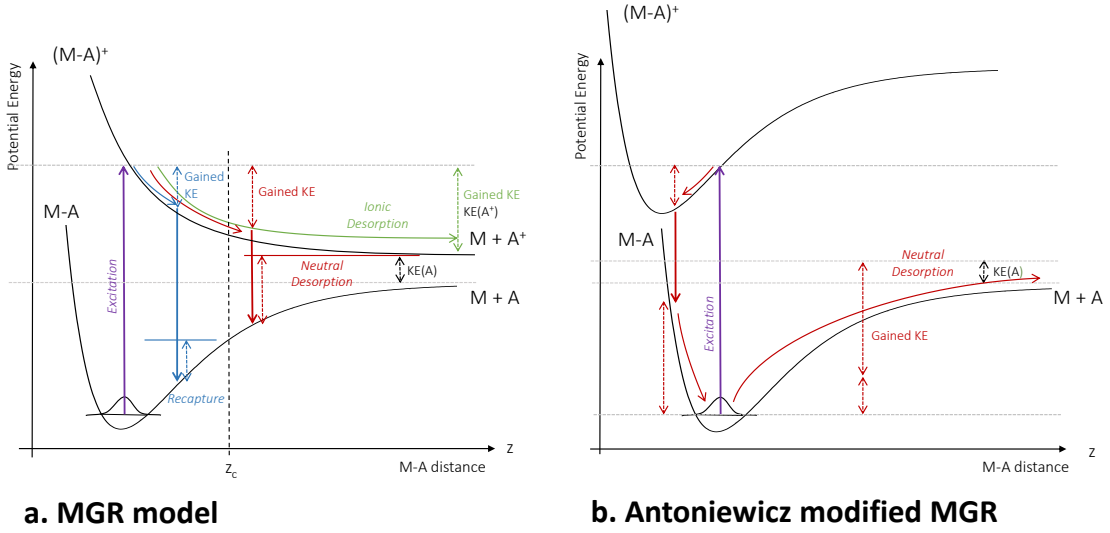

Figure II.11: **a.** Schematization of the MGR model. The ground and ionic state potential curves of the metal-adsorbate (M-A) bond are represented, with the latter being dissociative. After vertical excitation (violet up arrow), there are three possible outcomes depending on whether reneutralization (vertical down arrow) happens and when: if it does not happen the outcome is ionic desorption (green); if it happens after a critical distance z_c, neutral desorption happens (red); and if it happens before, recapture happens (blue). The balance of the kinetic energy gains are indicated in the different scenarii. **b.** The MGR model adapted by Antoniewicz to explain neutral desorption through a bound ionic state. Only neutral desorption is shown, but recapture can also happen in this configuration depending on when the excitation is quenched.

To give a little context, this model arose to try to account for the observed differences in ions desorbed by electron bombardment of chemisorbed molecules (mostly on metals) and the corresponding ion creation by electron impact on free molecules. The most important observation was the very small desorption cross-section of ions, but there were also differences in electron energy thresholds, branching ratios, etc. Also it seemed cleared that most of the desorbed molecules were neutral molecules and not ions.

The principle of the MGR model is sketched in fig.II.11a using potential energy curves with the coordinate being the surface-adsorbate distance. The first step is that electron impact leads to a Franck Condon transition from the ground state to a repulsive ionic state. The exact nature of the states being excited is left unsaid. This transition leads to nuclear motion of the ionized adsorbate away from the surface, which would lead to ion desorption with a cross section close to gas phase processes (10^{-17}-10^{-16} cm^2) if it were not for the second step of the process: electron transfer from the metal to reneutralize the ion, going back to the ground state curve. The outcome then depends on when the reneutralization occurs: if the adsorbate has acquired sufficient kinetic energy, it will escape the surface as a neutral molecule, otherwise it will be recaptured. A critical distance z_c can be defined on the surface-adsorbate coordinate after which reneutralization will lead to desorption. The same idea also applies for excited states below ionization, except ions are no longer a possible desorption product.

This model elegantly explains the experimental facts presented before, with the ion and neutral desorption cross sections depending on the rate of reneutralization. It applies well to a number of specific systems, especially the case of chemisorbed molecules on metals for which it was conceived. Detailed versions of the model can account for ESDIAD (Electron Stimulated Desorbed Ions Angle Distribution), a technique which was developed in the 70s where the angular distribution of desorbed ions is correlated to the orientation of bonds on the surface. The model also predicts an isotope effect: nuclear motion of heavier isotopes of a given adsorbate is slower, and therefore the recapture rate should be higher and the desorption cross section lower. In some experiments quantitative agreement with the model on cross section ratios is found.

But beyond these considerations, the MGR model introduces basic important ideas for understanding how electronic transitions cause desorption. The first one is that *potential electronic energy* can be converted into *kinetic nuclei energy* on repulsive parts of potential energy surfaces. The second one is that the lifetime and dynamics of excited states plays a very important role.

The first idea is quite general: we can basically have desorption whenever we have an electronic state that is repulsive relative to the surface - adsorbate coordinate, even in molecular ices. The problem is whether such an electronic state actually exists. In the case of physisorbed molecules adsorbed on metals, Antoniewicz [155] pointed out that ionic states should instead be attracted to the surface by the image potential, but that this does not preclude desorption: the ion acquires kinetic energy also by moving towards the surface, and when it is neutralized it finds itself on the repulsive part of the ground state potential and desorbs if sufficient kinetic energy is acquired. This is schematized in fig. II.11b. It is worth noting that this mechanism can readily be included in the frame of the MGR model: rather than the repulsive nature of the electronic state relative to the surface-adsorbate coordinates, what is important is the differences in equilibrium position of the ground and excited states that set the nuclei in motion.

II.3.2 Non-MGR models

Various models have been proposed to explain specific desorption experiments that deviate more or less from the MGR picture. Where the models are the most different are the cases that also deviate significantly from the systems for which MGR was initially conceived (chemisorbed molecules on metal surfaces). For example, a mechanism was proposed by Pooley [156] and Hersch [157] to explain defect formation in alkali halide ionic solids, which can apply to the desorption of halogen atoms when occurring near the surface. The idea is that excitons created in the solid localize in the form of an electron bound in a large orbit around an $(X)_2^-$ center (where X is an halogen atom), where the two halogen atoms have become significantly closer than in the normal lattice. When the exciton recombines radiatively, the two X atoms find themselves much closer than they should and repel each others, and the kinetic energy acquired leads to desorption.

This picture looks a lot like an Antoniewicz mechanism: two atoms get close in an excited state potential curve and when going back to the ground state find themselves on a repulsive part of the ground state potential. The essential difference is in the quenching step: the exciton decays radiatively, on a timescale completely different from the electron transfer from a metal to an ionized chemisorbate (which was the original point of the MGR

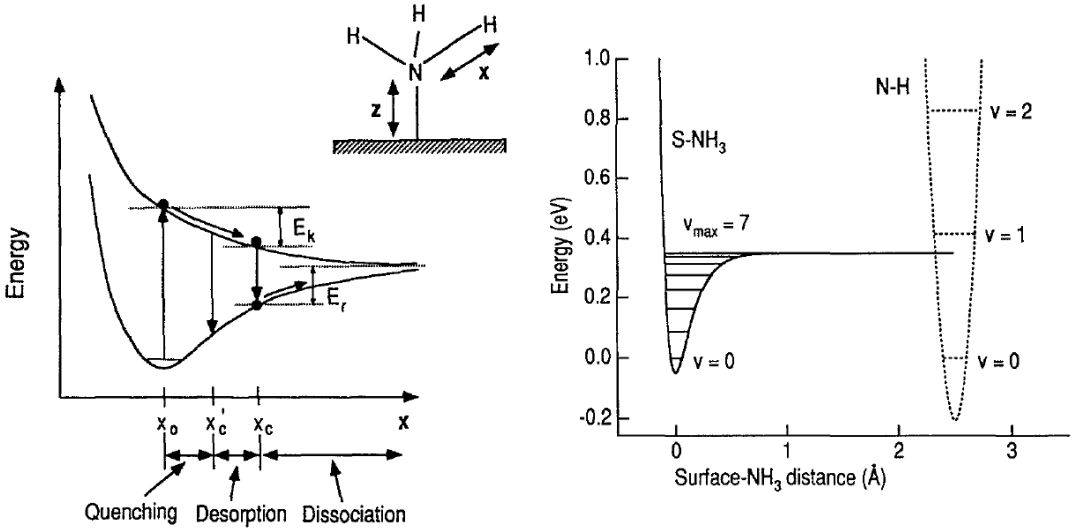

Figure II.12: Principle of the desorption mechanism of NH_3 on GaAs. Adapted directly from ref. [159]
. See the text for details on the mechanism.

model on the MG side: proving that very fast transfers occurred on metal surfaces). One could nonetheless argue that, in a broad sense, this is still an MGR-like model.

One model that had a lot of historical importance and is non-MGR is the Knotek-Feibelman model [158]. It was originally presented to explain desorption of positive ions (O^+) from ionic solids such as TiO_2. The desorption of O^+ is particularly counter-intuitive since in the solid, oxygen exists in the form of O^{2-}. What happens is that the Ti^{4+} is core-excited, but cannot undergo Auger decay because it has no valence electrons left. Instead an interatomic Auger decay happens and several electrons are stripped from the neighbouring O^{2-} which becomes O^+. An initially negative ion becoming positive in an ionic solid will feel a reversed electrostatic potential which will expel it.

This mechanism, although it fully applies only mostly to these type of ionic solids, pointed out the importance of core excitations, which despite having much lower cross sections than valence excitations, can lead to specific mechanisms that may dominate the desorption process. Another important development linked to core excitation is the importance of two-hole excitations (such as the ones obtained after Auger decay), which again are much less likely than one-hole excitations by direct excitation but also tend to be much longer lived and localized. More detailed discussions on these topics exist in the various articles of the proceedings of the DIET I conference [146].

There is another important class of mechanisms that was suggested for example in ref. [160], which is the nonradiative conversion of electronic energy into vibrational modes and subsequent coupling to desorption, taking inspiration from the mechanisms of gas phase dissociation of large molecules. This type of mechanism is also different from MGR type mechanisms. To illustrate a case, we can discuss a study of NH_3 desorption physisorbed on GaAs(100) by Zhu et al. [159]. In this study, the authors found a strong isotope effect when comparing the desorption of NH_3 and ND_3. The effect is too strong to be explained

by a regular MGR mechanism. Instead, the authors suggest a mechanism which is based on the vibrationally excited molecules that result from quenching of the electronically excited state. If sufficient vibrational excitation exist in the molecule, coupling to the surface-adsorbate bond can cause desorption. The excited state is dissociative relative to the internal bonds of the molecule, but can be quenched before complete dissociation, leading to high vibrational excitation of the molecule depending on how much the N-H bond has already been elongated. A "critical distance" on the potential energy surface is introduced similar to the one of the MGR mechanism (see fig. II.12), except that now this critical distance corresponds to the N-H distance required to have sufficient vibrational excitation in the quenched molecule. This critical distance is then proportional to the reduced mass of the N-H bond, resulting in a predicted isotopic effect involving the square root of the H/D ratio, instead of the square root of the NH_3/ND_3 ratio. This mechanism is interesting because it implies a sufficiently strong coupling between the internal vibration modes of the molecule and the surface-adsorbate bond, something which is backed up by experiments on IR desorption of NH_3 (i.e. by direct vibrational excitation of the molecules) [161]. Coupling can lead to excitation of substrate phonons (resonant heating) or to resonant or phonon-assisted tunnelling from the vibrationally excited state to a desorption continuum state. Zhu et al. [159] argue the latter case for NH_3 on GaAs and discuss in detail the energetics of this precise system.

The difference between this type of mechanism and MGR-type mechanisms is the absence of the concept of motion of the molecule being obtained on the repulsive parts of potential energy surfaces (although there is still nuclear motion in the excited dissociative state). Instead desorption is obtained by directly tunnelling into a continuum state of the physisorption potential well, as illustrated in fig. II.12. The quenching of the excited state is also very different in nature from the initial MGR.

II.4 A case study: desorption mechanisms from rare-gas solids

In this section, I will present the desorption mechanisms that have been elucidated for the case of rare-gas solids (RGS). RGS are the only systems close enough to molecular solids for which it can be said that the problem of desorption induced by electronic transitions has been mostly "solved", and the aim of this description is to see on what grounds this has been possible. It is also a good illustration of the principles developed previously in this chapter, as well as a source of inspiration for mechanisms in other systems.

II.4.1 Electronic excitations in RGS: excitons

Understanding the desorption mechanisms necessarily requires a very good understanding of the electronic excitations that are the initial point. While a lot is known about electronic states of molecules in the gas phase, the specificities of their condensed phase counterparts have not always been very much studied. The comprehension of desorption in RGS relies on the interest that the valence electronic excitations in this system - the RGS excitons - have sparked from very early on.

All four rare gases (Neon, Argon, Krypton and Xenon) in their condensed form are solids hosting excitons, in the sense commonly found for semiconductors and insulators of bound states appearing in the spectrum as a series of sharp peaks converging towards

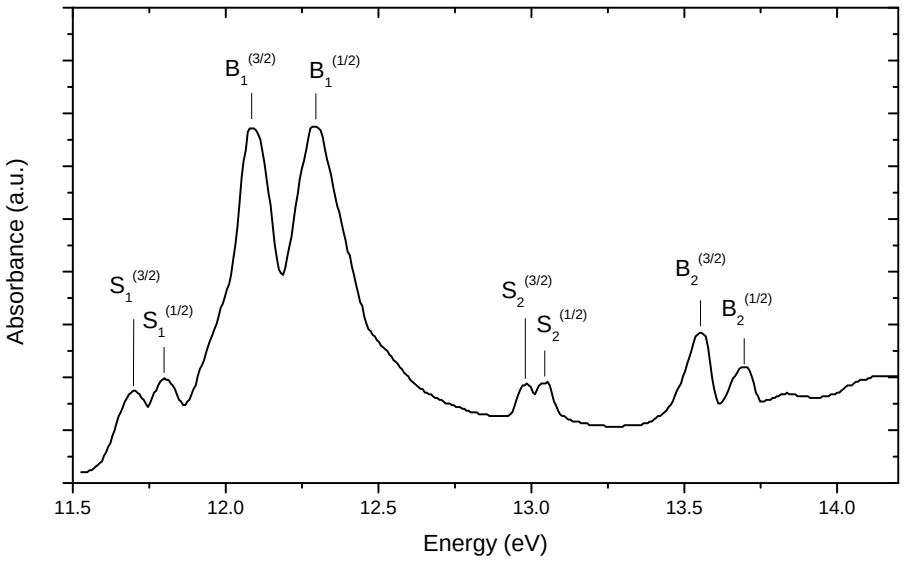

Figure II.13: Absorption spectrum of solid argon, adapted from ref. [165]. A thin film (40 Å) is used, which allows to see the surface excitons. The notation for the attribution of the peaks is B for a bulk and S for a surface exciton, the subscript is the number n in the exciton series and the superscript is the spin state.

the conduction band. RGS are a good example of the principles described previously for the fate of electronic states when going to the condensed phase: the first exciton of the series is intermediate between a Frenkel and a Wannier exciton, inheriting character from the corresponding gas phase Rydberg state and blue shifted compared with it, while the higher ones are fully Wannier excitons replacing the higher Rydberg states of the isolated atom. A large spin-orbit splitting makes it so that there are two series of excitons, singlet and triplet ones. These excitons can migrate in the solid. A lot of information on the properties of the RGS excitons can be found in a number of reviews [80, 162, 163, 164].

In addition, for each "bulk" exciton there exists a corresponding surface exciton, which only propagates at the surface. The surface also acts as a "trap" for bulk excitons because the energy of the surface exciton is lower than the bulk one. The bulk exciton can convert to a surface exciton but it cannot go back the other way. This is also a good illustration of the surface electronic state being somewhere "in-between" the bulk and the free molecules - in this case the blue shift compared with gas phase is less pronounced at the surface because repulsion by the neighbours due to the large radius of the state is reduced. Simultaneously the validity of this simple picture is challenged by the fact that in Kr and Xe, the first surface exciton is actually lower in energy than the corresponding gas phase Rydberg.

An example is given in fig. II.13 with the absorption spectrum of a very thin film of solid Argon adapted from ref. [165]. The film is thin enough to see the contributions of the surface excitons. The attributions of the different excitons are made on the figure: we see the n = 1 and 2 (first and second terms) of the four distinct series of surface and bulk, triplet and singlet excitons. Just like with Rydberg states, the intensity of the states decreases very rapidly with n. The cross-section of the first exciton is very high, around

~ 1 Å^2, compared with that of the electronic states of the solids we will see that tend to be around 0.1 Å^2 (the oscillator strength is not necessarily as different: the exciton peak is quite sharp).

Identifying the condensed phase electronic states and their nature is an important first step in the understanding of electronic desorption, but an even more important aspect is the dynamics of the excited state. Fortunately there is also a lot of information on this for the RGS excitons. Excitons are commonly associated with the idea of a delocalized excitation: the quasi-particle that is created propagates through the crystal as a wave. However, an exciton can also be localized by "trapping" in various manners. A trapped exciton is not necessarily immobile: the excitation can move by "hopping" from site to site in a diffusion-like behaviour. The existence of one or the other of these type of excitons will depend on the characteristics of the materials. In the molecular solids that we will consider later, in particular the amorphous ones, there is little evidence of excitation transport across the solid (which does not mean it does not exist), except perhaps in water ice to some degree. If we consider the valence electronic excitations in these solids as excitons, they are basically trapped excitons, which perhaps can migrate on short distances. In RGS though, both types of excitons coexist. The initial "free exciton", in a perfect crystal, can self-trap in two different forms. The first one is localization by inducing a local deformation of the lattice surrounding a specific excited atom, with a repulsion of the neighbouring molecules due to the spatial extent of the excited state. This creates a "cavity" with an excited atom at the center. The second one is the creation of a "molecular exciton" which is basically an excimer molecule inside the solid. Both these trapped excitons have energies lower than the free exciton and therefore the trapping cannot be reversed. Most of the studies on these different forms of the excitons in RGS have been done using luminescence techniques.

In addition to these considerations which are valid for a perfect crystal, defects and impurities are also exciton traps, and their density will influence the transport of excitons. Consequently the measured values for the diffusion length of excitons in the different RGS vary over orders of magnitude depending on the technique used to measure it and even for the same technique, and a lot of these discrepancies can be ascribed to different sample preparation. Obtaining a recipe for crystals that are reproducible from one lab to another seems to be a difficulty that illustrates well how the lack of proper control on the studied system is a problem.

The surface is also a form of "defect", and bulk excitons that reach the surface can be trapped there in the form of surface excitons, which is important for desorption.

II.4.2 Desorption mechanisms

In the case of the RGS, understanding of the dynamics of the excitons is already a long step towards understanding the electronic desorption mechanisms, because the two mechanisms that have been identified are associated with the two types of self-trapped excitons that have been presented before.

Consider first self-trapping as an excited atom in a cavity, and what happens when trapping occurs at the surface. As sketched in fig. II.14a, the repulsion forces exerted between the excited atom and the neighbours now will push the excited atom away from the surface. This has been called the "cavity ejection" mechanism. This mechanism

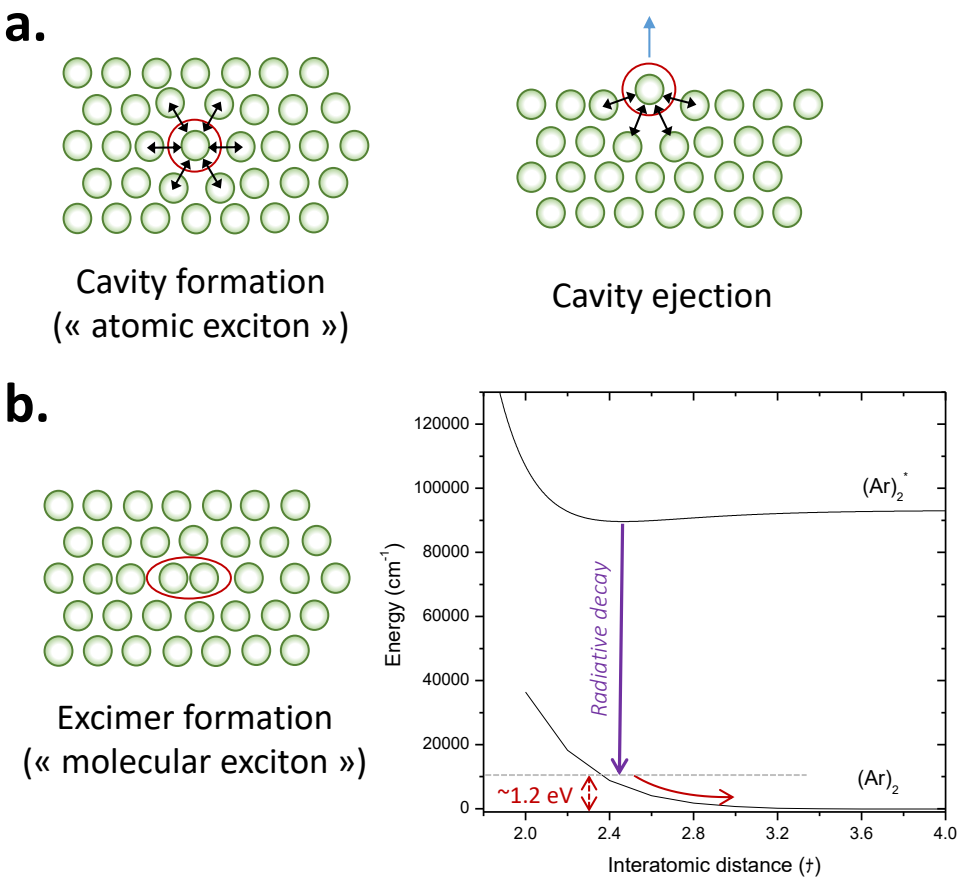

Figure II.14: Illustration of the desorption mechanisms in rare-gas solids. **a.** On the left, the formation of a cavity by self-trapping of an exciton as an "atomic exciton" in the matrix is illustrated. When this happens at the surface (right of the figure), the excited atom is ejected by the repulsive forces. **b.** On the left is shown the trapping of an exciton by formation of an excimer ("molecular exciton") in the matrix. On the right, the gain of kinetic energy of the two atoms on the ground state potential energy curve of the pair, after radiative decay of the excimer, is illustrated in the case of Ar (the curves come from the same references as in fig. II.4a).

corresponds to the first case presented in section II.1: the excited state is repulsive with respect to the atom - surface coordinate, which trivially leads to desorption as long as the excited state is not quenched rapidly. An important consequence of such a mechanism is that the atom desorbs in an excited state. One way to detect the desorption of excited atoms is if their lifetime is long enough (they are then called "metastable" particles) to reach a detector such as a microchannel plate set such as only atoms or molecules with sufficient internal energy can trigger a signal [166, 167]. But the technique that really allowed the study of this phenomenon in detail is the detection of luminescence. Ejected excited atoms decay radiatively, producing luminescence lines that are very well distinguishable from the radiative decay of the solid state excitons [168]. It was soon realized that this mechanism is most efficient in Ne [169, 170], works in Ar but not in Kr and Xe. The possibility of this mechanism is linked with the positive or negative value of the "electron affinity" of the solid. The repulsion energy of the cavity ejection mechanism comes from electron repulsion forces between the excited electron and the surrounding atoms. But there is a counter-acting force which comes from polarization of the dielectric medium by the excited atom. The sign of the sum of the two energies, the positive electron repulsion energy and the negative polarization energy, needs to be positive for the ejection mechanism to be possible (in other words, for the excited state surface potential to be repulsive relative to the atom-surface coordinate). This was confirmed precisely by also studying this mechanism for mixes of rare gases [171].

The second desorption mechanism is based on the "molecular" self-trapped exciton, i.e. the formation of an excimer in the solid. In an excimer the R-R equilibrium distance between the two R atoms is much shorter than in the ground state for the solid. The consequence is that when this excimer radiatively decays back to the ground state, the two R atoms repel each others (in other words, we fall back on a repulsive part of the ground state potential curve of the R-R pair). This is illustrated in fig. II.14b, with the potential curves of the Ar-Ar dimer. When this happens at the surface, the two atoms acquire significant kinetic energy and can therefore desorb. The kinetic energy involved has been predicted from the potential energy curves of the R-R pair (e.g. on fig. II.14b: about 1.2 eV is shared between the two Ar atoms) and from dynamics simulations and was compared with the measurements of the kinetic energy distributions of the desorbed atoms from the different RGS, finding very good agreement (a distribution of kinetic energy with a component centered around 0.6 eV for desorbing Ar atoms, for example) and demonstrating the mechanism [172, 173]. It is worth noting that this mechanism is quite close to the Hersch-Pooley mechanism for alkali halides mentioned previously, and follows a principle similar to the Antoniewicz mechanism, as already discussed.

There is a third "mechanism", identified for example by a tail of low kinetic energy desorbed atoms in the kinetic energy distributions, which consists in indirect sputtering of neighbouring atoms because of, for example, the excimer decay mechanism occuring in the sub-surface regions, triggering collisions around the surface.

The investigation of these desorption mechanisms has been aided a lot by the use of synchrotron radiation for selectively exciting precise excitons, but a lot of studies have also been made with other types of excitations such as energetic electrons [174, 175], low energy electrons [176], energetic ions [177, 178], X-rays [179]... Complications in these basic mechanisms occur when we have to also take into account higher energy excitations such as ionizations (creation of Ar^+, Ar_2^+ pairs...) and core excitations, and I have

not mentioned these here. The point is that a good understanding of the electronically induced desorption from the rare gas solids has emerged progressively because of a number of points:

- Thorough understanding of the excited states of the RGS and their dynamics
- The use of varied sources of excitations (photons, electrons, ions)
- The study of a variety of systems that are not restricted to the simple pure RGS: rare gas alloys, but also introduction of other molecules (e.g. [180, 181])
- The variety of techniques of investigation: looking at the different desorbed species (excited or ground state), angular and kinetic energy distributions, luminescence phenomena, and the very important use of dynamics simulations to compare with the experiments.

It is clear that the "elucidation of the desorption mechanisms" requires an approach from multiple angles to slowly erode the lack of understanding and progressively make a clear picture emerge.

II.5 Desorption from molecular ices

In the previous sections, I have presented some desorption mechanisms from the literature for molecules adsorbed on surfaces and for the rare-gas solids, these latter bringing us closer to actual molecular ices. I will present what is already known from the literature on the desorption mechanisms of some specific molecular ice systems in the relevant sections of the following chapters. Here I would like to give some general considerations on desorption from molecular ices.

How much can we transfer knowledge obtained on well-studied systems like the ones for which MGR-type mechanisms were developed (chemisorbed and physisorbed molecules on mostly metal surfaces, in particular) or rare-gas solids? Molecules adsorbed on surfaces are fairly different from molecular ices. First because the electronic structure may be significantly modified by interaction with the metal, but even when it is not the case the binding energies are different, the quenching of the excited state is different (and the lifetime longer for ices), etc... Rare-gas solids are closer but first, they are atomic and not molecular systems, and second they have some peculiar specificities.

First we can mention that binding energies in molecular ices are lower than for molecules adsorbed at surfaces. The absolute yields are therefore often higher, but this also has consequences on the possible mechanisms. Going back to the mechanism for NH_3 on GaAs desorption mentioned in section II.3.2 : the idea of tunnelling into a continuum of the physisorption well works here because the energetics of the system are such as to allow this process. A priori knowledge of a good coupling between the vibrational modes and surface-adsorbate mode is required to permit the suggestion of this mechanism. Coupling between vibrational modes and intermolecular modes in molecular ices should be weak, considering the gap in energy.

This is an illustration of how generalization of a previously proposed model to other systems than the one it was developed for may be difficult because the details of each sys-

tem matters. The same issue arises for MGR-type model which have for basic assumption a certain configuration of potential energy curves.

Another limit of the previously mentioned mechanisms is that the simplified picture of a single excited molecule interacting with a rigid surface is not really valid. The absence of the very fast quenching mechanisms (as is the case for excited molecules on metals) and the weak binding energy allow for considerable nuclear motion during the excited state lifetime, not only of the excited molecule itself but also of the neighbouring molecules that may reorient themselves into a more stable configuration. The evidence of indirect desorption mechanisms in a lot of different systems show that considering a specific molecule in interaction with a frozen matrix is not sufficient.

One mechanism that *can* be generalized to molecular ices, for example, is cavity ejection. It still requires knowledge of a property of the ice, namely electron affinity, but then this single property is predictive of the occurrence of the mechanism, which for example is active for N_2 ice but not for CO ice [182]. However, a positive electron affinity does not necessarily forbid the desorption of excited state species, showing that there are still more subtleties to the question [183, 182].

Finally, for all but the most simple ices, the role of chemistry in desorption cannot be understated. When a molecule has a lot of dissociative excited states and a complex photochemistry can occur, there will be a strong coupling between chemistry and desorption. Dissociation and subsequent recombination of the molecule can lead to "chemical desorption" due to the excess energy. The desorption of fragments of the molecules and photoproducts also becomes important.

Chapter III

Experimental methods

> L'ordre de précision croissante est un ordre d'instrumentalisation croissante, *donc de socialisation croissante*. [...] si l'on prétend par exemple trouver la largeur d'une frange d'interférence et déterminer, par les mesures connexes, la longueur d'onde d'une radiation, alors il faut non seulement des appareils et des corps de métiers, mais encore une théorie et par conséquent toute une Académie des Sciences. L'instrument de mesure finit toujours par être une théorie et il faut comprendre que le microscope est un prolongement de l'esprit plutôt que de l'oeil.
>
> Gaston Bachelard, *La formation de l'esprit scientifique*

This chapter is devoted to the description of the experimental techniques and the details of how the experiments were performed. Because I have worked on two separate set-ups, I will first discuss some aspects that are common to both set-ups, then proceed to describe each set-up in particular. For the experiments performed on SPICES II at LERMA, I separated the description of the synchrotron experiments and the part that was done in the laboratory, where I spent time developing the laser desorption + REMPI experiments.

III.1 Techniques

III.1.1 Ultra-high vacuum

The central element of both the SPICES 2 and the Multisystem set-up is an ultra-high vacuum (UHV) chamber. Ultra-high vacuum designates a vacuum between 10^{-9} and 10^{-12} mbar, which is more or less the ultimate pressure that can be achieved in an experimental set-up with practical purposes other than vacuum studies themselves.[a] A typical UHV chamber used for surface science studies reaches pressures of the order of 10^{-10}-10^{-11} mbar with standard UHV technology. The reason for using UHV in surface science in general comes from consideration of how long it takes for molecules of the residual gas to cover a surface with pollution. It can be shown that for adsorption of residual molecules with a sticking coefficient of 1 (all molecules that hit the surface are adsorbed) on a surface, the time it takes to form one monolayer of residual adsorbed molecules is linear with pressure and is approximately 1 s at 10^{-6} Torr. Adsorption of residual molecules is of course an issue when trying to study surface properties, and therefore in order to manage a reasonable measurement time (a few hours), pressures of the order of 10^{-10} mbar are required. In our case there is another reason to want a good vacuum: the residual vacuum is essentially our measurement background when we measure neutral desorption. PID and EID are measured in the gas phase: they correspond

[a] Pressures measured in the range of 10^{-14} mbar - a range where the measurement itself becomes the technological prowess - have been made [184]. A pumped and sealed glass bulb immersed in liquid helium, typical of the kind of apparatus used in the early days of UHV, can reach extremely low pressures that are not measurable.

to the increase of the partial pressure of a molecule (here measured with quadrupole mass spectrometry, see section III.1.2). Therefore we will obtain better signals with a lower residual pressure (especially considering that the molecules we are the most interested in, H_2O and CO, are common residual gases in UHV chambers).

Ultra-high vacuum requires some specific technology to be achieved and used. The proceedings of the CAS (Cern Accelerator School) that were dedicated to vacuum in 1999 and 2007 [185, 186] are invaluable introductory resources on many aspects of vacuum technology, although obviously geared towards accelerators (the proceedings of the 2017 edition are unfortunately not available yet). Here I will only give a brief introduction for the purpose of describing the systems and some notions that will be useful afterwards.

In a leak-tight chamber, the equilibrium pressure reached is a balance between two parameters: the pumping speed S and the outgassing Q. The first quantity, given typically in $l.s^{-1}$ or $m^3.s^{-1}$, characterizes the capacity to remove residual gas from the chamber and is linked to the pumps and the geometry of the chamber. The second one, given typically in $mbar.l.s^{-1}$, is the quantity of gas that desorbs from the materials present inside the chamber per unit of time. Indeed, all materials under vacuum outgas molecules that are adsorbed at their surface or dissolved in their bulk. Theoretically the ultimate pressure of a vacuum chamber is therefore:

$$P = \frac{Q}{S}$$

The pumps used in the vacuum systems described here comprise turbomolecular pumps, ion pumps and getter pumps. A turbomolecular pump is made of series of rotor-stator helix blade couples that capture molecules and impart them momentum towards the back of the pump, where the gas initially in the chamber is effectively compressed. This gas is then evacuated by a backing pump such as a scroll pump. In an ion pump, a plasma of electrons is generated by a high voltage and trapped in a magnetic field. The electrons ionize molecules from the residual gas, and the ions then impact the cathode of the pump where they react and stay trapped.

The principle of a getter pump is to have a material that can adsorb great quantities of gas in sufficiently deep wells that they are not re-released in the gas phase, effectively trapping the molecules that hit the material forever. Two classes of getter pumps are distinguished, evaporable and non-evaporable. For example the ion pump of the SPICES II set-up is also equipped with a Titanium sublimation pump. In this device, a Titanium filament is heated until evaporation such that the walls around are coated with a thin film of titanium, which can adsorb molecules. On the Multisystem set-up, a non-evaporable getter (NEG) pump is used. NEG materials are specific, mostly metal alloys (e.g. ZrVFe) that are porous, presenting a very high effective surface that makes metal sorption of a great quantity of molecules possible. Getter pumps in general need to be regenerated, because the amount of molecules that can be trapped is limited. This is why evaporable getters need to regularly be re-evaporated to renew the coating, and NEG pumps need to be re-activated after some times (by heating to high temperatures and evacuating the gas with a turbomolecular pump).

The last source of pumping that should be mentioned is cryopumping, evoked in chapter I. The principle of cryopumping is that on a cold enough surface, even simple physisorption is enough to keep a molecule trapped effectively forever. At a temperature of

10 K, most molecules (with the notable exception of H_2) will condense on the surface and stay trapped, being effectively removed from the gas phase. Going down to 6 K H_2 starts being condensed as well, and at temperatures of 1.8 K as for the cold bore of the LHC, it is cryopumped just as efficiently as other molecules (only Helium cannot be condensed). As mentioned in section I.2.2, cryopumping explains the vacuum performances of the LHC.

While there is no cryopump per se in SPICES II or in the Multisystem, there are cold surfaces when operating at low temperatures (the surface(s) and the cold parts leading to the substrate, see below). This will add to the total pumping speed. In fact, the cold surface in the Multisystem is both quite large and goes down to 5 K in the coldest part thanks to the use of passive liquid helium cooling, so that when operating at low temperature the cryopumping is the main source of pumping in the chamber, yielding a base pressure almost an order of magnitude lower than at high temperature.

The pumping speed that can be achieved in a vacuum chamber the size of which we have here, with regular means, is limited: it will usually be a few hundred $l.s^{-1}$ (a few thousand $l.s^{-1}$ with cryopumping in the Multisystem). In order to achieve ultra-high vacuum, it is therefore required to pay attention to the second parameter governing the base pressure, outgassing. Outgassing depends on the material and its conditioning, and varies on up to ten orders of magnitude. Therefore only a restricted list of materials are allowed inside a UHV chamber. This is why they are usually made of metal, and all-metal sealing with copper gaskets is used (and even then, some metals are not used). Polymers are used as scarcely as possible, and anything organic (grease, dust, hairs falling in the chamber...) should be carefully eliminated.

Outgassing can have different origins: it can come from the layers of adsorbed molecules at the surface of the material (mainly H_2O, hydrocarbons...) or from molecules dissolved *into* the material that diffuse to the surface and desorb. Outgassing decreases with time, as less and less molecules are available to desorb, but the time it takes to reach reasonable pressure may be of the order of months. This is why a bakeout procedure is usually made. All parts of the chamber are heated to temperatures of 100-200 °C (sometimes more) to accelerate significantly the desorption of molecules. In a non-baked chamber, H_2O usually dominates the residual vacuum, but once the bakeout has been done H_2 should be the main component. This comes from the two origins of outgassing mentioned: H_2O is adsorbed at the surface of the metal chamber, while H_2 can come from the dissolved H atoms in the bulk of the metal that diffused to the surface and recombined. The quantity and mobility of H_2O or oxygen atoms in bulk metal is very low. This bulk H is hard to deplete with a regular bakeout (but it is also not replenished when venting the chamber: as a consequence the older vacuum chambers tend to have less outgassing of H_2). This is also the difference between metals and polymers: water can be dissolved in bulk polymer in great quantities and diffuse/desorb efficiently once the polymer is under vacuum. It then takes a very long time and/or an efficient bakeout to deplete water from the bulk polymer.

III.1.2 Mass spectrometry

Mass spectrometry, more precisely quadrupole mass spectrometry, is the main detection technique employed in this work. The basic principle of mass spectrometry is to detect molecules and atoms -usually in their ionic form- as a function of their mass. This is most

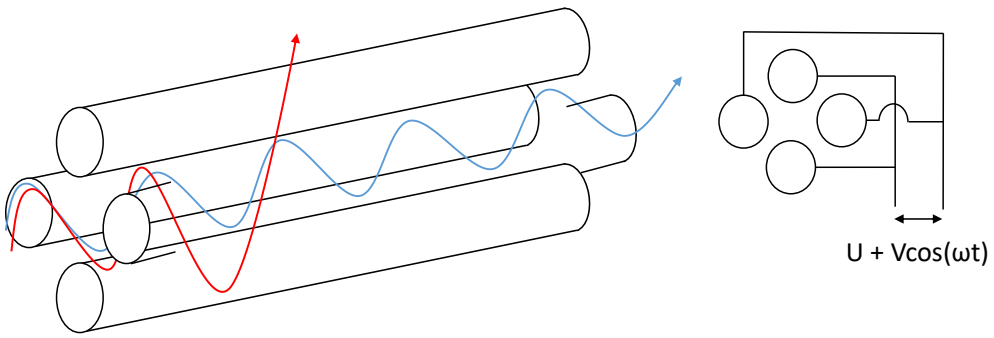

Figure III.1: Schematic design of a quadrupole mass filter. In blue is represented a stable ion trajectory through the quadrupole, in red an unstable one.

of the time done by manipulating the ions with electric and magnetic fields. The mass of a molecule already gives a lot of information on its nature - depending on the context it can unambiguously identify what species exactly is detected.

A mass spectrometer is made of three basic units: ionization source, mass filter, and detection. I will describe in the following these three units. Mass spectrometry will be used here as the main detection probe for both desorbing ions and neutral molecules, but also as an analyser of the residual gas in the UHV chamber. For the former use, we will be interested in calibrating our devices to derive absolute quantities. All these aspects are described in the following as well. For more details I will redirect to textbooks on the topic, which served as sources for the redaction of these parts [187, 188].

III.1.2.1 Mass filtering

One of the most basic ways to do mass spectrometry is time of flight mass spectrometry (TOF-MS). In TOF-MS the ions are captured by an extractor electric field and brought to a given kinetic energy, then are let drifting through a known length until they reach a detector. If a departure time t = 0 is well defined (e.g. using a pulsed ionization source, or a mechanical chopper...), the time that an ion of mass m will take to reach the detector is directly dependant on its mass, since the kinetic energy is fixed. Thus the signal detected as a function of arrival time can be inverted into a mass spectrum. It is also worth noting that the kinetic energy of the ions set by the electric field is actually proportional to their charge. Therefore the appropriate coordinate for the mass spectrum is not m but m/z: two particles with one having twice more charge but twice more mass than the other will have similar arrival times and will not be distinguished.

Quadrupole mass spectrometry does not work in a such a straightforward way. The mass discriminating part of a quadrupole mass spectrometer (QMS) is a quadrupole: four symmetrically positioned rods (see fig. III.1) with a voltage applied between them of the form $\pm(U + V\cos(\omega t))$ (each opposing rods are at the same potential). The trajectory of a charged particle inside such an electric field is governed by a set of nonlinear equations. It can be shown that in the relevant parameter space there are zones of stable trajectories (such as the one represented on fig. III.1 in blue) and zones of unstable trajectories (in

red in fig. III.1), depending on the values of U, V and ω, but also on the mass of the ion. The quadrupole can act as a mass filter when it is operated with a set of parameters such that the operation point is in a stable region only for a specific value of m/z. All ions with a different mass will have an unstable trajectory and hit the walls or the rods and be reneutralized.

It can be shown that the ratio U/V sets the resolution, i.e. the width of the range of m/z values that have stable trajectories. QMS are often operated at a so-called "unit resolution", which basically means that a peak at mass m contributes negligibly to the intensity measured at mass m+1 and m-1. It is therefore assumed here that the molecules all have integer masses, which is not exactly the case. Some mass spectrometers[b] have very high mass resolution which allows to discriminate molecules which are very close in mass, such as molecular oxygen O_2 and atomic sulfur S at mass 32.

A mass scan at constant resolution is then usually achieved by scanning the values of U and V while maintaining a constant U/V ratio. The fact that mass scanning only requires changing voltage amplitudes is what makes the operation of the QMS fast and easy. Standard QMS operate with typical values of $\omega \sim$ 1 - 4 MHz and U and V $\sim$ 100-1000 V, and in this mode of operation ions are usually brought to a kinetic energy of 10 eV for their passage through the quadrupole, for a trajectory of about 100 oscillations.

III.1.2.2 Ionization source

When ions are directly the particles we wish to detect (for example PID of ions in chapter VI or REMPI spectroscopy in section IV.1.2), there is no need for a ionization source internal to the detector. Only a way to capture the ions is needed, which is achieved using an "extraction" electric field. For example the Hiden QMS on SPICES II has at its tip a cone onto which a potential can be applied. A negative voltage will be used to capture positive ions and a positive voltage for negative ions.

However, to detect neutral molecules, they first need to be ionized. Many techniques have been deployed on different kinds of mass spectrometers, but the most common one by far and the one used here as well is electron-impact ionization. For this technique the ionization source consists of an electron emitting filament (a material, typically tungsten, emits electrons when it is heated enough) and an anode. The electrons are accelerated by the voltage between the filament and the anode. Electrons with a sufficient energy can ionize molecules and atoms for the reasons that were explained in the section on electron-matter interaction. The ionization source is operated at fixed electron energy to insure no variation of intensity due to the variation of ionization efficiency with electron energy. The electron energy is often 70 eV, or somewhere in this region (70-120 eV) because this is where the electron impact ionization cross-section of most molecules and atoms of interest is maximum.

The overall detection efficiency of a given molecule will therefore depend, among other things, on its ionization cross-section. The electron impact ionization cross-section of various molecules of interest at 70 eV are given in table III.1, in values absolute and relative to CO. Electron impact ionization at these energies can also be dissociative, so that ions other than the singly ionized parent molecule can be created, as is shown in

[b] for example, the ROSINA mass spectrometer of the ROSETA mission.

Table III.1: Partial electron impact ionization cross-section of a few molecules at 70 eV. A more detailed list of cross-sections used and the corresponding references are given in the appendix.

	Absolute (Å^2)	Relative to CO
$\sigma(CO^+/CO)$	1.76	1
$\sigma(C^+/CO)$	0.29	0.16
$\sigma(O^+/CO)$	0.19	0.11
$\sigma(N_2^+/N_2)$	1.88	1.06
$\sigma(H_2O^+/H_2O)$	1.23	0.7
$\sigma(H_2^+/H_2)$	0.93	0.52
$\sigma(Xe^+/Xe)$	4.67	2.62

the case of CO in the table. $\sigma(A^+/B)$ is the partial electron impact ionization cross-section of ion A^+ from the parent neutral molecule B. A complete table (table 7) of all the cross sections that have been used for quantification purposes in this work (see below) is given in appendix A along with all the references. It is worth noting that electron-impact ionization cross-section measurements are difficult, and therefore despite the claims of uncertainties ± 10% or better in the literature (based on the known sources of uncertainty), discrepancies of up to 30-40 % between the measurements of different groups can be observed.

III.1.2.3 Detection

There are two common techniques for ion detection after the mass filter. The first one is to simply use a Faraday cup, which will collect the ions and the generated current is then measured. This technique is basically limited by the state of the art in low-current reading. The limit is around 10^{-13} A with a corresponding partial pressure measurement limit around 10^{-9} mbar.

The other detection technique is to use a secondary electron multiplier (SEM). In this device, the incident ion is accelerated towards a dynode, which is made of a material with a high secondary electron yield (SEY). The ion creates secondary electrons, which are themselves accelerated and hit the dynode again, creating more electrons. This electron cascade creates a large current, up to 10^8 electrons per ion, which is then detected. The partial pressure measurement limit is much lower, down to 10^{-14}-10^{-15} mbar.

In practice, a lot of QMS offer the possibility of switching between Faraday cup and SEM detection. This is the case of the Balzers QMS of SPICES II and of the HiQuad QMS on the Multisystem. The SEM has a much better sensitivity but ages progressively, and it is not advisable to operate it in a pressure above 10^{-7} mbar. The Faraday cup can be used at higher pressures, up to $\sim 10^{-5}$ mbar (the limiting pressure is then mostly due to the operation limit of the ionization source filament). The SEM mode has been used almost exclusively in this thesis.

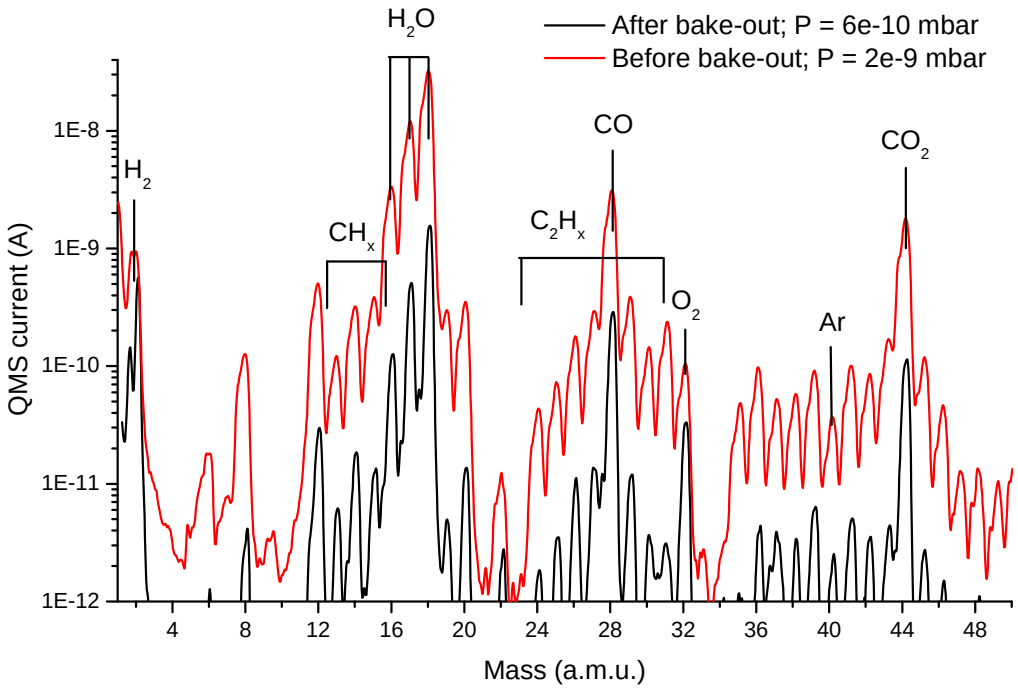

Figure III.2: Example of residual gas analysis mass spectra in SPICES II, before and after bake-out.

III.1.2.4 Residual gas analysis

QMS are commonly used in vacuum chambers as residual gas analysers (RGA), to probe the composition of the gas. There are only a limited number of molecules that are expected in the residual gas of a vacuum chamber, and they can therefore be identified by mass spectrometry with little ambiguity. The main residual molecules are H_2, H_2O, CO and CO_2. Because of electron-impact ionization, the fragment ions of these molecules will also appear in the mass spectrum.

Peaks that should be checked when performing residual gas analysis are those corresponding to hydrocarbons ($C_xH_y^+$), which are a sign of oil/grease pollution, and peaks like Ar (m/z = 40) or O_2 (m/z = 32) which are signs of a leak. There can also sometimes be pollutions by more exotic compounds: for example chlorinated pollution, signed by the presence of peaks at m/z = 35 and 37, is very hard to get rid of.

Fig. III.2 shows two mass spectra taken in SPICES II, before and after bake-out (for the first bake-out of the chamber after it was assembled). On the mass spectrum before bake-out water peaks dominate the spectrum and there is a lot of pollution peaks (CH_x etc). After bake-out most of the peaks have been reduced by an order of magnitude, while H_2 has only slightly decreased and is close to the water signal.

III.1.2.5 Kinetic energy analysis with an electrostatic deflector

The Hiden QMS of the SPICES II set-up comprises an electrostatic deflector for kinetic energy analysis. Analysis of some characteristics of this device are given in ref. [190].

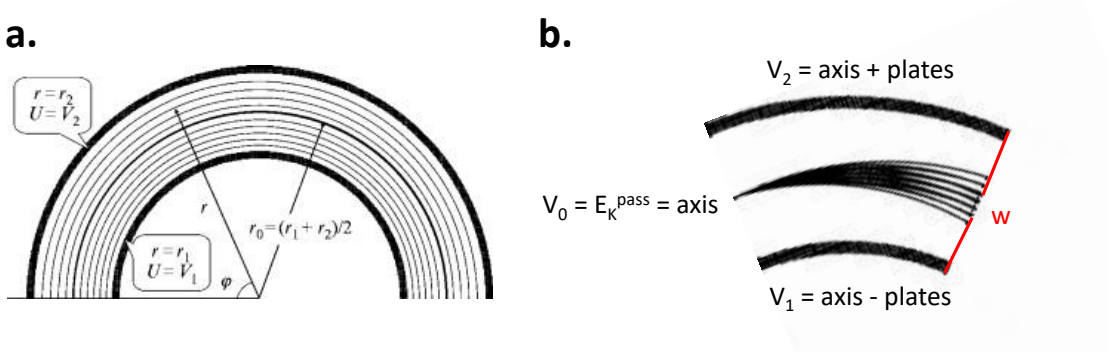

Figure III.3: Principle of the 45° sector field electrostatic analyser. **a.** Schematic drawing of a cylindrical sector field electrostatic deflector. The equipotential lines are shown. **b.** A 45° analyser as implemented on the Hiden QMS. Both figures are adapted from Yavor [189].

The analyser is a 45° sector field electrostatic analyser. It is based on the principle of the cylindrical sector field deflector, described e.g. in ref. [189]. In fig. III.3a, a cylindrical deflector is represented. With a voltage V_1 applied at $r = r_1$ and a voltage V_2 applied at $r = r_2$, the equipotential lines are circles and the electrostatic field only depends on r. In the 45° sector field analyser, as represented in fig. III.3b, the potential at the mean radius r_0 is called the axis (set by the axis voltage), and the potential applied at r_1 and r_2 is axis ± plates (set by the plates voltage). It can be shown [189] that the particles (singly charged here) that have a trajectory of constant radius r_0 in the deflector are those that satisfy the condition on their kinetic energy E_K:

$$E_K = \frac{V_2 - V_1}{2ln(r_2/r_1)}$$

The particles with different kinetic energy will be deflected above or below the axis. Only those with a kinetic energy fulfilling the condition will be able to go through the aperture w shown on fig. III.3b. In the geometry of the deflector used in the Hiden QMS, the plates voltage is set at 7.27 V and thus considering the values of r_1 (68 mm) and r_2 (82 mm) the kinetic energy for passage is 40 V. If the axis and plates voltages were set relative to the ground, then particles with initial kinetic energy 0 V (relative to the ground as well) would be accelerated to 40 V by the axis voltage when entering the QMS. To operate a kinetic energy filtering, the axis and plates voltages are set relative to a variable voltage "energy", which allows to offset the energy by which ions are accelerated upon entering the QMS, in order to have particles of a given kinetic energy brought to 40 V. For example, to filter particles with an initial kinetic energy of 3 V, the energy voltage is set at 3 V, so that the axis energy, which is -40 V relative to the energy voltage, is now -37 V relative to the ground, accelerating the 3 V particles to 40 V and allowing them to pass through the deflector.

One consequence of this operation principle is that the apparent kinetic energy of the particles (the one measured by the apparatus) is not necessarily the "true" kinetic energy, in the sense of their kinetic energy in field-free conditions in the vacuum, because the ions are usually not formed in a potential of 0 V. The extractor field for example creates a

non-zero potential for ions generated in the gas phase by laser ionization. The situation for ions leaving a surface is even more complicated, since we have to consider the work function of the solid, the possible charging effects, etc. Setting the absolute energy scale of the kinetic energy distributions we obtain is therefore difficult, except if we assume that the distribution should start at 0.

The resolution of this energy analyser is not extremely good. It is proportional to the aperture size w and the transmission energy (axis energy). Its value as given by Hiden is 1.7 V in standard operation conditions. As a consequence, only highly energetic ions can be differentiated with this apparatus. It works well for ion-induced desorption in the X-ray range (where kinetic energies can reach tens of eV), but is useless for e.g. attempting to obtain kinetic energy distributions of desorbing neutrals, which are expected to be below 1 eV (and may be scrambled by electron-impact ionization anyway). It should also be noted that there is no "full pass" mode for an electrostatic sector field analyser: any measurement made with the Hiden QMS is made at a given kinetic energy.

III.1.3 Ice growth

The molecular ice films that we investigate are grown onto cold substrates by vapour deposition. The molecule(s) of interest in gas phase are obtained either from gas bottles or from the vapour pressure of the liquid and let into an injection manifold, pumped with a turbomolecular pump. A low base pressure and flushing of the manifold a few times with the gas of interest insure a good purity of the injected gas. For liquids an additional step is required: the liquid has to be degassed from its dissolved volatiles (mostly CO and CO_2 in water, for example). This is done by the freeze-pump-thaw technique, where the liquid is frozen with liquid nitrogen, the overhead gas pumped, and then the liquid is thawed. During thawing large amounts of the dissolved gases will turn to the gas phase in the now empty overhead because their vapour pressures are much higher than that of the liquid host. The liquid is then frozen again, the overhead pumped, and the operation can be repeated a few times for complete elimination. Of course this only works for volatile impurities. Additional care is required when using deuterated products (mainly D_2O here): H/D exchanges happen easily with the residual gas and the surface adsorbed residues of the manifold and will result in an isotopically impure mix. It is usually necessary to flush a large number of times the manifold (but also the injection part under vacuum) to saturate the residues with deuterium and obtain a sufficiently pure gas.

A microleak valve separates the manifold from the UHV chamber and is used to inject very small partial pressures of gas into it. A tube is then used to guide the gas towards the surface. The principle of this guiding tube is shown in fig. III.4a. There is a plate at the outcome of the tube to "randomize" the direction of the molecules hitting the surface, in an attempt to minimize directional effect like growing of a thicker ice at the center of the substrate. A picture of the dosing tube used in the Multisystem is shown in fig. III.4b.

With this tube most molecules hit the surface, and the surface is sufficiently cool to have a sticking coefficient of one, so that few molecules will escape in the vacuum. This technique allows to deposit ice without having the pressure increase too much in the chamber. This is crucial for PID and EID studies where the background pressure of

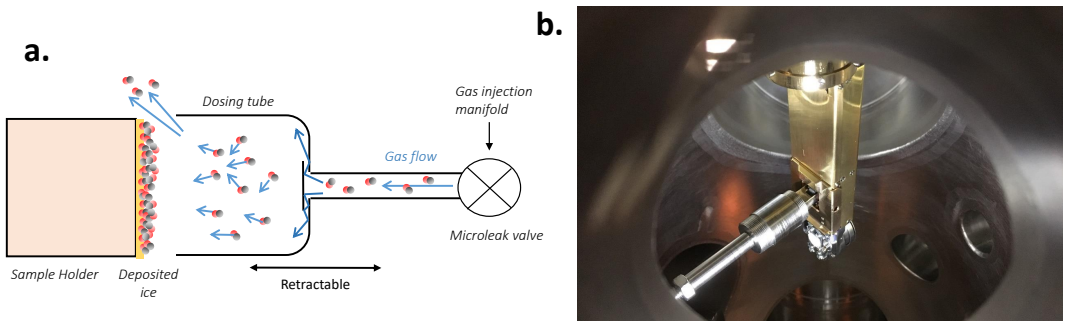

Figure III.4: Principle of the dosing tube for ice growth. **a.** Schematic drawing of the dosing tube. **b.** Picture of the dosing tube inside the Multisystem set-up, brought close to the cryomanipulator for dosing.

the deposited molecule in the chamber is what limits the sensitivity. How much pressure leaks out of the tube will depend on its size and the distance to the surface. For the SPICES II set-up, it was felt that it would be important to insure homogeneous coverage of the whole surface, so that the tube was made larger than the surface area. In the Multisystem, this is not possible and covering the whole surface is less important since the electron beam spot is small. The tube is therefore smaller than the surface (1 cm^2 vs 2.7 cm^2). This results in less leakage. From a rough estimation made with the QMS signal during injection, with the tube about 1 mm away from the surface, about 1 % of the injected gas leaks out in the Multisystem, but this can be reduced even more by bringing the tube even closer. At a tube-surface distance of about half a millimeter, the pressure in the Multisystem does not rise to more than a few 10^{-10} mbar even when dosing hundreds of monolayers of molecules, while for a similar dose the pressure in SPICES II would rise above 10^{-8} mbar (but this is not just due to the tube distance and size, as the pumping speed and the chamber geometries are different).

"Dosing" a reproducible amount of molecules on the surface requires having a reading of a signal proportional to the amount of injected molecules. In SPICES II, this signal is the partial pressure of the injected species read on the QMS (which comes from the small leakage of molecules that don't stick to the surface). In the Multisystem, it is the pressure decrease from a closed and calibrated volume of gas in the injection manifold. It is possible to calibrate the dosing (finding the proportionality between the measured signal and the ice thickness obtained), using the temperature-programmed desorption (TPD) method introduced in the next section.

The surfaces onto which the ices are grown vary, but the exploration of this underlying substrate effect has not been a focus of study during this work. We mostly work under the assumption that the substrate has no particular effect, because we use molecular ices thick enough to neglect these effects. The surfaces used are "technical" polycrystalline or amorphous surfaces, and not cleaned single crystal surfaces as are often used in surface science studies. "Technical" means that while we try to have polished, planar surfaces with no macroscopic structure and to avoid having our fingerprints on them, no particular cleaning procedure is made under vacuum (aside from baking out, but the bake out is mild in our chambers). The consequence is that there is certainly a layer or more of carbonaceous and oxygenated "dirt" at the surface. For example we would expect a

technical copper surface to consist of oxidized copper with traces of carbon "stuff".

III.1.4 Temperature-programmed desorption

Temperature-programmed desorption (TPD) experiments in the SPICES set-up have been developed and exploited mostly by Mikhail Doronin during his PhD and by Mathieu Bertin. The reader is referred to their respective PhD thesis [191] and HDR thesis [192] for more information on the technique and its applications. Here I will only introduce what is useful for the rest of the experiments.

TPD (sometimes called Temperature Desorption Spectroscopy, TDS) is a common surface science technique used to investigate adsorbates on surfaces, or use these adsorbates as probes of surface characteristics. The technique consists in depositing adsorbates (submonolayer or multilayer quantities) onto a surface, then to apply a controlled linear heating ramp, and monitor the partial pressure of the desorbed molecules as a function of temperature (typically using a QMS).

The kinetics of the desorption of molecules adsorbed on a surface is governed by the Polanyii-Wigner equation:

$$-\frac{dN_{ads}}{dt} = \nu N_{ads}^{n} \exp(\frac{-E_a}{kT})$$

$-\frac{dN_{ads}}{dt}$ is the flux of desorbing molecules (molecules.s^{-1}), N_{ads} the number of adsorbed molecules, k the Boltzmann constant and T the temperature. ν is a pre-exponential factor: it can be interpreted as the ratio between the partition function of the molecule in its adsorbed state and in its gas phase state (at least for physisorbed molecules)[c]. n is the kinetic desorption order. E_a is the adsorption energy of the molecule to the surface (i.e. the dissociation limit D_0 of the physisorption well).

In a TPD experiment, since a linear heat ramp is applied, the variable t can be replaced by the temperature T:

$$-\frac{dN_{ads}}{dt} = \frac{\nu N_{ads}^{n}}{\beta} \exp(\frac{-E_a}{kT})$$

Where β = dT/dt is the heat ramp. The TPD curve is then the detected signal on the appropriate mass channel of the QMS as a function of temperature. TPD can be used to derive parameters from the previous equations (ν, E_a), or to derive information on the structural arrangement of molecules on the surface, etc... It is also commonly used to identify a posteriori the composition of an ice, using the mass filter information.

Here TPD will mostly be useful for calibration purposes. TPD can be used to calibrate the thickness of the deposited molecular films. There are two ways to exploit TPD to obtain a thickness calibration, and they both rely on a distinction between the submonolayer and the multilayer regime.

One method is to exploit the fact that for some molecules (and some surfaces), the adsorption energy of the molecule to the surface is different from the adsorption energy to the multilayer ice. A significant enough difference will make the two classes of molecules

[c] It is common in both astrochemical studies and vacuum studies to see that the value of this pre-exponential factor for first-order desorption is $\sim 10^{13}$ s^{-1}, but this is only valid for small molecules (e.g. diatomics and H_2O).

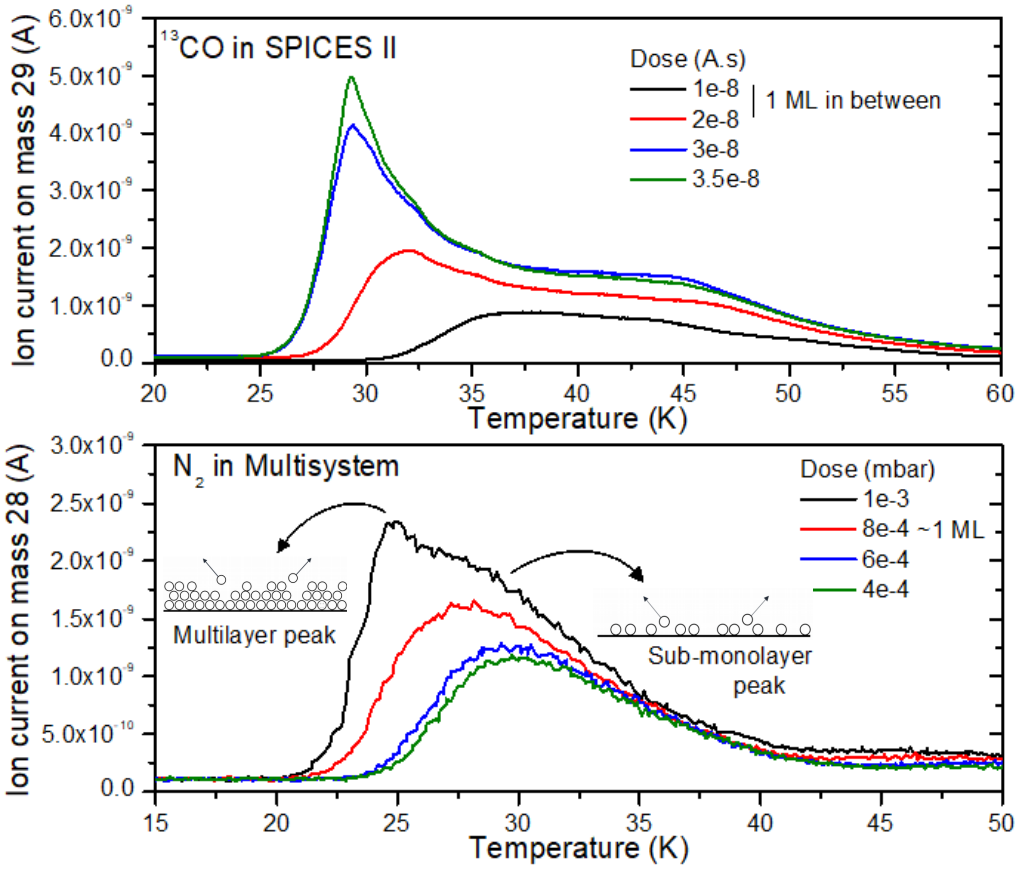

Figure III.5: TPD curves for thickness calibration of ^{13}CO ice in SPICES II (upper panel) and N_2 ice in the Multisystem (bottom panel). The legend of the curves in the upper panel is the integrated QMS signal on mass 29 during ice deposition. On the bottom panel, the legend is the pressure decrease in the closed injection volume. The approximate monolayer calibration, estimated from the apparition of the multilayer peak on the curves, is indicated. The TPD in SPICES II is made with a heat ramp of 12 K/min and in the Multisystem of 10 K/min.

appear at different temperatures in the TPD curve. Therefore the progressive growth of the multilayer peak as the amount of deposited molecule increases will mark the transition from monolayer to multilayer regime.

Conveniently, the monolayer for CO and N_2 are well identified by this method. Fig. III.5 shows examples of calibration TPDs for CO in SPICES II (upper panel) and for N_2 in the Multisystem (bottom panel). The multilayer and sub-monolayer peaks are clearly identified. As mentioned in the previous section, a "dose" of deposited molecules is given as an integrated leakage signal on the QMS for SPICES II, and as a pressure decrease from a calibrated and closed volume of injection for the Multisystem.

When this method cannot be used because the multilayer and sub-monolayer peaks are not distinguishable, there is another possibility to separate these two regimes. This

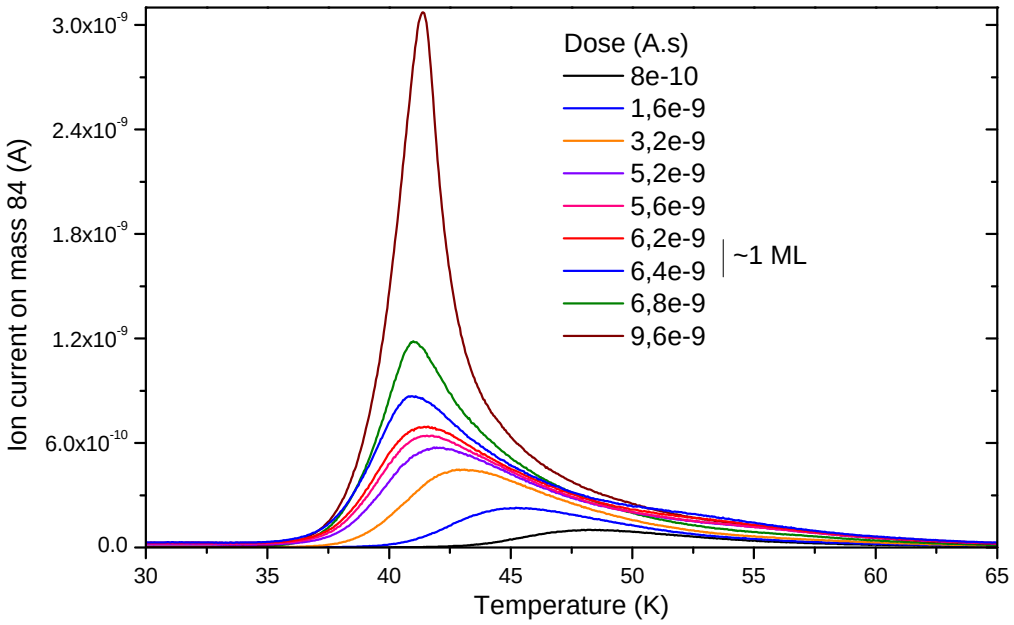

Figure III.6: TPD curves for thickness calibration of Kr ice in SPICES II. The approximate monolayer calibration, estimated from the transition from first order to zero order kinetics, is indicated. The legend of the curves in the upper panel is the integrated QMS signal on mass 84 during ice deposition.

one is based on the kinetic order of desorption. For multilayer desorption, the expected kinetic order is zero: when a molecule desorb, there is always a new molecule below that can also desorb later, so that the effective surface does not change during desorption and the desorption flux should be independent of the coverage. For sub-monolayer desorption, the number of available molecules for desorption decreases with time, so that a first order kinetics is expected. Zero and first kinetic order TPD curves behave differently: in the first order regime, when the coverage increases, the leading rise and maximum of the curve shift towards lower temperatures. In the zero order regime, the leading rise of all the curves is the same, while the maximum shifts towards higher temperatures when the coverage increases. The transition between the two regimes can therefore be identified and corresponds to the monolayer. An example is given for the case of Krypton ice in SPICES II in fig. III.6.

Sometimes none of the two above methods work. In the case of H_2O, for example, the TPD behaviour follows a more or less zero order kinetics even in the sub-monolayer regime. H_2O tends to form islands rather than a flat layer on metallic of graphitic surfaces, making this case more complicated and unsuitable for thickness calibration. It is, however, an example of how TPD can give information on the arrangement of molecules at the surface. For molecules like these, a thickness calibration can be extrapolated from the calibration of other molecules by taking into account the different QMS sensitivity factors.

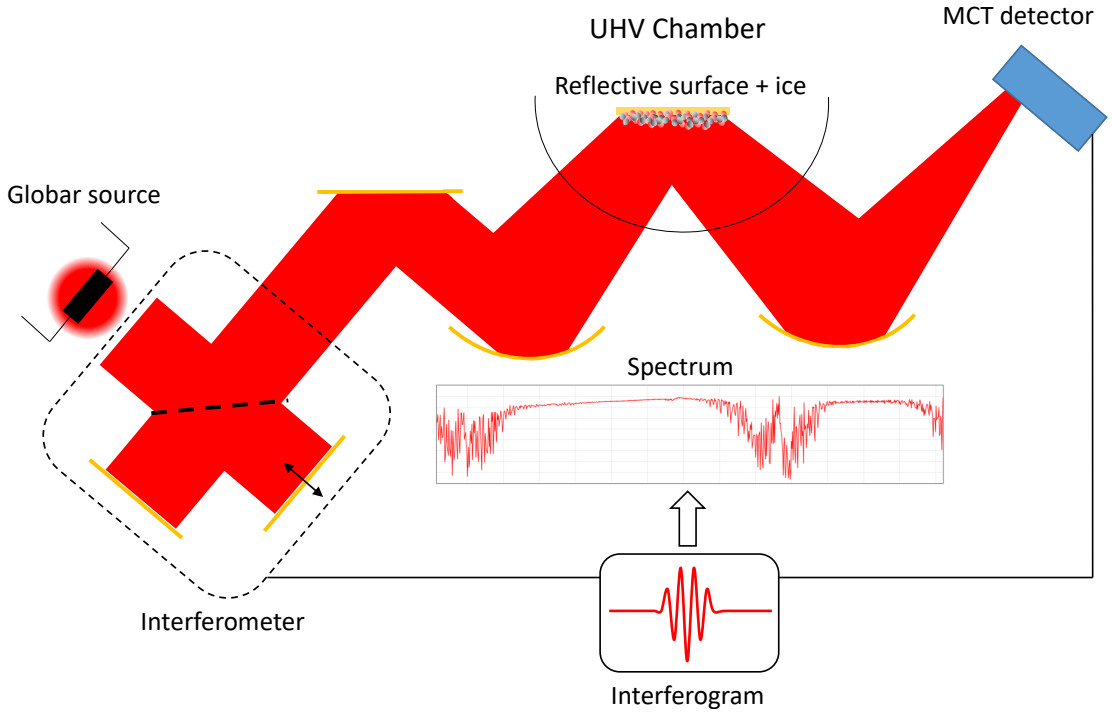

Figure III.7: Scheme of the FT-RAIRS set-up.

III.1.5 Infrared spectroscopy

Infrared spectroscopy is used in the SPICES II set-up as a way to probe the ice bulk. The general principle of IR spectroscopy is that in the infrared range (here the mid-infrared, 600 - 4000 cm^{-1} or 2.5-16 μm) the vibrational energy levels of molecules are probed, with sufficiently characteristic spectra that the composition of a gas or a thin bulk of condensed molecules can be determined.

The technique used here more specifically is FT-RAIRS: Fourier Transform Reflection Absorption InfraRed Spectroscopy. The scheme is presented on fig. III.7. An interferometer based on the principle of the Michelson interferometer (the actual design is more complicated than what is represented on the figure) is used with a globar (broadband IR source) as an input, and the ouput of the two superimposed coherent beams is then directed into the vacuum chamber and focused onto the surface. Some of the infrared light is absorbed by the ice bulk grown onto the surface and the beam is then reflected by the substrate and sent to an infrared detector (MCT, Mercury Cadmium Tellure). The signal as a function of optical path difference acquired while the mobile parts of the interferometer are moving forms an interferogram which is then Fourier-transformed to obtain the spectrum of the light, where the absorption of the molecules at specific frequencies appear. In FT-RAIRS the spectrum of the ice is obtained against a reference spectrum with the bare substrate, and the absorbance is deduced.

In the condensed phase, contrary to the gas phase, there are no rotational sub-levels and the IR spectra "simply" corresponds to the vibrational modes of the molecules. The IR spectrum allows to identify the presence of various molecules in the bulk of the ice, which

means that impurities (before irradiation) or products of chemistry (after irradiation) can be identified. The shifts, changes of shapes and splittings of peaks can also give information on the structure of the ice. However, not all molecules can be detected with infrared spectroscopy: for an electric dipole transition to occur, the dipole moment of the molecule needs to change during the vibration. For example N_2 is almost invisible by infrared spectroscopy: its symmetry forbids a dipole transition (it can be seen through a much weaker quadrupole transition).

Infrared spectroscopy in transmission can also be quantitative if the band strength of the observed transitions are known. Some caution is necessary because these band strengths can be sensitive to the structure of the ice and the molecular environment of the molecule but the technique is often used quantitatively. In FT-RAIRS quantification if more complicated. When light is reflected at the surface, the s-polarization (in plane) components of the incident and reflected light interfere destructively, and only the p-polarization (out of plane) component is left. In fact, the light is usually sent at a grazing angle (73° relative to the surface normal in SPICES II), to optimize the strength of the p component. Because of this, only molecules with a specific orientation (e.g. for diatomic molecules those that have their molecular axis normal to the surface) are probed and the technique is not directly quantitative. It is still possible to calibrate the signals but it needs to be done specifically for the set-up - the initial calibration of CO photodesorption relies on that.

III.1.6 Electron yield

A simple but very useful diagnosis tool, especially for experiments in the X-ray range or with electrons, is the total electron yield (TEY), which is the flux of outcoming electrons from the surface during irradiation. Ideally these electrons escaping the surface would be measured with an electron spectrometer, or even just a collecting cup. In the absence of such device it is still possible to have the information if the metallic surface onto which the ice is grown is electrically insulated. Then, electrons escaping the surface will create a current which can be read with a picoammeter (as the current is usually in the nA range).

This technique was implemented in the SPICES II set-up previous to the SEXTANTS runs in the soft X-ray range (2017). A copper substrate was isolated from the sample holder using a kapton foil, and a wire fixed to the surface and connected to a vacuum feed-through allowed the reading of the current. This diagnosis tool proved extremely useful for the experiments in the X-ray range: here electrons escape the ice surface following the Auger decay and the subsequent secondary electron cascade. Because the energy of the Auger electron is more or less always the same, the total number of electrons per absorbed photon is on average the same as well, and the TEY can be assumed to represent the absorption of the ice. Near the edge, and within say 100 eV of the IP, the dominant source of electrons remains the Auger electron and not the photoelectron if there is one, and this approximation stays valid. There would probably be a difference in the photon energy range where the photoelectron can also yield significant amounts of secondary electrons, but here the hypothesis seems safe.

The same technique is also used for electron irradiation in the Multisystem set-up, where it was directly part of the design of the sample holder. A whole part of the sample holder and the sample itself are isolated from the rest of the manipulator by a sapphire

plate, allowing current reading. In the case of electrons, the understanding of the current reading is more complicated because there are both electrons penetrating the surface and electrons leaving the surface. The flux of electrons escaping the surface is an interesting quantity called the secondary electron yield (SEY), which was introduced in section I.2. However, this quantity was difficult to measure on molecular ices because of charging issues. The other quantity we want access to is the flux of incident electrons on the surface. The way this is obtained is by applying a bias on a surface. By applying a sufficiently positive bias (+45 V), the secondary electrons, which have a relatively low kinetic energy (usually <20 eV) can no longer escape (they are recaptured when they leave the surface). The current reading then only corresponds to the incoming incident electrons. This gives the incident electron flux.

III.1.7 Calibration of EID and PID

In both set-ups, photon- and electron induced desorption of neutral species is mainly measured by the increase of partial pressure on a given mass channel of the QMS above the residual background of that channel. For ion detection the principle is similar, except that the background is essentially zero. Comparison of relative efficiencies requires at least subtraction of the background and division by the photon/electron flux, assuming a linear dependence to the flux. Here we also wish to obtain an *absolute* calibration, to obtain a number of desorbed molecules per incident photon/electron. This requires some more work. Different approaches were used here and can be compared. All the numbers related to calibration of desorption are compiled in Appendix A.

III.1.7.1 Absolute calibration methods

First of all, we need to obtain an absolute calibration for at least one given system. What we wish to do is to relate the current read on the QMS i_n on the appropriate mass channel n to the flux $(dN/dt)_X$ of desorbing molecules X, assuming these two quantities are related by a proportionality factor k_X. Assuming only species X contributes to mass channel n:

$$\frac{dN}{dt} = k_X i_n$$

One way to find k_X is to relate the loss of molecules in the condensed phase to the desorbing flux of molecules. This is what has been done for calibrating the photodesorption yield of CO in 2010 [193], using FT-RAIRS spectroscopy. The integrated area of the absorption band of solid CO is proportional to the amount of CO on the substrate, and can be calibrated to an absolute number of molecules by measuring it for different thicknesses of ice (themselves calibrated by TPD). Relating loss in the solid to desorption is only possible assuming that only desorption of the intact species contributes to solid loss. This works well when there is no dissociation and no significant photochemistry going on in the ice, hypotheses that are related and are well verified for CO in the VUV range in particular, but are wrong for a number of other systems.

Another possibility for calibration is to assume that the flux of desorbing molecules creates a uniform partial pressure raise in the chamber, and that the signal read on the QMS is proportional to that partial pressure increase. Indeed, the desorbing flux of molecules X can be related to a partial pressure increase Δp_X by the following relation:

$$\Delta p_X = \frac{k_B T}{S_X} \left(\frac{dN}{dt} \right)_X$$

With T the temperature of the molecules, and S_X the pumping speed for species X. The increase of partial pressure is proportional to the current i_n in the QMS. The proportionality factor for this, c_X ($A.Pa^{-1}$), can be obtained easily by gas injection of X in the chamber and comparison of the QMS signal to the pressure reading of a calibrated Bayard-Alpert gauge. This method assumes that molecules are thermalized and a partial pressure is well defined. In particular, this means for example that the signal detected should not depend on the position of the QMS in the chamber. This is only valid if the QMS is far enough from the surface: in SPICES II, the QMS is quite close and sees directly the surface, and we instead assume that most of the detected signal is due to molecules coming directly from the surface (and we do observe that the signal depends on the position of the QMS relative to the surface). In the Multisystem, on the other hand, this condition should be satisfied (see below). However, this method also requires a measurement of the pumping speed, which can be done, but the effective pumping speed near the surface may differ from the measurement, as will be explained later.

A third method consists in taking advantage of the calibration of TPD. TPD calibration allows the deposition of precisely one monolayer of molecules, which corresponds to a known number of molecules. In a TPD experiment, all these molecules are desorbed from the surface and detected by the QMS. By simple integration of the equation relating dN/dt to i, the integral of the TPD signal is proportional to the number of desorbed molecules:

$$N_X = k_X \int i_n \mathrm{d}t$$

Assuming k_X is the same in the TPD and PID/EID experiments, we know the two other quantities and can derive it this way.

Throughout this work, we will assume that the calibration factor of a molecule is always the same, as long as the geometry of the chamber and the settings of the QMS do not change. There are possible limitations to this assumption. A first one is related to the angular distribution of the desorbed molecules: if it is too different from one experiment to another, it will affect the detected signal on the QMS. For the desorption of neutral molecules from amorphous ices, we do not expect strong angular effects, but it is still something to keep in mind. Another fact related to the detection of neutral species is that the QMS is a *density* detector and not a *flux* detector: the signal measured is proportional to the density of molecules at a given time at the entry of the detector, and not to the flux of molecules going through. How this affects the measured signal is well understood by considering that slower molecules spend more time in the ionization source than faster ones, and thus have a higher probability of being ionized and detected. There is therefore a kinetic energy bias in the detection. Still, we do not expect very high kinetic energies for desorbed neutral molecules either in most cases.

III.1.7.2 Relative calibration methods

What we will try to do is to take into account how the calibration varies for different molecules. From the absolute calibration of one molecule (here, CO), it is possible to

derive factors for other species. Among the techniques introduced above, TPD calibration is the one applicable to the most systems, but it cannot be used for species that are reactive and not easily available in gas form (e.g. radicals) or even for species for which TPD calibration is hard because of unusual kinetics (e.g. H_2O). This technique will therefore mostly be used as a consistency check. As mentioned before we cannot take into account factors like differences in angular distributions or kinetic energy on which we have no information anyway. Instead we will focus in the differences induced by the different parts of the QMS.

There are two different possibilities for obtaining the relative sensitivity of the QMS to different species. One is simply to measure the absolute sensitivity s of the QMS, in A.mbar^{-1}, by injecting the gas of interest so that it dominates the gas composition in the chamber (e.g. injecting 10^{-8} mbar background pressure of a gas), and dividing the QMS signal on the relevant mass channel by the pressure. The pressure gauge needs to be calibrated for such a measurement, and the correction factor for different types of gases taken into account. The ratio of the absolute sensitivity of the molecule of interest to that of the reference molecule (CO or N_2) gives the relative sensitivity directly. But this does not solve the problem of the species for which gas injection is not possible. Another approach is then to look at the effect of the different parts of the QMS.

In the ionization source, a contribution to the difference of sensitivities arises from the different electron impact ionization cross-sections of the species, as introduced in a previous sub-section. These cross sections can be obtained from the literature and the calibration factor corrected by the ratio of the cross-sections. Note that this implies single-ionization processes in the ionization source, whereas there is probably some degree of multiple impact effects[d].

The transmission of ions in the quadrupole also differs between ions of different m/z. It is usually assumed that the transmission function of the quadrupole can be expressed as a power function of the mass:

$$T \propto \left(\frac{m}{z}\right)^{\alpha}$$

However, justification of this dependence of the transmission on mass is hardly found in any textbook, so that I could not find a theoretical basis for this power law and possible values of α.

The last factor to be taken into account is the detection efficiency of the SEM. Here also a power law of m/z is sometimes mentioned in the literature. Yates for example mentions [194] a $m^{-0.5}$ dependence, without giving an explanation. In this case however a simple rationalization of the changes of detection efficiency in the SEM can be given, since the principle of the SEM is not governed by parameters as complex as the quadrupole mass filter. The factor in the SEM gain that can change here is the ion-impact SEY (secondary electron yield), i.e. the average number of electrons ejected from the surface by the initial incident ion. The kinetic energy of the incident ions is set by the dynode voltage, but the SEY depends on the energy deposition at the surface by the ion as explained in the previous chapter (although possibly in regime where nuclear stopping and not electronic stopping dominates). The stopping power in the approximations of the Bethe theory does

[d] As seen in the presence in the mass spectra of some gases such as the rare gases of the multiply-ionized atom at a level above what is expected from the literature cross sections, for example.

not depend on the nature of the nuclei, but it does depend on its charge and its *velocity*, which is the relevant parameter in the theory, and not kinetic energy. This would explain the $m^{-0.5}$ dependence: at fixed kinetic energy, velocity will decrease as $m^{-0.5}$.

In addition we may add that there are also potential losses of ions in the QMS due to the ion optics that bring ions from one part of the QMS to another and that set the kinetic energy of the ions for optimal operation. These losses may also depend on the m/z of the ions.

For practical purposes, we will consider a global apparatus function of the QMS that includes all the above factors except the ionization source, and we will assume that it can be described by a power law of the m/z of the ions. For the calibration of neutrals, we are only interested in the relative apparatus function (AF), therefore we will set AF(CO) = 1. There are different ways to obtain the apparatus function: for the Multisystem HiQuad QMS, by looking at the sensitivity calibration of the different gases tested (H_2, H_2O, CO, N_2, Ar and CO_2), including their fragmentation pattern, and by dividing these by the ionization impact cross-sections, there seem to be an apparatus function power law of m^{-1}.

For the QMS in SPICES II, I used instead only two gases, acetone and xenon, with fragmentation patterns covering a wide range of masses. By the same principle (dividing by the ionization cross-section) I find a power law of $m^{-1.5}$ for the Balzers QMS apparatus function and $m^{-0.5}$ for the Hiden QMS apparatus function.

III.1.7.3 Fragments and reflected light

In addition, and no matter what the calibration method used is, we need to consider the cases where more than one species contributes to a given mass channel. For example, we may wish to see if there is a signal of desorbing atomic C from CO ice, but we need to consider that electron impact ionization of CO also yields C^+ ions that need to be subtracted from the signal. For this the partial ionization cross section needs to be known, and the apparatus function has to be taken into account as well. The corrected signal is obtained thus:

$$i_C^{corr} = i_{12} - \frac{\sigma(C^+/CO)}{\sigma(CO^+/CO)} \frac{AF(12)}{AF(28)} i_{28}$$

In summary, the yield of a desorbing species per incident photon is given by:

$$Y_X = k_X \frac{i_X^{corr}}{\Phi_{ph}}$$

With k_X obtained either from a TPD calibration, or from the known k_{CO} by:

$$k_X = \frac{s_X}{s_{CO}} k_{CO} = \frac{AF(X)\sigma(X^+/X)}{\sigma(CO^+/CO)} k_{CO}$$

During the 2016 synchrotron runs in SPICES II, the configuration of the chamber (see below) was such that a small part of the incident synchrotron light was reflected into the QMS used for neutrals detection. This caused a spurious signal on all mass channels, rising linearly with a threshold around 11 eV. In order to take this into account, the signal on a "dummy" mass channel (m/z = 90 which does not correspond to any species we could

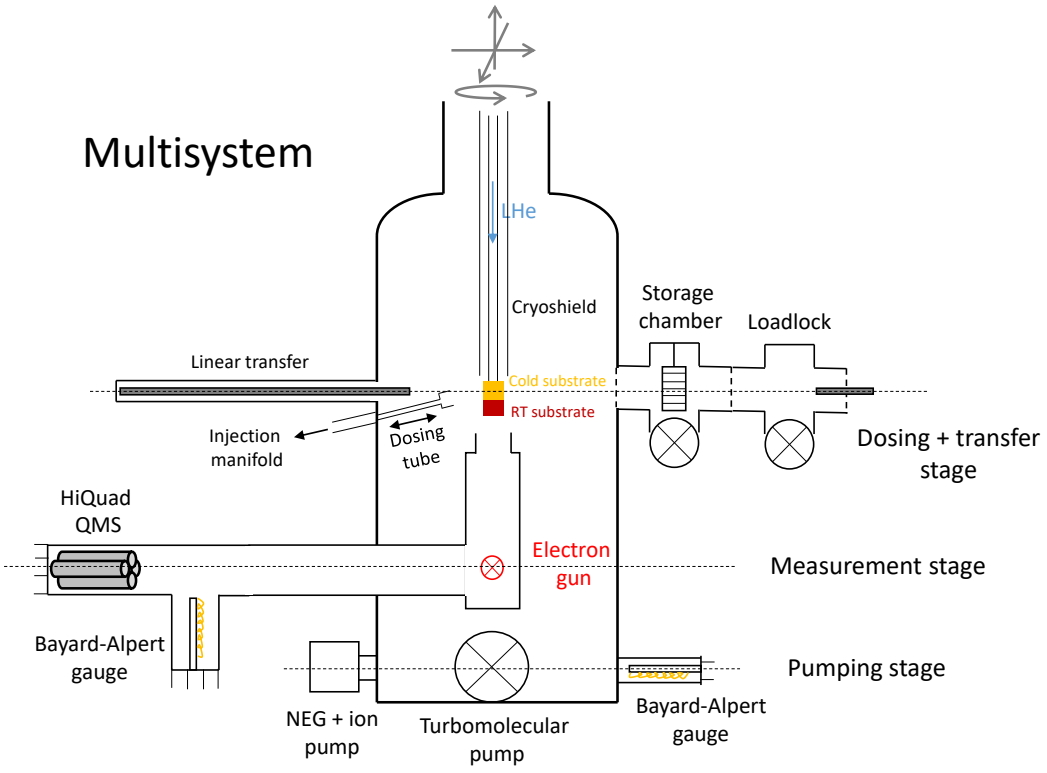

Figure III.8: Drawing of the Multisystem set-up. A description is given in the text.

have in the chamber) was recorded and subtracted from the desorption signal - the signal was usually small so it is not too much of a problem. In subsequent runs where a similar chamber geometry was used we ensured during the alignment step that the reflection was off the QMS.

III.2 Electron-induced desorption studies at CERN

III.2.1 The Multisystem set-up

The Multisystem[e] is the set-up that I have used at CERN to study electron-induced desorption (EID). This set-up was designed by Bernard Henrist and Vincent Baglin and assembled by them and Michal Haubner, with the idea of having a modular (hence its name) UHV chamber to study properties linked with non-thermal desorption and electron emission of surfaces exposed to irradiation (electrons, photons, ions). I participated to the commissioning of the set-up and the EID measurements on molecular ices were the first systematic measurements made on it.

The main chamber of the system is an ultra-high vacuum mu-metal (an alloy with a high magnetic permeability, that shields the interior of the chamber from parasitic magnetic fields) chamber pumped by a turbomolecular pump and a NEG cartridge. A

[e] A rather unsatisfying name, but we did not come up with a better one yet.

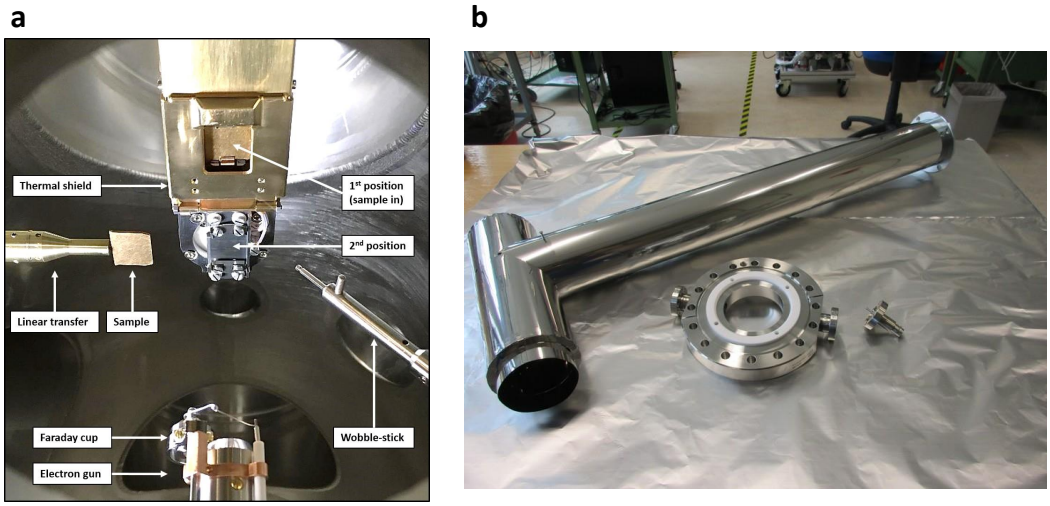

Figure III.9: **a.** View inside the main UHV chamber, with the cryomanipulator at the center and some other elements labeled on the picture. **b.** The molecule collector, not yet inserted in the chamber. Inside the chamber, the shorter tube is vertical and is where the manipulator is inserted. The longer tube is attached to a flange which leads to the QMS and a pressure gauge (cf. fig III.8).

drawing of the chamber is shown in fig. III.8. At the center is a cryomanipulator with movements in the XYZ directions and rotation around the Z axis, cooled down with liquid Helium. At the tip is a sample holder. A view of the manipulator inside the chamber is shown in fig. III.9a. The upper part of the sample holder can be cooled down to about 9 K (ultimate temperature achieved so far, but because of thermal issues after having to work on the sample holder, for most experiments presented in chapter V the base temperature was about 13 K), while the lower part is held at room temperature. We can see on the figure that in both the upper and lower part of the sample holder, a sample can be inserted. The samples used look like the one that is at the tip of the linear manipulator on the figure: they are flag-type substrates (surface $\sim$ 2.7 cm^2). For the experiments presented here the nature of the substrate is not considered important and its influence was not investigated. We used either a technical OFHC copper substrate or a gold-coated stainless steel substrate. On the lower part, a phosphorus screen was inserted. The back of the lower part is also equipped with two Faraday cups. Both this phosphorus screen and the Faraday cups were used to characterize the electron beam. For both sample slots, the sample is kept electrically isolated by a sapphire plate, which allows to measure the substrate current (see section III.1.6).

The sample can easily be changed in this set-up, using the linear manipulator shown on the figure and two annex vacuum chambers. A first chamber is used to store samples under vacuum, and the other to transfer a new sample from outside to the storage chamber. When the cryostat is at room temperature, it takes less than 30 minutes to change a sample.

The chamber is equipped with an electron gun (Kimball), with a theoretical range of electron energy 5 - 2000 eV. The measurements were carried out in the 150 - 2000 eV

range. The beam was incident normal to the surface. For each energy, the beam was set in order to obtain a clean spot of about 0.1 cm^2. The beam was checked to be gaussian with the Faraday cups. The exception was that for energies 1500 eV and more, the beam could no longer be focused tightly enough to obtain the same conditions. Larger and less well defined spots were used, which means measurements at these energy carry more uncertainty. Measurements were not made below 150 eV because the shape of the beam becomes harder to control properly (it is not visible on the phosphorus screen), but also because chargeing of the molecular ices made it difficult to have good measurements.

The composition of the residual gas of the chamber was monitored using a quadrupole mass spectrometer (HiQuad), which is also used for the desorption measurements.

In order to deposit condensed gas on the surface, an injection system is used. The principle was described in section III.1.4. Gas from an injection manifold is brought into a closed, known volume where the pressure is measured by a capacitance gauge. A microleak valve is then used to let gas into the chamber through a dosing tube, which can be brought very close to the surface so that most gas sticks and the rest of the chamber is not contaminated. The investigated gases are CO, N_2, Ar, CO_2, and H_2O, as well as some isotopes of these: $^{15}N_2$, $^{13}CO_2$ and D_2O. For H_2O and D_2O, the liquids in pyrex vials were purified by several freeze-pump-thaw cycles and the vapour pressure above the liquid was let into the manifold.

One particularity of the set-up that was implemented in 2018 is the use of a "molecule collector"[f]. The measurement of electron-induced desorption involves measuring the increase of partial pressure of the species of interest when bombarding the surface with the electron beam. In order to increase the sensitivity of the measurement, a new system was tested. The collector is an L shaped tube attached to the flange of the chamber which leads to the QMS and into which the manipulator can be inserted (see a picture of the collector fig. III.9b). The pumping speed inside the collector is thus limited, with the only apertures being the margin between the manipulator and the collector entrance, and a small hole to allow the electron beam to hit the sample inside. With the pumping speed reduced, the increase of partial pressure when irradiating the sample is increased. Based on measurements made inside and outside the collector for N_2 EID, it is estimated that the collector brings an improvement of a factor of ~ 8 to the signal-to-noise ratio.

III.2.2 Measurement procedure

We wish to obtain the EID yield as a function of electron energy for a number of systems. For this, a molecular ice is grown by the procedure explained previously. The cryomanipulator is then inserted in the molecule collector so that the cold substrate is in front of the electron gun. The surface is set at a voltage of +45 V to prevent secondary electrons from escaping the surface (this was tested to not change the EID yield, but it does change the incident electron energy, which is taken into account). The current read on the substrate when irradiating is therefore the incident electron current. The ice is irradiated at a given electron energy for about 20-30 seconds, usually with a beam current of around 100 nA, and the desorption signal of the relevant species is recorded on the QMS as an increase of partial pressure. Simultaneously, the substrate (incident beam) current is recorded with a Keithley picoammeter. The procedure is repeated for a series of electron

[f] Actual name used in the lab: the siphon.

energies. There is little room in the molecule collector to wiggle around and change the irradiation spot for each electron energy, so everything is done on the same spot. We can insure that this does not bias the EID yield by repeating the experiments with a different order of measurement. Because some ices do exhibit some ageing (change of yield with electron dose) the measurements can indeed be affected, but except for specific cases the irradiation time was short enough that it was not an issue.

Once the data is recorded, the processing is done by taking the average value of the QMS current during irradiation for each energy, dividing by the beam current, and converting to EID yield by the procedure explained earlier. The rms noise of the QMS measurement is taken as a measurement uncertainty for the error bars of the plots of chapter V. We thus consider that there is no uncertainty on the beam current measurement. There may be other sources of uncertainty (as mentioned above, the differences in beam size, for example...) but they are not quantifiable. The uncertainty on the absolute yield is also difficult to evaluate when it is calibrated with the TPD method: we cannot expect better than a 50 % uncertainty for these kinds of measurements, though.

III.3 SPICES II at LERMA

The details of the SPICES II set-up for the different synchrotron experiments and the laser desorption/REMPI lab experiments will be given in the next sections. I will briefly describe the main chamber here. The SPICES II set-up at LERMA was designed by Pascal Jeseck, Patrick Marie-Jeanne, Jean-Hugues Fillion and Mathieu Bertin and assembled in early 2016, during my master's internship with the team. It is an upgrade of the previous SPICES set-up, dedicated to the study of thermal and non-thermal desorption of molecular ices for astrophysical purposes. A drawing of the set-up is shown in fig. III.10. The UHV chamber is pumped by a turbomolecular pump and an ion pump + titanium sublimation pump down to $\sim 3\times 10^{-10}$ mbar at room temperature after bakeout, and 1×10^{-10} mbar at cryogenic temperature. A cryostat head is at the center of the chamber, with the sample holder at its tip. It is mounted on a differentially-pumped rotation system, with also an XY movement possible. Cryogenic cooling is made using a closed-cycle Helium compression cryostat, reaching 10-16 K at the sample depending on what is used on the sample holder. Substrates (square surfaces 1.5 × 1.5 cm^2) are glued on the copper sample holder. We have available an HOPG surface (Highly Oriented Pyrolytic Graphite), a polycrystalline gold surface, or an OFHC (Oxygen-Free High Conductivity) copper surface. Since 2017 the copper surface is electrically insulated from the ground, allowing electron yield measurements. However this has raised the base temperature of the sample holder from 12 K to 15-16 K, and we have suspicions that the copper surface itself might be above 20 K.

In the main plane of the chamber, a dosing tube as presented earlier is connected to the injection manifold for gas injection. Two separate lines are available on the gas injection manifold. The ice, once deposited, can be probed by FT-RAIRS as explained earlier as well. The spectrometer is a Bruker vec22 model with a resolution of ~ 1 cm^{-1} (which is more than enough for condensed phase measurements), and the detector a liquid nitrogen cooled MCT. Two QMS are available: a smaller Balzers model for neutral detection and RGA, and a bigger Hiden Analytical EQS model for ion detection with kinetic energy

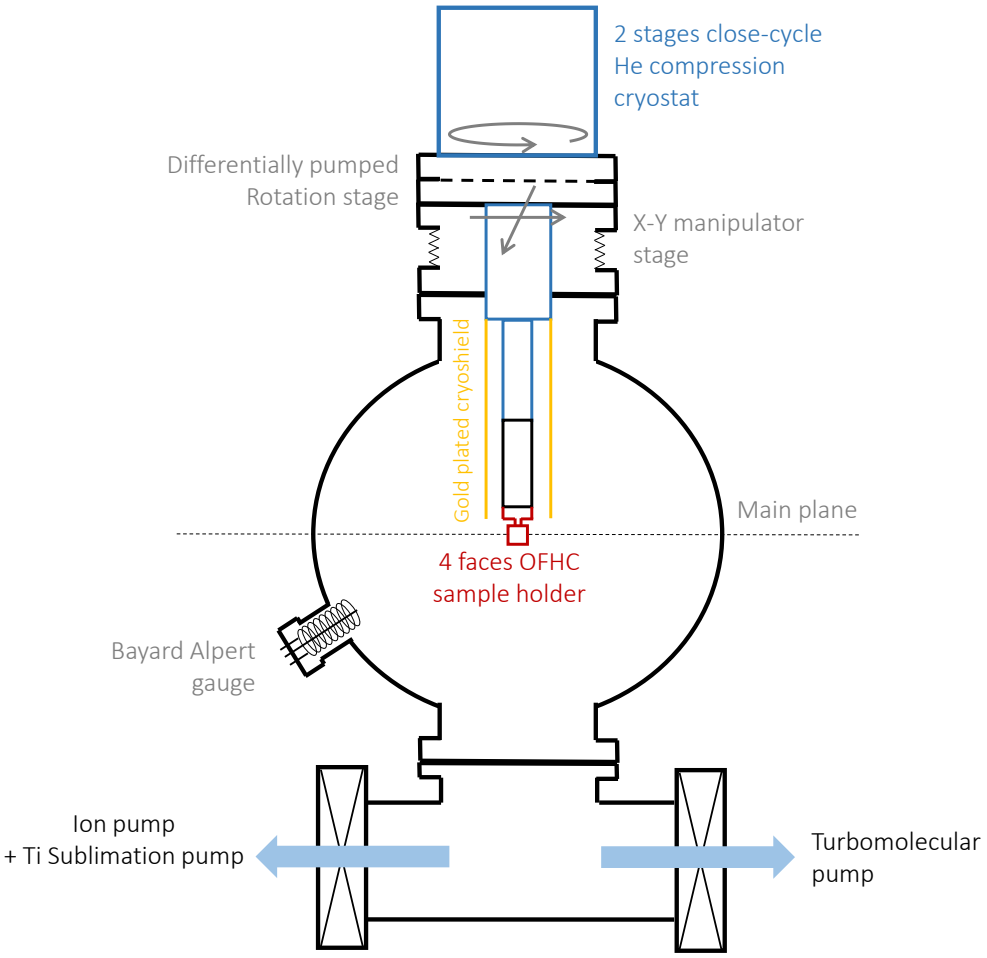

Figure III.10: Drawing of the SPICES II set-up. A description is given in the text.

analysis. The Hiden QMS also has a ionization source for neutral detection but it turned out to be less performing than the Balzers QMS for that purpose. Two quartz windows on opposite sides allow to let a UV laser through for REMPI spectroscopy. A differential pumping stage on one of the flanges is used for connection either to the VUV generation cell in the lab or to the synchrotron lines. The geometry will be more clear when looking at fig. III.11 and III.18 that will be explained later.

III.4 Synchrotron-based experiments

A lot of the experiments presented here were obtained during beamtime runs at SOLEIL, a 3rd generation synchrotron facility open for user projects. Experiments in the VUV range were performed on the DESIRS beamline, and experiments in the soft X-ray range on the SEXTANTS beamline. Here I will present how we make use of synchrotron light and describe how the experiments were performed on the two beamlines.

III.4.1 Synchrotron light and its advantages

As mentioned in chapter I, a relativistic charged particle with a radial acceleration emits synchrotron radiation, with a wide continuous spectrum, shown in fig. I.7. Synchrotron facilities are one class of particle accelerators that aim to harness synchrotron radiation for its unique properties. The most important aspect of synchrotron radiation is the continuous spectrum up to high energies: synchrotron radiation is basically the only way to produce light above the VUV range (up to hard X-ray energies) of *any photon energy* (with the help of monochromators), with a high photon flux and a coherent, well collimated beam. Synchrotron light sources typically use electrons, which are accelerated initially by a linear accelerator (linac) then accelerated again in a booster ring, and injected in a storage ring, where they are used to generate synchrotron radiation. The radiation can be generated simply using bending magnets, but insertion devices can be used to obtain a brighter light. These devices (wigglers or undulators) make the electrons undergo oscillations. The SOLEIL synchrotron has a storage ring of 354 m circumference and electrons of a nominal energy of 2.75 GeV are used. It is a source optimised for an "intermediate" energy range (tender X-rays), allowing efficient VUV and soft X-ray beamlines as well.

III.4.2 Experiments on the DESIRS beamline

The DESIRS beamline is an undulator-based beamline dedicated to VUV (5 - 40 eV) light. There are two operation modes of the beamline that we use. In the first one, a monochromator is used. It covers the 5 - 20 eV range and offers a resolution of $\sim$ 40 meV at 10 eV for a flux of $\sim 10^{13}$ ph.s^{-1} (depending on the setting of the aperture slits). In this mode continuous scans of the photon energy can be performed to obtain (photodesorption) spectra. However, this photon flux can be insufficient to obtain a measurable signal. The second mode uses the monochromator as a mirror at the zeroth order, therefore the beam consists of the direct output of the undulator. It consists of a spectrum of harmonics, the fundamental being set by the users, which have a spectral width of about 1 eV (the form is approximately lorentzian but can be quite asymmetric at some photon energies). The flux reached is then up to 10^{15} ph.s^{-1}. Scanning is no longer possible but the much higher flux allows measurement of low desorption yields.

A specificity of this beamline is the use of gas filters to ensure that no higher harmonics of the undulator is left in the beam. Rare gases are transparent in the VUV up until their ionization threshold, except for a few Rydberg lines, and can therefore be used for that purpose. Different ranges of photon energy are available depending on the rare gas used: 6-12 eV (Xe), 7-14 eV (Kr), 8-16 eV (Ar) and 10.5-21 eV (Ne). The high end of the energy is the first IP of the gas. Above 21 eV fundamental photon energy, the harmonics are simply cut-off by the optics, and the 5-6 eV range is available using an MgF_2 window. Most of the results presented in chapter IV were done using the Krypton filter in the 7- 14 eV range. Another specificity of the beamline is the possibility to control the polarization of the beam. In our experiments we only used the vertical (in the lab referential) polarization, since it is the one for which the line is the most efficient in terms of flux and undulator operation. It corresponds to an in-plane polarization of the incident beam at the surface.

The chamber is connected on branch B of the beamline, which is designed to accommodate user external chambers, in a windowless fashion using a differential pumping

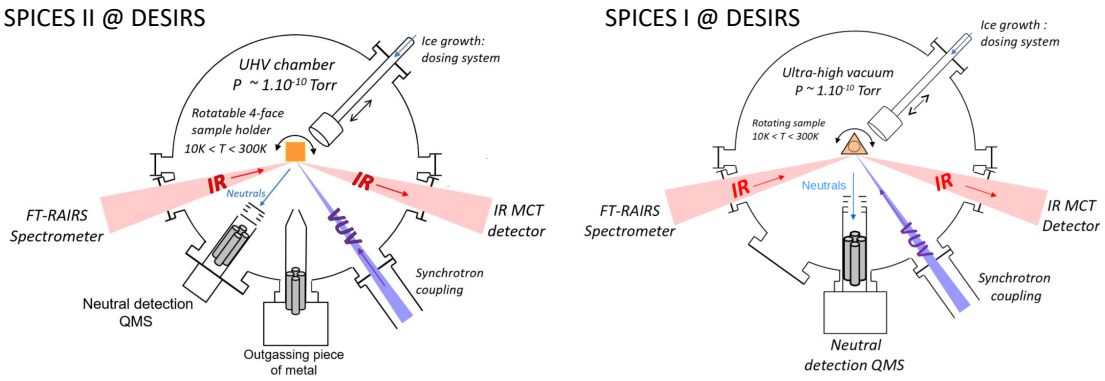

Figure III.11: Configuration of the SPICES II (left) and SPICES I (right) chambers at the DESIRS beamline.

set-up to preserve the ultra-high vacuum. The configuration of SPICES I (2009-2015) and II (2016-now) at the DESIRS beamline are represented on fig. III.11. The beam hits the surface at a 45° angle on a spot of a size of ~ 0.6 cm^2. The photon flux is measured right before the chamber using a NIST calibrated Si photodiode, AXUV for the first order beam and SXUV for the zero order one. Some representative fluxes are plotted in fig. III.12. The FT-RAIRS allows to check the composition of the ice before irradiation, and to probe possible photochemistry after.

The measurement procedure depends on the mode of the beamline used. When possible, we use the monochromator and continuously scan the photon energy (typically, from 7 to 14 eV) while recording the relevant masses on the QMS (the Balzers QMS for neutral molecules: the photon energy is too low to have ions desorbing). A photodesorption spectrum (not calibrated yet) is directly obtained this way. The photodesorption signal we measure is usually much lower than the background due to residual pressure. This is not a problem when the background is flat and can be easily subtracted, but this is not always the case. Ideally, a well baked-out chamber and the use of isotopically labeled species to avoid polluted channels provide a very good background against which sensitive measurements can be made (we can estimate that a desorption yield of $\sim 10^{-4}$ molecules/photon can be detected with first order light on a clean channel). In practice, the problem with synchrotron runs is that time is constrained and experiments made without pause for the full four or five days. Dosing an ice already introduces the species that we wish to measure in the chamber, polluting its mass channel, so that we have to wait for the background pressure to decrease before a measurement. Then the ice is flashed by a TPD, releasing again a lot of molecules in the chamber. As this process is repeated the background progressively worsens. Even a desorption yield of $\sim 10^{-3}$ molecules/photon can become difficult to measure after a while.

The noise is not the only problem: background subtraction when the background is not flat can be a problem. It is always assumed that an analytical fit of the background, typically using a polynomial function, can be made, but that remains an assumption that may not always be verified, and background subtraction can easily distort the spectra.

Background subtraction is the first step of the processing of the raw data into a photodesorption spectrum. For that, I used the background subtraction routine of Origin.

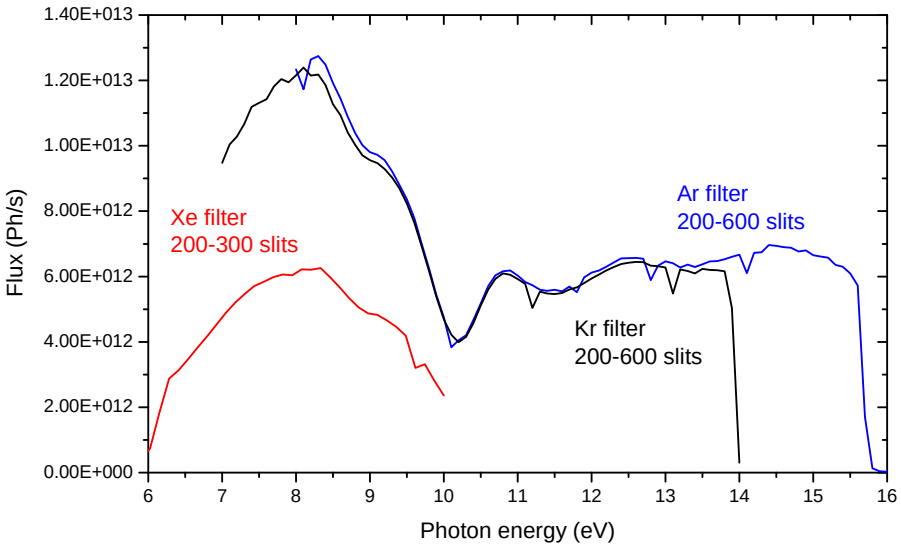

Figure III.12: Photon flux on the DESIRS beamline for different filters and slit settings. Measured with a NIST calibrated AXUV photodiode, right before the beam enters the SPICES chamber.

The next step is to convert the time abscissa into a photon energy abscissa. The QMS acquisition computer and the beamline control computer are not connected: synchronization is made "manually" by noting at which point of the acquisition the scan starts. One could then assume that it is possible to convert time to photon energy by a linear relation. It turns out that this method does not work: for each point in the scan, aside from the dwell that we set at 2 seconds, there is a time needed to move the monochromator and the undulator to the right energy of a few seconds. This latency is not fixed: there is a spread of duration for each point centered around 6 seconds but going from 4 to 9 seconds. This needs to be taken into account by interpolating the time-to-energy data of the scan to the time column of the QMS data. Neglecting this can result in significant differences, such as shifts in the features and distortions in regions where the flux is structured.

Once the data is converted to an energy scale, it is divided by the flux and by the absolute calibration factor as explained in a section above. A photodesorption spectrum with yields in molecules per incident photon as a function of photon energy is thus obtained.

The procedure for measurements at the zeroth order is simpler, since we irradiate the ice at fixed photon energies for a few seconds and record the signal on the QMS. Background subtraction is easier and the signal is then converted to photodesorption yield by dividing by the flux and calibration factor. Points are usually taken every 0.5 eV, which does not allow to resolve any fine structure, especially considering the spectral width of the light.

III.4.3 Experiments on the SEXTANTS beamline

The SEXTANTS beamline is also an undulator-based beamline, dedicated to experiments in the soft X-ray range (100 - 1000 eV). For the results presented here, we only worked around the O 1s edge (in the 520-600 eV range) where the monochromator used offers an

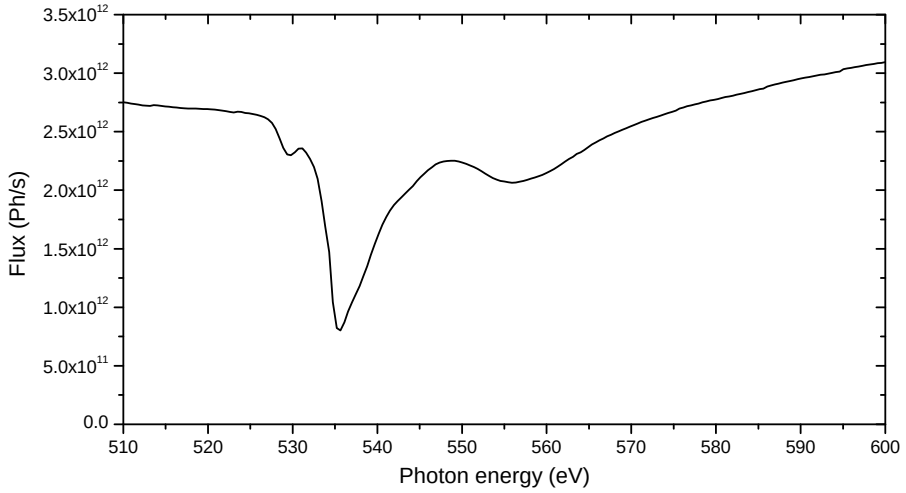

Figure III.13: Photon flux on the SEXTANTS beamline (510-600 eV). Measured with a Si photodiode, right before the beam enters the SPICES chamber.

ultimate resolution of $\sim$ 80 meV. The line is only used in monochromatized mode, but the flux is varied by changing the aperture slits (although this also affects the resolution). Higher order harmonics of the undulator are not a concern in this energy range because of optics cut-off. The flux measured in the relevant range by a Si photodiode before entry in the SPICES chamber is displayed in fig. III.13. This flux is for slits settings 20 μm, corresponding to a resolution of $\sim$ 120 meV. Other slit settings used are either 100 μm (at 600 eV, resolution 300 meV and flux 1.5×10^{13} ph.s^{-1}) or 5 μm (at 600 eV, resolution 90 meV and flux 8.5×10^{11} ph.s^{-1}). The flux spectrum does not change with the slit settings. We can see in fig. III.13 that the flux is structured, notably by absorption in O 1s range.

The configuration of SPICES II at SEXTANTS is displayed in fig. III.14. Polarization can also be controlled on this beamline, and we used the horizontal polarization setting to obtain a 50 % in-plane and 50 % out of plane polarization relative to the surface, since the beam is incident at 45° relative to the surface normal. The FT-RAIRS is only used to check the initial composition of the ice, since the irradiated spot is too small relative to the total area probed by the IR beam to see the consequences of photochemistry. The measurement procedure is relatively similar to the one on the DESIRS beamline: the photon energy is continuously scanned while the signal of selected neutral molecules (on the Balzers QMS) or ions (on the Hiden QMS) are monitored. Additionally, on the Hiden QMS the kinetic energy at which detection is made has to be chosen (there is no "full pass" mode for the deflector). In order to check that the kinetic energy chosen does not distort the "full" spectrum, kinetic energy distributions of ions are taken at different fixed photon energies. These kinetic energy distributions are also used to properly quantify ion desorption. The total electron yield (TEY) is also recorded as a function of photon energy for all scans.

The calibration of the results obtained for neutral desorption is relatively similar as what was done in the VUV range; however since the "reference" absolute calibration by FT-RAIRS cannot be done in this range (there is too much chemistry, and the discrepancy

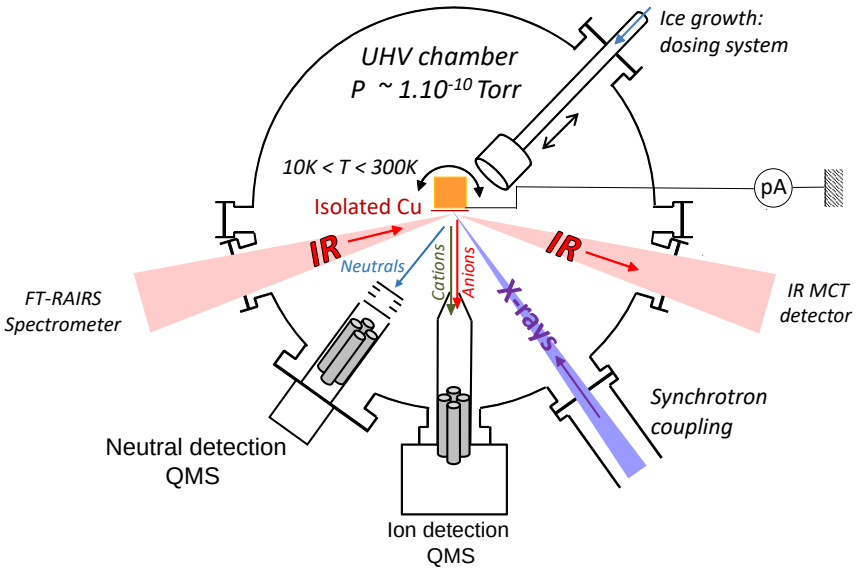

Figure III.14: Configuration of the SPICES II chamber at the SEXTANTS beamline.

between the size of the irradiation spot and the IR spot is too large), the TPD calibration method was used. For ion desorption, we do not have a method to obtain an absolute calibration right now, so that in order to estimate the yields we used literature values as a reference. The kinetic energy distribution of the C^+ ion from CO at 550 eV is integrated and divided by the flux to obtain a number of ion counts per incident photon. The reference value for C^+ desorption from CO at 550 eV is the one given by Rosenberg et al. [140]. The value given in this paper is 4 $\times 10^{-6}$ ion/photon for a detection efficiency of 100 %, but the detection efficiency of their apparatus was later estimated to 20 % [195]. Assuming a yield of 2 $\times 10^{-5}$ ion/photon for C^+ at 550 eV we obtain a detection efficiency for our own apparatus of 2 %, which does not seem unreasonable for a QMS. We then assume that the efficiency follows the power law $(m/z)^{-0.5}$ mentioned earlier for quantification of the other ions. In the absence of a way to cross-check this quantification, it is deemed temporary and should be taken as an order of magnitude estimate.

III.5 Development of a UV laser desorption and spectroscopy set-up in the lab

An amount of time which is not proportional to the space devoted to it in this manuscript has been spent on the development of a set-up at the LERMA laboratory, using lasers for both desorption and characterization of the desorbing molecules. The idea is that (i) beamtime at the synchrotron is limited: it is difficult to make systematic investigations and tests that would take a lot of time, and (ii) characterization of the desorbing molecules by laser spectroscopy is very interesting but would not be practical at the synchrotron because setting up a laser there would be complicated.

For this, a desorption source is required, ideally in the VUV range since this is mainly where the electronic levels of the molecules of interest lie. In the following sections, I will

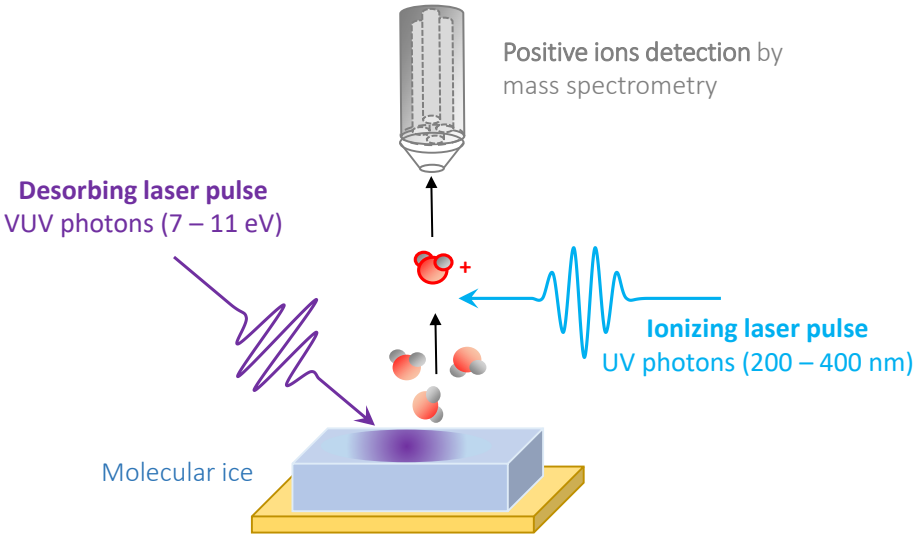

Figure III.15: Experimental scheme of the VUV desorption + REMPI spectroscopy set-up.

describe the set-up developed for laser desorption and for REMPI spectroscopy. Some first results will be presented in the next chapter.

The set-up of the experiment that we are aiming for is schematized in fig. III.15. In this experiment a nanosecond VUV laser pulse (7-11 eV) is used to desorb molecules by exciting a specific electronic state of the solid. A second nanosecond UV pulse (200-400 nm) ionizes the desorbed molecules, and the cations are detected by mass spectrometry. Ionization occurs about 1 cm above the surface, and is basically instantaneous with respect to the temporal width of the distribution of the desorbed molecules at this point (a few tens of μs). Therefore only molecules of velocity $v = d/t_{delay}$ (where d is the distance from the surface to the ionization point and t_{delay} is the time delay between the desorption and ionization pulses) are ionized and detected. By varying the time delay, a time-of-flight (TOF) spectrum, and therefore the translation energy distribution of the desorbed molecules, can be obtained. In addition, ionization is strongly enhanced when the photon energy of the ionizing pulse (or a multiple of that) is resonant with a rovibrational level of an excited state of the molecules. Scanning the photon energy of the ionizing pulse gives a REMPI spectrum (see below) from which the rotational and vibrational quantum state distributions of the desorbed molecules can be obtained. With both the kinetic and internal energy distributions, characterization of the desorbed molecules is thus complete.

III.5.1 UV and VUV laser desorption

III.5.1.1 VUV generation

Most studies of photodesorption that attempt to reach VUV wavelength use either a hydrogen discharge lamp, which gives a broadband spectrum and continuous irradiation, or a laser with a fixed wavelength, which allows to have a monochromatic and pulsed

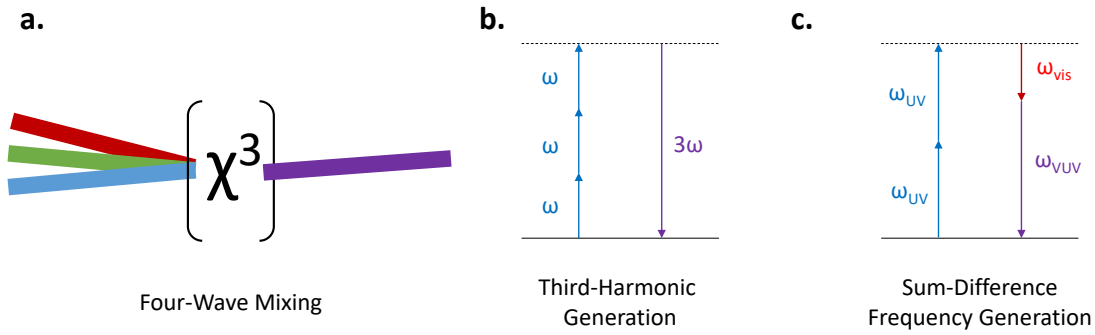

Figure III.16: **a** Principle of third-order nonlinear effects. **b** The Third-Harmonic Generation scheme. **c** The Sum-Difference Frequency Generation scheme.

irradiation. The lasers used are exciplex lasers: the wavelength of the ArF and F_2 lasers, respectively, fall at 193 nm and 157 nm, or 6.4 eV and 7.9 eV. It is desirable, to excite precisely the electronic states of the molecules we want, to have instead a more tunable laser source. This is, however, fairly complicated: there are no nonlinear crystals that are transparent in the VUV region so the doubling and tripling schemes of tunable lasers stop around 200 nm. VUV laser pulses can be generated using instead a gas as a nonlinear medium, but using a χ^3 (third order nonlinear optical susceptibility) effect since isotropic media have a zero χ^2. This kind of technique has been explored for more than 40 years [196] and is installed in several laboratories, but there is no commercial set-up for it.

Let us explain briefly the principle of VUV generation by four-wave mixing (fig. III.16a) in our case. The principle is to obtain higher frequency light from the mixing of lower frequencies by a third-order nonlinear effect. In this type of four-wave mixing, there are three input photons for one output photon (the VUV photon). Different schemes are then possible: one is Third Harmonic Generation (THG) where the three input photons are the same (fig. III.16b), another is Sum-Difference Frequency Generation (SDFG) where two photons are added and one subtracted (fig. III.16c).

The principle was tested during my master's internship, by tripling the 355 nm output of the pump of one of the lasers in a Xenon gas, yielding 118 nm light. The results will not be detailed here. VUV light was detected using a home-made photoelectric detector, using two metallic plates with a high voltage between them and sending the beam on one of the plates. The photoelectrons ejected by the VUV beam are accelerated towards the other plate and a current is measured. From rough estimations, we concluded that the energy of the VUV pulses obtained in the optimal conditions, around 1 nJ per pulse at 10 Hz, was too low for our applications. We therefore decided to move on to a four-wave mixing, sum-difference-frequency generation (SDFG) scheme, which should yield higher energies, but requires two different lasers.

The general theory of four-wave mixing in isotropic media in a focused geometry is presented in Bjorklund [197]. In this theory the four parameters that determine the output power of the VUV beam P_{VUV} are the number density of the tripling medium N (or concretely for us the pressure), the power of the input beams, the phase difference of the VUV and other beams Δk and the confocal parameter b of the beam (which is assumed to be a Gaussian beam, transverse, 0th mode in both directions). The form of

the formula giving the VUV power output depends on the scheme (THG, SDFG...).

The analysis shows that for THG, the output is nonzero only if Δk (which is equal to k_{VUV} - $3k_{UV}$ in this case) is negative. This is only possible if the medium has a negative dispersion (the optical index decreases with increasing wavelength), and usually dispersion is positive. Rare gases have a negative dispersion on the blue side of their resonances, but the tripling process is severely limited to a few specific wavelength ranges. Another downside of THG is that it is a non-resonant process: if we were to try working on a resonance of the rare gas, the generated VUV photon would immediately be re-absorbed as it is resonant as well.

SDFG is much more favourable: there it is possible to use a resonant scheme. The scheme is drawn in fig. III.16c. The UV laser used for the two up photons can be tuned to a resonance of the rare gas used, while the visible down photon is used to tune the wavelength of the VUV. In SDFG, the condition that maximizes the output is $\Delta k = 0$, which is also more convenient as the positive or negative dispersion of the gas does not matter. More precisely we have:

$$P_{VUV} \propto \chi^2 P_{vis} P_{UV}^2 N^2 exp(-bCN)$$

where Δk has been replaced by CN. The refractive index of a gas is proportional to the density N, so that Δk is as well, and this is why we introduce the intensive quantity C instead. We can see that once the power of the lasers is set, we need to optimize $N^2 exp(-bCN)$. The optimal value of b is 0, so that maximizing power requires focussing as much as possible. The optimum value of the density (i.e. of the gas pressure in the cell) is N = 2/bC. It is also possible to increase the efficiency of the tripling in wavelength regions where the rare gas used has negative dispersion: another gas, with positive dispersion, can then be used to "phase-match" and insure $\Delta k = 0$, therefore optimizing the power output [198]. It is also then possible to increase the pressure of the tripling gas above what would normally be optimal, taking advantage of the N^2 dependence of the output.

There are limits to how much the pressure, focussing and power of the input lasers can be increased: plasma formation, re-absorption of the VUV by the gas, saturation of the resonance, etc... and the optimal working point has to be found experimentally.

III.5.1.2 Practical implementation

A drawing of the set-up used for VUV generation is showed in fig. III.17. The principle is the following: one or several UV laser beams are focused by a regular quartz lens in a tripling cell, which has been pumped then filled with a static pressure of the rare gas used for tripling. Focussing is necessary to achieve third order nonlinear effects. A VUV pulse is thus generated. The different beams come out of the tripling cell through a LiF lens (since it is now necessary to have a material transparent to VUV light), which should make the VUV beam parallel. The beams enter a separation chamber, pumped to a primary vacuum of $\sim 10^{-2}$ mbar. A LiF prism is used to separate the VUV beam from the UV one(s). The VUV beam is then redirected into the SPICES chamber, passing through a LiF window separating the ultra-high vacuum from the separation chamber.

The goal to achieve VUV generation by SDFG will be to use a pulsed nanosecond dye laser (Quantel) pumped by a doubled Nd:YAG at 532 nm, to generate a tunable

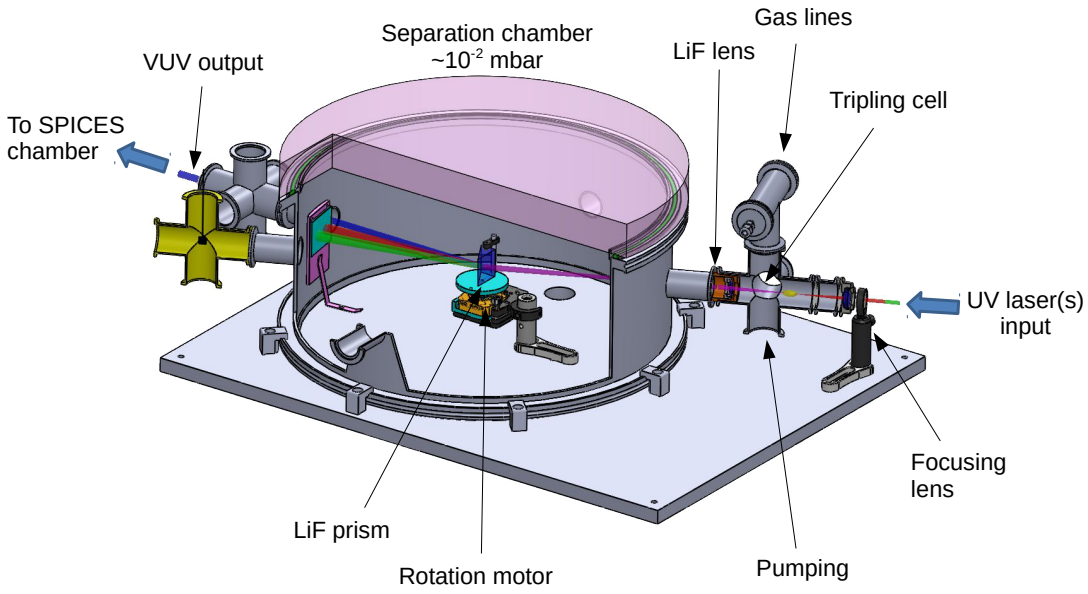

Figure III.17: Schematic drawing of the VUV generation set-up.

beam that will be doubled and then mixed for either tripling or DFG with the 1064 nm of the YAG, landing between 200 and 250 nm. This beam will be tuned on a 2-photon resonance of Krypton or Xenon. The second laser beam will come from another tunable pulsed nanosecond Quantel dye laser. The most efficient working region of such dye lasers is around 550 - 710 nm. Tuning this laser will tune the final wavelength of the VUV beam. A list of interesting 2-photon resonances in Kr and Xe has been identified.

Since the second, visible dye laser is not working, it is possible to start working with a non-tunable VUV beam if it lands on a relevant wavelength (typically in the absorption region of CO). The current plan is to use a 355 nm YAG from a borrowed laser and the 212.55 nm resonance of Krypton to obtain VUV at 151.6 nm, close to v = 1 of the A - X region of CO.

III.5.2 REMPI spectroscopy

REMPI stands for Resonance-Enhanced Multi-Photon Ionization, which as its name indicates is a multiphoton ionization scheme, therefore a nonlinear process usually done using a pulsed laser. It takes advantage of the fact that the multiphoton ionization process will be greatly enhanced if some multiple of the photon energy is resonant with an electronic transition of the molecule. Using a tunable monochromatic laser and monitoring the ion yield, it is therefore possible by scanning the wavelength to probe the electronic transitions of the molecules. These transitions in turn give information on the population of molecules in the ground state (rotational, but also spin, vibrational and even electronic states other than the ground state). A REMPI scheme is dubbed "N+M" when the resonant transition is an N-photon transition and it requires M more photons to exceed the ionization threshold.

In the gas phase at room temperature, for the molecules we are considering here, only the v = 0 vibrational level of the electronic ground state will be populated. We may however make an electronic transition from this state to different vibrational levels of different excited electronic states. We will assume that each vibronic band is well separated (which is the case here), and therefore when we do a REMPI spectrum we are probing a transition between the ground state v" = 0 and one specific vibrational level v' of an excited electronic state. We are therefore probing only the rotational population (and possibly the nuclear spin population) of this ground state. With desorbing molecules we may expect vibrationally excited molecules or even electronically excited ones, which makes many more transitions possible. But we will again assume that we are always probing one specific transition from the rotational levels of one populated vibronic level to those of another one empty vibronic level. Considering the wavelength range on which we can make a wavelength scan (3-4 nm without having to change the laser optimization, and even then a 4 nm scan would be done in several steps), it is not reasonable to think that the vibrational populations can be probed with a single REMPI scan. Instead these populations would be accessible by integrating the rotational populations obtained for each ground state vibrational level.

Consequently we need to understand the rotational sub-structure of a given vibronic transition. As mentioned briefly in chapter II, the structure of a rotational level in first order is of the form BJ(J+1), with B a rotational constant and J the quantum number associated with the total angular momentum. J is an integer for molecules with an even number of electrons (e.g. CO) and a half-integer for those with an odd number of electrons (e.g. NO). For a 1 photon transition, the transition selection rule for the rotational part (we assume otherwise an electric dipole allowed transition, governed by the Franck-Condon principle) is $\Delta J = 0, \pm 1$. For a 2-photon transition, we would have $\Delta J = 0, \pm 1, \pm 2$. Usually the transitions observed are grouped into "branches" depending on the ΔJ they correspond to. We speak of O, P, Q, R, S branches for ΔJ = -2, -1, 0, +1 or +2, respectively. Theoretically, one branch is enough to obtain information on the rotational populations, but sometimes looking at multiple branches can be useful to have access to a large range of J values on a scan that does not span a too long range of wavelengths.

III.5.3 Desorption + REMPI set-up

A summary of the practical implementation of the desorption + REMPI set-up is given in fig. III.18.

For the desorption part, a Quantel dye laser (pumped at 532 nm with a pulsed YAG with around 5 ns pulses, Q-switched at 10 Hz) with an output tripled to the deep UV range is used. It can be used as the UV laser part of the SDFG VUV generation scheme by tuning it to the relevant resonance (in which case the visible beam from another laser on the figure is also present). For the time being (as the visible laser was not available), experiments in the lab have been performed on NO, a molecular ice which absorbs above 200 nm and therefore does not require VUV generation. Instead the tripled output of the Quantel dye laser (doubling + mixing in crystals) has been used for desorption. A DCM dye is used to generate laser light at 639 nm and the final wavelength used is 213 nm, the maximum energy that can be reached being around 1.8 mJ per pulse when

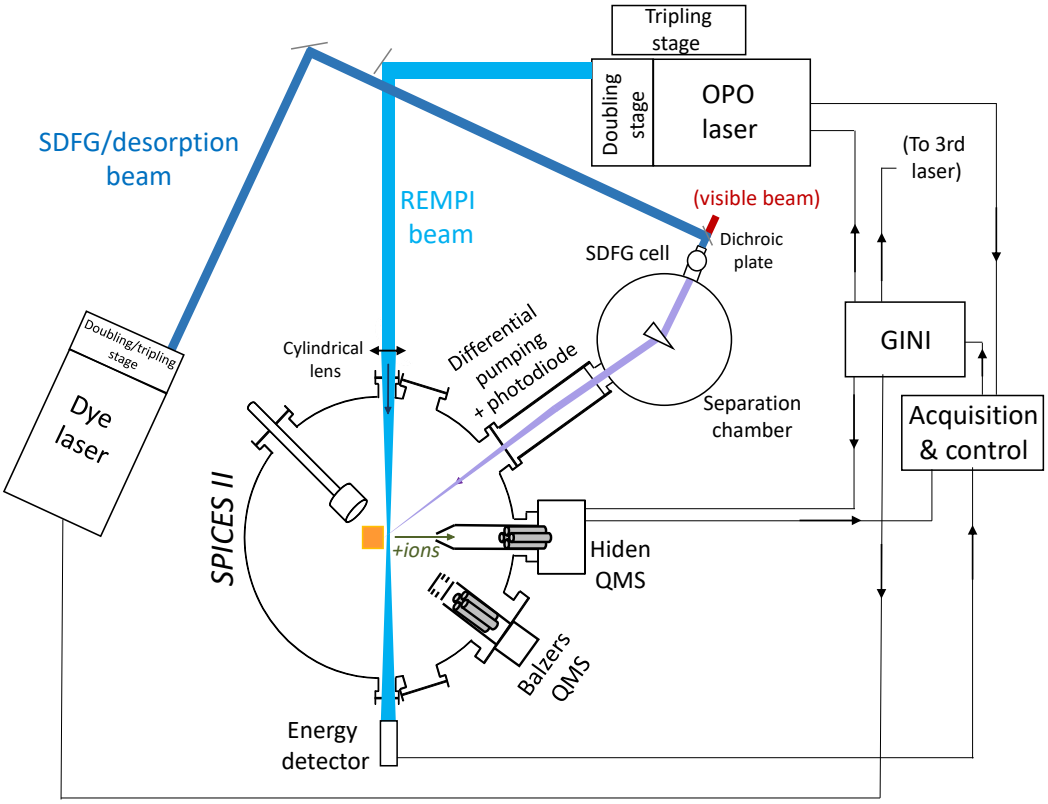

Figure III.18: Drawing of the overall set-up of the desorption + REMPI experiments. Details are given in the text.

exiting the laser. Since the optical path to the SPICES chamber is relatively long (two mirrors, two lenses and the LiF prism), only about 0.6 mJ is left when arriving at the chamber (which is nonetheless enough). The optical path is the same as for the VUV scheme. The two lenses at the entry and exit of the SDFG cell can be used to adjust the focalisation of the beam to the surface (here it was not particularly focused: the two lenses served mostly to correct for the divergence of the beam after an optical path of several meters). The separation chamber is connected to SPICES II by a differential pumping stage (but remains separated by a LiF windows from this differential pumping stage, which is mostly used at SOLEIL). This stage contains an SXUV photodiode for future VUV beam measurements. The energy of the desorption beam is presumed to stay constant during the course of the measurements, which is usually the case. This can be checked if necessary by catching one of the reflections of the beam in the LiF prism, where a few μJ can be measured.

REMPI spectroscopy is made using an OPO (optical parametric oscillator) pulsed nanosecond laser. An OPO makes use of a nonlinear effect where a "pump" wavelength is divided into two longer wavelengths of different energies. The shorter wavelength is called the signal and the longer one the idler. This effect is made in a crystal, where in the appropriate referential one angle relative to the incident light sets the wavelengths of the outcoming lights (the other angle setting the phase matching required for the effect). The

pump here is again a YAG laser, tripled to 355 nm (operating at 10 Hz and generating pulses of around 5 ns as well). Because of the stability and spectral width required for REMPI spectroscopy, the pump has injection seeding: a small single-wavelength laser light is injected in the cavity of the pump to force a single mode. Here the signal output of the OPO is used and doubled to $\sim$ 230 nm for the NO experiments. The resolution achieved after the doubling stage is nominally ~ 0.005 cm^{-1}. The beam is weakly focused by a 500 mm cylindrical lens (strong focusing is not required here, and we only focus in the plane parallel to the surface). The energy required for not saturating the REMPI signal in the 1+1 scheme for NO is actually relatively low, and therefore the beam is attenuated using a UV-transparent quartz dye cell filled with a very diluted solution of black ink[g]. The energy of the laser is measured continuously during a scan using an energy detector placed on the other side of the chamber, since it can vary by a factor of a few during the scan.

Synchronization of the lasers and the Hiden QMS used for ion detection is made using a GINI (Générateur d'Impulsions Numériques Informatisé, from the Institut des Sciences Moléculaires d'Orsay), an impulsion generator that controls the flash lamps and Q-switch of the three lasers, and the acquisition window of the QMS. The GINI is controlled by a computer. A labview program also receives back signals from the lasers and the QMS, and synchronizes the QMS data with the wavelength of the OPO laser (for a REMPI scan) or with the delay between the desorption and REMPI pulses (for a TOF scan). Examples of the use of this set-up will be presented in chapter IV.

[g]No less than five different types of inks were tested before finding one that does not degrade too much with time.

Chapter IV
VUV photon-induced desorption

> Le ciel s'était éclairci. Au-dessus de nous, les nuages de méthane s'ouvraient par trouées comme des plaques élargies de rouille. Les filets d'ammoniac, rebondissant sur la chape d'oxygène de la ville, s'étaient rabattus sur le Dehors, où ils dériveraient lentement, flottant d'abord au-dessus du Nakkarst puis continuant leur voyage au-delà, longtemps, jusqu'aux agrégats de glace, dans ce monde crevassé de cratères fixes et froids qui, en quatre milliards d'années, n'avaient jamais vu le soleil.
>
> Alain Damasio, *La Zone du Dehors*

This chapter is devoted to studies that have been made on photon-induced desorption (PID) in the VUV range. To the exception of section IV.1.2, which presents some first results on laser desorption of NO, all of the data presented here is synchrotron data obtained on the DESIRS beamline during experimental runs that were done during my PhD or my master's internship, or older ones for which the data had not been treated yet. This work is very much in line with what has been developed by the team since 2010. It is divided in two parts, one for the exploration of pure ice systems, and the other for composite systems, exploring indirect desorption effects. Previously the pure systems CO [193], N_2, O_2 [199], CO_2 [200] and CH_3OH [54] have been studied in the team. Here I will present some new results on CO, the work I have done on CH_4 and NO (which have been published [201, 202], the articles are reproduced in the appendix as paper I and II), as well as results obtained on H_2O, NH_3 and some organic molecules (mostly HCOOH). This more or less completes a first survey of the main components of interstellar grains (and cold vacuum surfaces), in their pure form. This does not mean that understanding of photodesorption processes in these pure ices has been achieved, as will be shown in the first section with new results obtained on CO ice. It does not mean either that the numbers required for astrochemical models are definitively known, because pure ice studies are obviously limited, although unavoidable. The second section on indirect desorption is also in line with the work that has been done on CO-induced desorption by the team, in isotopic CO [203], N_2/CO [204], CO_2 [200] and CO:CH_3OH [54] systems. We will try to see if the data obtained on a wider variety of systems (rare gases, O_2 on CO and these same species on H_2O) can help us understand better the indirect photodesorption processes.

IV.1 Pure ice systems

The study of pure ice systems is a prerequisite of the understanding of photodesorption. Although arguably only CO, CO_2 and H_2O are the pure ice systems directly relevant to the interstellar medium application, even a purely empirical determination of the photodesorption yield of a given molecule in an ice matrix resembling more that of the icy mantles needs a previous pure ice study to be properly made. I will come back to the

astrophysical relevance of pure ices in a later section. For a better understanding of PID mechanisms, it is obvious that studying simple systems first is mandatory.

IV.1.1 CO

CO ice has been the testbed molecule of photodesorption studies for astrophysical purposes in the last decade and more. It is a seemingly simple system, and extremely relevant for astrophysics. But what also drives the studies that keep being made on this system is the fact that despite this apparent simplicity, a number of aspects are still not understood.

One of the advantages of CO is its high dissociation threshold (11.1 eV [205]). Because of that, UV photochemistry in CO ice is not very efficient. Reactions are still possible between excited CO^* and CO below 11 eV, and photochemical studies have been made (see [206], and section VI. for more details), but high fluxes and fluences are required. With the low fluxes we use here we can almost neglect photochemistry, which is very convenient. In particular, this allows to calibrate absolute photodesorption yields by equating loss of CO molecules in the ice bulk as measured by IR spectroscopy, and number of photodesorbed molecules [193] (see section III.1.7). Another advantage of CO ice is that the photodesorption yield is high, and therefore easier to measure.

IV.1.1.1 Recent studies on CO photodesorption

Investigations of CO photodesorption have been in part driven by the lack of clear agreement between absolute values of the photodesorption yields. This in turn led to an exploration of what parameters could vary between the different experiments and which ones were relevant. Table IV.1 summarizes the studies that have determined absolute photodesorption yields for CO photodesorption. The first studies of Öberg et al. [207, 208] used a broadband hydrogen discharge lamp, which is a lamp dominated by Ly-α photons at 10.2 eV and with some lower energy photons in the 8-9 eV region from H_2 bands. In these UV lamp studies a window is used (MgF_2 or LiF) which means that there is a cut-off around 11 eV. Öberg et al. found a photodesorption yield of 3×10^{-3} molecules/photon for CO deposited at 15 K, with no thickness dependence down to 2 ML. It was also observed that the photodesorption yield decreases down to $\sim 1 \times 10^{-3}$ when the deposition temperature is increased to 22-27 K. The study of Munoz-Caro et al. [209] later found a much higher photodesorption yield of 3.5×10^{-2} molecules/photon for CO deposited at 15 K and even higher yields at 7 K. No ice thickness dependence was found down to 5 ML.

It was already realized at this point that photodesorption yields should depend on the spectrum of the light used [207], and that this could explain some discrepancies, but the definitive proof was brought by the measurement of photon energy-resolved photodesorption yields, using the synchrotron method [193]. The photodesorption spectrum of CO[a] is shown in fig. IV.1 and compared with the previously introduced absorption spectrum of solid CO. The two match very well. This photodesorption spectrum provides some basic confirmations, such as the fact that the desorption process indeed occurs from excitation of the CO ice and not the underlying substrate, and is mediated by electronic

[a] Some differences between this spectrum, published in ref. [201], and the one in Fayolle+2011 should be noted: the features at photon energy > 11 eV are much higher in the present spectrum because of a problem in the earlier flux calibration. The ratio between the first few vibrational bands is also slightly different, but I do not have a clear explanation for that (perhaps background subtraction issues).

Table IV.1: Recent publications on photodesorption from CO ice

Reference	Yields* (x10^{-2} mol/photon)	Deposition T (K)	
Öberg+2007,2009a [207, 208]	0.1 - 0.3	15, 22, 27	
Muñoz-Caro+2010 [209]	3.5 - 6.3	7, 8, 15	
Fayolle+2011 [193]	0.3 - 5	18	Wavelength-resolved (7-14 eV)
Bertin+2012 [203]		14	Isotopic layers: indirect desorption
Chen+2013 [210]	6.4 - 22	14	
Van Hemert+2015 [211]	0.4		Molecular dynamics simulation
Paardekooper+2016 [212]	0.14	20	
Muñoz-Caro+2016 [91]	1.5 - 6.5	8 - 20	
Díaz+2019 [213]	4 - 5	11	Deposition angle and method

* Extreme values of the photodesorption yield of CO per incident photon reported in these studies.

transitions. It also explains some diffences in the previously mentioned yields. The spectrum of the H discharge lamp of Munoz-Caro et al. [209] is also reproduced in fig. IV.1. The exact spectral composition of the light from these lamps depend on their operating conditions - in particular the ratio of Ly-α photons to continuum photons around 8-9 eV. Because the photodesorption yield of CO is quite low at the Ly-α, the photodesorption yield obtained will depend strongly on the operation condition of the lamps. This is the object of the study of Chen et al. [210] which does show some very different values of the photodesorption yield for different lamp settings.

The advantage of having a quantified and *wavelength-resolved* photodesorption spectrum is that it is possible to calculate the yields expected for light of any given spectral composition by simply taking a weighted average of the yields, where the weights are the normalized spectrum of the light. This is also very useful for deriving astrophysically relevant yields, as detailed in Fayolle et al. [193] (see also section IV.3 later). Considering a lamp completely dominated by Ly-α light, the photodesorption yield of Öberg et al. can be reconciled with our wavelength-resolved yields. On the other hand, if we calculate the expected photodesorption yield using the spectrum of Munoz-Caro et al, we find a yield of $\sim 1 \times 10^{-2}$ molecules/photon, still in disagreement with their values.

However, aside from the light spectrum, it seems clear that there is another parameter

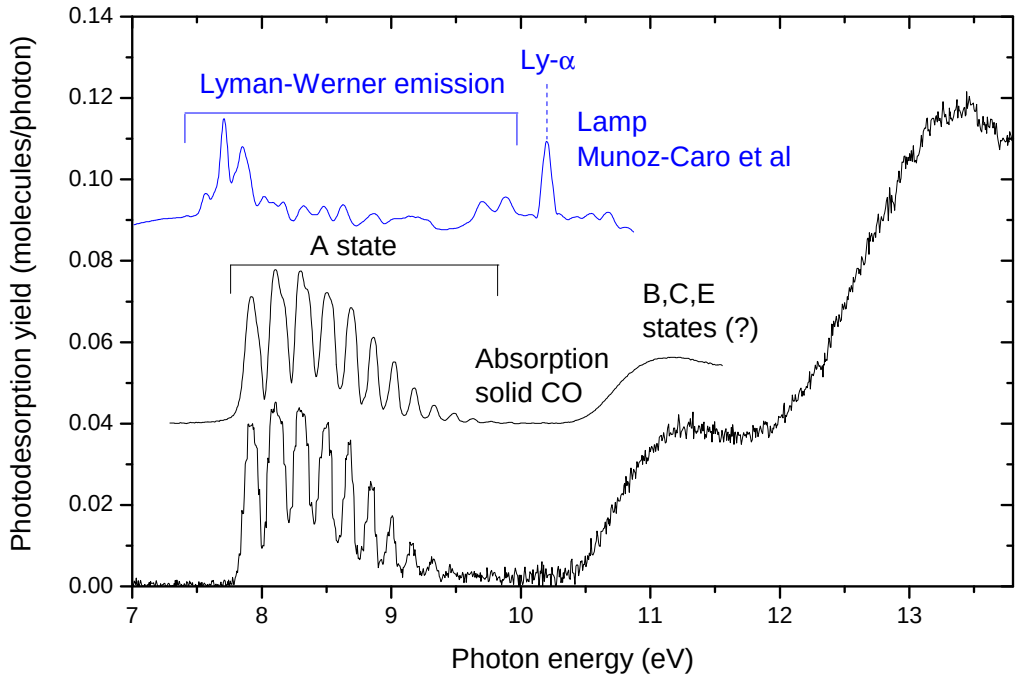

Figure IV.1: Photodesorption spectrum of 20 ML CO ice deposited at 10 K. The absorption spectrum of solid CO at 10 K from ref. [121] is shown for comparison. See section II.2.3 for attributions of the solid CO spectrum. Also shown is the spectral distribution of the hydrogen discharge lamp used by Munoz-Caro et al [209].

that affects the photodesorption yield of CO: ice deposition temperature. This parameter was more systematically explored by Munoz-Caro et al. recently [91] and is indicated for the various experiments in table IV.1. Their study is confined to the 8 - 20 K range because above 20 K, CO ice undergoes a phase transition. A variation of a factor of 5 is observed in the yields between 8 and 20 K with a linear decrease with temperature. At 18 K (the temperature for which the spectrum of Fayolle et al. was taken), the predicted photodesorption yield is 2.2×10^{-2} molecules/photon, only a factor of 2 higher than the expected value mentioned previously.

Taking into account the deposition temperature and the wavelength dependence, it is possible to reconcile the values of Öberg et al, Munoz-Caro et al. and Fayolle et al. to within a factor of 2, which is satisfying considering the large experimental errors on these values. However it is more difficult to explain the more extreme values of Chen et al. ($> 5 \times 10^{-2}$ molecules/photon at 14 K) and Paardekooper et al. (1.4×10^{-3} molecules/photon at 20 K, versus 1×10^{-2} molecules/photon expected from their lamp spectral distribution and the spectrum of Fayolle et al.). There are basically three possible sources of discrepancy, aside from those already mentioned of deposition temperature and light spectrum:

- Errors in the calibration of the desorbing flux of molecules
- Errors in the calibration of the photon flux

- Differences in experimental parameters that have not been identified but change the intrinsic photodesorption yield

It is clear that, in addition to making sure the first two items are properly ruled out for our own experiments (we cannot simply assume other experiments have errors), we need to pay attention to the third item and try to explore different parameters. A recent study by Diaz et al. [213] has explored the influence of the ice deposition method on photodesorption yields. The ice deposition method presumably can influence the structure of the ice, as discussed by the authors, just like the deposition temperature parameter. There is a slight change in photodesorption yield when the ice is deposited at a high angle ($\sim 70°$), resulting in a rougher surface according to the authors.

Investigating the deposition temperature dependence is particularly important for us. If the results found by Munoz-Caro et al. are confirmed, then we need to pay particular attention to our own deposition temperature because our CO spectra are recalibrated each run on the previous data, and are then used subsequently to calibrate every other molecule as well. Therefore an error in the CO recalibration because of surface temperature differences would have dire consequences on every other quantified results.

IV.1.1.2 Thickness and deposition temperature dependence of CO photodesorption

So far we have not been able to reproduce the results on deposition temperature. Some tests made in 2012 did not show convincing differences between ices deposited at 14 K and 18 K, but possible issues with a drift of the QMS gain throw some doubts on these results. More recently during the 2018 runs, we obtained the results shown on fig. IV.2 for 20 ML CO ices deposited at 16 and 20 K on the insulated Cu substrate (the apparent structure around 13 eV is an artifact from the flux correction, as Rydberg lines of the rare gas filter can cause structures to appear in the flux)

There is no significant difference between the two spectra, while a factor of 2 difference would be expected from the results of Munoz-Caro et al. [91]. However there is some doubt on the actual temperature of the substrate, as mentioned in chapter III. Because of the electrical insulation the thermal contact is not optimal between the copper substrate and the sample holder, so that the substrate may actually be above 20 K already when the sample holder is at 16 K. This means that we have no conclusive data on deposition temperature effects for the UV photodesorption of CO. I have not observed any effect of deposition temperature on EID from CO ice (see chapter IV), but the mechanisms are not necessarily the same (the origin of this deposition temperature dependence is not clear anyway). Therefore it is urgent to obtain synchrotron data for this parameter.

We have also explored the thickness dependence of CO photodesorption. Previous studies all agree that there is no thickness dependence of the photodesorption yields down to $\sim$ 2-5 ML, and our own isotopic layer experiments [203] (see below) locate precisely the photodesorption process to the first three layers of the ice. But this is only for excitation of the A - X transition below 10 eV. Lamp experiments use a window that cuts around 11 eV and therefore higher electronic states are not excited. In our own experiments we have access to these states but in the early publications [193, 203] there are issues with the high energy side because of flux calibration errors in this region and the fact that during

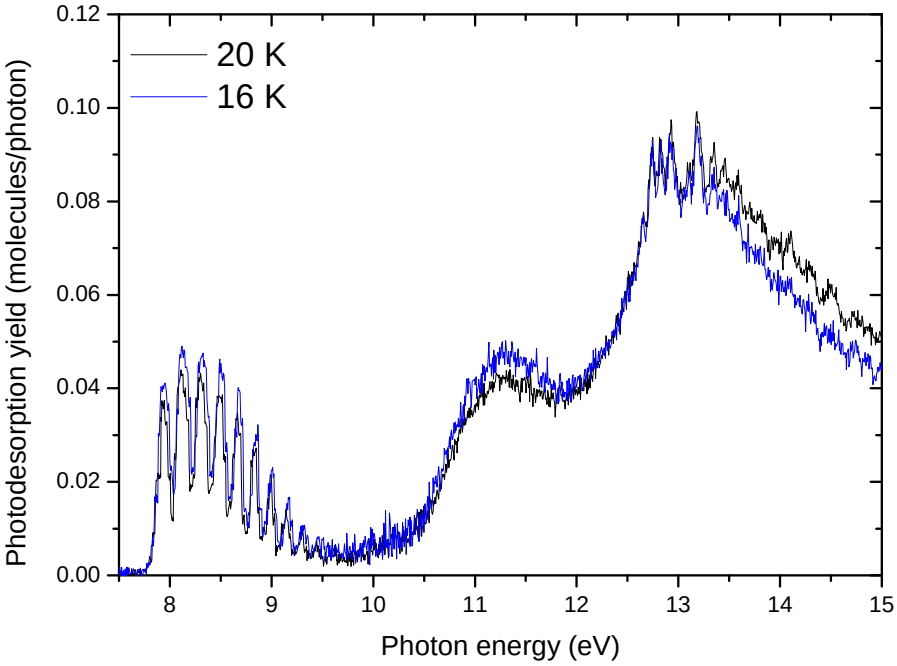

Figure IV.2: Photodesorption spectra of 20 ML CO at deposition temperatures of 16 K and 20 K. See text for the uncertainty regarding the actual temperature of the substrate.

one of the runs the photon flux was unusually low in this energy range on the beamline, because of carbon contamination.

More recently we came back to the exploration of the thickness parameter, during the 2016 runs in SPICES II. Fig. IV.3 shows the photodesorption spectra of CO as a function of ice thickness, for deposition at 12 K. It is clear that the behaviour is different between the A - X region, where the photodesorption yield is saturated at 3 ML, and the region above 10 eV where the signal keeps increasing up to 20 ML. In the inset the evolution of the integrated signal of the two regions 7 - 10 eV and 10 - 14 eV as a function of ice thickness is plotted and shows well this different behaviour. The high energy behaviour can be fitted with an inverse exponential decay ($A(1 - e^{-t/\tau})$) yielding a characteristic thickness of $\sim$ 7 ML.

A thickness dependence of photodesorption indicates transport of energy from below the surface to the top monolayer. The isotopic layer study in Bertin et al. [203] shows this quite well. A figure from this paper is reproduced in fig. IV.4. The principle is to prepare a ^{12}CO ice, and then to deposit layers of isotopically labeled ^{13}CO on top. The desorption of the two different isotopes can be distinguished by mass spectrometry. This indicates that the molecules that actually *desorb* are really the surface-most ones, with a very strong diminution of ^{12}CO desorption as soon as 1 ML of ^{13}CO is deposited on top. However, the desorbing molecule is not necessarily the one that absorbed the photon. Isotopes of CO can also be distinguished because they have slightly different vibrational constants, which becomes clearly visible in the high v peaks of the A - X transition. This shows that with 1 ML of ^{13}CO on ^{12}CO, ^{13}CO desorbs with the spectral signature of ^{12}CO (see fig. IV.4), thus demonstrating that sub-surface ^{12}CO molecules absorbed the

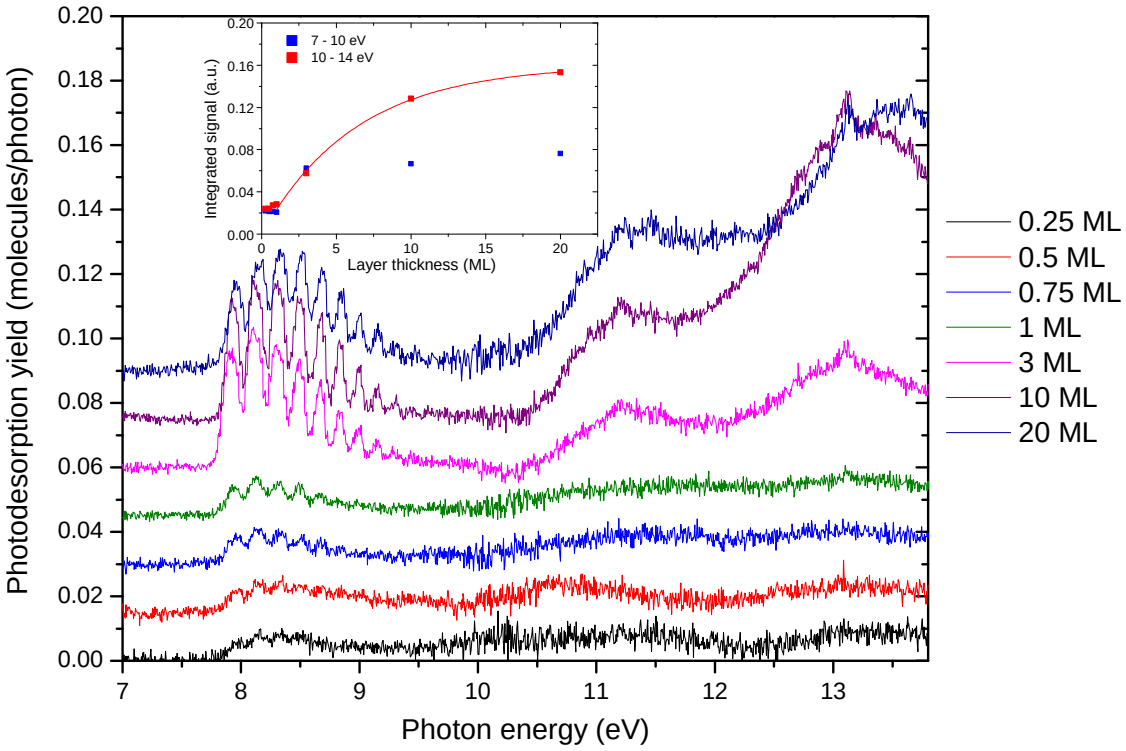

Figure IV.3: Thickness dependence of CO photodesorption for CO ice deposited at 12 K. Inset: integrated photodesorption signal in the 7-10 eV and 10 - 14 eV regions as a function of ice thickness. The dots are the experimental points and the curve an exponential decay fit. The two series of points have been scaled arbitrarily.

photons and transferred their energy to the surface molecules. This stops being the case after deposition of 3 ML of ^{13}CO on top. This indirect desorption mechanism will be discussed abundantly later in this chapter. The exact mechanism of energy transfer in indirect desorption was explored in other layered systems.

We have little clues regarding energy transport to the surface in the region above 10 eV either, but the list of possible culprits is limited. Electrons are not involved here like they are in the X-ray range and for primary electron irradiation (low energy electrons from the substrate do not have an effect here). We are not creating energetic fragments either (see the case of H fragments in H_2O below). Most probably a migration of electronic energy is involved. We can recall that while the exact nature of the higher lying electronic states of CO is not well identified, whether they are broadened Rydberg states, Wannier excitons, have conduction band character etc... they are by nature spatially extended and not localized on a single molecule. The radius of a higher lying Wannier exciton or Rydberg states already spans several monolayers of molecules. This could lead to energy transfers because of a simple overlap. The exponential decay fit made on the thickness dependences are not backed up by a physical interpretation and were used simply to obtain a characteristic thickness, but it is worth noting that if the energy transport is diffusion-like it is a good first approximation.

From a mechanistic point of view, there is an interesting quantity that we can now

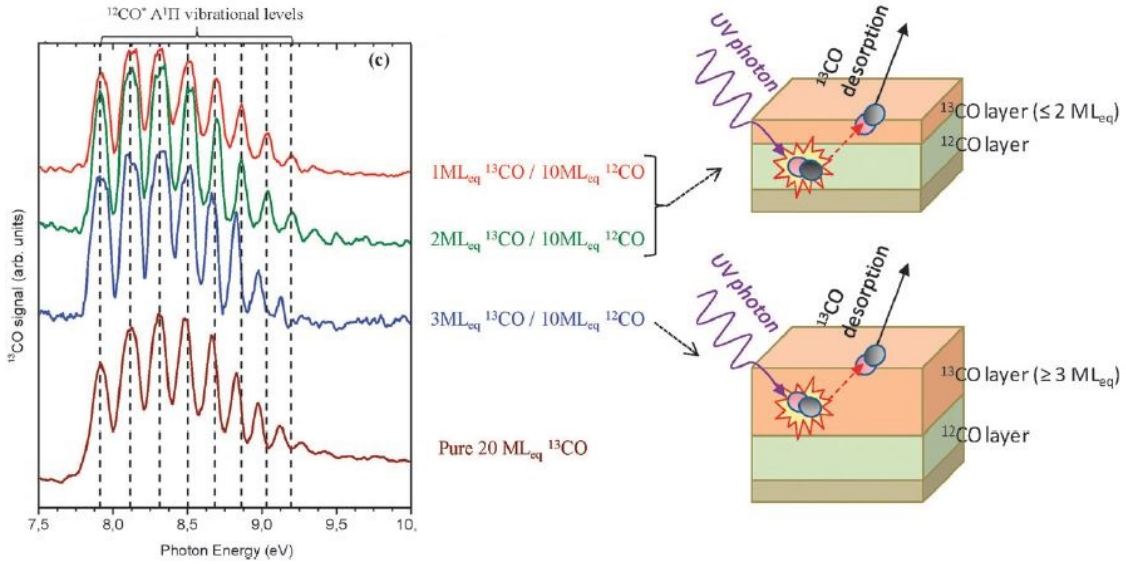

Figure IV.4: Photodesorption of ^{13}CO for layers of ^{13}CO deposited on top of a ^{12}CO ice. The spectral signatures of ^{12}CO in ^{13}CO desorption show an indirect desorption mechanism sketched on the figure. Reproduced directly from Bertin et al. [203].

derive which is the number of molecules desorbed per *absorbed photon*, instead of the usual yield per incident photon. The yield per absorbed photon is more intrinsic in the sense that it eliminates one parameter which is the absorption probability of the ice. Estimating this quantity requires knowing the absorption cross section of the solid. Fortunately they have been estimated for a variety of astrophysically relevant molecular ices recently [214, 215]. But another parameter required is to estimate the depth of molecules that can be "involved" in the desorption process. A molecule too deep in the ice can absorb a photon but we know it will never lead to desorption, so we should not take it into account. Here in the case of CO, below 20 K and in the A - X region, the "photodesorption-relevant" depth is well constrained to 3 ML from the isotopic labelling experiments. The yield per absorbed photon is then given by:

$$Y^{abs} = \frac{Y^{inc}}{1 - e^{-\sigma N}}$$

With σ the absorption cross-section (in cm^2) and N the density of molecules considered to be involved in photodesorption (number of monolayers times surface density of molecules). This formula is derived simply from the fact that the number of absorbed photons at a given depth in the ice is the number of incident photon multiplied by $1-e^{-\sigma N}$. It is worth noting that in most cases here, considering the absorption cross-sections of small molecules ices in the VUV range and the kind of depth involved (a few tens of ML at most), the product σN is small enough that the ice is optically thin and the factor reduces to just σN.

At 8.1 eV, considering a depth of 3 ML (N = 2.4 $\times 10^{15}$ molecules/cm^2), an absorption cross-section of 1.6 $\times 10^{-17}$ cm^2 [214] and a photodesorption yield per incident photon of 4.3 $\times 10^{-2}$ molecules/photon, we obtain a yield of almost 1 (1.14) desorbed molecule

per absorbed photon. Extrapolating the absolute cross-section of ref [214] (for which the spectrum cuts off at 10.6 eV) to the relative spectrum of ref [216] (cutting off at 11.5 eV and therefore resolving the first broad peak), we can estimate the absorption cross-section at 11.2 eV to be 6.7 $\times 10^{-18}$ cm^2. Assuming the "infinite thickness" photodesorption yield at 11.2 eV is reached for the 20 ML ice of fig. IV.3, this yield is 4.6 $\times 10^{-2}$ molecules/photon. For a relevant photodesorption depth of 10 ML, we find a yield per absorbed photon at 11.2 eV of almost 1 (0.9) desorbed molecules per absorbed photon as well.

The yield per absorbed photon is therefore unity (although the experimental errors are large). Such a result does not necessarily mean that all absorption events lead to exactly one molecule desorbing, because some events could lead to desorption of 2 molecules, compensating for events where no desorption occurs. However, it is still clear that the efficiency of the photodesorption process is quite large.

IV.1.1.3 Photodesorption mechanisms

A few theoretical studies have attempted simulations of CO desorption, giving interesting insights on the mechanisms. A series of early work by Dzegilenko & Herbst [217, 218, 219] investigated the non-thermal desorption of CO physisorbed on various surfaces. They modelled the coupling between the internal vibration mode of CO, its librational (frustrated rotation) mode, the CO-surface mode (physisorption) and the phonon bath of the system, looking at how energy could end up in the initially ground state physisorption mode when the vibrational and librational modes are initially excited. One basic and important conclusion of this study is that simply putting energy in the vibrational mode does not lead to desorption. Instead significant librational energy is required, because the coupling is much more efficient between libration and physisorption. The Debye frequency of the lattice is also an important parameter, with higher desorption probability for lower Debye frequencies. This last feature is specific to the mixed quantum-classical calculations and was not found in their purely classical calculations. It is counter-intuitive because the relaxation rate is higher for the non-rigid, low Debye frequency lattices, but it seems that a highly rigid surface also hinders desorption. The details of the desorption mechanism is described in their papers.

More recently Van Hemert et al. [211] published calculations on the desorption induced by *electronic excitation* (in the A-X transition) of *condensed CO*, which is much closer to our own conditions. They simulated CO clusters, either amorphous or crystalline, and calculated the ground state and excited potential surfaces of the CO dimer. Two mechanisms are described. For the surface molecules, a direct mechanism is found which is "MGR-like" and close to mechanisms like Hirsche-Pool or the excimer-mediated mechanism of rare gases (see chapter II). Basically, the excited CO molecule evolves on the potential energy surface of the excited state (and the surrounding molecules as well, rearranging in a configuration favourable for the excited state) until it is quenched back to the ground state, and there it lands on an unfavourable position and orientation with respect to the rest of the clusters (i.e. on an energetically elevated point of the ground state potential surface). Because of that, the molecule will then acquire kinetic energy and desorb. The other mechanism is an indirect mechanism (termed "kick-out" in the paper) where a molecule next to the excited one is ejected. This mechanism is not described in great detail, but is different from the "kick-out" by H atom that was found

for H_2O desorption (see below) and seems to involve high vibrational excitation of the sub-surface, initially excited molecule transfering kinetic energy to a neighbour molecule because of the large amplitude of the nuclei motions. It accounts for ~ 30 % of the total photodesorption yield. Another important finding is that, similarly to what was found by Dzegilenko & Herbst, simple vibrational excitation does no lead to desorption. Even putting a CO molecule in an extremely high (v = 40) vibrational state will not cause desorption to occur. It should be noted that this conclusion on the lack of efficiency of vibrational excitation for desorption is also confirmed by experiments on CO adsorbed on Ni(100) and pumped in its vibrational mode with intense IR free-electron laser pulses[b] [220].

These results are in qualitative agreement with our results: a direct and an indirect mechanism are found, and there is no dependence on the photon energy of the yield per absorbed photon (coherent with the fact that the photodesorption spectrum follows the absorption spectrum). Quantitatively however, the calculations predict a yield of 4×10^{-3} molecules/ incident photon, significantly lower than our experimental values. The ratio of indirect to direct desorption is also lower than what our isotopic layer experiments seem to indicate. In addition, the calculations predict an increase of desorption probabilities with increasing temperature, in contradiction with the results of Munoz-Caro et al. [91]. Calculations remain nonetheless precious for a better understanding of mechanisms. Indeed, it is predicted that molecules desorbed through the direct mechanism are highly vibrationally excited, while molecules desorbed by the indirect mechanism have little internal and translational energy. This is something that can be explored in SPICES II using the set-up developed for desorption + REMPI experiments, that will be presented in the next section.

All of the above is valid for the desorption mechanism in the A-X state, but I have shown earlier that the thickness dependence of the higher-lying states above 10 eV is different, indicating also a different desorption mechanism that will also need to be investigated. Desorption mechanisms are shown here to be excited state dependent within the same molecular system.

IV.1.2 NO

The main motivation for studying NO is that this molecule has a number of convenient properties for being a test molecule for the laboratory-based experiments that were developed throughout my PhD (see section III.5 and below). These properties are that:

- The electronic states of the molecule are such that REMPI schemes are accessible above 350 nm for 2+1 REMPI and around 225 nm for 1+1 REMPI. These wavelengths are easily accessible through respectively doubling and tripling of the output of tunable ns lasers.

- Solid NO has a broad electronic state accessible above 200 nm, which for the same reason mentioned above allows 1 photon desorption experiments without having to use a VUV laser scheme: the tripled output of a dye laser is sufficient.

[b] This is not published data as it is a negative result but it is mentioned in the cited "General Discussion" of a Faraday Discussion p22 by H. Zacharias.

- Possibly for the two above reasons, in surface science desorption + REMPI studies NO is a seminal system, therefore there is an extensive literature on it. Although as often these mostly concern chemisorbed molecules on well-defined metal surfaces (see ref [221] and references therein), there are even some studies of multilayer [222] or physisorbed sub-monolayer [223, 224] NO that are very extensive, providing a good reference for first tests.

As will be shown in the corresponding section, the NO molecule does not have only advantages for desorption + REMPI studies.

Before starting the laboratory studies, NO photodesorption was studied at the synchrotron to obtain a photodesorption spectrum and the absolute yields as a starting point. This is described in the first sub-section. It turns out that NO is not an irrelevant molecule for an astrophysical context either: while undetected in ice mantles it is expected to be present at the percent level. The astrophysical relevance of the synchrotron data is detailed in the published paper II [202] which is reproduced in the appendix.

NO is also another molecule in the series of diatomic molecules (CO, N_2, O_2) which allows some inter-comparisons of the photodesorption results. But some particularities of the NO molecule and the NO solid must be noted before moving on to photodesorption. NO distinguishes itself by being an open-shell molecule: it has an unpaired electron which makes it reactive and gives it different electronic properties. Its dissociation limit (6.5 eV in the gas phase [205]) and ionization potential (9.26 eV in the gas phase [205]) are relatively low compared with those of CO or N_2. In this sense it is closer to O_2, which has an unusual triplet ground state and a low dissociation limit (5.1 eV in the gas phase [205]).

In the solid form, NO is less volatile than other diatomic molecules, with a binding energy roughly estimated at 200 meV from our TPD experiments: it desorbs around 55 K, instead of the 30-35 K typical of the most volatile molecules. Another interesting particularity is that in solid form NO forms dimers, bonded by the N atoms, due to the unpaired electron. This fact was studied early on by X-ray diffraction [78], IR spectroscopy [225] and UV spectroscopy [226]. The NO dimer bond is weak (86 meV [227] in the gas phase) but the dimerization still affects the electronic properties significantly, as we will see later.

We have direct evidence that dimers are formed in our experimental conditions as well from IR spectroscopy. Fig. IV.5a shows the IR spectrum of NO ice deposited at 12 K. There are not one but two peaks, at 1775 cm^{-1} and 1864 cm^{-1} in the NO vibration region. These peaks correspond respectively to the antisymmetric ν_5 and symmetric ν_1 stretch vibration modes of the *cis* dimer [228], which is the most stable form of the dimer. Other forms like the *trans* dimer, the NO monomer and some other forms of *cis* dimers can be observed isolated in rare-gas matrices by IR spectroscopy as well [229, 230]. The bands are quite broad here.

Fig. IV.5b shows an experiment where IR spectra of the ice were taken continuously during a slow TPD experiment (2 K/min). It is noticeable that upon annealing there are significant changes to the two peaks, happening at 47 K. The antisymmetric mode is shifted to 1788 cm^{-1}, the widths of both peaks are significantly reduced and their intensity varies as well. The TPD shown in the inset of the figure also shows an inflection at 47 K (notice the intensity is in log scale). All of this is a sign of a change of structure in

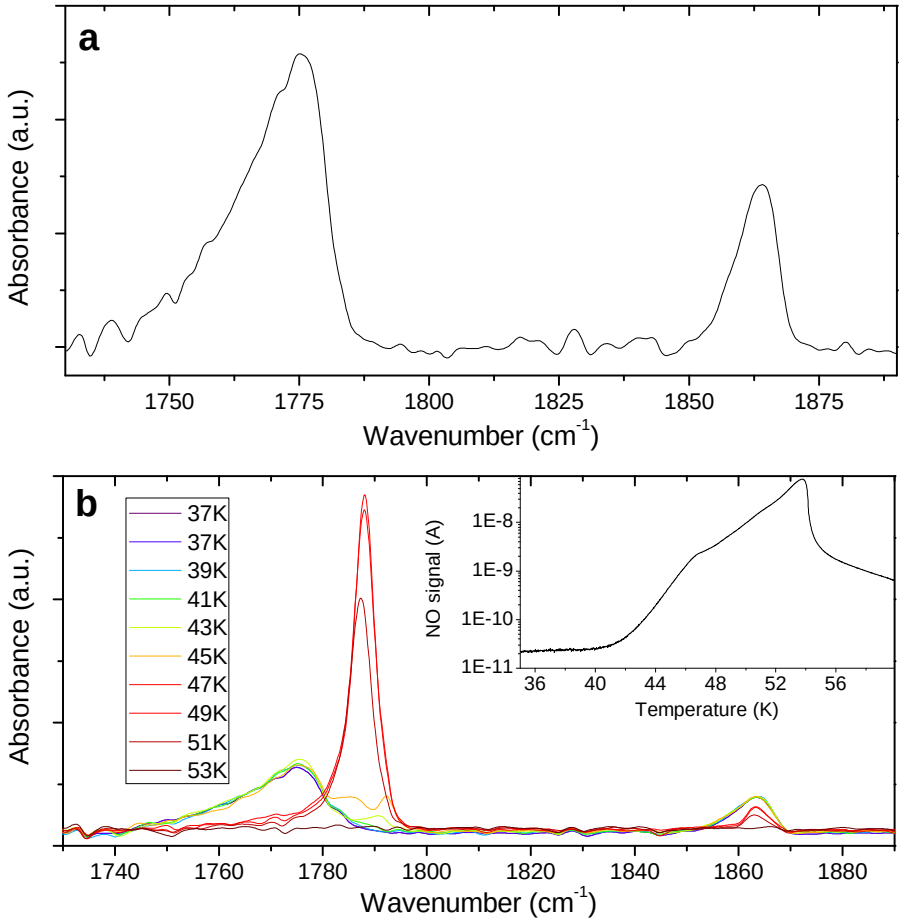

Figure IV.5: **a.** Infrared spectrum of 50 ML NO ice deposited at 12 K with no further annealing. The only visible peaks in the 700-3500 cm^{-1} region are those shown here. Attribution is made in the text. **b.** IR spectra of the same NO ice taken continuously while slowly heating the ice (2 K/min). In the inset the TPD is shown.

the ice, i.e. a phase transition. The low temperature phase is certainly more disordered than the high temperature one, hence the difference in peak widths, but it is unclear whether the high temperature phase is crystalline or simply a more ordered amorphous phase. Studies of the NO dimer so far have been made in isolation matrices, so that it is difficult to compare the wavenumbers of the peaks to derive information on the meaning of the peak shifts regarding the structure of the ice and the NO dimer. Environment effects clearly have an effect since the peak position of the ν_5 depends on the type of matrix [225, 228, 230]. The effect of phase was not explored here: for the synchrotron experiments we only grew low-temperature amorphous ices, and the laboratory based results are very preliminary.

IV.1.2.1 Synchrotron wavelength-resolved study

The experiments presented here were performed on the DESIRS beamline during the 2016 runs with the newly assembled SPICES 2 set-up. It should be noted that as explained in section III.1.7, during these runs parasitic photon signal appeared in the QMS and had to be corrected. The experiments were performed at 12 K on HOPG, copper and gold surfaces, using various ice thicknesses, and with different flux settings.

On fig. IV.6, adapted from paper II, the photodesorption spectrum of 10 ML NO ice on HOPG is shown on the bottom panel. On the top panel the gas phase absorption and solid phase absorption spectra of NO are shown. The photodesorption spectrum was not made in a single scan, instead a 6-12 eV and a 8-15 eV scan were combined, using respectively the Xenon and Argon filters on the beamline. It was not possible to go below 6 eV[c], so that half of the peak centered around 6 eV is missing. Looking at the absorption spectrum we can still assume that 6 eV is the maximum of the peak. The scan was made on a "fresh" (immediately after growing) ice, using wide photon energy steps (0.3 eV) to avoid ice ageing problems (see next subsection), after we concluded that there was no fine structure in the spectrum that would be missed because of the rough steps.

Let us first focus on the absorption. The broad peak centered at 6 eV was the first evidence for suggesting that NO forms dimers in the condensed phase [226]. This attribution of the broad peak as an electronic state of the NO dimer is further confirmed by the gas phase spectrum of the NO dimer, which presents a similar peak, although less broad [232]. The 6 eV peak was thus attributed to a charge transfer state. The attribution of the rest of the features of the solid phase spectrum is not clear: there is a weak broad feature at 8.4 eV and the absorption then rises up until 11.5 eV. The ionization threshold in the solid is 7.8 eV [233] and is not particularly marked here. The strong features above 10.5 eV in the gas phase spectrum correspond to autoionizing Rydberg states converging towards excited states of NO^+ [231].

Coming back to photodesorption, we see that the spectrum follows well the absorption spectrum. The desorption yield keeps rising above 11.5 eV until the highest photon energy measured, 15 eV. The absolute value of the photodesorption yield is fairly high, 2.10^{-2} molecules/incident photon at the maximum of the 6 eV peak and going up to 8.10^{-2} molecules/incident photon at 15 eV. This is typical of the diatomic molecule systems studied so far. The yield per *absorbed* photon cannot be properly evaluated as the absorption cross-section of solid NO is not known. If we assume a cross-section of 1×10^{-17} cm^2 at 6 eV and a relevant photodesorption thickness of 1-3 ML we obtain a yield per absorbed photon at 6 eV of $\sim$ 0.5 - 2 molecules desorbed per absorbed photon. The actual number is therefore probably closer to unity than to, say, 10^{-2}, but it is still not very informative because the interpretation changes quite a lot if the value is 2 (which requires explaining why multiple molecules are desorbed on average after one photon absorption, perhaps taking into account the dimer structure of the ice) or if it is 0.3 (which means a large part of the energy goes into other dissipation pathways than photodesorption).

The yields presented above are valid for a "fresh" ice but we observed that they evolved with time. NO is the first system in this manuscript for which we introduce the notion of ageing which is important for most of the molecular ices when studying photodesorption.

[c] It is actually possible to go lower in energy on the beamline by changing the polarization mode, but we were not aware of that at the time.

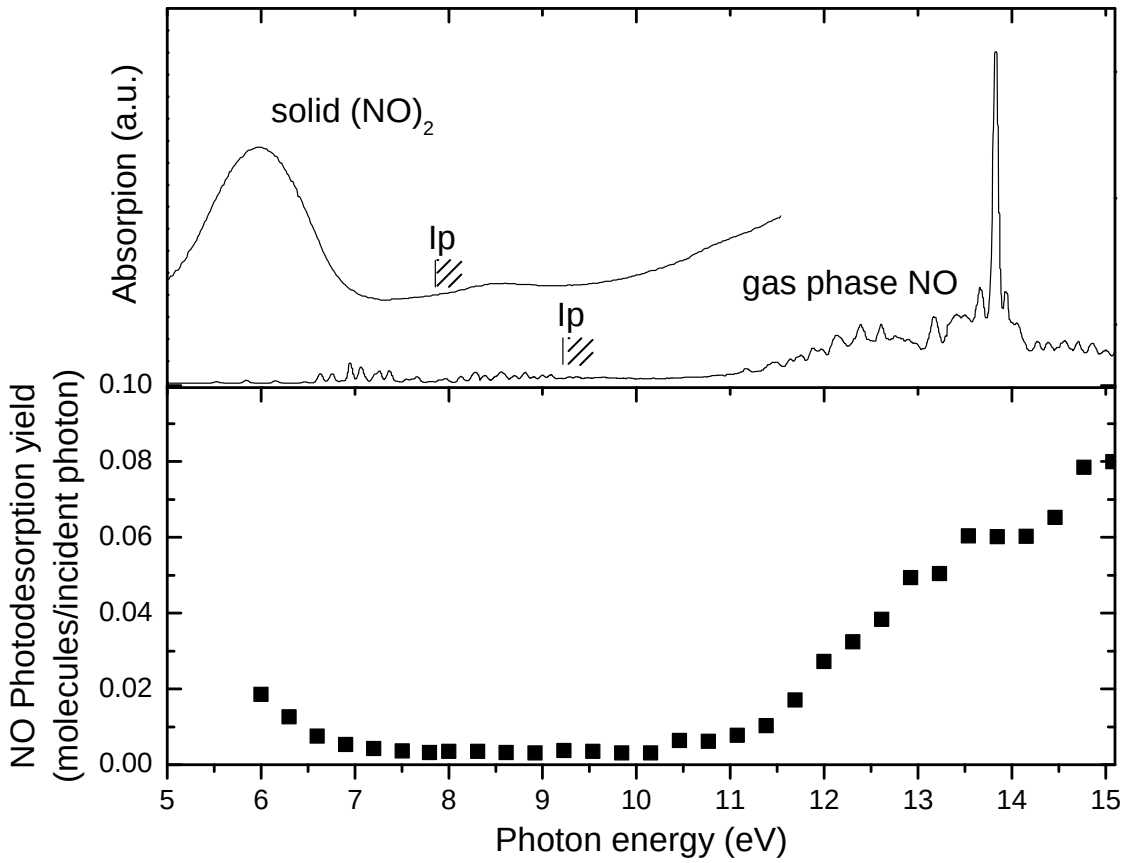

Figure IV.6: Absorption and photodesorption spectra of NO. Top panel: gas phase absorption adapted from ref [231] and solid phase absorption adapted from ref [216] of NO. In the solid phase, NO forms $(NO)_2$ dimers. Bottom panel: photodesorption spectrum of NO desorbing from 10 ML NO ice on the HOPG substrate. See the text for details.

"Ageing" is the gradual photo-induced modification of the ice as it is irradiated during the measurement. It is manifest from the changes in measured photodesorption yields with photon dose. Fig. IV.7 shows the result of four successive scans on the same 10 ML NO ice between 7 and 14 eV, done with the usual setting of the beamline (25 meV steps with a few seconds per step, same flux as mentioned previously). What we see is a diminution of the photodesorption yield with the successive scans, with a factor of 2 at 13.8 eV between the first and the last one (3.10^{16} photons.cm^2).

The origin of ageing is not entirely clear: one possibility is that the photons induce structural changes in the ice. For example, we saw earlier that annealing the ice changes its structure: it is possible that energy deposition by photons has the same effect. It could also make structural changes that are different from what is obtained by annealing. Unfortunately we did not have IR spectroscopy available during these experiments to monitor possible changes of the $(NO)_2$ vibrational signatures[d]. Another possible source of change is the photochemistry. As mentioned previously, the dissociation limit of NO

[d]The FT-RAIRS spectrometer was brought to the synchrotron but stopped working after a few hours.

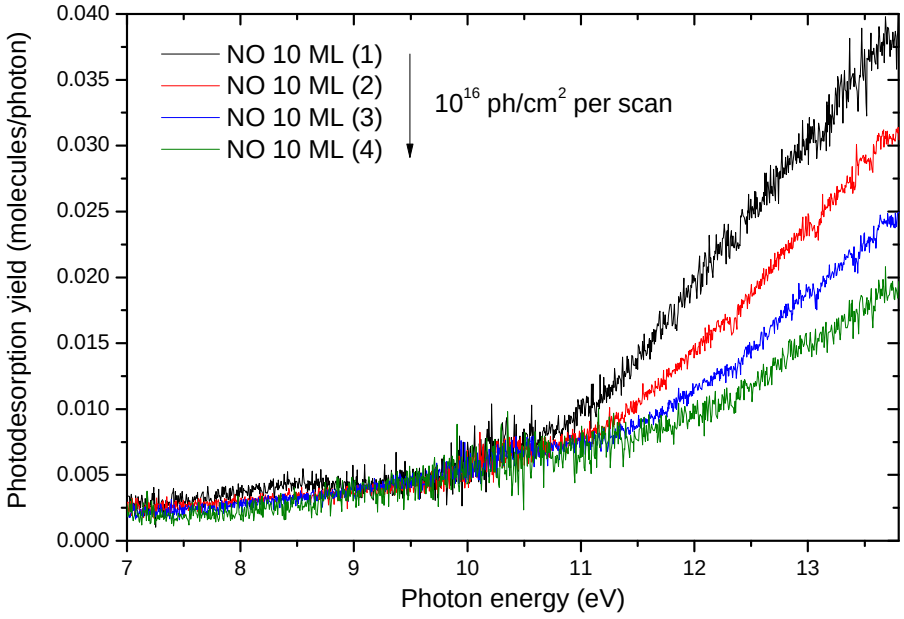

Figure IV.7: Photodesorption spectra of NO for four consecutive scans on the same 10 ML ice on the Au substrate. Each scan corresponds to an approximate dose of 10^{16} photons.cm^{-2}.

(6.5 eV) is accessible by the photons we use and the N and O radicals can react to form other products. Again we could not probe the photochemistry of the bulk by IR spectroscopy, but we can also look at what species other than NO are desorbing.

Aside from the NO molecule itself, we looked for N and O desorption but no signal was left after correction from the cracking. We also tried looking for NO_2 and N_2O desorption, as those are the expected products of NO VUV photolysis (at least in gas phase [229] and in rare-gas matrices [230]), but no signal was detected. O_2 was not detected either. We did detect an N_2 signal, but as this is on the polluted m/z = 28 channel it is quite noisy. It is shown in fig. IV.8 along with the NO signal from the same already irradiated ice. N_2 is also a product of gas phase NO photolysis and it is therefore not surprising to see it desorbing. The N_2 desorption yield is fairly high, almost comparable to the NO yield. It should be noted however that this is for an NO ice that had already been irradiated $> 3 \times 10^{16}$ photons.cm^{-2}: N_2 can accumulate in the ice and its photodesorption yield can depend on the irradiation dose.

Overall the evidence we have in our experiments for photochemistry in NO ice is scarce aside from N_2 photodesorption, but from the literature it is clear that some photochemistry occurs. The relation to ageing, on the other hand, is not clear. In order to mitigate the effect of ageing on our results, we first slightly reduced the flux by reducing the slits (6.4 10^{12} ph.s^{-1} instead of 1.2 10^{13} ph.s^{-1}). Since the spectra did not show any sharp structure, we also decreased the number of scan steps to 0.3 eV per step. Overall this resulted in a decrease of a factor of 10 of the total fluence per scan (from 10^{16} ph.cm^2 to 10^{15} ph.cm^2). Fig. IV.9 shows three repeated scans on a 20 ML NO ice between 8 and 15 eV, and in these conditions no ageing is seen.

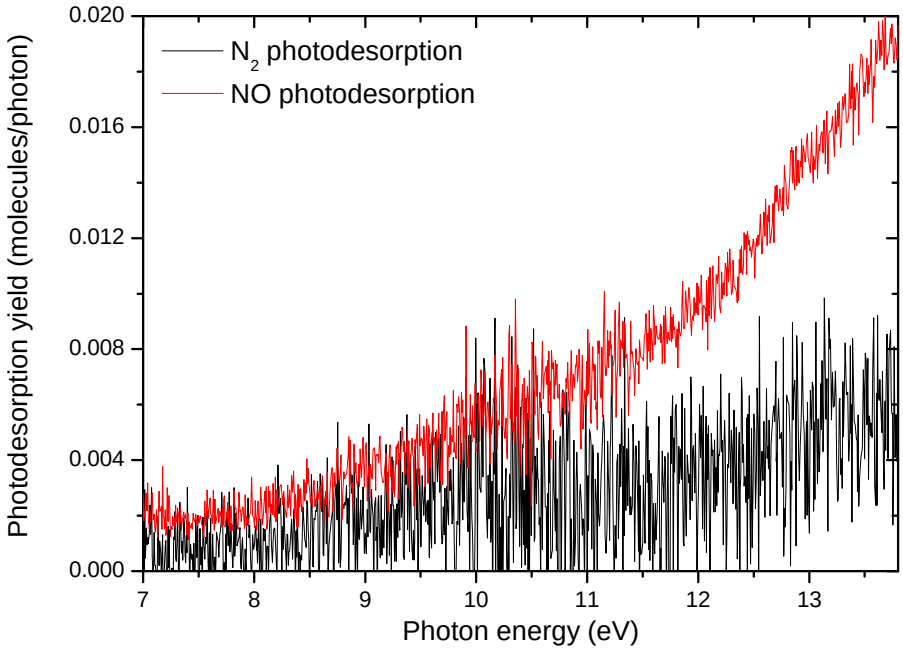

Figure IV.8: Photodesorption spectrum of N_2 from NO ice on the Au substrate (corresponding to the 4th scan of fig. IV.7). Also shown is the NO photodesorption yield of the corresponding scan.

The effect of thickness was also investigated. Fig. IV.10 shows the photodesorption spectra of NO ices with thicknesses varying between 0.5 and 20 ML on HOPG. First it should be noted that the apparent structures that deviate from the monotonous increase we saw in the case of continuous scans earlier are not always reproducible and are artifacts linked with the rough steps of the scan that appear after correction by the photon flux. There is a trend of increase of the photodesorption yield from 1 to 15 ML (although by a maximum of 50% only) but this is somewhat mitigated by the fact that the 20 ML ice has a photodesorption yield slightly lower than the 10 and 15 ML ices, suggesting that the trend may not be completely significant. The 0.5 ML ice has a significantly lower yield (by a factor of $\sim$2), which is expected from the fact that less molecules are available to desorb at the surface. It seems that the photodesorption yield is almost saturated already at 1 ML since the increase afterwards is not huge. Therefore the surface confinement of the photodesorption process in the case of NO is very marked, more than for CO.

This study of NO photodesorption is incomplete (relative to what could have been done with the current set-up) because (i) the photo-induced effects on the IR spectrum of the ice could not be obtained, which could have shed light on the ageing and photochemistry effects, and (ii) the ageing, N_2 desorption and thickness effects were not investigated for the 6 eV electronic state and it has not been completely imaged. However it was enough to bring some directions for the laser based experiments. The photodesorption mechanisms have not been discussed either yet: it will be done in the next section when the literature on NO laser desorption will be discussed to show what these experiments can bring.

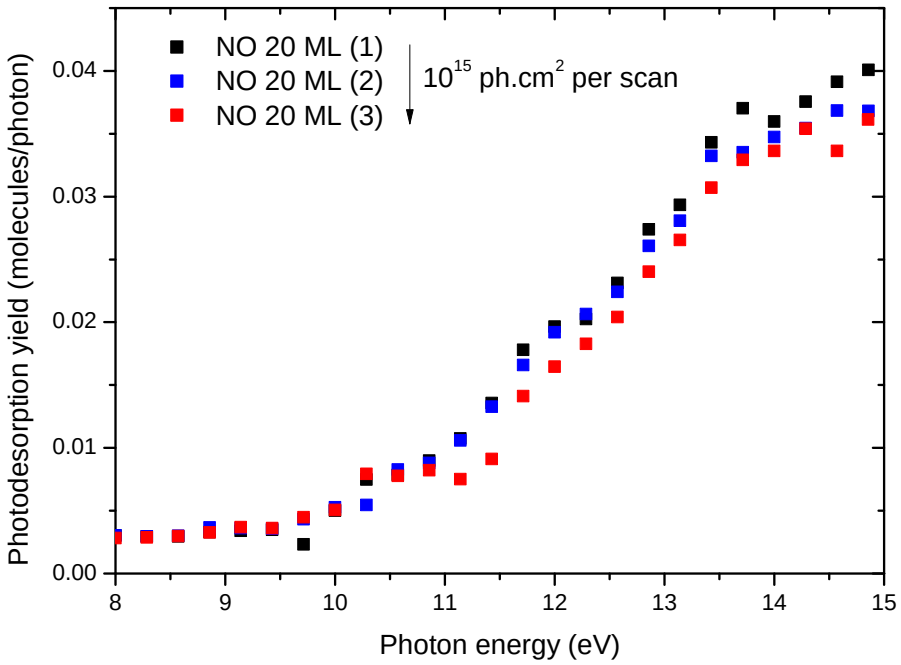

Figure IV.9: Photodesorption spectra for three consecutive scans on the same 20 ML NO ice on the Cu substrate between 8 and 15 eV. The ageing effect is mitigated by reducing the total fluence per scan ($\sim 10^{15}$ ph.cm^2).

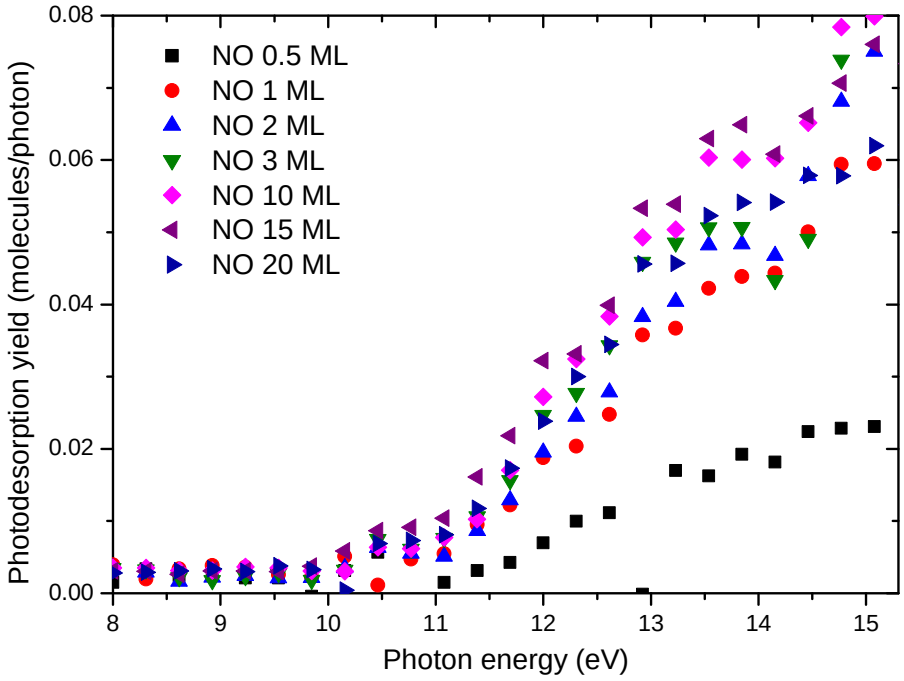

Figure IV.10: Thickness dependence of NO photodesorption. The photodesorption yield of NO is shown for different ice thicknesses (0.5 to 20 ML) grown on the HOPG substrate.

IV.1.2.2 NO gas phase REMPI

Before going into desorption + REMPI experiments, I need to present the gas phase REMPI experiments that are prerequisite to understand the REMPI spectra obtained afterwards. Gas phase spectra also provide a test of the data treatment method.

The chosen vibronic transition here is the first one, the $A^2\Sigma^+(v''=0) \longleftarrow X^2\Pi(v'=0)$ transition. This transition is low enough (around 225 nm) to allow for a simple 1+1 REMPI scheme - it is the only one accessible without having to use the tripling stage of the OPO laser used for REMPI. Even in a 1+1 scheme, the spectrum remains nonetheless fairly complicated due to the open-shell nature of the NO molecule. Fig. IV.11 shows a gas phase REMPI spectrum at 300 K taken in SPICES II (pressure P $\sim 5 \times 10^{-8}$ mbar), displaying an overview of the transition (5 different scans were made to obtain this spectrum). Below is shown a simulation of that same transition made using PGOPHER[e], with parameters from [103], slightly adjusted. The simulation shows the line intensities above (without any broadening taken into account) and the different branches below. The display of the branches is perhaps the most convenient one to understand the structure of the spectrum.

The ground state of the NO molecule is a $^2\Pi$ state, and therefore there is a spin-orbit splitting of the levels. This spin-orbit splitting is of 124 cm^{-1} here, which is larger than the rotational level spacing, so we can consider that the ground state is split into two nuclear spin levels, labeled F1 and F2, both of which have their own rotational sub-structure. The splitting is nonetheless small enough that the rotational structure due to both levels will overlap in the spectrum. This splitting is at the origin of the two distinct branch origins that we see on the branch plot of fig. IV.11. The upper electronic A state on the other hand is a Σ^+ state and therefore there is no spin-orbit splitting. The correct rotational quantum number here is N rather than J, N being the total angular momentum without the spin, i.e. $\vec{J} - \vec{S}$. N is an integer here. There are now two series of degenerate rotational levels, corresponding to J = N - 1/2 (labeled F1) and J = N + 1/2 (labeled F2). The situation is more clear when drawn on a rotational level diagram, shown in fig. IV.12. The different branches are labeled P, Q, R for ΔJ = -1, 0, 1 respectively, and in addition they are labeled '2' or '22' for a transition from F2 to F2, '1' or '11' for F1 to F1, and '12' for F2 to F1 (and inversely). This makes a total of 12 possible branches, some of which are degenerate, which makes 8 actual different branches on the spectrum. They are attributed in fig. IV.11.

The spectrum shown in fig. IV.11 has been corrected from the variations of laser intensity. In order to do that it was first necessary to check the laser intensity dependence of the signal. An example is shown in fig. IV.13. We can see three distinct regimes in this figure: at first there is a quadratic dependence of the ion signal to the laser power, then a linear one, and then we reach saturation. In the first regime neither the resonant step nor the ionization step are saturated, and we have the quadratic dependence expected for a 2-photon process. Above a threshold (here 25 μJ per pulse) the ionization step is saturated and therefore we reach a 1-photon like process. Then above another threshold the transition is saturated. Ideally we would like to work in a linear regime for all transitions, to avoid saturation issues and be able to simply correct the spectrum by the

[e]PGOPHER is a free software developed by C. Western for simulating and fitting rotational, vibrational and electronic spectra and available online at http://pgopher.chm.bris.ac.uk/ see also ref. [234].

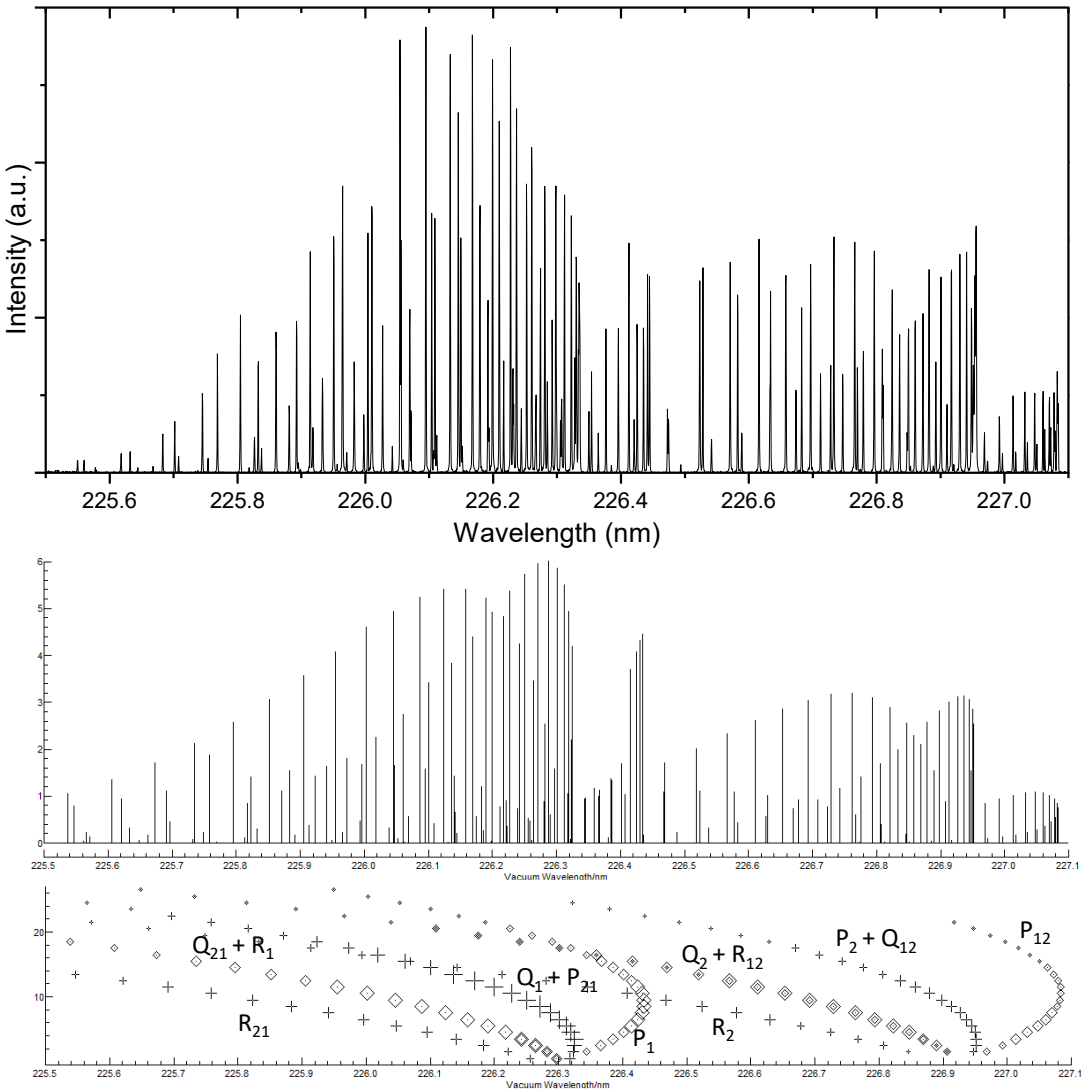

Figure IV.11: Gas-phase REMPI spectrum of the $A^2\Sigma^+(v''=0) \longleftarrow X^2\Pi(v'=0)$ transition of NO at 300 K. The top panel is the experimental spectrum. The middle panel is a spectrum simulated with PGOPHER (Ground state parameters: band origin 948 cm^{-1}, rotational constant B = 1.701 cm^{-1}, spin-orbit splitting A = 124.87 cm^{-1}; excited state parameters: band origin 45074 cm^{-1}, rotational constant B = 1.9925 cm^{-1}). The last panel is the attribution of the different branches. REMPI laser power: $\sim$ 40-70 μJ/pulse. Accumulation per wavelength step of 50 laser pulses at 10 Hz, 0.5 pm per step.

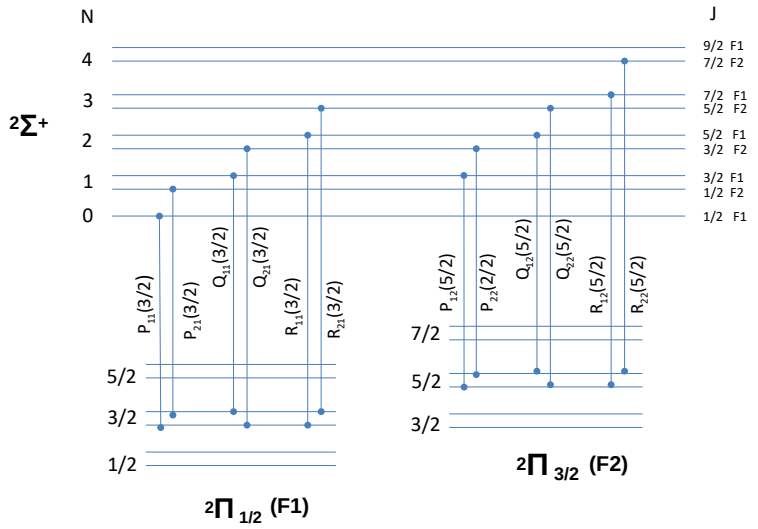

Figure IV.12: Rotational diagram of the NO $A^2\Sigma^+$ and $X^2\Pi$ electronic levels.

laser power. Care has to be taken to stay in the same regime over the course of a scan.

To extract information on the rotational population from the spectrum, the procedure is the following: once each peak has been identified with the help of the simulation, the spectrum (corrected by the laser power) is fitted with a multipeak fit routine with lorentzians. The area of each peak is proportional to the population of the initial level. However, to compare different peak areas we need to take into account the line strength for each transition - at least the part that changes for different rotational levels involved. That part is the Hönl-London factor. Here I used the Hönl-London factors for each transition calculated by PGOPHER. The line intensity divided by the Hönl-London factor gives the relative population of the different J levels. If we can assume the population to follow a Maxwell-Boltzmann distribution (which is obviously the case for a gas phase spectrum), we can extract a characteristic rotational temperature by making use of the fact that:

$$I_{J',J"} = S_{J',J"}(2J" + 1)exp(\frac{BJ"(J" + 1)}{kT_{rot}})$$

where $I_{J',J"}$ is the line intensity for the transition from a J" level to a J' level and $S_{J',J"}$ the corresponding Hönl-London factor. The 2J"+1 factor corresponds to the degeneracy of the level. By tracing ln(I/S) as a function of BJ"(J"+1), we should obtain a linear relation from which T_{rot} can be extracted. This is shown in fig. IV.14 where such a population diagram has been plotted for the P_{12}, P_2+Q_{12} and Q_2+R_{12} branches of the previously presented spectrum. The fit gives a temperature of 267 K, which is not too far from the expected 290 K.

IV.1.2.3 NO desorption + REMPI

For the desorption/REMPI experiments, desorption is done using the Quantel laser tuned at 213 nm (5.82 eV), slightly on the red side of the absorption bump of solid NO. All experiments were done for 50 ML solid NO ices grown at 16 K, some annealed to 49

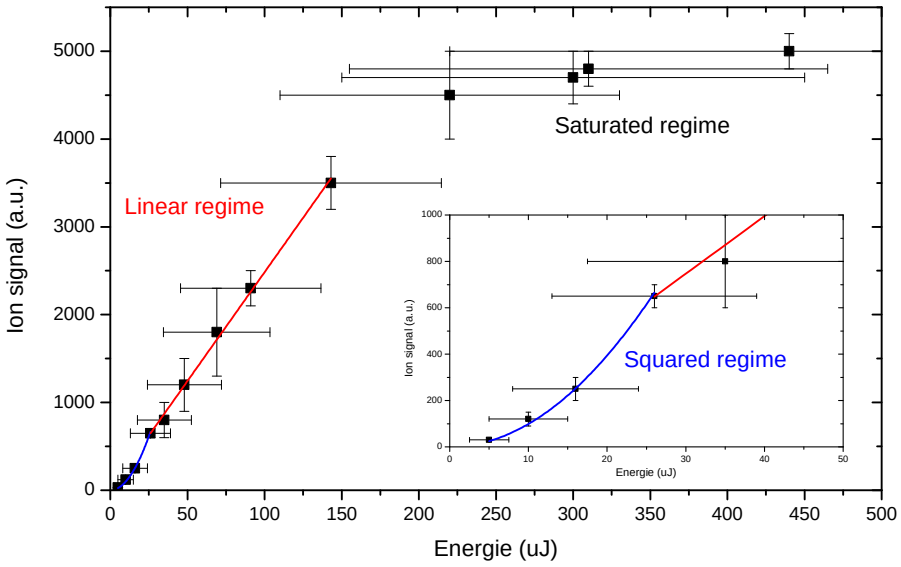

Figure IV.13: Dependence of the REMPI ion signal to the laser power. Laser fixed on the J' = 9.5 line of the Q_{12}+P_2 branch. Horizontal error bars estimated from the shot to shot noise of the laser, vertical error bars from the ion signal noise.

K and others not (the intention was to explore this parameter but it does not seem to change much). In these experiments, in addition to the REMPI laser power, the signal intensity depends also on the desorption laser power and on the intrinsic desorption signal. The desorption laser operates at fixed photon energy, and when it works well/is correctly set, its average power does not vary over time. There is however a shot-to-shot noise which adds to the uncertainty of the measurement. The dependence of the signal to the desorption laser power is shown in fig. IV.15. We see that it is linear at first, confirming a 1-photon process regime, but becomes superlinear afterwards. The superlinear regime is avoided here. The intrinsic desorption signal has an initial transitory regime, with a decrease of desorption over time. It reaches rapidly a regime where desorption only decreases slowly, in which all measurements were done. It is possible that this ageing still affects the measurements, but it is difficult to take into account.

Due to the way our set-up works, we do not have access to the "total" rotational population via the REMPI spectrum directly. There are two types of measurements we can do: we can either do a REMPI spectrum at a *fixed time of flight* (where we therefore probe the rotational population for only those molecules of a given kinetic energy), or we can do a time of flight (TOF) measurement (by varying the delay between the laser pulses) at a fixed wavelength, on a given line. To obtain the full rotational population, we would have to make a TOF measurement on every line transition and integrate the kinetic energy distributions. This is for example what was done in ref. [223], which is very similar to what we are trying to do. I have not done this here: I will instead show qualitatively what kind of results we can obtain with this set-up.

An example of TOFs is shown on fig. IV.16. The two TOFs were taken for J' = 3.5 and J' = 17.5 of the P_{12} branch. The oscillations we see in the TOF come from oscillations of the REMPI laser power, which I did not correct for. Also shown on the

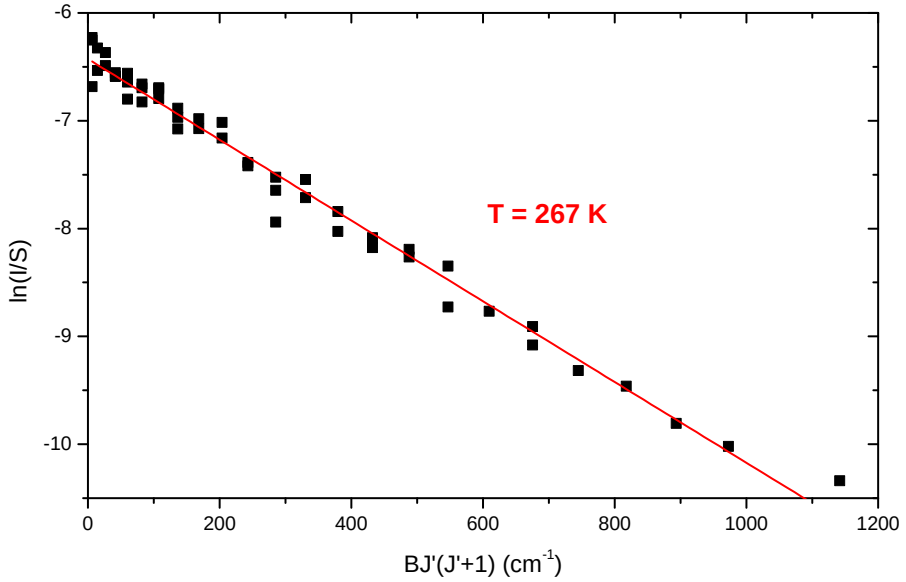

Figure IV.14: Rotational population of gas phase NO at 300 K. Plotted is the log of the line intensity I (integrated area of the peak, corrected by laser power) for a given J" level, divided by the Hönl-London factor, as a function of BJ"(J"+1). In red the result of a Maxwell-Boltzmann fit is shown along with the fitted temperature T_{rot}. In such a representation the slope is $1/kT_{rot}$.

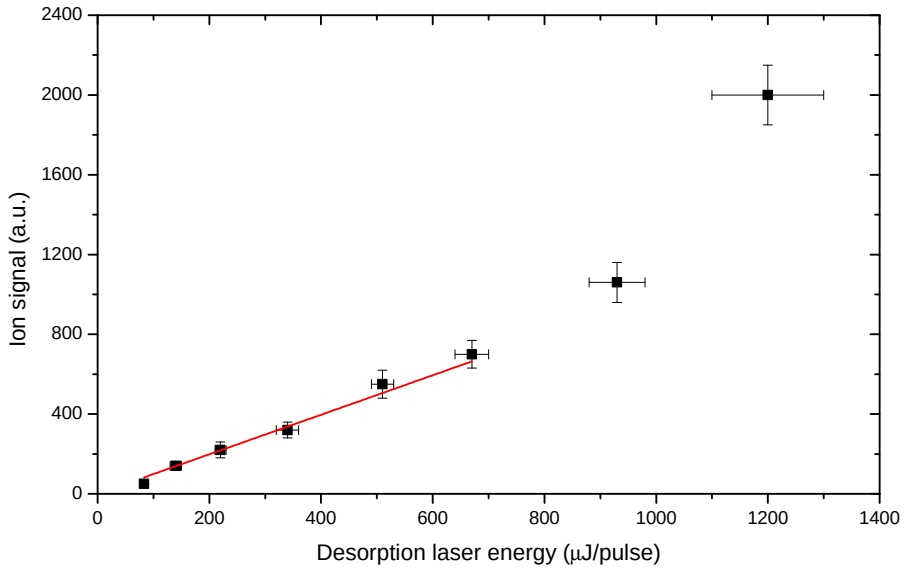

Figure IV.15: Dependence of the ion signal to the desorption laser energy (at 213 nm). On the J' = 3.5 line of the Q_{12}+P_2 branch. Horizontal error bars estimated from the shot to shot noise of the laser, vertical error bars from the ion signal noise.

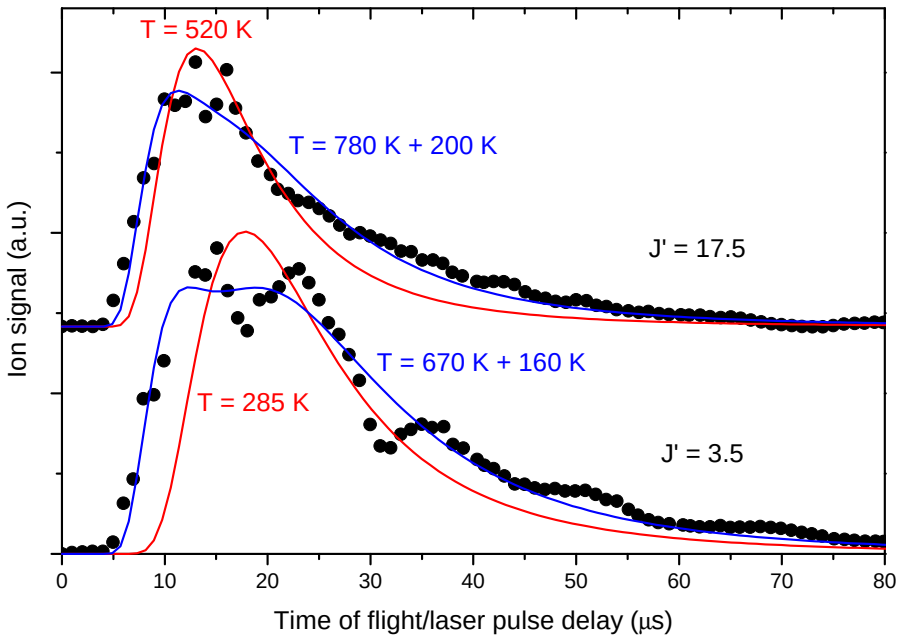

Figure IV.16: Time of flights for two different lines, J' = 3.5 and J' = 17.5 in the P_{12} branch. In red the result of a fit with a single Maxwell-Boltzmann distribution is shown, and in blue the result of a fit with a two-component Maxwell-Boltzmann distribution. The fitted temperatures are also indicated on the figure. Desorption laser energy $\sim$ 300 μJ/pulse, REMPI laser energy $\sim$ 40-80 μJ/pulse.

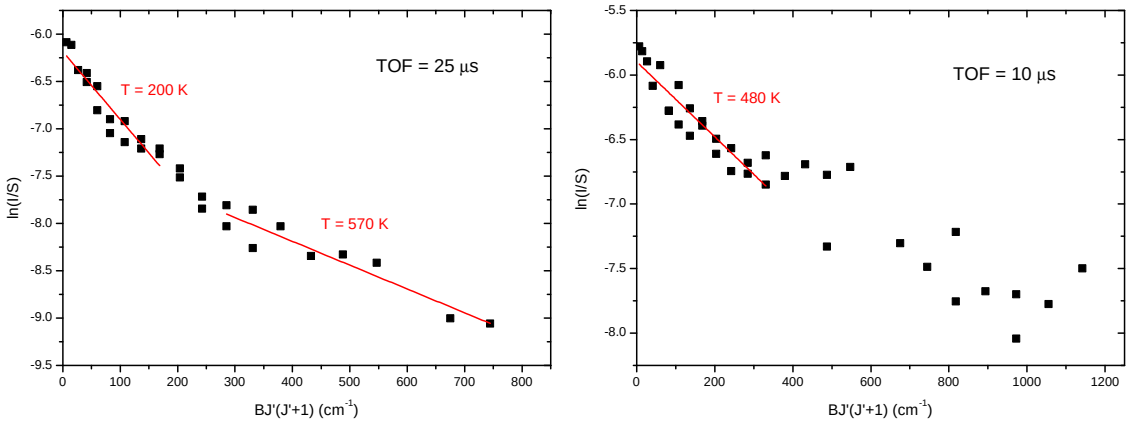

Figure IV.17: Rotational populations (similar to fig. IV.14) of desorbed NO for a TOF of 25 μs (on the left) or 10 μs (on the right). In red fits with Maxwell-Boltzmann distributions and the fitted temperatures are indicated. Desorption laser energy $\sim$ 80 μJ/pulse, REMPI laser energy $\sim$ 50-70 μJ/pulse.

figure are fits with either one or two Maxwell-Boltzmann (MB) distributions. The TOFs clearly cannot be fitted by single MB distributions. The result is much better with two, but that does not necessarily mean that there are two components with physical meaning at thermal equilibrium. It is also clear that the distribution for J' = 17.5 has a stronger fast component than the J' = 3.5 one. This result is coherent with what was obtained in ref. [223], where a correlation between translational and rotational energy was found.

Conversely, the rotational distributions of two REMPI spectra taken with two different TOF values of 10 μs and 25 μs (a fast and a slow TOF, as seen on fig. IV.16) are shown in fig. IV.17. The distribution cannot be fitted with a single linear relation as was done for the gas phase spectrum. We can see a linear behaviour for the low J but a deviation for higher J. For the TOF = 25 μs spectrum we can also make a linear fit of the high J, but again whether this corresponds to a physical meaning of two distinct rotational populations at thermal equilibrium cannot be answered with just these plots. These results are also again qualitatively coherent with those of ref. [223], although the temperatures found are not identical. As expected from a correlation between translational and rotational energy, the 10 μs TOF spectrum is "hotter" than the 25 μs one.

One of the reasons for using NO as a "test" molecule" for the desorption + REMPI experiments was the availability of very detailed studies on this system (multilayer condensed NO dimers) or very similar ones (monolayer physisorbed NO dimers on non-metal surfaces) in the literature, notably Natzle et al. [222], Jackson et al. [223] and Simpson et al. [224]. In these studies the vibrational, rotational, spin and translational distributions are obtained. In addition, other parameters such as thickness, laser power, laser wavelength... were investigated. As a result the discussion of the different possible mechanisms, as we do in this chapter for several systems, becomes more precise, since mechanisms can be ruled out by the wealth of experimental information. Natzle et al. [222] suggest internal conversion of the excited NO dimer to a state that dissociates towards ground state monomers, or a vibrational "hot spot" mechanism. Jackson et al. [223] suggest a mechanism reminding of the excimer desorption mechanism for rare-gas

solids, with a diminution of the N-N distance of the dimer in the excited state, with the molecules ending up on a repulsive part of the ground state curve after relaxation, but with a vibrational excitation of the monomers acquired because of the difference in N-O equilibrium distances in the excited state.

Although it does not necessarily bring a definitive answer on the desorption mechanisms, the internal and translational energy distributions of the desorbed molecules do allow to prune some mechanisms among all the possibilities, by discussing the energy balance of the processes and which mechanisms are coherent with e.g. vibrationally excited molecules, translational-rotational energy correlation, non-statistical distributions, etc... This kind of information will now be available with SPICES II, thanks to the developed set-up. The possibility of testing mechanisms predicted for CO has been mentioned in the previous sections; other possibilities abound, as NO and H_2O ices are basically the only molecular ices for which this kind of measurement has been made.

IV.1.3 CH_4

The results presented here on CH_4 photodesorption come from earlier synchrotron runs that were made with the first SPICES set-up but for which the data had not been treated and analyzed. They have been published in paper I [201] reproduced in the appendix and a lot of what is presented here summarizes the paper, although not all of the data is present in it. Notably the ageing and thickness effects were briefly mentioned but not shown directly in the paper. For the astrophysical relevance of CH_4 and its photodesorption see sections 1 and 5 of the paper. All the experiments presented here were made at 10 K on a gold substrate, using isotopically labeled $^{13}CH_4$.

In fig. IV.18, the gas phase absorption of CH_4 [235] and two different spectra of solid CH_4 [236, 237] are shown in the top panel and the photodesorption spectrum of CH_4 from a 20 ML CH_4 ice is shown in the bottom panel. Again we will first comment on the gas phase and solid phase absorption spectra. For the free CH_4 molecule the occupied valence orbitals consist of a triply degenerated $1t_2$ orbital and a deeper $2a_1$ orbital. The empty valence orbitals are quite high in energy [235] and the corresponding transitions from $1t_2$ to these are not visible in the "low-energy" (< 14 eV) part of the spectrum. Instead the features seen on fig. IV.18 are attributed to Rydberg transitions. For a highly symmetric molecule like methane there is a strong Jahn-Teller effect involved in the Rydberg transitions and the ionization (basically the T_d symmetry is unstable and therefore broken for the CH_4^+ ion). The two features seen at 9.5 and 10.1 eV in the gas phase spectrum are both attributed to $1t_2 \rightarrow 3s$ transitions, but the first one is converging towards the most stable D_{2d} symmetry of the ion and the second one to the C_{3v} symmetry [112]. The rest of the features are not precisely defined on the spectrum but have been attributed to higher Rydberg transitions. The IP is at 12.5 eV in the gas phase [238]. The dissociation limit is 4.4 eV [239] and the electronic states presented above are dissociative. In ref. [238], Kameta et al. have been able to distinguish the neutral dissociation cross-section and the ionization cross-section, showing that the ionization cross-section overtakes neutral dissociation only above 14 eV. Ionization of methane is not dissociative until 13.25 eV, the threshold for $CH_3^+ + H^-$ formation, while the threshold for $CH_3^+ + H$ is at 14 eV [240].

For solid CH_4, two spectra are shown. The older spectrum of Koch and Skibowsky

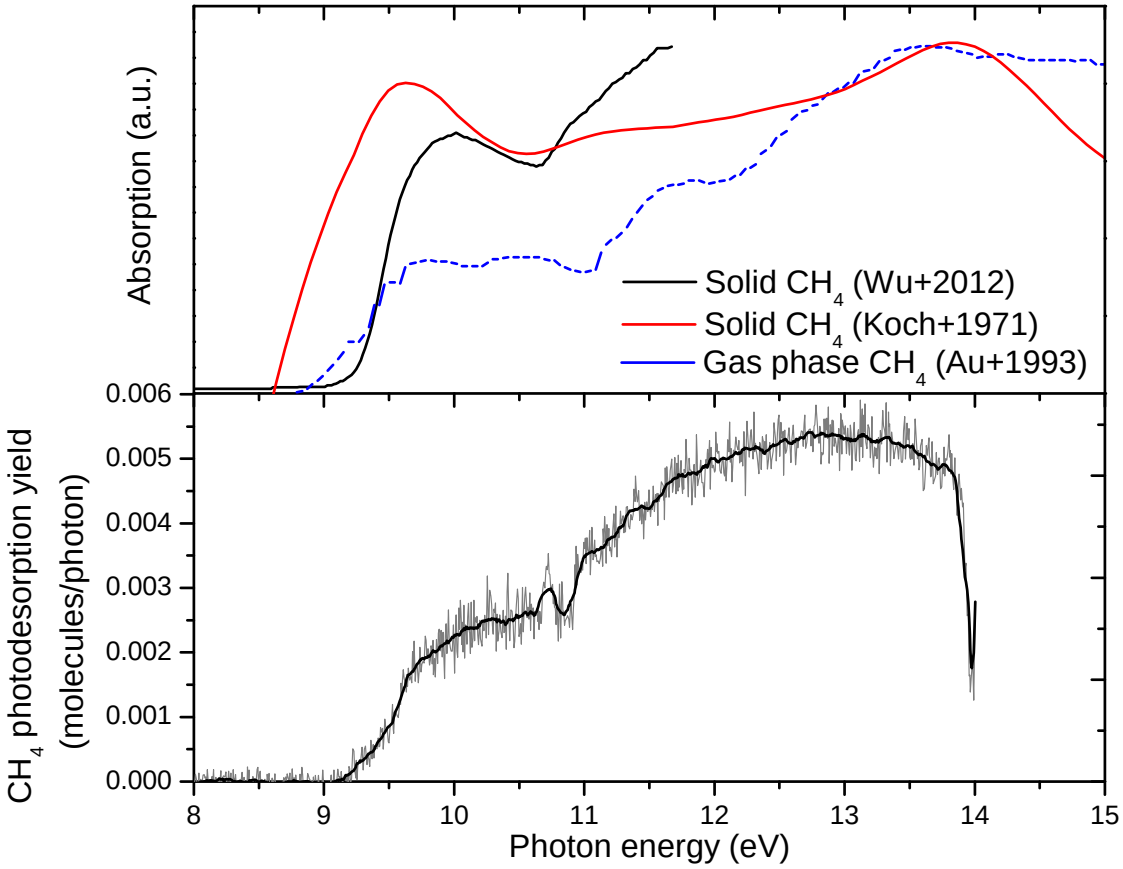

Figure IV.18: Absorption and photodesorption spectra of CH_4. Top panel: absorption spectra of solid CH_4 from ref. [237] (black line) and from ref. [236] (red line) and gas phase CH_4 from ref. [235] (dashed blue line). All spectra are arbitrarily scaled. Bottom panel: photodesorption spectrum of CH_4 from a 20 ML CH_4 ice (the last points are not significant).

[236] is shown because it has been measured up until high energies, but there is probably an issue with the absolute energy scale because the onset of absorption disagrees with more recent spectra [237, 215] (including our photodesorption spectrum) of 0.5 eV. The Koch spectrum has also been taken under different experimental conditions, at 30 K. In the solid spectrum, there is only one peak left at 10 eV. It has been suggested [112] that the Rydberg transitions are replaced by Wannier excitons, although the exciton series is not particularly clear. The solid phase IP is around 11.3 eV [85].

The photodesorption spectrum of CH_4 from CH_4 ice (bottom panel of fig. IV.18) is overall similar to the solid phase absorption spectrum. It resembles well to the spectrum of Wu et al, where there is a marked increase after the minimum at 10.6 eV. The resemblance to the spectrum of Koch and Skibowsky is less clear, but since this spectrum seems less reliable we cannot conclude that there is any significant deviation of the photodesorption spectrum from the absorption.

Ageing effects were also observed in CH_4. In fig. IV.19 three consecutive scans on

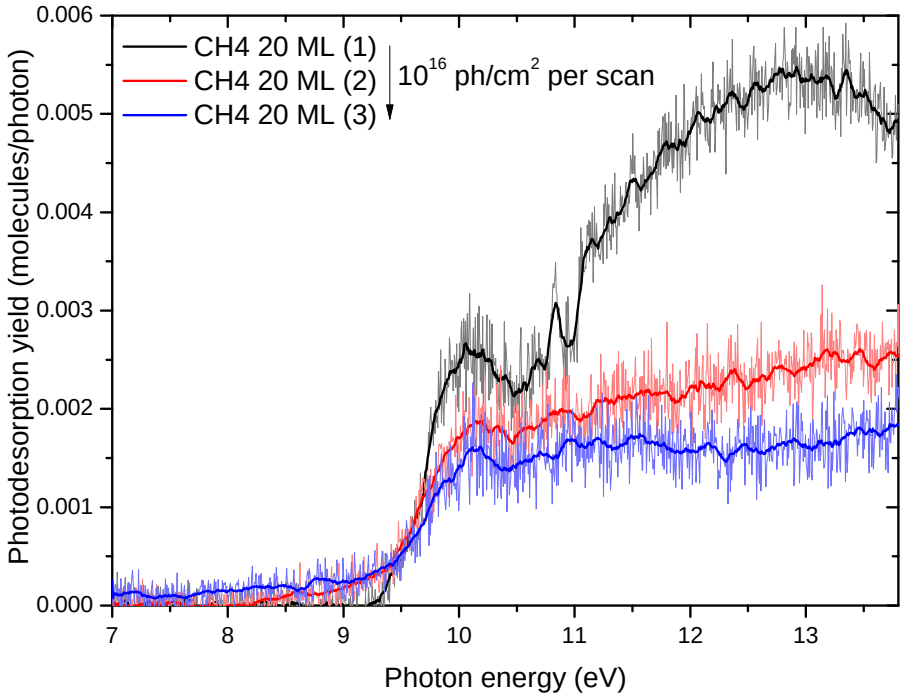

Figure IV.19: Photodesorption spectra for three consecutive scans on the same 20 ML CH_4 ice, with a photon dose of $\sim 10^{16}$ photons.cm^2 per scan. The ageing effect is visible.

the same 20 ML CH_4 ice are shown. We can see that the spectrum evolves. There is a strong diminution (factor of 2) of the photodesorption yield above 11 eV and a bit less pronounced at 10 eV (factor of 1.4) between the first and the second scan. The yield still decreases with the third scan but less so. It is therefore possible that the ageing of CH_4 rapidly reaches a steady state. We can also see on the third scan that the photodesorption yield is no longer exactly zero before 9.2 eV. This non-zero yield is unambiguous in the raw scans, with a clear step above the noise when the scan begins. This could be linked with the creation in the ice of C_xH_y photoproducts which absorb in this region [112].

Once again, ageing could be attributed both to structural changes and photochemistry. The trend observed between the first, second and third scan suggests an initial structural change, as photochemistry in CH_4 ice is not expected to reach a steady state, instead going to higher hydrocarbon chains. But the two possibilities could play a role on different time scales.

We also obtained a photodesorption spectrum from a thin (1.4 ML) ice, which we can compare to the thicker 20 ML ice. It is shown in fig. IV.20. What we see is a very similar photodesorption yield around the 10 eV peak but a significant difference after 11 eV with a much lower yield for the thin ice. Presently and in the absence of a more thorough investigation of thickness dependence we cannot conclude whether this behaviour is truly due to a thickness dependence of the photodesorption yield or an effect of ageing during the scan on the thin ice (ageing could conceivably be faster for a thin ice). It seems nonetheless that for the electronic state at 10 eV at least, photodesorption is very surface-confined as the yields are similar between the two ices, which is an interesting

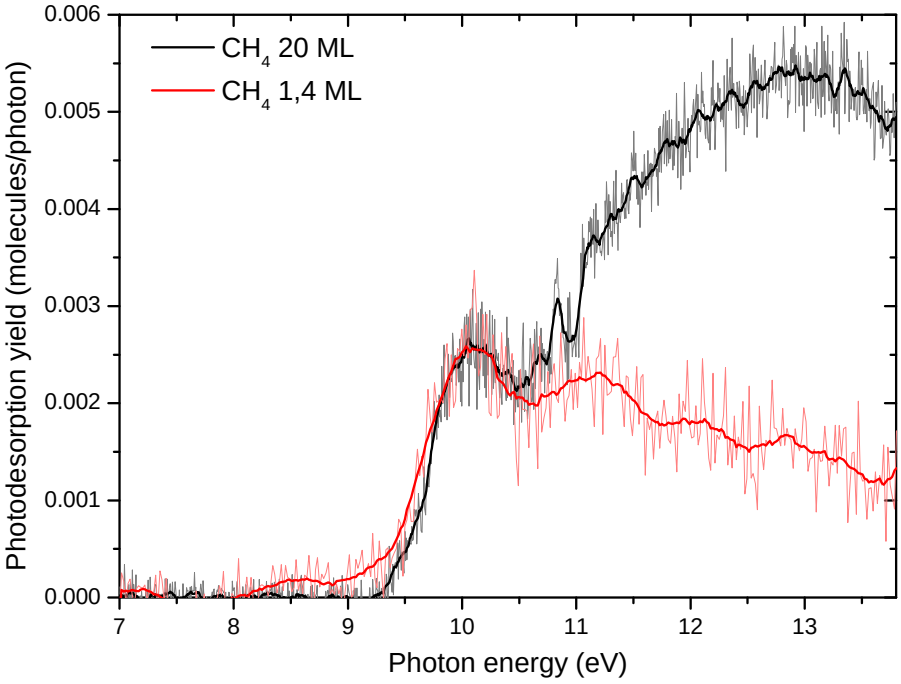

Figure IV.20: Thickness dependence of CH_4 photodesorption, with the photodesorption spectra of a thick (20 ML) and a thin (1.4 ML) ice.

conclusion. A similar conclusion was suggested in paper I on the basis of the CH_4/CO layer experiments that will be presented in a future section.

We looked for the desorption of fragments CH_3, CH_2 and CH, but after correction from the cracking in the QMS no signal was left. This does not necessarily put a strong constraint on their photodesorption yield, considering the correction for the cracking and the intrinsic noise of these mass channels. But it does mean that their desorption yield is not comparable to that of CH_4. Possibly these fragments react before having the possibility to desorb. Something we have not looked at is the desorption of photoproducts of methane chemistry, which was only briefly mentioned previously. Methane is not only easily dissociated, its chemical network upon irradiation is basically unrestricted in the sense that bigger and bigger hydrocarbon chains can be formed upon further and further irradiation. Numerous experiments on the photochemistry [241, 242] and irradiation chemistry [243, 244, 245, 246] of methane confirm this fact. A consequence for desorption is that a number of these photoproducts can also desorb. Here the only hint of that we obtained is a clear signal on mass 28 ($^{13}C_2H_2^+$), which could correspond to C_2H_2 desorption but also to the cracking of any number of bigger C_xH_y molecules. The fact that heavier hydrocarbons than CH_4 desorb is confirmed by the study done in the group of G. Munoz-Caro (see PhD thesis of G. Cruz-Diaz [247]), although in this study they surprisingly could not detect intact CH_4 desorption (perhaps due to different flux conditions). This desorption of heavier hydrocarbons has already been observed and studied for ion irradiation/sputtering (see ref. [35] and references therein). It is not especially common to see photoproducts significantly heavier than the parent molecule

desorbing in pure ices. It is clearly a wide subject that would merit more attention in the future.

Considering the ageing effects are not well understood, I will discuss only the first spectrum, CH_4 20 ML desorption. In terms of absolute yields, CH_4, despite being weakly bound, has lower yields (2.5×10^{-3} molecule/incident photon at 10 eV) than the diatomics but still higher yields than the more strongly bound isoelectronic NH_3 and H_2O or the heavier organic molecules. While basic parameters like binding energy and mass play a role in photodesorption, yields cannot be reduced to these parameters only. An interesting calculation is introduced in paper I which is linked to the previously introduced calculation of the photodesorption yield per absorbed photon. The results given here differ slightly from the paper because some numbers have been updated. Basically, we can divide the outcomes of the event "absorption of a photon at the surface of the ice" into three possibilities:

- Photodesorption of a CH_4 molecule
- Effective destruction of a CH_4 molecule (creation, and possibly desorption, of photoproducts, fragments... other than CH_4)
- Relaxation of the energy in the ice, through various pathways (including reformation of CH_4 after chemical reactions), without removal of CH_4 in any way

This classification is a "simple" picture which does not represent a microscopic reality where, for example, one absorption event could lead to desorption of multiple molecules, or where chemistry involves multiple absorption events, but statistically it makes sense. The initial absorption and the first two pathways can be quantified, yielding a quantification for the third one. The absorption cross-section at 10.2 eV (Lyman-α) is 1.5×10^{-17} cm^2 [215], the photodesorption yield per incident photon 2.5×10^{-3} molecule/incident photon and the effective photodestruction cross-section 3×10^{19} cm^2 (value obtained with a Ly-α dominated UV lamp[f]). This results on average to 0.15 desorbed CH_4 per absorbed photon (assuming 1.5 ML involved in photodesorption at most, as seen in the 1.4 ML spectrum), and 0.02 destroyed CH_4 per absorbed photon, leaving more than 80% of cases where effectively no CH_4 is removed. This is to compare to the case of CO where an average of 1 desorbed molecule per absorbed photon was found (at 10 K) in the previous section. In CH_4 energy dissipation seems more efficient.

One difference between CH_4 and CO is that in CH_4 dissociation dominates the electronic excitation. Dissociation should also play a role in CH_4 photodesorption. It introduces new possibilities for desorption aside from the direct and indirect mechanisms described for CO. One is linked with the fact that the chemistry of the reactive fragments created by dissociation partly leads back to CH_4. The reaction is exothermic and can lead to desorption of the newly formed molecule, which is analogous to the chemical desorption process introduced in section I.1.2 (except here the fragments are created by photons, which is not necessarily the general case). In fact, in ices cage effects can lead to a "geminate" recombination where the dissociated molecule immediately reforms because the fragments do not escape. Aside from this "photochemical" desorption, another

[f]Value from Ilsa Cooke (private communication), slightly lower than the published value of 5×10^{19} cm^2 [248] that was used in the paper.

possibility is that the fragments issued from dissociation can have significant kinetic energy, especially the light H fragments. This can lead to a "kick-out" mechanism, which is basically the ejection of a molecule by a collision with these "hot" fragments. This kick-out mechanism has been explored in particular for H_2O photodesorption, and will be expanded on in the dedicated section. If we consider dissociation plays an important role in CH_4 photodesorption at 10 eV, it could seem surprising that the photodesorption yield still follows the absorption in the region above 11.5 eV where non-dissociative ionization becomes more and more important. One possibility is that CH_4^+ ions quickly recombine with electrons and that the recombination is dissociative, leading back to the same processes.

But this does not explain why so much energy is dissipated without leading to desorption/destruction in CH_4 compared with CO. What is important is that dissociation can also be seen as a dissipation mechanism: even if it leads eventually to reformation of CH_4, energy is lost in lattice distortions, kinetic energy of the fragments which is dissipated away in collisions, etc... and once the molecule reforms, the exothermic energy is partitioned into the various degrees of freedom available. This is where another difference comes into play: CH_4 is a polyatomic molecule, with therefore multiple possible vibrations modes (whereas a diatomic molecule only has one), which allows more coupling to loss channels [249].

In conclusion, the results obtained on CH_4 show that it is a system where desorption, at least in the first electronic state, is confined to the very surface. It is also a system where dissociation plays an important role, possibly opening new photodesorption mechanisms but also acting as a dissipation channel for energy. Another important factor in dissipation is the number of atoms constituting the molecules, which sets the number of degrees of freedom that open loss channels not necessarily coupled to desorption either. Dissociation and polyatomicity can explain why this weakly bound, light molecule has desorption yields much lower than diatomics like CO or NO.

IV.1.4 H_2O

H_2O was the first molecular ice for which photodesorption was studied for an astrophysical context in the VUV range [17]. Its status as the main component of interstellar (and many planetary) ices and as one of the most important molecules in space led to many subsequent studies. Because of its importance across many other fields, photodesorption studies on water ice also exist outside of astrophysical considerations (in contrast to other molecules which have mostly been studied as adsorbates on specific surfaces), and it is also a better characterized system than most. H_2O photodesorption needs to be mentioned if only because considerable work exists on this topic, but I will also present recently obtained new results from synchrotron studies. The interpretations are still preliminary but the findings are definitely interesting.

IV.1.4.1 Water ice structure and electronic spectrum

The structure of thin water ice films grown from vapour deposition under vacuum can be broadly divided into three categories: porous amorphous (p-ASW for porous Amorphous Solid Water), compact amorphous (c-ASW) and crystalline. There are structural variations within these categories. Crystalline ice is usually hexagonal (Ih), which is the

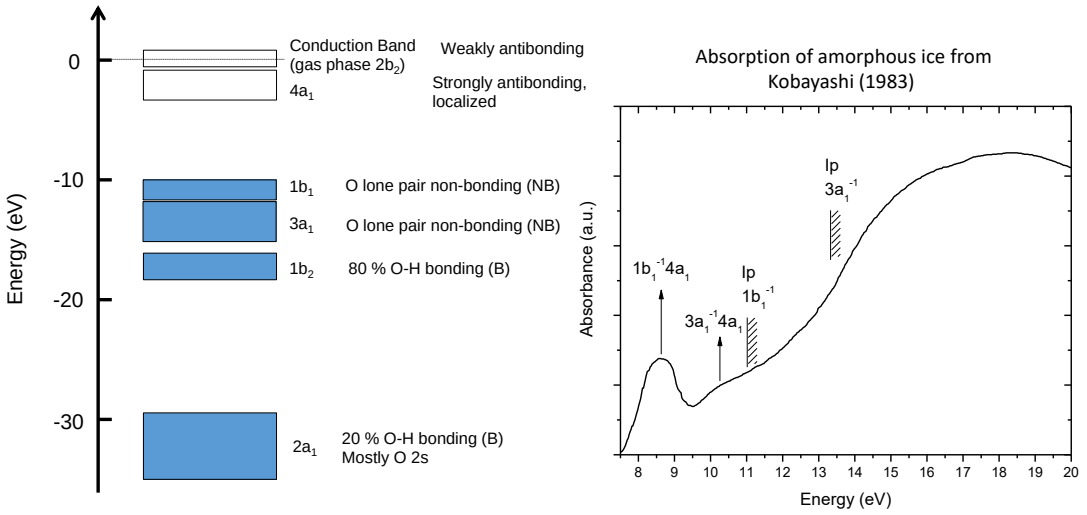

Figure IV.21: Electronic valence structure and absorption spectrum of water ice. The absorption spectrum on the right is taken from Kobayashi [86] and the electronic structure is determined from UPS and XPS experiments referenced in [255, 256].

thermodynamically stable phase also commonly found at ambient pressure and temperatures, but can also be cubic, and usually is quite far from a perfect crystal (in experiments), with polycrystalline aspect and many defaults. The amorphous phases present a continuum of porosity. All have in common that in the bulk, the water molecules are almost all tetrahedrally bonded, donating two and accepting two hydrogen bonds each. Crystalline phases present an ordered oxygen lattice but hydrogen disorder. The topic of ice structure under many different conditions is well reviewed in ref. [250]. In chapter VI, the structural studies of ice using X-ray spectroscopies (Auger electron, X-ray emission, etc) are also discussed.

In our experimental conditions, we consider that we grow p-ASW when we deposit at 15 K, and c-ASW when we deposit at 90 or 100 K (based e.g. on Kimmel et al. [94] and our own tests). This can be tested by probing the effective adsorption surface by TPD. Above 130 K the ice starts becoming crystalline, which can be observed by IR spectroscopy. The structure does not just depend on deposition temperature (and subsequent annealing), although it is the main parameter: deposition angle and deposition rate, for example, can also play a role. This has been explored in details in the literature [93, 94, 251]. Throughout this manuscript the work presented has been done on c-ASW. This is in part motivated by the fact that water ice has mostly been observed in amorphous phases in space (in particular in the ISM), although crystalline ice can be found in the solar system. Porous ice is known to get compactified by irradiation [252, 253], while crystalline ice gets amorphized [254], leading to c-ASW in regions where thermal annealing does not happen.

The valence electronic structure of water ice is recalled in fig. IV.21, with the different electronic levels (bands) and the absorption spectrum adapted from ref. [86]. Information on the electronic structure comes mainly from UPS, XPS and photoabsorption experiments and are summarized in refs. [255, 256]. Valence orbitals retain a lot of their gas phase character when they become valence bands in the solid, so the gas phase notations

are kept, although the hydrogen bonding does introduce some shifts and broadening. The exception is the $2b_2$ orbital which becomes a conduction band, and is therefore delocalized. The two highest occupied valence orbitals of the gas phase, $1b_1$ and $3a_1$, are nonbonding oxygen lone pair electrons. The O-H bound comes mostly from the $1b_2$ and $2a_1$ orbitals. The first two excitations that are seen in the absorption spectrum are transitions from respectively the $1b_1$ and $3a_1$ orbitals to the empty orbital $4a_1$ (which has a mixed 3s Rydberg / valence antibonding character). These transitions in the solid are often discussed in terms of exciton bands. The ionization threshold in the solid phase is located at 11 eV.

IV.1.4.2 Photodesorption yields and mechanisms in the literature

The first study of astrophysical relevance in the literature is the one by Westley et al. [17] and was made using a UV hydrogen discharge lamp and measuring the yield using a quartz microbalance to monitor the loss of material in the ice. Their conclusion is that the photodesorption yield varies with photon dose (increasing up to a saturation limit) and with irradiation temperature (the ice structure and deposition temperature are not stated in the paper), with absolute yields around 3 - 8 $\times 10^{-3}$ molecules per photon. They found desorption of the photoproducts O_2 and H_2 as well.

The study by Öberg et al. [52] agrees on the desorbed photoproducts, in addition detecting OH desorption at a level only twice lower than H_2O, and they state that desorption of other products is much lower. They disagree with the photon flux and fluence dependence found by Westley et al., which is ascribed to water re-deposition during the Westley experiment. They find a (small) thickness dependence and a temperature dependence which are modeled by a simple fit. The absolute yields are around 1 - 4 $\times 10^{-3}$ molecules/photon and represent *total* yields, measured by infrared spectroscopy loss of H_2O molecules from the solid phase. The values are estimated by differentiating loss due to chemistry and loss due to photodesorption by the presumed different kinetic order of the processes. Finally, they see no difference between H_2O and D_2O ice photodesorption.

A more recent study by Cruz-Diaz et al. [257], still using a UV lamp, but detecting desorption directly in the gas phase with a calibrated QMS (with a method similar to ours), found results in overall agreement with the preceding ones with a few points of difference. Their H_2O yield is 1.3 - 2.5 $\times 10^{-3}$ molecules/photon, but they also find a significant yield for O_2 desorption. They also find a factor of $\sim$2 lower yield for D_2O photodesorption.

H_2O photodesorption has also been studied by laser desorption [258, 259]. Nishi et al. [258] investigated photodesorption of NH_3 and H_2O at 248 and 193 nm, so that for H_2O this is a 2-photon process. They suggested an interesting mechanism. First, they suggest that the excitons created in the ice should end up localizing either at the surface or just below the surface (see the paper for more details). Then, they consider what happens to a pair of surface-subsurface molecule when one of the molecules is excited, and argue that the increase of the radius of electron density causes an increase of electron repulsion energy at the intermolecular distance of the ground state, leading to translational motion of the surface molecule and detachment from the surface. This is reminiscent of the "cavity ejection" mechanism in rare gas solids, and it could be classified as an "MGR-like" mechanism in the broadest sense of the term. This is sketched in fig. IV.22 in the top left panel.

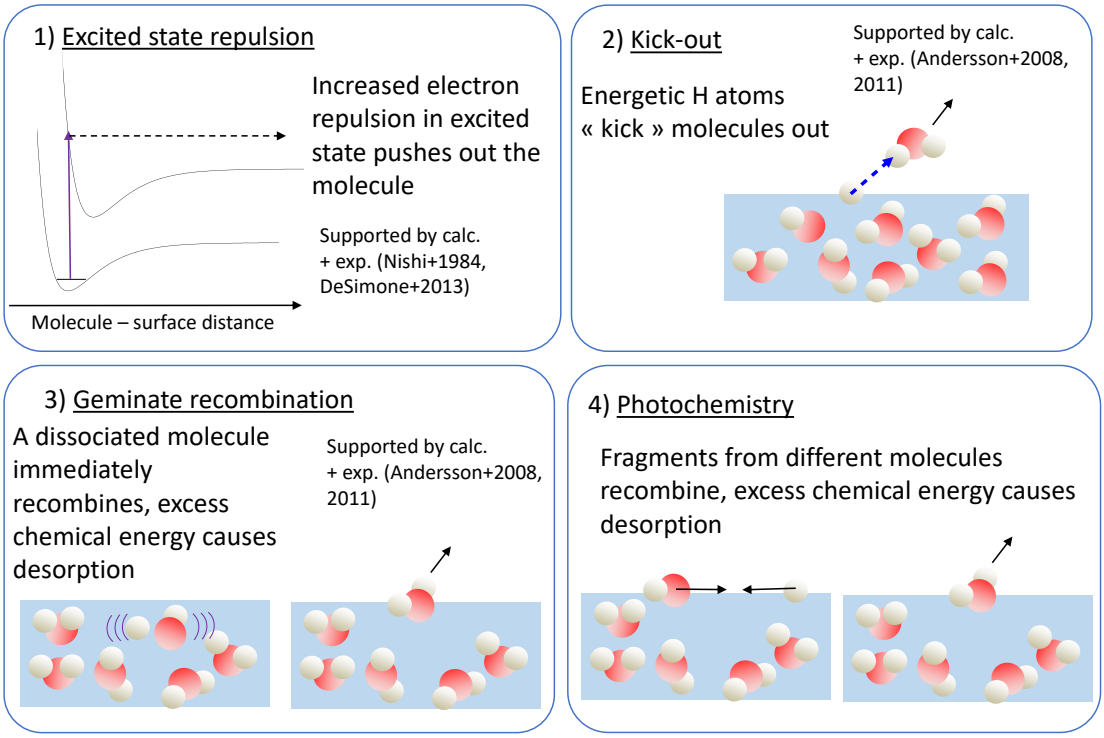

Figure IV.22: Summary of the proposed photodesorption mechanisms for intact water from water ice. See the text for details.

H_2O laser photodesorption was also the object of considerable work by japanese groups, a lot of which is summarized in a recent review [260]. In some of their work they have access to 1-photon desorption using an exciplex F_2 laser at 157 nm, a photon energy which is just at the onset of H_2O absorption. Laser desorption allows them to also use the technique of REMPI spectroscopy of the desorbed molecules presented earlier, which gives them precious information on the rotational and vibrational states of the molecules and the kinetic energy distributions.

There are also molecular dynamics simulations of H_2O photodesorption, which as always is very precious in unraveling mechanisms. A series of work were made by Andersson et al. [261] and continued by Arasa et al. [262, 263, 264]. These molecular dynamics simulations were confronted with the above-mentioned laser desorption + REMPI experiments to see if experiments could confirm the mechanisms inferred by the simulations [265].

Two mechanims are found in this way. The first one is the so-called "geminate recombination", where an H_2O molecule dissociates and immediately reforms and desorbs because of the excess energy. The second one is the "kick-out" mechanism: H_2O dissociation creates H atoms with a lot of kinetic energy, because energy partition favors the very light fragment. These fast H atoms move freely in the ice and can collide with other water molecules that are subsequently ejected. The laser desorption + REMPI experiments are *coherent* with some qualitative features expected of these two mechanisms, but saying that they definitely confirm them is a bit premature, as other mechanisms such as the one of Nishi et al. can also be expected to give similar features. In fact, this interpretation

has been challenged by other experimental and molecular dynamics investigations which favor the electron repulsion mechanism [266].

The proposed mechanisms for intact H_2O desorption are thus:

1. Electron repulsion increases in the excited state H_2O^*-H_2O pair (Nishi+1984 [258], De Simone+2013 [266])
2. Kick-out by fast H atoms (Andersson+2011 and other studies of these groups)
3. "Geminate" recombination of OH + H in H_2O (Andersson+2011 and other studies of these groups)
4. In addition, recombination at the surface of OH + H from diffusing fragments originating from different molecules

They are also summarized in fig. IV.22. The last item cannot be captured by molecular dynamics simulations which do not take into account subsequent reactions after dissociation, but according to our new experimental results it cannot be neglected.

IV.1.4.3 Experimental results from synchrotron study

We have studied photodesorption from c-ASW grown at 100 K at the synchrotron. The ices were 20 ML thick and maintained at different temperatures for irradiation. We used the zero order beam (higher flux and 1 eV width) because the flux with the first order monochromatic beam was too low to obtain any signal. The results for H_2O are presented in fig. IV.23. We observe desorption of H_2O, O_2, H_2 and OH, but no desorption of H_2O_2 or HO_2, which is coherent with previous studies. The trend observed with temperature, a slight increase of H_2O desorption and a larger increase of O_2 and H_2 desorption with increasing temperatures, is also in agreement with previous works. Regarding the absolute yields, we have slightly lower H_2O yields ($\sim 8 \times 10^{-4}$ molecules/photon at 10 eV) than Cruz-Diaz et al. [257] but considering the uncertainty on the absolute calibration this is a very good agreement, unlike for other molecules[g]. O_2 yields agree as well but OH yields are about 5 times lower. The absolute yields on H_2 are not considered very reliable considering the difficulties of calibrating the QMS apparatus function at this mass. For H_2, there is also a fluence dependence of the photodesorption yield, which increases of 40 % over the course of 40 minutes of irradiation ($\sim 10^{18}$ ph/cm^2)

New information is brought by the photon energy resolved yields. In the top left panel of fig. IV.23 a comparison is made with the absorption spectrum of Kobayashi. The spectrum is not well resolved because of the 1 eV width of the zero order beam, and therefore the structures are not clearly seen, but nonetheless we can observe that photodesorption is: (i) more efficient in the second exciton band, around 10 eV, than in the first one at 8.4 eV, and (ii) less efficient above the ionization threshold ($\sim$ 11 eV [86]) than below. Point (ii) can be explained by the fact that ionization is not dissociative (most of the mechanisms presented so far rely on dissociation) and the simple "single-hole" states are short-lived and easily migrate away [255]. The first point is more difficult to explain, as both electronic states are dissociative: in fact in the gas phase the first state is completely dissociative while the case of the second one is somewhat more complicated.

[g] which is actually surprising considering the disagreement we have on the CO yields used in both cases for calibration...

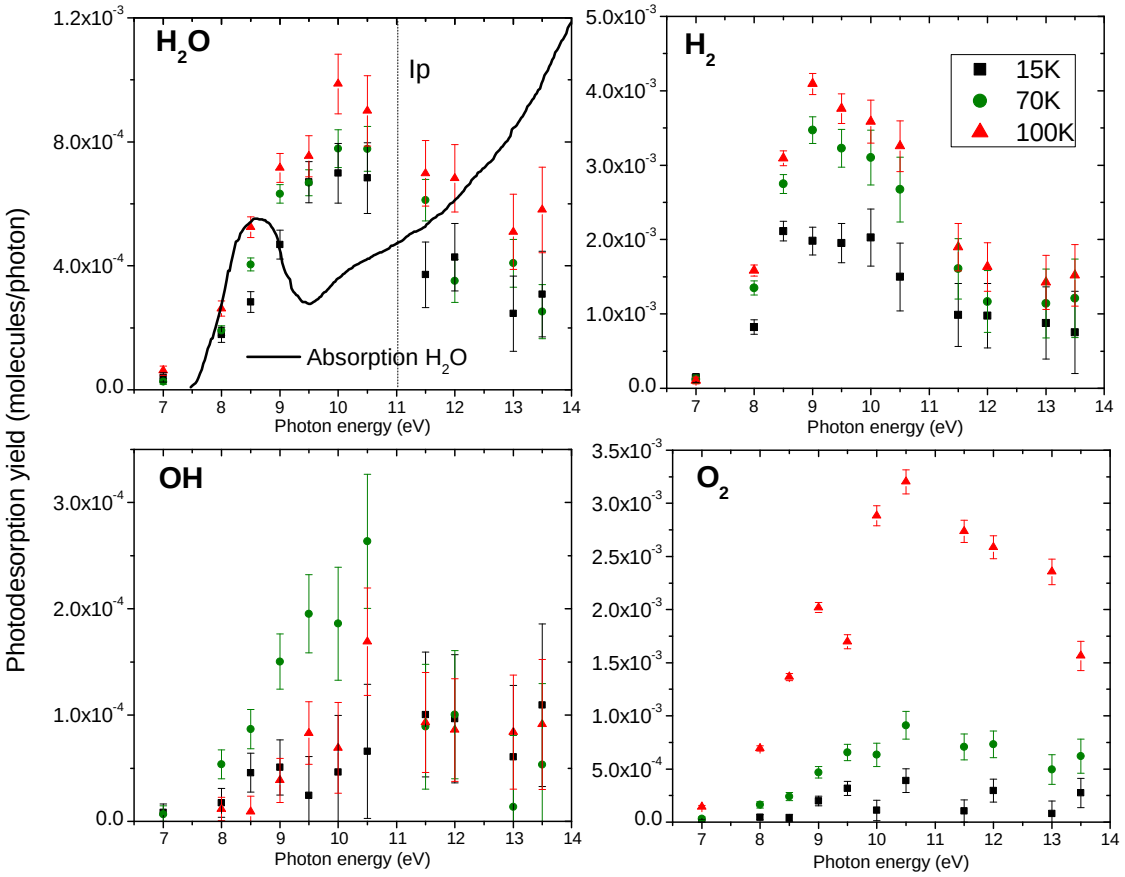

Figure IV.23: Photodesorption spectra of H_2O, O_2, H_2 and OH from 20 ML compact amorphous H_2O ice, at different temperatures. In the top left panel the absorption spectrum of amorphous ice [86] is reproduced for comparison.

We have also obtained interesting results on isotopic effects: the photodesorption spectra and yields for D_2O ice are presented in fig. IV.24. There is a drastic isotope effect with a photodesorption yield almost 8 times lower than H_2O for D_2O (1.2×10^{-4} molecules/photon at 10 eV) and 2-4 times higher for OD than OH (4×10^{-4} molecules/photon at 10 eV for OD vs. 1-2 $\times 10^{-4}$ molecules/photon for OH). This is not in agreement with what is reported by previous experimental studies.

In order to better understand these isotope effects, it is also interesting to look at the details of the irradiation temperature effect first. This is presented in fig. IV.25, with the photodesorption yield at 10.2 eV as a function of irradiation temperature for all species except OH, for which the signal was too weak in these experiments. We see a trend where photodesorption yields of H_2O, O_2, H_2 and their deuterated counterparts are constant until about 70 K then linearly rise. The only exception to this trend is OD (although the error bars are quite large).

First, let us discuss the desorption of O_2 and H_2. The desorption of these species is linked with chemistry: even for H_2, the direct dissociation of H_2O into H_2 + O is not the most likely pathway [260]. Experiments done with low-energy electron irradiation showed

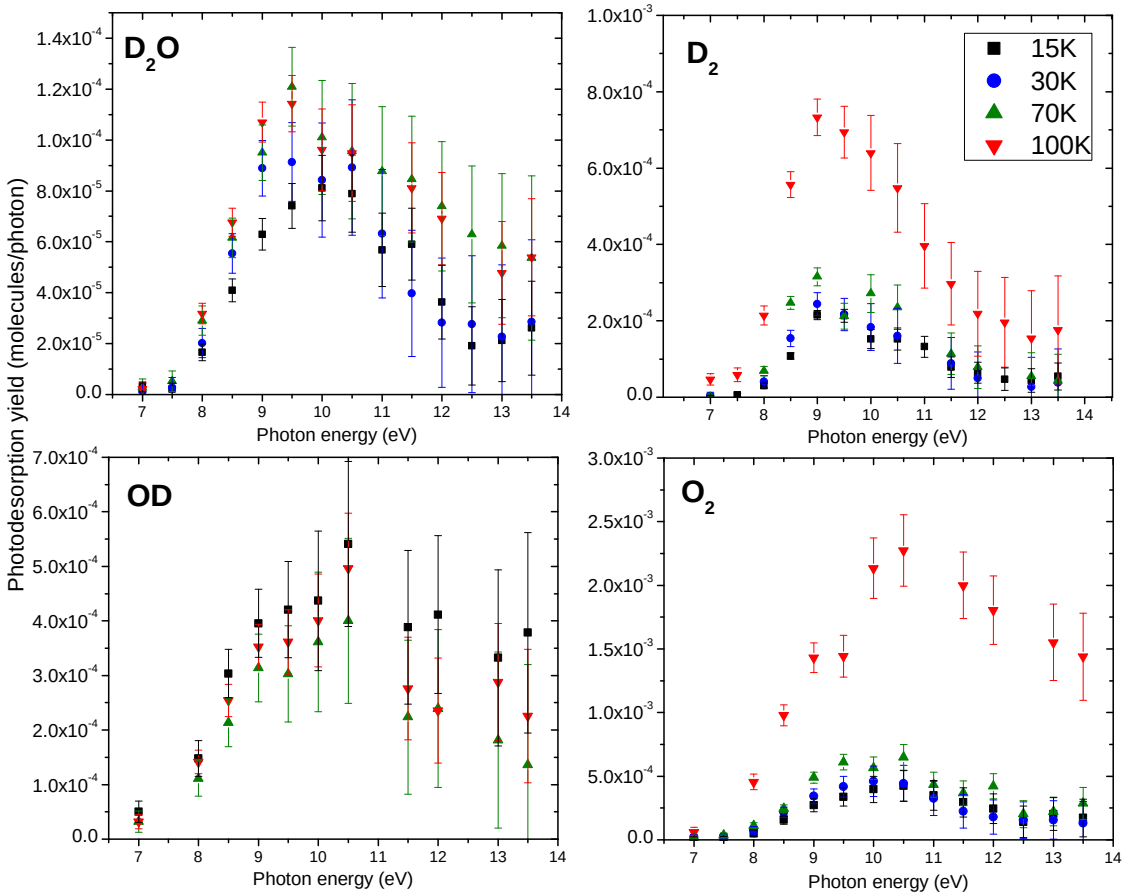

Figure IV.24: Photodesorption spectra of D_2O, O_2, D_2 and OD from 20 ML compact amorphous D_2O ice, at different temperatures.

that production of desorbing H_2 and O_2 happens mostly at the interfaces [267, 268], although *energy* migration from the bulk (in the form of excitons) occurs. The results from desorption + REMPI studies also agree with indirect mechanisms like H + H recombination for H_2 [260]. Formation and desorption of O_2 involves intermediate species like H_2O_2. The surface chemistry itself should not be particularly enhanced around 70 K. In fact, at such a temperature H atoms desorb and are therefore removed, decreasing the efficiency of chemistry. Photodesorption yields could also increase with temperature because above the thermal desorption threshold of a given species, it will desorb immediately upon being formed even without further sources of energy. This could perhaps have been the case for O_2 (although thermal desorption of O_2 from the ice should start already around 30-40 K), but it definitely cannot be the case for H_2 :above 25 K all surface H_2 already desorbs. Instead, what seems to be the most likely is that 70 K is the activation temperature of the diffusion of OH and other radicals in the *bulk* of the ice. The radicals of bulk origin can therefore reach the surface and enhance surface chemistry, leading to enhanced desorption of H_2 and O_2.

Now, considering the similar threshold for the increase of H_2O desorption, this suggests that surface chemistry *also* plays a role in H_2O desorption: this is the 4th item mentioned

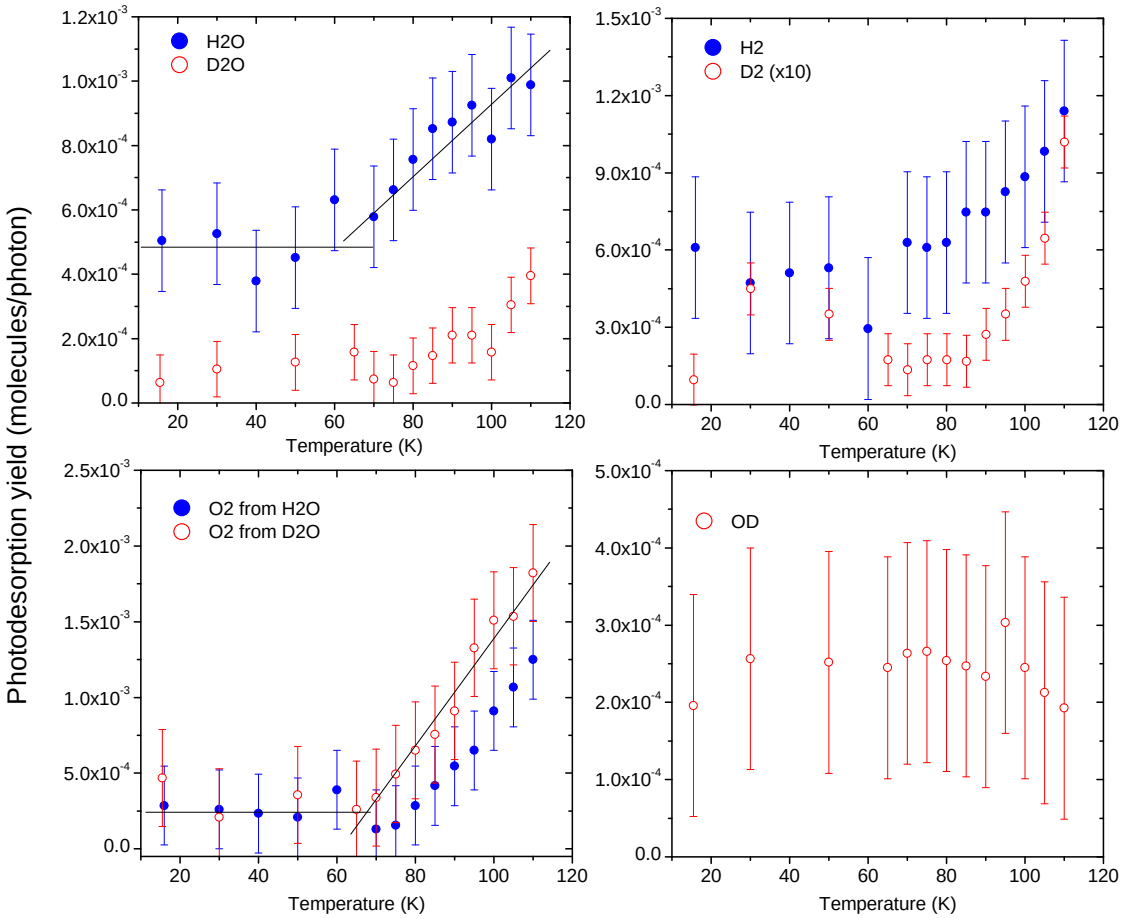

Figure IV.25: Photodesorption yields from 20 ML H_2O and D_2O compact amorphous ices, as a function of irradiation temperature, at a fixed photon energy of 10.2 eV.

at the end of the last subsection. The increase is not as dramatic because it is only one mechanism on top of others that are likely at play. The constant desorption of OD is also coherent with this picture: OD/OH desorption is a more direct mechanism, originating from the dissociation of D_2O/H_2O at the surface. It is therefore not increased by the diffusion of bulk OD/OH (a diffused bulk OD/OH can react at the surface but does not desorb: kinetic energy from the direct dissociation of a surface molecule is necessary for that).

Coming back now to the isotope effects: the observed H_2O/D_2O ratio cannot be explained by the kick-out mechanism. D atoms are created with less kinetic energy than H atoms but transfer momentum more efficiently to water molecules, and molecular dynamics calculations predict a photodesorption of D_2O about 2 times *more* efficient than H_2O. These same calculations do not find any difference for the geminate recombination mechanism. An isotope effect could be expected for the excited state electron repulsion mechanism, since it is an MGR-type mechanism (if the excited state is quenched before sufficient separation of the molecule pair, then the molecule does not desorb). However this would involve the mass ratio of H_2O and D_2O, which is not very high: MGR-type

mechanisms do not lead to isotope ratios as large as the one observed here. It is possible instead that the isotope effect stems from the mechanism that is not taken into account in simulation: non-geminate recombination. It is striking that while D_2O desorption decreases, OD desorption increases. While summing OD + D_2O and OH + H_2O yields does not give similar results, it is probable that part of the lower D_2O desorption yield is the result of more OD escaping the surface before chemical reaction. A higher OD desorption yield than for OH *is* found in molecular dynamics simulations [263, 264], explained by the fact that OD radicals obtain more kinetic energy upon D_2O dissociation than OH radicals do upon H_2O dissociation, for momentum conservation reason (the mass ratio of the fragments imply that OD gets 10% of the available kinetic energy while OH only gets 6%). In the MD simulations, OD desorption is factor of ~ 3 larger than OH desorption, which is very close to what we obtain here (e.g. at 100 K and 10 eV we have a factor of ~ 5, which considering all the error bars is very close). There is a discrepancy in the absolute values of OH/OD desorption which are higher by a factor of 2-4 in the MD simulations compared with our experiments, bu this can be attributed to the absence of chemistry, and thus OH/OD consumption, in these simulations.

In conclusion, this work provides the first wavelength-resolved photodesorption yields of parent molecules, photoproducts and fragments from H_2O and D_2O ice (c-ASW). These photodesorption spectra show a maximum of the desorption yield in the second exciton band (theoretical works and experimental laser desorption works so far have focused on the first band), with a clear lower efficiency of desorption above the ionization threshold, demonstrating once again an electronic state-dependence of the intrinsic efficiency of photodesorption. The two other major experimental findings are a strong isotopic effect in D_2O/H_2O desorption (D_2O yield much lower than H_2O yield, which is the reverse of what is predicted by MD simulations, and OD yield higher than OH yield), and a temperature effect with an increase of the desorption yield of H_2O/D_2O, D_2/H_2 and O_2 (but not OD) above 70 K. Both of these facts are consistent with our proposed explanation that non-geminate recombination at the surface of the ice (a mechanism not included in simulations) is dominant in the desorption of intact H_2O/D_2O from the ice. Diffusion of fragments from the bulk above 70 K and subsequent chemistry at the surface explain the observed temperature effects. Removal of OD at a higher rate than OH from the ice surface, and therefore reduced non-geminate recombination, is suggested to explain the observed isotope effects. The role of dissociation and chemistry is crucial in photodesorption for this system.

IV.1.5 NH_3

NH_3 is another important component of icy mantles, as mentioned in chapter I. This study was made in the framework of a collaboration with the group of A. Lafosse who studied low energy (<20 eV) EID of neutral molecules from NH_3 ice (see PhD thesis of L. Sala [269]).

NH_3 is an interesting system for a number of reasons. First, it is like H_2O a hydrogen-bonded system, although the hydrogen bonds are weaker and the bonding network is different (several H atoms share the same lone pair). It also features under certain conditions a crystal exciton [112, 115] (in the sense mentioned in section II.2 of an actual *collective* excitation which is specific to the crystal and not the molecule, appearing as a

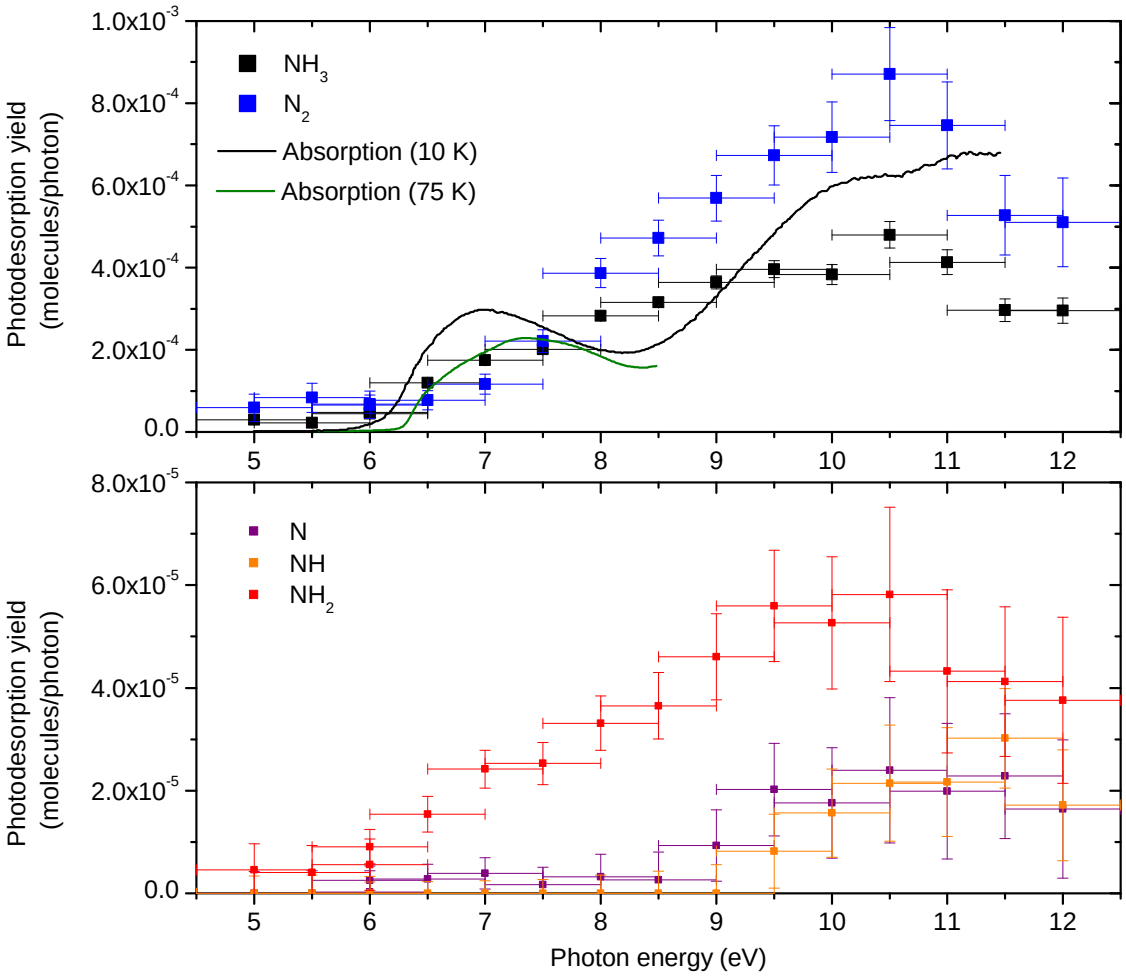

Figure IV.26: Photodesorption spectra of NH_3 and N_2 (top panel), NH_2, NH and N (bottom panel) from 20 ML NH_3 ice at 75 K. The horizontal error bars show the ∼1 eV FWHM of the zero order synchrotron beam. The vertical error bars represent relative errors due to the noise of the signal, and not absolute errors on the calibration. Also shown in the top panel are the absorption spectra of NH_3 ice for 10 K ice from Lu et al. [216] and from ice deposited at 10 K and annealed at 75 K from Mason et al. [115].

sharp peak at 6.4 eV). The first electronic states in the solid also seem to be very sensitive to the structure of the ice [115].

It would have been very interesting to see if a collective exciton also appears in the photodesorption spectrum or not, but unfortunately the photodesorption yield of NH_3 turned out to be slightly too weak ($<10^{-3}$ molecule/photon) for the use of first order light on the beamline. Instead a zero-order study was carried out, resulting in only broad structures being identifiable.

IV.1.5.1 Photodesorption spectra and yields

The photodesorption spectra of NH_3, but also N_2, NH_2, NH and N (which were all observed even after correcting for the cracking in the QMS) are presented in fig. IV.26. These spectra are for NH_3 ice deposited at 28 K and heated and maintained at 75 K (we will see later that the irradiation temperature does not matter too much for photodesorption). The absorption spectrum of NH_3 is shown also for two different conditions: the full spectrum (until 11.5 eV) of Lu et al. [216] corresponds to NH_3 ice deposited at 10 K, while the spectrum of Mason et al. [115], focused more on the low-energy side, corresponds to an ice deposited at 10 K but annealed to 75 K, which is similar to our own conditions. There is a noticeable blue-shift of the first peak of the absorption from 7 to 7.4 eV, but it is also clear that the shape becomes much less like that of a single peak. This first peak has been attributed from the gas phase feature in the same region, the $\tilde{A}$ state which is a Rydberg excitation from the $3a_1$ orbital, which is almost entirely of N lone-pair character, to the 3s a_1' orbital[h]. Subsequent gas phase features are also attributed to Rydberg transitions to 3p, 4s and 5s orbitals. Robin [112] however argues that Rydberg transitions should not exist in NH_3 ice and that therefore the observed peaks should correspond to valence transitions to σ^* orbitals, despite the fact that the condensed phase peaks have similar widths to the vibronic envelope of the gas phase electronic states. We are left with the conclusion that the attribution of the electronic spectrum of solid NH_3 is not entirely clear. The ionization potential (threshold) in the gas phase is 10.15 eV [205] and the shift of IP (vertical) from gas to solid is measured as 1.15 eV from UPS [270], assuming a similar shift of the threshold IP it should then land at 9 eV in the solid phase. This does mean that the Rydberg states $\tilde{D}$ and $\tilde{E}$ in the gas phase which converge towards the IP are lost or extremely broadened in the solid phase (no clear peaks are observed before 9 eV). The peak at 10.2 eV and above may correspond to super-excited neutral states. For example, a peak in the gas phase at 11.3 eV was suggested to be a transition to a valence σ^* orbital [271].

There seem to be a disagreement between NH_3 absorption and desorption spectra. In the photodesorption spectrum of NH_3, there is a continuous rise of the photodesorption yield from threshold to 10.5 eV, with no minimum around 8.5 eV as would have been expected from the absorption. The 1 eV spectral width of the synchrotron beam does blur our features but the structure of the spectrum is quite broad, so this result is still surprising. The same structure is observed for NH_3, N_2 and NH_2 desorption. It is however different for NH and N where a threshold of desorption at ∼9 eV is observed. This threshold is not too surprising for NH desorption considering gas phase photodissociation data. The thermochemical limit of dissociation of NH_3 into ground state NH($X^3\Sigma^-$) + H_2 is only 4.1 eV [271] but this reaction is forbidden. The threshold of formation of NH^* in either the $b^1\Sigma^+$ or $c^1\Pi$ states is precisely around 9 eV as determined both from fluorescence photodissociation and electron impact dissociation [272, 273, 271]. The N desorption threshold on the other hand is more mysterious, as I could not find information on direct dissociation of NH_3 into N, which is presumably not very likely and should have a high energy threshold. Here a process involving multiple steps is more likely.

The desorption was also studied as a function of *ice temperature* (but not deposition

[h] In this excited state the point group of NH_3 changes from C_{3v} to D_{3h} and therefore the labelling of the orbital changes as well

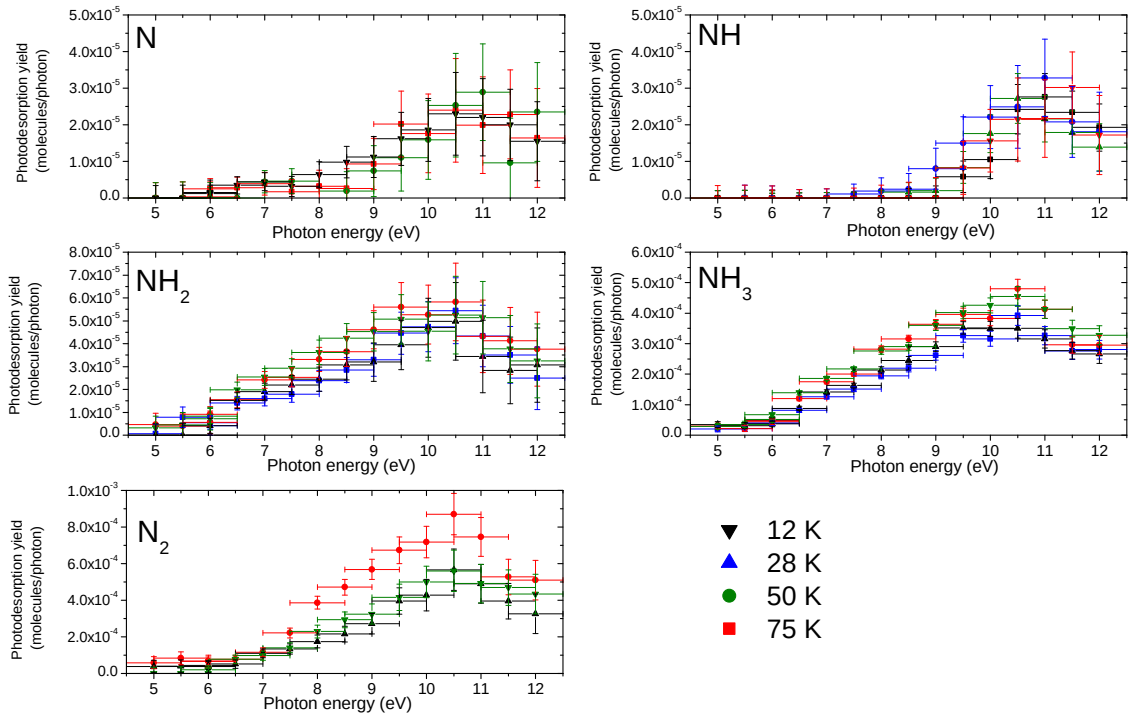

Figure IV.27: Photodesorption spectra of NH_3, NH_2, NH, N and N_2 from NH_3 ice as a function of ice temperature. The ices were all grown at 12 K then brought to and kept at the indicated temperature during the irradiation.

temperature). The ices were all deposited at 12 K, but were then maintained to either 12, 28, 50 or 75 K for irradiation. The results are presented in fig. IV.27. The data for N_2 and N at 28 K is absent because at this temperature CO outgassing from parts of the cryostat interfere with the signals. There is no notable difference between the spectra at different temperatures for any of the species, which again is a bit surprising considering the electronic states are supposed to be affected by the annealing of the ice, but these effects might be too faint to be detected with the zero order beam. The only effect of ice temperature is on the absolute desorption yields: there is a slight increase of NH_3 and N_2 with increasing temperature. The differences for the fragments are all within the (large) error bars of the experimental noise and are therefore not relevant.

Photodesorption from pure NH_3 was studied by Martin-Domenech et al. [274] with a hydrogen discharge UV lamp. Because NH_3 already absorbs at 193 nm (6.4 eV; photon energy of the ArF exciplex laser), photodesorption has also been studied at this wavelength by laser desorption [258, 275]. Both ref. [274] and [275] quantified the photodesorption. The value of Martin-Domenech et al. is 2×10^{-3} molecules/photon for intact NH_3 desorption, while our yield in the same photon range is $\sim 4 \times 10^{-4}$ molecules/photon. The origin of this disagreement is probably the disagreement that already exists in our respective values for CO photodesorption (see section IV.1.1), from which the other values are calibrated. Loeffler et al. [275] give a value of 1×10^{-3} molecules/photon at 6.4 eV, but this is a value derived from loss of NH_3 in the bulk (measured by a quartz microbalance). Our total photodesorption yield at 6.5 eV is $\sim 2 \times 10^{-4}$ molecules/photon, and a

loss of molecules due to photodesorption of $\sim 3 \times 10^{-4}$ molecules/photon if we equate N_2 desorption to the loss of 2 NH_3 molecules. The discrepancy can be attributed to loss of NH_3 by photochemistry in the bulk, which certainly takes place. In both these studies, N_2 and H_2 desorption is observed. As would be expected for these chemistry products, their desorption yield evolves (increasing by a factor of a few for N_2 [274]) with irradiation time, a factor that we did not investigate here.

Regarding the photodesorption mechanisms, I will mostly refer to previously discussed possibilities on other molecules. The (presumed) photodesorption mechanism of the fragments (at least NH and NH_2) is that kinetic energy is acquired on the dissociative excited state potential energy surface, which is enough for their desorption. For N_2, what should be explained is rather its formation mechanism, which can result from a variety of reaction pathways involving NH_2 (and perhaps NH fragments above 9 eV) and formation of intermediary species N_2H_x which are later dissociated. A lot of the reactions leading to N_2 formation are largely exothermic [269] and should provide enough energy for desorption if the reaction occurs at the surface. For intact NH_3 desorption, the same mechanisms discussed for H_2O can be evoked: exothermic reformation (geminate or not) of NH_3, hydrogen atom kick-out, and the electron repulsion mechanism suggested by Nishi et al. [258]. The small temperature dependence of NH_3 yields, the higher one for N_2 and the lack of temperature dependence of the fragments are similar to the H_2O case, suggesting similar mechanisms involving surface chemistry and it enrichment by bulk diffusion. A more precise temperature dependence study could perhaps unravel a threshold here as well. The previously mentioned (section II.3.2) study of NH_3 on GaAs(100) is interesting as well but implies a sufficiently strong coupling between the internal vibration modes of the molecule and the surface-adsorbate bond. This coupling should be different in the case of solid NH_3 and therefore the mechanism does not necessarily apply here. Since the evidence for this mechanism in NH_3 on GaAs relies on a strong isotopic effect, it suggests experiments on isotopes are nonetheless indicated.

The results obtained here are rather preliminary: as the above discussion shows we do not have experimental data that really allow an in-depth discussion of mechanisms. Still, we have again obtained wavelength-resolved photodesorption yields for the different desorbing species from NH_3 ice. We have measured the desorption of fragments NH_2, NH and N which was not done by Martin-Domenech et al. [274], and the wavelength resolution revealed a different threshold than NH_3 absorption for the desorption of NH and N. This can be explained for NH by a threshold for production of internally excited NH fragments. The observed desorption of N_2 with a yield of the same order as NH_3 is a testimony of the role played by chemistry in this system as well. NH_3 seems to be a system close to H_2O (which is not unexpected), with similar orders of magnitude for desorption yields, the desorption of photoproducts at a level similar or higher than the parent molecule, and the desorption of fragments at a lower yield. It is also worth noting that all of our results are in agreement with the results obtained by low-energy (<20 eV) electron irradiation of NH_3 ice in the group of A. Lafosse (see [269]).

IV.1.6 Other organic molecules

Recently, the team has started moving towards slightly larger, organic molecules which are a hot topic in ISM astrochemistry. Photodesorption studies were published recently

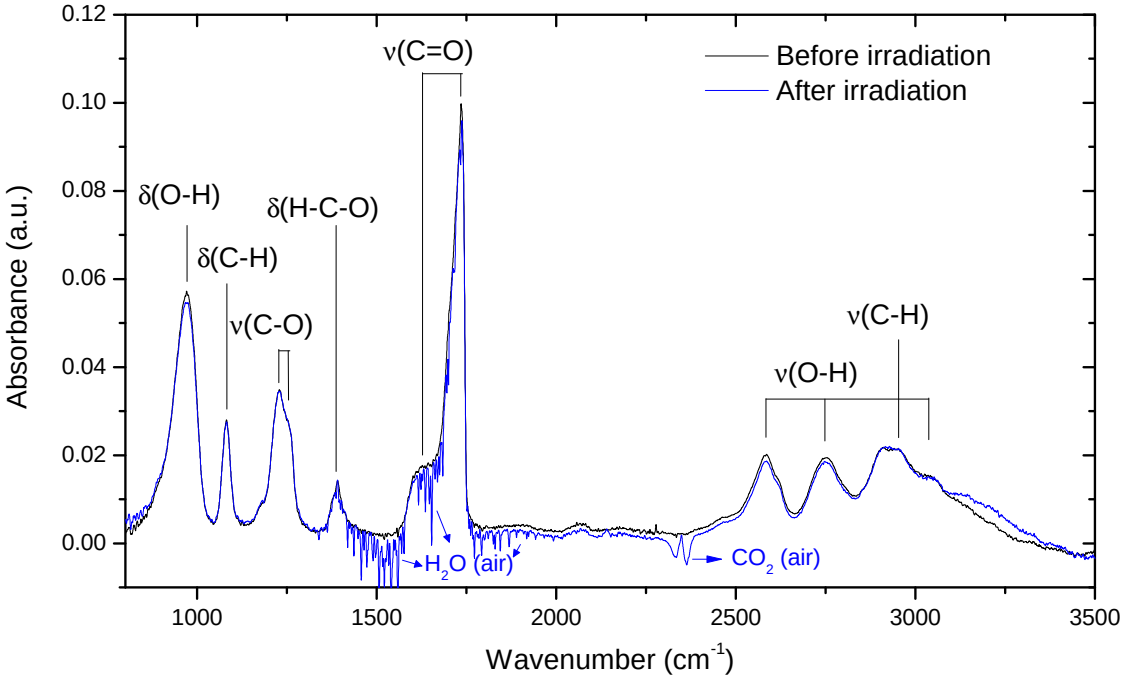

Figure IV.28: Infrared spectrum of 30 ML formic acid deposited at 90 K. Attributions of the peaks are indicated on the figure and discussed in the text. The black line corresponds to the spectrum before irradiation, and the blue line to the spectrum after irradiation.

on CH_3OH [54] and H_2CO [276], which I will mention here, but I will focus on data obtained on HCOOH since they are not published yet.

The noticeable trend observed in going towards larger molecules is that the photodesorption yield of the intact molecule decreases significantly, with a yield of $\sim 4 \times 10^{-4}$ molecules/photon for H_2CO, and down to $\sim 1 \times 10^{-5}$ molecules/photon for CH_3OH. The desorption of fragments then becomes largely dominant in the total photodesorption yield. In the case of H_2CO, both H_2 and CO desorb in the 5×10^{-3} molecules/photon range, and in the case of methanol, CH_3, OH and H_2CO are measured in the 10^{-5} molecules/photon range while CO dominates around 2×10^{-4} molecules/photon (H_2 was not quantified in the latter case).

IV.1.6.1 Photodesorption from HCOOH ice

The results presented here are preliminary: we focused on the photodesorption of various species from 30 ML pure HCOOH ice deposited at 90 K and irradiated at 15 K.

The structure of formic acid ice, from the available literature, seems fairly complicated. Formic acid easily forms dimers with two hydrogen bonds between the alkyl group H and the double-bonded O, but its crystal form consists of chains of HCOOH molecules with a single bond between each molecule [277]. Thin films of HCOOH seem to result in a varying mix of dimers, multimers and crystallites [278, 279, 280]. Evidence for this is obtained from IR spectroscopy or HREELS.

The RAIRS spectrum of HCOOH ice investigated here is presented in fig. IV.28.

A spectrum is presented before and after irradiation: the post-irradiation spectrum will be discussed later. The spectrum resembles well to the ones presented in ref. [279]. Attributions of the different modes are given on the figure. We observe bending modes of O-H (ν_5), C-H (ν_8) and H-C-O (ν_4) at respectively 970, 1081 and 1390 cm^{-1}. The H-C-O peak also has a shoulder at $\sim$ 1376 cm^{-1}. The O-H bending wavenumber is 40 cm^{-1} higher than reported in the other studies [279, 278, 280], but is very close to the value for crystalline α-HCOOH [281]. The modes for which the atoms are involved in the hydrogen bonding (the donor H of the O-H group and the acceptor O of the CO double bond) are expected to be the most affected by changes of structure in the solid: they are quite different for the crystal and the dimer. The stretching mode of single bond C-O is seen as a split peak at 1227 and 1253 cm^{-1} (there is a weak shoulder at 1180 cm^{-1} which we did not attribute). The C=O stretching is also split with a strong, very asymmetric peak at 1735 cm^{-1} and a broader and weaker peak at 1627 cm^{-1}. The position of these two peaks is again different from the values reported in the literature, but also different from the crystalline value. This peak is also expected to be very sensitive to the hydrogen bonding structure. The C-H stretch is seen at 2952 cm^{-1} while the O-H stretch is split into three very separated peaks at 2584, 2750 and 3040 cm^{-1}.

While the frequencies observed for some of the peaks suggest we have considerable crystalline structure in our ice even though it is deposited only a 90 K (crystallization is supposed to occur at higher temperatures, >100 K [278]), the splittings mentioned on some peaks are not attributable to the crystal since they are also present for lower temperature ices [279], in particular the ν(O-H) splittings. These splittings are attributed to the presence of long chains of HCOOH, not necessarily in a crystal structure [281]. The higher frequency peak of ν(C=O) is attributed to out of phase motion of the stretchings of neighbouring molecules, while the lower frequency one is the in phase motion. For the ν(O-H) the attribution is more complicated [281].

In conclusion it is possible that we have an intermediate structure with long HCOOH chains but without the complete ordering of a crystal. Our peaks match well these reported for crystalline HCOOH [281] while some differ from the values reported for thin film HCOOH deposited at lower temperatures [279, 280]. However, a lot of crystalline features pertain to the characteristics of long HCOOH chains, and crystalline structure is expected at a higher temperature than ours, so we do not think our ice is entirely crystalline. No evidence of peaks that could be attributed to the dimer (such as an O-H around 3110 cm^{-1}) are observed.

The photodesorption experiments were carried out using the zero order beam (therefore with a flux varying between 10^{14} and 10^{15} photons.s^{-1} and a spectral width of about 1 eV, see section III.4.2). A first series of measurement was made where we observed H_2CO, HCO, H_2O and OH. This first series is still interesting because this is where we observe an ageing effect. Points taken at similar energies but after more irradiation show significant changes of yields for some products. A second series of measurements were made, this time monitoring HCOOH, CO_2, O_2, CO and H_2O.

First of all, we have not observed any signal on mass channel 46 for HCOOH. This mass channel is not the most intense peak expected in the electron impact ionization mass spectrum of (gas phase) HCOOH, but the other ones, like the most intense one, HCO, correspond to molecules that could also conceivably desorb from the ice and cannot be used to obtain independently a measurement of HCOOH. From the noise on this channel

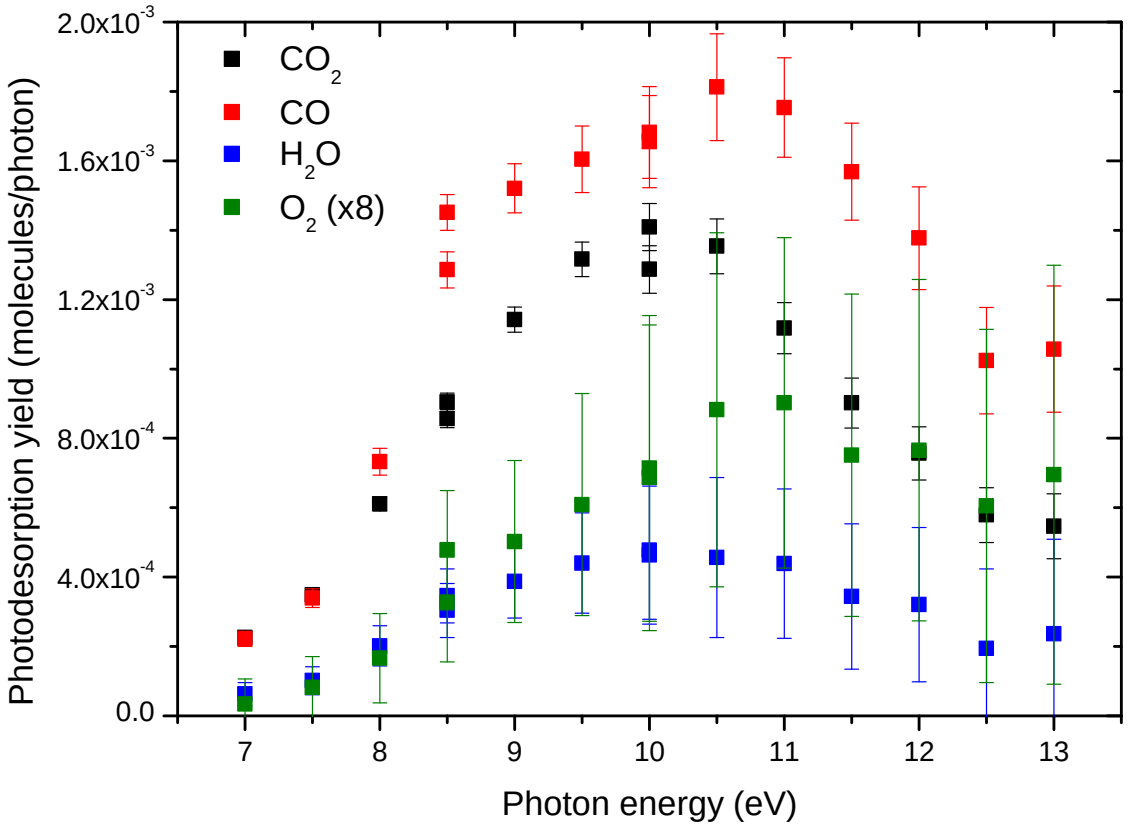

Figure IV.29: Photodesorption yields of CO_2, O_2, CO and H_2O from HCOOH ice (already irradiated with a photon dose of $\sim 1 \times 10^{17}$ photons.cm^2). Note that the O_2 yields have been multiplied by 8. Points at 8.5 and 10 eV were taken a second time at the end of the measurement to check for ageing.

(m/z = 46) we can estimate the upper limit put on the photodesorption yield of intact HCOOH to 2×10^{-5} molecules/photon. For this estimation, the partial electron impact ionization cross-section of HCOOH into $HCOOH^+$ is not known, so I have used the total electron impact ionization cross-section [282, 283] along with the ionization mass spectrum from the NIST.

Because the molecules investigated here all have a fragmentation pattern by electron impact ionization that can impinge on other monitored mass channels, some caution is necessary. In particular, the fact that HCOOH is not observed on the 46 mass channel makes it difficult to correct for its potential contributions to other channels. However, after examination of the fragmentation patterns and the relative intensities observed on the different channels, I can conclude that HCOOH can only significantly contribute to the HCO mass channel. No correction at all is required for the channels of CO_2, O_2, H_2CO and H_2O. The CO channels requires correction for CO_2 contribution only (H_2CO contribution is negligible), the HCO channel from H_2CO in addition to HCOOH, and the OH channel from H_2O. After correction for respectively H_2CO and H_2O contributions for the HCO and OH channels, it is already clear that no significant signal can be observed on

these channels. The species for which a photodesorption signal is detected are therefore CO_2, O_2, H_2CO, CO and H_2O.

The photodesorption yields of CO_2, CO, H_2O and O_2, taken during the second series of measurements, are displayed in fig. IV.29. Some points (at 8.5 and 10 eV) were measured a second time at the end to check for ageing. The photodesorption yields of H_2O for all series of measurements and the ones of H_2CO, which were only taken for the first series, are displayed in fig. IV.30. There the black points indicate the very first measurement points, and the red ones points measured later. Note that for this first series the points were taken in a random order.

To first comment on the ageing, it is clear that there is a strong decrease of H_2CO desorption after the beginning of the irradiation, while H_2O desorption seems fairly stable. We made a continuous following of CO_2 and H_2O desorption at fixed photon energy for 20 minutes between the two series of measurements, which confirmed a stable photodesorption yield for these two species. The origin of ageing is, again, not completely clear. A RAIRS spectrum was taken after the two series of measurements (fig. IV.28). There does not seem to be any drastic change in the spectrum: the most changes come from the parasitic absorption of gas phase H_2O and CO_2 in the parts of the spectrometer that are exposed to air. There is one change which is the apparition of a shoulder around 3200 cm^{-1}. This could correspond to the apparition of dimers in the solid, as this is around where the ν(O-H) mode of the dimer is expected, but the attribution is uncertain considering the fact that this is not a clearly defined peak and the baseline has changed somewhat between the two spectra. In addition this is also the region where the ν(O-H) mode of H_2O, which seems to be produced in the ice considering it desorbs, would also be expected. No other possible photoproducts peaks are observed. It should be noted that in zeroth order experiments, the flux is quite high but the total fluence not so much since each measurement point only takes a few seconds (the total fluence for the second series of measurements, for example, is estimated to less than 5 $\times 10^{16}$ photons/cm^2).

The shape obtained for the spectra cannot be compared to solid HCOOH VUV spectra because none exist to my knowledge. In the gas phase, the spectrum of HCOOH is quite complicated [284] with a number of different valence and Rydberg states overlapping. A first maximum is seen around 8.5 eV with mostly valence states contributing, although Rydberg transitions are already seen, and then a second rise occurs with Rydberg transitions converging towards the first ionization limit at 11.3 eV. But since solid HCOOH is a hydrogen bonded solid, we expect just like water and ammonia to see a strong perturbation of the gas phase states, even the valence ones, with possibly a blue-shift of the absorption onset as observed for these other two molecules.

In our photodesorption spectra at zeroth order all we see is a unique broad maximum at 10 eV, with no particular other features. Further assignment is hardly possible. There seem to be some differences in the spectra of the different fragments: the O_2 maximum occur at 11 eV and the low energy side of the CO points seem different from CO_2 and H_2O. But considering the uncertainty on these measurements and the lack of knowledge on the solid state electronic states, it is difficult to discuss the relevance of these differences.

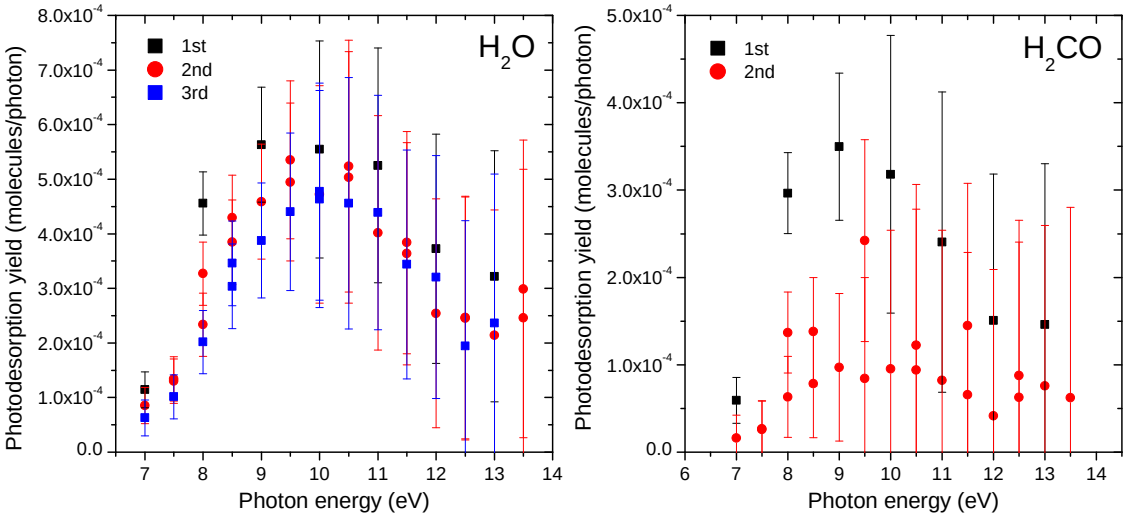

Figure IV.30: Photodesorption yields of H_2O (left panel) and H_2CO (right panel) from HCOOH ice (initially fresh ice). Black points were taken first, red points second and blue points third. See the text for more details.

IV.1.6.2 Photodesorption from organic molecules

Photodesorption from organic molecule ices has not been explored considerably so far: in addition to HCOOH, desorption from methanol [54, 285], H_2CO [276] and ethanol [286] has been studied.

It seems clear that desorption of the intact molecule from organic ices has a very low yield. H_2CO is still barely detected with 1st order beam and a yield of $\sim 1 - 4 \times 10^{-4}$ molecules/photon, but for methanol yields go down to 10^{-5} molecules/photon and intact HCOOH is not detected. This is a problem from an experimental point of view because we are reaching the limits of the capabilities of detection of our set-ups: comparison of the yields of different molecules is difficult. The fact that the yields become so low ties in with previous discussions on the photodesorption of NH_3, H_2O or CH_4. The binding energy certainly plays a role, but it cannot be the only factor as H_2O for example is quite strongly bound. The number of atoms, and therefore the number of degrees of freedom and the density of vibrational states is also an important factor. A "simple" DIET mechanism involving only the intact molecule is strongly competed by dissociation for most of these molecules, and the desorption mechanisms that stem from dissociation (kick-out, exothermic recombination) are all mitigated by the fact that the energy acquired by the molecule can be redistributed on many different internal modes of the molecules, leaving too little energy for desorption. On the other hand, I also pointed out that having many available and low-lying internal modes can be an advantage for desorption because coupling with intermolecular modes (phonons) also becomes easier.

The study of photodesorption from organic ices then becomes more about the inventory of the different desorbing fragments and products. This could bring information about dissociation in the condensed phase, which is not a particularly well constrained topic. It is also important for astrochemical models, as desorption of fragments could enrich the gas phase chemistry.

Some even larger molecules such as aromatic compounds have been well studied in condensed form[i], and since PAHs have a definitive astrophysical relevance perhaps moving on to the study of these systems would bring interesting insights.

IV.1.7 Perspectives and limits for pure ices

Results on many different pure ices have been presented here. I will try to draw some conclusions on the above results at the end of this chapter, but before going to the next section I will mention what perspectives we have on just pure ices studies and what are the limits of these studies that push us to explore processes like the indirect desorption that will be the object of the rest of the chapter.

There are many paths that can still be explored on just pure ice systems, as it is clear that we have not reached a complete understanding of these systems, and that we have not even exhausted what can be done with the current set-up, without any more diagnoses. First, it is necessary to settle the question of the deposition temperature for CO with a series of wavelength resolved and thickness dependent measurements. It would also be interesting to see if similar effects exist for N_2, as it is a relatively close system.

Still at the synchrotron, one parameter that has not been much explored so far is the polarization of the light. The DESIRS beamline offers the possibility of varying the polarization, but all measurements so far have been made using linear vertical polarization because it is optimal in terms of photon flux and undulator operation. Polarization could be particularly important and interesting for more crystalline or at least not completely disordered systems, such as CO above 20 K, crystalline CO_2, H_2O or NH_3, etc... From an astrophysical point of view the interest is not clear (except that the yields for a polarization relevant to astrophysical environments will need to be clarified if an effect is found) but differences of photodesorption yields may provide mechanistical insights. Some tests were realized on CO without being conclusive, but a test on N_2 provides the result shown in fig. IV.31: in linear horizontal polarization setting (i.e., considering the angle of incidence, a 50 % in-plane and 50 % out-of-plane polarization with respect to the surface), the photodesorption yield of N_2 between 12.3 and 13.7 eV ($b^1\Pi_u$ (v") - $X^1\Sigma_g^+$ (v' = 0) vibronic transitions) is twice higher than in vertical setting (fully in-plane polarization). There does not seem to be any v" specific enhancement, and this might be purely a difference of absorption of the different polarizations. Nonetheless, it is something worth investigating.

Other directions have been pointed out in the various sections: one problem that is not fully understood is ageing. Its nature is not completely clear and this is partly a consequence of the lack of knowledge and control on the exact structure of our systems. I would argue that the evidence we have so far does not point towards ageing being a bulk chemical modification in most systems. A bulk structural modification is still possible, although we have not observed anything on the infrared spectrum in the case of HCOOH, for example. But another possibility is a chemical and/or structural modification of the surface rather than the bulk. It is possible that the surface rearranges itself towards a more stable structure upon irradiation, resulting in lower yields. Chemical modification can also be different at the surface because diffusion of radicals can be expected to be different: if a layer of large amorphous carbon structures forms itself at the surface of irradiated CH_4 ice, for example, that could explain a diminution in the yield. Finally, it

[i] e.g. for the interest in molecular excitons in organic solids, see [287, 288, 289].

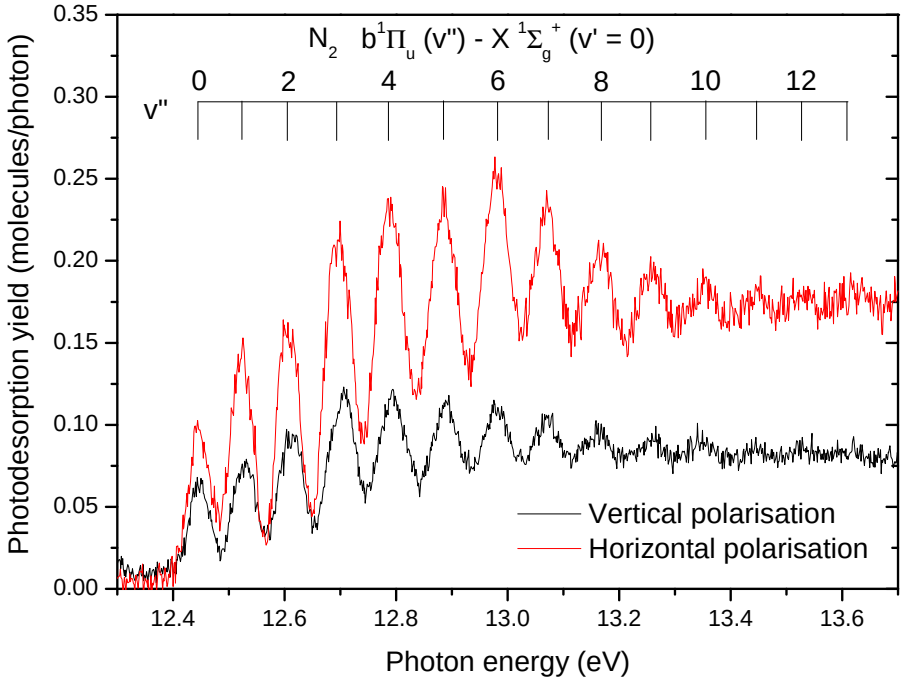

Figure IV.31: Photodesorption yield of N_2 in vertical (black line) and horizontal (red line) polarization settings. The vibronic peaks of the electronic transition are attributed on the figure.

is also possible that the first few molecules desorbing are molecules in particularly low-binding sites at the surface, of which there would only be a limited number (this has been suggested to explain some experiments on laser desorption of water, for example [259]). The existence of a few weakly bound sites at the surface has been found in Monte-Carlo simulations of CO ice growth [290]. If this is the case then what we observe is not really ageing but the rapid desorption and depletion of a few specific surface molecules, which would also bring the question of the surface structure of astrophysically relevant ices. All these surface effects would however require surface probes to be tested. Bulk and surface structural characterization and surface chemistry probe tools are definitely something that would bring new insights into the interaction of irradiation with molecular ices.

Although the synchrotron is a very powerful tool for the perspectives mentioned above, these studies are all characterized by the problem that they are time-consuming. Systematically exploring inter-linked parameters and dealing with time-dependence is not ideal when beamtime is limited. It is also clear that part of the reason why we are lacking data on some aspects or others of the photodesorption of several systems (CO, NO...) is that problems are only found during data treatment, after the synchrotron runs, with the next ones planned a year after when everything goes well. The development of the laboratory set-up should prove precious for more systematic studies, in addition to providing new probes of desorbed molecules. The perspectives of this set-up, which is on the verge of working, are exciting. Aside from measurements on CO, there is a large variety of interesting systems to study.

Studying pure ices is interesting by itself, from both a mechanistic and an astrophysical point of view, and it is also a mandatory step in the understanding of more complex systems like mixed ices. Still, it will be necessary to also move towards these more complex systems. For astrochemistry, the ices encountered are not pure (except perhaps some solar system ices). From a mechanistic point of view, aside from the intrinsic interest of studying the new mechanisms that emerge from having more complex systems, they can bring insights retrospectively on the pure systems, by bringing new information.

The effects of going from pure ice to mixes can be more or less (in the sense that they overlap somewhat) divided into three aspects:

- Indirect desorption, where one excited molecule induces desorption of another molecule
- Effects of the environment on energy relaxation, fragmentation, etc...
- Changes in the photochemistry and desorption of new photoproducts

The third item is very much tied to the large body of work that has been done on photochemistry and irradiation chemistry of molecular ices. Mixing molecules that can dissociate to create radicals such as OH, CH_x, NH_x etc will lead to a complex chemistry and some of the created products can desorb. See e.g. [286, 291] for studies of photodesorption from ice mixes that focus on this aspect. The second item is, for example, studied for CH_3OH:CO mixes [54] and there is certainly much to explore on the topic.

In this thesis however, the last two items have not been explored. Instead I focused on an exploration of the indirect desorption processes that happen in layered ice systems, which are model systems for understanding indirect desorption in general. This will be the object of the next section.

IV.2 Indirect desorption: model layered ices

Indirect desorption is defined here as a process where an electronic transition in a molecule leads to the desorption of a different molecule. This process is presumably common in pure ices (several of the mechanisms presented earlier consist in indirect desorption processes), but becomes particularly interesting (and can be probed) in mixed ices. In our experiments, we have access to a spectral information: the spectral signatures observed in a photodesorption spectrum are indication of the electronic state that led to the desorption of the molecule being observed. If we observe electronic transitions of a given molecule in the photodesorption spectrum obtained by monitoring another molecule, we have a measure of indirect desorption.

We would therefore like to measure the efficiency of this process, and understand what mechanism explains the indirect desorption. For this, we have opted to study model systems rather than mixes. We study layered systems, where a thick substrate ice will play the role of the absorber, and molecules adsorbed on top will play the role of the desorbed molecule. We have explored mostly two substrates, CO ice and H_2O ice, on which a variety of adsorbates have been tested, in an attempt to see which parameters drive the indirect desorption process. These substrates are also the main components of astrophysical ices and indirect desorption processes for these molecules is therefore very important.

Before going to the results, let us lay out some considerations on the mechanisms of indirect desorption. One first step for indirect desorption can be the transfer of energy between the underlying substrate to the adsorbate (just like there can be transfers from the bulk to the surface in pure ices). We can distinguish two types of energy transfers.

One is kinetic energy transfer, which is nothing more than a collision between a molecule having acquired kinetic energy and another surface molecule. The kick-out mechanism discussed for H_2O is a kinetic energy transfer, as is the "collision sputtering" mechanism discussed for the RGS in section II.4. If a sub-surface molecule acquires kinetic energy, (for example along the repulsive part of a potential energy surface, as rare gas atoms do in the excimer mechanism) or if it dissociates into fragments, it can collide with surface molecules and give them enough kinetic energy to directly desorb.

Another is transfer of internal energy, e.g. electronic or vibrational energy. There is an abundant literature on the migration of electronic energy in rare gases with transfer to impurities, for example. Such a transfer can be seen as fluorescence of the impurities is observed when exciting the host rare gas matrix (e.g. Au and Ag atoms [292], CO [293], O_2 and N_2 [177]). An example of indirect desorption is the desorption of excited Ar^* when exciting Ne atoms in a Ne:Ar mix [294]. These electronic energy transfers are proposed to happen by free exciton diffusion and recombination on impurities, or by Förster-Dexter type energy transfers. A Förster energy transfer occurs through dipole-dipole interactions on a relatively long-range (in the case of molecular solids, between molecules that are a few lattice sites away, although the process is mostly invoked in the context of chromophores in liquid solvents, for which interactions may occur at longer distance), requiring near-resonance between the energy levels. A Dexter transfer is an electron exchange between two close molecules (the wavefunctions need to overlap): the excited electron of a molecule is swapped for a valence electron of another, effectively transferring the electronic excitation. Förster long-range energy transfers can also occur

for vibrational excitations, as shown for example between CO molecules [295] or NO molecules [296] and from a CO to an O_2 molecule [297] isolated in rare gas matrices. Dzegilenko & Herbst [298] have shown in calculations that physisorbed CO could be desorbed by near-resonant energy transfer from a vibrationally excited O-H bond v = 1 (from a nearby water molecule or on a SiOH surface) to a vibrationally and librationally excited CO molecule in v = 1 and J = 7, again by dipole-dipole interactions.

Internal energy transfer, unlike kinetic energy transfer, does not explain directly desorption. The now excited molecules desorb "by their own means": this does not presume what the next step of the desorption process is. In Mann et al [180] the desorption of metastable N_2^* and CO^* molecules from Xe ice after electronic energy transfer from Xe to N_2 or CO is explained by a transfer of vibrational excitation to the adsorbate-substrate bond (see II.1 and II.3.2).

In the following, we will try to see whether the indirect desorption we observe is coherent with either of the two types of energy transfers presented before.

IV.2.1 CO-induced indirect desorption

I will start by presenting the results obtained on indirect desorption induced by CO, i.e. experiments where a thin layer of a given molecule is deposited on top of a CO ice. The first system for which indirect desorption was investigated in the team was CO and N_2 layers and mixes [204]. So far only results on CO-induced desorption have been published (for CH_4 [201] (paper I) and H_2CO [276], and to some degree CH_3OH [54]), and it is the process for which we have the most data.

We have considered that the best way to study CO-induced desorption was to study layered systems, i.e. approximately 1 ML of a molecule deposited on top of a pure CO ice, rather than mixed systems. Mixed systems add the supplementary confusion of dilution effects and it becomes difficult to disentangle "pure" indirect effects. However, there is an experimental difficulty with layered systems, which is precisely to consider that we have perfect layers. CO molecules in the ice are weakly bound, and when depositing a layer of other molecules on top, arriving at 300 K from the gas phase, it is likely that there is a "sputtering" effect during deposition of the overlayer where the incident molecules become buried a few layers into the CO ice, creating a "surface region" with a gradient of the incident molecules mixed with CO (with an uncontrolled mixing). The situation is sketched in fig. IV.32. There is some evidence of this effect in our experiments. It has also been mentioned in the literature before [167]. It is something to keep in mind when interpreting the results. Another important experimental factor is the uncertainty on the calibration of the absolute yields, which we will wish to compare. In all of the data to follow, the underlying CO substrate ice is 20 or 30 ML thick, grown at 10-12 K.

IV.2.1.1 Single layers

Let us first look at single layers of various molecules on CO ice. We have obtained data for a total of 7 adsorbates: N_2, Ar, Kr, Xe, O_2, CH_4 and H_2CO. The comparison of all these systems is instructive regarding the process.

In fig. IV.33, the photodesorption spectrum of 1 ML of N_2 deposited on top of a CO ice is presented, along with the spectra of pure N_2 and CO. In all the figures to follow, for the layered ices, the molecule indicated under parenthesis at the end of the legend

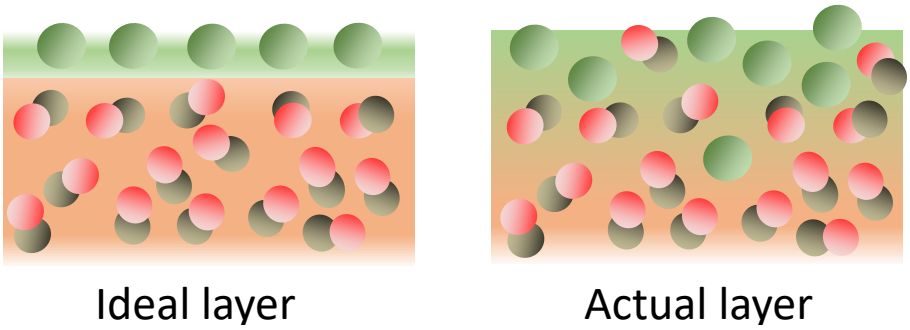

Figure IV.32: Ideal vs actual (inferred) layers on CO ice. During deposition of molecules the weakly bound CO molecules are scrambled and some mixing occurs.

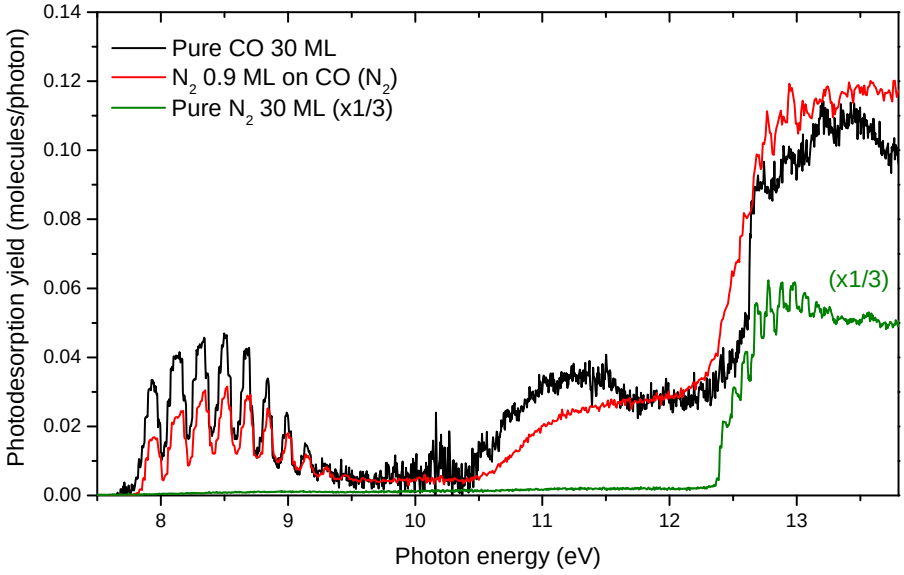

Figure IV.33: Photodesorption spectrum of N_2 from 0.9 ML of N_2 on CO ice. Also shown for comparisons are the photodesorption spectra of pure CO and pure N_2.

indicates the molecule being measured on the QMS. Solid N_2 only strongly absorbs above 12.4 eV: before that threshold (corresponding to absorption in the $b^1\Pi_u$ state), there are only transitions strictly forbidden in the gas phase, slightly relaxed in the solid but contributing only weakly to the absorption . Below 12.4 eV, the photodesorption spectrum of 1 ML N_2 on CO resembles completely to the CO spectrum, and even above 12.4 eV we can see a strong CO contribution. We see clearly in this example how the spectral information obtained with the synchrotron radiation unambiguously demonstrates indirect desorption. The case of CO-induced desorption is particularly convenient because the molecular signature of the vibrational progression of the A-X transition is very specific and can be easily identified in most spectra. Regarding the efficiency of the indirect process, the desorption of N_2 in the A-X region is about 2/3rd that of pure CO. This was also the case for the desorption of one monolayer of ^{13}CO on ^{12}CO ice, so that we can

say that the indirect process is as efficient for desorbing N_2 as it is for desorbing CO.

The photodesorption spectra for single layers of the rare gases (at least as close as we could get) on CO ice are shown in fig. IV.34. The photodesorption spectra of the pure RGS are also indicated to show where their absorption features are expected to contribute. There are some experimental difficulties with the RGS, in particular Krypton and Xenon. For masses (84 for Kr and 130 for Xe were the ones we used) that lie in a very different mass range from the one we commonly use, the apparatus function of the QMS is very different as well (the sensitivity ratio, measured by injecting pressures of the two gases, between CO and Xe in SPICES II on the Balzers QMS is about 100), so some supplementary caution is required when considering the absolute yields and thickness calibrations. In addition, the problem of the deposited molecules burying under the CO ice is clearly present here (as we will confirm later). For all three rare gases, there is a very clear indirect CO photodesorption signal, and the estimate of the photodesorption yield is relatively similar in all three cases and lower than for N_2, but still around 1×10^{-2} molecules/photon. For Xe the estimated deposited layer is 2 ML, but we still see mostly CO contribution in the 8-9 eV region, probably because a lot of the Xe has been buried in the CO ice.

On fig. IV.35, the photodesorption spectra of a single layer of O_2, CH_4 and H_2CO (0.4 ML in the latter case) are shown along with their pure ice photodesorption spectra for comparison. In these cases there is no real concern about the thickness and photodesorption yield calibration (within the usual error bars). CH_4 does not absorb below 9.5 eV and the CO molecular signatures are very clear. The photodesorption yield is much lower than the previously shown ones: 1.5×10^{-3} molecules/photon. O_2 does absorb in the region but with no particular structure, while we can discern the vibronic bands of the A-X CO transition superimposed on the O_2 absorption on the layer spectrum. We can estimate that the CO contribution amounts to around 1.5×10^{-3} molecules/photon. As for H_2CO, it absorbs as well in the whole region of the spectrum, and the signal is very noisy, but we can still see a bump around 8 eV that is not present on the pure H_2CO spectrum. We can estimate the magnitude of the CO indirect desorption contribution to 10^{-4} molecules/photon.

IV.2.1.2 Multiple layers and other systems

In addition to the single layer systems we can look at what happens to the desorption of the layered molecule and of the underlying CO as a function of the number of deposited layers. The idea was initiated to see whether there could be some long range energy transfers with indirect desorption in multilayers. This approach has instead highlighted, for several systems, a clear mixing of the layered molecule with the CO ice instead of perfect layers. Some representative examples are shown in fig. IV.36. On the left the desorption of the layered molecule is shown, and on the right the desorption of the underlying CO that has been recorded simultaneously is presented. In the Ar/CO system, we see that for Ar desorption the CO signatures progressively disappear (and those of Ar become more and more visible) as the thickness of Ar increases. Nonetheless, the CO signatures are still visible in Ar desorption even with 10 ML of Ar deposited on CO. Conversely if we look at CO desorption, the CO signatures are strongly decreased even with only 1 or 2 ML of Ar on top. In addition, for the thicker layers CO desorbs with the signatures of

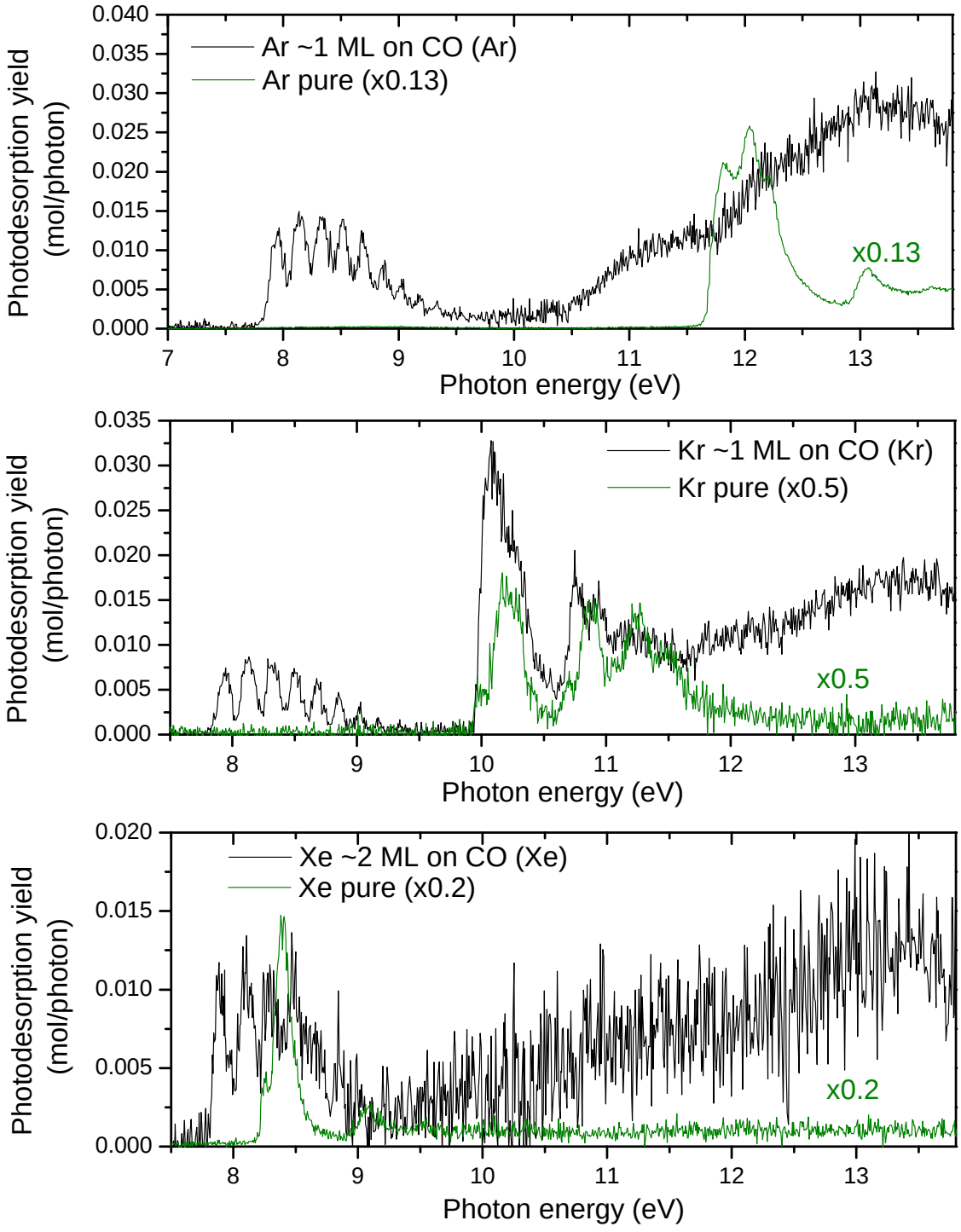

Figure IV.34: Photodesorption spectra of single layers of the rare gases on CO ice. Top: photodesorption of Ar from 1 ML Ar on CO and from pure Ar. Middle: photodesorption of Kr from 1 ML Kr on CO and from pure Kr. Bottom: photodesorption of Xe from 2 ML Xe on CO and from pure Xe. See text on the uncertainty on thickness calibration and absolute yields.

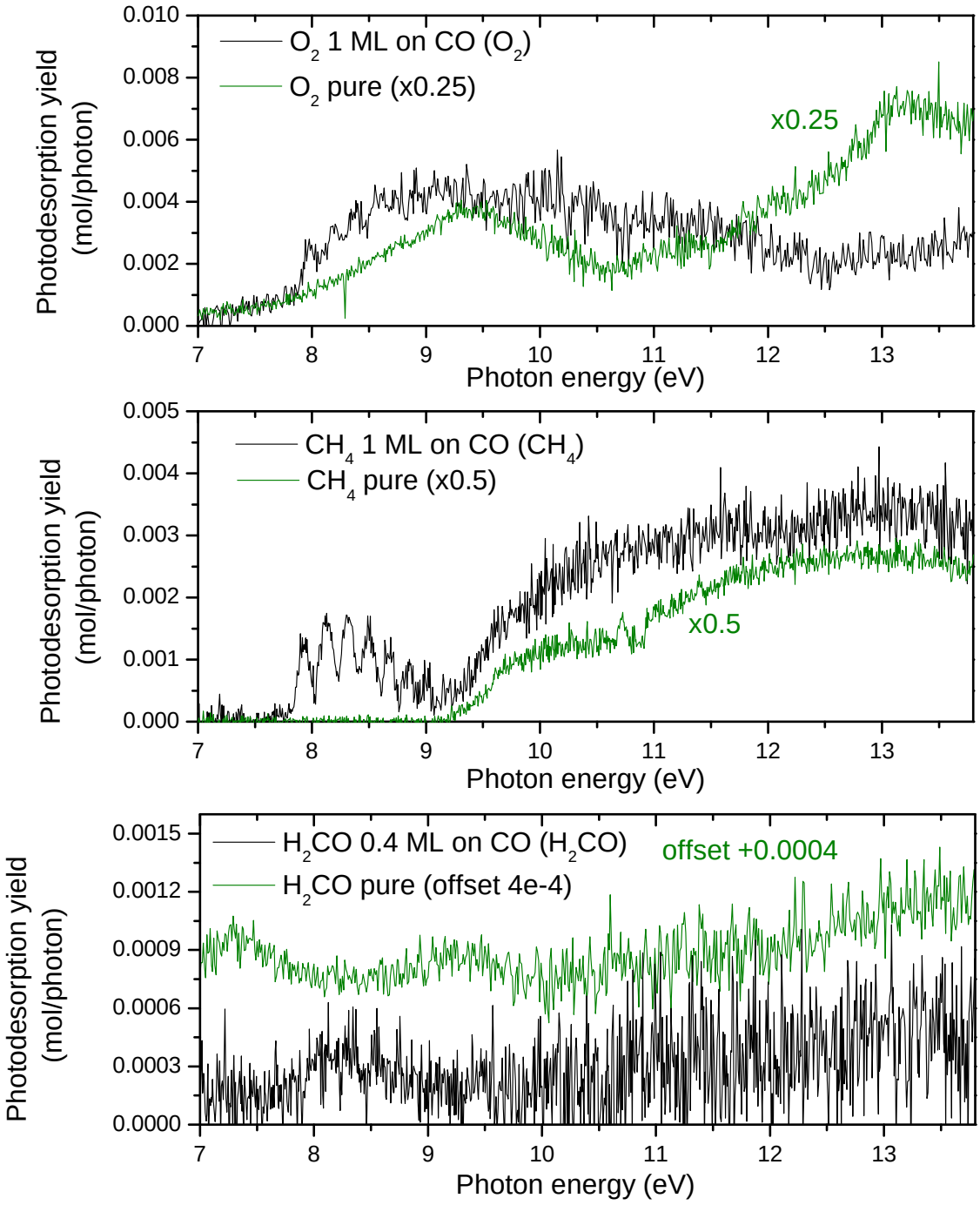

Figure IV.35: Photodesorption spectra of O_2, CH_4 and H_2CO single layers on CO. Top: photodesorption of O_2 from 1 ML O_2 on CO and from pure O_2. Middle: photodesorption of CH_4 from 1 ML CH_4 on CO and from pure CH_4. Bottom: photodesorption of H_2CO from 0.4 ML H_2CO on CO and from pure H_2CO.

Ar excitation instead, with a quite strong signal. On the Ar desorption, the Ar excitons (including the surface exciton) are also slightly blue-shifted (of $\sim$ 0.1 eV) in the 10/14 ML Ar layers spectra compared with the pure Ar case, although this is barely visible on the figure with this scale. All of this indicates the presence of CO at the surface even in the case of the thickest layers, although it is certainly not the major species.

In the O_2/CO system the observations are fairly similar. Looking at the O_2 desorption spectra it is clear that the contribution of O_2 absorption signatures increases with thickness, but the CO signatures are nonetheless visible up to the O_2 5 ML layer. The desorption of CO is again decreased but the vibrational progression of the A-X state remains visible, with some O_2 signatures contributing. The case of CH_4/CO is different: CO desorption is strongly suppressed with only 1 ML of CH_4 on top, and is not measurable anymore for 3 ML CH_4 (not shown). For the 3 ML CH_4 on CO system the spectral signature of CO has also disappeared completely. It seems that the lighter CH_4 molecule does not sputter CO upon deposition and forms neat layers, with results reminding of what was found for ^{13}CO/CO [203]: desorption happens mostly at the surface (top 1 ML) and indirect desorption from the top 3 ML.

The systems N_2/CO [204], Kr/CO and Xe/CO display a behaviour similar to O_2/CO and Ar/CO (not shown). It seems that only for the light CH_4 molecules neat layers are formed, for the rest we have to assume that there is a degree of mixing which we do not have access to, and therefore precise comparisons between the systems become difficult. Fortunately the indirect desorption efficiencies we found span two orders of magnitude, so comparisons are still possible.

In addition to the systems already presented, layers of H_2O on CO were investigated, but no H_2O desorption could be detected. This is not necessarily surprising: it only constrains the CO-induced desorption process in that case to $< 3{\times}10^{-3}$ molecules/photon. H_2O layers deposition strongly suppresses CO desorption, lending credit to the formation of neat layers for this lighter molecule as well. Strong CO desorption suppression is also observed for H_2CO [276].

Layers were not directly investigated for CH_3OH, only CO:CH_3OH mixes. There is no particular evidence of CO-induced desorption in this data [54]. Again this is not unexpected because the desorption of methanol itself in pure methanol is very weak. Another system where "mixes" were previously investigated is CO_2. Irradiation of pure CO_2 leads to the formation of large quantities of CO in the ice, and CO spectral signatures star to appear in the CO_2 desorption yields after a long irradiation time [200]. We estimate the data for processed ices from this paper as more or less equivalent to a 1:1 CO:CO_2 mix, and the CO-induced desorption of CO_2 is of the order of $\sim 1 \times 10^{-3}$ molecules/photon in that case. This is not a layer system, so comparison with the other systems is not direct, but the order of magnitude of the indirect desorption contribution should be similar, as is the case for N_2 [204] for example.

IV.2.1.3 Discussion

The previously presented results show that CO-induced indirect photodesorption exists for all systems that were investigated (except for H_2O, but probably simply because it was not strong enough to be detected, which was not unexpected) but that the efficiency spans more than two orders of magnitudes, depending on the system. We may then

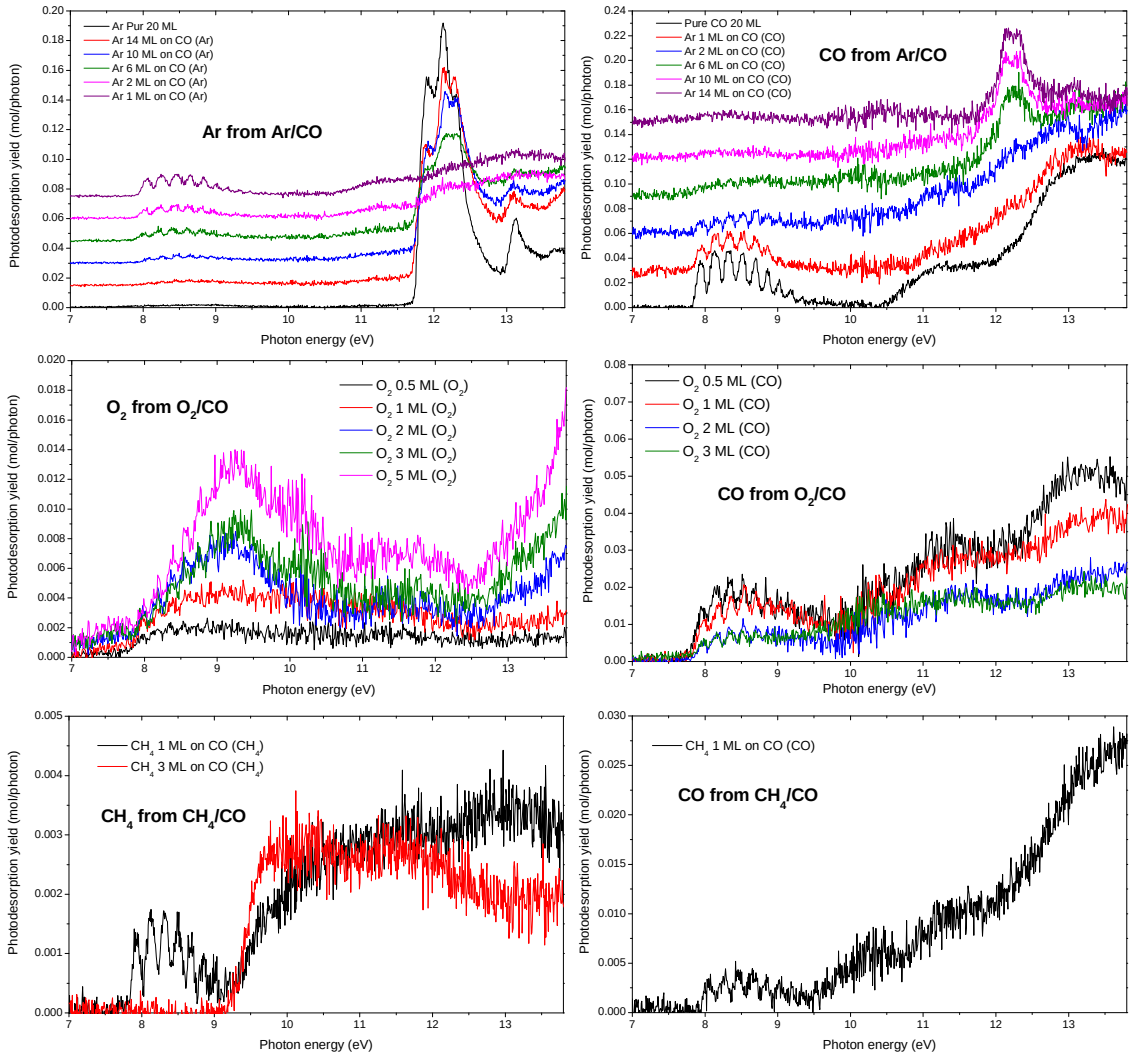

Figure IV.36: Photodesorption spectra of multiple layers of Ar, O_2 and CH_4 on CO. Top: photodesorption of Ar (left) and CO (right) from Ar on CO for several thicknesses. Middle: photodesorption of O_2 (left) and CO (right) from O_2 on CO for several thicknesses. Bottom: photodesorption of CH_4 (left) and CO (right) from CH_4 on CO for several thicknesses.

Table IV.2: Summary of the systems for CO-induced desorption.

System	Indirect yield* (mol/photon)	Mass (a.m.u.)	Number of atoms
$^{13}CO/CO$	3×10^{-2}	29	2
$^{15}N_2/CO$	3×10^{-2}	30	2
$^{18}O_2/CO$	1.5×10^{-3}	36	2
Ar/CO	1.5×10^{-2}	40	1
Kr/CO	8×10^{-3}	84	1
Xe/CO	1×10^{-2}	130	1
$^{13}CH_4/CO$	1.5×10^{-3}	17	5
$CO:CO_2$	1×10^{-3}	44	3
H_2CO/CO	1×10^{-4}	30	4

* Contribution of CO-induced indirect desorption to the photodesorption yield of the molecule for single layer systems (except for CO_2, see the text), at the maximum of the absorption in the A-X region (8.3 eV)

either assume that (i) there is a single mechanism explaining all of indirect desorption in all the studied systems, with an efficiency varying with parameters that we would like to identify, or (ii) there are multiple mechanisms with varying degrees of efficiencies for different systems. In the following we will first focus on the first case, because it is not really possible to disentangle much if we consider multiple mechanisms from the beginning, but it is worth keeping in mind that it remains a possibility.

The list of the systems studied is summarized in table IV.2, along with the estimated efficiency, as measured by the indirect photodesorption yield of the molecule at the maximum of the A-X CO transition, and the mass and number of atoms of the molecule. Indeed, among the relevant varying parameters that we can identify is the mass of the molecule, which will play a role if there is a kinetic energy transfer. The number of atoms is linked with the number of internal degrees of liberty of the molecule, which can also be important for energy redistribution. Another important parameter in desorption is of course the binding energy of the molecule. This parameter is not really known, nor can it be easily measured, for molecules adsorbed on CO ice[j]. However, we expect that for the systems pure CO and Ar, N_2, CH_4 and O_2 on CO the binding energies will all be close, of the order of 100 meV. They might be higher for H_2CO, CO_2, Kr and Xe (up to 200-300 meV).

When discussing the efficiency of the indirect desorption process, it should be kept in mind that the absolute photodesorption yield depends among other things on the surface coverage of the molecule when we are in a sub-monolayer regime.

The rare gases were initially chosen as a simple series of system where we can vary the mass and binding energy parameters (simultaneously, unfortunately) in the order Xe > Kr > Ar without having to worry about other confusing factors. We see a very similar efficiency for all three rare gases, which would mean that mass and binding energies are irrelevant here, at least within the uncertainties of our experiment, which as mentioned

[j]because TPD experiments cannot be performed without evaporating also the CO ice.

before include uncertainties on the surface amount of the adsorbates and the calibration of the yields. Such a result is surprising and would seem to rule out a kinetic energy transfer mechanism such as the one discussed in section IV.1.1. However, we do not know exactly how the desorption efficiency depends on the amount of kinetic energy transferred nor how much of the initial $\sim$ 8 eV of the photon is transferred: if the kinetic energy transferred is much higher than the binding energy, no significant effect of mass or binding energy would be expected. The fact that the indirect desorption process works for the rare gases with an efficiency not too far from the pure CO yield rules out any sort of energy transfer to internal modes of the desorbed atom. The first electronic levels of Ar and Kr are well above the energy of the A-X transition, so no electronic energy transfer is possible. Second, there is no notion of vibrational or librational modes to which energy could be transferred here.

The case of CH_4 has been discussed in paper I already. The photodesorption yield of CH_4 from CH_4 on CO is much lower than the previously discussed system, almost two orders of magnitude lower than pure CO. The mass of the molecule is a factor of about two lower than CO, but the binding energy should be relatively close. There is a fundamental difference between a polyatomic molecule like CH_4 and a diatomic molecule like CO or N_2, however: CH_4 has much more internal degrees of freedom, with several vibrational modes and combinations of modes for example. This could help "wash out" any transferred energy if it is partitioned into the different modes. A similar explanation could hold for the case of CO_2, for which the indirect desorption yield is relatively similar. In the case of H_2CO, we again have a polyatomic molecule, which is also coherent with low observed indirect desorption yield. However, its mass is close to CO, and its binding energy to CO ice might be a bit higher than for the other systems but it is not much larger than CO_2 or CH_4, so it is not clear why its CO-induced indirect photodesorption yield is an order of magnitude lower than for these molecules. It is not out of question that H_2CO forms dimers at the surface of CO and therefore is more difficult to desorb.

A very important system for interpretation is O_2/CO. O_2, N_2 and CO are all diatomic molecules with very similar masses and binding energies. However, while the photodesorption yield of pure CO and of N_2 from N_2/CO are very similar, the photodesorption yield of O_2 from O_2/CO is more than an order of magnitude lower (table IV.2). If we were to consider a kinetic energy transfer mechanism, similar yields would be expected for all three molecules as they have similar masses and degrees of freedom. Such a mechanism is therefore apparently not coherent with the O_2 indirect desorption yield.

Let us see now what conclusions can be drawn, assuming a single mechanism picture. First, it seems clear that internal energy transfer is not involved here because the indirect desorption yield for the rare gases is almost as high as for N_2. Another possibility presented earlier is direct kinetic energy transfer. In section IV.1.1 the proposed mechanisms for CO photodesorption were presented. Aside from the main "direct" mechanism, an indirect mechanism mediated by highly vibrationally excited CO molecules was suggested: this would precisely correspond to direct kinetic energy transfer. For such a mechanism, we would expect a correlation to appear between indirect desorption efficiency and mass, but I mentioned earlier that such a dependence could be washed out depending on how much energy is transferred compared with the binding energy of the molecules. This still would not explain the comparison of the O_2, N_2 and CO data where there are little confusing factors but very different indirect yields.

At this point, the most likely conclusion is that we cannot keep the single mechanism picture. We could imagine processes of desorption that do not involve direct kinetic energy or internal energy transfers: the formation of "excited complexes" leading to an RGS excimer like desorption mechanism (see II.4) for example is one, but the likelihood of explaining all of the data with such a mechanism is low. However, a coherent picture can still emerge if we consider that the system O_2/CO in particular is specific. Indirect desorption by highly vibrationally excited CO molecules, which is the indirect mechanism proposed by MD simulations, is coherent with the high indirect desorption yield for N_2 and the rare gases as long as we assume that the dependence of the desorption probability on mass and binding energy is not very marked. The indirect desorption efficiency of polyatomic molecules is then strongly reduced for the reasons mentioned above.

The particularity of the O_2/CO system could come from channels for energy loss competitive to desorption. One such possibility would be competition with chemistry, for example through a reaction of the type $CO^* + O_2 \longrightarrow CO_2 + O$. Another is that O_2 is one of the few adsorbates studied where electronic energy transfer is actually possible from CO excited in the A state. Electronic energy transfer could occur, and lead e.g. to O_2 dissociation without desorption of the molecule.

In conclusion, the study of a wide variety of adsorbates reveal that in the general case, CO induced indirect desorption is not mediated by internal energy transfer but by direct kinetic energy transfer via highly vibrationally excited molecules. The process is very efficient for small rigid molecules (N_2, RG atoms), with little apparent dependence on mass and binding energy. However, it becomes much less efficient for larger and "softer" molecules with more degrees of freedom (CH_4, H_2CO). While the CO indirect desorption mechanism retains a high importance in astrophysics, as will be shown later, it is unlikely to help desorbing large complex organic molecules as could have been hoped at first. The number of internal degrees of freedom seems to be the key parameter governing the indirect desorption yields. There are also exceptions to this general case, as shown for the O_2/CO system, that need to be treated separately.

IV.2.2 H_2O-induced desorption

In the following I will present results on the indirect desorption induced by H_2O, by studying again layered system, this time on water ice. Both H_2O and D_2O ice were studied, using a compact amorphous ice grown at 100 K. One advantage of compact water is that there is no problem of layered molecules burying inside the ice, which is bound much more strongly than CO ice. One disadvantage is that the surface of water ice is not exactly flat: the effective surface is larger than for a flat surface, and therefore we can expect that "one monolayer" deposited on water ice will not exactly correspond to an effective monolayer. This is represented on fig. IV.37. Nonetheless the data obtained should be more precisely inter-comparable.

IV.2.2.1 Results on single and multilayers on H_2O and D_2O

Five different layer molecules were explored (CO, N_2, Ar, Kr and Xe layered on H_2O or D_2O ices). For Xenon we never detected any sign of indirect desorption, so the results are not shown. The results for single layers on H_2O ice are presented in fig. IV.38. N_2 and Ar do not absorb in the region shown here below 11 eV (N_2 only has very weak

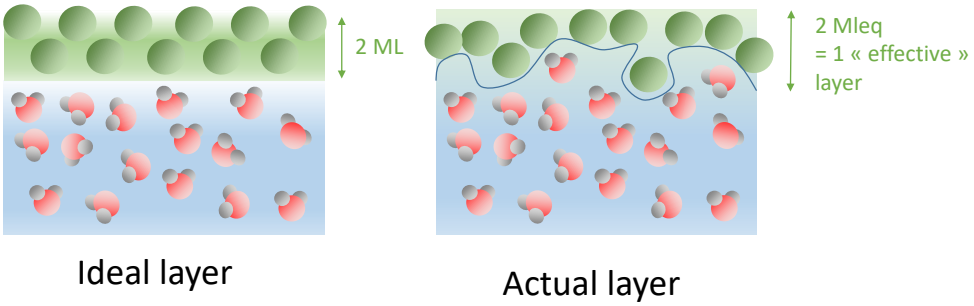

Figure IV.37: Ideal vs actual layers on water ice. The water ice surface is not flat, leading to a larger effective surface and a lower effective number of layers.

forbidden transitions in this region [215]). We see that they are nonetheless desorbed, but there is an interesting difference with the H_2O absorption spectrum (taken from Lu et al. [216]): the desorption spectra are shifted by about 0.4 eV. The maximum of the first band is around 8.6 eV on the absorption spectrum, but the desorption spectra peak at 9 eV. This shift is present on all scans and perfectly reproducible. I will come back to its interpretation later. For Kr/H_2O, the Krypton starts absorbing around 9.7 eV, but we still have a clear H_2O indirect desorption signature before that. The signal is noisy, so that the shift is less visible but is present here as well. For CO/H_2O, the difficulty is that CO does absorb in the same region as water. It is clear that H_2O indirect desorption contributes, as we see desorption around 10.5 eV where CO does not absorb and the shape of the desorption spectrum in the 8-9.5 eV region is quite different from pure CO. I have shown here the result for 0.5 ML CO on H_2O because the contribution of H_2O is more visible than for 1 ML. The yields obtained for different adsorbates therefore span over one order of magnitude, which is less than for CO, although we have not explored as many systems.

Results for single layers on D_2O ice are shown in fig. IV.39. Here the photodesorption spectra are compared with the absorption spectrum of D_2O from Cruz-Diaz et al [299]. The absorption spectrum of D_2O is blue-shifted by about 0.1 eV (maximum of the first band at 8.7 eV) compared with H_2O. The photodesorption spectra are still shifted relative to the absorption in this case, with a maximum remaining around 9 eV. The commentaries that can be made on these spectra are similar as for H_2O: the one marked difference is that the indirect photodesorption yields are overall higher for D_2O single layers.

In fig. IV.40, the results for multiple layers for a few representative systems (N_2/H_2O, Ar/D_2O and CO/D_2O) are shown. These results are interesting: we see that for indirect desorption, in the case of N_2 and Ar (the relevant region of H_2O absorption is shown in the insets), the maximum of yield is actually reached around 3-5 ML on top of the ice. The efficiency decreases afterwards but the water features remain present in the spectra at 10 ML. This is partly due to the larger effective surface area of water ice mentioned earlier: the calibration indicated for the layer thicknesses is a "flat surface" calibration. There may be a factor of 2 or 3 more effective surface area on water ice. The fact that even for 10 ML Ar on D_2O, the surface exciton at 11.7 eV dominates over the bulk excitons which are not even well defined confirms that we do not have 10 effective layers of Argon

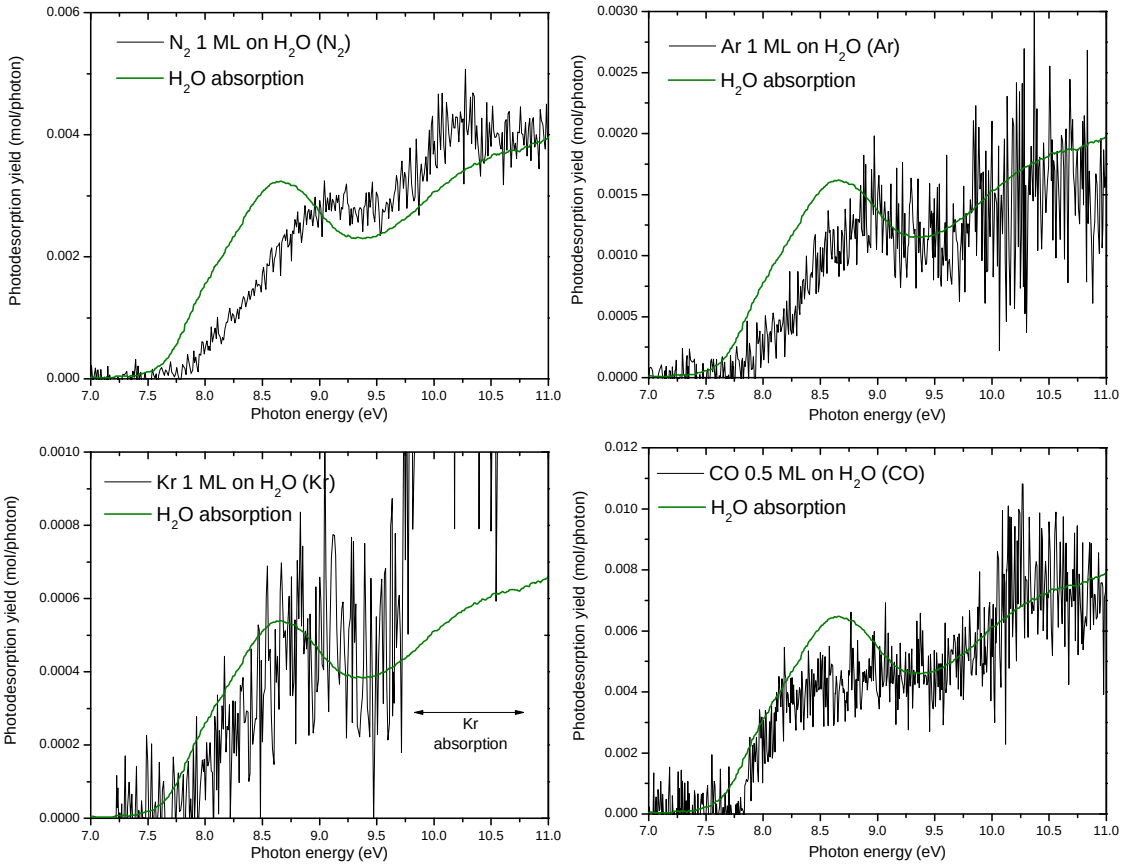

Figure IV.38: Photodesorption spectra of N_2 (top left), Ar (top right), Kr (bottom left) and CO (bottom right) single layers on H_2O compact amorphous ice. The absorption spectrum of H_2O from Lu et al. [216] is shown each time for comparison.

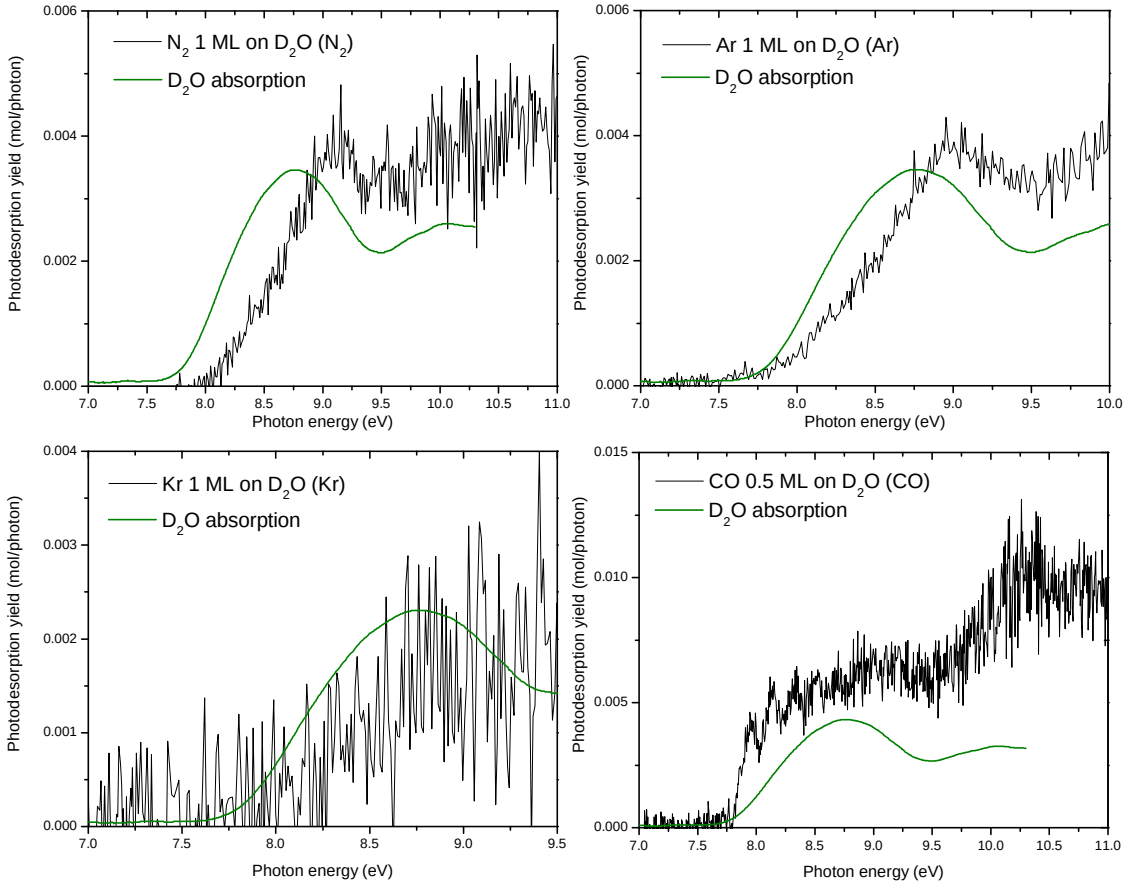

Figure IV.39: Photodesorption spectra of N_2 (top left), Ar (top right), Kr (bottom left) and CO (bottom right) single layers on D_2O compact amorphous ice. The absorption spectrum of D_2O from Cruz-Diaz et al. [299] is shown each time for comparison.

Table IV.3: Summary of the systems for H_2O-induced desorption.

Layered molecule	Indirect yield[a] (mol/photon)		Mass (a.m.u.)	Binding energy[b] (meV)
	on H_2O	on D_2O		
^{13}CO	4×10^{-3}	6×10^{-3}	29	122
$^{15}N_2$	3×10^{-3}	4×10^{-3}	30	99
Ar	1.4×10^{-3}	3.8×10^{-3}	40	75
Kr	5×10^{-4}	1.5×10^{-3}	84	118

[a] Contribution of H_2O-induced indirect desorption to the photodesorption yield of the molecule for single layer systems at 9 eV. [b] Binding energy on compact amorphous H_2O determined by TPD experiments in sub-monolayer regime, taken from Smith et al [81].

here (compare with e.g. the results for Ar/CO in fig. IV.36). But it also seems that the indirect desorption process is not completely surface-confined here: we should have multilayers for 10 ML deposited, therefore we can estimate that the transfer of energy from the underlying water ice can probably reach the second or third effective layer. For CO we cannot see these effects since CO absorption quickly starts to dominate the photodesorption spectrum.

IV.2.2.2 Discussion

Similarly to what was said earlier for CO, we may consider a single mechanism to explain H_2O induced indirect desorption for a start, but there may be multiple at play. Interestingly there is already a case of H_2O induced indirect desorption in the literature. In the papers of Thrower et al. [300] and Marchione et al. [301, 302] the desorption of benzene adsorbed in sub-monolayer quantities on water ice by electrons (200-400 eV) is reported. They show that benzene is efficiently desorbed by excitation of the underlying water ice and subsequent migration of the water excitons to excite the benzene through the hydrogen bond between benzene and water. In particular, changing the substrate to a less hydrogen bonded one drastically reduces the efficiency of the process [302].

This process is certainly specific to species that can form strong hydrogen bonds with the water ice, allowing electronic energy transfer. We are not in such a case here: as for CO, the observation of indirect desorption of Argon clearly rules out any energy transfer to internal energy of the desorbing molecule.

Aside from that, the experimental facts that we have are the indirect photodesorption yields summarized in table IV.3. The masses are also indicated, and the binding energies for monolayers on ASW since those can be and have been experimentally determined (all values are taken from Smith et al. [81]). We see that we have in order of indirect desorption yields CO $\sim$ N_2 > Ar > Kr for a given substrate (H_2O or D_2O) and that the yields on D_2O are always higher. The indirect yields for CO should of course be taken with caution as CO also absorbs at 9 eV and this contribution is difficult to take into account. In addition we also need to explain the shift of the desorption spectra compared with the absorption spectra.

Since energy transfer to internal energy modes of the desorbing molecule has been rejected, the second immediate possibility that was also evoked for CO is direct kinetic

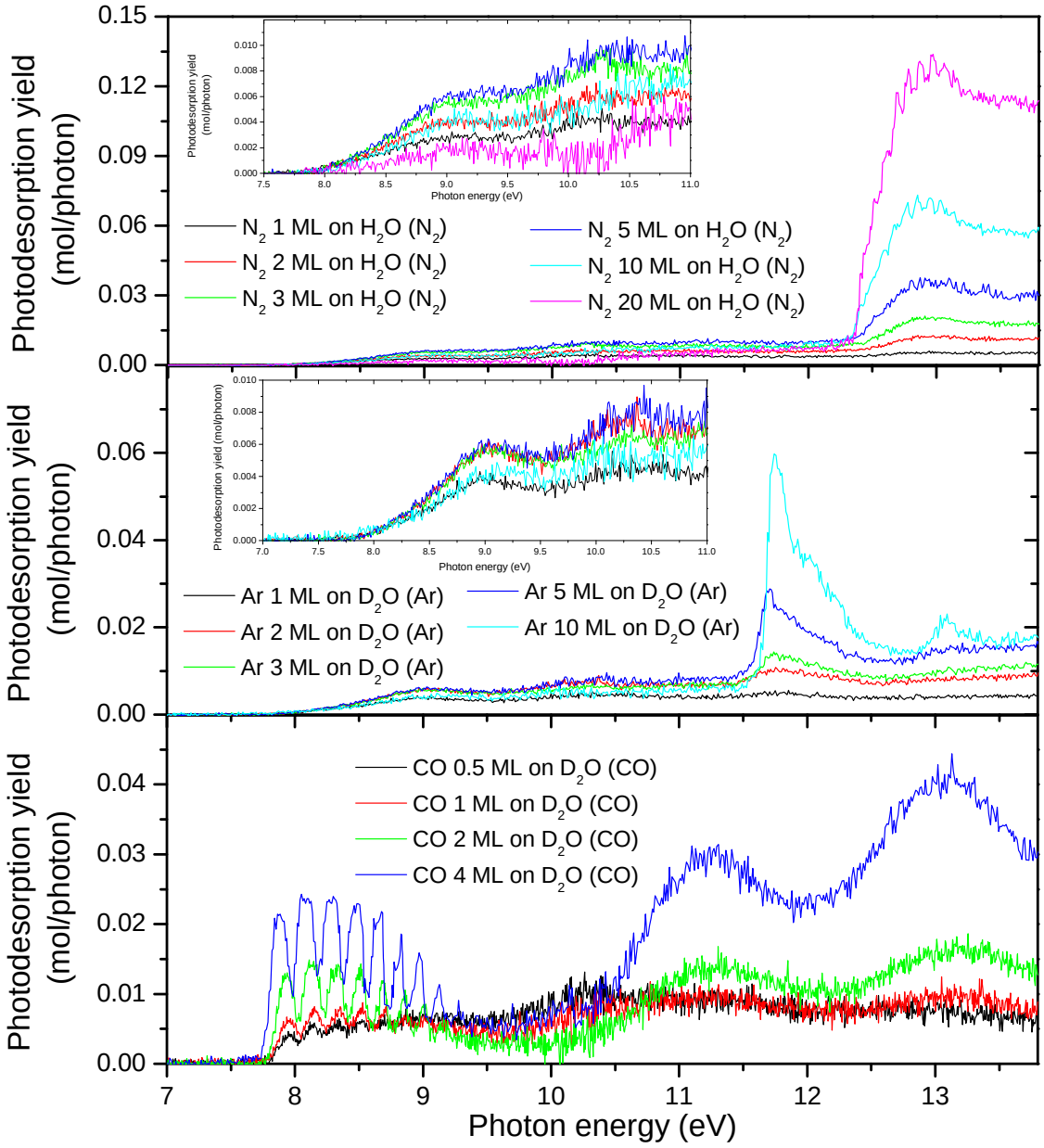

Figure IV.40: Photodesorption spectra of multiple layers of N_2 (top), Ar (middle) and CO (bottom) on respectively H_2O, D_2O and D_2O compact amorphous ice.

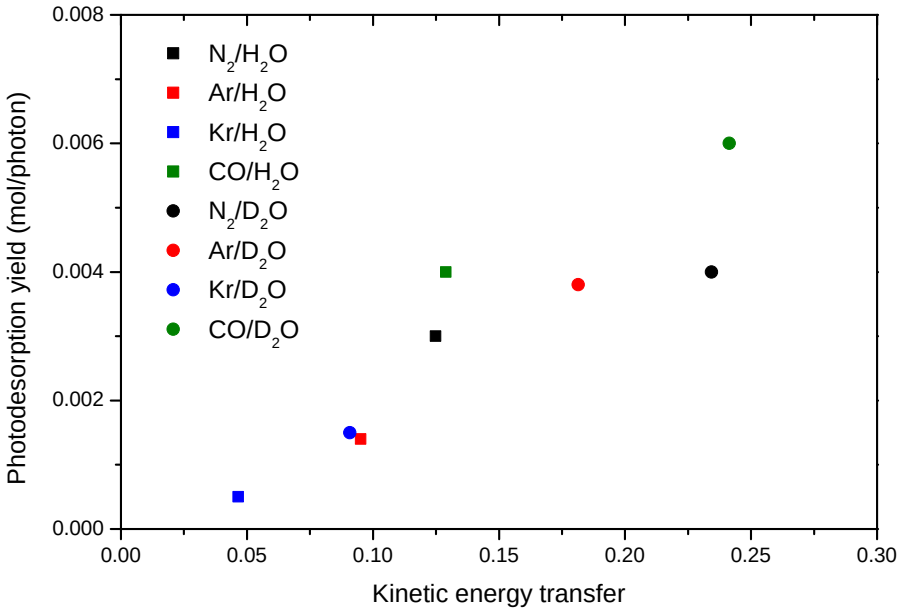

Figure IV.41: Indirect photodesorption yield for the different single layer systems, as a function of kinetic energy transfer for a head-on elastic collision between the layer molecule and an H or D atom (see text for the formula). The indirect photodesorption yield is the photodesorption yield measured at 9 eV.

energy transfer. In this case, it would correspond to the "kick-out" mechanism by energetic H/D atoms discussed in section IV.1.4 for the desorption mechanisms of pure H_2O. This mechanism has been put forward by molecular dynamics calculations on the pure H_2O system. Such a mechanism is actually well suited to explain all of our experimental observations. Since the kick-out is basically a collision, we expect its efficiency to depend on mass: this is indeed what is observed in the indirect desorption efficiencies. The efficiency should also depend on the binding energy of the species to the ice, but all our species have relatively close values of binding energy to ice here, and the order of these values does not follow the order of the desorption efficiencies: the mass effect seems to dominate.

The kick-out also explains the larger indirect desorption efficiency for D_2O ice: while D atoms get less kinetic energy when dissociating D_2O (because of momentum conservation), they also transfer their kinetic energy much more efficiently than H atoms. The molecular dynamics simulations that have been done on isotope effects in water desorption do show a more efficient kick-out effect for D atoms [264]. It is also worth to emphasize that the observed isotope effect is *not* the same as the one observed for H_2O and D_2O desorption from the pure ices, where D_2O desorption is lower than H_2O desorption. It is therefore sensible to look for a different mechanism for indirect desorption than what was suggested for the pure ice.

As for the observed shift of the photodesorption spectra, it may also be explained by the kick-out mechanism by considering that the excess kinetic energy of the fragments issued from dissociation of the water molecules should increase with photon energy. An

increase of "intrinsic" efficiency (indirect photodesorption yield per absorbed photon) with photon energy, due to the higher kinetic energy of the fragments, would indeed cause a shift towards higher energy of the spectrum.

At this point, we may summarize the results by plotting the indirect photodesorption yield against the fraction of the kinetic energy that is transferred by the energetic H/D atom to the layer molecule if we consider a simple hard sphere classical elastic collision. In such a case the efficiency of kinetic energy transfer is:

$$\frac{E_{transf}}{E_{ini}} = \frac{4m_1m_2}{(m_1+m_2)^2}$$

where E_{ini} is the initial kinetic energy and m_1 the mass of the kicking H/D atom and E_{transf} the transferred kinetic energy and m_2 the mass of the kicked surface molecule. The plot is shown in fig. IV.41. All the results go in the right qualitative direction (increase of indirect desorption efficiency with transferred fraction). It is difficult to comment more because we do not have a precise idea of how the photodesorption yield would vary with the kinetic energy imparted to the desorbing particle (we could see a somewhat linear relation in this plot but it would probably be bold to make such a claim), and because there are additional confusing factors anyway such as binding energy. However we do know approximately how much energy H and D atoms initially have upon H_2O/D_2O dissociation [263]: considering the dissociation energy of water is $\sim$ 5.4 eV and about 0.7 eV of the energy goes into vibrational and translational energy of OH/OD, there is about $\sim$ 2 eV left for H/D atoms (D atoms have slightly less, but not so much) for photon energies around 8 eV. This means that in the hard sphere collision model and for the systems considered here there is between 100 meV and 500 meV of kinetic energy transferred, which is of the same order as the binding energies of the systems. Therefore it is clear that we are in a regime where mass and binding energy of the adsorbate on one part, and initial kinetic energy and transfer efficiency for H/D atoms on another part, will affect the indirect desorption efficiencies.

Considering this mechanism does not require direct neighbouring of the excited substrate and desorbed surface molecules, it can also explain the observed layer thickness dependence of the indirect desorption yields: the energetic H/D atoms can travel a few ML to reach the surface.

In conclusion, all experimental observations seem to be coherent with a kick-out mechanism. The other mechanisms discussed for pure water desorption do not seem to apply here: geminate or non-geminate recombination happening in the water could conceivably liberate chemical energy that might eject neighbouring molecules, but then we would expect desorption yields depending mostly on the binding energy of the molecule. The isotope effect of the photodesorption spectra shifts cannot be explained in that case. Conversely, although we showed that non-geminate recombination was an important mechanism for desorption of intact water in pure water ice in a previous section, we also show here through indirect desorption that the kick-out mechanism is not to be excluded, although it does not seem to be dominant for pure water ice.

It should be noted that only diatomic or atomic adsorbates have been studied here: it is possible that for polyatomic molecule we would observe as for CO a reduction of indirect desorption yields. Adsorbate-specific exceptions could also be found to the kick-out mechanism, e.g. for adsorbates that are strongly hydrogen-bonded to the water ice,

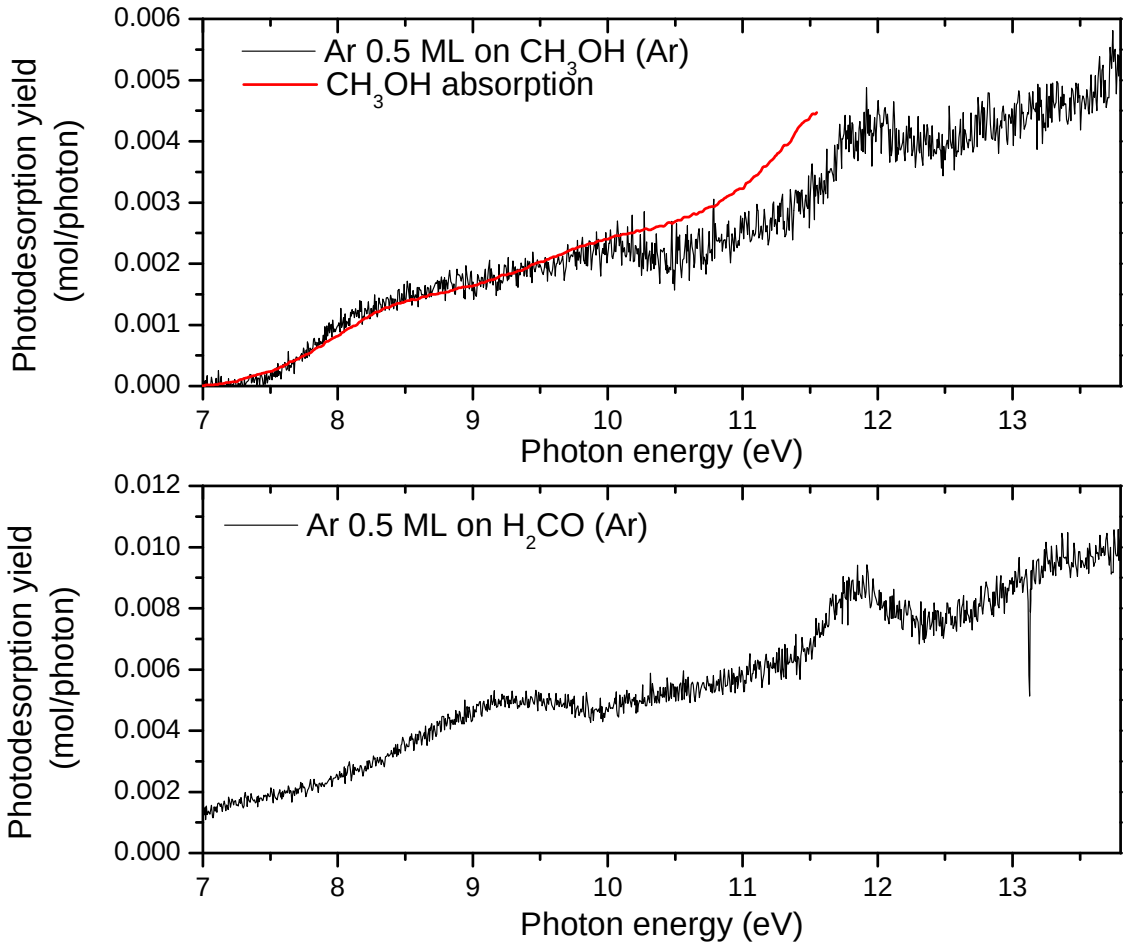

Figure IV.42: Photodesorption spectra of Ar from 0.5 ML Ar on CH_3OH (top) and on H_2CO (bottom). For CH_3OH the absorption spectrum of the pure methanol ice is also shown, taken from ref. [303].

where electronic energy transfer seems possible as evidenced for C_6H_6/H_2O [301].

IV.2.3 Other systems

Aside from indirect desorption from CO and H_2O, we have looked at a few other systems. In particular we have tried to use argon single layers as a probe of the "desorption spectrum" of ices where first-order monochromatic experiments are not possible for the parent molecules because of the low desorption yields. In fig. IV.42 the desorption spectra of 0.5 ML Ar on CH_3OH and H_2CO are shown. The spectra show clearly the spectral signatures of the two underlying ices. This suggests that the indirect desorption process works for many different systems. The indirect desorption yields of Ar in these two systems and in Ar/CO and Ar/H_2O are all close (especially when the differences of absorption cross-section of the ices is taken into account): the order of magnitude of the indirect desorption yield seems to depend more on the desorbing adsorbate than on the substrate

absorbing ice. This may be because the binding energy, which should be a crucial parameter, depends more on the adsorbate than on the substrate. This is also despite the fact that the mechanisms of indirect desorption for CO ice and H_2O ice are different. For the two other substrates considered here, we may again exclude transfer to internal energy because Argon desorption is observed, but without further study we cannot say much more - although it should be noted that these two substrates will also be prone to dissociation and creation of energetic H fragments like H_2O. It would be therefore interesting to investigate the desorption of Argon (and perhaps other molecules) on CO_2 or N_2 ices, for example, to try to determine how universal the indirect desorption phenomenon could be.

IV.3 Implementation in astrochemical models spectral dependence

For UV photodesorption, the question is no longer whether it is important or not to take it into account in models: the process is implemented in a lot of different models and is necessary to explain various observations, as explained in chapter I. The question is rather how the process should be implemented: what aspects of the complex process we are dealing with should be taken into account.

Most of the works that have been done on photodesorption have considered pure ice systems. The astrophysically relevant work that has been done on photodesorption in this last decade or so has been briefly reviewed in a book chapter recently [304] and also as part of reviews on broader topics [12, 6, 305]. This includes works that have not been mentioned in the previous sections on pure ices, e.g. on CO_2 [306, 307, 308, 309, 310] or O_2 [311].

At "first order", what really should be taken into account in models is the molecular dependence of the photodesorption yields. This is the first basic parameter for which yields vary over orders of magnitude. Such a conclusion is not new, but the present manuscript emphasizes it again as in the yields we have measured and that were not previously published, the yield for NO is in the 10^{-2} mol/photon range while intact HCOOH from HCOOH ice is constrained to $< 2 \times 10^{-5}$ mol/photon. Ideally, for each molecule the wavelength-resolved photodesorption yields need to be measured to obtain numbers that are appropriate for different astrophysical environments. Another advantage of our wavelength-resolved yields is that for the systems for which first-order measurements are possible, the photon flux used is much smaller than the one typically obtained with broadband lamps or pulsed lasers, which brings us a little bit closer to astrophysically relevant conditions.

Using monochromatized light has the advantage over broadband sources that the measurements are more controlled, and that the results can be used to derive yields relevant to any situation. Indeed, each environment has its own UV photon spectrum, as shown in chapter I, and the ISRF spectrum for example is very different from cosmic-ray secondary UV photons. When the molecule has a structured photodesorption spectrum the effect of the environment spectrum on the average yields can be important (and, as a consequence, using a UV source with a broadband spectrum will give results that are only valid for that specific spectrum that may or may not be representative of an astrophysical

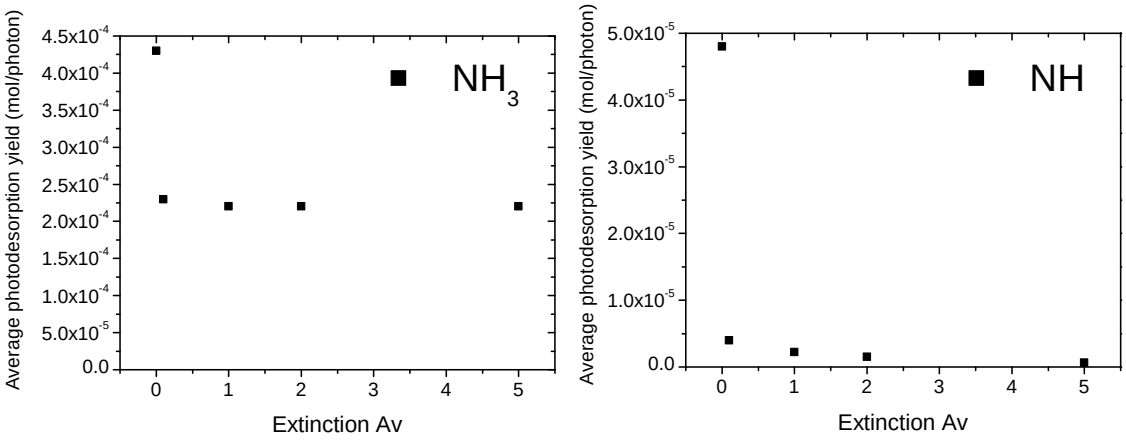

Figure IV.43: Average photodesorption yields of NH_3 and NH in a PDR environment at different extinctions A_v. Photodesorption yields from the pure NH_3 ice at 75 K have been used along with spectra calculated with the Meudon PDR code, as explained in the text.

environment).

An average yield Y_{avg} that can be used in a model using a rate equation of the type presented in section I.1.2.2 can be calculated for a specific environment using our data. The average yields are calculated from the wavelength-resolved yields by taking a weighted average of the yield spectrum, where the weight is the photon density spectrum of the considered astrophysical environment. The formula is the following:

$$Y_{avg} = \frac{\int y(\lambda)\Phi(\lambda)d\lambda}{\Phi(\lambda)d\lambda}$$

Where Y_{avg} is the photodesorption yield per "average" photon in the environment considered, $y(\lambda)$ is the wavelength-resolved photodesorption yield, and $\Phi(\lambda)$ is the photon density spectrum of the environment considered.

Let us take an example that will illustrate the importance of wavelength-resolved yields. Photon-Dominated Regions (PDRs), as we have seen in chapter I, are often modelled as a one-dimensional molecular cloud, with an external UV source on one side and the one dimension being equivalently the column density traversed by the UV photons, or the visual extinction A_v. As A_v increases, the total photon flux decreases, but the spectrum of the photons also changes, as illustrated previously in fig. I.3. The consequence is that the Y_{avg} considered for photodesorption should *also* change with A_v.

A concrete example of the importance of this fact can be seen by using the recent paper of Furuya & Aikawa on nitrogen fractionation [312]. In this paper, the authors investigate the origin of nitrogen fractionation (differences of the $^{15}N/^{14}N$ ratio in the gas phase compared with the normal abundance) in a PDR. Their proposed mechanism for the observed depletion of ^{15}N in the gas phase is the following: the $^{14}N^{15}N$ molecule is more photodissociated than the $^{14}N_2$ molecule because of a phenomenon called self-shielding (absorption of the photons with energies corresponding to transitions of $^{14}N_2$ by the abundant $^{14}N_2$ molecule "shields" other $^{14}N_2$ molecules from these dissociative photons, which is not the case for the much less abundant $^{14}N^{15}N$ whose transitions

Table IV.4: Average photodesorption yields of molecules[a] for different astrophysical environments.

	ISRF ($A_v = 0$)	ISRF ($A_v = 2$)	Secondary photons
CO	1.9×10^{-2}	1.2×10^{-2}	1.3×10^{-2}
N_2	1×10^{-2}	1.7×10^{-3}	8.3×10^{-3}
NO	9×10^{-3}	4.7×10^{-3}	1.1×10^{-2}
O_2	9.3×10^{-3}	6.9×10^{-3}	9.6×10^{-3}
CH_4	1.4×10^{-3}	2.9×10^{-4}	2.2×10^{-3}
H_2O	3.8×10^{-4}	3×10^{-4}	5.5×10^{-4}
NH_3	4.3×10^{-4}	2.2×10^{-4}	4.2×10^{-4}
CO_2	2.9×10^{-4}	1.5×10^{-5}	2.5×10^{-4}
H_2CO	5×10^{-4}	4.2×10^{-4}	4×10^{-4}
CH_3OH	1.2×10^{-5}	1×10^{-5}	1.5×10^{-5}

[a] Photodesorption yield of the parent molecule from the pure ice, disregarding dependences to various parameters like ice thickness (the ice is assumed to be representative of the infinite thickness ice), ice temperature, etc. Values have a ± 50 % uncertainty.

are slightly shifted compared with the regular isotope). This enriches the gas phase in ^{15}N atoms, some of which will stick to grains and be hydrogenated into NH_3, effectively staying trapped in the solid phase. The solid phase is therefore enriched in ^{15}N. But one mechanism counteracts this depletion process: photodesorption of NH_3 back to the gas phase. In their paper, they show that the isotopic ratio $^{15}N/^{14}N$ in the PDR is very sensitive to the photodesorption yield of NH_3.

It is therefore interesting to look at how the photodesorption yields vary as a function of A_v, using the spectra calculated with the Meudon PDR code that were introduced in section I.1.1.4. Using the above mentioned formula, the result for NH_3 is shown in fig. IV.43 (left panel). We see that the only visible difference in yields for NH_3 is between the $A_v = 0$ spectrum and the other ones. This is because as soon as there is a little extinction, large parts of the spectrum above 11.2 eV are completely absorbed, and this is where the photodesorption yield of NH_3 is higher. This absorption does not change enough between different A_v other than 0 that there can be a significant difference for a molecule like NH_3 which desorbs in basically the whole range. A difference is visible in the case of NH, shown in the right panel of fig. IV.43. This is because the photodesorption threshold for NH is higher than NH_3, around 9 eV, so it is more affected by the changes at high energy in the spectra.

The magnitude of the effect of having different UV spectra therefore varies depending on the spectrum of the molecule. The values derived for different astrophysical environments for all the molecules (parent molecule desorbing from the pure ice) for which wavelength-resolved yields have been obtained are summarized in table IV.4. The UV spectra considered are the ISRF at $A_v = 0$ and $A_v = 2$ (calculated by F. Le Petit using the Meudon PDR code, see I.1.1.4) and the spectrum for secondary UV photons created by cosmic rays inside a dense cloud (introduced in section I.1.1.4).

A few comments can be made on how yields vary for different molecules in different

environments. For the ISRF, the yield is more or less an average of the photodesorption yield over the whole range since there are photons at all energies. What matters for the two other environments is whether most of the photons are at an energy where the ice does not absorb - for the secondary UV photons, the Ly-α (10.2 eV) is an important contribution, and for $A_v = 2$ photons above 11.2 eV are basically all absorbed. Molecules with a structureless spectrum spanning most of the photon energy range (O_2, H_2O, NH_3, H_2CO, CH_3OH) show very little variation of their average photodesorption yield for different environments. We see a drop in the yield for secondary UV photons compared with the ISRF for molecules that do not absorb strongly at the Ly-α (e.g. CO, N_2) but it is not a huge drop: despite the Ly-α dominating the spectrum in terms of line intensity, its weight in the integrated number of photons remains "only" 50 %, and the rest is more or less evenly distributed over the 7-13.6 eV range. The effect is much more dramatic for the attenuated ISRF ($A_v = 2$) versus non-attenuated. The average yield for molecules that have most of their absorption above 11.2 eV (N_2, CH_4, CO_2) drops by an order of magnitude. It should be noted that this effect had not been shown in the previous papers of the team, since we only very recently obtained the PDR spectra calculated by F. Le Petit. This emphasizes even more the importance of wavelength-resolved spectra, but also points out the importance of the environment photon density spectra that are considered. The spectrum of the "source", whether it be the ISRF or another one like a nearby star, may differ significantly from the local spectrum that has been attenuated by gas and dust. On this topic, one should also consider with caution spectra dominated by atomic and molecular lines like the secondary UV spectrum or the TW Hya spectrum (fig. I.2), where the width of the lines are very important in determining the actual weight, in integrated photon flux, of a given line relative to the continuum or the other lines.

The average yields derived from wavelength-resolved photodesorption yields from pure ices, such as these presented above, are good first order values for models as long as:

- There is a consensus on the value. We saw that there is a spread of value for CO photodesorption that remains not entirely explained. On the other hand there is a rather good agreement for H_2O photodesorption.
- There is no parameter that affects the yields of the pure ice "to the first order" (i.e. by more than a factor of 2-3). The temperature deposition effect found by Munoz-Caro et al [91] would be such a first order effect, as there is a factor of 5 between the extremes of the measured yields. The temperature effect for H_2O, or the deposition angle effect for CO, are "second order" effects: they do not change the order of magnitude of the yield.
- The pure ice yield is a representative yield for that molecule: in mixed ice the yield is not affected too much aside from the dilution effect.

The last item brings us to the question of the investigation of ice mixes. Arguably the only pure ice systems relevant for astrochemical modelling of the ISM are H_2O, CO and CO_2 (and perhaps CH_3OH in some regions). All other molecules are found in too low abundances and with no evidence of pure phases, so that the really relevant studies would involve the molecule in a matrix of H_2O or CO, or even in a more "realistic" mix of molecules using the observed abundances (see chapter I). This does not mean that

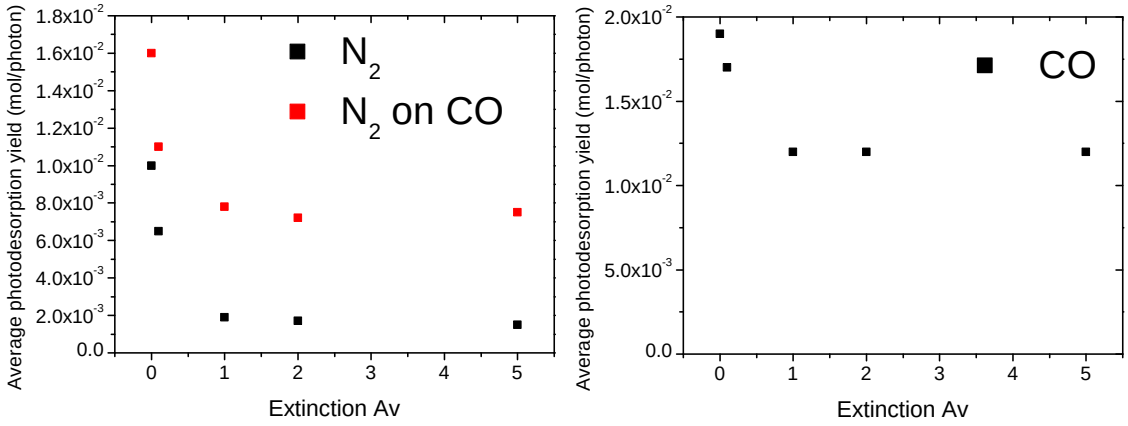

Figure IV.44: Average photodesorption yields of N_2, CO and N_2 from N_2/CO in a PDR environment at different extinctions A_v. Photodesorption yields from the N_2 and CO pure ices and from a 1 ML N_2/CO ice have been used along with spectra calculated with the Meudon PDR code, as explained in the text.

the studies that have been made on other pure ices are useless for the ISM (and they could definitely be relevant for planetary science). First because the study of pure ices is a prerequisite to the study of mixes, but also because the matrix environment may not have a significant effect on the photodesorption yield of the intact molecule (aside from a simple dilution effect). Still, now that we have a good overview of most relevant molecules in their pure form, and although a thorough physical understanding of the various systems has not been achieved yet, from an astrophysical point of view it is necessary to move on to mixed systems. Which has already been done: works on photodesorption from mixed ices already exist (see e.g. [286, 291]). One type of work is what has been presented in the section on indirect desorption, where we focused on a more precise understanding of one aspect of ice mixes. Another is the study of molecules in CO or H_2O matrices: CH_3OH:CO and H_2CO:CO mixes have been investigated in our team [54, 276]. Although the measurements are difficult because of the low yields, the effect of the CO matrix on e.g. H_2CO desorption does not seem to be drastic. In any case, it seems to me that any subsequent study of the photodesorption of molecules should always in addition to the pure ice, include a study of the effect of an H_2O and a CO matrix on photodesorption as a basic start. This is particularly true for the systems to which we will naturally tend to move to, organic molecules, as the matrix may have significant effects on the fragmentation and chemistry of these easily dissociated molecules.

Let us take one example that illustrates how one of the effects of having mixed ices, indirect desorption, which we have abundantly studied in the previous section, changes the average photodesorption yields. Fig. IV.44 is similar to the previously shown fig. IV.43: it shows the average photodesorption yield as a function of A_v, this time for N_2 and CO for the pure ices and N_2 for the 1 ML N_2/CO system. For pure N_2 the difference of yields between $A_v = 0$ and $A_v = 5$ is dramatic, as was already shown in table IV.4, because almost all of the photodesorption yield is above 12.4 eV. But this effect should be mitigated in real ices because when N_2 coexists with CO, CO-induced desorption will have an important effect on the N_2 yield, since CO also absorbs in the

low-energy region (below 10.2 eV). This is abundantly clear on the figure: the average yield of N_2 at $A_v \geq 1$ is four times higher when CO-induced indirect desorption is taken into account. One of the objectives of the study of CO-induced indirect desorption was that if we could find parameters that correlate with the efficiency of the process, we could have simplified astrophysical implementation of indirect processes (which as we see here can be important). H_2O-induced indirect desorption should have similar implications.

IV.4 Conclusions

Some important progresses have been made in this chapter on the understanding and quantification of VUV photon-induced desorption in molecular ices.

First, photon-induced desorption is a molecule-dependent process, which was already known but is further emphasized here by measurements on pure ice systems that had not been measured before (NO, CH_4, HCOOH).

Second, photon-induced desorption is a wavelength-dependent process. The availability of wavelength-resolved photodesorption yields data is expanded to new systems (NO, CH_4, H_2O, NH_3 and (preliminary) HCOOH) and includes an inventory of the desorbing fragments and photoproducts. We have shown how this can be particularly important for astrochemical models, where wavelength dependence can have as much as an order of magnitude effect on the average yields depending on the UV photon density spectrum of the considered environment. These wavelength-resolved results also allow to show in the case of H_2O that the intrinsic efficiency of the photodesorption process is electronic state dependent.

Photon-induced desorption is a surface process: molecules desorbing come from the very surface of the ice. But deeper layers can be involved in the desorption process, through energy transport, indirect desorption, diffusion of bulk fragments and products, etc. It was shown before this thesis that this "near-surface region" is confined to about 3 ML in the case of CO in the A-X region (8-9 eV). Here we show this depth is molecule dependent: in the case of CH_4 and NO, thickness dependence measurements confine desorption to the very first monolayer. But it is also excited state dependent: in the case of CO the thickness dependence study shows that for the electronic states above 10 eV, the depth involved in desorption is about 10 ML, contrary to the 3 ML of the A-X state. This dependence makes astrochemical modelling more complicated.

Direct and indirect photodesorption mechanisms have been evidenced for CO ice and H_2O/D_2O ice. The indirect mechanisms are of a different nature for the two ices: for H_2O the hypothesis of a kinetic energy transfer mechanism from hot H/D fragments to the desorbates provides a satisfying explanation to all experimental facts, i.e. desorption yields for the different systems studied, H/D isotope effects and shift of the desorption spectrum relative to the absorption spectrum. For CO similarly a form of kinetic energy transfer is likely at play, although of a different nature since it involves highly vibrationally excited molecules. The efficiency of indirect desorption for CO is highly affected by the number of internal degrees of freedom of the adsorbate, and some adsorbate-specific exceptions can occur as for O_2/CO. Indirect mechanisms are almost not taken into account in astrochemical models but should be very important since CO and H_2O constitute the main matrices in which molecules are found in ice mantles.

I have also shown the increasing importance of dissociation and chemistry when going to larger systems. Strong evidence for the role played by non-geminate recombination (i.e. chemistry) in the desorption of intact water from water ice was found: chemistry opens new desorption pathways. But chemistry and dissociation also constitute energy dissipation pathways that are in competition with desorption, as I showed in the case of CH_4. When moving to larger organic molecules like HCOOH, the desorption of fragments takes an increasingly important place, and this should have consequences on the gas phase chemistry in astrochemical models because of the desorption of radicals.

A new laser desorption/laser spectroscopy set-up has been developed and successfully tested on the NO molecule, showing promising possibilities for the future study of e.g. CO, allowing the testing of mechanisms predicted by theory.

The perspectives are numerous for further studies of VUV photon-induced desorption. There are some interesting pure ice systems left that could be studied, mostly complex organic molecules that are detected in many regions including protoplanetary disks, like CH_3CN. As pointed out earlier in the chapter, there is also a necessity to turn to mixed systems. The model layers that have been studied to understand better indirect desorption are a first important step, but effects of having molecules in CO and H_2O matrix such as dilution and chemistry need also to be investigated. One type of experiment that may be interesting would be to make a mix of different molecules in proportions representative of what is typically found in grain mantles, and try to measure desorption of all the different species without attempting to obtain a finer understanding of mechanism. This is experimentally challenging because of the limitations of mass spectrometry, where we need to be able to disentangle the different mass channels.

One element of study that is somewhat lacking even for "pure" molecules is the sub-monolayer regime and the effect of the substrate. A few results on thickness dependence of photodesorption have been shown here, and the few layers regime already shows a decrease of the photodesorption yield of e.g. CO. But when we reach the sub-monolayer regime, substrate absorption may become more important. A recent example showed that C_2H_2 deposited on tholins (Titan aerosol-analogs) is photodesorbed in the near UV range (at 355 nm/3.5 eV) by absorption of the underlying substrate [313]. This article is also interesting as it shows how the implications of photodesorption may extend to environments of significantly different pressure and chemical conditions than what we have explored here, like the Titan atmosphere.

One issue with all the above-mentioned perspectives is that they are all experimentally challenging considering the detection limits of our apparatus. Matrix diluted molecules, ice mixes or sub-ML regimes all imply lower yields than for the pure ices, and for larger organic molecules we are also reaching the limits of what we can measure for the desorption of the parent molecules.

The newly developed laser desorption/REMPI set-up is also promising for this, as the sensitivity of the laser ionization detection scheme is very high, therefore provided that the desorption source is sufficient it will allow the study of some of these systems. Laser ionization is also much more selective than mass spectrometry and could allow otherwise complicated identification of desorbing species.

Chapter V

Electron-induced desorption

> If was one thing all people took for granted, was conviction that if you feed honest figures into a computer, honest figures come out. Never doubted it myself till I met a computer with a sense of humor.
>
> Robert Heinlein, *The Moon is a Harsh Mistress*

In this chapter, I will present the results I obtained on electron-induced desorption (EID) from molecular ices at CERN. These were the first systematic measurements made on the newly commissioned Multisystem set-up, therefore the measurements stayed confined to relatively simple systems: pure, thick molecular ices. I did measurements on N_2, Ar, CO, CO_2 and H_2O/D_2O. The goals are to obtain quantified numbers for EID, try to interpret the curves of EID yield versus electron energy and what information can be obtained from them, and explore some parameters that could be relevant (e.g. ice temperature and phase). The electron energy is systematically varied between 150 and 2000 eV. We did not investigate the energies below 150 eV because (i) it is difficult to insure beam quality and electrons reaching the sample at these low energies and (ii) for condensed gas, charging problems can occur (2 keV, on the other hand, is the limit of the electron gun). We will also investigate which species desorb for the ices where chemistry occurs, the influence of the temperature of the ice during irradiation, or the temperature of deposition of the ice, which can change its structure. The N_2 and Ar ices, which are "chemically inactive", will be good systems to try to understand the EID yield curves without the further complication added by chemistry, which is discussed for CO, CO_2 and H_2O ices. The effect of impurity doping of Argon ice on EID is also discussed.

The measurement procedure is described in chapter III along with the description of the set-up used. A few important reminders: the error bars on EID graphs correspond to the noise (rms) on the mass signal measurements. The point at 2 keV (and also possibly the one at 1.5 keV) is not completely reliable because of beam focusing issues. The experiments are done with a +45 V bias on the surface (which does not affect the yields) so that measuring the sample current gives access directly to the incident flux of electrons, which is always around 100 nA. This measurement is of course important to obtain absolute EID yields. Thicknesses and irradiation times are chosen so as to avoid significant beam damage (which occurs fast with electrons, even at a flux of only 100 nA), but this does not exclude the fact that there are sometimes transitory effects on the desorption yield, which will be discussed when it is relevant.

V.1 Chemically inactive pure ices: N_2 and Ar

V.1.1 Interpretation of EID yield curves

Before showing the details of the N_2 and Ar results, I will use their EID yield curves as examples to show the basic interpretation we can have of the shape of these curves. Measurements of desorption (sputtering is the term often employed in the literature) by energetic electrons and ions are usually rationalized by assuming that the desorption yield is proportional to some power of the stopping power for the projectile-target couple considered. Often a linear or a quadratic dependence on the stopping power is found. This is explained by the fact that for energetic enough projectiles that will traverse the whole ice, what is important for desorption is the energy deposited "near the surface" (a notion which I will come back to later), and this is captured by the stopping power. If desorption occurs through a "single event" (event= excitation or ionization of a molecule) process, a linear relation is expected, but multiple event processes can also occur (in particular when the density of deposited energy is high), leading to superlinear relations.

In fig. V.1, the EID yield of N_2 for a 500 ML ice grown and irradiated at 14 K is

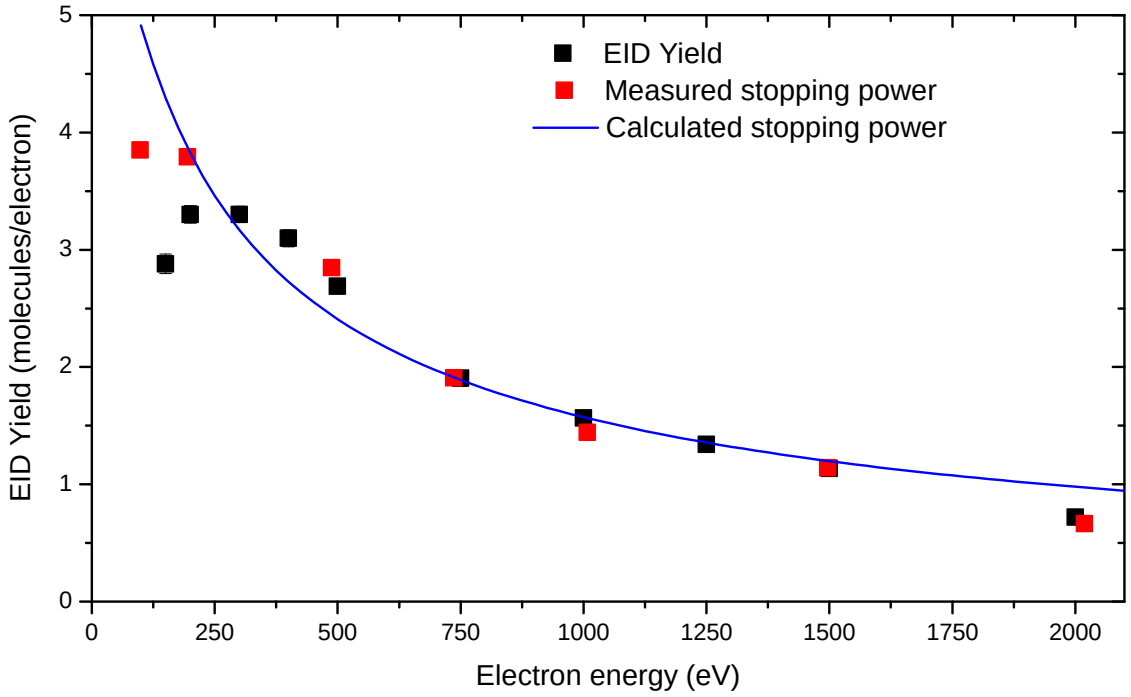

Figure V.1: EID yield of N_2 from 500 ML N_2 ice grown and irradiated at 14 K. Also shown for comparison is the calculated stopping power using the modified Bethe formula introduced in chapter II and the measured stopping power of ref. [133].

shown. We can see that there is a maximum around 200-300 eV and a progressive decrease as we go towards higher energies. This is compared with the calculated stopping power dE/ds using a modified Bethe formula (see section II.2.4) and the measured stopping power dE/dz of ref. [133], which we recall are two different quantities since one is the energy loss along the s coordinate of the electron path and one is the energy loss along the z coordinate which is the distance to the surface. We see a good agreement, in particular with the measured stopping power, at high energies but deviations at low energies. For N_2 a linear dependence with the stopping power of the desorption yield was found for low stopping powers [35], including keV electron measurements [314] (note that here the authors fit their data best with $S_e^{1.15}$, which is probably because the calculated stopping power does not exactly match the actual stopping power), which is coherent with what is found here as well.

Deviations at low energy from the stopping power can be understood because we transition to a different regime of energy deposition. Electrons of lower energy have higher stopping powers (up to a certain point, but the stopping power seems to be increasing at least down to 100 eV) but also lower penetration depths. When they deposit all of their energy in the "near-surface" region, the stopping power is no longer a relevant quantity. This "near-surface" region is similar to the notion already developed in the case of UV photons in chapter IV: it is the region below the surface that is relevant for desorption. In other words, it is the depth for which, if an excitation happens within this depth, desorption can happen at the surface through energy or particle transport mechanisms.

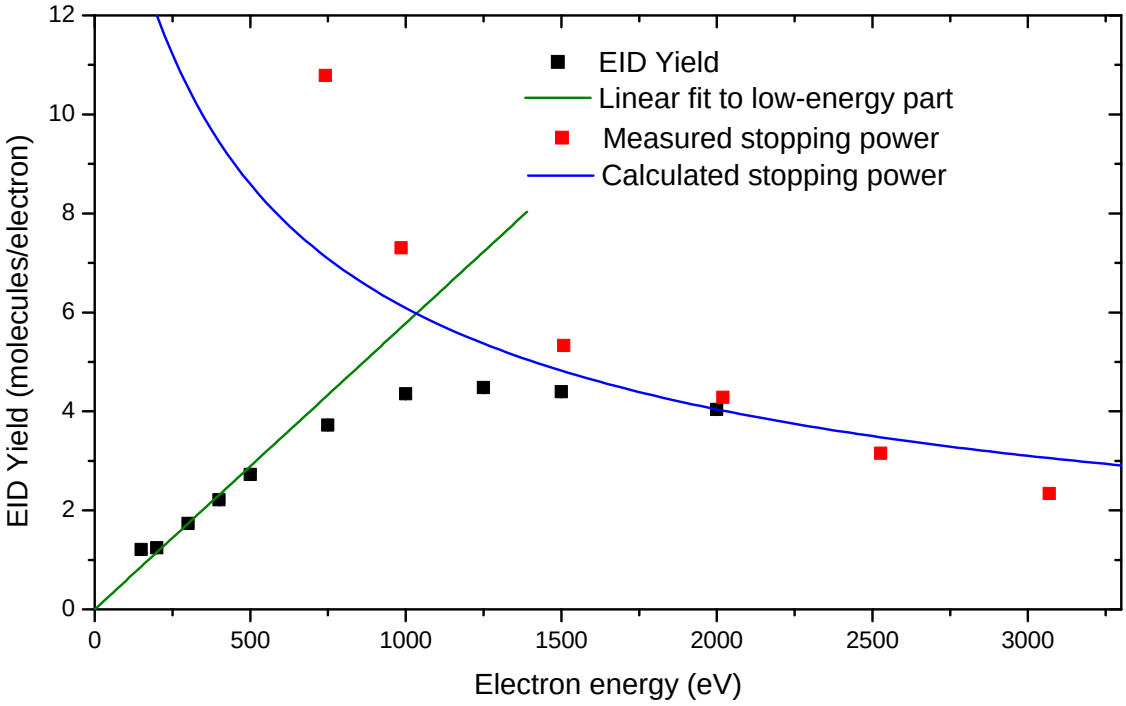

Figure V.2: EID yield of Ar from 500 ML Ar ice grown and irradiated at 14 K. Also shown for comparison is the calculated stopping power using the modified Bethe formula introduced in chapter II and the measured stopping power of ref. [133].

In the limit of low-energy electrons (typically from 150 eV down to 20 eV here), the desorption yield should be proportional to the total energy of the electron, since all of the energy is deposited near the surface. We then see a maximum in the yield curve which corresponds to the transition between the regime of penetration limited to the near-surface region, and penetration much deeper than the near-surface region. Note that the situation for electrons below 20 eV would be different since resonant structures appear in this region and different processes like DEA can be active (see II.2.4.4).

The first regime is better seen for Ar, where the transition occurs at much higher electron energy (evidence of a regime of yield proportional to electron energy for N_2 would have required measurements below 150 eV). The EID yield of a 500 ML Ar ice grown and irradiated at 14 K is presented on fig. V.2. Up until 500 eV the desorption yield is linear with electron energy (the lowest point at 150 eV is off because of charging issues). The regime in which the yield is proportional to stopping power is not visible with our range limited to 2 keV.

Therefore, the shape of the EID yield curve should be indicative of this "near-surface" depth for different ices, i.e. of the length of transport, although quantitative determination seems difficult. In the following I will use the term "desorption-relevant depth" or "transport scale" to qualify it.

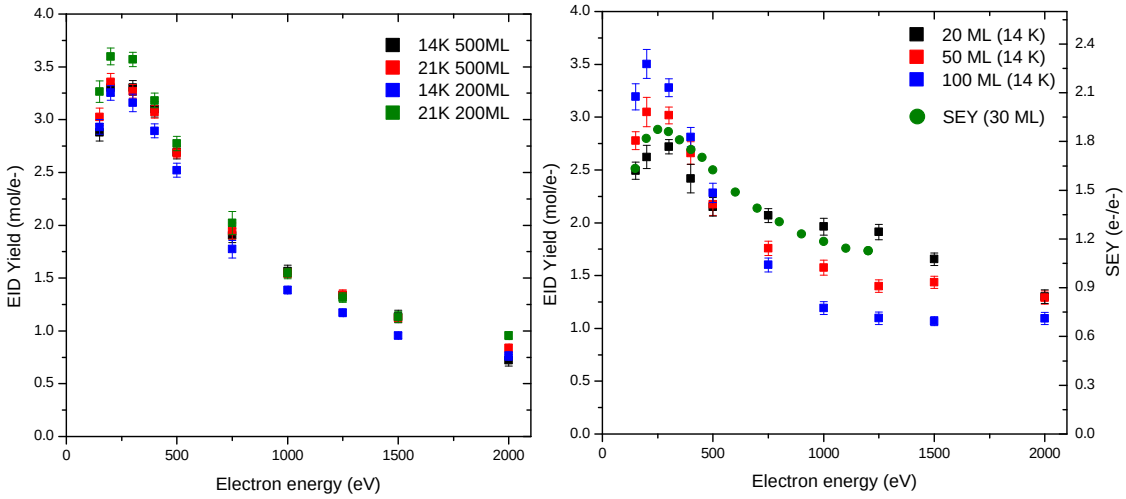

Figure V.3: N_2 EID yield for different ice thicknesses and deposition temperatures. Left panel: curves for 500 ML and 200 ML ices for deposition temperatures of 14 and 21 K. Right panel: curves for different ice thicknesses. Also the secondary electron yield (SEY) of 30 ML N_2 from ref. [315] is shown.

V.1.2 N_2

Experiments were performed on both regular N_2 and isotopically labeled $^{15}N_2$. No differences were observed, as expected, and I will only present the results for $^{15}N_2$ here since the signal/noise ratio is better. The only desorbing species observed was N_2 itself, although it is possible that very small amounts of N or N_3 desorb as well. One advantage of nitrogen ice is that it exhibits green luminescence when irradiated with electrons, which allows to cross-check the shape and position of the electron spot directly on the sample.

On the left side of fig. V.3, results for four different ices are shown, for 200 and 500 ML thicknesses and for a deposition temperature of the ice of 14 and 21 K. The deposition temperature of the ice does not have an effect here. We checked that the temperature at which the ice is maintained during the irradiation (from 14 to 22 K; above 22 K thermal desorption becomes more important than EID) does not have an effect either (not shown). There is no particular indication in the literature for any change of structure of N_2 ice as a function of deposition temperature (for example the density remains constant [77]), so these results are not surprising. There are also no significant difference between the two thicknesses, which indicates that we have already reached a saturated yield at 200 ML.

Results for thinner ices are shown on the right side of fig. V.3. When we reach down to 20 ML, the curve "flattens" with a higher yield at high electron energies and a slightly lower yield around the maximum. To explain why the curve flattens for thinner films, we need to take into account the substrate. Indeed, electrons with a penetration depth higher than the film thickness will reach the substrate. Excitations of the substrate could then take place and influence the yield, but another factor is the reflection of electrons on the substrate. In particular, gold has a high reflection coefficient for electrons, e.g about 0.4 at 2 keV [316]. If the penetration depth of the electrons is higher than twice the thickness of the film, then electrons can reflect on the substrate and make their way to

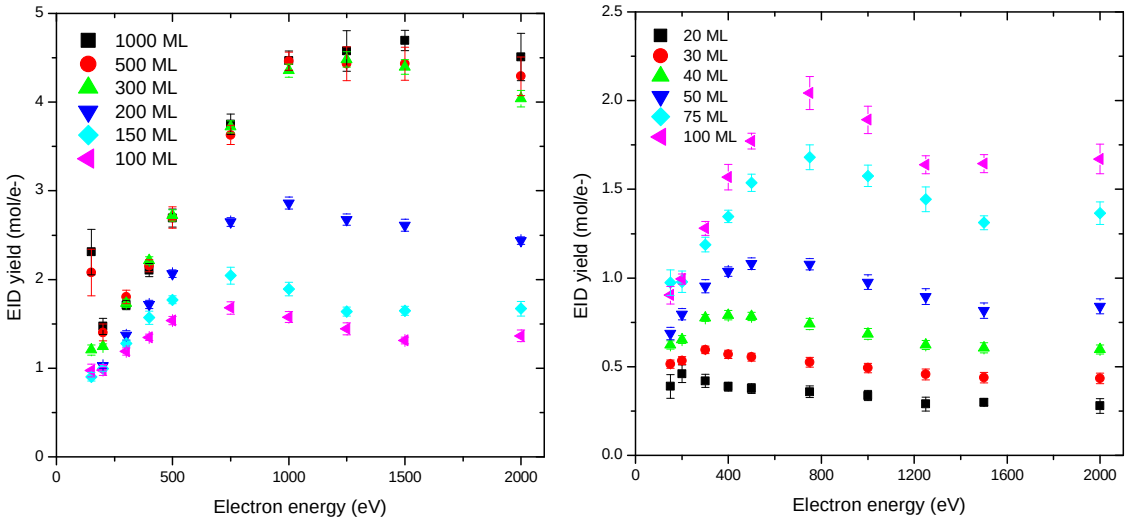

Figure V.4: Ar EID yield for different ice thicknesses. High thicknesses are on the left panel and low thicknesses on the right panel. All ices were deposited and irradiated at 14 K.

the surface again, depositing more energy, and making the desorption yield higher, which is what is observed on the curves.

On the figure is also shown a measurement of the secondary electron yield (SEY) of N_2, taken from Kuzucan et al. [315]. The SEY curve, which was measured for a 30 ML ice, closely resembles the EID curves of about the same thickness (20 ML). This similarity suggests that the drivers of energy transport from the bulk to the surface are the secondary electrons. The characteristic desorption-relevant depth that was discussed earlier should then correspond to the escape depth of secondary electrons (about 30 Å or 10 ML). This is coherent with the shape of the curve.

The absolute EID yield for N_2 reaches about 3.3 molecules/electron at the maximum. The yield at 1 keV is 1.6 molecules/electron, which compares very well with the value of 1.8 molecules/electron found in ref. [314] and quantified using a quartz microbalance. In ref. [317] the value indicated is about 2.5 molecules/electron, which is not too far either.

V.1.3 Ar

The EID yield of solid Argon as a function of electron energy and ice thickness is displayed in fig. V.4, with the high thicknesses on the left side and the low thicknesses on the right side.

The shape of the EID yield curve changes depending on the thickness up to about 300 ML, with the maximum shifting to higher energies. Above 300 ML the shape and intensity become stable, with only marginal changes for the highest electron energies. According to the previously mentioned interpretation of the EID curve, the shape is characteristic of the transport length scale. The change of shape as a function of thickness is therefore a good illustration of this principle. Below 300 ML, the desorption-relevant depth is limited by the thickness of the film. Above 300 ML saturation is reached, meaning the

desorption-relevant depth for the semi-infinite film is about 300 ML. This gives rise to a curve with a maximum in electron energy much higher than previously, around 1250 eV.

The reason for such a large transport scale is the nature of the electronic excitations of solid argon. As explained in detail in section II.4, the excitons in Argon can migrate over rather large distances. Typically, measurements in the literature estimate this length to be around 200-300 nm, (e.g. [173]) which is coherent in order of magnitude with the threshold estimated here (300 ML corresponding to about 100 nm).

It is worth noting that the EID yield curves of Ar differ from the SEY curves reported in ref. [318], where the maximum of the curve keeps shifting and increasing well beyond 300 ML. It is therefore possible that in the case of Ar, EID and SEE (secondary electron emission) are decorrelated.

The mechanisms of desorption for Argon and other rare gases are more or less elucidated, as explained in detail in section II.4. In that section I mostly described mechanisms linked with the excitons: more energetic irradiation sources like electrons and ions can also ionize Ar, but it is often assumed that electron recombination will occur and we will fall back on the usual excitons, although electron recombination does liberate some energy that can lead to desorption. A very detailed discussion can be found in e.g. Reimann et al. [177].

The thickness dependence that we observe here has also been reported in a lot of other studies on electron and ion sputtering of rare gases [174, 177] with very similar results. A modelling of this thickness dependence based on a diffusion model of the excitations created finds very good agreement for diffusion lengths of $\sim$ 200-300 Å, i.e 70-100 ML, which is in good agreement with what is found here (the saturation occurs at 300 ML but the characteristic thickness should be around 100-150 ML, even though the thickness curves cannot be fitted by simple exponential decay functions).

Quantitatively, the yield of 4.5 Ar atoms/electron at 1 keV is in good agreement with previously reported results by Tratnik [317] ($\sim$ 5 atoms/el) and Ellegaard et al. [174] (2.5 atoms/el) for thick argon films.

V.1.4 Ar mixed with impurities: effects of ice composition

A few preliminary experiments were made on the effect of ice composition for EID. The chosen system is Argon ice dopped with impurities (small amounts of CO or N_2). The idea stems from the interpretation presented above of the EID yield curve, and the notion that added impurities should act as exciton sinks and reduce the length of energy transport in the ice.

The results for Argon desorption from Ar:N_2 (on the left) and Ar:CO (on the right) mixed 500 ML ices with 100:5 and 100:2 compositions for each are shown in fig. V.5. The composition was checked by TPD afterwards. We see in the figures that the shape is modified, with for example curves maxima shifted to 1 keV for Ar:N_2 100:2 and 750 eV for Ar:N_2 100:5, and for both Ar:CO ices they are shifted to about 750 eV (probably lower for the 100:5 one). The Ar:CO curves end up resembling closely to the curve of the 75 ML Ar ice. This is an indication that the diffusion length of the excitons has actually been reduced to a bit less than this value (perhaps 60 ML). The Ar:N_2 curves, on the other hand, indicate a larger diffusion length of the excitons, resembling more the 150-200 ML pure Ar curves in terms of shape, but with a desorption yield increased by a factor

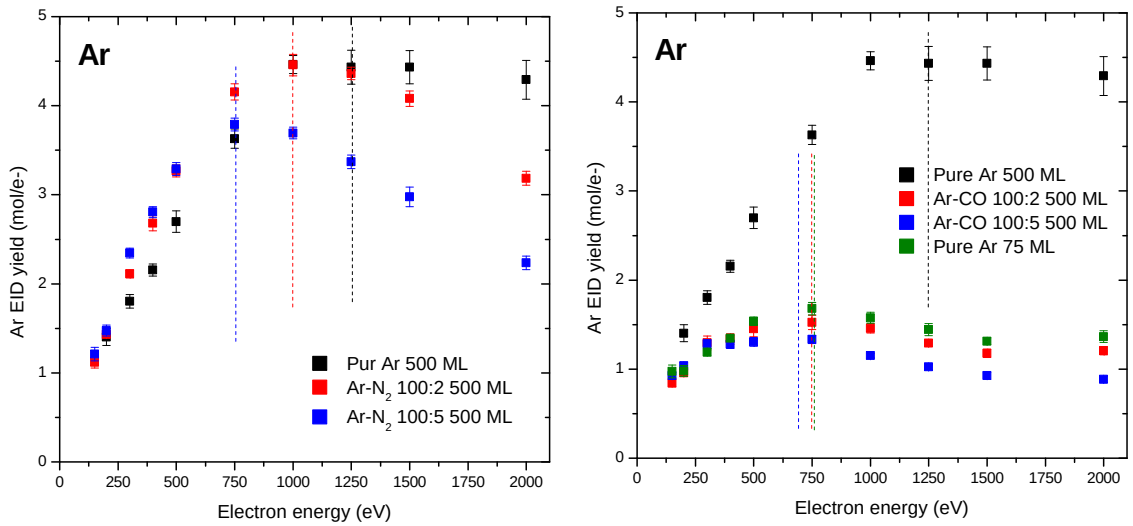

Figure V.5: Ar desorption from Ar ice mixed with CO and N_2 impurities. Left panel: Ar desorption from 500 ML mixed Ar:N_2 100:2 and 100:5 ices, along with the 500 ML pure Ar curve for comparison. Right panel: Ar desorption from 500 ML mixed Ar:CO 100:2 and 100:5 ices, along with the 500 ML and 75 ML pure Ar curves for comparison. The approximate maximum of each curve is indicated by dashed vertical lines.

of ∼2. The results confirm the idea that impurities lower the diffusion length of excitons, as "measured" by the EID yield curve of Argon. However, while CO does not seem to change the desorption efficiency of Ar, N_2 does.

The desorption of the impurities themselves is displayed in fig. V.6, on the left for N_2 and on the right for CO. The curve for N_2 seems relatively flat. The points at 200-250 eV are outliers because charging can occur at these energies. The CO curves look more regular at first sight, in the sense that they resemble typical curves for ices like pure CO where the energy transport is limited by the secondary electrons. But the CO signal in these experiments is initially decreasing, and the first point was done at 300 eV which is the highest point on the curve. It is therefore possible that CO exhibits a relatively flat curve as well. Whichever is the case, the EID yield curves of the impurities do not resemble that of Argon for the corresponding ice. This is fairly puzzling as well. One possibility is that there are multiple components in these curves, for example one with a high energy maximum and one with a low energy maximum, resulting in something that looks more flat.

These results are, again, preliminary, but it seems that there are interesting phenomena to investigate here. What is found for Ar desorption is well rationalized by the interpretation we developed of the EID yield curve (except for the increase of Ar desorption efficiency for Ar:N_2 mixes).

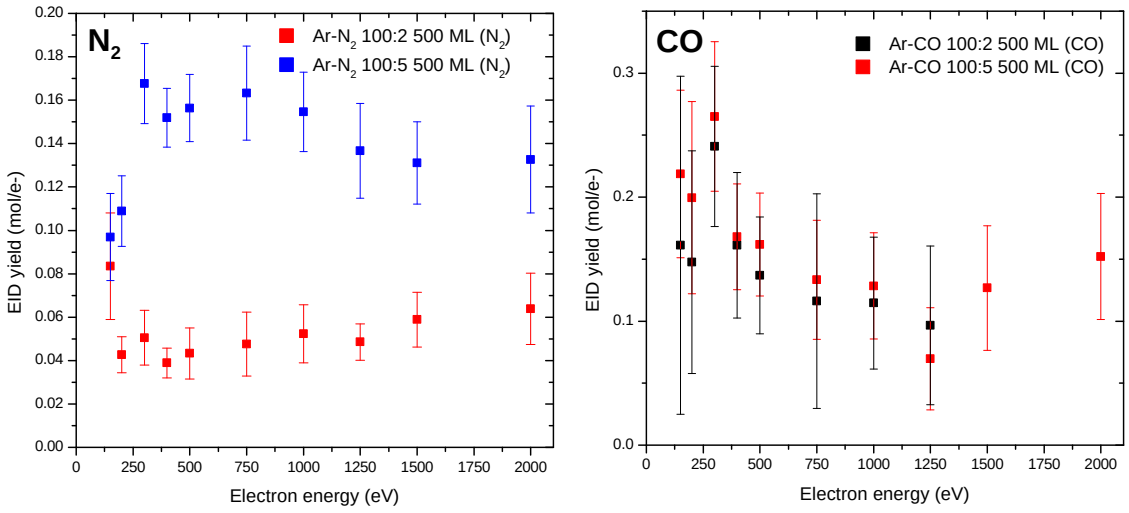

Figure V.6: N_2 and CO desorption from Ar ice mixed with N_2 and CO impurities. Left panel: N_2 desorption from 500 ML mixed Ar:N_2 100:2 and 100:5 ices. Right panel: CO desorption from 500 ML mixed Ar:CO 100:2 and 100:5 ices.

V.2 CO, CO_2, H_2O and the role of chemistry

V.2.1 CO

The EID yield for CO ices of different thicknesses and deposition temperatures are shown in the left panel of fig. V.7. Once again, a typical curve with a maximum at 300 eV is observed. The yield, however, is much higher than for N_2. For high thickness films, no effect of thickness on the EID yield is seen. Measurements of CO EID for thin films were made difficult by the high EID yield of the molecule and the modification of the film during irradiation: too much of the ice was processed or removed during the measurement (for an EID yield of 10 mol/electron and an irradiation at 100 nA on a 0.1 cm^2 spot the removal rate is about 3 ML/minute). Also shown for comparison is the CO SEY from Kuzucan et al. [315], which differs a bit from the EID curves. However this SEY curve was measured at a thickness of 30 ML, which certainly explains the discrepancy at high electron energies. The maximum of the SEY occurs at 200 eV and is clearly different from the 300 eV maximum of the EID, which could indicate additional transport pathways rather than simply secondary electrons - recall the thickness dependence that was found in chapter IV for VUV PID of CO - but this remains speculative.

Our value of ∼3.8 CO molecules/electron at 1 keV is close to the value of Tratnik [317] (∼4.5 molecules/el) but higher than the values reported by Schou et al. and Brown et al. [319] which are below 1 molecule/el. The studies of ion and keV electron sputtering of CO [319, 35] found a quadratic dependence of the yield with the stopping power down to the lowest stopping powers (electrons of a few keV, i.e. stopping powers even lower than ours). This quadratic dependence could explain why CO yields are high compared with N_2 yields, despite the fact that these isoelectronic molecules have comparable yields in the VUV range. The exact reason for such a quadratic dependence is not clear: at low stopping powers, single ionization events are spatially well separated. It is possible that

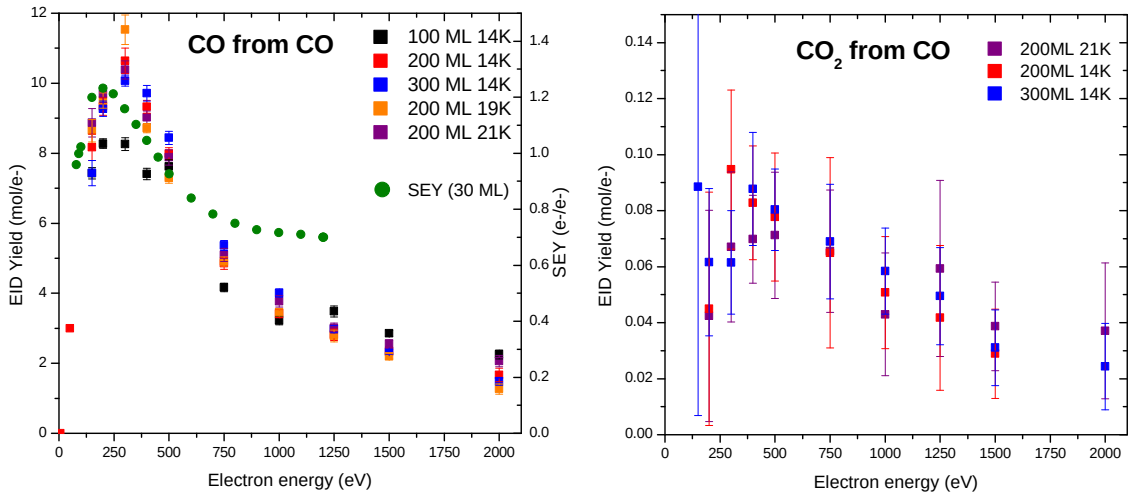

Figure V.7: CO and CO_2 EID yield from CO ice under different conditions. Left panel: CO EID yield for different thicknesses and deposition temperatures. The SEY of 30 ML CO from ref. [315] is also shown. Right panel: CO_2 EID yield from CO for different thicknesses and deposition temperatures.

chemistry plays a role here. The desorption mechanisms may therefore differ from the ones discussed in the VUV range in chapter IV.

An important finding is that no effect of the deposition temperature is seen here - and in this set-up there should not be any issue with the measurement of the temperature of the sample - contrary to what has been observed in the VUV range, cf. section IV.1.1. This again suggests different mechanisms at play.

Contrary to the previous molecules, a lot of chemistry can already happen during the irradiation of a CO ice, as many carbon chain species can be formed. This will be discussed again in the next chapter, as more probes of the chemistry are available for the soft X-ray experiments. Although we cannot probe the chemistry happening in the ice here, we can observe one of the main products desorbing in the gas phase, CO_2. The EID yield of CO_2 from a CO ice is shown in the right panel of fig. V.7. The yield is very small (two orders of magnitude smaller than CO) and therefore the error bars are large, so it is difficult to confirm whether there is a difference in the shape of the EID curves between CO and CO_2.

V.2.2 CO_2

Solid carbon dioxide is an ice that can no longer be called "simple" like the previous ones: first because it has a complex range of possible structures, like water, and second because chemistry now plays a prominent role in the effects of radiation. CO_2 films can be crystalline or amorphous to various degrees depending on the conditions of preparation of the ice. The ice is amorphous when deposited at a temperature of 14 K (the base temperature of our set-up) and becomes more and more crystalline when it is heated up to 75 K (above this temperature, the ice starts to significantly sublimate) [97]. Deposition temperature also significantly affects the density and porosity, with an ice 40% less dense

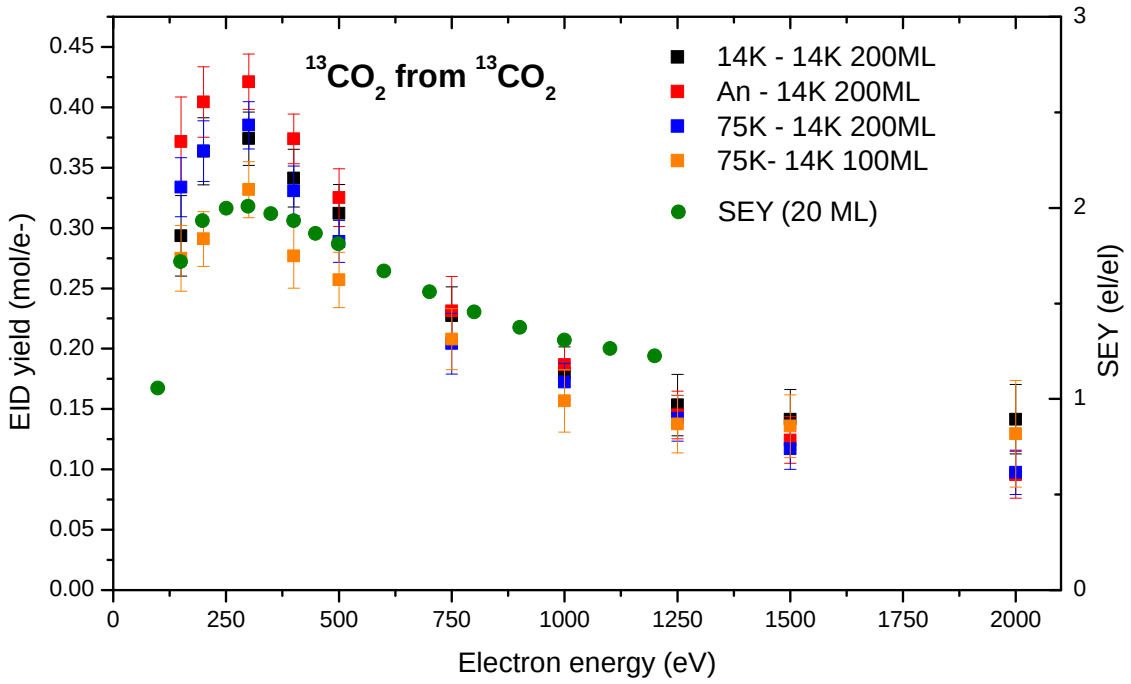

Figure V.8: EID yield of CO_2 from CO_2 ice, for three different structures of the ice (see the text). In the labels, the first temperature corresponds to the structure of the ice (grown at 75 K, annealed to 75 K or grown at 14 K), the second one to the irradiation temperature. The thickness of the ice is indicated after. Also shown is the SEY for CO_2 ice from ref. [315].

when deposited at 14 K than when deposited at 75 K [79].

Experiments were done on both regular CO_2 and isotopically labeled $^{13}CO_2$. As for N_2 only the experiments with the isotope will be presented here. Three different phases of the ice are investigated: one where the ice is grown at 14 K and irradiated as is (amorphous ice), one where the ice is grown at 14 K then annealed to 75 K, and one where the ice is directly deposited at 75 K. The latter two are different, which is seen from the fact that CO_2 ice directly deposited at 75 K can be seen with the naked eye on the surface. A 200 ML ice is usually too thin to be visible. Here a very clear and colored square with iridescence is observed. Presumably the ice grown at 75 K is the most crystalline one and this crystallinity is at the origin of this optical property. In the figures to follow, the ices are labeled 14 K or 75 K when they are grown at 14 K or 75 K and "An" when they are grown at 14 K and annealed to 75 K. The second temperature indicated on the figures is the irradiation temperature, which for now will always be 14 K. The thickness dependence was not explored in detail, but sometimes two different thicknesses are made for the same ice phase.

The results for desorption of CO_2 are displayed in fig. V.8. The yields and shape of the curves for all three phases are very close. The yield for the 100 ML ice are slightly lower. The curves are again compared with the SEY results of Kuzucan et al. [315], which have the same maximum at 300 eV. The SEY curve is flatter (higher at high electron energies

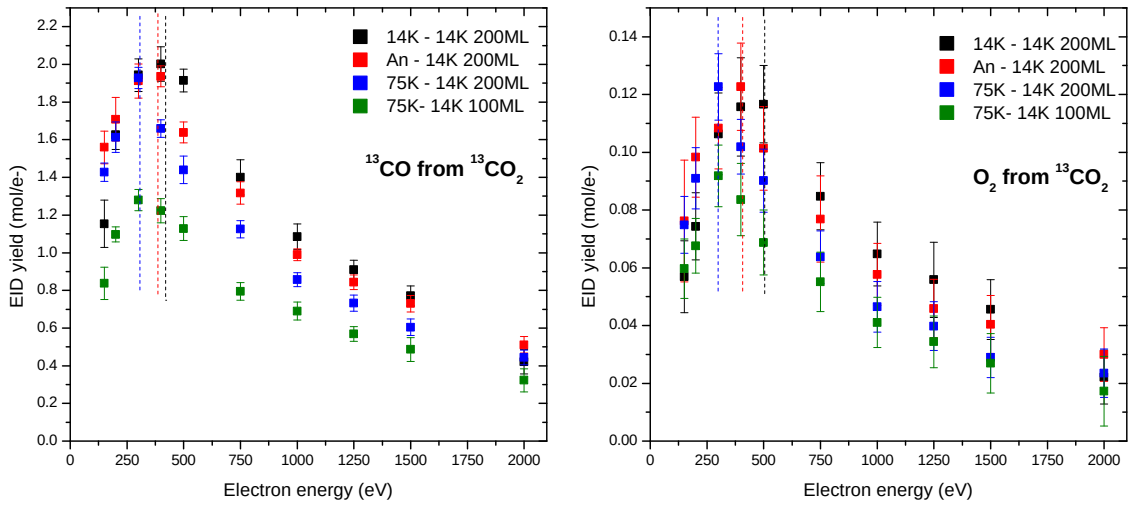

Figure V.9: EID yield of CO and O_2 from CO_2 ice for different structures of the ice. The structures are the same as for the previous figure. For the labels, the first temperature corresponds to the structure of the ice (grown at 75 K, annealed to 75 K or grown at 14 K), the second one to the irradiation temperature. The thickness of the ice is indicated after. The approximate maximum of each curve is indicated by dashed vertical lines.

relative to the maximum) but this is again ascribed to thickness differences, as the SEY was measured for 20 ML. Measurements on CO_2 sputtering with keV electrons do not seem to exist, but some measurements have been made with ions [320, 321]. Again, a quadratic dependence to the stopping power was found (although the number of points is limited).

The reason why we can say CO_2 is an ice for which chemistry and dissociation dominate the desorption is because the most abundant desorbing species is not the parent molecule CO_2 but a product of dissociation, CO. Also observed desorbing is O_2, although the yield is lower. This is consistent with all studies of desorption from CO_2, whether the ones with ions or the ones with VUV photons [200, 310]. The desorption yields of CO and O_2 for the same ices that were presented in the previous figure are shown in fig. V.9. Although the absolute yields do not differ significantly for different structures of the ice (which is consistent with the result of Sie et al. for VUV photons [310]), there is a difference in the shape of the curves. As we go from the more crystalline ice (deposited at 75 K) to the more porous and amorphous one (deposited at 14 K), there is a shift towards higher energies of the maximum (CO: 300 eV for 75 K, between 300 and 400 eV for An, 400 eV for 14 K; O_2: 300 eV for 75 K, 400 eV for An, 500 eV for 14 K).

This effect can also be seen from a different angle by plotting instead the curves of the three desorbing products (normalized arbitrarily for comparison) for either the 75 K ice or the 14 K ice, which is done in fig. V.10. In this figure we see that for the crystalline 75 K ice (left panel), the maximum of the curve occurs basically at the same energy (300 eV) for all three species, despite some differences between the relative intensities. On the other hand, for the porous amorphous 14 K ice (right panel), we see that the maximum is similar as for the 75 K ice for CO_2 but shifts towards higher energies for CO and even more for O_2. Considering the interpretation we have of the EID yield curves, where the

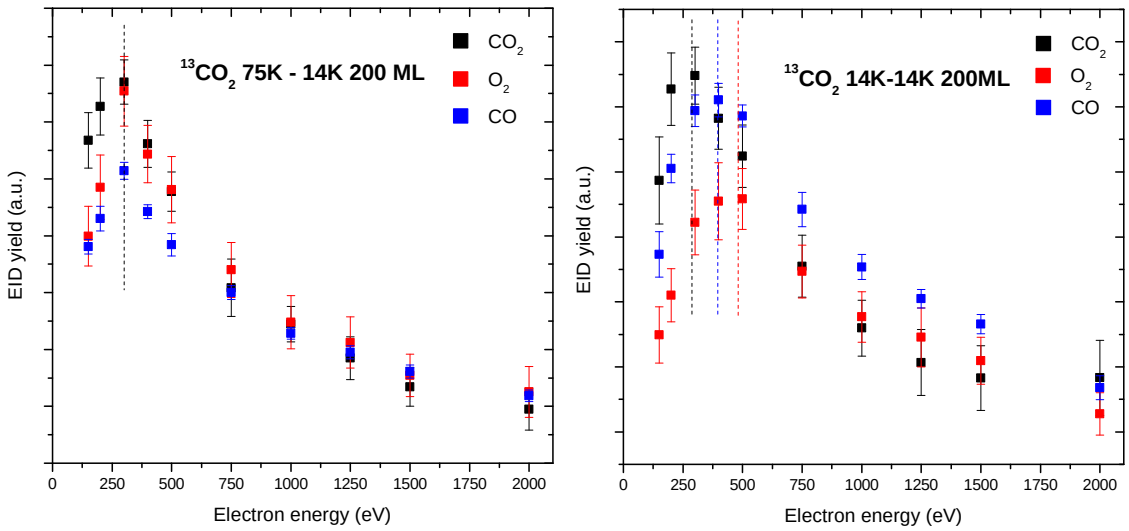

Figure V.10: Comparison between the yields of CO, O_2 and CO_2 for the crystalline (left panel) and the porous amorphous (right panel) CO_2 ices. The approximate maximum of each curve is indicated by dashed vertical lines.

maximum characterizes the depth involved in the desorption process, this means that for the 14 K ice deeper layers are involved in the desorption of O_2 than for CO, and for CO than for CO_2 - but this is not the case for the 75 K ice. This is well explained by considering the desorption mechanisms of these different species. Desorption of CO_2 can involve chemistry but also more direct processes. Desorption of CO is similar: it can desorb directly by dissociation of CO_2 but also reform from chemical processes. As for O_2, the direct dissociation of CO_2 is not likely to yield it and therefore chemistry has to be involved in its formation and subsequent desorption. When the ice is porous and amorphous, radicals formed by dissociation of bulk CO_2 can reach the surface, react and enhance chemistry, which will affect the most, in order, O_2, then CO, then CO_2, considering the weight that chemistry should play in the formation and desorption of these three species. This is why we see this shift in the EID yield curves. Such a phenomenon does not occur for crystalline CO_2 where bulk radicals cannot reach the surface (at least not at 14 K).

Some experiments were also carried out at a higher irradiation temperature (50 or 65 K). While this does not have any significant effect on the desorption of CO_2, there are some changes for CO and O_2. During irradiation at 14 K, there is a transitory regime for CO and O_2 desorption, with a quick rise over the first few tens of seconds and then a slower rise over the first few minutes (for a beam current of the order of 100 nA), towards an asymptotic value that was used in the previously shown curves. This is well explained by the contribution of chemistry and/or multiple step processes (e.g. CO_2 dissociation into CO + O, then excitation of CO and desorption) to the desorption of these species. When the ice is irradiated at a higher temperature (65 K), which is above the thermal desorption temperature of CO and O_2, the transitory regime becomes longer, with a rising time of 10 or 15 minutes. Both transitory regimes are shown in the case of O_2 in fig. V.11. The signal measured at 65 K is orders of magnitude higher. Comparing the yields, however,

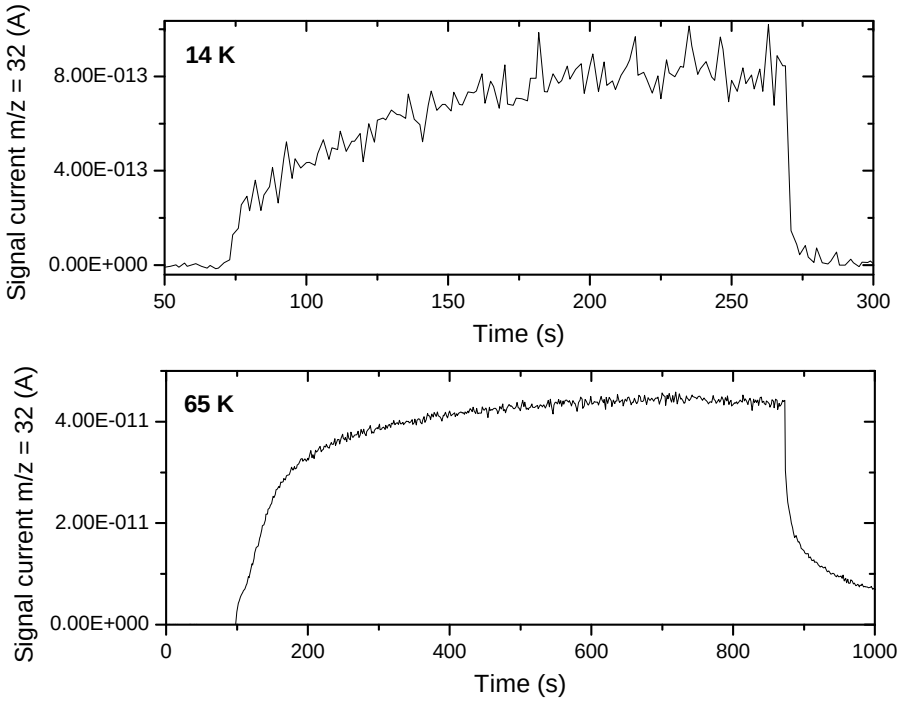

Figure V.11: O_2 desorption signal as a function of time, for a 200 ML crystalline (grown at 75 K) ice irradiated at either 14 K (upper panel) or 65 K (lower panel).

is difficult, because the pumping speed of a species is clearly not the same below or above its thermal desorption temperature, and in this chamber cryopumping is very high. The TPD calibration method only works for the desorption below the cryopumping threshold. It is therefore difficult to say how different the yields are at higher temperatures. This is something that would gain to be explored.

V.2.3 H_2O

Water ice has been discussed already in chapter IV and will be discussed again in chapter VI: it is one of the common threads of this manuscript. The EID yield curve of H_2O from water ice is shown in fig. V.12 for different phases and temperatures of the ice. The same recipe as in SPICES for growing different phases of ice was followed: the ice is grown at 15 K to obtain porous amorphous water (p-ASW), at 100 K to obtain compact amorphous water (c-ASW) and 140 K for crystalline water. The irradiation temperature can then also be varied. It is clear from fig. V.12 that the phase does not have significant effects on the desorption of H_2O. The yields for higher irradiation temperatures are systematically higher, but not by much, as was also found for the VUV range.

The shape of the curves does not look too different from the other ices where secondary electrons dominate energy transport. The SEY of water ice adapted from ref. [323] is also shown on fig. V.12. While the maxima look similar between the SEY and EID curves, the shape are not exactly the same but it is difficult to comment more, especially since our data points are noisy.

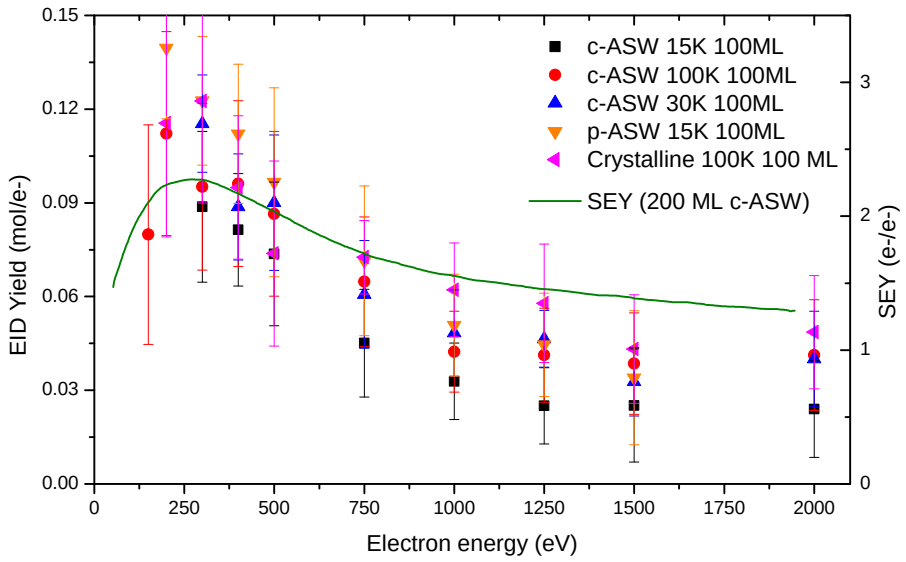

Figure V.12: EID yield curve of H_2O from water ice, for different phases and irradiation temperatures. The SEY from ref. [322] is also shown.

We have also made experiments on D_2O ice, and the results displayed in fig. V.13 that show the EID yield of D_2O from compact amorphous D_2O ice at 15 or 100 K show that the isotope effect we have observed in the VUV range is present here as well. We find the same factor of ~ 5 between the desorption of H_2O and D_2O.

Unfortunately, the set-up is not adapted for the detection of desorbing radicals, as they would react on the walls of the collector before reaching the QMS which is far away. Therefore we could not measure OH and OD desorption and compare them. We did measure the desorption of H_2 and O_2, but we encounter a similar problem as for the desorption of CO and O_2 from CO_2 when the temperature is high: the cryopumping speed which dominates changes a lot and its measurement is complicated, making quantification impossible at temperatures other than 15 K.

Therefore on fig. V.14, only the results obtained at 15 K for the desorption of H_2/D_2 and O_2 from H_2O/D_2O ice are shown, for c-ASW and p-ASW. The shape of the curves are not especially informative at different temperatures anyway. It should also be kept in mind that the desorption of H_2 and O_2 have time dependences as well: the points were taken when the signal had reached a relatively stable value.

The literature on EID (and ion sputtering) from water ice is much larger than for other molecular ices. Only those that look at neutral desorption will be mentioned here, as we have not looked at desorbing ions. Detailed studies of ion sputtering of water by light and heavy ions [319, 324, 254, 36] show, among other things, that the sputtering yield is proportional to the square of the stopping power on a very large range of values. This dependence, which points to a dominating mechanism requiring the cooperation of two different excitations/ionizations, is interesting for us because it is also coherent with the picture developed in chapter IV of chemistry/non-geminate recombination playing an important role in water desorption.

There has been studies of EID by low-energy electrons [325, 326], as well as numerous

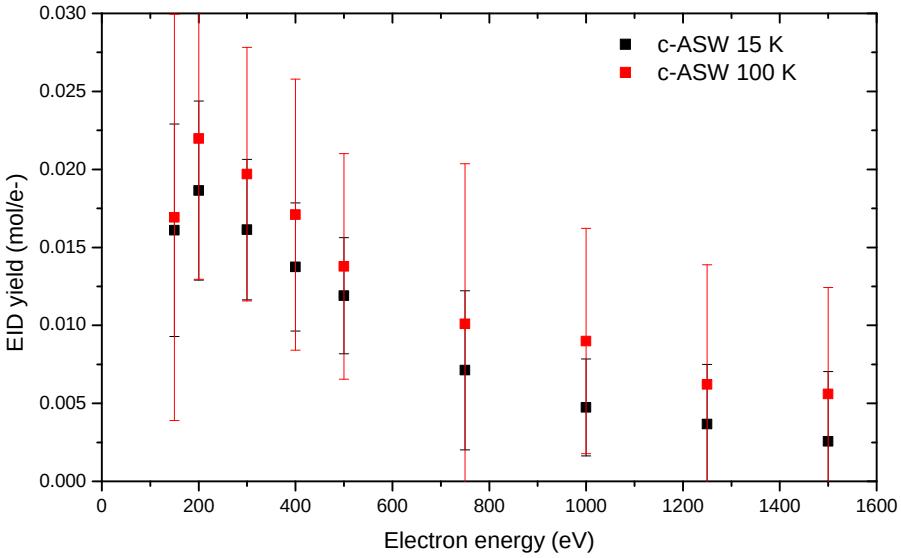

Figure V.13: EID yield curve of D_2O from c-ASW D_2O ice, at two different irradiation temperatures.

studies in the group of Petrik and Kimmel [267, 327, 328], and more recent ones in the group of McCoustra [302, 329], that point to the complexity of the energy transport and chemistry leading to production of H_2 and O_2, in particular (this is not an exhaustive account of the papers published on the topic). Those studies that are quantitative [327, 329] agree with our results at least in the order of magnitude: more precise comparison is difficult because they look at the H_2O loss from the bulk, but with a total estimated loss of 0.5-3 molecules/electron in ref. [327] for 87 eV electrons and 0.1-0.5 molecules/electron for 200-300 eV electrons in ref. [329] we are close to our own numbers. On the other hand, an isotope effect like the one we have seen is not mentioned in these works.

V.3 Relevance of the data to astrophysical and accelerator contexts

The relevance of electron-induced desorption for accelerator vacuum dynamics is relatively straightforward, and has mostly been exposed already in chapter I. Electrons are a particularly important component of the non-thermal desorption processes because of the acceleration of photoelectrons by electric fields that bring them to energies where they most efficiently interact (hundreds of eV). The added issue of electron clouds further stresses the importance of electrons. The relevance of the specific system of thick molecular ices is less obvious: as also mentioned in chapter I it covers relatively fringe cases. However, knowledge on molecular ice systems can certainly be transferred to the case of physisorbed molecules on technical surfaces. The quantified numbers themselves are not necessarily applicable but the ideas are.

In astrochemistry, on the other hand, the relevance of electron-induced desorption is not entirely clear - in particular for the interstellar medium: it is not a non-thermal

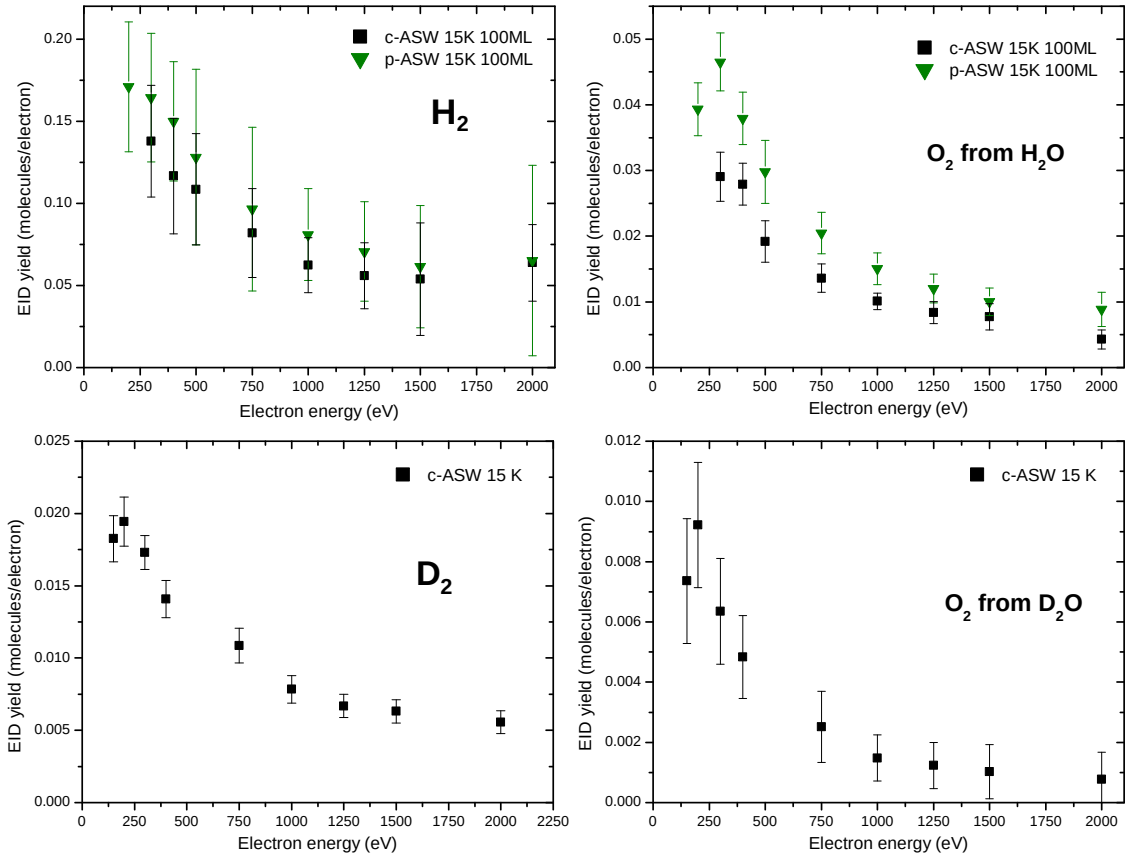

Figure V.14: EID yield curves of H_2 (top left) and O_2 (top right) from H_2O ice for c-ASW and p-ASW at 15 K, and D_2 (bottom left) and O_2 (bottom right) from D_2O ice for c-ASW at 15 K.

desorption process taken into account in models of regions of the ISM. Studies of electron-induced desorption that claim astrophysical relevance usually justify this by the fact that electrons, in particular low-energy electrons, are an important part of the effect that all types of energetic radiations (X-rays, cosmic rays, solar wind and all types of energetic charged particles that can be generated by magnetic effects in space) generate in solids. While this is definitely the case, it is worth asking ourselves whether there could also be directly a flux of electrons hitting ices in some regions of space.

Electrons are part of cosmic rays, but these are very energetic electrons. The "low-energy" part (keV to Mev) of the CR electron spectrum is very poorly constrained: data near the Solar System from Voyager 1 only go down to a few MeV [330]. The local energy spectrum of a given region is, in any case, difficult to infer. At low energies, the electrons interact a lot and are likely to be strongly attenuated, making it difficult for them to penetrate the dense media that are of interest for us. The high energy electrons do penetrate but precisely because they interact weakly: they will not have any significant effect on ices (the desorption yield predicted by extrapolating the stopping power to the MeV region is orders of magnitude lower, and above the MeV energies, the energy loss regime changes as mentioned in chapter II).

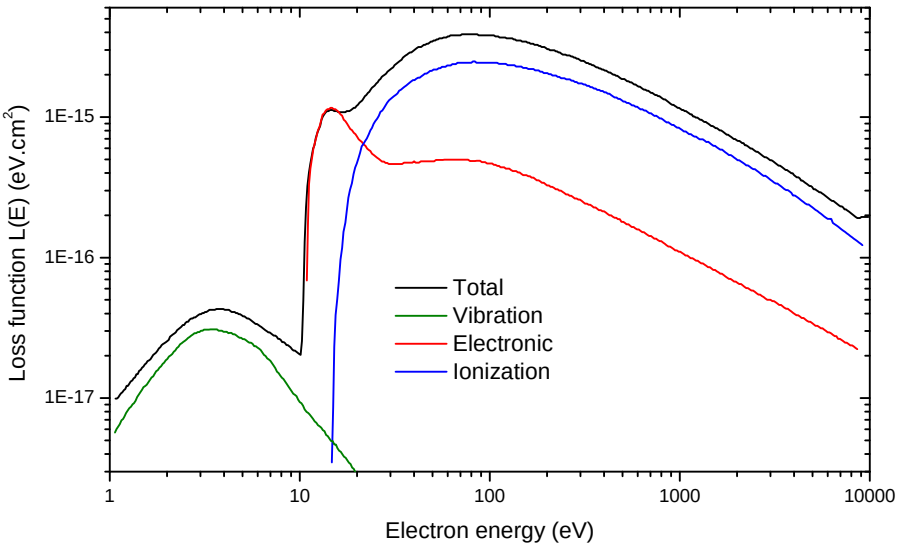

Figure V.15: Loss function of electrons in H_2, as a function of electron energy. The total loss function is displayed in black, and the contribution of vibration excitation, electronic excitation and ionization are displayed respectively in green, red and blue. The curves are directly taken from ref. [333].

There is a large number of electrons in astrophysical media created by a multitude of sources (such as cosmic ray ionization), with a typical density for cold neutral media of $n_{e-}/n_H \sim 10^{-6}$ [331]. However these electrons are thermalized to an electron temperature that does not exceed 10 000 K, i.e. 1 eV.

Instead the potential source of electrons of relevant energies that we need to explore are the non-thermalized secondary ones created in situ by more penetrating types of irradiations that ionize the medium. X-rays (such as the ones created by young stars) will generate keV electrons, while cosmic rays generate electrons of 20-50 eV mean energy depending on the CR energy and type (see e.g. [332]). The problem is whether these electrons will have any opportunity to reach grains. Electrons, contrary to UV photons, interact strongly with the H_2 composing the medium, and will be quickly inelastically scattered to sub-excitation energies, becoming thermalized. Estimating an electron flux spectrum impinging on grains for a given medium is therefore difficult. But the absolute value of the desorption flux induced by electron is not what we want to know in first intent. In terms of desorption, low-energy electrons will compete with the secondary UV photons generated by the same processes (X-rays or cosmic ray ionization and excitation of the medium by inelastic scattering of the secondary electrons), as well as with desorption by the primary X-rays and cosmic rays. Therefore, what we would like to know before going any further is whether electron-induced desorption is more efficient than the other processes linked with cosmic ray or X-ray irradiation of a medium.

First, let us consider the propagation of an electron in an H_2 medium with grains, with a typical grain density ratio relative to H_2 of $n_{grain}/n_{H_2} = 10^{-12}$. The inelastic scattering of the electron is governed by the stopping power dE/dx introduced in section

II.2.4, or equivalently by the loss function L where

$$n_H L(E) = \frac{dE}{dx}$$

The loss function L(E) of electrons in H_2 is shown in fig. V.15, reproduced from ref. [333]. We can see that an electron with an initial energy of a few tens of eV will be inelastically scattered very fast by exciting and ionizing the H_2 medium, until its energy is below $\sim$ 11 eV. For keV electrons it will take longer to reach that energy. Once the electron is sub-excitation for H_2, the inelastic scattering is dominated by the vibrational cross-section which is much lower. The electron can be considered irrelevant for desorption once it is below $\sim$ 6 eV, which is the approximate EID threshold for CO [334] and H_2O [325].

The average length l of medium traversed by an electron of initial energy E before going below 6 eV is given by:

$$l = \int_6^E \frac{1}{dE/dx} dE = \frac{1}{n_H} \int_6^E \frac{dE}{L(E)}$$

The average number of collisions with a grain per unit length, on the other hand, is given by $n_{grain}\sigma_{grain}$ with $\sigma_{grain} \sim \pi a^2 \sim 3 \times 10^{-10}$ cm^2 for a typical grain size a = 100 nm.

The average number of collisions with grains of an electron of initial energy E before going below 6 eV is therefore given by

$$P = \frac{n_{grain}\sigma_{grain}}{n_H} \int_6^E \frac{dE}{L(E)}$$

This calculation discounts the fact that there cannot be more than 1 collision with a grain for the electron, but since P << 1 it is not a problem.

We can calculate instead the average number of molecules desorbed by an electron of initial energy E by incorporating the EID yield Y_i(E) for a given species i:

$$\Gamma_i = \frac{n_{grain}\sigma_{grain}}{n_H} \int_6^E \frac{Y_i(E)}{L(E)} dE$$

Let us consider the case of low-energy (tens of eV) electrons created by cosmic rays. The exact energy does not really matter much because the inverse of the energy loss function is dominated by the 6-11 eV part[a]. The calculation yields P(50 eV) $\sim$ 6 $\times 10^{-5}$. For the yields, I extrapolate the experimental yields from 150 eV to 6 eV by assuming a mostly linear relation, for the arguments discussed before. This approximation is certainly questionable below 20 eV, where resonant structure and new processes like DEA are expected. However, the order of magnitude of the yield for the neutrals should not be wrong. For example, the measurements of EID of CO by 0-30 eV electrons of Rhakovskaia et al. [334] does show that there is a little structure in the yield but that the linear approximation should not be wrong by more than a factor of 2. The result is Γ_{CO} (50 eV) $\sim$ 2 $\times 10^{-5}$ molecules. The photodesorption yield by a typical secondary UV photon spectrum for CO is 3 $\times$ 10^{-3} molecule/photons. Assuming the number of secondary

[a] As a side note, this means that it would be more relevant to directly measure EID in this low-energy range, instead of extrapolating values at 150 eV down to 6 eV as is done afterwards.

photons created by cosmic rays is of the same order of magnitude as the number of secondary electrons (according to ref [29] one ionization event by a cosmic ray creates on average 0.3 UV photons), we see that secondary UV photons should clearly dominate (attenuation of UV photons is mostly due to dust, so we can consider that any created UV photon will encounter a grain with a probability close to 1).

KeV electrons produced by X-rays have a better fighting chance, as the inelastic scattering cross section is (initially) lower, it requires a lot more scattering events before the electron goes sub-excitation, and the EID yield is higher. The calculations yield P(1 keV) $\sim 2 \times 10^{-4}$ and $\Gamma_{CO}(1 \text{ keV}) \sim 1 \times 10^{-3}$ molecules, which is indeed two orders of magnitude higher than the previous number and closer to the UV photon yield. This number does not account for a slight increase in yield that would be caused by the secondary low-energy electrons created during the scattering of the 1 keV electron. However, we also need to take into account that a lot of secondary UV photons are created that way - more than in the case of cosmic-ray ionization. It is therefore likely that the influence of electron-induced desorption will remain lower than photodesorption in this case as well.

These calculations could certainly be much more refined but they already give an idea of how relevant electron-induced desorption is likely to be in interstellar media. It seems clear that the influence of cosmic-ray generated electrons can be neglected, while the case is less clear cut for X-ray generated electrons. Regions where significant X-ray radiation exists are therefore particularly complex in terms of desorption process, with the competition of X-rays, primary and secondary UVs, secondary electrons, cosmic rays, etc... These conclusions are limited to the interstellar medium, but EID could also be relevant in different regions of space: comets and icy moons that are bathed in energetic particles [324].

V.4 Conclusions and perspectives on electron-induced desorption

Conclusions regarding the astrophysical and vacuum relevance of the data have been outlined in the previous section. Quantitative data for the electron-induced desorption of the different species from CO, N_2, Ar, CO, CO_2 and H_2O/D_2O ices have been provided in the 150-2000 eV range. Some quantitative measurements already exist in the literature and seem to agree with our findings, giving confidence in the calibration method used. Our measurements further expand these already existing measurements, in particular in terms of energy range and by probing desorbing neutrals other than the parent molecule. Using this quantified data, I provided an estimation of whether electrons produced by primary cosmic rays or X-rays could compete with UV photodesorption from secondary UV photons. The balance is not in favour of electrons but it could be worth investigating in further details.

The mechanistic discussions in this chapter have been relatively limited, partly because a lot has been said already in previous chapters and because desorption of neutrals by electrons occurs through excitations and ionizations of similar nature as those probed in the VUV range, the main difference being the spatial closeness of successive excitations by a specific electron. It has nonetheless been pointed out that this difference can result in different mechanisms, as seen in the quadratic stopping power dependence of the yield for some species. The exploration of the effect of irradiation temperature on desorption

shows that this parameter does not play a role in the desorption from N_2 and CO. For ices displaying important chemistry like CO_2 and H_2O, irradiation temperature plays an important role in the desorption of volatile products, and a somewhat lesser role in the desorption of the parent molecules, but investigations were complicated by the transitory aspects and the impossibility to properly quantify the results. Deposition temperature did not show any effect for N_2 and CO either - for CO, an effect similar to the one discussed in chapter IV in the VUV range could have been expected. The phase of CO_2 does play a role in desorption, not so much on the yields but on the shape of the EID curve. As for water, there is no effect on H_2O desorption and the results for H_2 and O_2 are again not conclusive. Finally, although mostly thick films have been used, the effect of thinner films on yields and EID curve shape can be rationalized as has been explained above.

The main idea that I have developed in this chapter from a fundamental/mechanistic point of view is that electron-induced desorption can be used as a tool to probe the depth below the surface that is involved in desorption processes, i.e. the scale of transport of energy or fragments/products from bulk to surface. The relation between the shape of the EID yield curve as a function of electron energy, and this desorption-relevant depth, is I think well illustrated in the specific case of Argon. A detailed thickness study on this ice, where a characteristic energy migration length of $\sim$ 100-150 ML is found due to exciton diffusion, showed how the shape of the curve evolves with thickness when that thickness is less than the migration length and limits the EID yield. The experiments where impurities were added into Argon are also good examples of the way the curve is affected by changes of the energy transport scale.

For "semi-infinite" films where the transport scale is lower than the thickness, the EID yield curve becomes characteristic of that transport scale. From then, I concluded that for N_2 and CO at the very least, the desorption-relevant depth ($\sim$ 10 ML) is simply dominated by the scattering length of secondary electrons. However, interesting conclusions are reached for the desorption of CO_2, where the porous amorphous ice displays an increased depth involved in desorption for O_2 and CO compared with CO_2, which is not present for the crystalline ice. The shape of the EID yield curve can be used as a probe of this desorption-relevant depth, indicating transport of energy or species from the bulk to the surface. A detailed thickness study as was done for Ar could do this as well, but thin films measurements are complicated by fast erosion, and the substrate starts becoming relevant and affects the shape of the curve.

It should be possible, if sufficient data of good quality is available on the stopping power and penetration of electrons (particularly low-energy electrons) in the various molecular solids, to develop a more quantitative model of the EID yield curves. It would require some assumptions on the physical processes of transport, though. If such a thing is possible, then it will also require some experimental efforts to obtain EID curves with more points and that extend to a larger energy range. Extrapolation to a wider electron energy range should be possible, considering some dependence with the stopping power for the high energy side using what is known from the literature, and using a linear relation between 150 and 20 eV (or even below but keeping in mind that the approximation is crude), but direct measurements would obviously be preferred if they can be done later. Use of low-energy electrons should be possible in this set-up, although beam characterization has to be properly made and charging of the ice can be a problem. The hard limit on high-energy electrons is 2 keV, but it would be worthwhile to see if obtaining a better

beam shape, and therefore more reliable data, above 1.3 keV can be done.

Chapter VI

X-ray photon-induced desorption

> Reality is that which, when you stop believing in it, doesn't go away.
>
> Philip K. Dick, *I Hope I Shall Arrive Soon*

Photodesorption in the soft X-ray range is a new line of research for the team. All the results presented in this chapter were obtained in 2017 on the SEXTANTS beamline of the SOLEIL synchrotron and constitute a first exploration of the two systems that are of major interest for us: H_2O and CO ice. I will show that the results are interesting from an astrophysical point of view, and that there is a rich physics to be explored, especially for water. New results obtained in 2019 cannot be included in this manuscript but bring complementary information on water and explore new systems such as N_2, NH_3 or CH_3OH.

I mentioned in chapter II that interest in core excitations in the context of the extended DIET community had grown quite a lot in the 80s and 90s. Again most of the focus has been on physisorbed and chemisorbed species on surfaces rather than molecular ices, to the exception of the rare gases (e.g. [335]) and water (e.g. [336]), and some isolated studies on other systems [140, 337]. The concepts and ideas developed in these studies will be of great inspiration here nonetheless.

From the astrophysical point of view, X-ray photodesorption is not a process that is currently considered in models despite the presence of X-rays in regions of the interstellar medium (protoplanetary disks, for example). The literature on experimental investigations relevant to astrophysics (with quantifications and appropriate contextualization) of the process is scarce. Some studies have been made by a Brazilian group [338, 339, 340, 341, 342], but are restricted to ion desorption and done mostly at fixed photon energies. Their studied systems are also more oriented towards organic molecules. Our results on X-ray desorption from water ice were the first published quantification of neutral desorption [55], which we show to be much higher than ion desorption. Very recently, the collaboration of Munoz-Caro and Chen have started investigating X-ray photodesorption as well, with a focus more towards chemistry and formation of new molecules in mixed ices [343, 344].

There is a lot to be explored in X-ray photodesorption, because we do not only have access to desorption of neutrals, but also of ions, and there are plenty of cations and even some anions that desorb. With the set-up we have at SEXTANTS described in chapter III, we can detect all these desorbing species and their photodesorption spectra, but also simultaneously measure the total electron yield (TEY) and therefore have the absorption spectrum of the ice for precisely each scan. For ions, deviations between the TEY and the photodesorption spectrum seem to be common and bring a lot of information on the desorption processes specific to each of them. As this is a "first exploration" of the system, I will for each system interpret the absorption spectrum, look at the inventory of desorbing molecules, and see what can be said on the desorption processes from the available literature and the comparison of the spectra.

A first basic distinction that I will try to make in terms of mechanism is between processes mediated by the Auger electron and the subsequent cascade of secondary electrons, and those stemming from the core-excited molecule in its final state. The former class of processes has been called X-ray induced Electron-Stimulated Desorption (XESD) in the literature, and the latter "true Photon-Induced Desorption" (true PID), so I will keep these terms here. The distinction is schematized in fig. VI.1. Scattering of the Auger electron in the ice creates secondary electrons and secondary excitations, which when they end up near the surface, can trigger desorption. On the other hand, after Auger decay the initially excited molecule is left in a usually highly excited state (2h or 2h1e, see chapter

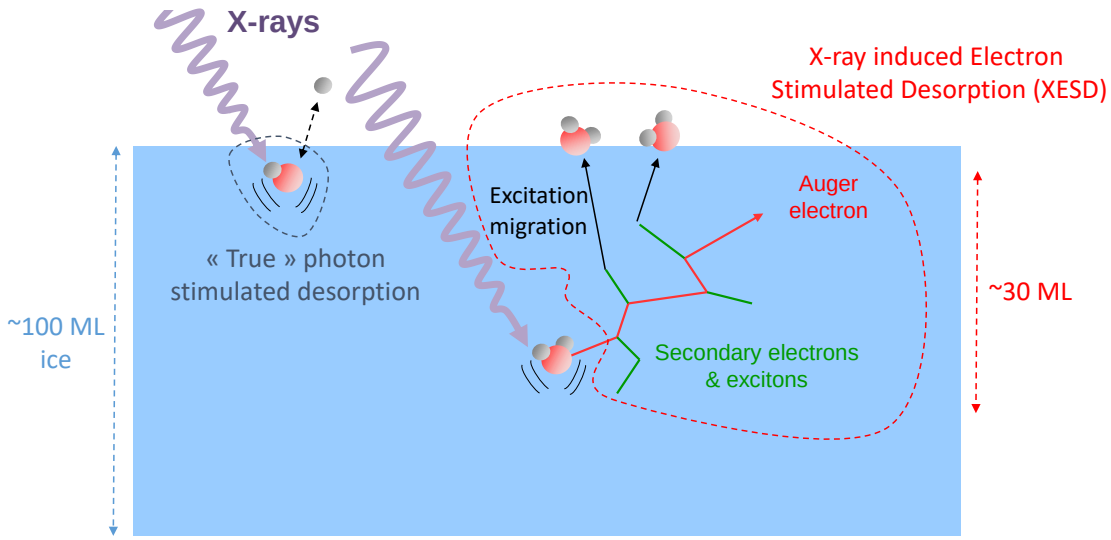

Figure VI.1: The distinction between XESD and true PID. XESD (in red) stems from the scattering of the Auger electron in the ice, which creates secondary electrons (in green) and excitation, that can migrate to the surface. The scattering occurs on a typical length scale of 30 ML. True PID (in blue) stems from the initially core-excited molecule that ends up in a very excited state. The ice here (either CO or H_2O) is about 100 ML thick.

II) and can cause desorption too.

VI.1 H_2O X-ray photodesorption

The first system studied is water ice, for all the reasons already mentioned in previous chapters regarding its importance for various contexts. A lot of the results obtained have already been published or will be published soon in the form of paper III and IV, and therefore this chapter will be relatively short despite the abundance of results because I will only summarize the main ones.

In these experiments, we studied compact amorphous water (c-ASW), i.e. water ice grown at 90 K, with a thickness of 100 ML. We investigated two irradiation temperatures: 15 K and 90 K. No other parameter was varied. We have then looked at the desorption of neutrals, cations and anions. In addition for each scan the total electron yield is recorded simultaneously.

VI.1.1 Ice absorption spectroscopy and structure

The total electron yield curves obtained in our experimental conditions at 15 and 90 K are presented in fig. VI.2. Let us recall that the TEY is assimilated to the absorption of the ice, because each photon absorption event will lead to exactly one Auger electron of a roughly similar energy ($\sim$ 500 eV here) being ejected, and the subsequent scattering and secondary electron cascade will yield the same average number of secondary electrons. The dominant contribution to the TEY are the secondary electrons created by the Auger

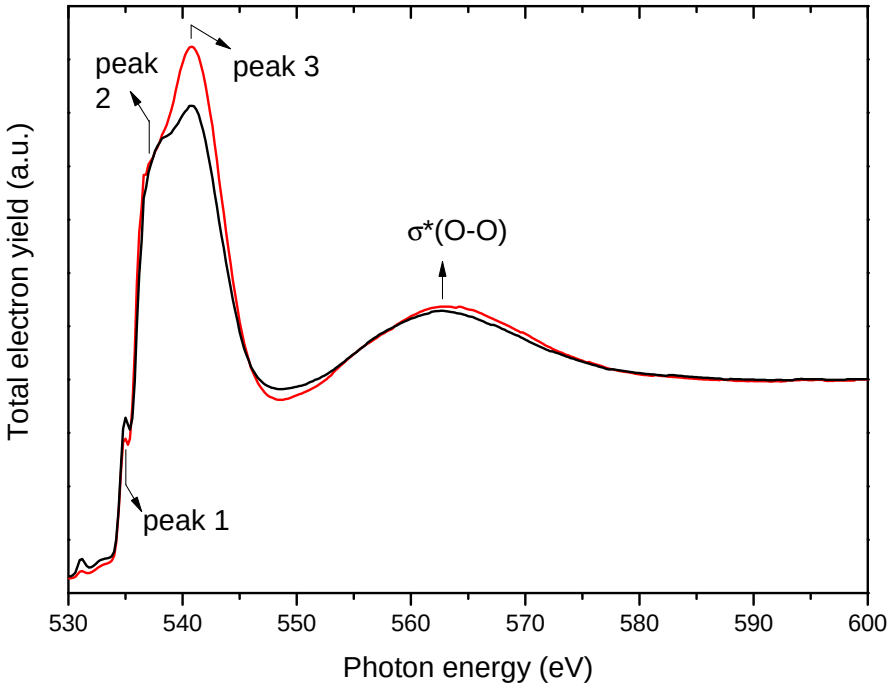

Figure VI.2: Total electron yield (TEY) as a function of photon energy at 15 K (black trace) and 90 K (red trace) from water ice grown at 90 K (c-ASW). The curves have been normalized at 600 eV.

cascade. The probing depth of the technique, corresponding roughly to the radius of the electron cascade, is about 100 Å[345] ($\sim$ 30 ML). The contributions of the bulk of the ice are thus presumably dominant, although the surface roughness of amorphous ice may increase the surface contributions and make the estimation of probing depth more complicated. Since the ice is 100 ML thick, the contribution of the substrate to the TEY is low (and mostly flat). It is worth noting that some low energy electrons could conceivably come from the substrate into the ice, because their inelastic mean free path increases below a few eV, but then they are not likely to overcome the work function and escape into the vacuum.

The electronic structure of water has already been recalled in chapter II and IV, and I will only focus on the specificities of the core-excitation spectrum here. In condensed phase, all spectra of the different forms of water in the core excitation region display three features with varying relative intensities, which I will simply call peak 1, 2 and 3 here for reasons explained below. These are seen on our TEY spectra at 535, 537.2 and 541 eV respectively. The peak at 563 eV is the first EXAFS oscillation (see section II.). On this feature, it is worth noting that although I call it "first EXAFS oscillation", it is close enough to the edge (which is at 537.4 eV in the condensed phase [346, 347]) that it cannot be treated accurately by the simple EXAFS theory. Multiple scattering calculations are necessary [348], and in the last reference Parent et al. chose to call this peak an "intermolecular σ^*(O-O) resonance" instead, which can be defended.

Most early works on water core excitation [349, 350, 348] attributed the first three

features according to the gas phase features, with the first peak being inherited from the $4a_1$ free molecule orbital, the second from the $2b_2$ orbital, and the third corresponding to Rydberg orbitals that are heavily modified in condensed phase because of their spatial extension. This is in line with more recent work [351] interpreting the first peak as a localized state of core-excitonic nature, therefore little affected by hydrogen bonding and inheriting from the free molecule $4a_1$ orbital, while the third one corresponds to a state delocalized along the H-bond network, bearing no relation with the free molecule, but coherent with the solid state notion of a conduction band.

Another interpretation has also been proposed. As mentioned in the introduction, X-ray absorption spectroscopy and related techniques have been used to fuel the debate regarding the structure of liquid water and other forms of condensed water. The interpretation takes into account the fact that in condensed phase, all water molecules are not necessarily equivalent. Even in the crystalline phases, the picture of a non-distorted, tetrahedrally bonded molecule does not hold due to the presence of the surface, various defects, grain boundaries and admixtures of amorphous ice in even the best crystalline samples. Calculations have shown the X-ray spectrum of water to be strongly dependant on the bonding of the molecule [352]. In particular, single H-bond donor molecules (i.e. with a free hydrogen) exhibit different features from fully coordinated molecules. These calculations in addition to considerable amounts of experimental data on various forms of condensed water (see refs [98, 353] and references therein) lend credit to the following interpretation: peak 1 and 2 of the spectra, called pre- and main-edge in these references, gain intensity from weakly coordinated, and in particular single donor (SD) species, while peak 3 (called the post-edge) gains intensity from fully coordinated species. The core difference between this interpretation and the previous one is whether there can be a localized excitation contributing to the pre-edge feature for fully coordinated species in the ice. The transposition of gas-phase peak interpretations to the condensed phase is therefore not so clear, which is why we adopted the labels peak 1, 2 and 3 for this paper.

We will use the second theory as a framework of interpretation of our TEY data. The difference of the spectra at 15 and 90 K (fig.VI.2) can thus be interpreted as follow. We see that at 90 K, the post-edge (peak 3) is more intense and sharper than at 15 K, while the pre-edge (peak 1) is slightly decreased. We can conclude that at 90 K, more fully coordinated species with less distorted H-bond are probed. The ice is grown at 90 K, which yields a compact amorphous structure, and we do not expect cooling it from 90 to 15 K to change that structure. However we are not probing a pristine ice: the high photon flux used modifies the ice, as expected for any type of irradiation [354]. The irradiation should create defects and trapped species that change the local structure, affecting the hydrogen-bond network. The differences between the two temperatures should stem from the fact that at 90 K, the ice more easily regenerates itself, as defects and trapped species can diffuse and molecules can more easily rearrange themselves. This is why more fully-coordinated species with sharper features (peak 3) are observed at 90 K.

In addition to the features of water, some additional peaks can be seen in the pre-edge region, marking the presence of fragments and products of the photo-induced chemistry in the ice. Fig. VI.3 shows the TEY between 524 and 536 eV at either 15 or 90 K. The observed peaks can be attributed to various species other than H_2O created by X-ray irradiation in the ice: we see the O, OH and HO_2 radicals as well as O_2 and H_2O_2. The intensity of these peaks do not change upon further irradiation of the ice, showing that

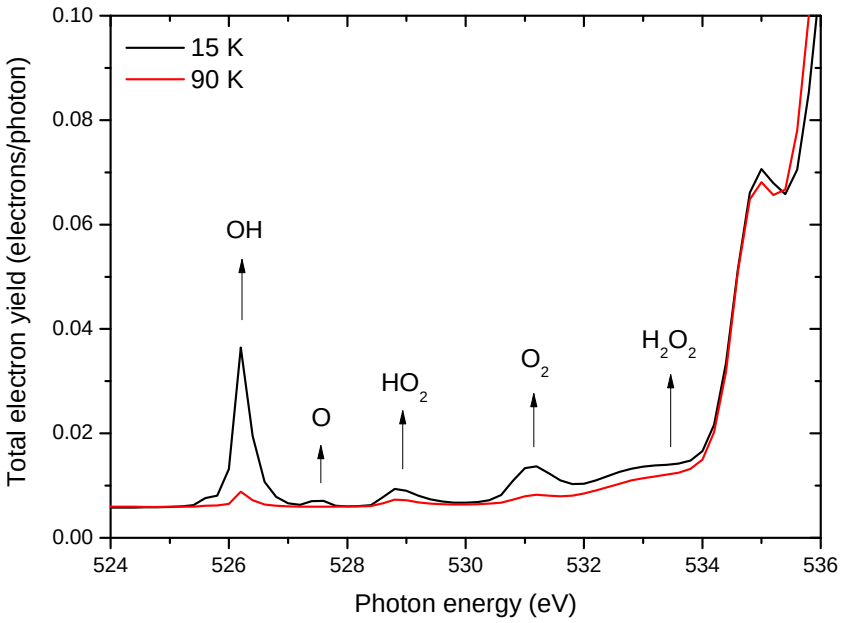

Figure VI.3: Total electron yield (TEY) as a function of photon energy in the pre-edge region at 15 K (black trace) and 90 K (red trace) from a compact ASW ice grown at 90 K. Attribution of the peaks following Laffon et al. [355] are indicated.

we are probing a steady state. In this steady state, Laffon et al. [355] estimated from the peak intensities that these chemical products amount to no more than a few percent of the ice. Pure water ice shows a resiliency to irradiation, i.e. most of the photochemistry occurring leads back to H_2O as the end product. More radicals and products are observed at 15 K than at 90 K: at 90 K the radicals have become mobile and are consumed by chemistry, while O_2 is thermally desorbed. Only H_2O_2 stays relatively stable. The X-ray induced chemistry in the ice is discussed in more detail in paper IV.

VI.1.2 Desorption of neutral species, and astrophysical relevance of X-ray photodesorption

The desorption of neutral species has been developed the most in paper III, with a few additional elements in paper IV.

The neutral species detected in desorption are H_2O, O_2 and H_2, coherent with the results obtained for electrons and UV photons. The spectra of all these species (see paper III and IV) all follow the TEY well. The quantified photodesorption yields at 550 eV are summarized in table VI.1, including the tentative quantification of cations and anions (see section on the quantification). We can clearly see there that desorption of neutrals is far above desorption of ions.

Desorption of neutrals is likely dominated by XESD, as argued in the papers. While definitive proof is not possible, there are some arguments in favour of this conclusion. One is that the photodesorption spectra of neutrals follows the TEY. It is a weak argument, because while an XESD process *necessarily* follows the TEY (electrons created at

Table VI.1: Photodesorption yields (molecules/incident photon) of all detected species at 550 eV from water ice at 90 K

	90 K	15 K		90 K	15 K		90 K	15 K
H_2O	3.8×10^{-3}	3.4×10^{-3}	H^+	1×10^{-4}	4.3×10^{-5}	H^-	1.3×10^{-5}	6.5×10^{-6}
H_2	8.9×10^{-3}	5.3×10^{-3}	H_2^+	5×10^{-7}	1.6×10^{-7}	H_2^-	3×10^{-10}	
O_2	6.3×10^{-3}	4×10^{-4}	H_3^+	2.5×10^{-9}		O^-	1.3×10^{-7}	2.3×10^{-8}
OH	$< 1 \times 10^{-3}$	$< 1 \times 10^{-3}$	O^+	3.6×10^{-8}	2.8×10^{-8}	OH^-	2.2×10^{-8}	6.4×10^{-9}
			OH^+	6×10^{-9}	4.6×10^{-9}	H_2O^-	3×10^{-10}	
			H_2O^+	3×10^{-9}	3.7×10^{-9}	O_2^-	8×10^{-10}	
			H_3O^+	1.2×10^{-8}	1.6×10^{-8}			
			O_2^+	2.9×10^{-8}				
			$(H_2O)_3H^+$	1.9×10^{-8}	2.4×10^{-8}			

different photon energies are undistinguishable and will lead to the same effects, therefore these effects should be proportional to the total number of electrons), it is not *sufficient*: it would make sense for a true PID process to follow the absorption spectrum, as we have mostly observed to be the case for valence excitations in chapter IV. The argument becomes strong when it is reversed and there is a deviation of the photodesorption spectrum from the TEY, signing a true PID process, as we will see for ion desorption. Another experimental argument is that it is possible to estimate the photodesorption yield per *absorbed* photon (see paper III for the details), with a result of 0.2 H_2O molecules per absorbed photon. This is very close to what we found for EID of H_2O (chapter V) at 500 eV (0.1 H_2O molecules per incident electron). The EID yield at 500 eV is more or less what we would expect the contribution of XESD to the X-ray photodesorption yield to be. Therefore it is at least possible to say that possible true PID processes do not have a contribution to the yield that is not much larger than XESD.

XESD dominating for neutral desorption is sensible in the picture we have of how the energy of the initial photon is distributed in the ice. Most of the energy of the initial photon goes into the Auger electron and therefore into the secondary events, which suggests they should dominate desorption. Putting it in numerical terms, since there is one true PID event for 20-25 secondary events (single ionization + creation of a secondary electron that can cause one valence excitation), if all those events have similar partial cross sections for desorption (within an order of magnitude), then the secondary events will obviously dominate. For this to be true, we need the secondary events to be energetically sufficient to lead to desorption. Desorption of neutral species has a threshold around 8 eV for UV photons, which is an upper limit for electrons (which could also for example excite a lower triplet state of water). Therefore "simple" valence excitations are sufficient to cause desorption. Valence ionizations are apparently less efficient (see chapter IV) but can cause desorption as well. This means first that secondary electrons are energetically able to desorb neutral species, and second that the single ionization events which dominate the inelastic scattering of the Auger electron can cause desorption of neutral species as well. The only way true PID could dominate in such a case is if the true PID process, involving the highly excited initial molecule, is much more efficient than these "simple" excitations to desorb molecules. I do not see a reason to believe this, and the comparison of the PID yield per absorbed photon with the EID yield at 500 eV does not lend credit to this hypothesis.

We can also compare the efficiency of the X-ray photodesorption process to the UV process. In the UV range, at 10 eV we can estimate a yield of 8×10^{-3} H_2O molecules per *absorbed* photon. X-ray photodesorption is therefore more efficient in this sense, with 0.2 H_2O molecules per absorbed photon, but if we consider instead the yield per deposited eV in the ice we obtain roughly the same numbers (8×10^{-4} desorbed H_2O molecules per eV in the UV range and 4×10^{-4} desorbed H_2O molecules per eV in the X-ray range, which considering all the sources of errors is reasonably close). This is consistent with the picture developed above of domination of secondary events in the X-ray range that are of the same nature as the primary events in the UV range: the fact that the yield per eV is lower in the X-ray range can even be explained by the lower efficiency of ionization (compared with valence excitations) to desorb molecules. Since photodesorption of neutral species is likely dominated by secondary valence excitations, as explained above, the question of the desorption mechanisms is the same problem as for UV photodesorption and the same

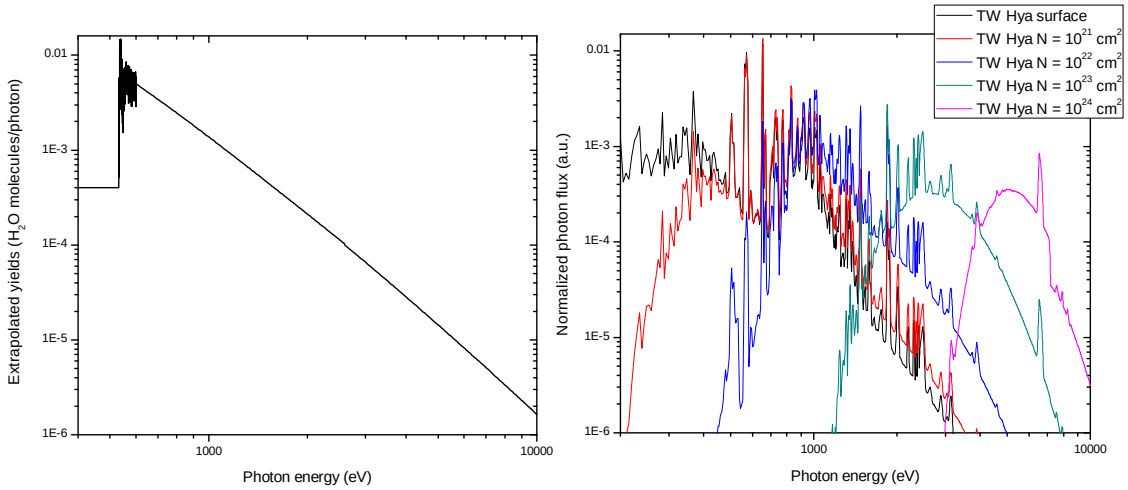

Figure VI.4: **a.** Photodesorption yield of H_2O from c-ASW at 15 K extrapolated up to 10 keV and down to 200 eV. **b.** X-ray emission spectrum of TW Hya adapted from [30] and spectra of the same spectrum after attenuation by different column densities N of dust and gas (see text). All spectra have been normalized for comparison.

possibilities discussed in chapter IV apply.

Let us now turn to the astrophysical relevance of these results. Neutral desorption is the most important for astrophysics since they are the most abundant desorbing species by a large margin. The question is then whether X-ray photodesorption has an impact and how to implement it in astrochemical models. This is developed in detail in paper III.

The photon energy range that has been used in this work (520-600 eV) is much smaller than the typical spectrum of an astrophysical object - in astrophysical models spectra usually go up to 10 keV, and the spectrum of a young star has significant intensity up to several keV. Our data therefore needs to be extrapolated. Fortunately this is not too hazardous: above 600 eV and up to 10 keV, (i) we can consider that the photodesorption yield of neutrals will follow the absorption spectrum, as it does near the edge, (ii) the absorption cross-section of the ice can be approximated by the gas phase cross section, because well above resonance the transition is almost entirely atomic O 1s in character and is not perturbed by the environment (except for the weak EXAFS oscillations), and (iii) up to 10 keV the absorption cross-section is dominated by the core ionization process by a photoelectric process (Compton scattering becomes important above 10 keV). Below 520 eV, the extrapolation is more complicated to make because the process is no long core excitation/ionization, but as we will see later this region is hardly relevant anyway. The result of the extrapolation of the photodesorption yield of H_2O, using the gas phase absorption cross section of H_2O from ref. [356], is shown in fig. VI.4a.

The second problem to consider is what the spectrum of photons hitting the ice grains in a typical environment will look like. Measured X-ray spectra of, for example, young stars of protoplanetary disks (e.g. TW Hydrae [30]) exist, but because the X-ray spectrum spans such a large photon energy range, the photons will be attenuated with a very different cross section depending on their energy. Soft X-ray photons (<1 keV) are much

Table VI.2: Average photodesorption yields of intact water (H_2O molecules per incident photon, c-ASW at 15 K) for the X-ray spectra of TW Hydrae at different attenuations.

	Average photodesorption yield
TW hydrae spectrum	$2.3 \pm 1.2 \times 10^{-3}$
$n_H = 10^{21}$ cm^2	$2.5 \pm 1.3 \times 10^{-3}$
$n_H = 10^{22}$ cm^2	$1.2 \pm 0.6 \times 10^{-3}$
$n_H = 10^{23}$ cm^2	$1.2 \pm 0.6 \times 10^{-4}$
$n_H = 10^{24}$ cm^2	$1.2 \pm 0.6 \times 10^{-5}$

more heavily attenuated than harder ones. The spectrum therefore depends on the column density of gas and dust between the star and the regions of icy dust grains. In order to estimate the impact of attenuation, I used the attenuation cross-sections of ref. [357] and the above mentioned measured spectrum of TW hydrae and calculated the X-ray spectrum for different column densities of gas. The result is shown on fig. VI.4b (an example with another type of X-ray spectrum is shown in paper III supplementary materials).

Using the extrapolated energy-differentiated photodesorption yields and the calculated spectra, a weighted averaged photodesorption yield for a given column density of gas can be calculated (this is the same calculation that was presented in section IV.3). The results in table VI.2 show that the yield indeed decreases quite a lot when the column density becomes high. This is a conclusion similar to the one reached in chapter IV, where taking into account attenuation of photons above 11.2 eV in the VUV range sigificantly affected the average photodesorption yields. It emphasizes yet again the importance of considering the local photon spectrum.

A rough estimation introduced in paper III shows X-ray photodesorption has the potential to be relevant in parts of a protoplanetary disk. The comparison is made between X-ray photodesorption, UV photodesorption and cosmic rays desorption in a part of the disk where UV photons of the star have been completely attenuated and the remaining X-rays compete with cosmic rays and cosmic-ray induced UV photons. The estimation was made by taking data from the T Tauri star model of protoplanetary disk physico-chemistry of Walsh et al. [358, 359] for the fluxes and densities. This shows that the X-ray photodesorption process is at least worth taking into account in models to see what kind of impact it could have, and our results open the way to such an implementation.

VI.1.3 Desorption of ions

Results on the desorption of ions from water ice are the focus of paper IV. This part will mostly summarize the most interesting findings that came out of the investigation of the different ions.

The ions I will talk about here are H^+, H^- and the oxygen fragments (O^+, OH^+, H_2O^+, O^- and OH^-). A discussion of the desorption of protonated clusters $(H_2O)_nH^+$ can be found in the paper as well. The following parts will be largely similar to the corresponding sections in paper IV with a number of reformulations, but are presented here in the main text because they are worth highlighting.

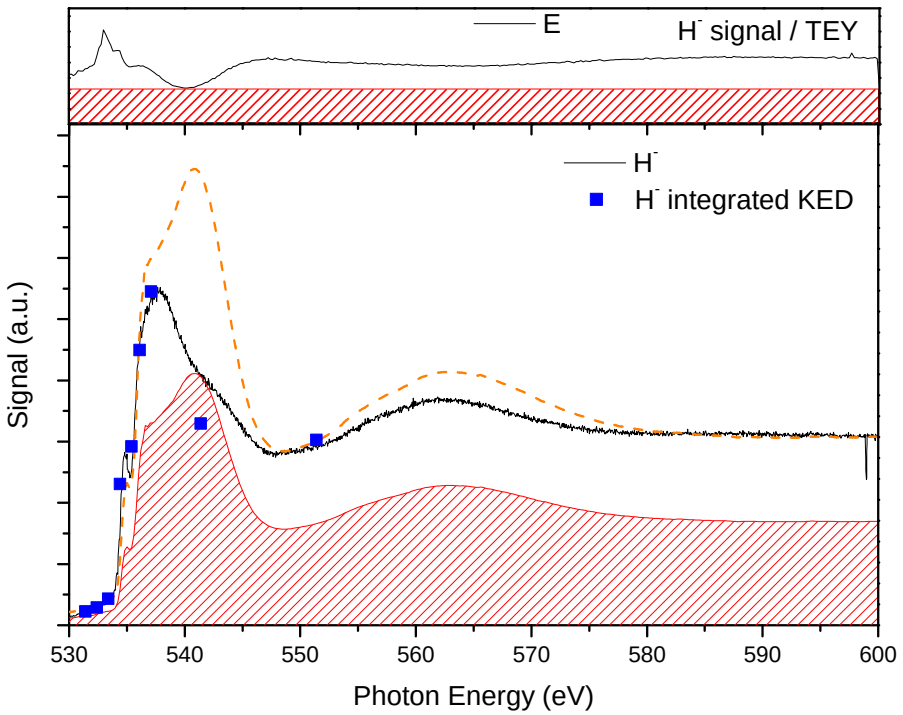

Figure VI.5: Photodesorption spectrum of H^- at 90 K, at the maximum of kinetic energy (black trace). In blue dots the integrated KEDs of H^- at 90 K are indicated. The TEY is indicated twice with two different normalizations, by the dashed orange trace and the hashed red area. The inset above represents the H^- signal divided by the TEY. The red hashed area constrained by the minimum of this curve corresponds to the maximum contribution of XESD to H^- desorption.

VI.1.3.1 H^- desorption

The photodesorption spectrum of H^- at 90 K is shown in fig. VI.5. This is a spectrum taken at the maximum of the kinetic energy distribution of H^- (around 6 eV). The TEY is represented twice, in orange dashes fitting the H^- spectrum above 580 eV and as a red hashed area under the H^- curve. The deviations of the H^- spectrum from the TEY are clear. They remain clear in the integrated kinetic energy distributions (KEDs) indicated in blue dots on fig. VI.5, and are therefore not an effect of kinetic energy filtering. From these deviations we can already estimate the maximum contribution of XESD to H^- desorption: this is the purpose of the red hashed TEY and of the inset above the figure, which represents the H^- signal divided by the TEY. Since the contribution of XESD to desorption necessarily follows (spectrally) the TEY, in this representation the contribution of XESD is a flat line and it is constrained by the minimum of the curve. The hashed red area is the maximum contribution of XESD to desorption and represents 60 % of the signal. The corresponding area is shown in the main figure as well.

In consequence, true photodesorption processes represent at least 40 % of H^- desorption (with varying contributions depending on the photon energy). A true photodesorption process means that the initially core-excited molecule is fragmented into one

anion and highly charged cation fragments. Such processes have been observed in the gas phase (e.g. [360, 361, 362] for water), but are minor dissociation pathways compared with fragmentation involving only neutrals and cations. Electrons on the other hand can induce anion desorption by processes such as dissociative electron attachment (DEA), which is specific to electron excitation, and ion-pair dissociation. These processes have been studied extensively [363, 364].

If we compare H^- photodesorption to the TEY represented by the dashed curve in fig. VI.5, we see that intensity is mostly missing in peak 3 and in the EXAFS oscillation. This means that the true PID processes must be less efficient there. Interestingly there is a lot of H^- signal above the edge that cannot be explained by XESD (see the inset of fig. VI.5), meaning that even when the final state is a 2h state, there are dissociation pathways leading to anions. We could have expected 2h1e final states to be more likely to yield anions than 2h states but it does not seem to be the case. Another explanation is needed for the specific spectral regions where desorption of H^- is suppressed. The common point of peak 3 and the EXAFS oscillation is that they are linked with the coordination shell of the molecules: peak 3 has been interpreted as having intensity deriving mostly from four-coordinated molecules. This means that the fully coordinated, bulk molecules do not efficiently lead to anion desorption by true PID processes.

VI.1.3.2 Oxygen fragments desorption

Our estimated desorption yields for oxygen-bearing fragments are much lower than H^+(table VI.1). The observation of low yields of oxygen-bearing fragments (O^+, OH^+, H_2O^+) desorbing from water ice is a common feature of not only soft X-ray irradiation [336], but also XUV irradiation [366] and medium energy (100-200 eV) electrons [367]. Studies of anion desorption by dissociative electron attachment (DEA) of low-energy (<20 eV) electrons on water ice also reported very low O^- and OH^- desorption signals [368]. Explanations for these low yields have been suggested before, as summarized in paper IV.

Looking at the spectrum of these oxygen fragments brings interesting information on the mechanisms of desorption, supporting some hypotheses on the low desorption yields. The photodesorption spectrum of O^+ at 90 and 15 K is represented in fig. VI.6. The spectrum is evidently completely different from the TEY. What we see are two peaks at 533.5 and 536.1 eV in the spectrum at 90 K, and two additional peaks at 531.2 and 539.7 eV at 15 K. The two peaks in the spectrum at 90 K can be attributed to H_2O_2 resonances, as seen from the gas phase spectrum represented on the figure (shifted to match the first peak). The first peak of H_2O_2 is visible in the TEY and was already attributed above. The two additional peaks at 15 K can be attributed to O_2 resonances: again the first one is clear in the TEY at 15 K and had already been attributed before. The ion desorption yield of O^+ from condensed O_2 is shown in the figure.

This spectral information shows that the desorption of O^+ is dominated by direct excitation and dissociation (therefore a true photodesorption process) of products of the photochemistry, which are present only at the few percent level in the ice. We cannot exclude that the concentration of photoproducts is higher at the surface than in the bulk, because diffusion of radicals, and the subsequent chemistry, can be different at the surface. Still, considering the relative abundances, the desorption of O^+ through excitation of these photoproducts must be much more efficient than through XESD or direct excitation of

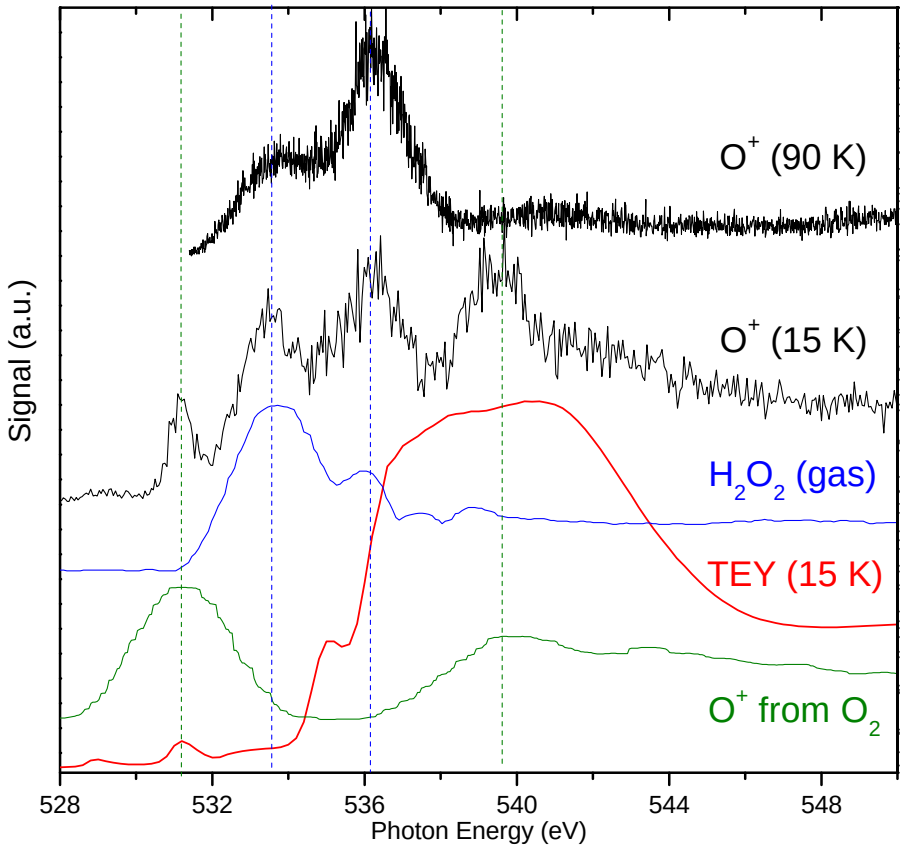

Figure VI.6: Photodesorption spectrum of O^+ at 90 K and 15 K. Also shown: the TEY at 15 K (red trace), the gas phase core absorption spectrum of H_2O_2 (blue trace), adapted from ref.[365] and shifted to match the H_2O_2 first peak, and the O^+ ion desorption yield from pure O_2 ice adapted from ref. [140].

H_2O.

This strong contribution of H_2O_2 (and O_2 at 15 K) is also seen in the desorption spectra of the other oxygen-bearing fragments, OH^+, H_2O^+, O^- and OH^-. All the figures are shown in paper IV. The details of the spectra for each ions differ: for H_2O^+ and OH^+ for example, contributions of water to the spectrum are still visible, and the anions have other specificities. Here I will discuss this common point of photoproducts contributing much more to the desorption spectra of these ions than H_2O.

What we suggest is that a lot can be explained by simply considering kinetic energy partition between the fragments during dissociation. For dissociation of an isolated molecule, momentum conservation implies that the part of the available energy that goes into kinetic energy of the fragments is partitioned such that the energy going to a given fragment is proportional to 1 - m_f/m_p, where m_f/m_p is the ratio of the masses of the fragment and the parent molecule. In the condensed phase this is only an upper limit because of the surrounding molecules constraining movement. In dissociation of an isolated water molecule into two fragments H and OH (regardless of their charge), momentum conservation implies that the H fragment takes away ∼94% of the kinetic energy, and

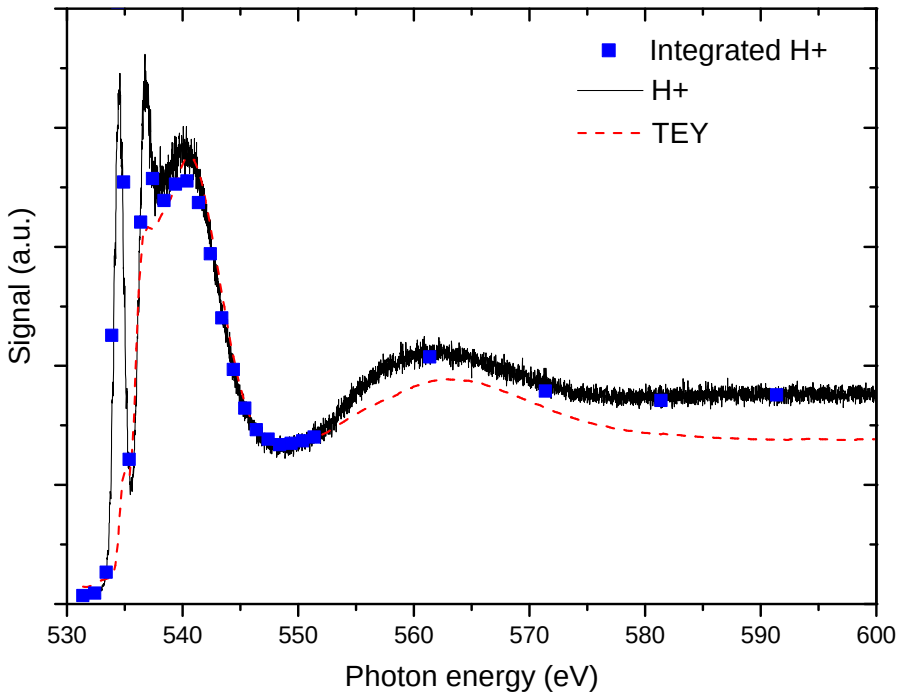

Figure VI.7: Photodesorption spectrum of H^+ at 90 K, at the maximum of kinetic energy (~ 7 eV) (black trace). The blue dots correspond to integrated kinetic energy distributions of H^+ taken at different photon energies. The TEY is shown in dashed orange.

little is left for the oxygen-bearing fragment. In the case of dissociation into three fragments, the symmetry of the molecule also plays a role: it has been observed in Coulomb explosion of molecules that the central atom has much less kinetic energy because the recoil energy of the peripheric fragments compensate[369]. This would be the case for dissociation of H_2O in H + O + H. Low kinetic energy implies that the ion will not be able to overcome the desorption barrier. If we consider now H_2O_2 and O_2, we see that dissociation will rupture an O-O bond and yield fragments of almost similar masses, so that a roughly equal partition of the kinetic energy can happen. We could expect at least some oxygen-bearing fragments from dissociation of H_2O_2 to have enough kinetic energy to desorb, whereas those originating from dissociation of H_2O would not, explaining the experimental facts. More details are given in paper IV: other factors should also be taken into account, to explain the different weight of the H_2O and H_2O_2 in the different oxygen fragments for example.

VI.1.3.3 H^+ desorption

As can be seen in table VI.1 from the estimated yields, H^+ is by far the most abundant desorbing ion, and in consequence it is the only one that has really been studied so far (in desorption by core-excitation of water ice). The photodesorption spectrum of H^+, at the maximum of the kinetic energy distribution (we will see later that this is important) is shown in fig. VI.7, along with the TEY for comparison and points corresponding to integrated kinetic energy distributions of H^+ taken at fixed photon energies. The

latter allows to show that the spectrum we show, which is a kinetic-energy differentiated spectrum like all of those we take for ions, is not significantly biased compared with the integrated spectrum, except perhaps near the first intense peak.

The interesting aspect of this spectrum is the way it deviates from the TEY. Where peak 1 would have been expected at the threshold of absorption, we have instead a much more intense and red-shifted peak which I will call peak 1', at 534.4 eV. There is also a more intense and sharper peak 2 at 536.8 eV. Above 550 eV, there is also a difference with the EXAFS oscillation appearing shifted of about 1 eV, and a different slope in the continuum (which could be the reason for the apparent shift of the EXAFS peak). The first study on H^+ desorption by Rosenberg et al. [349] already noticed the intense peak 1' and the deviation above 550 eV. They first suggested that the differences should arise from the electronic signatures of surface molecules, that should differ from bulk ones because of the differences in coordination. They performed an EXAFS analysis of bulk ice from the electron yield, but could not achieve a similar analysis on the H^+ data, concluding that it was not possible to obtain the O - O distance at the surface because processes like XESD also contributed to H^+ desorption in the continuum.

A lot of work afterwards focused on the interpretation of peak 1'. Detailed investigations in the group of D. Menzel [336, 370, 371] gave access to a lot of information. The surface origin of peak 1' is reinforced by the observation that the intensity of this peak saturates at 2-3 ML thickness, while the rest of the spectrum only saturates above 40 ML, suggesting an important bulk XESD contribution (∼50 % according to the authors). Peak 1' also displays an interesting polarization dependence, with an intensity peaking for a polarization normal to the surface and disappearing for a polarization parallel to the surface. The detailed interpretation is complex, because this is not the behaviour expected for maximization of transition probability of molecules with an H bond pointing outwards. H^+ ions in general show an angular distribution peaked towards the surface normal. Overall the interpretation strongly points towards peak 1' originating from the surface molecules, with a dangling O-H pointing roughly normal to the surface. In Coulman et al. [336], they suggested an "ultrafast" dissociation mechanism associated with peak 1': ultrafast dissociation, which has mostly been studied in the gas phase, corresponds to the dissociation of a molecule within the lifetime of the core hole, before Auger decay takes place (see e.g. [372] for a review).

Interesting insight was brought by the work of Mase et al. ([373, 374] and references therein). Their apparatus allows to do coincidence studies for surface processes. At fixed photon energy (controlling the initial state), the desorbing H^+ ions are detected in coincidence with the Auger electron. This is a powerful technique because the energy of the Auger electron contains information on the *final* state, i.e. which orbitals are involved in the 2h or 2h1e final state. Their results for photon energies other than peak 1' (above or below continuum) show that the most probable final states (from the intensity of the different peaks in the non-coincidence Auger spectrum) are those involving the non-bonding orbitals $1b_1$ and $3a_1$, which makes sense because they are the shallower ones. If we label NB the nonbonding orbitals and B the bonding ones ($1b_2$ and $2a_1$), the intensity of the final states goes in order $(NB)^{-2} > (B)^{-1}(NB)^{-1} > (B)^{-2}$. This order is reversed for the coincidence spectrum: more H^+ are produced by $(B)^{-2}$ final states than by $(NB)^{-2}$ final states, despite the lower probability of obtaining the first ones. This is sensible as well: removing electrons from bonding orbitals increases the probably of dissociation

of the excited molecule, yielding H^+ fragments. If the initial excitation is in peak 1', however, no particular preference for any final state is seen in the coincidence spectrum of Auger electrons. This is interpreted as follows: what happens for this resonance is *not* ultrafast dissociation, because no trace of Auger decay of the OH fragment is observed in the spectrum, but there is still a "fast" dissociation process in which the O-H bond is significantly elongated during the core hole lifetime. This will lead to dissociation and H^+ ejection no matter what the final state of the excited molecule is, because the dissociation has already started in the initial state. This last conclusion is also the one reached in the later papers from the Menzel group [371].

This picture is further confirmed by our measurement of kinetic energy distributions of H^+ ions at peak 1' and elsewhere. The KED at peak 1' is significantly narrower with a lower maximum (see paper IV). This is explained by the fact that the KED reflects the potential energy surface of the state(s) that led to desorption: in the case of peak 1', most of the kinetic energy of the ion is already acquired on the PES of the core excited state, while elsewhere the KE is acquired on the PES of the final state. There is a multitude of final states that yield different kinetic energies for H^+ [255, 256], explaining the broader distribution.

VI.2 CO X-ray photodesorption

Experiments on the X-ray photodesorption of CO ice were conducted at the SEXTANTS beamline in the vicinity of the O 1s threshold. CO was a natural choice both because it is the second most important molecule in astrophysical ices, and a common vacuum pollutant, and because it has been well investigated by the team in the VUV range, opening the possibility of comparisons. The energy range and experimental conditions were similar to those described for the experiments on H_2O: we prepared a 100 ML thick ice deposited at 15 K and irradiated between 520 and 600 eV, monitoring the TEY, the desorption of neutral species on the Balzers QMS and cations and anions on the Hiden QMS. Because CO ice charges up and is chemically modified much more than water ice, we used lower photon fluxes: $\sim 7 \times 10^{11}$ ph.s^{-1} for most of the scans, although some were done at higher flux. This did not hinder the sensitivity as on the other hand the desorption yields were higher.

A consequence of the chemical modifications is that the nature of the ice evolves a lot after several scans, meaning that the ice has to be renewed more frequently and that interpretations have to take into account the alterations. Therefore I will first discuss the information we can obtain on the modifications of the ice through the evolution of TEYs. Next I present the results on neutral species, then those on ions. The section on ions is subdivided again: first I discuss the charging and ageing effects and their consequences on ion desorption, then I present the mass spectrum of cations where a plethora of species were observed, and finally I discuss the spectral signatures of selected cations, plus the one of O^-, the only anion observed with significant intensity. Afterwards, I use these results to discuss X-ray induced photochemistry of solid CO as it is revealed by these experiments in comparison to the existing literature. I also discuss the astrophysical implications.

VI.2.1 Effects of the irradiation: TEY evolution

In order to interpret the absorption spectrum of solid CO near the O edge, as obtained from the TEY measurements, let us first look at the spectrum of gas phase CO in this region. A moderate resolution EELS spectrum of CO between 530 and 560 eV, taken from Hitchcock et al. [375], along with high resolution photoionization spectra in specific regions taken from Püttner et al. [376], are shown in fig. VI.8. As in the case of H_2O, the attributions of the near edge in the gas phase are relatively straightforward since the peaks consist in well-spaced transitions of an electron from the 1s to the empty orbitals. Here the transitions are also vibrationally resolved, indicating that the core-hole states are bound. The first and strongest feature is the $1s^{-1}\pi^*$ resonance (1σ-2π transition), centered at 534.4 eV. The 2π orbital is the only empty valence orbital of CO, as all the above-lying states are already of Rydberg character. The bottom left of fig. VI.8 is a zoom onto the π^* resonance with well-resolved vibrational peaks. On the bottom right of fig. VI.8, we see the promotion of a 1s electron to the Rydberg orbitals, with many different states attributed on the figure and again resolved vibrational peaks. The ionization potential is 542.54 eV and we see clearly the convergence of the Rydberg states to it. We also see on the top panel of the figure that the continuum is not featureless: there is a strong bump at 550 eV which is a shape resonance [375]. The weak feature at 556 eV and possible even weaker shoulders higher in energy are not discussed in the

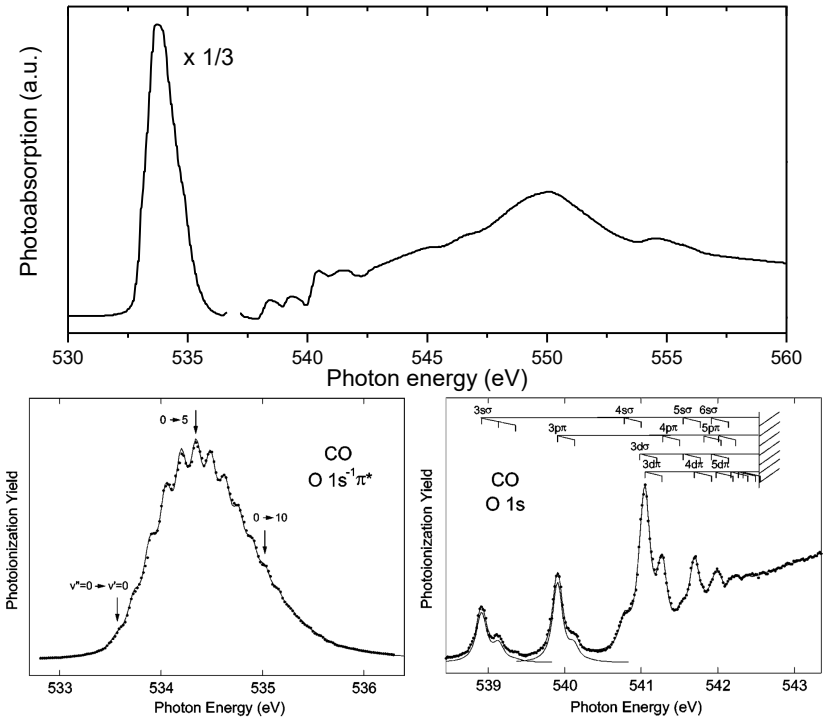

Figure VI.8: Photoabsorption spectrum of gas phase CO in the O 1s region. The top panel is an EELS (electron energy loss spectrum) giving an overall view at moderate resolution between 530 and 560 eV, taken from Hitchcock et al. [375] (figure adapted from ref [137]). The bottom right and left panels are high resolution photoionization spectra taken from Püttner et al. [376]. On the bottom left is the $1s^{-1}\pi^*$ resonance, and on the bottom right are the Rydberg transitions up to the ionization continuum.

literature on CO absorption. These do not seem to be artifacts as we also find them in our TEY measurements for solid CO. The most simple attribution is multielectron features. Above threshold, resonances are often traces of doubly-excited states (2h2e, with a core hole and a valence hole). Such features were clearly observed, with well-resolved numerous 2h2e peaks corresponding to Rydberg progressions towards an excited core ionized state, in the continuum after the C edge of CO [377]. However they occurred closer to the edge, only a few eV above threshold. Here a resonance about 17 eV above threshold should correspond to more highly excited states, or to 2h1e states (shake-up). A shake-up peak has been observed in an XPS experiment on gas phase CO [378] around 16 eV above the main peak, and it is the most intense shake-up peak. This seems to correspond well to the observed peak in absorption.

Turning now to solid phase CO, on fig. VI.9 is presented the absorption spectrum of CO condensed at 15 K obtained from measuring the TEY of a freshly grown ice. The spectrum for solid CO was reported in the photodesorption study of Rosenberg et al. [140], which had a low spectral resolution ($\sim$ 8 eV) and where most of the peaks seen here could not be resolved. Jugnet et al. [379] have imaged the $1s^{-1}\pi^*$ resonance for chemisorbed, gas phase and solid CO, showing the exact match of the energy and width of the peak for solid and gas phase CO - which is what we have used to cross-check the

absolute energy scale of our spectra. A TEY spectrum of solid CO up to 560 eV was also shown in a DIET conference proceedings [380]. Many X-ray studies have been made on CO chemisorbed on various surfaces [139, 379, 381, 382], but the spectra obtained are quite different from the bulk CO one.

First, it is worth mentioning that even the first scan made on a fresh ice already probes a slightly modified ice, as was the case with water. But contrary to water ice, CO ice does not reach a chemical steady state during the irradiation, as the chemistry occurring does not in majority lead back to CO. Instead much more complex species based on carbon chains can be formed. I will come back to this later. On the top panel of fig. VI.9, although it is faint with this scale, peaks at 527.4 and 531.2 eV can be attributed to atomic O and molecular O_2, just like in water ice, signs that some photoproducts have already started to accumulate. Therefore even in this spectrum any faint peaks should be considered with caution before attributing them to CO features.

With that said, the spectrum of solid CO resembles a lot to the gas phase spectrum. A strong resonance centered at 534.4 eV corresponds to the $1s^{-1}\pi^*$ transition. Although the vibrational bands are not as well resolved on our TEY, superimposing the gas phase $1s^{-1}\pi^*$ resonance from ref. [376] and ours (with a minor shift of 0.15 eV of the absolute scale) shows a perfect match, confirming the result of ref [379]. The core electronic state must therefore not be very much modified when going from the free to the condensed molecule. In the region where transitions to the Rydberg orbitals used to be in the gas phase (539 - 542 eV) we see a series of more or less well resolved bumps. There is a clear one at 539.9 eV, another at 544.7 eV, and at least two shoulders around 541.4 eV and 543.4 eV, with possibly more broader peaks contributing here. As expected, the Rydberg states become very broad peaks in the condensed phase, and it is difficult to say much more about the nature of these peaks, as the way the electronic states are modified is not really clear. Contrary to the π^* resonance, no vibrational structure is observed, but considering the width of the peaks it is difficult to say if this is simply due to all the peaks overlapping or to a real modification of the electronic states. Contrary to the gas phase, the ionization threshold is not visible: it occurs in the gas phase at 542.4 eV and should be lower in the condensed phase for the arguments developed in chapter II (as mentioned in chapter IV, the first IP of CO is red-shifted of ∼1.5 eV in the VUV region). Overall what we observe in this region is very reminiscent of what is observed in the 10-15 eV region of the condensed CO spectrum: conversion of Rydberg states to blue-shifted broad peaks with the ionization threshold not visible somewhere in the middle. Since most these peaks are above the IP, they can no longer be treated as "Rydberg states" or as Wannier excitons. It should be noted that in ref. [380], it is suggested that the peak at 544.7 eV is in fact a multiple scattering oscillation. The presence of shoulders in the red side of this peak was not observed in this reference due to insufficient resolution, but this does not necessarily preclude the possibility of one or more peaks being multiple scattering features. I do not see an a priori argument for clearing the attribution of this peak. Lastly we observe a large peak at 550.5 eV and a more faint one at 556 eV, with possibly very weak additional features at higher photon energies (560-570 eV). Since these peaks are also present in the gas phase, it is sensible to attribute them in the same way: the 550 eV peak is a shape resonance as well, and the weak features correspond probably to multielectron excitations. The existence of corresponding features in the gas phase shows that these are not EXAFS oscillations.

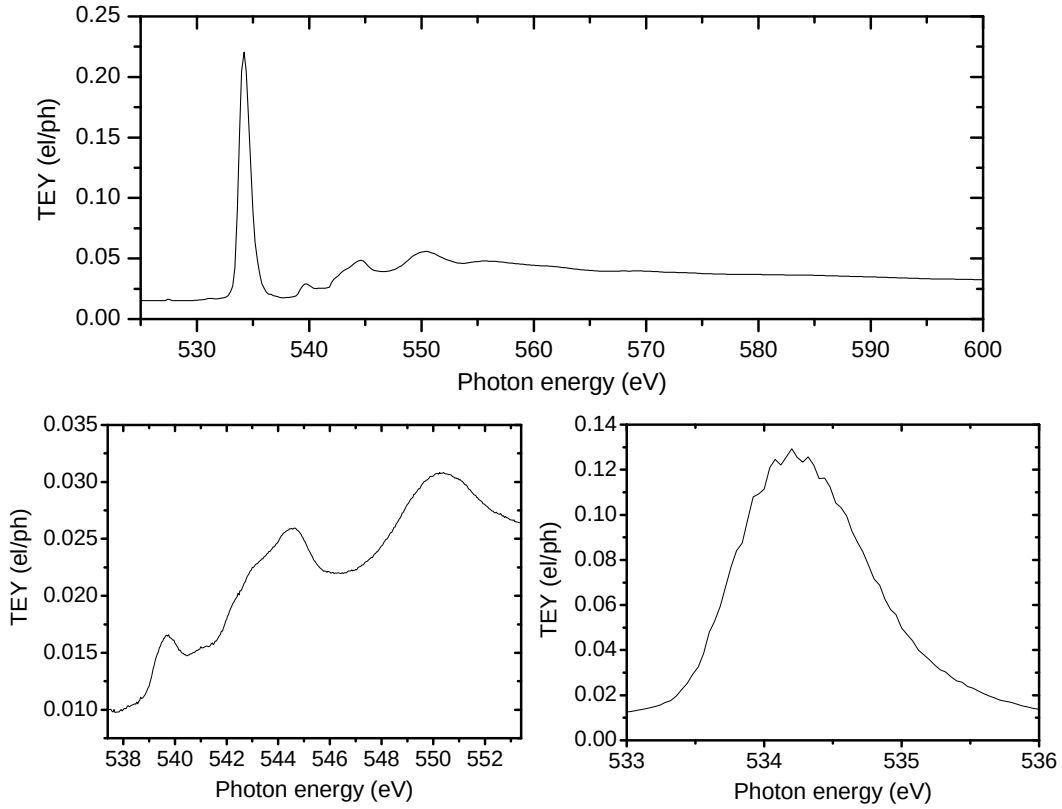

Figure VI.9: Photoabsorption spectrum of solid CO, measured with the TEY. The top panel shows the whole spectrum from 525 to 600 eV, taken with a positive value on the extractor of the Hiden QMS which increases the absolute value of the TEY (in electron per photon) relative to the field-free value. Bottom panels are scans made with more scan steps on specific regions of the spectrum, recorded with negative values of the extractor (which is why the absolute TEY value do not match with the top panel). The bottom right panel is a zoom onto the 533-536 eV region (π^* resonance) and the bottom left panel is a zoom onto the 537-553 eV region. Attributions are made in the text. The spectral resolution of the light is ∼80 meV.

Contrary to the case of water ice, the TEY evolves with the photon dose received, a sign of the chemical evolution of the ice. This is shown in fig. VI.10. In fig. VI.10a, the TEYs of four successive scans (photon dose $\sim 2 \times 10^{16}$ photons.cm^{-2} per scan) on a fresh ice are shown, along with the TEY of an ice that received a very high photon dose (total dose difficult to estimate as this ice was used for testing various things). In fig. VI.10b the TEYs of sixteen successive short scans (photon dose $\sim 4 \times 10^{15}$ photons.cm^{-2} per scan) on a fresh ice are shown. We see on fig. VI.10a that the overall shape of the TEY changes with photon dose: (i) the $1s^{-1}\pi^*$ peak decreases, (ii) the baseline increases and (iii) the various features in the 539-550 eV region become progressively blurred, and are almost lost for the high dose ice. In addition, small peaks corresponding to the photoproducts

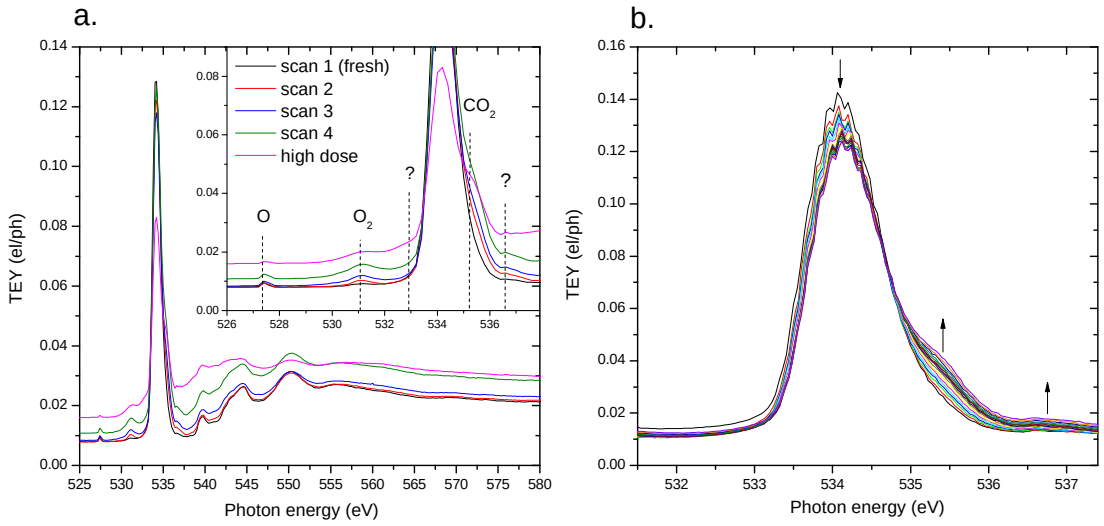

Figure VI.10: Evolution of the total electron yield (TEY) of solid CO with photon dose. **a.** Total electron yield for four consecutive scans on an initially fresh ice (scans labeled 1 to 4), photon dose $\sim 2 \times 10^{16}$ photons.cm^2 per scan, and total electron yield of an ice having received a much higher photon dose ($> 2 \times 10^{17}$ photons.cm^2; scan labeled "high dose"). The inset is a zoom in the region where photoproducts peaks can be seen. These peaks are attributed on the figure. **b.** Total electron yield for sixteen consecutive short scans on an initially fresh ice, photon dose $\sim 4 \times 10^{15}$ photons.cm^2 per scan. The arrows indicate which peaks increase or decrease during irradiation.

increase in intensity (some attributions are made in the inset of fig. VI.10a). As mentioned previously, two of these peaks, at 527.4 and 531.2 eV, can respectively be attributed to atomic O and molecular O_2. We see in fig. VI.10b in more detail the growth of two other peaks, one at 535.2 eV and a smaller one at 536.6 eV. The first one, in the right shoulder of the π^* peak of CO, can be attributed to CO_2 (based on the gas phase position of the π^* resonance of CO_2 [383]), which is therefore the main product of the chemistry in the ice. The second one, on the other hand, cannot be easily attributed. We can rule out the possibility of a second peak corresponding to O, O_2 or CO_2, as none of the other peaks of these species are expected in this region. But the variety of molecules combining carbon and oxygen that can be formed is very large, as we will see later. It is also possible that this single peak corresponds to the absorption of a class of several similar molecules. According to the other evidence we have from desorption and other photochemistry experiments in the literature (to be discussed in the next sections), the most likely candidates are C_2O and C_3O_2, and possibly also C_3O. At high enough photon dose, another peak at 533 eV appears on the left side of the $1s^{-1}\pi^*$ resonance that is not visible on fig. VI.10b but can be slightly discerned in fig. VI.10a (it is also much more visible in fig. VI.16 to be introduced later). Similarly there is no obvious attribution for this peak, which could also correspond to C_2O or C_3O_2, or other species of this kind. None of these molecules, which are not easily isolated in normal conditions, have available core excitation spectra, so that a definitive attribution is not possible. The progressive blurring of the features in the 539-550 eV region is also certainly due to the fact that the other species will contribute

in this region with other broad features and their ionization continuum. This blending of peaks prevents any specific attribution in this region. Another possible contribution to the changes of shapes observed in this region is the fact that all these states, whether they are inherited from Rydberg states, multiple scattering peaks etc, are naturally sensitive to the environment, due to their spatial extant. When the chemical evolution becomes significant they could be intrinsically affected (we will see later that it is probably not the case).

I made no attempt to quantify these photoproducts peaks as was done in the literature in the case of water. From the evolution of the TEYs, it is clear that the ice does not reach a steady state, at least not before a very high dose of photons. Photoproducts such as CO_2 and O_2 accumulate in the ice, at least up until the photon doses of $\sim 1\times10^{17}$ photons.cm^2 that correspond to the successive scans of fig. VI.10. For ices having received a very high photon dose the peaks of the photoproducts become blurred and it is not completely clear that their intensity has evolved much. The evidence that the ice still evolves then comes from this blurring of the features and the increase of the baseline.

VI.2.2 Desorption of neutral species

The photodesorption spectrum of the CO neutral molecule from solid CO in the O 1s region is shown in fig. VI.11. This spectrum was taken for an ice that had already been irradiated several times, but not to very high doses (scan 4 of fig. VI.10)[a]. Overall the spectrum, which is compared to the TEY (recorded simultaneously) on the figure, matches well with the absorption. There are some discrepancies (at the initial baseline at 525 eV and around 570 eV), but as often for neutral desorption there can be difficulties in background signal substraction that lead to artifacts in the spectrum. Still, the main features such as the $1s^{-1}\pi^*$ resonance and its CO_2 shoulder, the O_2 peak, the edge/post-edge region and the shape resonance are all recognizable and match with the TEY in relative intensities (although there seem to be some glitches in the signal around 540 eV). The inset shows a finer scan made around the $1s^{-1}\pi^*$ resonance, where we can see the slight vibrational features. Here background issues definitely hinder the comparison between TEY and photodesorption spectrum.

The other species that we could observe desorbing at low fluxes is CO_2. Fig. VI.12 shows three photodesorption spectra of CO_2: the first one was taken on a fresh ice, the second one immediately afterwards on the same ice, and the third one on another ice, that had been highly irradiated. Except the $1s^{-1}\pi^*$ resonance and its shoulder, the features of the absorption spectrum are hardly recognizable because of the noise. The spectrum still probably follows the TEY. We can see evolutions in the spectra with photon dose: from the first to the second scan, the desorption yield at the resonance more than doubles. The yields in the continuum, whether at 525 eV or 600 eV, increase as well (of a similar factor at 600 eV: more than doubled). Therefore the accumulation of CO_2 (and/or other species) in the ice has a strong influence on its desorption yield, suggesting a several step process (rather than immediate desorption of CO_2 upon formation). In the third scan, the yield at the resonance decreased, but so did the TEY (see the behaviour of highly irradiated ices in fig. VI.10). The yields at 525 eV and 600 eV, on the other hand, increased.

[a]Unfortunately it turned out that this is the only viable spectrum we have recorded for neutral CO desorption.

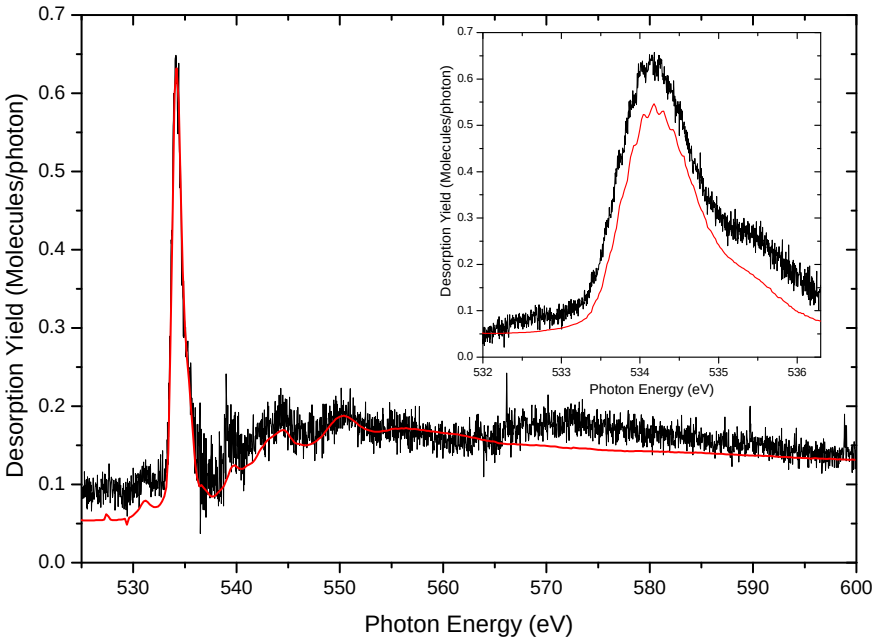

Figure VI.11: Photodesorption spectrum of neutral CO from solid CO near the O 1s edge. Added for comparison is the TEY (red line, normalized so as to roughly match the photodesorption spectrum). This ice had already received a photon dose of $\sim 6 \times 10^{16}$ photons.cm^2. Inset: photodesorption spectrum around the $1s^{-1}\pi^*$ resonance, from another ice. The vibrational structure is resolved. This ice had already been significantly irradiated ($> 1 \times 10^{17}$ photons.cm^2).

We also attempted to see the desorption of other neutral species by increasing the flux a lot, using $\sim 1.4 \times 10^{13}$ ph.s^{-1}. With this much higher flux the ice rapidly changes, and the experiment was done on an already irradiated ice. The only new species we could unambiguously observe was C_2O, shown on fig. VI.13 - or at least we saw a signal increase on mass 42. We could not observe O_2 desorption, but this channel was rather noisy, which does not give a very low constraint on the desorption yield ($< 1 \times 10^{-3}$ mol.ph^{-1} at the $1s^{-1}\pi^*$). C_5 was looked for and not found either. The detection of a mass 42 signal is clear despite the noise: the $1s^{-1}\pi^*$ is visible and the increase above the background at the beginning and end of the scan is unambiguous. It could however come from the cracking of other, bigger species in the QMS that were not detected here (e.g. C_3O_2). Desorption of neutral species other than CO were explored in ion sputtering [384] as well, and these authors observed CO_2, O_2, but also C_2, $(CO)_2$ and O. We did look for desorption of atomic O and C, but these mass channels are noisy and the cracking of CO in the ionization chamber of the QMS dominates the signal. After correction for the cracking, no clear signal was left.

The absolute photodesorption yield of neutral CO in the O 1s edge region is high (more than an order of magnitude higher than H_2O for example), but not that much higher than the yield of CO in the VUV region (see section IV.1.1). This is, of course, explained by the

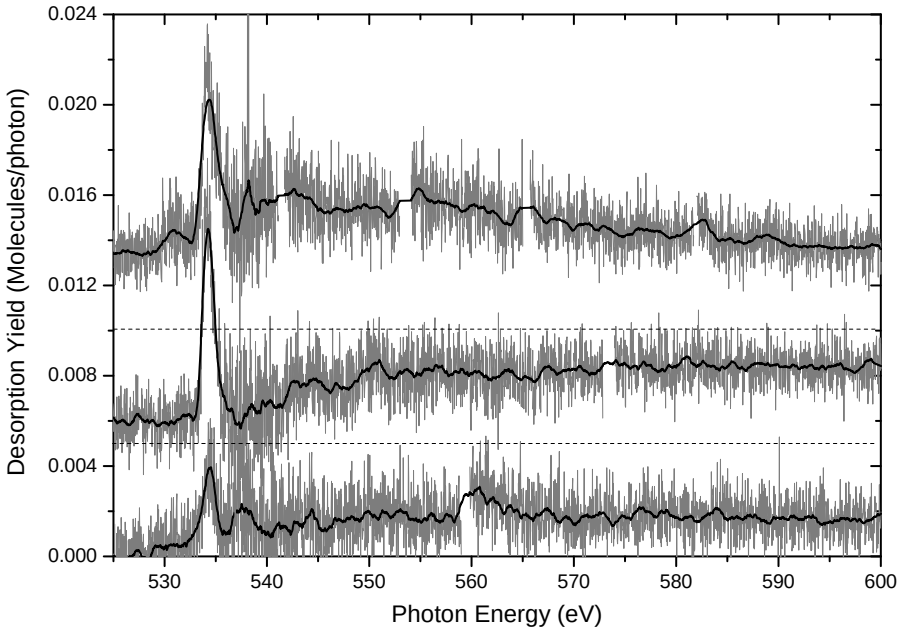

Figure VI.12: Photodesorption spectrum of neutral CO_2 from solid CO near the O 1s edge. Spectra for three different ices are presented (in grey is the raw data, the black line is a smooth). They have been vertically shifted for clarity; their baseline is indicated by the dashed lines. The bottom spectrum is for a fresh ice, the middle one was done immediately afterwards, and the upper one was done on another ice, that had already received a high photon dose ($> 3 \times 10^{17}$ photons.cm^2).

much lower absorption cross-section of core-electron excitations compared with valence-electron ones. We can therefore instead derive the photodesorption yield per absorbed photon as was done for H_2O in the previous section (see paper III for the details). Here, I will consider an absorption cross-section at 600 eV of 6×10^{-19} cm^2, which is the value for gas-phase CO [356] (as was the case for H_2O, condensed phase measurements do not exist, but the cross-section in this region is mostly atomic in nature anyway, and little influenced by the environment). The characteristic depth involved in photodesorption can be taken as $\sim$ 30 ML, which is the approximate mean free range of the Auger electron. This already presumes that CO desorption is dominated by the Auger cascade, and the electrons are the main carrier of energy - we saw in the VUV section on CO that there is no energy transport on long scales in solid CO. The yield per incident photon at 600 eV is ~ 0.15 mol.ph^{-1}. Therefore the yield per absorbed photon in the O 1s region is 8.4 molecules per absorbed photon. For the $A^1\Pi - X^1\Sigma^+$ transition I found a value of about 1 desorbed molecule per absorbed photon, so an order of magnitude less. This is rather similar to what was found for water. It is also worth noting that this value is very similar to the yields I found for electron-induced desorption from CO ice (see section V.2.1).

The absolute photodesorption yield of neutral CO_2 from solid CO is initially around 1×10^{-3} molecule per incident photon at 600 eV and goes up to 4×10^{-3} after some irradiation. There is therefore almost two orders of magnitude between the yields. This is also completely coherent with the values I found for CO_2 desorption from solid CO in

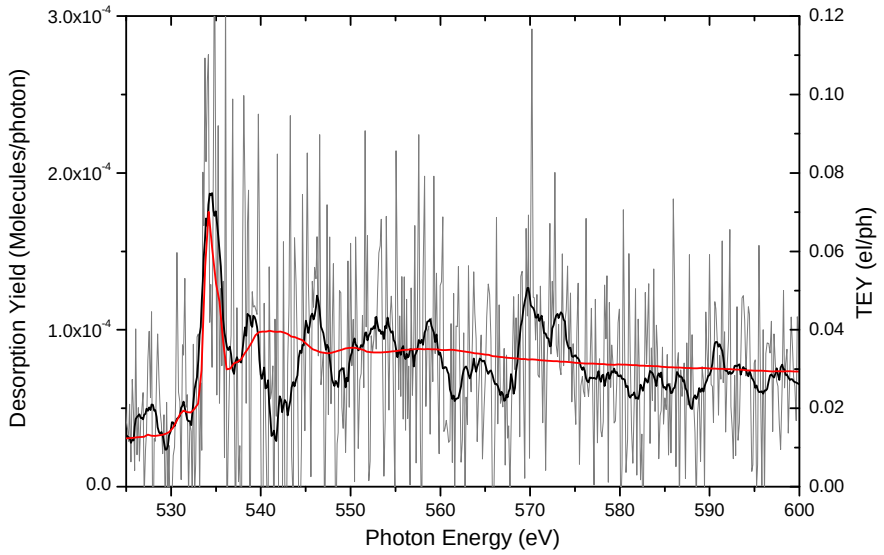

Figure VI.13: Photodesorption spectrum of neutral C_2O from solid CO near the O 1s edge. In grey is the raw data, the black line is a smooth. The TEY (red line, normalized so as to roughly match the photodesorption spectrum) is also shown for comparison. This ice had already been irradiated with a high photon dose and the scan was done with a high photon flux: $\sim 1.4 \times 10^{13}$ ph.s^{-1}.

electron-stimulated desorption. On the other hand, CO_2 desorption is not observed during the VUV irradiation of solid CO, although small amounts are formed in the ice. This highlights the main difference between an energy region where desorption and effects on the ice are limited to mostly non-dissociative valence excitations, and one where ionization and dissociation readily take place.

The photodesorption spectra of the species observed here follow the TEY (although this is mostly well visible for CO, the other spectra being noisy). This was also observed in ref [380] for desorption of neutral CO from solid CO, but also for desorption of neutral CO, O and C from chemisorbed CO on metal surfaces [385] (although in that case the mechanisms could be different). Therefore arguments similar to those developed for H_2O can be made for domination of XESD in the desorption process. The comparison between the yield for EID at 500 eV (section) and the yield per absorbed photon here shows a good match. The explanation that secondary electrons have sufficient energy to generate the "simple" valence excitations that are sufficient to desorb CO (as seen in VUV excitation) also holds. In fact, for CO, measurements of EID of neutrals for low energy electrons exist [334] and show a threshold at $\sim$ 6 eV (corresponding to the lowest lying excited state $a^3\Pi$, which is accessible by electron excitation). It is therefore straightforward that these secondary electrons, along with the primary Auger electron, which carry most of the energy of the initial photon, will dominate the desorption yield of at least neutral CO, and probably the other neutral species as well.

VI.2.3 Desorption of ions

VI.2.3.1 Ice charging and ageing

Before examining ion desorption in details, it is necessary to say a few words about issues intrinsic to these measurements that were encountered. One first "problem" is ice ageing, which was already mentioned previously. It is a problem in the sense that the system we study evolves with time/photon dose, which makes it less well defined and makes the study more complex, but at the same time it is also an object of study in itself since it is part of the interaction of ices with photons. We already saw how the TEYs give information on the evolution of the ice and how the photodesorption yield of neutral molecules can change with photon dose. The same is true for cations and anions: we expect ageing to change the yield with photon dose and therefore possibly bias the relative intensities of features on the spectra, etc.

However, there is another problem that is more specific to ion desorption: ice charging. We already mentioned this phenomenon in previous sections. While ice charging has not been a significant issue when studying water, here we have evidence that it has visible effects on the measurements. First, ice charging, because it changes the potential at the surface of the ice, can change the desorption yield of ions, which are sensitive to this potential. Another even more important problem is linked with the fact that we have a kinetic energy filter on the ion QMS. As explained in section II.1.2, the *apparent* kinetic energy measured by the detector is not directly the actual kinetic energy of the ion, but depends on the potential the ions are created in, which is affected by charging. The consequence is that the KED of a given ion can shift during a scan (which is made at fixed kinetic energy), skewing the measurement. It is something to keep in mind when interpreting the ion spectra to follow.

VI.2.3.2 Mass spectrum of cations

The first result obtained when we looked at the desorption of ions from core-excited solid CO was the mass spectrum of the cations. It is presented in the case of a ^{13}CO ice in fig. VI.14. We see a forest of peaks, evidence of a surprisingly large number of different species desorbing in ion form. The goal of this section is to try to disentangle this spectrum.

First, we can remark that it is not possible to cover all of these masses by simply making linear combinations of C and O atoms. Therefore other, parasitic atoms are involved in the chemistry that we see going on here. The conspicuous signal of H^+, along with the possible pollutants we expect, suggest that mainly hydrogen is involved and we see hydrogenated forms of $C_xO_y^+$ chains. The common pollutants of technical surfaces are chemisorbed water and hydrocarbon chains, while the residual gas of the chamber is mainly H_2 and, because we worked with the molecule during the same experimental runs, H_2O. These provide hydrogen either as pollutants in and on the ice, or even as reactants on parts of the QMS or the chamber (it cannot be completely excluded that some of the observed ions do not come directly from the surface). We will therefore have to keep this in mind when attributing the peaks.

Let us focus on the part of the spectrum before mass 32, where we expect small fragments. Here the number of peak is reasonable enough and we can discuss the attribution of all of them. The peaks are listed in table VI.3 along with their attribution. The

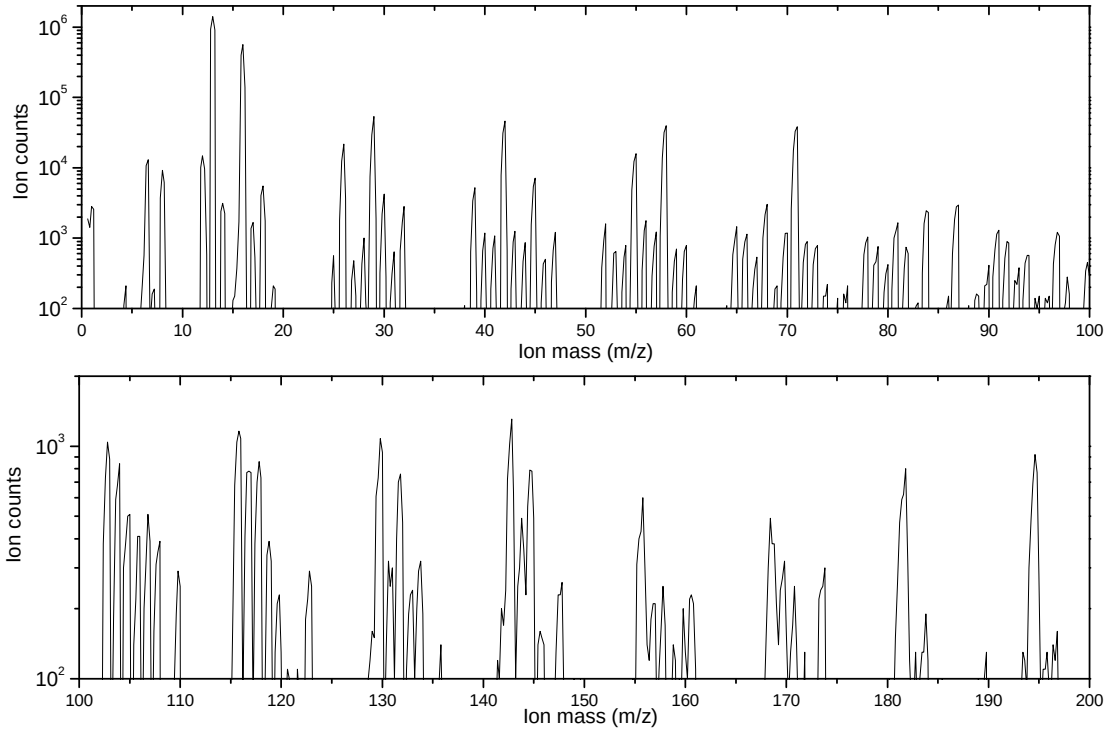

Figure VI.14: Mass spectrum of the cations desorbed from solid ^{13}CO by irradiation at 550 eV. The spectrum was accumulated for a duration of $\sim$ 300 s with a photon flux of 2.3×10^{12} ph.s^{-1}. The kinetic energy filter was set to 1.5 eV.

intensity relative to the $^{13}C^+$ (m/z = 13) peak is given, and has been corrected by the apparatus function of the QMS. However it should be kept in mind that this spectrum is taken at a given kinetic energy for a given photon dose (the ice on which this spectrum was taken had already absorbed some photons). For the reasons mentioned above, ice ageing and charging will certainly change the relative intensities of the peaks. Furthermore, the spectrum being taken at a given kinetic energy also skews the relative intensities since the kinetic energy distributions of the different ions are different (this is mostly relevant for the lighter fragment ions like C^+ and O^+: the KED for large cations are probably not very different given our poor kinetic energy resolution).

The most abundant fragments are C^+ and O^+ (since we used ^{13}CO, in the absence of indication "C" always refers to ^{13}C in the rest of this section). The CO^+ ion is much weaker, at 6% of C^+. The only other peak with significant ($> 1\%$) intensity is C_2^+. As mentioned before we see H^+ signal, indicating hydrogen pollutants. In the region of the multiply-charged atoms we see C^{3+}, C^{2+} and O^{2+}, but also a faint trace of N^{2+}, indicating a very weak nitrogen pollution as well. This is also visible on the weak N^+ signal - although CH^+ could contribute to this mass as well, which makes it less reliable. There does not seem to be a CO^{2+} signal contributing at m/z = 14.5. Because we used isotopic ^{13}CO here, we can expect other isotopes of carbon and oxygen to be present at the percent level as well. This is why the signal at m/z = 12 is attributed to $^{12}C^+$, and the signals at m/z = 17 and 18 to $^{17}O^+$ and $^{18}O^+$ respectively. The latter two attributions

Table VI.3: Attribution and intensity of the desorbed cations from solid CO at 550 eV, between mass 1 and 32

Mass channel (a.m.u.)	Attribution*	Intensity rel. to $^{13}C^+$	Mass channel (a.m.u.)	Attribution*	Intensity rel. to $^{13}C^+$
1	H^+	2	18	$^{18}O^+$	0.46
4.3	C^{3+}	0.01	25	$^{12}CC^+$	0.05
6.5	C^{2+}	0.67	26	C_2^+	2.14
7	N^{2+}	0.01	27	HC_2^+	0.05
8	O^{2+}	0.52	28	$^{12}CO^+$	0.10
12	$^{12}C^+$	1.01	29	CO^+	5.57
13	C^+	100	30	HCO^+	0.45
14	N^+/CH^+	0.23	31	$H_2CO^+/C^{18}O^+$	0.07
16	O^+	44.2	32	O_2^+	0.31
17	$^{17}O^+/OH^+$	0.13			

* All carbon atoms are ^{13}C isotopes unless indicated otherwise.

are arguable because they could also correspond to pollutants such as OH^+ or H_2O^+. For this same reason, we can also expect isotopic variants of abundant ions to appear, like the very weak signal at m/z = 25 which I attribute to $^{12}C^{13}C^+$, and the $^{12}CO^+$ signal. Finally because of the hydrogen pollution, we can expect hydrogenated forms of the abundant molecules we see: this is the case of HC_2^+, HCO^+ and H_2CO^+, although $C^{18}O^+$ can also contribute to the latter signal (m/z = 31).

Moving on to the heavier cations, I will not try to attribute all the peaks. As mentioned previously, pollutants, hydrogen in particular, make the number of peaks larger than it should. Still, if we were to set an arbitrary limit and look only at the peaks whose intensity are $> 0.2\%$ of the C^+ peak, we would only end up with one peak (m/z = 56, 0.25% of C^+) that cannot be attributed to some $C_xO_y^+$ species, and it can be attributed to a singly hydrogenated form of another (rather intense) peak (HC_3O^+). If we consider all the peaks, there are many more (> 25) that cannot be attributed to $C_xO_y^+$, but almost all of them can be accounted for by singly hydrogenated forms ($HC_xO_y^+$) or isotopic variants of $C_xO_y^+$ ions that are detected.

The attributions of all the $C_xO_y^+$ ions that are detected are given in table VI.4. They are classified by family, depending on the number of oxygen atoms: thus we see C_x^+ for x = 2 to 15, C_xO^+ for x = 2 to 11, $C_xO_2^+$ for x = 1 to 6, $(CO)_x^+$ for x = 2 to 5, and $C_xO_5^+$ for x = 2 to 9. $C_4O_3^+$ and $C_3O_4^+$ are the only ions of their series that are detected, and $C_4O_6^+$ and $C_5O_6^+$ the only two of theirs, which is surprising but there is no other particular reason to think the attributions are wrong (no overlap with the hydrogenated or isotopic form of another species that we would expect to yield significant intensity). It should be noted that we only have access to the chemical formula of the compound here, without any information on the way the atom are arranged and if there are ion clusters included (for example, the $(CO)_x^+$ are assumed to form a series of singly charged CO clusters, but that is not necessarily the case). Although not shown in the table, the

Table VI.4: Attribution and intensity of the desorbed cations from solid CO at 550 eV, between mass 33 and 200.

Mass channel (a.m.u.)	Attribution*	Intensity rel. to $^{13}C^+$	Mass channel (a.m.u.)	Attribution*	Intensity rel. to $^{13}C^+$
39	C_3^+	0.63	42	C_2O^+	5.76
52	C_4^+	0.22	55	C_3O^+	2.24
65	C_5^+	0.22	68	C_4O^+	0.47
78	C_6^+	0.17	81	C_5O^+	0.28
91	C_7^+	0.23	94	C_6O^+	0.10
104	C_8^+	0.16	107	C_7O^+	0.10
117	C_9^+	0.16	120	C_8O^+	0.05
130	C_{10}^+	0.23	133	C_9O^+	0.05
143	C_{11}^+	0.29	146	$C_{10}O^+$	0.04
156	C_{12}^+	0.14	159	$C_{11}O^+$	0.03
169	C_{13}^+	0.12			
182	C_{14}^+	0.20			
195	C_{15}^+	0.24			
45	CO_2^+	0.92	106	$C_2O_5^+$	0.08
71	$C_3O_2^+$	6.12	119	$C_3O_5^+$	0.08
84	$C_4O_2^+$	0.43	132	$C_4O_5^+$	0.16
97	$C_5O_2^+$	0.23	158	$C_6O_5^+$	0.06
110	$C_6O_2^+$	0.06	171	$C_7O_5^+$	0.06
			184	$C_8O_5^+$	0.05
			197	$C_9O_5^+$	0.04
58	$(CO)_2^+$	5.78	100	$C_4O_3^+$	0.08
87	$(CO)_3^+$	0.52	103	$C_3O_4^+$	0.20
116	$(CO)_4^+$	0.24	148	$C_4O_6^+$	0.06
145	$(CO)_5^+$	0.18	161	$C_5O_6^+$	0.05

* All carbon atoms are ^{13}C isotopes unless indicated otherwise.

hydrogenated form of the carbon chains HC_x^+ were systematically found in the spectrum, with an intensity close to equal to that of the corresponding C_x^+ peak.

Four ions show significantly higher intensity than the rest: C_2O^+ (6%), C_3O^+(2%), $(CO)_2^+$ (6%) and $C_3O_2^+$ (6%). Everything else is in the 0.05-1% range. This is another argument for the C_2O or C_3O_2 neutral forms being the most likely candidate in the attribution of the unknown peak of section VI.1. Surprisingly, the CO_2^+ ion is not very intense, despite being the most abundant neutral product after CO. This shows that it is necessary to be cautious in extrapolating ion desorption yields to other quantities such as neutral desorption yields or total produced species. The evolution of the intensity of the series of ions is interesting: while the C_xO^+, $C_xO_2^+$ and $(CO)_x^+$ show a clear decrease with increasing x, this is not the case for the C_x^+ and $C_xO_5^+$ series. The reason for these trends is not clear yet to me.

The first study of X-ray induced ion desorption from CO ice by Rosenberg et al. [140] only reported C^+, O^+, CO^+, C_2O^+ and $(CO)_2^+$, but a lot of the cations we detected here were also seen by Scheuerer et al. in the Menzel group, although this is only mentioned in a DIET conference proceedings [380]. The most abundant ions were also observed desorbing in the deep valence region of solid CO by XUV excitation (30-60 eV) [386]. Most of the ions were also seen in ion bombardment (1 keV Ar^+) of solid CO [387]. The relative intensities reported in these works all seem in reasonable agreement with ours.

VI.2.3.3 Spectral signatures

The spectra of some selected cations among all those observed, basically the most abundant ones, were investigated. We looked into the most details at C^+, O^+ and CO^+, and also the only anion we observed, O^-, but I will also present spectra of C_2^+, C_2O^+, C_3O^+, $C_3O_2^+$ and $(CO)_2^+$.

The interpretation of all the spectra presented here need to take into account the problems of charging and ageing developed in a previous section. In the duration of a long scan (typically 520-600 eV) the kinetic energy distributions are expected to shift enough to have a potentially visible effect on the spectrum, even more if different parts of the spectrum yield ions with intrinsically different kinetic energy distributions. Furthermore, ageing will cause an overall slow decrease of the ion signal during the spectrum.

The photodesorption spectrum of C^+ on a relatively fresh ice (scan 2 of fig. VI.10a) is presented in fig. VI.15 (top panel) along with the integrated KEDs at fixed photon energies (blue dots). Overall the features of CO absorption are all clearly seen. The relative intensity of the π^* resonance (534.4 eV) and the edge/post-edge region (538-550 eV) is not the same than on the TEY (shown for comparison on the figure), but because of the problems previously mentioned it is difficult to assess if this difference has a physical signification or if it is a measurement artifact from this spectrum. The integrated KEDs are closer to the TEY in terms of relative intensity of these two regions, therefore I would be inclined to say that there is no significant difference. The slope of the decrease of the continuum is higher on the photodesorption spectrum than on the TEY, which I attribute to an ageing effect. Once again the integrated KEDs are closer to the TEY. One difference is the small peak visible at 555 eV on the spectrum of C^+, which is red-shifted compared with the (presumably) corresponding peak on the TEY at 556 eV. Part of the shift could be due to the difference of the decreasing slopes of the continuum in the two spectra.

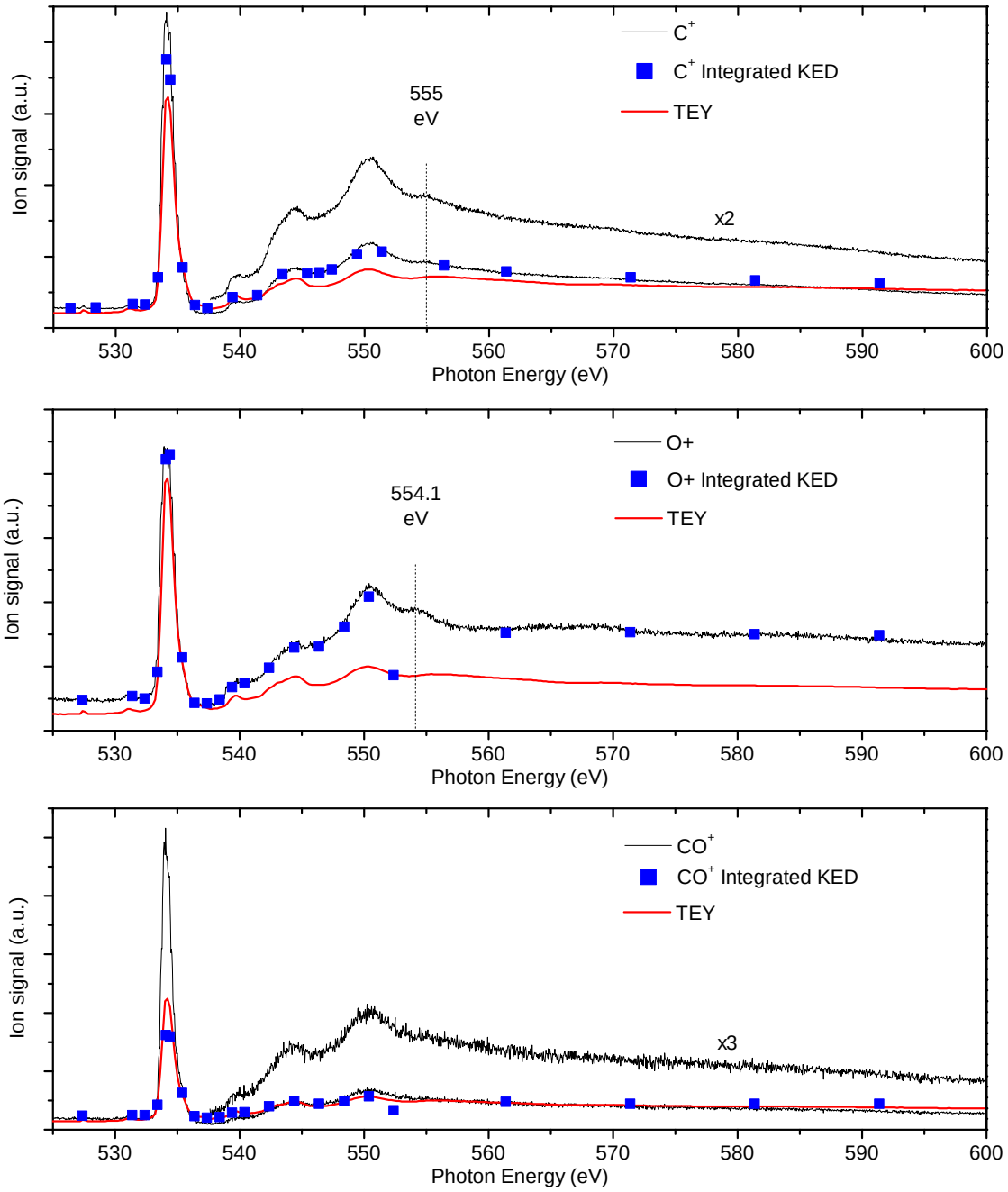

Figure VI.15: Photodesorption spectra of C^+ (top panel), O^+ (middle panel) and CO^+ (bottom panel) from condensed CO. The spectrum taken at the (initial) maximum of the KED is the black trace, which has been magnified above 540 eV for C^+ and O^+ to show better the structures. In blue dots are the integrated KEDs at different photon energies. The TEY is shown in red for comparison (normalized so as to best match the desorption spectra).

The photodesorption spectrum of O^+, taken on the same ice, is shown in fig. VI.15 (middle panel) and similarly displays all the features of CO absorption. This time, however, the relative intensity of the π^* to the edge/post-edge region is lower than the TEY, and it is confirmed by the integrated KEDs which show very good agreement with the spectrum (except for an odd point at 551.4 eV). Here it is clear that production of O^+ is higher above 538 eV than it is at 534.4 eV on the resonance. In addition, there is a feature at 554.4 eV instead of the 556 eV of the TEY which is quite clear (this time there is no difference in the continuum decreasing slopes between O^+ spectrum and TEY).

The photodesorption spectrum of CO^+, taken on the same ice as well, is shown in fig. VI.15 (bottom panel). For the spectrum displayed the π^* is much more intense than the edge/post-edge and continuum region compared with the TEY, but this is not confirmed by integrated KEDs which indicate instead a slightly lower relative intensity. A feature at 555 eV is very faintly visible in the spectrum, therefore seeming red-shifted compared with the TEY and at the same position as for C^+.

Thus for these spectra taken on a relatively fresh ice, only two deviations from the TEY are seen: (i) a clear lower relative desorption yield at the π^* for O^+ and (ii) something happening around the small peaks above the shape resonance, that are present at 556 eV in the TEY, 555 eV for C^+ and CO^+ (barely visible in the latter; the red-shift could partly originate from the steeper decreasing continuum in these desorption spectra compared with the TEY) and 554.1 eV for O^+. I will discuss this second point later after the data on O^- will have been presented.

It is interesting to also look at the spectra of these ions in the case of a heavily processed ice (the "high dose" ice of fig. VI.10a). They are displayed in fig. VI.16. On the left side of the figure the full spectra are shown, on the right side shorter scans around the π^* were made. On the right side figures we see that in all three cases the 533 eV peak is not visible on the photodesorption spectra, while it is obvious in the TEY. As for the CO_2 peak at 535.2 eV, it is weak enough on C^+ and O^+ that we cannot see an actual bump. It can be discerned in the CO^+ spectrum but seems weaker than on the TEY. Since the spectra of C^+ and O^+ do not follow the TEY, we can conclude that XESD is not dominant in their desorption yield in this region. We can also conclude that desorption of C^+ and O^+ by true PID following π^* core-excitation of CO is significantly more efficient than for core-excitation of CO_2 or the species contributing at 533 eV.

Let us now look at the full spectra (left side figures of fig. VI.16). The case of CO^+ seems clear: it looks very similar to the TEY, except for the slope of the continuum whose steeper decrease in the CO^+ spectrum is attributed to ageing. There could be some deviations, as mentioned before, but they are too slight to be reliable considering the charging and ageing issues. In the case of C^+ the photodesorption spectrum looks very similar to the one taken on a fresh ice (fig. VI.15), with clearly visible CO absorption features. This is in contrast with the TEY, where as mentioned in a previous section the CO features become blurred and the region between 538 and 560 eV is heavily changed. The case of O^+ is again intermediate: while the photodesorption spectrum for the aged ice differs from the TEY, it is not similar to O^+ of the fresh ice. The shape resonance and the peak at 554.1 eV are still visible, but there are more features than the CO ones contributing in the edge/post-edge region.

All of this rules out the idea suggested before that the intrinsic features of CO absorption are modified by the ageing. Instead the modifications in the 538-550 eV region

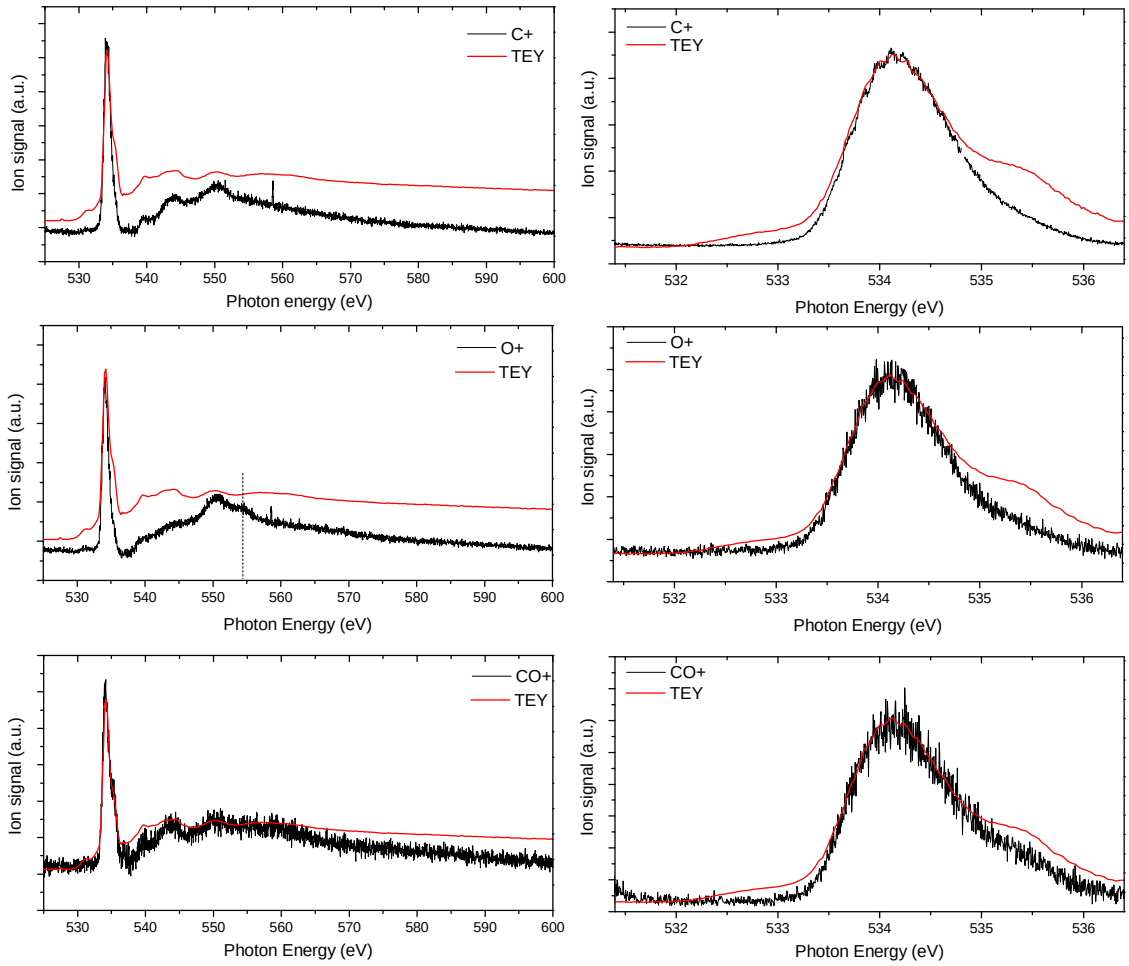

Figure VI.16: Photodesorption spectra of C^+ (top panels), O^+ (middle panels) and CO^+ (bottom panels), in full range (left panels) or near the π^* resonance (right panels). These spectra were taken on a CO ice that had already received a high photon dose.

of the TEY are due to additional contributions of the new photoproducts.

Looking at the desorption of ions in the deep valence region (25-60 eV) of condensed CO is instructive [386]. What has been observed is desorption of C^+ and O^+ with a photon energy threshold for desorption at 30 eV and a maximum yield around 50 eV, attributed to satellite states of CO. These states are typically the final states reached after spectator Auger decay of core-excited CO (i.e. below threshold). The 1:5 ratio in intensity between C^+ and O^+ observed is close to the ratio we see here at 534.4 eV (1:3.5). The study was not pushed to higher energies where the contribution of double ionization dominates, so that we cannot see whether in this region (which corresponds to the final states obtained after Auger decay of core ionized states, above threshold) the ratio between O^+ and C^+ changes. There is, though, a slight difference at the highest shown energies around 60 eV where the ratio O^+/C^+ does increase. In our case, above threshold, the ratio is close to 1:2. For CO^+, there is similarly a desorption with a threshold around 28 eV increasing up to 50-60 eV involving satellite states. However, desorption of CO^+ is also observed

through excitation of resonances in the 14-25 eV region, which are attributed to doubly excited Rydberg states.

This allows us to discuss the desorption mechanisms for these three cations. The desorption of C^+ and O^+ are fairly straightforward to explain through true PID: below threshold, Auger decay leads to satellite/2h1e which have been shown to trigger desorption of these ions, through the dissociative character of some of these highly excited states of the ions (most states other than X, A and B of CO^+ are dissociative in the gas phase). Above threshold, the 2h final states after Auger decay dissociate the molecule because of Coulomb explosion, yielding C^+ and O^+ fragments with a lot of kinetic energy which should not have issues desorbing. The Auger electrons released in the ice can similarly excite these same states, but they are rather high in energy, since a threshold at 30 eV has been observed in photodesorption. This is clearly not reachable by secondary electrons. Even their excitation cross-section by the Auger electron must no be very high, even though such data is difficult to obtain. The data obtained on C^+ and O^+ desorption from fresh ices did not allow to conclude on the XESD/true PID distinction because it followed the TEY (except for the π^* resonance for O^+). But the comparison to desorption spectra from highly irradiated ices brought us new insights, with clear deviations from the TEY at the π^* but also in the 538-560 eV region. Since the experimental results show deviations from the behaviour expected for XESD (desorption spectrum following the TEY), we may conclude with reasonable certainty that true PID dominates for O^+ and C^+. Going further, it is clear from the C^+ spectrum from the highly irradiated ice (fig. VI.16), which looks like the pristine ice TEY, that true PID from CO yields C^+ desorption much more efficiently than true PID from other molecules.

The case of CO^+ is different. The mechanisms for CO^+ desorption in the first place are more complicated. The CO^+ ion needs to be formed with sufficient kinetic energy to overcome the desorption barrier: CO^+ desorption is not observed after single ionization [386]. It was suggested for the doubly excited states, that a reduction of the intermolecular distance by forming a CO^* + CO dimer followed by autoionization and repulsion could explain the desorption. For the satellite states it was proposed instead that the excited $(CO^+)^*$ could deexcite by ionizing a neighboring molecule, creating a CO^+ - CO^+ repulsion [386]. We could therefore imagine similar mechanisms for true PID: formation of CO^+ - CO^+ pairs, either below or above threshold. Regarding the XESD vs. true PID question, the fact that the desorption threshold of CO^+ is at much lower energies thanks to the doubly-excited states increases the weight of XESD, not just because of the Auger electron but also because the high energy tail of the secondary electrons (say 15-20 eV) could conceivably excite these states as well. Comparison with electron-stimulated desorption of ions from condensed CO would be interesting here. Our experimental evidence does not go against the possibility of XESD playing an important role.

The results obtained here on condensed CO are quite different from those obtained in the Menzel group on CO chemisorbed on metal surfaces [139, 382, 385]. In these works, the desorption spectra of C^+ and O^+ (and O^{2+}) are very different from the absorption, and multielectron features play a much more prominent role. There are clear high energy features (around 550 and 570 eV) associated with 2h2e and 3h3e excitations that dominate the spectra. This is explained by the fact that more "simple" excitations are efficiently quenched by the substrate. Dissociation and desorption of ionic fragments thus require highly localized states like the doubly or triply excited states. Their result for CO^+, on

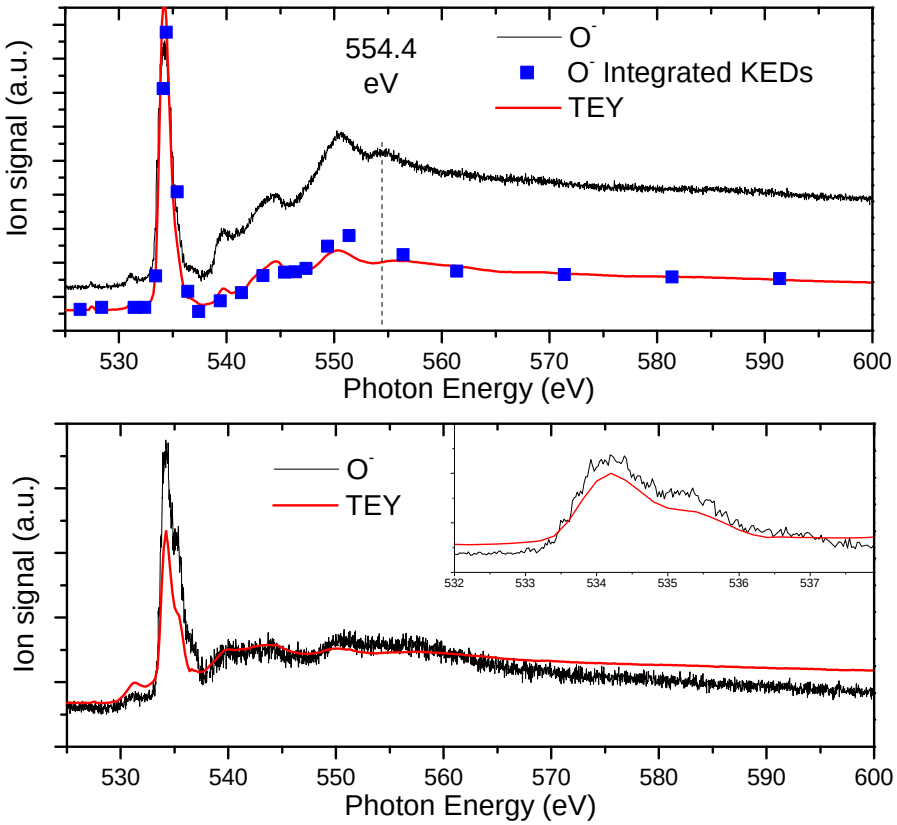

Figure VI.17: Photodesorption spectrum of O^- for a fresh ice (top panel) and a highly processed ice (bottom panel). Also shown on the top panel are the integrated KEDs for O^- (blue dots) and the TEY (red line). The TEY is also shown in red in the bottom panel. The inset of the bottom panel is a zoom in the π^* region.

the other hand, follow closely their absorption spectrum.

We also looked at the desorption of anions. Only one anion was observed with significant intensity, O^-. C^- was also observed with more than 30 times less signal, and the ion count was not sufficient to study it in more detail. This is not entirely surprising: anion desorption from DEA by low energy electrons on condensed CO mostly yields O^- and 10 times less C^-, with also a higher electron energy threshold for C^- [388]. Studies of core-excited/ionized CO fragmentation in anions are lacking: the only studies to my knowledge [389, 390] only mention O^- but never says that C^- is not observed. In any case, this observation is probably simply a consequence of the higher electron affinity of oxygen.

The photodesorption spectrum of O^- is shown on fig. VI.17, for a fresh ice on the top panel (along with the integrated KEDs) and for a highly processed ice on the bottom panel. Looking at the spectrum for the fresh ice, there are no strong difference with the TEY, and the integrated KEDs show that the relative intensity of the π^* and the rest of the spectrum are similar to the TEY. The one difference with the TEY is the presence of a peak at 554.7 eV, very close to what is observed for O^+. For the processed ice, O^- still follows the TEY quite well, with the distorted features in the edge/post-edge region being

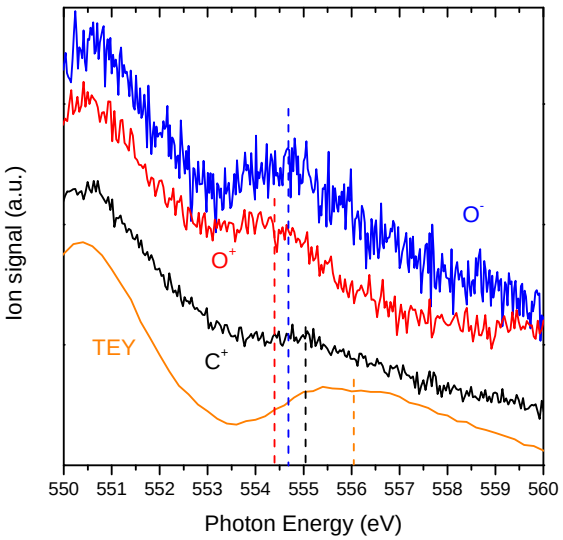

Figure VI.18: Zoom in the 550-560 eV region of the O^+, O^- and C^+ photodesorption spectra and the TEY. The scaling is arbitrary and used to show clearly the peaks around 555 eV.

clearly observed. This is in contrast with the behaviour of O^+ and C^+. Furthermore, if we zoom onto the π^* (inset of the bottom panel), the CO_2 peak is quite strong, as is the following peak at 536.6 eV. Even for CO^+ the contribution of the non-CO peaks for the highly processed ice was not as strong.

All of this suggests that either XESD (and thus DEA, or ion-pair dissociation) plays an important role in O^- desorption, or that the true PID processes leading to its formation are just as efficient for non-CO molecules as they are for CO. It may seem surprising that true PID processes would yield anions as efficiently above and below the core ionization threshold, which would suggest ruling out true PID dominating the yield. However, in gas phase core ionization, the O^- yield does not decay to zero above threshold: there is still significant intensity in the data of ref [390]. This requires the formation of the ion pair C^{3+} + O^-, a pathway that should have a low probability but is viable. This condition is furthermore relaxed in condensed phase where processes like intermolecular coulombic decay (ICD) or charge transfer can split positive charges over several molecules. More studies on anion production by core ionization of CO in the gas phase, such as the coincidence anion/cation measurements that have been done on water and other molecules recently [362, 391], would bring more insights.

We can now conclude on the peak(s) that are observed around 555 eV in the different photodesorption spectra and the TEY. To have a better view of these peaks a zoom is made in fig. VI.18 of the 550-560 eV region for the TEY and O^+, O^- and C^+. A peak appears in the TEY at 556 eV that has been attributed to a 2h1e (shake-up, excited core ion) state following XPS data. One peak appears at 555 eV for C^+ but it is faint and there is some uncertainty on whether this red-shift could come from differences in the slope of the decreasing continuum. However the peaks are clearly visible and unambiguous in the spectra of O^+ and O^-, and red-shifted to respectively 554.4 and 554.7 eV. The explanation I can suggest is the following: since the 556 eV peak of the TEY is attributed to a 2h1e

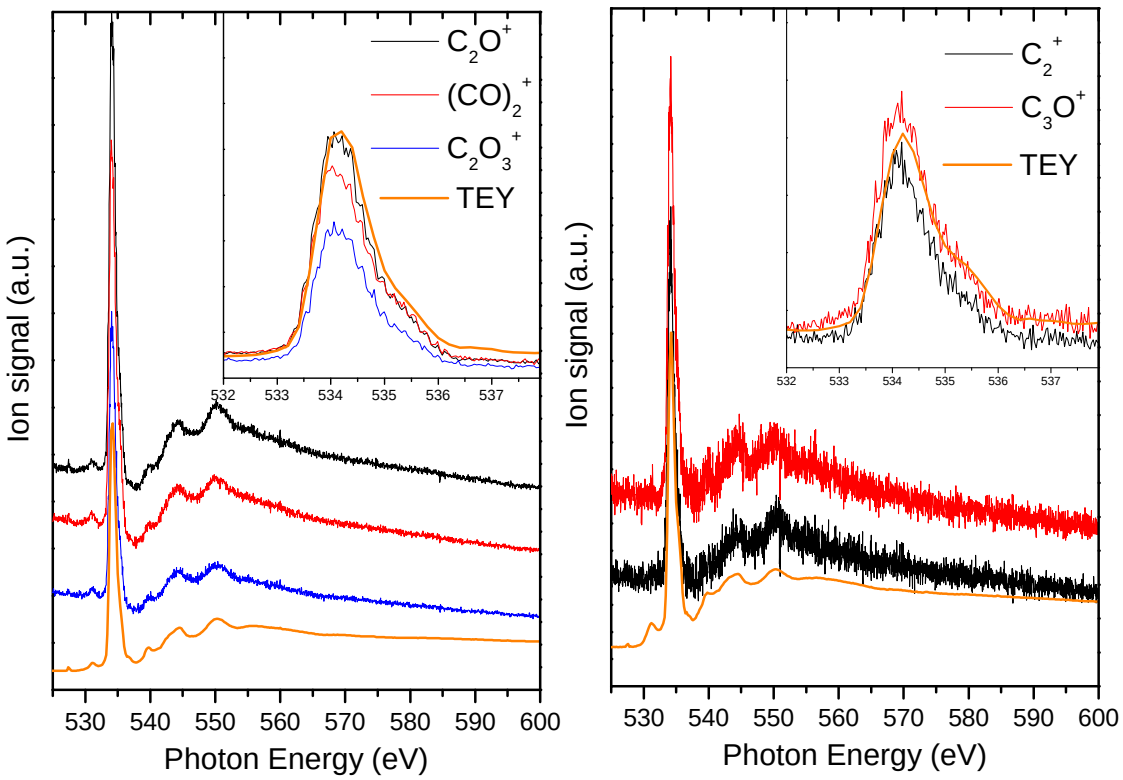

Figure VI.19: Photodesorption spectra of C_2O^+, $(CO)_2^+$ and $C_3O_2^+$ (left panel), and C_2^+ and C_3O^+ (right panel). For each panel the corresponding ice had already received about two scans worth of photons prior. The respective TEYs are also shown for comparison in orange. The spectra have been offset for clarity.

state, we can expect a series of 2h2e (doubly-excited) Rydberg states converging to this excited core ion slightly below in energy, although their excitation cross-sections may be low. Anions have often been used as tracers of doubly-excited states above ionization thresholds, either in the valence or core region [392, 393, 361], precisely because charge conservation requires that dissociation of an initially positively charged state into an anion also involve highly positively charged fragments, which makes these dissociation pathways minor (or even forbidden: O^- formation after core ionization of gas phase H_2O and decay to a two-hole state is impossible). Doubly-excited states with low excitation cross-sections (therefore invisible in photoabsorption) but involving a neutral initial state thus become visible in the ion yield spectra. Indeed, it is for O^- that the peak (here at 554.4 eV) is the most visible. Similarly, these 2h2e state could have a particularly high O^+ desorption yield which make them appear in the O^+ spectrum. If a red-shift does exist for C^+ and CO^+ similar explanations can hold.

Let us now move on to the photodesorption spectra of C_2^+, C_2O^+, C_3O^+, $C_3O_2^+$ and $(CO)_2^+$, presented in fig. VI.19. In all cases the spectra were taken on ices for which this was the third scan, so that they were still relatively fresh (CO features still largely recognizable and dominant but clear presence of CO_2 in the shoulder of the π^* resonance). No KEDs were made for these ions, so that we cannot check the effect of charging and

kinetic energy bias on these spectra. However, there is no particularly strong deviation from the TEY visible on any of these spectra. There are slight differences between the various spectra and the TEY, but not large enough to warrant a detailed discussion here.

Desorption of these bigger ions, not just these which we just discussed but also the others, is hard to explain by simple ionization of their neutral equivalent formed in the ice. The reason for that is similar to the arguments explaining why simple ionization of CO does not lead to CO^+ desorption. Desorption of these ions could conceivably occur from fragmentation of bigger molecules, but then the lighter fragments would take away most of the dissociation energy, and therefore observation of the biggest ions would require even larger molecules that could break up into two large fragments, and these are probably not very abundant. Instead, the most likely explanation is that these ions desorb immediately upon their formation via ion-neutral reactions, owing to the exothermicity of the reaction. For example (see ref. [386]) C_2O^+ can be formed via C^+ + CO or $(CO^+)^*$ + CO (exothermicity 2.8 eV in the gas phase [394]), and $C_3O_2^+$ via C_2O^+ + CO (exothermicity more than 6 eV [386] in the gas phase). Exothermic addition reactions of C^+, CO^+ or C_2O^+ to existing C_xO_y species could explain the variety of ions observed in desorption. This would also explain why the desorption yield of CO_2^+ is so low: simple ionization of the abundant CO_2 in the ice does not lead to desorption and CO_2^+ is not created via ion-neutral reaction (at least not with significant excess energy).

VI.2.4 Discussion on X-ray induced photochemistry

The previously presented results allow me to discuss more specifically the X-ray induced photochemistry in comparison to what was done in the literature. The goal of this study was not to study photochemistry: no attempts were made to properly quantify products creation and derive kinetics. This was already done for various types of irradiation in the literature. Still, our results show interesting complementarity with other studies because in the ice chemistry community the analysis probes used are almost always infrared spectroscopy and TPD. In contrast, tools such as X-ray absorption spectroscopy and photon-stimulated ion desorption are almost never used.

VI.2.4.1 CO irradiation chemistry

CO chemistry can be initiated by C and O radicals resulting from CO dissociation. However, CO dissociation requires a lot of energy, with a gas phase dissociation threshold of 11.1 eV [205]. Considering that this threshold is not likely very different in the condensed phase, but that ionization kicks in around 12.5 eV and the first three electronic states of CO^+ are not dissociative, there is only a narrow range of excitation energy for which CO is dissociated into C and O. However this region corresponds well to the maximum of the typical secondary electron energy distribution. Another source of radical production by secondary electrons is dissociative electron attachment (occuring resonantly around 10-12 eV as well for CO). A C and O fueled chemistry is therefore certainly taking place. But CO chemistry also occurs below 11.1 eV, as shown by the studies that were done using VUV photons [206, 395]. Indeed, electronically excited CO^* is itself a reactive species, and the reaction CO^* + CO $\longrightarrow$ CO_2 + C is the well known kickstarter of chemistry in this energy range [396]. Finally, the CO^+ ions created by simple ionization events

and the ion fragments like C^+ and O^+ created by higher energy ionization (in particular core-excited/-ionized dissociation) are the source of ion-neutral chemical reactions, as mentioned in the previous section. Ions formed will presumably recombine shortly afterwards with electrons, undergoing for some of them dissociative recombination into new species and radicals.

The most relevant work to compare with here is the one of Ciaravella et al. [397, 398], since it is the only one having studied directly X-ray photochemistry. Their experiments were done using either broadband (0.25-1.2 keV) or monochromatic (300, 550 eV) light. Using transmission IR spectroscopy and TPD, they found production of several C_x (x = 3, 5, 8, 9), C_xO (x = 2 - 6) and C_xO_2 (x = 1, 3, 5, 7) molecules, similar to these we saw in the form of cations. The most abundant detected molecules are CO_2, C_3O_2, C_3 and C_2O, coherent with the results we obtain for cations and neutral desorption. Interestingly, they found an effect where for a very high flux of photons, the amount of species created and CO destruction by unit of fluence actually becomes lower than for experiments at lower fluxes, although the reason for that is not clear.

Most studies of the photochemistry/irradiation chemistry of CO have been done using hydrogen lamps (VUV photons) [206, 395], energetic electrons [399] or energetic ions [387, 400, 401, 402, 395, 403, 404]. Since the processes leading to chemistry are mostly similar, these studies can be compared to soft X-ray photochemistry as well.

The studies made using VUV photons ($\leq$11 eV) mentioned before [206, 395] are interesting because the only starting point of chemistry is the previously mentioned reaction of CO^* with CO to form CO_2 and C. Since no O atoms are produced in this reaction, this somewhat restricts the chemical possibilities, but the major products of CO chemistry are suboxides like C_2O or C_3O_2, which are already observed with VUV irradiation and well explained by reactions of the type C + CO $\longrightarrow$ C_2O and C_2O + CO $\longrightarrow$ C_3O_2. Species observed by IR spectroscopy in these studies are C_2O, CO_2, C_3O_2 (in both studies), C_3, C_3O (ref. [206]), C_5O_2 and C_7O_2 (ref. [395]) and can all be explained by the above reactions.

The study of Jamieson et al. [399], made using 5 keV electron bombardment of CO ice, has a very thorough discussion of CO chemistry, with detailed aspects for each species and families of species. They detected C_x (x = 3, 6), C_xO (x = 2-7) and C_xO_2 (x = 1, 3-5). These authors also proposed a chemical network and attempted to derive rate constants for each reactions based on their results. However, they made the assumption that CO chemistry was essentially based on the CO^* initial reaction, arguing that they saw no trace of O atom chemistry and that ions were negligible. In our study we have through XAS the evidence that there is a considerable amount of O and O_2 accumulated in the ice (which cannot be observed through IR spectroscopy), and the ion desorption shows also how ions can play a role. Although the irradiation sources are different, it seems unlikely to me that with 5 keV electrons, ion and O chemistry can be neglected. The CO^* reaction does explain almost all of the observed products, and the qualitative conclusions are mostly the same, but it is likely that quantitatively things become more complex as we go from VUV irradiation to ionizing radiation.

The works that were done using ion bombardment do mention the role of ionization [384, 401]. At the very least, dissociative recombination of CO^+ with an electron yielding C and O fragments should be considered, but I also mentioned earlier that the desorption of ions was most likely due to exothermic ion-neutral reactions, rather than ionization

of already formed neutral species. Another interesting aspect of these ion bombardment studies is the investigation of the residue that is left after long irradiation of CO ice and heating of the surface up to 200 K. This leaves nonvolatile species ($\sim$ 1% in mass of the initial ice in their experiment) that have been shown to have an average C:O stoichiometry of 3:1 using Rutherford backscattering (RBS). This is higher than what was originally assumed, which was that C_3O_2 polymers were formed [405, 384].

A series of species that were not observed in the other experiments probing the solid phase are the chains with more than 2 oxygens (for example the series of $C_xO_5^+$ ions that we attributed in table VI.4). If this attribution is not a mistake, this suggests the possibility of reactions involving for example O^+ as well and leading to this kind of ions, although none of these were observed in the gas phase [406]. Here we see the complementarity of the different techniques: it is delicate to assert that C_xO_5 species exist in the solid without further confirmation by infrared spectroscopy or other solid probe techniques.

VI.2.4.2 Comparison of different probes of chemistry

Detection of chemistry using infrared spectroscopy has the advantage that a detection asserts the presence of the neutral species inside the ice. Ion desorption, on the other hand, is an indirect method: first because we detect ions, and second because we only detect those ions that desorbed to the gas phase. We can assume that if an ion is detected in desorption, it has been formed in the ice. It is, however, arguable that the corresponding neutral species is formed in the ice as well: as mentioned in the previous section the desorption of these ions is probably the result of an ion-neutral chemistry that directly forms the ion, and to have the neutral form present in the ice we need the recombination of that ion with an electron to not be dissociative. The carbon chains and suboxides that we observe here are not very stable species. Furthermore some of the ions we observe are probably clusters (stabilized by ion-dipole interactions) that do not really exist in the same way in the condensed phase. For some species it is reasonable to assume that their neutral equivalent does exist in the condensed phase, but then the relative intensity of the ion peaks give very little information on the relative abundances in the condensed phase: while there seems to be some correlation for several ions (the most abundant ions are also the most abundant condensed phase neutral species), I pointed out earlier that it does not work at all for CO_2, the most abundant neutral product, since CO_2^+ desorption is quite low. While retrieving relative abundances from infrared spectroscopy is not trivial, it is still possible if enough data on band strengths is available.

On the other hand, ion desorption (i) is so sensitive, due to the essentially zero background and the ease of ion control, capture and detection, that many more species are detected than in infrared spectroscopy, and (ii) it is not limited in the detectable species in the same way as infrared spectroscopy where only infrared active species can be observed (excluding e.g. C, O, C_2, O_2...). Here only species with overlapping m/z ratio are ambiguous.

In the infrared spectroscopy experiments, TPD is also often used to derive supplementary information on the (neutral) products present in the condensed phase, but TPD is limited by the fact that bringing thermal energy to the ice also modifies it, potentially modifying the chemistry, breaking unstable species, etc... In addition neutral detection by

Table VI.5: Average photodesorption yields of intact CO (CO molecules per incident photon of "average" energy for the given environment) for the X-ray spectra of different regions at different attenuations.

	TW Hya (young star)	MKN231 (ULIRG)
Source spectrum	8.8×10^{-2}	2.9×10^{-2}
$n_H = 10^{21}$ cm^2	7.8×10^{-2}	2.3×10^{-2}
$n_H = 10^{22}$ cm^2	3.9×10^{-2}	4.6×10^{-3}
$n_H = 10^{23}$ cm^2	3×10^{-3}	5×10^{-4}
$n_H = 10^{24}$ cm^2	3.2×10^{-4}	1.7×10^{-4}

electron impact ionization makes the secure detection and identification of big molecules or fragments a delicate task.

One solid phase probe that we had access to here is X-ray absorption spectroscopy (XAS). XAS is far from being as sensitive to a variety of newly formed species as infrared spectroscopy, especially in our set-up which has not really been optimized for doing XAS experiments. But it is a precious complementary probe, which as mentioned earlier can reveal species which are not detectable by IR spectroscopy, here O and O_2 (but we could probably have detected C and C_2 as well near the C edge). Although we have not attempted a quantification here, it should be possible as was done for water [407].

Multiplying different probing techniques, in any case, can only be beneficial to the advancement of irradiation chemical studies of ices.

VI.2.5 Astrophysical yields

We can, as we did for water, derive desorption yields per "average" photon for different X-ray environments relevant to astrophysics. The procedure is similar and is based on the same assumptions detailed in section VI.1 and in paper III, thus I will refer to these for more details. It is assumed first that the photodesorption yield will follow the absorption of solid CO from 600 eV to 10 keV. This assumption is probably slightly wrong, as previously mentioned for water, because after a few hundreds of eV the photoelectron starts playing an important role (around 800 eV it has an energy of $\sim$ 250 eV, and the electron-stimulated desorption yield is maximal at this energy). Then, the second hypothesis is that the absorption of solid CO in this energy range is the same as the absorption of gas phase CO. This, on the other hand, is quite reasonable because the absorption of the core shells is mostly atomic in nature in this range, and hardly perturbed by external factors. An extrapolated photodesorption yield of CO, shown in fig. VI.20, is thus derived. This extrapolated yield is weighted-averaged with the same spectra presented in section to obtain values that represent what the "average" photodesorption yield would be in a region of space where the X-ray spectrum would be of this kind. These values are given in table VI.5. Extra caution should be taken when considering the validity of these numbers, because as we saw the yield of CO depends on the ageing of the ice. This should not change the order of magnitude of the yields (which is what we aim at here...) but there could easily be a factor of two between a fresh ice and a processed ice, from the observations we have made in the previous section.

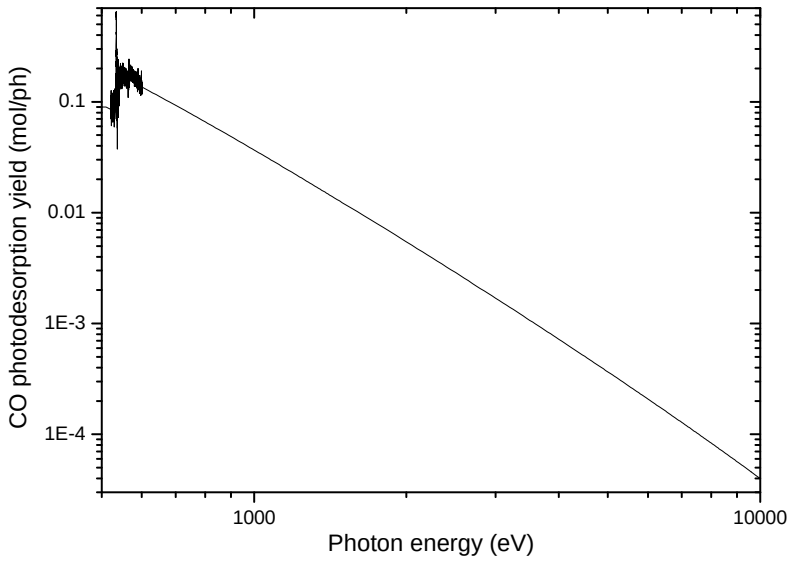

Figure VI.20: Photodesorption yields of neutral CO from solid CO, extrapolated up to 10 keV. See the text for more details on the extrapolation.

The comments that can be made on the evolution of these yields with the density traversed and with the spectrum are mostly that same as they were for water (see paper III): as harder X-rays contribute to the spectrum, the average photodesorption yield becomes lower. One important difference with water is that CO freezes out on grains at much lower temperatures (< 20 K), and thus deeper into clouds. Looking at the numbers from the table, it is likely that the average X-ray photodesorption yield for CO at a relevant location in a disk will be lower (in the few 10^{-3} mol/photon range) than the average yield for UV photons (10^{-2} mol/photon). In such a location UV from the disk will probably not penetrate, but X-ray photodesorption will compete with cosmic ray desorption and photodesorption by cosmic ray induced secondary UV photons. The precise calculation is not easy to make, but if the yield is lower and the photon flux is lower as well, X-ray photodesorption will lose to the other processes. Its relevance could come about again if the interior of the disk is shielded against cosmic rays, as was suggested recently [31]. This data can nonetheless be implemented in astrochemical models, as only a full model investigation will give the final word on the relevance of the X-ray photodesorption process.

VI.3 Conclusions on X-ray photodesorption

Photodesorption in the soft X-ray range has been explored for our two most important systems: H_2O and CO ice. The diagnoses in this energy range are more rich than for VUV photons and electrons, as not just neutrals could be measured but also desorbing cations and anions, as well as the absorption spectrum through the total electron yield. Photodesorption spectra have been obtained for many different species, and for the most part this is the first time that such a measurement has been made.

The quantified photodesorption of neutral species for both CO and H_2O ices - again,

the first measurement of this kind in this energy range - allows implementation of the X-ray photodesorption process in models. I showed how the data obtained can be translated to numbers that are directly relevant to astrochemical models, and made an estimation suggesting a potentially significant effect of X-ray photodesorption in the ISM, in particular in planet-forming disks. Our studies are part of a blossoming interest for the impact of X-rays in astrochemistry. Comparisons of the photodesorption spectra with the TEY and of the estimated yields per absorbed photon with the EID yields from the previous chapter suggest that the desorption of neutral species is dominated by the XESD process, i.e. by the Auger electron scattering and the secondary electrons.

For most ions, on the contrary, photodesorption is dominated by true PID processes, i.e. desorption processes mediated by the relaxation of the initially core-excited molecule, which is left in a highly excited state after Auger decay. This is seen in particular in the fact that the photodesorption spectra of a lot of ions are very different from each others, especially in the case of H_2O ice. Once again photodesorption can be excited state-dependent: desorption of H^+ from H_2O is strongly enhanced in the dangling H peak at 534.4 eV, while desorption of H^- is suppressed in the "four-coordinated molecules" state at 540 eV. The excited state dependence of the desorption of these ions can conversely give information on the nature of these excited states. The identification of strong signatures of photoproducts like H_2O_2 and O_2 in the photodesorption spectra of "oxygen fragments" (O^+, O^-, OH^+...) showed that true PID processes involving core-excitation of these photoproducts were much more efficient than processes involving excitation of the water molecules. For CO, the desorption spectra of O^+ and O^- reveal doubly-excited states embedded in the post-edge continuum around 555 eV that are not visible in the absorption spectrum and where desorption of these two ions is enhanced.

X-ray irradiation is at the same time a vector of photochemistry and a probe of that photochemistry: the absorption spectrum where different species can be observed and the desorption of some neutral and ionic species are all probes that are complementary to techniques more traditionally used for investigation of the irradiation chemistry of molecular ices, a topic of great relevance for astrophysics. This is particularly obvious in the case of CO where the plethora of observed cations, up to very large species, indicate how much chemistry is going on.

Conclusion

> Anyone moderately familiar with the rigours of composition will not need to be told the story in detail; how he wrote and it seemed good; read and it seemed vile; corrected and tore up; cut out; put in; was in ecstasy; in despair; had his good nights and bad mornings; snatched at ideas and lost them; saw his book plain before him and it vanished; acted people's parts as he ate; mouthed them as he walked; now cried; now laughed; vacillated between this style and that; now preferred the heroic and pompous; next the plain and simple; now the vales of Tempe; then the fields of Kent or Cornwall; and could not decide whether he was the divinest genius or the greatest fool in the world.
>
> Virginia Woolf, *Orlando*

The stated objective of this thesis was to bring a better understanding of photon and electron induced desorption for the specific system of molecular ices, and to apply this understanding to the contexts of astrochemistry and vacuum dynamics.

Let us briefly summarize what has been done. Using two recently assembled set-ups (SPICES II at LERMA and the Multisystem at CERN), the PID and EID of a large number of molecular ice systems has been explored. For each systems, the desorption of the different species we could detect was characterized and quantified, and photodesorption spectra or EID yield curves as a function of electron energy were obtained. Synchrotron measurements were made in the VUV range (5-14 eV, mostly 7-14 eV) and the soft X-ray range (O 1s, 520-600 eV) for PID. A range of 150-2000 eV was explored for electrons. Parameters such as ice thickness, deposition temperature and irradiation temperature were explored for some systems. In addition to these measurements, considerable advance was made on the development of a laboratory laser desorption/laser spectroscopy set-up at LERMA, which will allow quantum-state and kinetic energy resolved measurements of desorption. It was successfully tested for the NO ice system, and shows promising possibilities for future work.

Answering to the first question of what desorbs goes from trivial in some simple molecular ices where only the parent molecule is detected, to one of the main stakes of the study when the number of desorbing fragments and photoproducts, as well as their quantitative importance, increases, but also when the investigation of desorbing ions in the case of the soft X-rays is added. A wide panel of different systems has been presented

in this manuscript.

The spectrally-resolved data, afforded by synchrotron radiation, obtained for PID is one of the most important particularities of our work. It allows electronic state selective measurements of photodesorption and reveals the electronic state dependence of the desorption of some species. In the VUV range this is the case of CO, where two different mechanisms are expected for the electronic states above and below 10 eV, but also for H_2O which has a maximum desorption efficiency in the second exciton band and a reduced efficiency above the ionization threshold. Still in the VUV range selective excitation is what allows the investigation of indirect desorption in unprecedented details. In the soft X-ray range, the photodesorption spectra of ions show deviations from the absorption, indicating some electronic states are more (H^+ desorption by the surface dangling O-H state) or less (H^- desorption in the "four-coordinated" peak at 540 eV) efficient for desorbing these ions. Spectral resolution is also what allows to reveal the domination of photoproduct (O_2, H_2O_2) excitation in the desorption of "oxygen fragment" ions (O^+, O^-, OH^+...). The wavelength dependent data has also been shown to be crucial for obtaining accurate yields for astrochemical modelling. I showed how photodesorption in both the VUV and soft X-ray ranges critically depends on the local photon density spectra considered, and how taking into account attenuation of the "source" spectra by gas and dust is important. The importance of indirect desorption processes for astrophysics have also been demonstrated in this manuscript, through the exploration of the efficiency of the process in CO and H_2O ices, which are the main components of ice mantles.

Soft X-ray photodesorption and electron-induced desorption are processes that are not currently considered in astrochemical models. Our quantitative measurements for a number of systems (the first of this kind in the case of soft X-ray photodesorption) give the possibility to take them into account. They allow preliminary estimations of whether these effects will be important or not. I concluded that electron-induced desorption will generally have a less important effect than UV photodesorption, but not by a margin large enough that investigating further the impact of this process should be discarded, considering the uncertainties of the estimation made. Soft X-ray photodesorption, on the other hand, should be the dominant source of non-thermal desorption in some specific regions. It is now left to astrochemical modelling to determine whether the process has a significant impact.

One unifying thread of this manuscript is the notion of "desorption-relevant depth" or "near-surface region": the number of layers below the surface where excitations can participate to desorption. This is linked with transport of energy or particles in the ice: electronic excitations, whether mobile excitons or transferred localized excitations, secondary and Auger electrons, energetic fragments and diffusing volatile products of chemistry can exist and migrate to the surface, and the depth below the surface involved can vary from just the very top monolayer to hundreds of layers. In the VUV range, I showed that desorption could be very surface-confined in the case of CH_4 or NO, or involve the first 2-3 ML when indirect desorption is involved, such as is the case for CO in the A-X region: the depth is molecule dependent. But it is also excited state dependent, as shown for CO where a different depth is observed for the states above 10 eV. It also depends on the composition of the systems when the ice is not pure, as we see for the two cases studied in indirect desorption. Systematic investigation of the indirect photodesorption process on CO and H_2O ices for a wide variety of species have

been performed. The processes for the two different substrates are of a different nature but both lead to desorption of species with variable efficiencies. For electrons I showed that the shape of the EID curve depended on the desorption relevant depth. Depending on the molecule it can be controlled by the scattering length of the secondary electrons (around $\sim$ 10 ML), as for N_2 and CO, or by migration of the electronic excitation in the case of Ar (more than 100 ML in that case). I showed that for porous CO_2, while secondary electrons seem to dominate the desorption-relevant depth for the desorption of CO_2, diffusion of fragments controlled the depth for desorption of CO and O_2: the desorption depth for a given system also depends on which desorbate we look at. In the X-ray range, for H_2O I estimated the desorption-relevant depth for neutral desorption to about 50 ML, taking into account both Auger electron scattering and exciton diffusion. But for the same system, there is a resonance in H^+ desorption that corresponds to a surface-specific state, which is therefore completely surface-confined. Understanding the desorption-relevant depth and which factor dominates that depth is an integral part of the understanding of desorption mechanisms, but also of the wider topic of energy transport in molecular ices. It is also a supplementary difficulty for modelling, since it depends on the ice, on the specific excited state or the electron energy, on the desorbate, and probably other factors such as temperature.

Another emerging theme in this thesis is the tight link between desorption and chemistry. Chemistry and dissociation are simultaneously a possible cause of desorption and a competition for desorption processes. Their importance in desorption is obvious when we observe desorption of fragments and irradiation products, which is the case for many systems. But I showed strong evidence that chemistry is also involved, through the non-geminate recombination process, in the VUV desorption of the intact water molecule from water ice. On the other hand, evaluating the intrinsic effiency of the photodesorption process in dissociative systems compared with competitive pathways (as was done for CH_4 in the VUV range) shows how chemistry and dissociation are also sources of energy dissipation, resulting in overall lower desorption yields.

There are many open perspectives of the further study of PID and EID from molecular ices. I have outlined in chapter IV what kind of systems we could move towards: pure ices of larger organic molecules, ice mixes of varying complexity, or the sub-monolayer regime. All these explorations are experimentally challenging in terms of detection but do not require much more than what we already have at our disposal. These same systems could also be studied in the soft X-ray range and with electrons, as inter-comparisons of the different sources have proven to be fruitful. Simpler systems should not be discarded, because we are far from having understood everything, but new techniques are requires for deeper investigations: laser spectroscopy of the desorbed molecules is one of them. The immediate perspective for the set-up is the investigation of the direct and indirect desorption mechanisms on CO ice, but possibilities abound for e.g. water direct and indirect desorption, REMPI of fragments (e.g. CO and H_2 from H_2CO)... In the soft X-ray range, desorption of ions seems extremely promising, as the desorption often seems dominated by true PID processes that therefore gives information on the core electronic states dynamics involved.

Going beyond what it is immediately possible to do, one of the elements that is lacking in general is a better understanding of the structure and the electronic states of molecular ices, which is a basic prerequisite to the further understanding of electronic and nuclei

dynamics. What happens at the surface in terms of structure and chemistry is particularly interesting but particularly difficult to probe. Surface specific spectroscopy methods, and luminescence studies for the evolution of electronic states for example, are among the long term investigations that could help bring a better understand of PID and EID - among other questions that these studies would answer.

In terms of context, while the present work has focused a lot on astrochemistry of the ISM, it would be interesting to explore further what kind of consequence the processes we study could have in vacuum dynamics, in planetary science (e.g. icy airless bodies, but also frozen molecules on aerosols in moons like Titan), or even other fields that have not yet been considered. New interesting systems and angles of study could be found that way.

Appendix A: Calibration values

In table 7, the calibration values relative to CO for the Balzers QMS in SPICES II are given (see III.1.7). The partial ionization cross-sections are taken from the literature, the reference being given at the end of the line. The transmission function of the QMS relative to CO is calculated using the power law TF $\propto (m/z)^{1.5}$ determined by calibration experiments where injections of acetone and xenon were performed, and setting the value for CO (m/z = 28) to 1. These values have been used to calibrate neutral desorption data from chapter IV and chapter VI. The ion desorption data from chapter VI, measured with the Hiden Analytical QMS, required only the QMS transmission function, for which a power law TF $\propto (m/z)^{0.5}$ was found.

In table 6 the QMS sensitivity (A.mbar^{-1}) determined against a calibrated Bayard-Alpert gauge by injection of the gas in the chamber is given for the Multisystem. The calibration is directly deduced from the ratio of the sensitivities. For O_2 no injection were made, we assumed a transmission function close to N_2.

Table 6: QMS sensitivity and calibration factor for quantification in the Multisystem.

	RGA sensitivity (A.mbar^{-1}	Calibration (rel. to N_2)
N_2	0.33	1
Ar	0.25	0.76
CO	0.35	1.1
CO_2	0.21	0.63
O_2	N/A	0.8
H_2	1	3
H_2O	0.33	1
D_2O	0.33	1

Table 7: QMS calibration factors for neutrals quantification in SPICES.

Species	Fragment (m/z)	Partial EI ionization cross section (Å^2)	QMS TF (rel. to CO)	Cal. factor (rel. to CO)	Ref.
CO	CO^+ (28)	1.78	1	1	[408]
	C^+ (12)	0.29	3.6	0.59	[408]
	O^+ (16)	0.19	2.3	0.25	[408]
N_2	N_2^+ (28)	1.88	1	0.95	[409]
	N^+ (14)	0.55	2.8	0.87	[409]
N	N^+ (14)	1.52	2.8	2.4	[410]
O_2	O_2^+ (32)	1.57	0.8	0.71	[409]
	O^+ (16)	0.73	2.3	0.95	[409]
H_2	H_2^+ (2)	0.93	*6*	3.1	[409]
	H^+ (1)	0.075	N/A	N/A	[409]
H_2O	H_2O^+ (18)	1.62	1.9	1.7	[411]
	OH^+ (17)	0.95	2.1	1.1	[411]
	O^+ (16)	0.16	2.3	0.21	[411]
OH	OH^+ (17)	1.85	2.1	2.2	[412]
CO_2	CO_2^+ (44)	2.74	0.5	0.77	[411]
	CO^+ (28)	0.11	1	0.06	[411]
NO	NO^+ (30)	2.42	0.9	1.2	[413]
	N^+ (14)	0.65	2.8	1	[413] + NIST
CH_4	CH_4^+ (16)	1.71	2.3	2.2	[408]
	CH_3^+ (15)	1.42	2.6	2.1	[408]
	CH_2^+ (14)	0.35	2.8	0.55	[408]
	CH^+ (13)	0.18	3.2	0.3	[408]
CH_3	CH_3^+ (15)	1.73	2.6	2.5	[414]
	CH_2^+ (14)	1.1	2.8	1.7	[414]
CH_2	CH_2^+ (14)	1.67	2.8		[414]
NH_3	NH_3^+ (17)	1.59	2.1		[415]
	NH_2^+ (16)	1.27	2.3		[415]
	NH^+ (15)	0.09	2.6		[415]
	N^+ (14)	0.03	2.8		[415]
NH_2	NH_2^+ (16)	3.8	2.3		[416]
NH	NH^+ (15)	2.1	2.6		[416]
HCOOH	$HCOOH^+$ (46)	1.19	0.5		[282]
	CO_2^+ (44)	0.2	0.5		[282]
	H_2CO^+ (30)	0.03	0.9		[282]
	HCO^+ (29)	1.95	1		[282]
	CO^+ (28)	0.34	1		[282]
	OH^+ (17)	0.33	2.1		[282]

Bibliography

[1] E. F. van Dishoeck; "Astrochemistry: Overview and Challenges"; arXiv preprint arXiv:1710.05940 (2017). 2

[2] E. F. van Dishoeck; "Astrochemistry of Dust, Ice and Gas: Introduction and Overview"; Faraday Discussions **168**, p. 9 (2014). 2, 3

[3] A. G. G. M. Tielens; "The Molecular Universe"; Proceedings of the International Astronomical Union **7**, pp. 3–18 (2011). 2

[4] E. Herbst; "The Synthesis of Large Interstellar Molecules"; International Reviews in Physical Chemistry **36**, pp. 287–331 (2017). 2

[5] A. G. G. M. Tielens; "The Molecular Universe"; Reviews of Modern Physics **85**, pp. 1021–1081 (2013). 2

[6] K. I. Öberg; "Photochemistry and Astrochemistry: Photochemical Pathways to Interstellar Complex Organic Molecules"; Chemical Reviews **116**, pp. 9631–9663 (2016). 2, 6, 167

[7] E. Herbst & E. F. van Dishoeck; "Complex Organic Interstellar Molecules"; Annual Review of Astronomy and Astrophysics **47**, pp. 427–480 (2009). 2, 16

[8] A. A. Boogert, P. A. Gerakines & D. C. Whittet; "Observations of the Icy Universe"; Annual Review of Astronomy and Astrophysics **53**, pp. 541–581 (2015). 2, 6, 7, 8

[9] P. Caselli & C. Ceccarelli; "Our Astrochemical Heritage"; The Astronomy and Astrophysics Review **20**, p. 56 (2012). 2

[10] E. F. van Dishoeck, E. Herbst & D. A. Neufeld; "Interstellar Water Chemistry: From Laboratory to Observations"; Chemical Reviews **113**, pp. 9043–9085 (2013). 2

[11] G. M. Muñoz Caro & E. Dartois; "Prebiotic Chemistry in Icy Grain Mantles in Space. An Experimental and Observational Approach"; Chemical Society Reviews **42**, p. 2173 (2013). 2

[12] C. J. Bennett, C. Pirim & T. M. Orlando; "Space-Weathering of Solar System Bodies: A Laboratory Perspective"; Chemical Reviews **113**, pp. 9086–9150 (2013). 2, 7, 8, 12, 167

[13] M. J. Mumma & S. B. Charnley; "The Chemical Composition of Comets—Emerging Taxonomies and Natal Heritage"; Annual Review of Astronomy and Astrophysics **49**, pp. 471–524 (2011). 2, 8

[14] B. A. McGuire; "2018 Census of Interstellar, Circumstellar, Extragalactic, Protoplanetary Disk, and Exoplanetary Molecules"; The Astrophysical Journal Supplement Series **239**, p. 17 (2018). 3

[15] T. P. Snow & B. J. McCall; "Diffuse Atomic and Molecular Clouds"; Annual Review of Astronomy and Astrophysics **44**, pp. 367–414 (2006). 4

[16] V. Wakelam, E. Bron, S. Cazaux, F. Dulieu, C. Gry, P. Guillard, E. Habart, L. Hornekær, S. Morisset, G. Nyman, V. Pirronello, S. D. Price, V. Valdivia, G. Vidali & N. Watanabe; "H 2 Formation on Interstellar Dust Grains: The Viewpoints of Theory, Experiments, Models and Observations"; Molecular Astrophysics **9**, pp. 1–36 (2017). 4

[17] M. S. Westley, R. A. Baragiola, R. E. Johnson & G. A. Baratta; "Photodesorption from Low-Temperature Water Ice in Interstellar and Circumsolar Grains"; Nature **373**, pp. 405–407 (1995). 4, 13, 127, 129

[18] L. B. F. M. Waters; "Dust in Evolved Stars"; in "Astrophysics of Dust," , volume 309p. 229 (2004). 5

[19] N. Ysard, M. Köhler, A. Jones, M.-A. Miville-Deschênes, A. Abergel & L. Fanciullo; "Dust Variations in the Diffuse Interstellar Medium: Constraints on Milky Way Dust from *Planck* -HFI Observations"; Astronomy & Astrophysics **577**, p. A110 (2015). 5

[20] A. Garcia; *Évolution de la porosité des grains: une solution aux problèmes de formation planétaire?*; Ph.D. thesis (2018). 6

[21] M. Godard; *Les carbones amorphes hydrogenes: observations, synthèse et caracterisation en laboratoire de poussières interstellaires*; Ph.D. thesis (2011). 6

[22] E. Dartois, L. d'Hendecourt, F. Boulanger, M. Jourdain de Muizon, M. Breitfellner, J.-L. Puget & H. J. Habing; "Molecular Gas Phase Counterparts to Solid State Grain Mantles Features: Implication for Gas/Grain Chemistry"; Astronomy and Astrophysics **331**, pp. 651–660 (1998). 6

[23] E. F. van Dishoeck, E. A. Bergin, D. C. Lis & J. I. Lunine; "Water: From Clouds to Planets"; in "Protostars and Planets VI," (University of Arizona Press) (2014); ISBN 978-0-8165-3124-0. 7

[24] W. M. Grundy, D. P. Cruikshank, G. R. Gladstone, C. J. A. Howett, T. R. Lauer, J. R. Spencer, M. E. Summers, M. W. Buie, A. M. Earle, K. Ennico, J. W. Parker, S. B. Porter, K. N. Singer, S. A. Stern, A. J. Verbiscer, R. A. Beyer, R. P. Binzel, B. J. Buratti, J. C. Cook, C. M. Dalle Ore, C. B. Olkin, A. H. Parker, S. Protopapa, E. Quirico, K. D. Retherford, S. J. Robbins, B. Schmitt, J. A. Stansberry, O. M. Umurhan, H. A. Weaver, L. A. Young, A. M. Zangari, V. J. Bray, A. F. Cheng, W. B. McKinnon, R. L. McNutt, J. M. Moore, F. Nimmo, D. C. Reuter, P. M. Schenk, S. A. Stern, F. Bagenal, K. Ennico, G. R. Gladstone, W. M. Grundy, W. B. McKinnon, J. M. Moore, C. B. Olkin, J. R. Spencer, H. A. Weaver, L. A. Young, T. Andert, O. Barnouin, R. A. Beyer, R. P. Binzel, M. Bird, V. J. Bray, M. Brozović, M. W. Buie, B. J. Buratti, A. F. Cheng, J. C. Cook, D. P. Cruikshank, C. M. Dalle Ore, A. M. Earle, H. A. Elliott, T. K. Greathouse, M. Hahn, D. P. Hamilton, M. E. Hill, D. P. Hinson, J. Hofgartner, M. Horányi, A. D. Howard, C. J. A. Howett, D. E. Jennings, J. A. Kammer, P. Kollmann, T. R. Lauer, P. Lavvas, I. R. Linscott, C. M. Lisse, A. W. Lunsford, D. J. McComas, R. L. McNutt Jr., M. Mutchler, F. Nimmo, J. I. Nunez, M. Paetzold, A. H. Parker, J. Wm. Parker, S. Philippe, M. Piquette, S. B. Porter, S. Protopapa, E. Quirico, H. J. Reitsema, D. C. Reuter, S. J. Robbins, J. H. Roberts, K. Runyon, P. M. Schenk, E. Schindhelm, B. Schmitt, M. R. Showalter, K. N. Singer, J. A. Stansberry, A. J. Steffl, D. F. Strobel, T. Stryk, M. E. Summers, J. R. Szalay, H. B. Throop, C. C. C. Tsang, G. L. Tyler, O. M. Umurhan, A. J. Verbiscer, M. H. Versteeg, G. E. Weigle II, O. L. White, W. W. Woods, E. F. Young & A. M. Zangari; "The Formation of Charon's Red Poles from Seasonally Cold-Trapped Volatiles"; Nature **539**, pp. 65–68 (2016). 8

[25] R. Gredel, S. Lepp & A. Dalgarno; "The C/CO Ratio in Dense Interstellar Clouds"; The Astrophysical Journal **323**, pp. L137 – L139 (1987). 9, 10

[26] C. M. Johns-Krull & G. J. Herczeg; "How Hot Is the Wind from TW Hydrae?" The Astrophysical Journal **655**, p. 345 (2007). 9, 11

[27] J. S. Mathis, P. G. Mezger & N. Panagia; "Interstellar Radiation Field and Dust Temperatures in the Diffuse Interstellar Matter and in Giant Molecular Clouds"; Astronomy & Astrophysics **128**, pp. 212–229 (1983). 8, 9

[28] C. Cecchi-Pestellini & S. Aiello; "Cosmic Ray Induced Photons in Dense Interstellar Clouds"; Monthly Notices of the Royal Astronomical Society **258**, pp. 125–133 (1992). 10

[29] C. J. Shen, J. M. Greenberg, W. A. Schutte & E. F. van Dishoeck; "Cosmic Ray Induced Explosive Chemical Desorption in Dense Clouds"; Astronomy & Astrophysics **415**, pp. 203–215 (2004). 10, 13, 194

[30] H. Nomura, Y. Aikawa, M. Tsujimoto, Y. Nakagawa & T. J. Millar; "Molecular Hydrogen Emission from Protoplanetary Disks. II. Effects of X-Ray Irradiation and Dust Evolution"; The Astrophysical Journal **661**, p. 334 (2007). 11, 205

[31] L. I. Cleeves, E. A. Bergin, C. Qi, F. C. Adams & K. I. Öberg; "Constraining the X-Ray and Cosmic-Ray Ionization Chemistry of the TW Hya Protoplanetary Disk: Evidence for a Sub-Interstellar Cosmic-Ray Rate"; The Astrophysical Journal **799**, p. 204 (2015). 11, 238

[32] C. Rab, M. Güdel, P. Woitke, I. Kamp, W.-F. Thi, M. Min, G. Aresu & R. Meijerink; "X-Ray Radiative Transfer in Protoplanetary Disks: The Role of Dust and X-Ray Background Fields"; Astronomy & Astrophysics **609**, p. A91 (2018). 11

[33] G. Randall Gladstone, W. R. Pryor & S. Alan Stern; "Lyα@Pluto"; Icarus **246**, pp. 279–284 (2015). 12

[34] L. T. Greenberg; "Photodesorption from Interstellar Dust Grains"; in "Interstellar Dust and Related Topics," pp. 413–419 (Springer) (1973). 13

[35] R. E. Johnson, R. W. Carlson, T. A. Cassidy & M. Fama; "Sputtering of Ices"; in "The Science of Solar System Ices," , volume 356, edited by M. S. Gudipati & J. Castillo-Rogez; pp. 551–581 (Springer New York, New York, NY) (2013); ISBN 978-1-4614-3075-9 978-1-4614-3076-6. 13, 125, 177, 183

[36] E. Dartois, M. Chabot, T. I. Barkach, H. Rothard, B. Augé, A. N. Agnihotri, A. Domaracka & P. Boduch; "Cosmic Ray Sputtering Yield of Interstellar H2O Ice Mantles : Ice Mantle Thickness Dependence"; Astronomy & Astrophysics **618**, p. A173 (2018). 1809.09180. 13, 189

[37] T. Pino, M. Chabot, K. Béroff, M. Godard, F. Fernandez-Villoria, K. Le, L. Breuer, M. Herder, A. Wucher, M. Bender, D. Severin, C. Trautmann & E. Dartois; "Release of Large Polycyclic Aromatic Hydrocarbons and Fullerenes by Cosmic Rays from Interstellar Dust. Swift Heavy Ion Irradiations of Interstellar Carbonaceous Dust Analogue"; Astronomy & Astrophysics (2019). 13

[38] A. Léger, M. Jura & A. Omont; "Desorption from Interstellar Grains"; Astronomy & Astrophysics **144**, pp. 147–160 (1985). 14

[39] J. Najita, E. A. Bergin & J. N. Ullom; "X-Ray Desorption of Molecules from Grains in Protoplanetary Disks"; The Astrophysical Journal **561**, p. 880 (2001). 14

[40] R. T. Garrod, V. Wakelam & E. Herbst; "Non-Thermal Desorption from Interstellar Dust Grains via Exothermic Surface Reactions"; Astronomy and Astrophysics **467**, pp. 1103–1115 (2007). 14

[41] F. Dulieu, E. Congiu, J. Noble, S. Baouche, H. Chaabouni, A. Moudens, M. Minissale & S. Cazaux; "How Micron-Sized Dust Particles Determine the Chemistry of Our Universe"; Scientific Reports **3** (2013). 14

[42] Y. Oba, T. Tomaru, T. Lamberts, A. Kouchi & N. Watanabe; "An Infrared Measurement of Chemical Desorption from Interstellar Ice Analogues"; Nature Astronomy (2018). 14

[43] M. Minissale, F. Dulieu, S. Cazaux & S. Hocuk; "Dust as Interstellar Catalyst: I. Quantifying the Chemical Desorption Process"; Astronomy & Astrophysics **585**, p. A24 (2016). 14

[44] J. Harju, J. E. Pineda, A. I. Vasyunin, P. Caselli, S. S. R. Offner, A. A. Goodman, M. Juvela, O. Sipilae, A. Faure, R. L. Gal, P. Hily-Blant, J. Alves, L. Bizzocchi, A. Burkert, H. Chen, R. K. Friesen, R. Guesten, P. C. Myers, A. Punanova, C. Rist, E. Rosolowsky, S. Schlemmer, Y. Shirley, S. Spezzano, C. Vastel & L. Wiesenfield; "Efficient Methanol Desorption in Shear Instability"; arXiv:1903.11298 [astro-ph] (2019)1903.11298. 14

[45] F. Le Petit, C. Nehme, J. Le Bourlot & E. Roueff; "A Model for Atomic and Molecular Interstellar Gas: The Meudon PDR Code"; The Astrophysical Journal Supplement Series **164**, pp. 506–529 (2006). 15

[46] M. Ruaud, V. Wakelam & F. Hersant; "Gas and Grain Chemical Composition in Cold Cores as Predicted by the Nautilus Three-Phase Model"; Monthly Notices of the Royal Astronomical Society **459**, pp. 3756–3767 (2016). 15

[47] J. Kalvāns; "Ice Chemistry in Starless Molecular Cores"; The Astrophysical Journal **806**, p. 196 (2015). 15

[48] L. Podio, I. Kamp, C. Codella, S. Cabrit, B. Nisini, C. Dougados, G. Sandell, J. P. Williams, L. Testi, W.-F. Thi, P. Woitke, R. Meijerink, M. Spaans, G. Aresu, F. Ménard & C. Pinte; "Water Vapor in the Protoplanetary Disk of DG Tau"; The Astrophysical Journal **766**, p. L5 (2013). 15, 17

[49] C. Walsh, T. J. Millar, H. Nomura, E. Herbst, S. W. Weaver, Y. Aikawa, J. C. Laas & A. I. Vasyunin; "Complex Organic Molecules in Protoplanetary Disks"; Astronomy & Astrophysics **563**, p. A33 (2014). 15

[50] C. N. Shingledecker & E. Herbst; "A General Method for the Inclusion of Radiation Chemistry in Astrochemical Models"; Physical Chemistry Chemical Physics (2018). 15

[51] J. Kalvāns; "The Effect of Selective Desorption Mechanisms During Interstellar Ice Formation"; The Astrophysical Journal **803**, p. 52 (2015). 15, 16

[52] K. I. Öberg, H. Linnartz, R. Visser & E. F. van Dishoeck; "Photodesorption of Ices. II. H2O and D2O"; The Astrophysical Journal **693**, pp. 1209–1218 (2009). 16, 129

[53] C. Walsh, S. Vissapragada & H. McGee; "Methanol Formation in TW Hya and Future Prospects for Detecting Larger Complex Molecules in Disks with ALMA"; Proceedings of the IAU Symposium 332S, Astrochemistry VII - Through the Cosmos from Galaxies to Planets (2017). 16, 17

[54] M. Bertin, C. Romanzin, M. Doronin, L. Philippe, P. Jeseck, N. Ligterink, H. Linnartz, X. Michaut & J.-H. Fillion; "UV Photodesorption of Methanol in Pure and CO-Rich Ices: Desorption Rates of the Intact Molecules and the Photofragments"; The Astrophysical Journal **817**, p. L12 (2016). 16, 98, 140, 144, 147, 149, 154, 171

[55] R. Dupuy, M. Bertin, G. Féraud, M. Hassenfratz, X. Michaut, T. Putaud, L. Philippe, P. Jeseck, M. Angelucci, R. Cimino, V. Baglin, C. Romanzin & J.-H. Fillion; "X-Ray Photodesorption from Water Ice in Protoplanetary Disks and X-Ray-Dominated Regions"; Nature Astronomy **2**, pp. 796–801 (2018). 16, 198

[56] D. Hollenbach, M. J. Kaufman, E. A. Bergin & G. J. Melnick; "Water, O2, and Ice in Molecular Clouds"; The Astrophysical Journal **690**, pp. 1497–1521 (2009). 16

[57] P. Caselli, E. Keto, E. A. Bergin, M. Tafalla, Y. Aikawa, T. Douglas, L. Pagani, U. A. Yíldíz, F. F. S. van der Tak, C. M. Walmsley, C. Codella, B. Nisini, L. E. Kristensen & E. F. van Dishoeck; "First Detection of Water Vapor in a Pre-Stellar Core"; The Astrophysical Journal **759**, p. L37 (2012). 16

[58] R. Le Gal, E. Herbst, G. Dufour, P. Gratier, M. Ruaud, T. H. G. Vidal & V. Wakelam; "A New Study of the Chemical Structure of the Horsehead Nebula: The Influence of Grain-Surface Chemistry"; Astronomy & Astrophysics **605**, p. A88 (2017). 16

[59] V. Guzmán, J. Pety, J. R. Goicoechea, M. Gerin & E. Roueff; "H $_2$ CO in the Horsehead PDR: Photo-Desorption of Dust Grain Ice Mantles"; Astronomy & Astrophysics **534**, p. A49 (2011). 16

[60] K. Willacy & W. D. Langer; "The Importance of Photoprocessing in Protoplanetary Disks"; The Astrophysical Journal **544**, pp. 903–920 (2000). 16

[61] C. Dominik, C. Ceccarelli, D. Hollenbach & M. Kaufman; "Gas-Phase Water in the Surface Layer of Protoplanetary Disks"; The Astrophysical Journal Letters **635**, p. L85 (2005). 16

[62] M. R. Hogerheijde, E. A. Bergin, C. Brinch, L. I. Cleeves, J. K. Fogel, G. A. Blake, C. Dominik, D. C. Lis, G. Melnick, D. Neufeld *et al.*; "Detection of the Water Reservoir in a Forming Planetary System"; Science **334**, pp. 338–340 (2011). 17

[63] V. N. Salinas, M. R. Hogerheijde, E. A. Bergin, L. Ilsedore Cleeves, C. Brinch, G. A. Blake, D. C. Lis, G. J. Melnick, O. Panić, J. C. Pearson, L. Kristensen, U. A. Yıldız & E. F. van Dishoeck; "First Detection of Gas-Phase Ammonia in a Planet-Forming Disk: NH3 , N2H+, and H2O in the Disk around TW Hydrae"; Astronomy & Astrophysics **591**, p. A122 (2016). 17

[64] H. Terada & A. T. Tokunaga; "Multi-Epoch Detections of Water Ice Absorption in Edge-on Disks Around Herbig Ae Stars: PDS 144n and PDS 453"; The Astrophysical Journal **834**, p. 115 (2017). 17

[65] K. I. Öberg, K. Furuya, R. Loomis, Y. Aikawa, S. M. Andrews, C. Qi, E. F. van Dishoeck & D. J. Wilner; "Double DCO^+ Rings Reveal Co Ice Desorption in the Outer Disk Around Im Lup"; The Astrophysical Journal **810**, p. 112 (2015). 17

[66] K. I. Öberg, V. V. Guzmán, K. Furuya, C. Qi, Y. Aikawa, S. M. Andrews, R. Loomis & D. J. Wilner; "The Comet-like Composition of a Protoplanetary Disk as Revealed by Complex Cyanides"; Nature **520**, pp. 198–201 (2015). 17

[67] M. T. Carney, M. R. Hogerheijde, R. A. Loomis, V. N. Salinas, K. I. Öberg, C. Qi & D. J. Wilner; "Increased H2CO Production in the Outer Disk around HD 163296"; Astronomy & Astrophysics **605**, p. A21 (2017). 17

[68] P. A. Redhead; "The First 50 Years of Electron Stimulated Desorption (1918–1968)"; Vacuum **48**, pp. 585–596 (1997). 17, 47

[69] A. J. Dempster; "A New Method of Positive Ray Analysis"; Physical Review **11**, pp. 316–325 (1918). 17

[70] Y. Isikawa; "The Desorption of the Adsorbed Hydrogen on a Platinum Plate by the Impact of Slow Electrons"; Proceedings of the Imperial Academy **18**, pp. 246–250 (1942). 17

[71] V. Baglin; "The LHC Vacuum System: Commissioning up to Nominal Luminosity"; Vacuum **138**, pp. 112–119 (2017). 19

[72] V. Baglin, I. Collins, O. Gröbner, C. Grünhagel & B. Jenninger; "Molecular Desorption by Synchrotron Radiation and Sticking Coefficient at Cryogenic Temperatures for H2, CH4, CO and CO2"; Vacuum **67**, pp. 421–428 (2002). 20

[73] R. Cimino, M. Commisso, D. R. Grosso, T. Demma, V. Baglin, R. Flammini & R. Larciprete; "Nature of the Decrease of the Secondary-Electron Yield by Electron Bombardment and Its Energy Dependence"; Physical Review Letters **109**, p. 064801 (2012). 20

[74] C. Herbeaux, P. Marin, P. Rommeluère, V. Baglin & O. Gröbner; "Photon Stimulated Desorption of Unbaked Stainless-Steel Vacuum Chambers"; Vacuum **60**, pp. 113–122 (2001). 20

[75] F. Le Pimpec, O. Gröbner & J. Laurent; "Electron Stimulated Molecular Desorption of a Non-Evaporable Zr–V–Fe Alloy Getter at Room Temperature"; Nuclear Instruments and Methods in Physics Research Section B: Beam Interactions with Materials and Atoms **194**, pp. 434–442 (2002). 20

[76] I. Vegard; "Struktur Und Leuchtfähigkeit von Festem Kohlenoxyd"; Zeitschrift für Physik **61**, pp. 185–190 (1930). 28

[77] M. Satorre, M. Domingo, C. Millán, R. Luna, R. Vilaplana & C. Santonja; "Density of CH4, N2 and CO2 Ices at Different Temperatures of Deposition"; Planetary and Space Science **56**, pp. 1748–1752 (2008). 28, 29, 179

[78] W. J. Dulmage, E. A. Meyers & W. N. Lipscomb; "On the Crystal and Molecular Structure of N2O2"; Acta Crystallographica **6**, pp. 760–764 (1953). 28, 108

[79] W. Schulze & H. Abe; "Density, Refractive Index and Sorption Capacity of Solid CO2 Layers"; Chemical Physics **52**, pp. 381–388 (1980). 28, 185

[80] I. Y. Fugol'; "Excitons in Rare-Gas Crystals"; Advances in Physics **27**, pp. 1–87 (1978). 28, 52

[81] R. S. Smith, R. A. May & B. D. Kay; "Desorption Kinetics of Ar, Kr, Xe, N2, O2, CO, Methane, Ethane, and Propane from Graphene and Amorphous Solid Water Surfaces"; The Journal of Physical Chemistry B **120**, pp. 1979–1987 (2016). 28, 162

[82] S. A. Sandford & L. J. Allamandola; "The Volume- and Surface-Binding Energies of Ice Systems Containing CO, CO2 and H2O"; Icarus **87**, pp. 188–192 (1990). 28

[83] H. J. Fraser, M. P. Collings, M. R. S. McCoustra & D. A. Williams; "Thermal Desorption of Water Ice in the Interstellar Medium"; Monthly Notices of the Royal Astronomical Society **327**, pp. 1165–1172 (2001). 28

[84] K. Jacobi & H. H. Rotermund; "UV Photoemission from Physisorbed Atoms and Molecules: Electronic Binding Energies of Valence Levels in Mono-and Multilayers"; Surface Science **116**, pp. 435–455 (1982). 28

[85] F.-j. Himpsel, N. Schwentner & E. E. Koch; "Ultraviolet Photoemission Spectroscopy of Solid Nitrogen and Oxygen"; physica status solidi (b) **71**, pp. 615–621 (1975). 28, 123

[86] K. Kobayashi; "Optical Spectra and Electronic Structure of Ice"; The Journal of Physical Chemistry **87**, pp. 4317–4321 (1983). 28, 38, 128, 131, 132

[87] N. Schwentner, F. J. Himpsel, V. Saile, M. Skibowski, W. Steinmann & E. E. Koch; "Photoemission from Rare-Gas Solids: Electron Energy Distributions from the Valence Bands"; Physical Review Letters **34**, pp. 528–531 (1975). 28

[88] L. Meyer; "Phase Transitions in Van Der Waal's Lattices"; in "Advances in Chemical Physics," , edited by I. Prigogine & S. A. Rice; pp. 343–387 (John Wiley & Sons, Inc., Hoboken, NJ, USA) (2007); ISBN 978-0-470-14361-2 978-0-471-69921-7. 29

[89] R. Luna, G. Molpeceres, J. Ortigoso, M. A. Satorre, M. Domingo & B. Maté; "Densities, Infrared Band Strengths, and Optical Constants of Solid Methanol"; Astronomy & Astrophysics **617**, p. A116 (2018). 29

[90] L. Vegard; "Die Struktur derjenigen Form von festem Stickstoff, die unterhalb 35,50 K stabil ist"; Zeitschrift für Physik **58**, pp. 497–510 (1929). 29

[91] G. M. Muñoz Caro, Y.-J. Chen, S. Aparicio, A. Jiménez-Escobar, A. Rosu-Finsen, J. Lasne & M. R. S. McCoustra; "Photodesorption and Physical Properties of CO Ice as a Function of Temperature"; Astronomy & Astrophysics **589**, p. A19 (2016). 29, 100, 101, 102, 107, 170

[92] J. P. Devlin & V. Buch; "Surface of Ice as Viewed from Combined Spectroscopic and Computer Modeling Studies"; The Journal of Physical Chemistry **99**, pp. 16534–16548 (1995). 29

[93] K. P. Stevenson; "Controlling the Morphology of Amorphous Solid Water"; Science **283**, pp. 1505–1507 (1999). 29, 128

[94] G. A. Kimmel, K. P. Stevenson, Z. Dohnálek, R. S. Smith & B. D. Kay; "Control of Amorphous Solid Water Morphology Using Molecular Beams. I. Experimental Results"; The Journal of Chemical Physics **114**, pp. 5284–5294 (2001). 29, 128

[95] J. A. Noble, C. Martin, H. J. Fraser, P. Roubin & S. Coussan; "Unveiling the Surface Structure of Amorphous Solid Water via Selective Infrared Irradiation of OH Stretching Modes"; The Journal of Physical Chemistry Letters **5**, pp. 826–829 (2014). 29

[96] R. M. Escribano, G. M. Munoz Caro, G. A. Cruz-Diaz, Y. Rodriguez-Lazcano & B. Mate; "Crystallization of CO2 Ice and the Absence of Amorphous CO2 Ice in Space"; Proceedings of the National Academy of Sciences **110**, pp. 12899–12904 (2013). 29

[97] J. He & G. Vidali; "Characterization of Thin Film CO2 Ice through the Infrared Nu1+nu3 Combination Mode"; Monthly Notices of the Royal Astronomical Society **473**, pp. 860–866 (2018). 29, 184

[98] A. Nilsson, D. Nordlund, I. Waluyo, N. Huang, H. Ogasawara, S. Kaya, U. Bergmann, L.-å. Näslund, H. Öström, P. Wernet, K. Andersson, T. Schiros & L. Pettersson; "X-Ray Absorption Spectroscopy and X-Ray Raman Scattering of Water and Ice; an Experimental View"; Journal of Electron Spectroscopy and Related Phenomena **177**, pp. 99–129 (2010). 29, 201

[99] A. Rosu-Finsen, J. Lasne, A. Cassidy, M. R. S. McCoustra & D. Field; "Spontaneous Polarization of Solid CO on Water Ices and Some Astrophysical Implications"; Phys. Chem. Chem. Phys. **18**, pp. 5159–5171 (2016). 29

[100] O. Plekan, A. Rosu-Finsen, A. M. Cassidy, J. Lasne, M. R. S. McCoustra & D. Field; "A Review of Recent Progress in Understanding the Spontelectric State of Matter"; The European Physical Journal D **71** (2017). 29

[101] G. Brivio & T. Grimley; "Dynamics of Adsorption/Desorption at Solid Surfaces"; Surface Science Reports **17**, pp. 1–84 (1993). 29

[102] J. M. Hollas; *Spectroscopie: cours et exercices* (Dunod, Paris) (2000); ISBN 978-2-10-003945-6. 29

[103] G. Herzberg; *Spectra of Diatomic Molecules*; number by Gerhard Herzberg ; 1 in Molecular Spectra and Molecular Structure; 2nd edition (van Nostrand, New York) (1987); ISBN 978-0-442-03385-9. 29, 115

[104] H. Lefebvre-Brion, Robert W. Field, TotalBoox & TBX; *The Spectra and Dynamics of Diatomic Molecules.* (Elsevier Science) (2004); ISBN 978-0-08-051750-6. 29

[105] E. Biémont; *Spectroscopie moléculaire: structures moléculaires et analyse spectrale* (2010); ISBN 978-2-8041-5065-5. 29

[106] P. Slavıćek, R. Kalus, P. Paška, I. Odvárková, P. Hobza & A. Malijevský; "State-of-the-Art Correlated *Ab Initio* Potential Energy Curves for Heavy Rare Gas Dimers: Ar2, Kr2, and Xe2"; The Journal of Chemical Physics **119**, pp. 2102–2119 (2003). 32

[107] Y. Mizukami & H. Nakatsuji; "Potential Energy Curves of the Ground, Excited, and Ionized States of Ar $_2$ Studied by the Symmetry Adapted Cluster-configuration Interaction Theory"; The Journal of Chemical Physics **92**, pp. 6084–6092 (1990). 32

[108] G. L. Wolk & J. W. Rich; "Observation of a New Electronic State of Carbon Monoxide Using LIF on Highly Vibrationally Excited CO($X\ ^1\ \Sigma\ ^+$)"; The Journal of Chemical Physics **79**, pp. 12–18 (1983). 32

[109] M. Eidelsberg, J.-Y. Roncin, A. Le Floch, F. Launay, C. Letzelter & J. Rostas; "Reinvestigation of the Vacuum Ultraviolet Spectrum of CO and Isotopic Species: The B1Σ+ ↔ X1Σ+ Transition"; Journal of Molecular Spectroscopy **121**, pp. 309–336 (1987). 31

[110] D. L. Cooper & K. Kirby; "Theoretical Study of Low-lying $^1\Sigma^+$ and $^1\Pi$ States of CO. I. Potential Energy Curves and Dipole Moments"; The Journal of Chemical Physics **87**, pp. 424–432 (1987). 31

[111] W. Chan, G. Cooper & C. Brion; "Absolute Optical Oscillator Strengths for Discrete and Continuum Photoabsorption of Carbon Monoxide (7–200 eV) and Transition Moments for the X 1Σ+ - A 1Π System"; Chemical Physics **170**, pp. 123–138 (1993). 34, 36, 37

[112] M. B. Robin; *Higher Excited States of Polyatomic Molecules. Vol. 1: [...]* (Acad. Press, New York, NY) (1974); ISBN 978-0-12-589901-7. 35, 36, 122, 123, 124, 135, 137

[113] V. L. Broude, Ė. I. Rašba & E. F. Šeka; *Spectroscopy of Molecular Excitons*; number 16 in Springer Series in Chemical Physics (Springer, Berlin) (1985); ISBN 978-3-540-12409-2 978-0-387-12409-4. 35

[114] H. G. Hixson, M. J. Wojcik, M. S. Devlin, J. P. Devlin & V. Buch; "Experimental and Simulated Vibrational Spectra of H2 Absorbed in Amorphous Ice: Surface Structures, Energetics, and Relaxations"; The Journal of Chemical Physics **97**, p. 753 (1992). 35

[115] N. J. Mason, A. Dawes, P. D. Holtom, R. J. Mukerji, M. P. Davis, B. Sivaraman, R. I. Kaiser, S. V. Hoffmann & D. A. Shaw; "VUV Spectroscopy and Photo-Processing of Astrochemical Ices: An Experimental Study"; Faraday Discussions **133**, p. 311 (2006). 35, 135, 136, 137

[116] A. S. Davydov; "The Theory of Molecular Excitons"; Soviet Physics Uspekhi **7**, pp. 145–178 (1964). 36

[117] R. S. Knox; *Theory of Excitons* (Academic Pr., New York) (1972); ISBN 978-0-12-607765-0. 36

[118] F. Messina, E. Vella, M. Cannas & R. Boscaino; "Evidence of Delocalized Excitons in Amorphous Solids"; Physical Review Letters **105**, p. 116401 (2010). 36

[119] B. Katz, M. Brith, B. Sharf & J. Jortner; "Rydberg States of Benzene in Rare-Gas Matrices"; The Journal of Chemical Physics **50**, pp. 5195–5203 (1969). 36

[120] F. Vigliotti & M. Chergui; "Rydberg States in the Condensed Phase Studied by Fluorescence Depletion Spectroscopy"; The European Physical Journal D **10**, p. 379 (2000). 36

[121] H.-C. Lu, H.-K. Chen, B.-M. Cheng, Y.-P. Kuo & J. F. Ogilvie; "Spectra in the Vacuum Ultraviolet Region of CO in Gaseous and Solid Phases and Dispersed in Solid Argon at 10 K"; Journal of Physics B: Atomic, Molecular and Optical Physics **38**, pp. 3693–3704 (2005). 36, 37, 101

[122] Y.-J. Chen, G. M. Muñoz Caro, S. Aparicio, A. Jiménez-Escobar, J. Lasne, A. Rosu-Finsen, M. R. S. McCoustra, A. M. Cassidy & D. Field; "Wannier-Mott Excitons in Nanoscale Molecular Ices"; Physical Review Letters **119** (2017). 37

[123] L. Lee & M. Suto; "Quantitative Photoabsorption and Fluorescence Study of H2O and D2O at 50-190 Nm"; Chemical Physics **110**, pp. 161–169 (1986). 38

[124] J. H. Fillion, R. van Harrevelt, J. Ruiz, M. Castillejo, A. H. Zanganeh, J. L. Lemaire, M. C. van Hemert & F. Rostas; "Photodissociation of H2O and D2O in B, C, and D States (134-119 Nm). Comparison between Experiment and Ab Initio Calculations"; The Journal of Physical Chemistry A **105**, pp. 11414–11424 (2001). 38

[125] H. A. Bethe; *Selected Works of Hans A Bethe: (With Commentary)*; *World Scientific Series in 20th Century Physics*, volume 18 (WORLD SCIENTIFIC) (1997); ISBN 978-981-02-2876-7 978-981-279-575-5. 38, 39

[126] H. A. Bethe & J. Ashkin; "Passage of Radiations through Matter"; in "Experimental Nuclear Physics," , volume 1 (1953). 38, 39, 40, 41

[127] M. Inokuti; "Inelastic Collisions of Fast Charged Particles with Atoms and Molecules—The Bethe Theory Revisited"; Reviews of Modern Physics **43**, pp. 297–347 (1971). 38, 39, 40

[128] D. C. Joy & S. Luo; "An Empirical Stopping Power Relationship for Low-Energy Electrons"; Scanning **11**, pp. 176–180 (1989). 38, 41

[129] A. Mozumder; *Fundamentals of Radiation Chemistry* (Elsevier) (1999); ISBN 978-0-12-509390-3. 38, 41

[130] E. Alizadeh & L. Sanche; "Precursors of Solvated Electrons in Radiobiological Physics and Chemistry"; Chemical Reviews **112**, pp. 5578–5602 (2012). 38, 39

[131] J. A. LaVerne & A. Mozumder; "Penetration of Low-Energy Electrons in Water"; Radiation Research **96**, p. 219 (1983). 41

[132] P. Hovington, D. Drouin, R. Gauvin, D. C. Joy & N. Evans; "CASINO: A New Monte Carlo Code in C Language for Electron Beam Interactions-Part III: Stopping Power at Low Energies"; Scanning **19**, pp. 29–35 (2006). 41

[133] A. Adams & P. K. Hansma; "Practical Range and Energy Loss of 0.1-3-keV Electrons in Thin Films of N2 , O2 , Ar, Kr, and Xe"; Physical Review B **22**, pp. 4258–4263 (1980). 42, 43, 177, 178

[134] S. Valkealahti, J. Schou & R. M. Nieminen; "Energy Deposition of keV Electrons in Light Elements"; Journal of Applied Physics **65**, pp. 2258–2266 (1989). 42, 43

[135] M. Øhlenschlaeger, H. Andersen, J. Schou & H. Sørensen; "The Range of 1-3 keV Electrons in Solid Oxygen and Carbon Monoxide"; Radiation Protection Dosimetry **13**, pp. 61–64 (1985). 42

[136] L. Sanche; "Electron Resonances in DIET"; Surface science **451**, pp. 82–90 (2000). 44

[137] J. Stöhr; *NEXAFS Spectroscopy* (Springer, Berlin; London) (2011); ISBN 978-3-642-08113-2. 44, 214

[138] D. C. Koningsberger (Editor); *X-Ray Absorption: Principles, Applications, Techniques of EXAFS, SEXAFS and XANES*; number 92 in Chemical Analysis (Wiley, New York) (1988); ISBN 978-0-471-87547-5. 44

[139] R. Treichler, W. Wurth, W. Riedl, P. Feulner & D. Menzel; "Core Excitation-Induced Photodesorption of Molecular and Fragment Ions from CO Adsorbates on Metal Surfaces"; Chemical Physics **153**, pp. 259–281 (1991). 46, 215, 230

[140] R. A. Rosenberg, P. J. Love, P. R. LaRoe, V. Rehn & C. C. Parks; "K-Shell Photoexcitation of Solid N2, CO, NO, O2, and N2O"; Physical Review B **31**, p. 2634 (1985). 47, 88, 198, 209, 214, 226

[141] M. Piancastelli; "The Neverending Story of Shape Resonances"; Journal of Electron Spectroscopy and Related Phenomena **100**, pp. 167–190 (1999). 47

[142] D. Lichtman & Y. Shapira; "Photodesorption: A Critical Review"; Critical Reviews in Solid State and Materials Sciences **8**, pp. 93–118 (1978). 47

[143] P. Avouris & R. E. Walkup; "Fundamental Mechanisms of Desorption and Fragmentation Induced by Electronic Transitions at Surfaces"; Annual Review of Physical Chemistry **40**, pp. 173–206 (1989). 47

[144] T. E. Madey; "History of Desorption Induced by Electronic Transitions"; Surface science **299**, pp. 824–836 (1994). 47

[145] D. Menzel; "Thirty Years of MGR: How It Came about, and What Came of It"; Nuclear Instruments and Methods in Physics Research Section B: Beam Interactions with Materials and Atoms **101**, pp. 1–10 (1995). 47

[146] N. H. Tolk, M. M. Traum, J. C. Tully & T. E. Madey; *Desorption Induced by Electronic Transitions DIET I: Proceedings of the First International Workshop, Williamsburg, Virginia, USA, May 12-14, 1982* (Springer Berlin Heidelberg, Berlin, Heidelberg) (1983); ISBN 978-3-642-45552-0 978-3-642-45550-6. 47, 50

[147] W. Brenig, D. Menzel, G. Ertl & R. Gomer (Editors); *Desorption Induced by Electronic Transitions DIET II*; *Springer Series in Surface Sciences*, volume 4 (Springer Berlin Heidelberg, Berlin, Heidelberg) (1985); ISBN 978-3-642-82549-1 978-3-642-82547-7. 47

[148] R. H. Stulen, M. L. Knotek, G. Ertl & R. Gomer (Editors); *Desorption Induced by Electronic Transitions DIET III*; *Springer Series in Surface Sciences*, volume 13 (Springer Berlin Heidelberg, Berlin, Heidelberg) (1988); ISBN 978-3-642-73730-5 978-3-642-73728-2. 47

[149] G. Betz, P. Varga, G. Ertl, R. Gomer & H. K. V. Lotsch (Editors); *Desorption Induced by Electronic Transitions DIET IV*; *Springer Series in Surface Sciences*, volume 19 (Springer Berlin Heidelberg, Berlin, Heidelberg) (1990); ISBN 978-3-642-84147-7 978-3-642-84145-3. 47

[150] A. R. Burns, E. B. Stechel & D. R. Jennison; *Desorption Induced by Electronic Transitions DIET V: Proceedings of the Fifth International Workshop, Taos, NM, USA, April 1-4, 1992* (Springer Berlin Heidelberg, Berlin, Heidelberg) (1993); ISBN 978-3-642-78080-6. 47

[151] D. Menzel & R. Gomer; "Desorption from Metal Surfaces by Low-Energy Electrons"; The Journal of Chemical Physics **41**, p. 3311 (1964). 47

[152] D. Menzel & R. Gomer; "Desorption from Surfaces by Slow-Electron Impact"; The Journal of Chemical Physics **40**, pp. 1164–1165 (1964). 47

[153] P. A. Redhead; "Interaction of Slow Electrons With Chemisorbed Oxygen"; Canadian Journal of Physics **42**, pp. 886–905 (1964). 47

[154] P. A. Redhead; "Desorption of CO and O+ From Polycrystalline Mo Surfaces by Slow Electron Impact"; Applied Physics Letters **4**, pp. 166–167 (1964). 47

[155] P. R. Antoniewicz; "Model for Electron- and Photon-Stimulated Desorption"; Physical Review B **21**, pp. 3811–3815 (1980). 49

[156] D. Pooley; "F-Centre Production in Alkali Halides by Electron-Hole Recombination and a Subsequent [110] Replacement Sequence: A Discussion of the Electron-Hole Recombination"; Proceedings of the Physical Society **87**, pp. 245–256 (1966). 49

[157] H. N. Hersh; "Proposed Excitonic Mechanism of Color-Center Formation in Alkali Halides"; Physical Review **148**, pp. 928–932 (1966). 49

[158] M. L. Knotek & P. J. Feibelman; "Ion Desorption by Core-Hole Auger Decay"; Physical Review Letters **40**, pp. 964–967 (1978). 50

[159] X.-Y. Zhu, M. Wolf, T. Huett & J. M. White; "Laser-induced Interaction of Ammonia with GaAs(100). II. Desorption Dynamics"; The Journal of Chemical Physics **97**, pp. 5868–5875 (1992). 50, 51

[160] J. C. Tully; "Direct and Indirect Mechanisms of Stimulated Desorption"; in "Desorption Induced by Electronic Transitions DIET I," , volume 24, edited by V. I. Goldanskii, R. Gomer, F. P. Schäfer, J. P. Toennies, N. H. Tolk, M. M. Traum, J. C. Tully & T. E. Madey; pp. 31–38 (Springer Berlin Heidelberg, Berlin, Heidelberg) (1983); ISBN 978-3-642-45552-0 978-3-642-45550-6. 50

[161] T. Chuang, H. Seki & I. Hussla; "Infrared Photodesorption: Vibrational Excitation and Energy Transfer Processes on Surfaces"; Surface Science **158**, pp. 525–552 (1985). 51

[162] I. Fugol'; "Free and Self-Trapped Excitons in Cryocrystals: Kinetics and Relaxation Processes"; Advances in Physics **37**, pp. 1–35 (1988). 52

[163] N. Schwentner, E.-E. Koch & J. Jortner; *Electronic Exitations in Condensed Rare Gases*; number 107 in Springer Tracts in Modern Physics (Springer, Berlin) (1985); ISBN 978-3-540-15382-5 978-0-387-15382-7. 52

[164] G. Zimmerer; "Excitons in Rare-Gas Solids: Exotic or Model-Like?" Journal of Luminescence **125**, pp. 287–293 (2007). 52

[165] V. Saile, M. Skibowski, W. Steinmann, P. Gürtler, E. E. Koch & A. Kozevnikov; "Observation of Surface Excitons in Rare-Gas Solids"; Physical Review Letters **37**, pp. 305–308 (1976). 52

[166] H. Shi, P. Cloutier, J. Gamache & L. Sanche; "Dynamics of Low-Energy-Electron Stimulated Desorption of Metastable Particles from N 2 Condensed on Xe and Kr Films"; Physical Review B **53**, p. 13830 (1996). 55

[167] H. Shi, P. Cloutier, J. Gamache & L. Sanche; "Mechanisms of Metastable N2 and Kr Electron Stimulated Desorption from N2 Kr Double Layer and Mixed Films"; Surface science **380**, pp. 385–396 (1997). 55, 149

[168] F. Coletti & J. Debever; "Self-Trapping of Excitons at the Surface of Rare Gas Solids and Its Manifestation in Luminescence and Desorption"; Journal of Luminescence **31-32**, pp. 927–929 (1984). 55

[169] I. Arakawa, D. Weibel, T. Nagai, M. Abo, T. Hirayama, M. Kanno, K. Mitsuke & M. Sakurai; "Angular and Kinetic Energy Distributions of the Desorption of Ne Metastable Induced by Excitons at the Surface of Solid Ne"; Nuclear Instruments and Methods in Physics Research Section B: Beam Interactions with Materials and Atoms **101**, pp. 195–199 (1995). 55

[170] ł. Dutkiewicz, R. Pędrys & J. Schou; "Molecular-Dynamics Simulation of Ejection Processes in Electronically Excited Solid Ne"; Europhysics Letters (EPL) **36**, pp. 301–306 (1996). 55

[171] M. Runne & G. Zimmerer; "Excitonic Excitations and Desorption from Rare-Gas Solids"; Nuclear Instruments and Methods in Physics Research Section B: Beam Interactions with Materials and Atoms **101**, pp. 156–168 (1995). 55

[172] D. J. O'Shaughnessy, J. W. Boring, S. Cui & R. E. Johnson; "Ejected-Atom Energy Spectra from Electronically Excited Rare-Gas Solids"; Physical Review Letters **61**, pp. 1635–1638 (1988). 55

[173] G. Zimmerer; "Electronic Sputtering from Rare-Gas Solids"; Nuclear Instruments and Methods in Physics Research Section B: Beam Interactions with Materials and Atoms **91**, pp. 601–613 (1994). 55, 181

[174] O. Ellegaard, R. Pedrys, J. Schou, H. Sørensen & P. Børgesen; "Sputtering of Solid Argon by keV Electrons"; Applied Physics A **46**, pp. 305–312 (1988). 55, 181

[175] T. Adachi, T. Hirayama, T. Miura, I. Arakawa & M. Sakurai; "Absolute Measurements of the Total PSD and ESD Yields at the Surface of Solid Krypton"; Surface Science **528**, pp. 60–66 (2003). 55

[176] P. Rowntree, H. Sambe, L. Parenteau & L. Sanche; "Formation of Anionic Excitations in the Rare-Gas Solids and Their Coupling to Dissociative States of Adsorbed Molecules"; Physical Review B **47**, p. 4537 (1993). 55

[177] C. T. Reimann, W. L. Brown & R. E. Johnson; "Electronically Stimulated Sputtering and Luminescence from Solid Argon"; Physical Review B **37**, pp. 1455–1473 (1988). 55, 148, 181

[178] D. J. O'Shaughnessy, J. W. Boring, J. A. Phipps & R. E. Johnson; "Absolute Differential Yields of Condensed Rare Gases Sputtered by keV Ions"; Surface science **203**, pp. 227–244 (1988). 55

[179] W. Wurth, G. Rocker, P. Feulner, R. Scheuerer, L. Zhu & D. Menzel; "Core Excitation and Deexcitation in Argon Multilayers: Surface-and Bulk-Specific Transitions and Autoionization versus Auger Decay"; Physical Review B **47**, p. 6697 (1993). 55

[180] A. Mann, P. Cloutier, D. Liu & L. Sanche; "Excitation-Energy Transfer and Metastable-Particle Desorption from Electron-Bombarded Xe Films with N 2 and CO Top Layers"; Physical Review B **51**, p. 7200 (1995). 56, 149

[181] A. Hayama, T. Kuninobu, T. Hirayama & I. Arakawa; "Desorption of Metastable Particles Induced by Electronic Excitation at the Surface of Rare-Gas Solid with Physisorbed Hydrogen"; Journal of Vacuum Science & Technology A: Vacuum, Surfaces, and Films **16**, pp. 979–983 (1998). 56

[182] H. Shi, P. Cloutier & L. Sanche; "Low-Energy-Electron Stimulated Desorption of Metastable Particles from Condensed N 2 and CO"; Physical Review B **52**, p. 5385 (1995). 57

[183] A. Mann, G. Leclerc & L. Sanche; "Metastable-Atom Desorption and Luminescence Stimulated by Low-Energy Electron Impact on Condensed Kr, Xe, and Xe/Kr Films"; Physical Review B **46**, pp. 9683–9690 (1992). 57

[184] P. A. Redhead; "Extreme High Vacuum"; (1999). 60

[185] S. Turner; "CAS - CERN Accelerator School : Vacuum Technology"; (1999). 61

[186] D. Brandt; "CAS - CERN Accelerator School and ALBA Synchrotron Light Facility : Course on Vacuum in Accelerators"; (2007). 61

[187] P. H. Dawson (Editor); *Quadrupole Mass Spectrometry and Its Applications* (North-Holland Publ. Co, Amsterdam) (1976); ISBN 978-0-444-41345-1. 63

[188] J. H. Gross; *Mass Spectrometry* (Springer Berlin Heidelberg, Berlin, Heidelberg) (2011); ISBN 978-3-642-10709-2 978-3-642-10711-5. 63

[189] M. Yavor; "Chapter 6 Electrostatic Energy Analyzers"; in "Advances in Imaging and Electron Physics," , volume 157pp. 213–258 (Elsevier) (2009); ISBN 978-0-12-374768-6. 67

[190] E. Hamers, W. van Sark, J. Bezemer, W. Goedheer & W. van der Weg; "On the Transmission Function of an Ion-Energy and Mass Spectrometer"; International Journal of Mass Spectrometry and Ion Processes **173**, pp. 91–98 (1998). 66

[191] M. Doronin; *Adsorption on Interstellar Analog Surfaces: From Atoms to Organic Molecules*; Ph.D. thesis; Université Pierre et Marie Curie-Paris VI (2015). 70

[192] M. Bertin; *Laboratory Astrophysics Studies of Thermal and Photon-Induced Desorption from Molecular Ices*; Ph.D. thesis (2019). 70

[193] E. C. Fayolle, M. Bertin, C. Romanzin, X. Michaut, K. I. Öberg, H. Linnartz & J.-H. Fillion; "CO Ice Photodesorption: A Wavelength-Dependent Study"; The Astrophysical Journal **739**, p. L36 (2011). 75, 98, 99, 100, 102

[194] J. T. Yates; *Experimental Innovations in Surface Science* (Springer International Publishing, Cham) (2015); ISBN 978-3-319-17667-3 978-3-319-17668-0. 77

[195] C. C. Parks; *The Auger Decay Mechanism in Photon-Stimulated Desorption of Ions From Surfaces*; Ph.D. thesis (1983). 88

[196] C. R. Vidal; "Four-Wave Frequency Mixing in Gases"; in "Tunable Lasers," pp. 57–113 (Springer) (1992). 90

[197] G. C. Bjorklund; "Effects of Focusing on Third-Order Nonlinear Processes in Isotropic Media"; IEEE Journal of Quantum Electronics **11**, pp. 287–296 (1975). 90

[198] G. Hilber, A. Lago & R. Wallenstein; "Broadly Tunable Vacuum-Ultraviolet/Extreme-Ultraviolet Radiation Generated by Resonant Third-Order Frequency Conversion in Krypton"; JOSA B **4**, pp. 1753–1764 (1987). 91

[199] E. C. Fayolle, M. Bertin, C. Romanzin, H. A. M Poderoso, L. Philippe, X. Michaut, P. Jeseck, H. Linnartz, K. I. Öberg & J.-H. Fillion; "Wavelength-Dependent UV Photodesorption of Pure N2 and O2 Ices"; Astronomy & Astrophysics **556**, p. A122 (2013). 98

[200] J.-H. Fillion, E. C. Fayolle, X. Michaut, M. Doronin, L. Philippe, J. Rakovsky, C. Romanzin, N. Champion, K. I. Öberg, H. Linnartz & M. Bertin; "Wavelength Resolved UV Photodesorption and Photochemistry of CO2 Ice"; Faraday Discussions **168**, p. 533 (2014). 98, 154, 186

[201] R. Dupuy, M. Bertin, G. Féraud, X. Michaut, P. Jeseck, M. Doronin, L. Philippe, C. Romanzin & J.-H. Fillion; "Spectrally-Resolved UV Photodesorption of CH4 in Pure and Layered Ices"; Astronomy & Astrophysics **603**, p. A61 (2017). 98, 99, 122, 149

[202] R. Dupuy, G. Féraud, M. Bertin, X. Michaut, T. Putaud, P. Jeseck, L. Philippe, C. Romanzin, V. Baglin, R. Cimino & J.-H. Fillion; "The Efficient Photodesorption of Nitric Oxide (NO) Ices: A Laboratory Astrophysics Study"; Astronomy & Astrophysics **606**, p. L9 (2017). 98, 108

[203] M. Bertin, E. C. Fayolle, C. Romanzin, K. I. Öberg, X. Michaut, A. Moudens, L. Philippe, P. Jeseck, H. Linnartz & J.-H. Fillion; "UV Photodesorption of Interstellar CO Ice Analogues: From Subsurface Excitation to Surface Desorption"; Physical Chemistry Chemical Physics **14**, p. 9929 (2012). 98, 100, 102, 103, 105, 154

[204] M. Bertin, E. C. Fayolle, C. Romanzin, H. A. M. Poderoso, X. Michaut, L. Philippe, P. Jeseck, K. I. Öberg, H. Linnartz & J.-H. Fillion; "Indirect Ultraviolet Photodesorption From CO:N2 Binary Ices — an Efficient Grain-Gas Process"; The Astrophysical Journal **779**, p. 120 (2013). 98, 149, 154

[205] G. Herzberg & K. P. Huber; *Molecular Spectra and Molecular Structure* (Van Nostrand Reinhold, New York London) (1979); ISBN 978-0-442-23394-5. 99, 108, 137, 234

[206] P. A. Gerakines, W. Schutte & P. Ehrenfreund; "Ultraviolet Processing of Interstellar Ice Analogs I. Pure Ices"; Astronomy & Astrophysics (1996). 99, 234, 235

[207] K. I. Öberg, G. W. Fuchs, Z. Awad, H. J. Fraser, S. Schlemmer, E. F. van Dishoeck & H. Linnartz; "Photodesorption of CO Ice"; The Astrophysical Journal **662**, pp. L23–L26 (2007). 99, 100

[208] K. I. Öberg, E. F. van Dishoeck & H. Linnartz; "Photodesorption of Ices I: CO, N2 , and CO2"; Astronomy and Astrophysics **496**, pp. 281–293 (2009). 99, 100

[209] G. M. Muñoz Caro, A. Jiménez-Escobar, J. á. Martín-Gago, C. Rogero, C. Atienza, S. Puertas, J. M. Sobrado & J. Torres-Redondo; "New Results on Thermal and Photodesorption of CO Ice Using the Novel InterStellar Astrochemistry Chamber (ISAC)"; Astronomy & Astrophysics **522**, p. A108 (2010). 99, 100, 101

[210] Y.-J. Chen, K.-J. Chuang, G. M. Muñoz Caro, M. Nuevo, C.-C. Chu, T.-S. Yih, W.-H. Ip & C.-Y. R. Wu; "Vacuum Ultraviolet Emission Spectrum Measurement of a Microwave-Discharge Hydrogen-Flow Lamp in Several Configurations: Application to Photodesorption of CO Ice"; The Astrophysical Journal **781**, p. 15 (2013). 100

[211] M. C. van Hemert, J. Takahashi & E. F. van Dishoeck; "Molecular Dynamics Study of the Photodesorption of CO Ice"; The Journal of Physical Chemistry A **119**, pp. 6354–6369 (2015). 100, 106

[212] D. Paardekooper, G. Fedoseev, A. Riedo & H. Linnartz; "A Novel Approach to Measure Photodesorption Rates of Interstellar Ice Analogues. The Photodesorption Rate of CO Ice Reinvestigated"; Astronomy & Astrophysics (2016). 100

[213] C. G. Díaz, H. C. de Lucas, S. Aparicio, G. M. M. Caro, N.-E. Sie, L.-C. Hsiao & Y.-J. Chen; "Accretion and Photodesorption of CO Ice as a Function of the Incident Angle of Deposition"; Monthly Notices of the Royal Astronomical Society (2019). 100, 102

[214] G. A. Cruz-Diaz, G. M. Muñoz Caro, Y.-J. Chen & T.-S. Yih; "Vacuum-UV Spectroscopy of Interstellar Ice Analogs: I. Absorption Cross-Sections of Polar-Ice Molecules⋆"; Astronomy & Astrophysics **562**, p. A119 (2014). 105, 106

[215] G. A. Cruz-Diaz, G. M. Muñoz Caro, Y.-J. Chen & T.-S. Yih; "Vacuum-UV Spectroscopy of Interstellar Ice Analogs: II. Absorption Cross-Sections of Nonpolar Ice Molecules⋆"; Astronomy & Astrophysics **562**, p. A120 (2014). 105, 123, 126, 159

[216] H.-C. Lu, H.-K. Chen, B.-M. Cheng & J. Ogilvie; "Absorption Spectra in the Vacuum Ultraviolet Region of Small Molecules in Condensed Phases"; Spectrochimica Acta Part A: Molecular and Biomolecular Spectroscopy **71**, pp. 1485–1491 (2008). 106, 111, 136, 137, 159, 160

[217] F. Dzegilenko & E. Herbst; "Classical Dynamics of Adsorbate–Surface Systems: Application to Nonthermal Desorption"; The Journal of Chemical Physics **100**, pp. 9205–9214 (1994). 106

[218] F. Dzegilenko, E. Herbst & T. Uzer; "Mixed Quantum-classical Calculations on the Nonthermal Desorption of Physisorbed CO"; The Journal of Chemical Physics **102**, pp. 2593–2603 (1995). 106

[219] F. N. Dzegilenko & E. Herbst; "Effect of Coupling between Frustrated Translation and Libration on the Nonthermal Desorption of Physisorbed CO: Three-dimensional Quantum Calculations"; The Journal of Chemical Physics **104**, pp. 6330–6337 (1996). 106

[220] "General Discussion"; Faraday Discussions **168**, p. 423 (2014). 107

[221] F. M. Zimmermann & W. Ho; "State Resolved Studies of Photochemical Dynamics at Surfaces"; Surface science reports **22**, pp. 127–247 (1995). 108

[222] W. C. Natzle, D. Padowitz & S. J. Sibener; "Ultraviolet Laser Photodesorption of NO from Condensed Films: Translational and Internal Energy Distributions"; The Journal of Chemical Physics **88**, pp. 7975–7994 (1988). 108, 121

[223] R. C. Jackson, J. C. Polanyi & P. Sjövall; "Photodissociation Dynamics of (NO)2 on LiF(001): Characterization of Vibrationally Excited NO Fragments"; The Journal of Chemical Physics **102**, p. 6308 (1995). 108, 118, 121

[224] C. Simpson, P. Griffiths, J. Curry & M. Towrie; "The Photolysis of NO Dimers, Adsorbed on an MgF2 Surface, at 248 Nm"; Chemical Physics Letters **250**, pp. 342–348 (1996). 108, 121

[225] W. G. Fateley, H. A. Bent & B. Crawford; "Infrared Spectra of the Frozen Oxides of Nitrogen"; The Journal of Chemical Physics **31**, pp. 204–217 (1959). 108, 109

[226] J. Granier-Mayence & J. Romand; "Spectre d'Absorption De l'Oxyde Azotique Solide Entre 2400 A et 1600 A"; Compte-Rendu de l'Académie des Sciences **258**, p. 1148 (1953). 108, 110

[227] E. A. Wade, J. I. Cline, K. T. Lorenz, C. Hayden & D. W. Chandler; "Direct Measurement of the Binding Energy of the NO Dimer"; The Journal of Chemical Physics **116**, p. 4755 (2002). 108

[228] J. F. Canty, E. G. Stone, S. B. Bach & D. W. Ball; "Matrix Isolation and Theoretical Studies of ONNO: Assignment of a New Combination Band and Density Functional Calculations"; Chemical physics **216**, pp. 81–89 (1997). 108, 109

[229] A. G. Leiga & H. A. Taylor; "Far-Ultraviolet Photolysis of Nitric Oxide"; The Journal of Chemical Physics **42**, pp. 2107–2112 (1965). 108, 112

[230] F. Legay & N. Legay-Sommaire; "Infrared Spectroscopy, Infrared Photoconversion, and Ultraviolet Photodissociation of NO Dimers in Neon and Nitrogen Matrices"; The Journal of Chemical Physics **102**, pp. 7798–7806 (1995). 108, 109, 112

[231] W. Chang, G. Cooper & C. Brion; "Absolute Optical Oscillator Strengths for the Photoabsorption of Nitric Oxide (5–30 eV) at High Resolution"; Chemical Physics **170**, pp. 111–121 (1993). 110, 111

[232] E. Forte & H. Van Den Bergh; "The Heat of Formation of the Nitric Oxide Dimer and Its UV Spectrum"; Chemical Physics **30**, pp. 325–331 (1978). 110

[233] M. Bertolo & K. Jacobi; "NO Adsorption on Pd(111) in the Temperature Range between 20 and 300 K"; Surface Science **226**, pp. 207–220 (1990). 110

[234] C. M. Western; "PGOPHER: A Program for Simulating Rotational, Vibrational and Electronic Spectra"; Journal of Quantitative Spectroscopy and Radiative Transfer **186**, pp. 221–242 (2017). 115

[235] J. W. Au, G. Cooper, G. R. Burton, T. N. Olney & C. E. Brion; "The Valence Shell Photoabsorption of the Linear Alkanes, CnH2n+2 (n = 1-8) : Absolute Oscillator Strengths (7-220 eV)"; Chemical Physics pp. 209–239 (1993). 122, 123

[236] E.-E. Koch & d. M. Skibowski; "Optical Absorption of Gaseous Methane, Ethane, Propane and Butane and Reflection of Solid Methane and Ethane in the Vacuum Ultraviolet"; Chemical Physics Letters **9**, pp. 429–432 (1971). 122, 123

[237] Y.-J. Wu, C. Y. R. Wu, S.-L. Chou, M.-Y. Lin, H.-C. Lu, J.-I. Lo & B.-M. Cheng; "Spectra and Photolysis of Pure Nitrogen and Methane Dispersed in Solid Nitrogen With Vacuum-Ultraviolet Light"; The Astrophysical Journal **746**, p. 175 (2012). 122, 123

[238] K. Kameta, N. Kouchi, M. Ukai & Y. Hatano; "Photoabsorption, Photoionization, and Neutral-Dissociation Cross Sections of Simple Hydrocarbons in the Vacuum Ultraviolet Range"; Journal of Electron Spectroscopy and Related Phenomena **123**, pp. 225–238 (2002). 122

[239] G. Herzberg & G. Herzberg; *Electronic Spectra and Electronic Structure of Polyatomic Molecules*; number by Gerhard Herzberg ; Vol. 3 in Molecular Spectra and Molecular Structure; 2nd edition (Krieger Publ, Malabar, Fla) (1991); ISBN 978-0-89464-270-8. 122

[240] P. Plessis, P. Marmet & R. Dutil; "Ionisation and Appearance Potentials of CH_4 by Electron Impact"; Journal of Physics B: Atomic and Molecular Physics **16**, pp. 1283–1294 (1983). 122

[241] J.-I. Lo, M.-Y. Lin, Y.-C. Peng, S.-L. Chou, H.-C. Lu, B.-M. Cheng & J. F. Ogilvie; "Far-Ultraviolet Photolysis of Solid Methane"; Monthly Notices of the Royal Astronomical Society **451**, pp. 159–166 (2015). 125

[242] J.-B. Bossa, D. M. Paardekooper, K. Isokoski & H. Linnartz; "Methane Ice Photochemistry and Kinetic Study Using Laser Desorption Time-of-Flight Mass Spectrometry at 20 K"; Phys. Chem. Chem. Phys. **17**, pp. 17346–17354 (2015). 125

[243] R. I. Kaiser & K. Roessler; "Theoretical and Laboratory Studies on the Interaction of Cosmic-Ray Particles with Interstellar Ices. III. Suprathermal Chemistry–Induced Formation of Hydrocarbon Molecules in Solid Methane (CH_4), Ethylene (C_2H_4), and Acetylene (C_2H_2)"; The Astrophysical Journal **503**, pp. 959–975 (1998). 125

[244] G. Baratta, M. Domingo, G. Ferini, G. Leto, M. Palumbo, M. Satorre & G. Strazzulla; "Ion Irradiation of CH4-Containing Icy Mixtures"; Nuclear Instruments and Methods in Physics Research Section B: Beam Interactions with Materials and Atoms **209**, pp. 283–287 (2003). 125

[245] C. J. Bennett, C. S. Jamieson, Y. Osamura & R. I. Kaiser; "Laboratory Studies on the Irradiation of Methane in Interstellar, Cometary, and Solar System Ices"; The Astrophysical Journal **653**, p. 792 (2006). 125

[246] A. L. F. de Barros, V. Bordalo, E. Seperuelo Duarte, E. F da Silveira, A. Domaracka, H. Rothard & P. Boduch; "Cosmic Ray Impact on Astrophysical Ices: Laboratory Studies on Heavy Ion Irradiation of Methane"; Astronomy & Astrophysics **531**, p. A160 (2011). 125

[247] G. A. Cruz-Diaz; *PhD Thesis: VUV-Spectroscopy and Photodesorption of Interstellar Ice Analogues*; Ph.D. thesis; Universidad Autonoma de Madrid (2015). 125

[248] K. I. Öberg, E. F. van Dishoeck, H. Linnartz & S. Andersson; "The Effect of H2O on Ice Photochemistry"; The Astrophysical Journal **718**, pp. 832–840 (2010). 126

[249] A. Nitzan; *Chemical Dynamics in Condensed Phases: Relaxation, Transfer and Reactions in Condensed Molecular Systems*; Oxford Graduate Texts (Oxford University Press, Oxford ; New York) (2006); ISBN 978-0-19-852979-8. 127

[250] T. Bartels-Rausch, V. Bergeron, J. H. E. Cartwright, R. Escribano, J. L. Finney, H. Grothe, P. J. Gutiérrez, J. Haapala, W. F. Kuhs, J. B. C. Pettersson, S. D. Price, C. I. Sainz-Díaz, D. J. Stokes, G. Strazzulla, E. S. Thomson, H. Trinks & N. Uras-Aytemiz; "Ice Structures, Patterns, and Processes: A View across the Icefields"; Reviews of Modern Physics **84**, pp. 885–944 (2012). 128

[251] Z. Dohnálek, G. A. Kimmel, P. Ayotte, R. S. Smith & B. D. Kay; "The Deposition Angle-Dependent Density of Amorphous Solid Water Films"; The Journal of Chemical Physics **118**, pp. 364–372 (2003). 128

[252] M. Palumbo, G. Baratta, G. Leto & G. Strazzulla; "H Bonds in Astrophysical Ices"; Journal of Molecular Structure **972**, pp. 64–67 (2010). 128

[253] E. Dartois, J. J. Ding, A. L. de Barros, P. Boduch, R. Brunetto, M. Chabot, A. Domaracka, M. Godard, X. Y. Lv, C. F. Mejía Guamán, T. Pino, H. Rothard, E. F. da Silveira & J. C. Thomas; "Swift Heavy Ion Irradiation of Water Ice from MeV to GeV Energies: Approaching True Cosmic Ray Compaction⋆"; Astronomy & Astrophysics **557**, p. A97 (2013). 128

[254] E. Dartois, B. Augé, P. Boduch, R. Brunetto, M. Chabot, A. Domaracka, J. J. Ding, O. Kamalou, X. Y. Lv, H. Rothard, E. F. da Silveira & J. C. Thomas; "Heavy Ion Irradiation of Crystalline Water Ice: Cosmic Ray Amorphisation Cross-Section and Sputtering Yield⋆"; Astronomy & Astrophysics **576**, p. A125 (2015). 128, 189

[255] D. E. Ramaker; "Comparison of Photon-Stimulated Dissociation of Gas-Phase, Solid and Chemisorbed Water"; Chemical Physics **80**, pp. 183–202 (1983). 128, 131, 212

[256] M. T. Sieger, W. C. Simpson & T. M. Orlando; "Electron-Stimulated Desorption of D+ from D2O Ice: Surface Structure and Electronic Excitations"; Physical Review B **56**, p. 4925 (1997). 128, 212

[257] G. A. Cruz-Diaz, R. Martín-Doménech, E. Moreno, G. M. Muñoz Caro & Y.-J. Chen; "New Measurements on Water Ice Photodesorption and Product Formation under Ultraviolet Irradiation"; Monthly Notices of the Royal Astronomical Society **474**, pp. 3080–3089 (2018). 129, 131

[258] N. Nishi, H. Shinohara & T. Okuyama; "Photodetachment, Photodissociation, and Photochemistry of Surface Molecules of Icy Solids Containing NH $_3$ and Pure H $_2$ O Ices"; The Journal of Chemical Physics **80**, pp. 3898–3910 (1984). 129, 131, 138, 139

[259] J. Bergeld & D. Chakarov; "Photo Ejection of Water Molecules from Amorphous Ice Films"; The Journal of Chemical Physics **125**, p. 141103 (2006). 129, 146

[260] A. Yabushita, T. Hama & M. Kawasaki; "Photochemical Reaction Processes during Vacuum-Ultraviolet Irradiation of Water Ice"; Journal of Photochemistry and Photobiology C: Photochemistry Reviews **16**, pp. 46–61 (2013). 130, 132, 133

[261] S. Andersson & E. F. van Dishoeck; "Photodesorption of Water Ice"; Astronomy and Astrophysics **491**, pp. 907–916 (2008). 130

[262] C. Arasa, S. Andersson, H. M. Cuppen, E. F. van Dishoeck & G.-J. Kroes; "Molecular Dynamics Simulations of the Ice Temperature Dependence of Water Ice Photodesorption"; The Journal of Chemical Physics **132**, p. 184510 (2010). 130

[263] C. Arasa, S. Andersson, H. M. Cuppen, E. F. van Dishoeck & G. J. Kroes; "Molecular Dynamics Simulations of D $_2$ O Ice Photodesorption"; The Journal of Chemical Physics **134**, p. 164503 (2011). 130, 135, 165

[264] C. Arasa, J. Koning, G.-J. Kroes, C. Walsh & E. F. van Dishoeck; "Photodesorption of H2O, HDO, and D2O Ice and Its Impact on Fractionation"; Astronomy & Astrophysics **575**, p. A121 (2015). 130, 135, 164

[265] S. Andersson, C. Arasa, A. Yabushita, M. Yokoyama, T. Hama, M. Kawasaki, C. M. Western & M. N. R. Ashfold; "A Theoretical and Experimental Study on Translational and Internal Energies of H2O and OH from the 157 Nm Irradiation of Amorphous Solid Water at 90 K"; Physical Chemistry Chemical Physics **13**, p. 15810 (2011). 130

[266] A. J. DeSimone, V. D. Crowell, C. D. Sherrill & T. M. Orlando; "Mechanisms of H2O Desorption from Amorphous Solid Water by 157-Nm Irradiation: An Experimental and Theoretical Study"; The Journal of chemical physics **139**, p. 164702 (2013). 131

[267] N. G. Petrik & G. A. Kimmel; "Electron-Stimulated Production of Molecular Hydrogen at the Interfaces of Amorphous Solid Water Films on Pt(111)"; The Journal of Chemical Physics **121**, pp. 3736–3744 (2004). 133, 190

[268] N. G. Petrik, A. G. Kavetsky & G. A. Kimmel; "Electron-Stimulated Production of Molecular Oxygen in Amorphous Solid Water"; The Journal of Physical Chemistry B **110**, pp. 2723–2731 (2006). 133

[269] L. A. Sala; *Low-Energy Electron Induced Chemistry in Supported Molecular Films*; Ph.D. thesis; Université Paris Sud (2018). 135, 139

[270] A. J. Yencha, H. Kubota, T. Fukuyama, T. Kondow & K. Kuchitsu; "Penning Ionization Electron Spectroscopy and Photo-Electron Spectroscopy of Molecular Solids. II. Ammonia and Water"; Journal of Electron Spectroscopy and Related Phenomena **23**, pp. 431–440 (1981). 137

[271] S. Leach, H.-W. Jochims & H. Baumgärtel; "VUV Photodissociation of Ammonia: A Dispersed Fluorescence Excitation Spectral Study"; Phys. Chem. Chem. Phys. **7**, pp. 900–911 (2005). 137

[272] B. Gelernt, S. Filseth & T. Carrington; "Quenching and Radiative Lifetimes for NH(b1Σ+, $\Upsilon' = 0$)"; Chemical Physics Letters **36**, pp. 238–241 (1975). 137

[273] U. Müller & G. Schulz; "Electron Impact Dissociation of the NH_3 Molecule: Absolute and Relative Cross Sections for NH*($c\ ^1\Pi$, $A\ ^3\Pi$), NH^+ *($C\ ^2\Sigma^+$, $B\ ^2\Delta$, $A\ ^2\Sigma^-$), and NH^*_2 ($A\ ^{\sim 2}A_1$) Fragment Emissions"; The Journal of Chemical Physics **96**, pp. 5924–5937 (1992). 137

[274] R. Martín-Doménech, G. A. Cruz-Díaz & G. M. Muñoz Caro; "UV Photoprocessing of NH3 Ice: Photon-Induced Desorption Mechanisms"; Monthly Notices of the Royal Astronomical Society **473**, pp. 2575–2582 (2017). 138, 139

[275] M. J. Loeffler & R. A. Baragiola; "Photolysis of Solid NH_3 and NH_3 –H_2O Mixtures at 193 Nm"; The Journal of Chemical Physics **133**, p. 214506 (2010). 138

[276] G. Féraud, M. Bertin, C. Romanzin, R. Dupuy, F. Le Petit, E. Roueff, L. Philippe, X. Michaut, P. Jeseck & J.-H. Fillion; "VUV Photodesorption and Photofragmentation of Formaldehyde (H2CO)-Containing Ices"; ACS Earth and Space Chemistry (2019). 140, 144, 149, 154, 171

[277] F. Holtzberg, B. Post & I. Fankuchen; "The Crystal Structure of Formic Acid"; Acta Crystallographica **6**, pp. 127–130 (1953). 140

[278] J. Cyriac & T. Pradeep; "Structural Transformation in Formic Acid on Ultra Cold Ice Surfaces"; Chemical Physics Letters **402**, pp. 116–120 (2005). 140, 141

[279] S. E. Bisschop, G. W. Fuchs, A. C. A. Boogert, E. F. van Dishoeck & H. Linnartz; "Infrared Spectroscopy of HCOOH in Interstellar Ice Analogues"; Astronomy & Astrophysics **470**, pp. 749–759 (2007). 140, 141

[280] I. Martin, M. Bertin, A. Domaracka, R. Azria, E. Illenberger & A. Lafosse; "Chemistry Induced by Low-Energy Electrons in Condensed Multilayers of Pure Small Organic Acids"; International Journal of Mass Spectrometry **277**, pp. 262–268 (2008). 140, 141

[281] R. C. Millikan & K. S. Pitzer; "The Infrared Spectra of Dimeric and Crystalline Formic Acid"; Journal of the American Chemical Society **80**, pp. 3515–3521 (1958). 141

[282] S. Pilling, A. C. F. Santos, W. Wolff, M. M. Sant'Anna, A. L. F. Barros, G. G. B. De Souza, N. V. De Castro Faria & H. M. Boechat-Roberty; "Ionization and Dissociation of Cometary Gaseous Organic Molecules by Solar Wind Particles - I. Formic Acid"; Monthly Notices of the Royal Astronomical Society **372**, pp. 1379–1388 (2006). 142, 246

[283] P. Możejko; "Calculations of Electron Impact Ionization Cross Section for Simple Biomolecules: Formic and Acetic Acids"; The European Physical Journal Special Topics **144**, pp. 233–237 (2007). 142

[284] S. Leach, M. Schwell, F. Dulieu, J.-L. Chotin, H.-W. Jochims & H. Baumgärtel; "Photophysical Studies of Formic Acid in the VUV. Absorption Spectrum in the 6–22 eV Region"; Phys. Chem. Chem. Phys. **4**, pp. 5025–5039 (2002). 143

[285] G. A. Cruz-Diaz, R. Martín-Doménech, G. M. Muñoz Caro & Y.-J. Chen; "Negligible Photodesorption of Methanol Ice and Active Photon-Induced Desorption of Its Irradiation Products"; Astronomy & Astrophysics **592**, p. A68 (2016). 144

[286] R. Martín-Doménech, G. M. Muñoz Caro & G. A. Cruz-Díaz; "Study of the Photon-Induced Formation and Subsequent Desorption of CH3OH and H2CO in Interstellar Ice Analogs"; Astronomy & Astrophysics **589**, p. A107 (2016). 144, 147, 171

[287] G. W. Robinson; "Electronic and Vibrational Excitons in Molecular Crystals"; Annual Review of Physical Chemistry **21**, pp. 429–474 (1970). 145

[288] E. Koch & A. Otto; "Vacuum Ultra-Violet and Electron Energy Loss Spectroscopy of Gaseous and Solid Organic Compounds"; International Journal for Radiation Physics and Chemistry **8**, pp. 113–150 (1976). 145

[289] M. B. Robin; *Higher Excited States of Polyatomic Molecules. Vol. 2: ...* (Acad. Press, New York, NY) (1975); ISBN 978-0-12-589902-4. 145

[290] S. Cazaux, R. Martín-Doménech, Y. J. Chen, G. M. Caro & C. G. Díaz; "CO Depletion: A Microscopic Perspective"; The Astrophysical Journal **849**, p. 80 (2017). 146

[291] H. Carrascosa, L.-C. Hsiao, N.-E. Sie, G. M. M. Caro & Y.-J. Chen; "$\hat{}{13}$CO and $\hat{}{13}$CO$_2$ Ice Mixtures with N$_2$ in Photon Energy Transfer Studies"; Monthly Notices of the Royal Astronomical Society (2019). 1903.11906. 147, 171

[292] A. Schrimpf, B. Herkert, L. Manceron, U. Schriever & H.-J. Stöckmann; "Exciton Trapping at Au and Ag Atoms in Rare Gas Matrices"; physica status solidi (b) **165**, pp. 469–480 (1991). 148

[293] J. Becker, O. N. Grigorashchenko, A. N. Ogurtsov, M. Runne, E. V. Savchenko & G. Zimmerer; "Thermoluminescence from CO-Doped Solid Ar"; Journal of Physics D: Applied Physics **31**, pp. 749–753 (1998). 148

[294] D. E. Weibel, T. Nagai, T. Hirayama, I. Arakawa & M. Sakurai; "Electronic Energy Transfer in Rare-Gas Solid Alloys Studied by Photon Stimulated Desorption"; Langmuir **12**, pp. 193–198 (1996). 148

[295] H. Dubost & R. Charneau; "Laser Studies of Vibrational Energy Transfer and Relaxation of CO Trapped in Solid Neon and Argon"; Chemical Physics **12**, pp. 407–418 (1976). 149

[296] I. Hadj Bachir, R. Charneau & H. Dubost; "Intermolecular Transfer of Vibrational Energy in Matrix Isolated NO. High Vibrational States, Electronic Excitation and Dissociation"; Chemical Physics **177**, pp. 675–692 (1993). 149

[297] A. Salloum & H. Dubost; "Vibrational Energy Transfer from CO to O2 in Rare Gas Matrices." Chemical Physics **189**, pp. 179–204 (1994). 149

[298] F. Dzegilenko & E. Herbst; "V - V,R, Excitation of Librational Energy for CO Physisorbed on Ice and Silica"; Chemical Physics Letters **234**, pp. 216–220 (1995). 149

[299] G. A. Cruz-Diaz, G. M. M. Caro & Y.-J. Chen; "Vacuum-UV Absorption Spectroscopy of Interstellar Ice Analogues. III. Isotopic Effects"; Monthly Notices of the Royal Astronomical Society **439**, pp. 2370–2376 (2014). 159, 161

[300] J. D. Thrower, A. G. M. Abdulgalil, M. P. Collings, M. R. S. McCoustra, D. J. Burke, W. A. Brown, A. Dawes, P. J. Holtom, P. Kendall, N. J. Mason, F. Jamme, H. J. Fraser & F. J. M. Rutten; "Photon- and Electron-Stimulated Desorption from Laboratory Models of Interstellar Ice Grains"; Journal of Vacuum Science & Technology A: Vacuum, Surfaces, and Films **28**, pp. 799–806 (2010). 162

[301] D. Marchione, J. D. Thrower & M. R. S. McCoustra; "Efficient Electron-Promoted Desorption of Benzene from Water Ice Surfaces"; Phys. Chem. Chem. Phys. **18**, pp. 4026–4034 (2016). 162, 166

[302] D. Marchione & M. R. S. McCoustra; "Electrons, Excitons and Hydrogen Bonding: Electron-Promoted Desorption from Molecular Ice Surfaces"; Phys. Chem. Chem. Phys. **18**, pp. 29747–29755 (2016). 162, 190

[303] Y.-P. Kuo, H.-C. Lu, Y.-J. Wu, B.-M. Cheng & J. Ogilvie; "Absorption Spectra in the Vacuum Ultraviolet Region of Methanol in Condensed Phases"; Chemical Physics Letters **447**, pp. 168–174 (2007). 166

[304] G. M. Muñoz Caro & R. Martín Doménech; "Photon-Induced Desorption Processes in Astrophysical Ices"; in "Laboratory Astrophysics," , volume 451, edited by G. M. Muñoz Caro & R. Escribano; pp. 133–147 (Springer International Publishing, Cham) (2018); ISBN 978-3-319-90019-3 978-3-319-90020-9. 167

[305] M. McCoustra & J. Thrower; "Exciton-Promoted Desorption From Solid Water Surfaces"; in "Reference Module in Chemistry, Molecular Sciences and Chemical Engineering," p. B9780124095472139101 (Elsevier) (2017); ISBN 978-0-12-409547-2. 167

[306] C. Yuan & J. T. Yates; "Lyman-α Photodesorption from CO2(Ice) at 75 K: Role of CO2 Vibrational Relaxation on Desorption Rate"; The Journal of Chemical Physics **138**, p. 154303 (2013). 167

[307] C. Yuan & J. T. Yates; "Isotope Effect in the Photochemical Decomposition of CO2 (Ice) by Lyman-α Radiation"; The Journal of Chemical Physics **138**, p. 154302 (2013). 167

[308] C. Yuan & J. T. Yates; "Radiation Damage and Associated Phase Change Effect on Photodesorption Rates From Ices — Lyα Studies of the Surface Behavior of CO_2 (Ice)"; The Astrophysical Journal **780**, p. 8 (2014). 167

[309] R. Martín-Doménech, J. Manzano-Santamaría, G. M. Muñoz Caro, G. A. Cruz-Díaz, Y.-J. Chen, V. J. Herrero & I. Tanarro; "UV Photoprocessing of CO2 Ice: A Complete Quantification of Photochemistry and Photon-Induced Desorption Processes"; Astronomy & Astrophysics **584**, p. A14 (2015). 167

[310] N.-E. Sie, G. M. M. Caro, Z.-H. Huang, R. Martín-Doménech, A. Fuente & Y.-J. Chen; "On the Photodesorption of CO $_2$ Ice Analogs: The Formation of Atomic C in the Ice and the Effect of the VUV Emission Spectrum"; The Astrophysical Journal **874**, p. 35 (2019). 167, 186

[311] J. Zhen & H. Linnartz; "UV-Induced Photodesorption and Photochemistry of O2 Ice"; Monthly Notices of the Royal Astronomical Society **437**, pp. 3190–3201 (2014). 167

[312] K. Furuya & Y. Aikawa; "Depletion of Heavy Nitrogen in the Cold Gas of Star-Forming Regions"; The Astrophysical Journal **857**, p. 105 (2018). 168

[313] B. Fleury, M. S. Gudipati, I. Couturier-Tamburelli & N. Carrasco; "Photoreactivity of Condensed Acetylene on Titan Aerosols Analogues"; Icarus **321**, pp. 358–366 (2019). 173

[314] O. Ellegaard, J. Schou, H. Sørensen & P. Børgesen; "Electronic Sputtering of Solid Nitrogen and Oxygen by keV Electrons"; Surface science **167**, pp. 474–492 (1986). 177, 180

[315] A. Kuzucan, H. Neupert, M. Taborelli & H. Störi; "Secondary Electron Yield on Cryogenic Surfaces as a Function of Physisorbed Gases"; Journal of Vacuum Science & Technology A: Vacuum, Surfaces, and Films **30**, p. 051401 (2012). 179, 180, 183, 184, 185

[316] H. So/rensen & J. Schou; "Interaction between Solid Nitrogen and 1–3-keV Electrons"; Journal of Applied Physics **49**, pp. 5311–5318 (1978). 179

[317] H. Tratnik; *Electron Stimulated Desorption of Condensed Gases on Cryogenic Surfaces*; Ph.D. thesis (2006). 180, 181, 183

[318] J. Cazaux, Y. Bozhko & N. Hilleret; "Electron-Induced Secondary Electron Emission Yield from Condensed Rare Gases: Ne, Ar, Kr, and Xe"; Physical Review B **71** (2005). 181

[319] W. L. Brown, W. M. Augustyniak, K. J. Marcantonio, E. H. Simmons, J. W. Boring, R. E. Johnson & C. T. Reimann; "Electronic Sputtering of Low Temperature Molecular Solids"; Nuclear Instruments and Methods in Physics Research Section B: Beam Interactions with Materials and Atoms **1**, pp. 307–314 (1984). 183, 189

[320] W. Brown, W. Augustyniak, E. Simmons, K. Marcantonio, L. Lanzerotti, R. Johnson, J. Boring, C. Reimann, G. Foti & V. Pirronello; "Erosion and Molecule Formation in Condensed Gas Films by Electronic Energy Loss of Fast Ions"; Nuclear Instruments and Methods in Physics Research **198**, pp. 1–8 (1982). 186

[321] R. E. Johnson, L. Lanzerotti, W. L. Brown, W. Augustyniak & C. Mussil; "Charged Particle Erosion of Frozen Volatiles in Ice Grains and Comets"; **123**, pp. 343–346 (1983). 186

[322] S. Jurac, R. A. Baragiola, R. E. Johnson & E. C. Sittler; "Charging of Ice Grains by Low-Energy Plasmas: Application to Saturn's E Ring"; Journal of Geophysical Research **100**, p. 14821 (1995). 189

[323] N. Hilleret, V. Baglin, B. Henrist, E. Mercier & C. Scheuerlein; "Ingredients for the Understanding and the Simulation of Multipacting"; in "10th Workshop on LEP-SPS Performance," pp. 130–135 (2000). 188

[324] R. E. Johnson; "Photolysis and Radiolysis of Water Ice"; in "Physics and Chemistry at Low Temperatures," pp. 297–339 (2011). 189, 194

[325] G. A. Kimmel, T. M. Orlando, C. Vézina & L. Sanche; "Low-energy Electron-stimulated Production of Molecular Hydrogen from Amorphous Water Ice"; The Journal of Chemical Physics **101**, pp. 3282–3286 (1994). 189, 193

[326] G. A. Kimmel & T. M. Orlando; "Low-Energy (5–120 eV) Electron-Stimulated Dissociation of Amorphous D2O Ice: D(2S), O(3P2, 1, 0), and O(1D2) Yields and Velocity Distributions"; Physical Review Letters **75**, pp. 2606–2609 (1995). 189

[327] N. G. Petrik & G. A. Kimmel; "Electron-Stimulated Sputtering of Thin Amorphous Solid Water Films on Pt(111)"; The Journal of Chemical Physics **123**, p. 054702 (2005). 190

[328] N. G. Petrik, A. G. Kavetsky & G. A. Kimmel; "Electron-Stimulated Production of Molecular Oxygen in Amorphous Solid Water on Pt(111): Precursor Transport through the Hydrogen Bonding Network"; The Journal of Chemical Physics **125**, p. 124702 (2006). 190

[329] A. G. M. Abdulgalil, A. Rosu-Finsen, D. Marchione, J. D. Thrower, M. P. Collings & M. R. S. McCoustra; "Electron-Promoted Desorption from Water Ice Surfaces: Neutral Gas-Phase Products"; ACS Earth and Space Chemistry **1**, pp. 209–215 (2017). 190

[330] A. C. Cummings, E. C. Stone, B. C. Heikkila, N. Lal, W. R. Webber, G. Jóhannesson, I. V. Moskalenko, E. Orlando & T. A. Porter; "Galactic Cosmic Rays in the Local Interstellar Medium: Voyager 1 Observations and Model Results"; The Astrophysical Journal **831**, p. 18 (2016). 191

[331] P. R. Maloney, D. J. Hollenbach & A. G. G. M. Tielens; "X-Ray–Irradiated Molecular Gas. I. Physical Processes and General Results"; The Astrophysical Journal **466**, p. 561 (1996). 192

[332] M. Chabot; "Cosmic-Ray Slowing down in Molecular Clouds: Effects of Heavy Nuclei"; Astronomy & Astrophysics **585**, p. A15 (2016). 192

[333] T. Cravens, G. Victor & A. Dalgarno; "The Absorption of Energetic Electrons by Molecular Hydrogen Gas"; Planetary and Space Science **23**, pp. 1059–1070 (1975). 192, 193

[334] O. Rakhovskaia, P. Wiethoff & P. Feulner; "Thresholds for Electron Stimulated Desorption of Neutral Molecules from Solid N2, CO, O2 and NO"; Nuclear Instruments and Methods in Physics Research Section B: Beam Interactions with Materials and Atoms **101**, pp. 169–173 (1995). 193, 221

[335] D. Menzel; "Valence and Core Excitations in Rare Gas Mono-and Multilayers: Production, Decay, and Desorption of Neutrals and Ions"; Applied Physics A **51**, pp. 163–171 (1990). 198

[336] D. Coulman, A. Puschmann, U. Höfer, H.-P. Steinrück, W. Wurth, P. Feulner & D. Menzel; "Excitation, Deexcitation, and Fragmentation in the Core Region of Condensed and Adsorbed Water"; The Journal of Chemical Physics **93**, pp. 58–75 (1990). 198, 208, 211

[337] D. Menzel, G. Rocker, H.-P. Steinrück, D. Coulman, P. A. Heimann, W. Huber, P. Zebisch & D. R. Lloyd; "Core Excitation, Decay, and Fragmentation in Solid Benzene as Studied by X-ray Absorption, Resonant Auger, and Photon Stimulated Desorption"; The Journal of Chemical Physics **96**, pp. 1724–1734 (1992). 198

[338] D. Andrade, H. Boechat-Roberty, S. Pilling, E. da Silveira & M. Rocco; "Positive and Negative Ionic Desorption from Condensed Formic Acid Photoexcited around the O 1s-Edge: Relevance to Cometary and Planetary Surfaces"; Surface Science **603**, pp. 3301–3306 (2009). 198

[339] D. P. P. Andrade, M. L. M. Rocco & H. M. Boechat-Roberty; "X-Ray Photodesorption from Methanol Ice: Ion Desorption by Soft X-Ray"; Monthly Notices of the Royal Astronomical Society **409**, pp. 1289–1296 (2010). 198

[340] S. Pilling & D. P. Andrade; "Employing Soft X-Rays in Experimental Astrochemistry"; arXiv preprint arXiv:1112.1991 (2011). 198

[341] S. Pilling & A. Bergantini; "The Effect of Broadband Soft X-Rays in SO_2 -Containing Ices: Implications on the Photochemistry of Ices Toward Young Stellar Objects"; The Astrophysical Journal **811**, p. 151 (2015). 198

[342] G. C. Almeida, S. Pilling, D. P. P. Andrade, N. L. S. Castro, E. Mendoza, H. M. Boechat-Roberty & M. L. M. Rocco; "Photodesorption and Photostability of Acetone Ices: Relevance to Solid Phase Astrochemistry"; The Journal of Physical Chemistry C **118**, pp. 6193–6200 (2014). 198

[343] A. Jimenez-Escobar, A. Ciaravella, C. Cecchi-Pestellini, C.-H. Huang, N.-E. Sie, Y.-J. Chen & G. M. M. Caro; "Photo-Desorption of H2O:CO:NH3 Circumstellar Ice Analogs: Gas-Phase Enrichment"; arXiv:1810.03302 [astro-ph] (2018)1810.03302. 198

[344] A. Ciaravella, A. Jiménez-Escobar, C. Cecchi-Pestellini, C.-H. Huang, N.-E. Sie, G. M. M. Caro & Y.-J. Chen; "Synthesis of Complex Organic Molecules in Soft X-Ray Irradiated Ices"; arXiv:1905.07958 [astro-ph] (2019)1905.07958. 198

[345] N. Tımneanu, C. Caleman, J. Hajdu & D. van der Spoel; "Auger Electron Cascades in Water and Ice"; Chemical Physics **299**, pp. 277–283 (2004). 200

[346] B. Baron & F. Williams; "X-ray Photoelectron Spectroscopy of Amorphous Ice"; The Journal of Chemical Physics **64**, pp. 3896–3897 (1976). 200

[347] G. R. Wight & C. E. Brion; "K-Shell Excitation of CH4, NH3, H2O, CH3OH, CH3OCH3 and CH3NH2, by 2.5 keV Electron Impact"; Journal of Electron Spectroscopy and Related Phenomena **4**, p. 25 (1974). 200

[348] P. Parent, C. Laffon, C. Mangeney, F. Bournel & M. Tronc; "Structure of the Water Ice Surface Studied by X-Ray Absorption Spectroscopy at the O K-Edge"; The Journal of Chemical Physics **117**, pp. 10842–10851 (2002). 200

[349] R. A. Rosenberg, P. R. LaRoe, V. Rehn, J. Stöhr, R. Jaeger & C. C. Parks; "K-Shell Excitation of D2O and H2O Ice: Photoion and Photoelectron Yields"; Physical Review B **28**, p. 3026 (1983). 200, 211

[350] M. Tronc & R. Azria; "Role of Morphology of D2O Ice (20 –160 K) in Low Energy Electron Stimulated Desorption of D- and O- Anions, and x-Ray Photon Stimulated Desorption of D+ Cations"; International Journal of Mass Spectrometry p. 7 (2001). 200

[351] J. S. Tse, D. M. Shaw, D. D. Klug, S. Patchkovskii, G. Vankó, G. Monaco & M. Krisch; "X-Ray Raman Spectroscopic Study of Water in the Condensed Phases"; Physical Review Letters **100** (2008). 201

[352] M. Cavalleri, H. Ogasawara, L. Pettersson & A. Nilsson; "The Interpretation of X-Ray Absorption Spectra of Water and Ice"; Chemical Physics Letters **364**, pp. 363–370 (2002). 201

[353] J. A. Sellberg, S. Kaya, V. H. Segtnan, C. Chen, T. Tyliszczak, H. Ogasawara, D. Nordlund, L. G. M. Pettersson & A. Nilsson; "Comparison of X-Ray Absorption Spectra between Water and Ice: New Ice Data with Low Pre-Edge Absorption Cross-Section"; The Journal of Chemical Physics **141**, p. 034507 (2014). 201

[354] E. Dartois, B. Augé, H. Rothard, P. Boduch, R. Brunetto, M. Chabot, A. Domaracka, J.-J. Ding, O. Kamalou, X.-Y. Lv, E. F. da Silveira, J.-C. Thomas, T. Pino, C. Mejia, M. Godard & A. de Barros; "Swift Heavy Ion Modifications of Astrophysical Water Ice"; Nuclear Instruments and Methods in Physics Research Section B: Beam Interactions with Materials and Atoms **365**, pp. 472–476 (2015). 201

[355] C. Laffon, S. Lacombe, F. Bournel & P. Parent; "Radiation Effects in Water Ice: A near-Edge x-Ray Absorption Fine Structure Study"; The Journal of Chemical Physics **125**, p. 204714 (2006). 202

[356] J. Berkowitz; *Atomic and Molecular Photoabsorption: Absolute Total Cross Sections* (Academic Press) (2002). 205, 220

[357] T. J. Bethell & E. A. Bergin; "Photoelectric Cross-Sections of Gas and Dust in Protoplanetary Disks"; The Astrophysical Journal **740**, p. 7 (2011). 206

[358] C. Walsh, H. Nomura, T. J. Millar & Y. Aikawa; "Chemical Processes in Protoplanetary Disks. II. On the Importance of Photochemistry and X-Ray Ionization"; The Astrophysical Journal **747**, p. 114 (2012). 206

[359] C. Walsh, H. Nomura & E. van Dishoeck; "The Molecular Composition of the Planet-Forming Regions of Protoplanetary Disks across the Luminosity Regime"; Astronomy & Astrophysics **582**, p. A88 (2015). 206

[360] W. C. Stolte, M. M. Sant'Anna, G. Öhrwall, I. Dominguez-Lopez, M. N. Piancastelli & D. W. Lindle; "Photofragmentation Dynamics of Core-Excited Water by Anion-Yield Spectroscopy"; Physical Review A **68** (2003). 208

[361] M. N. Piancastelli, R. Sankari, S. Sorensen, A. De Fanis, H. Yoshida, M. Kitajima, H. Tanaka & K. Ueda; "Resonant Auger Decay of Above-Threshold Core-Excited H2O"; Physical Review A **71** (2005). 208, 233

[362] C. Stråhlman, A. Kivimäki, R. Richter & R. Sankari; "Negative-Ion/Positive-Ion Coincidence Yields of Core-Excited Water"; The Journal of Physical Chemistry A **120**, pp. 6389–6393 (2016). 208, 232

[363] M. Tronc, R. Azria, Y. Le Coat & E. Illenberger; "Threefold Differential Electron-Stimulated Desorption Yields of D-Anions from Multilayer Films of D2O and ND3 Condensed on Platinum"; The Journal of Physical Chemistry **100**, pp. 14745–14750 (1996). 208

[364] W. C. Simpson, L. Parenteau, R. S. Smith, L. Sanche & T. M. Orlando; "Electron-Stimulated Desorption of D-(H-) from Condensed D2O (H2O) Films"; Surface science **390**, pp. 86–91 (1997). 208

[365] E. Rühl & A. P. Hitchcock; "Oxygen K-Shell Excitation Spectroscopy of Hydrogen Peroxide"; Chemical physics **154**, pp. 323–329 (1991). 209

[366] R. A. Rosenberg, V. Rehn, V. O. Jones, A. K. Green, C. C. Parks, G. Loubriel & R. H. Stulen; "The Photodissociative Ionization of Amorphous Ice"; Chemical Physics Letters **80**, pp. 488–494 (1981). 208

[367] J. Herring-Captain, G. A. Grieves, A. Alexandrov, M. T. Sieger, H. Chen & T. M. Orlando; "Low-Energy (5 – 250 eV) Electron-Stimulated Desorption of H+, H2+, and H+(H2O)n from Low-Temperature Water Ice Surfaces"; Physical Review B **72** (2005). 208

[368] X. Pan, H. Abdoul-Carime, P. Cloutier, A. D. Bass & L. Sanche; "D-, O- and OD- Desorption Induced by Low-Energy (0–20eV) Electron Impact on Amorphous D2O Films"; Radiation Physics and Chemistry **72**, pp. 193–199 (2005). 208

[369] T. A. Carlson; "The Coulomb Explosion and Recent Methods for Studying Molecular Decomposition"; in "Desorption Induced by Electronic Transitions DIET I," , volume 24, edited by V. I. Goldanskii, R. Gomer, F. P. Schäfer, J. P. Toennies, N. H. Tolk, M. M. Traum, J. C. Tully & T. E. Madey; pp. 169–182 (Springer Berlin Heidelberg, Berlin, Heidelberg) (1983); ISBN 978-3-642-45552-0 978-3-642-45550-6. 210

[370] R. Romberg, S. Frigo, A. Ogurtsov, P. Feulner & D. Menzel; "Photon Stimulated Desorption of Neutral Hydrogen Atoms from Condensed Water and Ammonia by Resonant O1s and N1s Excitation: Search for the Signature of Ultrafast Bond Breaking"; Surface Science **451**, pp. 116–123 (2000). 211

[371] R. Weimar, R. Romberg, B. Naydenov, D. Menzel & P. Feulner; "Dynamics of Ultrafast Dissociation of Hydrogenic Molecules by Resonant Antibonding Core Electron Excitation: Conclusions from Detuning Dependence of H+- Kinetic Energy Distributions from Condensed Films"; Chemical Physics Letters **510**, pp. 78–81 (2011). 211, 212

[372] P. Morin & C. Miron; "Ultrafast Dissociation: An Unexpected Tool for Probing Molecular Dynamics"; Journal of Electron Spectroscopy and Related Phenomena **185**, pp. 259–266 (2012). 211

[373] K. Mase, M. Nagasono, S. Tanaka, T. Urisu, E. Ikenaga, T. Sekitani & K. Tanaka; "Auger Electron Photoion Coincidence Technique Combined with Synchrotron Radiation for the Study of the Ion Desorption Mechanism in the Region of Resonant Transitions of Condensed H2O"; The Journal of Chemical Physics **108**, pp. 6550–6553 (1998). 211

[374] K. Mase, M. Nagasono, S.-i. Tanaka, T. Sekitani & S.-i. Nagaoka; "Ion Desorption from Molecules Condensed at Low Temperature: A Study with Electron-Ion Coincidence Spectroscopy Combined with Synchrotron Radiation (Review)"; Low Temperature Physics **29**, pp. 243–258 (2003). 211

[375] A. Hitchcock & C. Brion; "K-Shell Excitation Spectra of CO, N2 and O2"; Journal of Electron Spectroscopy and Related Phenomena **18**, pp. 1–21 (1980). 213, 214

[376] R. Püttner, I. Dominguez, T. J. Morgan, C. Cisneros, R. F. Fink, E. Rotenberg, T. Warwick, M. Domke, G. Kaindl & A. S. Schlachter; "Vibrationally Resolved O 1 s Core-Excitation Spectra of CO and NO"; Physical Review A **59**, p. 3415 (1999). 213, 214, 215

[377] M. Domke, C. Xue, A. Puschmann, T. Mandel, E. Hudson & D. A. Shirley; "Carbon and Oxygen K-Edge Photoionization of the CO Molecule"; CHEMICAL PHYSICS LETTERS p. 7 (1990). 214

[378] T. A. Carlson, M. O. Krause & W. E. Moddeman; "Excitation Accompanying Photoionization in Atoms and Molecules and Its Relationship to Electron Correlation"; Le Journal de Physique Colloques **32**, pp. C4–76–C4–84 (1971). 214

[379] Y. Jugnet, F. J. Himpsel, P. Avouris & E. E. Koch; "High-Resolution C 1s and O 1s Core-Excitation Spectroscopy of Chemisorbed, Physisorbed, and Free CO"; Physical Review Letters **53**, pp. 198–201 (1984). 214, 215

[380] R. Scheuerer, P. Feulner, G. Rocker, Z. Lin & D. Menzel; "Erosion of Pure and Alloyed Ices of Rare Gases and Small Molecules by Core Excitation"; in "Desorption Induced by Electronic Transitions DIET IV," , volume 19, edited by G. Ertl, R. Gomer, H. K. V. Lotsch, G. Betz & P. Varga; pp. 235–239 (Springer Berlin Heidelberg, Berlin, Heidelberg) (1990); ISBN 978-3-642-84147-7 978-3-642-84145-3. 215, 221, 226

[381] N. Mårtensson & A. Nilsson; "Core-Level Line Shapes of Adsorbates: Effects of Electronic and Vibrational Excitations"; Journal of Electron Spectroscopy and Related Phenomena **52**, pp. 1–46 (1990). 215

[382] R. Weimar, R. Romberg, S. P. Frigo, B. Kassühlke & P. Feulner; "Time-of-Flight Techniques for the Investigation of Kinetic Energy Distributions of Ions and Neutrals Desorbed by Core Excitations"; Surface science **451**, pp. 124–129 (2000). 215, 230

[383] G. Wight & C. Brion; "K-Shell Energy Loss Spectra of 2.5 keV Electrons in CO2 and N2O"; Journal of Electron Spectroscopy and Related Phenomena **3**, pp. 191–205 (1974). 217

[384] D. Chrisey, J. Boring, J. Phipps, R. Johnson & W. Brown; "Sputtering of Molecular Gas Solids by keV Ions"; Nuclear Instruments and Methods in Physics Research Section B: Beam Interactions with Materials and Atoms **13**, pp. 360–364 (1986). 219, 235, 236

[385] P. Feulner, R. Romberg, S. P. Frigo, R. Weimar, M. Gsell, A. Ogurtsov & D. Menzel; "Recent Progress in the Investigation of Core Hole-Induced Photon Stimulated Desorption from Adsorbates: Excitation Site-Dependent Bond Breaking, and Charge Rearrangement"; Surface science **451**, pp. 41–52 (2000). 221, 230

[386] L. Philippe, T. Hirayama, M. J. Ramage, G. Comtet, M. Rose, L. Hellner & G. Dujardin; "Molecular Reactions in Condensed Carbon Monoxide Studied by Ion Photodesorption"; The Journal of Chemical Physics **106**, pp. 7072–7079 (1997). 226, 229, 230, 234

[387] H. T. Jonkman & J. Michl; "Secondary Ion Mass Spectrometry of Small-Molecule Solids at Cryogenic Temperatures. 1. Nitrogen and Carbon Monoxide"; Journal of the American Chemical Society **103**, pp. 733–737 (1981). 226, 235

[388] L. Sanche; "Dissociative Attachment in Electron Scattering from Condensed O2 and CO"; Physical Review Letters **53**, pp. 1638–1641 (1984). 231

[389] W. C. Stolte, D. L. Hansen, M. N. Piancastelli, I. Dominguez Lopez, A. Rizvi, O. Hemmers, H. Wang, A. S. Schlachter, M. S. Lubell & D. W. Lindle; "Anionic Photofragmentation of CO: A Selective Probe of Core-Level Resonances"; Physical Review Letters **86**, pp. 4504–4507 (2001). 231

[390] D. L. Hansen, W. C. Stolte, O. Hemmers, R. Guillemin & D. W. Lindle; "Anion Formation Moderated by Post-Collision Interaction Following Core-Level Photoexcitation of CO"; Journal of Physics B: Atomic, Molecular and Optical Physics **35**, pp. L381–L386 (2002). 231, 232

[391] A. Kivimäki, C. Stråhlman, R. Richter & R. Sankari; "Fragmentation of Methanol Molecules after Core Excitation and Core Ionization Studied by Negative-Ion/Positive-Ion Coincidence Experiments"; The Journal of Physical Chemistry A **122**, pp. 224–233 (2018). 232

[392] G. Dujardin, L. Hellner, B. J. Olsson, M. J. Besnard-Ramage & A. Dadouch; "Negative-Fragment-Ion Formation by Photon Excitation of Molecules in the Vicinity of Their Core-Ionization and Direct-Double-Ionization Thresholds"; Physical Review Letters **62**, pp. 745–748 (1989). 233

[393] A. Dadouch, G. Dujardin, L. Hellner, M. J. Besnard-Ramage & B. J. Olsson; "Highly Excited Quasistable States of Neutral CO Lying up to the Double-Ionization-Energy Level"; Physical Review A **43**, pp. 6057–6065 (1991). 233

[394] M. T. Bowers, M. Chau & P. R. Kemper; "Reactions of Ions in Excited Electronic States: (CO+·)*+CO C2O+· + CO"; The Journal of Chemical Physics **63**, pp. 3656–3660 (1975). 234

[395] M. J. Loeffler, G. A. Baratta, M. E. Palumbo, G. Strazzulla & R. A. Baragiola; "CO2 Synthesis in Solid CO by Lyman-α Photons and 200 keV Protons"; Astronomy & Astrophysics **435**, pp. 587–594 (2005). 234, 235

[396] H. Okabe; *Photochemistry of Small Molecules* (Wiley, New York) (1978); ISBN 978-0-471-65304-2. 234

[397] A. Ciaravella, A. Jiménez-Escobar, G. M. Muñoz Caro, C. Cecchi-Pestellini, R. Candia, S. Giarrusso, M. Barbera & A. Collura; "Soft X-Ray Irradiation of Pure Carbon Monoxide Interstellar Ice Analogues"; The Astrophysical Journal **746**, p. L1 (2012). 235

[398] A. Ciaravella, Y.-J. Chen, C. Cecchi-Pestellini, A. Jiménez-Escobar, G. M. Muñoz Caro, K.-J. Chuang & C.-H. Huang; "Chemical Evolution of a CO Ice Induced by Soft X-Rays"; The Astrophysical Journal **819**, p. 38 (2016). 235

[399] C. S. Jamieson, A. M. Mebel & R. I. Kaiser; "Understanding the Kinetics and Dynamics of Radiation-induced Reaction Pathways in Carbon Monoxide Ice at 10 K"; The Astrophysical Journal Supplement Series **163**, pp. 184–206 (2006). 235

[400] R. Haring, R. Pedrys, D. Oostra, A. Haring & A. De Vries; "Reactive Sputtering of Simple Condensed Gases by keV Ions II: Mass Spectra"; Nuclear Instruments and Methods in Physics Research Section B: Beam Interactions with Materials and Atoms **5**, pp. 476–482 (1984). 235

[401] D. B. Chrisey, W. L. Brown & J. W. Boring; "Electronic Excitation of Condensed CO: Sputtering and Chemical Change"; Surface science **225**, pp. 130–142 (1990). 235

[402] A. Trottier & R. L. Brooks; "Carbon-Chain Oxides in Proton-Irradiated CO Ice Films"; The Astrophysical Journal **612**, pp. 1214–1221 (2004). 235

[403] M. E. Palumbo, P. Leto, C. Siringo & C. Trigilio; "Detection of C3O in the Low-Mass Protostar Elias 18"; The Astrophysical Journal **685**, pp. 1033–1038 (2008). 235

[404] E. Seperuelo Duarte, A. Domaracka, P. Boduch, H. Rothard, E. Dartois & E. F. da Silveira; "Laboratory Simulation of Heavy-Ion Cosmic-Ray Interaction with Condensed CO"; Astronomy and Astrophysics **512**, p. A71 (2010). 235

[405] T. Baird; "The Nature of the Solid Products from CO Radiolysis"; Carbon **10**, pp. 723–728 (1972). 236

[406] V. G. Anicich; "Evaluated Bimolecular Ion-Molecule Gas Phase Kinetics of Positive Ions for Use in Modeling Planetary Atmospheres, Cometary Comae, and Interstellar Clouds"; Journal of Physical and Chemical Reference Data **22**, pp. 1469–1569 (1993). 236

[407] S. Lacombe, F. Bournel, C. Laffon & P. Parent; "Radical Photochemistry in Oxygen-Loaded Ices"; Angewandte Chemie **118**, pp. 4265–4269 (2006). 237

[408] C. Tian & C. R. Vidal; "Cross Sections of the Electron Impact Dissociative Ionization of CO, CH4 and C2H2"; Journal of Physics B: Atomic, Molecular and Optical Physics **31**, p. 895 (1998). 246

[409] H. C. Straub, P. Renault, B. G. Lindsay, K. A. Smith & R. F. Stebbings; "Absolute Partial Cross Sections for Electron-Impact Ionization of H2, N2, and O2 from Threshold to 1000 eV"; Physical Review A **54**, p. 2146 (1996). 246

[410] E. Brook, M. F. A. Harrison & A. C. H. Smith; "Measurements of the Electron Impact Ionisation Cross Sections of He, C, O and N Atoms"; Journal of Physics B: Atomic and Molecular Physics **11**, pp. 3115–3132 (1978). 246

[411] O. J. Orient & S. K. Strivastava; "Electron Impact Ionisation of H2O, CO, CO2 and CH4"; Journal of Physics B: Atomic and Molecular Physics **20**, pp. 3923–3936 (1987). 246

[412] V. Tarnovsky, H. Deutsch & K. Becker; "Electron Impact Ionization of the Hydroxyl Radical"; The Journal of Chemical Physics **109**, p. 932 (1998). 246

[413] J. Lopez, V. Tarnovsky, M. Gutkin & K. Becker; "Electron-Impact Ionization of NO, NO2, and N2O"; International Journal of Mass Spectrometry **225**, pp. 25–37 (2003). 246

[414] V. Tarnovsky, A. Levin, H. Deutsch & K. Becker; "Electron Impact Ionization of CDx (X= 1-4)"; Journal of Physics B: Atomic, Molecular and Optical Physics **29**, p. 139 (1996). 246

[415] M. V. V. S. Rao & S. K. Srivastava; "Total and Partial Ionization Cross Sections of NH_3 by Electron Impact"; Journal of Physics B: Atomic, Molecular and Optical Physics **25**, pp. 2175–2187 (1992). 246

[416] K. N. Joshipura, M. Vinodkumar & U. M. Patel; "Electron Impact Total Cross Sections of CHx, NHx and OH Radicals Vis-à-Vis Their Parent Molecules"; Journal of Physics B: Atomic, Molecular and Optical Physics **34**, p. 509 (2001). 246

Paper I: Spectrally-resolved UV photodesorption of CH_4 in pure and layered ices

Astronomy & Astrophysics manuscript no. output
April 24, 2017
©ESO 2017

Spectrally-resolved UV photodesorption of CH_4 in pure and layered ices

R. Dupuy[1], M. Bertin[1], G. Féraud[1], X. Michaut[1], P. Jeseck[1], M. Doronin[1], L. Philippe[1], C. Romanzin[2] and J.-H. Fillion[1]

[1] Laboratoire d'Etude du Rayonnement et de la Matière en Astrophysique et Atmosphères (LERMA), Sorbonne Universités, UPMC Univ. Paris 06, Observatoire de Paris, PSL Research University, CNRS UMR 8112, F-75005, Paris, France

[2] Laboratoire de Chimie Physique (LCP), CNRS UMR 8000, Univ. Paris Sud, F-91400 Orsay, France

ABSTRACT

Context. Methane is among the main components of the ice mantles of interstellar dust grains, where it is at the start of a rich solid-phase chemical network. Quantification of the photon-induced desorption yield of these frozen molecules and understanding of the underlying processes is necessary to accurately model the observations and the chemical evolution of various regions of the interstellar medium.
Aims. This study aims at experimentally determining absolute photodesorption yields for the CH_4 molecule as a function of photon energy. The influence of the ice composition is also investigated. By studying the methane desorption from layered CH_4:CO ice, indirect desorption processes triggered by the excitation of the CO molecules are monitored and quantified.
Methods. Tunable monochromatic vacuum ultraviolet light (VUV) light from the DESIRS beamline of the SOLEIL synchrotron is used in the 7 - 13.6 eV (177 - 91 nm) range to irradiate pure CH_4 or layers of CH_4 deposited on top of CO ice samples. The release of species in the gas phase is monitored by quadrupole mass spectrometry, and absolute photodesorption yields of intact CH_4 are deduced.
Results. CH_4 photodesorbs for photon energies higher than ~9.1 eV (~136 nm). The photodesorption spectrum follows the absorption spectrum of CH_4, which confirms a desorption mechanism mediated by electronic transitions in the ice. When it is deposited on top of CO, CH_4 desorbs between 8 and 9 eV with a pattern characteristic of CO absorption, indicating desorption induced by energy transfer from CO molecules.
Conclusions. The photodesorption of CH_4 from pure ice in various interstellar environments is around $2.0 \pm 1.0 \times 10^{-3}$ molecules per incident photon. Results on CO-induced indirect desorption of CH_4 provide useful insights for the generalization of this process to other molecules co-existing with CO in ice mantles.

Key words. Astrochemistry – ISM: abundances – ISM: molecules – Molecular processes – Methods: laboratory: solid state Ultraviolet: ISM

1. Introduction

In cold and dense regions of the interstellar medium (ISM), such as dense molecular clouds or protoplanetary disks midplanes, interstellar dust grains are coated with an ice mantle, composed of molecules either accreted from the gas phase or formed directly on the surface. Due to the low temperatures in these regions (~ 10 K) thermal desorption is negligible, and the exchanges between the gas phase and those icy mantles are thus driven by non-thermal processes. Among them, desorption stimulated by UV photons emitted by nearby stars or secondary UV photons emitted by excited molecules is thought to play a significant role. Laboratory experiments in the last few years have aimed at quantitatively and qualitatively describing such photon-stimulated desorption (PSD) processes for astrophysically relevant ice analogs, (see e.g., Öberg et al. 2009; Hama et al. 2009; Fayolle et al. 2011; Yuan & Yates 2014; Martín-Doménech et al. 2016) which is required in order to explain the observations of molecule abundances in the gas and solid phases and to accurately model the chemical evolution in the concerned regions of the ISM. Photodesorption can also be relevant in other astrophysical media; it has been considered as one of the possible space-weathering agents of solar system bodies (Bennett et al. 2013).

CH_4 has been observed toward protostellar objects (Dartois et al. 1998; Boogert et al. 1998) in the gas and solid phase, with an estimated CH_4 gas to ice ratio of 0.3-0.5. CH_4 formation was proposed to occur on grains, and it was found to exist in polar ices containing H_2O and CH_3OH (Boogert et al. 1998). CH_4 is also detected in ices toward young stellar objects (YSOs) with a typical abundance of 1-10 % with respect to H_2O, while in quiescent clouds and cores only an upper limit of <3 % is found (Boogert et al. 2015). In cometary ices, the typical abundance relative to H_2O is 1 % (Mumma & Charnley 2011), lower than in the previously cited environments. The observations toward YSOs suggest that the dominant formation mechanism of CH_4 in the ISM is through hydrogenation of atomic C at the surface of grains (Öberg et al. 2008). Such a mechanism has been experimentally confirmed (Hiraoka et al. 1998). This implies that desorption from grains constitutes the main source of CH_4 in the gas phase. CH_4 abundances in the gas phase are poorly known mainly because of its lack of a permanent dipole moment, meaning that no detection is possible at radio wavelengths (Boogert et al. 2004). This lack of observational constraints makes it even

Article published by EDP Sciences, to be cited as https://doi.org/10.1051/0004-6361/201730772

more crucial to have accurate modeling parameters when assessing the available reservoir of CH_4. Indeed, methane is included in gas-grain models for cold clouds, disks, and illuminated regions such as photon-dominated regions (PDR) (Ruaud et al. 2016; Kalvans 2015; Hollenbach et al. 2009; Garrod & Pauly 2011; Cleeves et al. 2016).

Evaporation of CH_4 from the grain mantles is the first step of a gas phase chemistry leading to the formation of carbon chains (as in protostars and protoplanetary disks, see e.g., Sakai & Yamamoto (2013); Aikawa & Nomura (2006); Hassel et al. (2008)). Moreover, photodissociation products of methane initiate a chemical network that has been well experimentally studied in the gas phase, due to the fact that it is also very relevant to planetary science (Romanzin et al. 2005; Gans et al. 2011; Smith & Raulin 1999).

In the solid phase, CH_4 is also at the start of a rich chemical network. Laboratory experiments on the processing of pure CH_4 ice with energetic particles (Kaiser & Roessler 1998; Baratta et al. 2003; Bennett et al. 2006; de Barros et al. 2011) and UV photons (Lo et al. 2015; Bossa et al. 2015) as well as mixes with other astrophysically relevant molecules such as H_2O (Öberg et al. 2010; Hodyss et al. 2009), N_2 (Wu et al. 2012), CO (Maity et al. 2014) or N_2:CO (Hodyss et al. 2011) have yielded a great variety of products.

Non-thermal desorption/sputtering of methane by energetic ions and electrons has already been extensively studied (Johnson et al. 2013, and references therein). This is not the case for UV irradiation. Cruz-Diaz et al. (2016) observed CH_4 desorption when UV-irradiating a pure methanol ice, demonstrating a pathway to the release of methane in the gas phase other than direct methane photodesorption. However, in their study of pure CH_4 ice, they did not observe intact CH_4 photodesorption (Cruz-Diaz 2015). Instead, desorption of photoproducts such as C_2H_4 was seen. A recent study by Martín-Doménech et al. (2016) has also shown that a part of the reaction products (e.g., H_2CO) initiated by the methane photodissociation in mixed CH_4:H_2O ices is released in the gas phase during UV irradiation. However, they did not observe intact CH_4 photodesorption either. The present study is therefore, to our knowledge, the first report of CH_4 photodesorption from pure CH_4 ice. We have focused on the desorption of the intact CH_4 molecule, and obtained absolute photodesorption yields as a function of the UV photon energy between 7 and 13.6 eV. This allows one to derive photodesorption yields for any given astrophysically relevant UV field. In order to test the influence of the environment of the molecules on photodesorption, we also investigated the desorption of layers of CH_4 deposited on top of CO ice. CO is a very abundant component of interstellar ices, and has a high photodesorption yield (Fayolle et al. 2011), therefore its ability to indirectly induce desorption of other molecules (Bertin et al. 2013) could have important astrophysical implications.

2. Methods

Experiments were performed in the SPICES (Surface Processes & ICES) set-up, which has previously been described in detail (Doronin et al. 2015). It consists of an ultra-high vacuum (UHV) chamber with a base pressure of typically 10^{-10} mBar, within which a polycrystalline gold surface is mounted on a rotatable cold head that can be cooled down to ~10 K using a closed cycle helium cryostat. Ices of $^{13}CH_4$ (Eurisotop, >99.9% purity in ^{13}C) and CO (Air liquide, >99.9% purity) are dosed by exposing the cold surface (10 K) to a partial pressure of gas using a tube positioned a few millimeters away from the surface, allowing rapid growth without increasing the chamber pressure to more than a few 10^{-9} mBar. Ice thicknesses are controlled with a precision better than 1 monolayer (ML) via a calibration using the temperature programmed desorption (TPD) technique, as detailed in Doronin et al. (2015). The release of species in the gas phase is monitored by means of a quadrupole mass spectrometer (QMS).

The chamber is then coupled to the undulator-based DESIRS beamline (Nahon et al. 2012) at the SOLEIL synchrotron facility, which provides a monochromatic, tunable radiation beam hitting the sample at 45° incidence. The coupling is window-free to prevent cut-off of the higher energy photons. To acquire photodesorption spectra, the narrow bandwidth (~25 meV) output of a grating monochromator is continuously scanned between 7 and 14 eV. Higher harmonics of the undulator are suppressed using a Krypton gas filter. Typical photon fluxes as measured with a calibrated AXUV photodiode depend on the photon energy and vary between 5×10^{12} and 17×10^{12} photons.cm^{-2}.s^{-1}.

During the photon energy scan, the relative amount of photodesorbed molecules is recorded by the QMS. Each 25 meV photon energy step lasts about 5 s, which is sufficiently higher than the dwell time of the QMS (0.5 s). A typical scan thus lasts around 20 minutes, which corresponds to a total photon dose of ~10^{16} photons.cm^{-2}.

Once corrected from the background contribution and divided by the photon flux, the QMS signal I_i corresponds to the relative efficiency of photodesorption as a function of photon energy. This signal can then be converted to absolute photodesorption yields. For a given species i, the absolute photodesorption yield Y_i (in molecules per incident photons) is proportional to the signal I_i at the m/z ratio of species i, such that $Y_i = f_i \times I_i$. f_i can be further expanded into $f_i = g \times h_i$ where g is a factor intrinsic to the QMS and the geometry of our set-up, and h_i is a factor specific to each species i. In the case of CO, f_{CO} can be obtained by comparing the photodesorption signal of a pure CO ice taken during the experimental runs to the well-known CO absolute photodesorption yields (Fayolle et al. 2011). This calibration is then used as a basis to derive the proportionality coefficients f_i of the other species. This is done by correcting f_{CO} by molecule-dependent factors such as the electron-impact ionization cross-section, which characterizes the fact that CO and species i are not ionized with the same efficiency by the ionization chamber, and the apparatus function of our QMS, which characterizes the fact that ions with a different m/z ratio are not detected with the same efficiency by the QMS. Thus, for CH_4, we have:

$$Y_{CH_4} = f_{CH_4} \times I_{CH_4} = f_{CO} \times \frac{\sigma(CH_4^+/CH_4)}{\sigma(CO^+/CO)} \times \frac{AF(CH_4)}{AF(CO)} \times I_{CH_4} \quad (1)$$

where $\sigma(i^+/i)$ is the partial electron-impact ionization cross-section of the i^+ ion relative to its parent molecule i, and $AF(i)$ is the apparatus function of our QMS for species i ($AF(CO)$ is set to 1).

Until now we assumed that the QMS signal at a given m/z ratio originated from a single species i. However, due to cracking in the QMS, an ion can originate from different parent molecules, and the signal has to be corrected from the contribution of the irrelevant parent molecules. For example in our case, the signal measured on mass 16 (corresponding here to $^{13}CH_3^+$) could be originating from either desorbed CH_3 radicals or from desorbed CH_4 molecules that are cracked in the ionization chamber of the QMS. Thus in order to know if there is a signal originating from desorbing CH_3, the latter contribution has to be substracted using

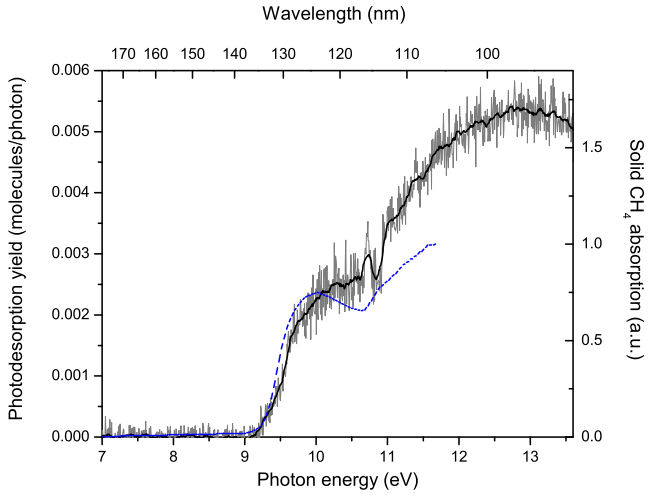

Fig. 1. $^{13}CH_4$ photodesorption spectrum of a 20 ML thick $^{13}CH_4$ ice at 10 K between 7 and 13.6 eV. The blue dotted line (right axis) is the absorption spectrum of pure CH_4 adapted from Wu et al. (2012).

the partial ionization cross-sections of CH_4 and CH_3:

$$I_{CH_3} = I_{CH_3^+} - \frac{\sigma(CH_3^+/CH_4)}{\sigma(CH_4^+/CH_4)} \times \frac{AF(CH_3)}{AF(CH_4)} \times I_{CH_4} \quad (2)$$

where $I_{CH_3^+}$ is the total signal measured on mass channel 16 and I_{CH_3} is the signal originating from desorbing CH_3 (so far we have assumed that ions in the QMS had only one parent molecule, i.e., $I_i = I_{i^+}$).

For similar reasons, $^{13}CH_4$ was used in order to distinguish it in mass spectrometry from O^+ fragments (m/z = 16, same as $^{12}CH_4^+$) originating from the cracking of CO in the QMS, during CH_4 layered on CO experiments. This consideration also brings up the possibility that part of the CH_4^+ signal detected originates not from desorbing CH_4 but from larger molecules formed by photolysis of the ice and photodesorbed. However, the expected photolysis products of solid CH_4, such as C_2H_2, C_2H_4, C_2H_6 or larger hydrogenated carbon-chains (e.g., Lo et al. (2015)) only lead to negligible CH_4^+ signal by electron-impact ionization at 70 eV.[1] We have therefore made the assumption that desorption of possible photoproducts from the solid methane does not participate to the recorded CH_4^+ signal, that is thus only related to the desorption of intact CH_4.

The calibration of our spectra is done using the apparatus function of our QMS as determined by calibration experiments using several molecules with well-known electron-impact cracking patterns and the partial electron-impact ionization cross-sections at 70 eV found in Tian & Vidal (1998) for CH_4 and CO. While the uncertainties on the relative photodesorption spectra are only due to experimental noise, background substraction and photon flux uncertainties, this calibration method introduces much larger uncertainties on the absolute photodesorption yields. We estimate a systematic 50% uncertainty on all the absolute photodesorption yields given for CH_4 hereafter.

3. Results

3.1. Pure CH_4 ice

Figure 1 shows the photodesorption yield as a function of photon energy of CH_4 from a pure, 20 ML-thick CH_4 ice. There is a threshold at 9.1 eV under which desorption is below our detection limit. A broad peak is centered around 10 eV, then desorption steadily increases from 10.5 eV onwards, with a maximum around 13 eV. The absorption spectrum of pure CH_4 adapted from Wu et al. (2012) is given for comparison, and it matches fairly well the desorption profile, at least until their cut-off energy. The 10 eV broad feature is less well defined in our desorption spectrum. The absorption spectrum taken by Koch & Skibowski (1971), which has a higher energy cut-off, suggests that the absorption continues to increase until around 14 eV. We did not use that spectrum here because it has a 0.5 eV red-shift compared with the spectrum from Wu et al. (2012). This is probably because of different experimental conditions; the spectrum by Koch & Skibowski (1971) was taken at 30K, where CH_4 is expected to be crystalline rather than amorphous (Hudson et al. 2015). The spectrum from Cruz-Diaz et al. (2014b), taken at 10K under UHV conditions as well and recorded at energies lower than 10.3 eV, agrees with the one by Wu et al. (2012).

The absorption spectrum of CH_4 in the gas phase has a threshold at 8.5 eV and two, rather than one, broad features centered at 9.7 and 10.5 eV. These two features have been attributed to the $1t_2$ -> 3s Rydberg transitions of respectively the D_{2d} and C_{3v} symmetries of the ion (Au et al. 1993). As discussed in Robin (1974), the equivalent feature at 10 eV in the solid spectrum can thus probably be attributed to excitons, which is also supported by calculations (Kunz 1983). The fact that the desorption spectrum matches the absorption spectrum and the attributions discussed here is clear evidence that desorption is initiated by an electronic transition. After 11 eV, the absorption of gas-phase CH_4 continues to increase as in the solid phase, although there are no clearly discernible features. Virtual valence orbitals are thought to be above the first ionization potential at 13.6 eV, therefore the absorption in this region has been attributed to overlapping Rydberg transitions. The ionization threshold of CH_4 in the gas phase is at 12.5 eV (Kameta et al. 2002) and is red-shifted by 1.2 eV in the solid phase (Himpsel et al. 1975) which puts it at 11.3 eV. In the gas phase, Kameta et al. (2002) have measured the relative weight of neutral dissociation and ionization in the absorption of CH_4. Below the ionization threshold, there is only neutral dissociation, but as the ionization channel opens, neutral dissociation decreases until only ionization processes occur, at 16 eV. Therefore, the desorption mechanisms at the origin of the 10 eV feature are likely different from those responsible for the desorption signal above 11 eV.

We have observed evidence of aging of the CH_4 ice: when it has already been processed by VUV irradiation, the desorption yield decreases. This means that despite our low fluence, which usually allows us to probe desorption processes without affecting the ice significantly, photochemistry and/or ice restructuration (due to release of energy in the bulk) must play a role. Systematic studies of the effect of processing will be required to understand the exact nature of the aging effect and how much it affects photodesorption. In the meantime we only present results for "fresh" ice.

The masses corresponding to the CH_3, CH_2, and CH fragments were also monitored during the photon irradiation. Once corrected from the cracking of desorbing CH_4 in the ionization chamber of the QMS, the remaining signals fall below our sensitivity level, meaning that we are unable to observe the desorption of these radicals if they do desorb. This is despite the fact that at least the CH_3 radical fragment has been detected as trapped in photolyzed methane ice (Lo et al. 2015) and matrix-isolated methane (Milligan & Jacox 1967).

[1] http://webbook.nist.gov/chemistry/

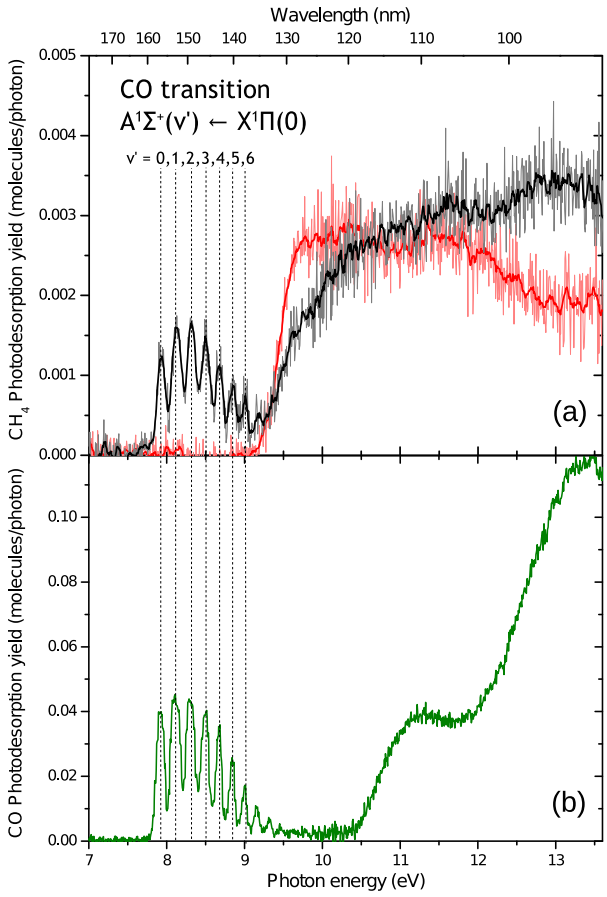

Fig. 2. (a) $^{13}CH_4$ photodesorption spectrum of 1 ML (black trace) and 3 ML (red trace) of $^{13}CH_4$ on top of 20 ML of CO ice at 10 K, between 7 and 13.6 eV. (b) CO photodesorption spectrum of a 20 ML thick pure CO ice at 10 K. Electronic transitions are indicated by vertical dashed lines.

3.2. CH_4 on top of CO ice

Figure 2b shows the photodesorption spectrum of a pure 20 ML-thick CO ice (measured at m/z=28 CO). Between 8 and 9 eV, this spectrum shows very characteristic peaks that correspond to the vibrational levels of the $A^1\Sigma \leftarrow X^1\Pi$ electronic transition of condensed CO. This feature allowed for labeling of the desorption at these energies as a DIET (Desorption Induced by Electronic Transition) process (Fayolle et al. 2011). It was later found that desorption in this region could be in great part attributed to an indirect mechanism (Bertin et al. 2012). "Indirect" here means that the desorbing molecule is not the one that has absorbed a photon. Instead, a CO molecule in the first few sub-surface monolayers of the ice is excited, then an energy transfer induces the desorption of another, surface-located CO molecule. Above 10.5 eV, two broad features are observed. The CO desorption mechanism for these two features is not clear, since in this region electronic states are dissociative and ionization can occur at 12.5 eV and above, which opens many more possibilities other than a 'simple' DIET mechanism, such as photo-electron induced desorption or neutral-neutral or ion-neutral recombination chemistry.

Figure 2a shows the photodesorption spectrum of 1 ML of CH_4 deposited on top of 20 ML of CO. The desorption profile is significantly changed as compared with the pure CH_4 ice. Between 8 and 9 eV, where CH_4 does not desorb in the pure ice case (Fig. 1), desorption peaks are observed that correspond to the signature peaks of CO excitation. This is a clear indication that an indirect desorption mechanism is at play. This indirect mechanism is schematized in Figure 3: the excitation of a sub-surface CO molecule is followed by an energy transfer to a CH_4 molecule at the surface, which then desorbs. The principle is identical to the indirect mechanism that was found in pure CO, and we discuss in section 4.2 the generalization of this 'CO-induced' desorption mechanism. The photodesorption of CH_4 on CO is a superimposition of the pure CO (Fig. 2b) and pure CH_4 (Fig. 1) profiles; while the peaks between 8 and 9 eV are entirely due to CO-induced indirect desorption, desorption around 10 eV unambiguously corresponds to CH_4 absorption and subsequent desorption, since CO absorption (and desorption) is very weak in this region. In the region above 11 eV, both molecules absorb significantly and they probably both contribute to the observed desorption of CH_4, although no clear features can be discerned.

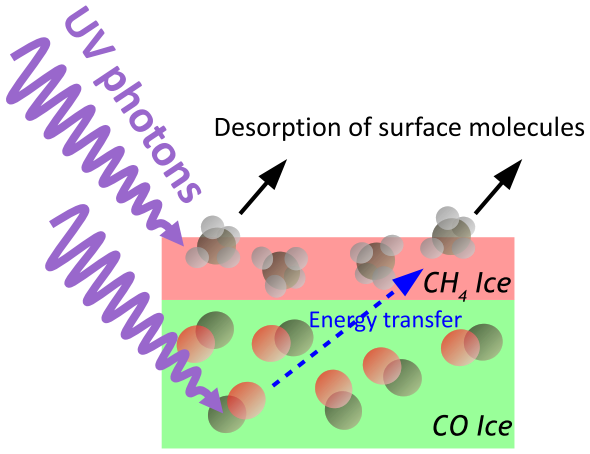

Fig. 3. Simplified scheme of the two desorption mechanisms at play: direct desorption of surface $^{13}CH_4$, and indirect desorption of surface $^{13}CH_4$ after energy transfer from underlying CO molecules.

In Figure 2a, also represented is the photodesorption spectrum of 3 ML of CH_4 deposited on top of 20 ML of CO. At this thickness, no CO-induced desorption is seen at all, and the spectrum looks like the photodesorption spectrum of 20 ML of CH_4 below 10.5 eV. In this system, indirect desorption is negligible if more than 3 ML of CH_4 are deposited on top of CO ice. Both the 1 and 3 ML layers of CH_4 on CO exhibit lower desorption yields in the region above 11 eV than in the case of the pure 20 ML ice, which suggests either a thickness dependence of the desorption in this region or that the ageing effect mentioned earlier is more efficient in thin layers. In this latter case, the ice could have aged as the scan occurred, resulting in a lower yield at high energies. The yield at high energy of the 3 ML layer is even lower than the 1 ML one, which is evidence that there is a contribution, although almost structureless, of CO-induced desorption in the latter case.

4. Discussion

4.1. Photodesorption mechanisms in pure CH_4 ices

In the relatively more simple case of molecules that do not dissociate upon VUV irradiation (e.g., CO under 10 eV, N_2), photodesorption has been attributed to a DIET process, which as discussed above can be direct or indirect, where the molecule stays intact throughout the process (Bertin et al. 2012, 2013).

Such a process cannot be excluded here, but the fact that the energy threshold for dissociation of CH_4 in the gas phase is much lower than the photon energy (Gans et al. 2011) suggests that new desorption pathways should be opened by photodissociation. Photodesorption initiated by molecular photodissociation is known to dominate in the case of H_2O. Molecular dynamics simulations on the photodesorption of H_2O ice (Andersson & van Dishoeck 2008; Andersson et al. 2011) have suggested a kick-out mechanism by energetic H fragments. This mechanism could be generalized to other molecules such as CH_4 that produce energetic fragments, including H, when photodissociated. Another possible process is where desorption occurs as the fragments of a molecule that dissociated, immediately recombine (geminate or direct recombination). Recombination can also occur for fragments coming from different molecules (secondary recombination); the fact that fragments are very energetic means that in condensed phase, they can travel far on the surface and in the bulk and react with other fragments. Such a process has been shown to exist for the UV photodesorption of O_2 (Fayolle et al. 2013) and CO_2 (Fillion et al. 2014; Martín-Doménech et al. 2015). Another indication that photodissociation and subsequent radical chemistry likely plays an important role in CH_4 desorption, is the desorption of heavier hydrocarbons such as C_2H_4 observed by Cruz-Diaz (2015) upon VUV irradiation of CH_4 ice.

One interesting piece of information that we can extract from our data is where the energy goes when photons are absorbed at the surface of the ice. The final outcomes of the initial event of a photon being absorbed by a molecule near the surface can be divided into three channels. Two measurable channels are (i) a CH_4 desorption event and (ii) the effective destruction of a CH_4 molecule. It should be noted that the second channel does not characterize photodissociation, since photodissociation can also lead to desorption or recombination into a CH_4 molecule. Rather, this outcome corresponds to photochemistry; radicals and/or photoproducts are created. The third is then (iii) the energy is relaxed through various pathways. The weight of this third channel can be deduced from the quantification of the initial step and the first two outcomes. The absorption cross-section of pure solid CH_4 at Lyman-α (10.2 eV) has been measured by Cruz-Diaz et al. (2014b) as 1.5×10^{-17} cm^2. Assuming that desorption occurs in the first three monolayers of the ice, we find a photodesorption yield of ~0.05 molecules desorbed per absorbed photon at Lyman-α. This value characterizes channel (i). Öberg et al. (2010) evaluated the effective photodestruction cross-section of pure CH_4 ice irradiated by a Lyman-α dominated discharge lamp as 5×10^{-19} cm^2, which corresponds to ~0.033 destroyed molecules per absorbed photons. We can consider this value to represent channel (ii) if we make the hypothesis that photodestruction is similar at the surface and in the bulk. Both values derived for channels (i) and (ii) are low and suggest that channel (iii) dominates; most of the absorbed energy is relaxed away.

These values can be compared with the photodesorption yields per absorbed photon derived by Cruz-Diaz et al. (2014a) for CO, which are above unity for all wavelengths, meaning that each photon absorption leads on average to one or even multiple desorption events. The energetics in these two cases are therefore very different. The photodesorption yield per absorbed photon of CH_4 is closer to the one found in Cruz-Diaz et al. (2014b) for O_2, another molecule where photodesorption has been linked to photodissociation.

Table 1. $^{13}CH_4$ photodesorption yields per incident photon for pure CH_4 ice in various interstellar environments

	Dense cores[a]	Protoplanetary Disks[b]	ISRF[c]
	(x 10^{-3} molecules/photon)		
Pure CH_4	2.2 ± 1.1	2.2 ± 1.1	2.0 ± 1.0

Notes. UV fields are taken from [a]Gredel et al. (1987), [b]Johns-Krull & Herczeg (2007) and [c]Mathis et al. (1983)

4.2. Desorption induced by CO molecules

The results obtained on layered CH_4:CO ices provide some insight into CO-induced desorption. In a previous study, N_2 overlayer desorption induced by the underlying CO ice excitation has been shown to be a very efficient process (Bertin et al. 2012). Indeed, the photodesorption yield of N_2 can reach up to ~ 2.5 $\times 10^{-2}$ molecule/photon at a photon energy of 8.3 eV when it is adsorbed onto CO ice, whereas it is almost zero when N_2 is pure. As can be seen in Fig. 2, the CH_4 desorption induced by the CO excitation barely reaches 2×10^{-3} molecule/photon at the same energy. It is interesting, therefore, to discuss this difference of one order of magnitude as compared with the case of N_2. The efficiency of the indirect process for different molecules can be driven by several parameters corresponding to the different steps of the mechanism: The inter-molecular energy transfer, the intra or inter-molecular energy relaxation once it has been transferred, and the binding energy of the molecule. CH_4 is as volatile as CO and N_2, and although no data is available on the CH_4-CO binding energy to our knowledge, it is reasonable to assume that it would not be very different from the CH_4 binding energy with itself (~100 meV, Smith et al. (2016)). If the energy transfer is simply a kinetic momentum transfer, since CH_4 is lighter than N_2 or CO, we would expect the transfer to be even more efficient. However, a good case can be made for the limiting step being intra or inter-molecular energy relaxation. Aside from a higher density of vibrational states into which energy can be partitioned, vibrational relaxation of polyatomic molecules is usually much faster than for diatomic molecules, due to the availability of relaxation pathways involving multiple vibration modes that do not exist for diatomic molecules (Nitzan 2006). Such an explanation also fits with the observed fact that in CH_3OH:CO ice mixtures, CO-induced desorption of CH_3OH is not observed (Bertin et al. 2016). Further investigations will aim at determining precisely what parameter(s) drive the efficiency of this process.

5. Astrophysical implications

5.1. Photodesorption yields of CH_4 from interstellar icy grains

By multiplying the photodesorption spectra we obtained with typical UV fields (with their integral normalized to unity) of different regions of the interstellar medium, we can derive average photodesorption yields for each of these regions. Table 1 gives such values for the dense core UV field calculated by Gredel et al. (1987), the protoplanetary disk field calculated by Johns-Krull & Herczeg (2007) and the interstellar radiation field (ISRF) estimated by Mathis et al. (1983). The UV field in dense cores and the regions of protoplanetary disks far away from the star comes from secondary UV photons generated by cosmic rays, and is dominated by Lyman-α photons (at 10.2 eV). The photodesorption of CH_4 being relatively efficient at Lyman-α (Fig. 1), the average desorption yield for those environments is

equal to the desorption yield at Lyman-α (Table 1 and Fig. 1). For the ISRF, where there is a higher contribution of lower-energy photons that do not efficiently photodesorb CH_4, the average desorption yield is slightly lower. These photodesorption yields are obtained for $^{13}CH_4$, but, considering the weak difference in mass, we expect about the same values for the $^{12}CH_4$ isotope.

We must, however, discuss the conditions of validity of these yields. They will depend on the accuracy of the UV field models for the considered region of the ISM, but also on how well our experimental conditions can be extrapolated to astrophysical ice mantles. They are thus only entirely valid for pure, thick ices of methane deposited at 10 K, that have not been further processed. "Thick" in the context of photodesorption experiments can be taken as a few tens of monolayers. Photodesorption is a surface process that mostly involves the first few monolayers of the ice, and although deeper layers can play a role to some extent, 20 monolayers can thus be considered "thick". The data obtained for 1 ML and 3 ML of CH_4 deposited on CO ice suggest, however, a thickness dependence of the photodesorption yields for thinner layers. Another factor that can affect photodesorption is ice morphology. Ice morphology is also linked to the deposition temperature of the ice in experiments and post-processing by UV photons or cosmic ray analogs, as has been extensively studied in the case of H_2O (e.g., Dartois et al. 2013, and references therein). A recent study by Muñoz Caro et al. (2016) has highlighted the influence of the physical properties of the CO ice on photodesorption: desorption yields for CO ices deposited between 7 and 20 K vary by up to a factor of 4. This effect has been attributed to the disorder of CO molecular dipoles affecting the energy transfer between molecules, and thus hindering the indirect desorption process mentioned in section 3.2.

Another important aspect to take into account is the molecular environment; CH_4 is not found pure in ice mantles. Observations (Boogert et al. 2015) and models (Garrod & Pauly 2011) currently point to a two-phase model of interstellar ices: One H_2O-rich phase, formed when hydrogenation of atoms is a dominant process and containing NH_3, CH_4 and CO_2, and one CO-rich phase containing CH_3OH and CO_2. According to this model, an astrophysically realistic situation would therefore rather be CH_4 in a water matrix, containing other elements such as NH_3 and CO_2. In a first approximation, the yields obtained for pure ices can be extrapolated to an astrophysical ice by simply weighing each yield by the relative abundance of the species. However, a different environment means different binding energies, relaxation dynamics, and chemistry, all of which can significantly affect photodesorption - not to mention indirect desorption induced by different molecules. The latter is evidenced by our studies of desorption induced by CO. A more realistic case that still needs to be studied is the photodesorption of methane from an H_2O-rich ice. The relative parts of desorption, destruction, and relaxation are likely to change in a water matrix, although it is hard to predict in which way desorption will be affected. Experiments by Öberg et al. (2010) show a much increased photodestruction cross-section for CH_4 mixed with H_2O, while experiments on CO deposited on amorphous solid water (ASW) showed a decreased photodesorption, attributed to the ability of dangling OH from the water matrix to evacuate energy into the bulk very efficiently (Bertin et al. 2012). A recent study by Martín-Doménech et al. (2016) on the photodesorption of CH_4:H_2O ices only showed the desorption of reaction products (CO and H_2CO) initiated by the methane photodissociation. In this case, the desorption yield of intact CH_4 from a H_2O-rich ice has not been measured. More experiments, which await further beamtime, will be required to investigate all these considerations and to quantify all these effects on the CH_4 photodesorption yields from a water-rich or a CO-rich environment.

5.2. Solar system

As mentioned in section 1, photodesorption may also be relevant in astrophysical contexts other than the ice mantles of interstellar grains, for example in the solar system. CH_4 is classified among the supervolatile molecules. In the ultra-high vacuum conditions of our experimental set-up, its sublimation temperature is around 30K. Therefore, non-thermal desorption will likely only matter for the coldest regions of the solar system, in places where the ice is never exposed to solar light and photodesorption occurs because of the interstellar UV photons and the solar UV photons scattered by the interplanetary medium. For example, a scenario was recently published (Grundy et al. 2016) where the red color of the poles of Charon observed by New Horizons are suggested to originate from products of the photolysis of condensed CH_4 by the back-scattered solar UV photons. The CH_4 in this scenario comes from the evaporation of Pluto and is continuously deposited on Charon and trapped at the poles where the temperature is low enough for its condensation. This is a typical case where thermal desorption does not occur and non-thermal desorption pathways may thus play a role in the gas/ice dynamics. While in this precise case, the deposition rate ($\sim 2 \times 10^8$ molecules.cm^{-2}.s^{-1}) is much higher than the photodesorption rate expected considering the measured VUV flux (3.5×10^7 photons.cm^{-2}.s^{-1} with mostly Lyman-α photons would mean $\sim 7.7 \times 10^4$ desorbed molecules.cm^{-2}.s^{-1}), this scenario, as suggested by its authors, may be extended to other, smaller objects around Pluto. The example of Nix is taken, where the deposition rate is estimated to be 20 000 times lower than for Charon, in which case photodesorption would probably start being significant.

6. Conclusions

Pure amorphous CH_4 ices at 10 K were irradiated with synchrotron light (91-177 nm – 7-13.6 eV), and spectrally-resolved absolute CH_4 photodesorption yields were measured. These yields strongly depend on the wavelength, with no desorption below $\approx$136 nm. Photodesorption yields were derived for pure CH_4 ices for various astrophysical environments: for dense cores and disks they were found to be $2.2 \pm 1.1 \times 10^{-3}$ molecules per incident photon, equal to the value at Lyman-α energy, and for diffuse ISM conditions a value of $2.0 \pm 1.0 \times 10^{-3}$ molecules per incident photon was found. These yields can be added to models, keeping in mind the limits of their validity as has been discussed. Thin layered ices were also studied (1 ML of CH_4 above CO ice), and gave a different CH_4 photodesorption spectrum, with spectral signatures from both CH_4 and CO. This showed that both direct (i.e., the molecule absorbing a VUV photon is the one desorbing) and indirect (i.e., the molecule absorbing a VUV photon is not necessarily the one desorbing) electronic induced desorption mechanisms are at play. Comparison of CO-induced desorption in the case of CH_4 with previously studied molecules allowed for discussion of the parameters driving this indirect process.

Acknowledgements. We acknowledge SOLEIL for provision of synchrotron radiation facilities under the project 20150760 and we would like to thank Laurent Nahon for assistance on the beamline DESIRS. This work was supported by the French program "Physique et Chimie du Milieu Interstellaire" (PCMI) funded by the Conseil National de la Recherche Scientifique (CNRS) and Centre National

d'Etudes Spatiales (CNES). Financial support from the LabEx MiChem, part of the French state funds managed by the ANR within the investissements d'avenir program under reference ANR-11-10EX-0004-02 is acknowledged. Fundings by the Ile-de-France region DIM ACAV program is gratefully acknowledged.

References

Aikawa, Y. & Nomura, H. 2006, The Astrophysical Journal, 642, 1152
Andersson, S., Arasa, C., Yabushita, A., et al. 2011, Physical Chemistry Chemical Physics, 13, 15810
Andersson, S. & van Dishoeck, E. F. 2008, Astronomy and Astrophysics, 491, 907
Au, J. W., Cooper, G., Burton, G. R., Olney, T. N., & Brion, C. E. 1993, Chemical Physics, 209
Baratta, G., Domingo, M., Ferini, G., et al. 2003, Nuclear Instruments and Methods in Physics Research Section B: Beam Interactions with Materials and Atoms, 209, 283
Bennett, C. J., Jamieson, C. S., Osamura, Y., & Kaiser, R. I. 2006, The Astrophysical Journal, 653, 792
Bennett, C. J., Pirim, C., & Orlando, T. M. 2013, Chemical Reviews, 113, 9086
Bertin, M., Fayolle, E. C., Romanzin, C., et al. 2013, The Astrophysical Journal, 779, 120
Bertin, M., Fayolle, E. C., Romanzin, C., et al. 2012, Physical Chemistry Chemical Physics, 14, 9929
Bertin, M., Romanzin, C., Doronin, M., et al. 2016, The Astrophysical Journal, 817, L12
Boogert, A., Gerakines, P., & Whittet, D. 2015, arXiv preprint arXiv:1501.05317
Boogert, A. C. A., Blake, G. A., & Öberg, K. 2004, The Astrophysical Journal, 615, 344
Boogert, A. C. A., Helmich, F. P., Van Dishoeck, E. F., et al. 1998, Astronomy and Astrophysics, 336, 352
Bossa, J.-B., Paardekooper, D. M., Isokoski, K., & Linnartz, H. 2015, Phys. Chem. Chem. Phys., 17, 17346
Cleeves, L. I., Bergin, E. A., Alexander, C. M. O., et al. 2016, The Astrophysical Journal, 819, 13
Cruz-Diaz, G. A. 2015, PhD thesis, Universidad Autonoma de Madrid
Cruz-Diaz, G. A., Martín-Doménech, R., Muñoz Caro, G. M., & Chen, Y.-J. 2016, Astronomy & Astrophysics, 592, A68
Cruz-Diaz, G. A., Muñoz Caro, G. M., Chen, Y.-J., & Yih, T.-S. 2014a, Astronomy & Astrophysics, 562, A119
Cruz-Diaz, G. A., Muñoz Caro, G. M., Chen, Y.-J., & Yih, T.-S. 2014b, Astronomy & Astrophysics, 562, A120
Dartois, E., d'Hendecourt, L., Boulanger, F., et al. 1998, Astronomy and Astrophysics, 331, 651
Dartois, E., Ding, J. J., de Barros, A. L., et al. 2013, Astronomy & Astrophysics, 557, A97
de Barros, A. L. F., Bordalo, V., Seperuelo Duarte, E., et al. 2011, Astronomy & Astrophysics, 531, A160
Doronin, M., Bertin, M., Michaut, X., Philippe, L., & Fillion, J.-H. 2015, The Journal of Chemical Physics, 143, 084703
Fayolle, E. C., Bertin, M., Romanzin, C., et al. 2013, Astronomy & Astrophysics, 556, A122
Fayolle, E. C., Bertin, M., Romanzin, C., et al. 2011, The Astrophysical Journal, 739, L36
Fillion, J.-H., Fayolle, E. C., Michaut, X., et al. 2014, Faraday Discussions, 168, 533
Gans, B., Boyé-Péronne, S., Broquier, M., et al. 2011, Physical Chemistry Chemical Physics, 13, 8140
Garrod, R. T. & Pauly, T. 2011, The Astrophysical Journal, 735, 15
Gredel, R., Lepp, S., & Dalgarno, A. 1987, The Astrophysical Journal, 323, L137
Grundy, W. M., Cruikshank, D. P., Gladstone, G. R., et al. 2016, Nature, 539, 65
Hama, T., Yokoyama, M., Yabushita, A., et al. 2009, The Journal of Chemical Physics, 131, 224512
Hassel, G. E., Herbst, E., & Garrod, R. T. 2008, The Astrophysical Journal, 681, 1385
Himpsel, F.-j., Schwentner, N., & Koch, E. E. 1975, physica status solidi (b), 71, 615
Hiraoka, K., Miyagoshi, T., Takayama, T., Yamamoto, K., & Kihara, Y. 1998, The Astrophysical Journal, 498, 710
Hodyss, R., Howard, H. R., Johnson, P. V., Goguen, J. D., & Kanik, I. 2011, Icarus, 214, 748
Hodyss, R., Johnson, P. V., Stern, J. V., Goguen, J. D., & Kanik, I. 2009, Icarus, 200, 338
Hollenbach, D., Kaufman, M. J., Bergin, E. A., & Melnick, G. J. 2009, The Astrophysical Journal, 690, 1497
Hudson, R. L., Gerakines, P. A., & Loeffler, M. J. 2015, Phys. Chem. Chem. Phys., 17, 12545
Johns-Krull, C. M. & Herczeg, G. J. 2007, The Astrophysical Journal, 655, 345
Johnson, R. E., Carlson, R. W., Cassidy, T. A., & Fama, M. 2013, in The Science of Solar System Ices, ed. M. S. Gudipati & J. Castillo-Rogez, Vol. 356 (New York, NY: Springer New York), 551–581
Kaiser, R. I. & Roessler, K. 1998, The Astrophysical Journal, 503, 959
Kalvans, J. 2015, The Astrophysical Journal, 803, 52
Kameta, K., Kouchi, N., Ukai, M., & Hatano, Y. 2002, Journal of Electron Spectroscopy and Related Phenomena, 123, 225
Koch, E.-E. & Skibowski, d. M. 1971, Chemical Physics Letters, 9, 429
Kunz, A. B. 1983, Physical Review B, 28, 3465
Lo, J.-I., Lin, M.-Y., Peng, Y.-C., et al. 2015, Monthly Notices of the Royal Astronomical Society, 451, 159
Maity, S., Kaiser, R. I., & Jones, B. M. 2014, The Astrophysical Journal, 789, 36
Martín-Doménech, R., Manzano-Santamaría, J., Muñoz Caro, G. M., et al. 2015, Astronomy & Astrophysics, 584, A14
Martín-Doménech, R., Muñoz Caro, G. M., & Cruz-Díaz, G. A. 2016, Astronomy & Astrophysics, 589, A107
Mathis, J. S., Mezger, P. G., & Panagia, N. 1983, Astronomy & Astrophysics, 128, 212
Milligan, D. E. & Jacox, M. E. 1967, The Journal of Chemical Physics, 47, 5146
Mumma, M. J. & Charnley, S. B. 2011, Annual Review of Astronomy and Astrophysics, 49, 471
Muñoz Caro, G. M., Chen, Y.-J., Aparicio, S., et al. 2016, Astronomy & Astrophysics, 589, A19
Nahon, L., de Oliveira, N., Garcia, G. A., et al. 2012, Journal of Synchrotron Radiation, 19, 508
Nitzan, A. 2006, Chemical dynamics in condensed phases: relaxation, transfer and reactions in condensed molecular systems, Oxford graduate texts (Oxford ; New York: Oxford University Press), oCLC: ocm62118341
Robin, M. B. 1974, Higher excited states of polyatomic molecules. Vol. 1: [...] (New York, NY: Acad. Press), oCLC: 832295923
Romanzin, C., Gazeau, M.-C., Bénilan, Y., et al. 2005, Advances in Space Research, 36, 258
Ruaud, M., Wakelam, V., & Hersant, F. 2016, Monthly Notices of the Royal Astronomical Society, 459, 3756
Sakai, N. & Yamamoto, S. 2013, Chemical Reviews, 113, 8981
Smith, N. S. & Raulin, F. 1999, Journal of Geophysical Research: Planets, 104, 1873
Smith, R. S., May, R. A., & Kay, B. D. 2016, The Journal of Physical Chemistry B, 120, 1979
Tian, C. & Vidal, C. R. 1998, Journal of Physics B: Atomic, Molecular and Optical Physics, 31, 895
Wu, Y.-J., Wu, C. Y. R., Chou, S.-L., et al. 2012, The Astrophysical Journal, 746, 175
Yuan, C. & Yates, J. T. 2014, The Astrophysical Journal, 780, 8
Öberg, K. I., Boogert, A. C., Pontoppidan, K. M., et al. 2008, The Astrophysical Journal, 678, 1032
Öberg, K. I., van Dishoeck, E. F., & Linnartz, H. 2009, Astronomy and Astrophysics, 496, 281
Öberg, K. I., van Dishoeck, E. F., Linnartz, H., & Andersson, S. 2010, The Astrophysical Journal, 718, 832

Paper II: The efficient photodesorption of nitric oxide (NO) ices: A laboratory astrophysics study

A&A 606, L9 (2017)
DOI: 10.1051/0004-6361/201731653
© ESO 2017

Astronomy & Astrophysics

Letter to the Editor

The efficient photodesorption of nitric oxide (NO) ices

A laboratory astrophysics study

R. Dupuy[1], G. Féraud[1], M. Bertin[1], X. Michaut[1], T. Putaud[1], P. Jeseck[1], L. Philippe[1], C. Romanzin[2], V. Baglin[3], R. Cimino[4], and J.-H. Fillion[1]

[1] Laboratoire d'Étude du Rayonnement et de la Matière en Astrophysique et Atmosphères (LERMA), Sorbonne Universités, UPMC Univ. Paris 06, Observatoire de Paris, PSL Research University, CNRS, 75005 Paris, France
e-mail: geraldine.feraud@upmc.fr
[2] Laboratoire de Chimie Physique (LCP), CNRS UMR 8000, Univ. Paris Sud, 91400 Orsay, France
[3] CERN, 1211 Geneva 23, Switzerland
[4] Laboratori Nazionali di Frascati (LNF)-INFN, 00044 Frascati, Italy

Received 26 July 2017 / Accepted 24 September 2017

ABSTRACT

The study and quantification of UV photon-induced desorption of frozen molecules furthers our understanding of the chemical evolution of cold interstellar regions. Nitric oxide (NO) is an important intermediate species in both gas-phase and solid-phase chemical networks. In this work, we present quantitative measurements of the photodesorption of a pure NO ice. We used the tunable monochromatic synchrotron light of the DESIRS beamline of the SOLEIL facility near Paris to irradiate NO ices in the 6–13.6 eV range and measured desorption by quadrupole mass spectrometry. We find that NO photodesorption is very efficient, its yield being around 10^{-2} molecule per incident photon for UV fields relevant to the diffuse and dense interstellar medium. We discuss the extrapolation of our results to an astrophysical context and we compare photodesorption of NO to previously studied molecules.

Key words. astrochemistry – ISM: abundances – ISM: molecules – molecular processes – methods: laboratory: solid state – ultraviolet: ISM

1. Introduction

Nitric oxide (NO) is an important molecule in the interstellar medium (ISM) and is a key intermediate species from atomic N to molecular N_2, at the basis of the synthesis of nitrogen hydrides (Herbst & Klemperer 1973; Akyilmaz et al. 2007; Hily-Blant et al. 2010; Le Gal et al. 2014). Gas-phase NO has been observed in extremely varied environments: in photon dominated regions (Jansen et al. 1995), in several molecular clouds (Ziurys et al. 1991; Gerin et al. 1992; Akyilmaz et al. 2007), in comet P/Halley (Wallis & Krishna Swamy 1987), in a circumstellar envelope (Quintana-Lacaci et al. 2013), and even in an extragalactic source (Martín et al. 2003).

Unfortunately, there is no observational evidence for the existence of NO in the icy mantles of dust grains; however, it has been reported several times that NO is highly likely to be present there. Indeed, observations of gas-phase nitrogen-containing molecules in several starless cores gave a much lower atomic N abundance than the cosmic N abundance (Hily-Blant et al. 2010), so ices should contain N-bearing molecules (10 to 34% of total nitrogen could be contained in ices around protostars, see Öberg et al. 2011). A critical review of the nitrogen budget can be found in Boogert et al. (2015). The abundance of NO in the interstellar solid phase is estimated at ~0.5 to 5% relative to H_2O (Charnley et al. 2001; Theulé et al. 2013; Ruaud et al. 2016) i.e. within the same order of magnitude as the observed NH_3 or CH_4 ice abundances (e.g. Öberg 2016). Spatially resolved observations of gas-phase NO in pre-protostellar cores have shown that NO is depleted in the core (Akyilmaz et al. 2007), i.e. there is a decrease in gas-phase NO in the core with respect to the edges. This depletion can be explained by condensation of gas-phase NO onto icy grains (Hily-Blant et al. 2010), therefore enriching the outer ice with solid NO. In addition to gas-phase condensation, NO could also be directly synthesized in the icy mantle; laboratory studies have shown that solid NO can be produced by electron-irradiation of H_2O:N_2 or CO:N_2 ice mixtures (Kim et al. 2011; Zheng et al. 2011).

It is commonly assumed that interstellar ices in dense cores are composed of two phases: an inner H_2O-rich phase containing NH_3, CH_4, and CO_2 and an outer CO-rich phase resulting from the gas-phase CO freeze-out on grains and containing CH_3OH and CO_2 (Boogert et al. 2015). In comparison to the major components of astrophysical ices, solid NO is rarely considered even though it could play an important role in molecular clouds. Only a few gas-grain models include NO ices in these environments (e.g. Charnley et al. 2001; Ruaud et al. 2016), whereas gas-phase NO is included in many models (e.g. Le Gal et al. 2014). There are also a few laboratory studies on NO ice chemistry and photoprocessing. In addition to NO formation in solid state (Kim et al. 2011; Zheng et al. 2011), it has been shown that solid state reaction of NO leads to more complex molecules such as NH_2OH and NO_2 (Congiu et al. 2012; Minissale et al. 2014). Moreover, hydrogenation and UV processing of ices containing NO in CO-, H_2CO-, or CH_3OH-rich ices lead to the formation of N-C containing molecules (Fedoseev et al. 2016), strengthening the importance of NO in the solid-phase chemistry.

In the colder regions of the ISM where grains temperatures are below the sublimation temperatures of condensed molecules,

the molecular gas-to-ice abundance ratio is believed to depend on the competition between accretion and non-thermal desorption processes (Bergin & Tafalla 2007). Among them, desorption stimulated by UV photons, so called UV photodesorption, can be an important mechanism (Dominik et al. 2005; Hogerheijde et al. 2011; Willacy & Langer 2000). This has motivated a number of laboratory studies in order to quantify the efficiency of this desorption process for a collection of small molecules in their solid phase (H_2O, CO, N_2, CO_2), which have shown that photodesorption is a rather complex process at the molecular scale, with associated yields depending on the molecule, but also on many parameters such as ice composition, thickness, temperature, etc. (e.g. Öberg et al. 2009; Muñoz Caro et al. 2016). A recent approach using tunable monochromatic light has been successful in providing photodesorption absolute yields in the vacuum ultraviolet (VUV) region (7–14 eV), highlighting the underlying photodesorption mechanisms and providing fundamental data that are independent from the energy profile of the irradiation source (Fayolle et al. 2011; Bertin et al. 2013; Fillion et al. 2014; Dupuy et al. 2017).

Among existing laboratory studies on the photodesorption of NO ice (for a review see Zimmermann & Ho 1995), none provide absolute photodesorption yields at astrophysically relevant wavelengths. We present *absolute* photodesorption spectra of pure NO ice between 6 and 13.6 eV (206.6 and 91.2 nm). This letter focuses on pure NO ice, as a first step, in comparison with another pure weakly bound species (CO) for which photodesorption spectra have been already measured in the same conditions.

2. Methods

Experiments are performed in the Surface Processes & ICES 2 (SPICES 2) set-up, a recent upgrade of the SPICES set-up of LERMA – Univ. Pierre et Marie Curie (France), which is especially designed for the high sensitivity and quantitative measurement of the photodesorption of neutrals and ions from molecular ices. It consists of an ultra-high vacuum (UHV) chamber with a base pressure of typically 10^{-10} mbar, within which a polycrystalline gold surface, a polycrystalline oxygen-free high conductivity (OFHC) copper surface, and a highly oriented pyrolytic graphite (HOPG) surface are mounted on a rotatable cold head that can be cooled down to ~10 K using a closed-cycle helium cryostat. Ices of nitric oxide NO (Airliquide, >99.9% purity) are grown in situ by exposing the HOPG cold surface (10 K) to a partial pressure of gas using a tube positioned a few millimetres from the surface, allowing rapid growth without increasing the chamber pressure to more than a few 10^{-9} mbar. Ice thicknesses are controlled with a precision better than 1 monolayer (1 ML corresponding to a surface molecular density of $\sim 1 \times 10^{15}$ cm^{-2}) via a calibration procedure using the temperature programmed desorption (TPD) technique, as detailed in Doronin et al. (2015).

The chamber is coupled to the undulator-based DESIRS beamline (Nahon et al. 2012) at the SOLEIL synchrotron facility, which provides monochromatic, tunable VUV light for irradiation of our ice samples. The coupling is window-free to prevent cut-off of the higher energy photons. To acquire photodesorption spectra, the synchrotron light from a normal-incidence grating monochromator (narrow bandwidth around 25 meV or 0.3 nm) is scanned between 6 eV (206.6 nm) and 13.6 eV (91.2 nm). Higher harmonics of the undulator are suppressed using argon and xenon gas filters. Photon fluxes are measured upstream of the SPICES 2 set-up with a calibrated AXUV photodiode. The flux depends on the photon energy, and varies between 1.1×10^{12} photons cm^{-2} s^{-1} at 6 eV, 8.9×10^{12} photons cm^{-2} s^{-1} at 8 eV, and 4.6×10^{12} photons cm^{-2} s^{-1} at 13.6 eV.

During the photon energy scan, the relative amount of photodesorbed NO molecules is recorded by a quadrupole mass spectrometer (QMS) from the Pfeiffer company, with a mass resolution of ~0.3 amu, as taken from the full width at half maximum of the mass peaks. A typical scan lasts around 3 min, which corresponds to a total photon fluence of at most $\sim 10^{15}$ photons cm^{-2}. We took care to limit the total fluence in each scan in order to get reproducible spectra, which are independent of the photon fluence. Under these conditions, N or O desorption from pure NO ice could not be detected, either because their photodesorption is ineffective, or because the related photodesorption signals fall below our sensitivity limit, mainly given by our signal-to-noise ratio.

Once corrected for the background contribution and divided by the photon flux, the QMS signal corresponds to the relative efficiency of photodesorption as a function of photon energy. The absolute photodesorption yield $y(\lambda)$ (in molecule per incident photon) is then deduced from that of CO (Fayolle et al. 2011) following a calibration procedure that takes into account NO electron impact ionization cross section in the ionization chamber of the QMS together with the apparatus function of the mass filter (see e.g. Dupuy et al. 2017). While the uncertainties on the relative photodesorption spectra are only due to experimental noise, background substraction, and photon flux uncertainties, this calibration method introduces much larger uncertainties on the absolute photodesorption yields. We estimate a systematic 40% uncertainty on the absolute photodesorption yields. The main source of error is the original calibration procedure of CO desorption yields in Fayolle et al. (2011); the other sources of error (flux, apparatus function, electron-impact ionization cross sections) are negligible in comparison.

3. Results and discussion

The NO photodesorption spectrum of 10 ML thick NO ice deposited on HOPG at 10 K is shown in Fig. 1. The photodesorption yield is absolute, representing the number of NO molecules desorbed per incident photon on the ice. Photodesorption of NO is found over the whole 6–13.6 eV energy range. The photodesorption yield changes as a function of wavelength: there is a maximum around 6 eV, then it is very weak from 7 eV to the Lyman α (121.6 nm, 10.2 eV). It reaches a threshold around 10.5 eV (118 nm) and increases strongly for higher energies until it attains 0.06 molecule/photon at 13.6 eV. The desorption spectrum looks like the absorption spectrum of solid NO from Lu et al. (2008) recorded between 5 and 11.5 eV. This striking similitude between the absorption spectrum of the condensed molecule and the photodesorption spectrum has been already observed in a number of systems, and is the signature that the electronic excitation responsible for the desorption takes place in the condensed molecular film, and not in the supporting substrate.

The assignment of the involved excited electronic states is ambiguous, especially as NO molecules are known to organize into dimer structures in the solid phase (Dulmage et al. 1953), but the comparison between solid-phase and gas-phase NO and $(NO)_2$ spectra from the literature gives useful insights (Fig. 1). Unfortunately, we could not find the gas-phase absorption spectrum of $(NO)_2$ at energies higher than 6 eV. Gas-phase electronic spectra of NO and of its dimer are totally different in the 6 eV region; the absorption is very weak and well structured for NO, whereas a very broad band with a maximum at 6 eV is observed for $(NO)_2$ (Forte & Van Den Bergh 1978) that has been assigned

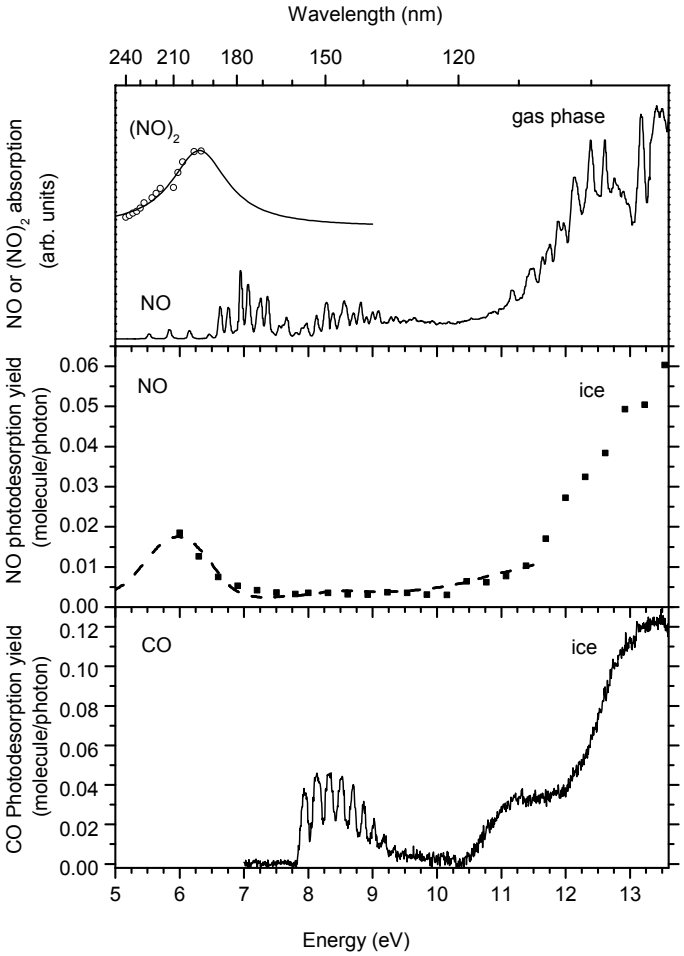

Fig. 1. *Upper panel*: electronic spectrum of gas-phase NO from Chang et al. (1993) and electronic spectrum of gas-phase $(NO)_2$ from Forte & Van Den Bergh (1978, open dots) and its Lorentzian fit (solid line). *Middle panel*: NO photodesorption spectrum of 10 ML thick NO ice on HOPG at 10 K between 6 and 13.6 eV (filled squares). Large energy steps of 0.3 eV were used to avoid ice ageing. Absorption spectrum of pure solid NO from Lu et al. (2008) between 5 and 11.7 eV (dashed line). The absorption spectrum is scaled to the photodesorption spectrum. *Lower panel*: CO photodesorption spectrum of a 20 ML thick CO ice on gold at 10 K between 7 and 13.6 eV (Dupuy et al. 2017).

to a charge transfer state (Levchenko et al. 2006). The state with a maximum at 6 eV observed in absorption or in photodesorption spectra from solid NO can thus be attributed to the electronic excitation of $(NO)_2$. The binding energy of NO dimers is not very strong (0.086 eV or 1.99 kcal mol^{-1} from Wade et al. 2002); therefore, the desorbing molecules are NO monomers and not dimers. For energies above 10.5 eV, the strong increase in the desorption signal could be due to upper electronic states of NO or of $(NO)_2$, mainly assigned to Rydberg series that are clearly visible in the NO gas-phase spectrum of Fig. 1 (Chang et al. 1993, and references therein). It could be argued that photoelectrons produced by NO ionization are also at the origin of the measured desorption signal above 10.5 eV. However, the ionization energy of solid NO is measured at around 7.8 eV (Bertolo & Jacobi 1990), and electron-induced desorption experiments have shown that NO molecules are desorbed even by 0 eV electrons, i.e. there is no desorption threshold. In our experiment, desorption does not increase above 7.8 eV; therefore, photoelectrons produced in the ice should not play a major role in the desorption processes in this energy range.

In the case of simple molecules such as CO and N_2, it has been shown that photodesorption is initiated by an electronic transition to a bound excited state, the relaxation of which subsequently leads to the desorption of a surface molecule. This process is referred to as an indirect desorption induced by electronic transition (DIET) process because the energy can be transferred from the excited molecule to the surrounding species (Bertin et al. 2012, 2013). For other molecules (CO_2, O_2, H_2O, CH_3OH), photodesorption can also be triggered by photodissociation of the molecule, followed by exothermic chemical recombination of the photofragments in the ice (Fillion et al. 2014; Fayolle et al. 2013; Bertin et al. 2016; Martín-Doménech et al. 2016; Cruz-Diaz et al. 2016) or momentum transfer between a photofragment and an intact molecule, also known as the kick-out mechanism (Andersson et al. 2011). In the case of NO, we have no evidence from our experiments that N or O atoms undergo photodesorption. The absence of efficient photodesorption of these light photofragments tends to rule out a potential kick-out mechanism. We cannot neglect photodesorption by photodissociation and exothermic chemical recombination of N and O atoms, i.e. reformation of NO molecules that can have enough energy to desorb. It is therefore difficult from our data set to conclude whether photodesorption is triggered by photochemistry, by an indirect DIET process, or both as has been observed in the case of solid CO_2 (Fillion et al. 2014). Finally, reactions between N or O fragments and intact NO are possible and could lead to the formation of bigger species, such as NO_2, during the irradiation.

It is interesting to compare NO photodesorption with that of the previously studied CO ice (Fayolle et al. 2011). It is clear from Fig. 1 that photodesorption spectra of pure NO and pure CO are very different in the 6–9.5 eV region. Photodesorption of NO is a structureless broad band with a maximum at 6 eV, whereas that of CO shows vibronic structures spanning from 8 to 9.5 eV. Both NO and CO desorb very weakly at Lyman-α, whereas above 10.5 eV the yields strongly increase. At high energy (>10.5 eV), CO photodesorption yields are larger in Dupuy et al. (2017) than in Fayolle et al. (2011), which we associate with an effect of the ice thickness, contrary to the lower energy part (7–10.5 eV) which has been found almost independent of the thickness for ices thicker than 3 ML (Bertin et al. 2012). This is an interesting effect, that goes beyond the scope of this article, and we plan to study it more thoroughly in the future.

The average photodesorption yield $Y_{\rm avg}$ for a given environment is derived using the formula

$$Y_{\rm avg} = \frac{\int y(\lambda)\phi(\lambda)\mathrm{d}\lambda}{\int \phi(\lambda)\mathrm{d}\lambda},$$

where $y(\lambda)$ is the experimental photodesorption yield (Fig. 1), and $\phi(\lambda)$ is the UV field of the environment. NO photodesorption is $Y_{\rm avg} = 1.3 \pm 0.5 \times 10^{-2}$ molecule/photon for an inner core radiation field, and $Y_{\rm avg} = 1.1 \pm 0.4 \times 10^{-2}$ molecule/photon for the interstellar radiation field (ISRF; see Sect. 2 for an estimation of the uncertainties). Two typical UV fields were used: the ISRF from Mathis et al. (1983) relevant for the diffuse ISM or at the edges of dense molecular clouds (Heays et al. 2017), and inner cloud fields generated by the interaction between cosmic rays and H_2 (Gredel et al. 1987). Pure NO and pure CO photodesorption yields are of the same order of magnitude, both in dense core and in ISRF conditions. The very high yields from pure NO ices appear to be typical of weakly interacting diatomic molecules.

It is clear from the absorption spectrum of solid NO from Lu et al. (2008) that NO should still be desorbed by photon energies below 6 eV, which are missing in our experimental data due to technical limitations. However, if we extrapolate our photodesorption yields between 5 and 6 eV using the shape of the absorption spectrum, we find similar photodesorption yields within experimental errors for ISRF conditions. Indeed, half of the NO photodesorption yield comes from 12–13.6 eV photons.

Some insights on NO presence in different phases of ices can be deduced from laboratory experiments and observations. NO is a volatile species, an intermediary case between very volatile molecules such as O_2, CO, or N_2 and heavier molecules such as H_2O or CO_2. Spatially resolved observations of NO and N_2H^+ in dense cores have shown that NO and N_2 depletions occur at the dense core centre (Akyilmaz et al. 2007; Pagani et al. 2012), implying that NO and N_2 could coexist in the outer layer of the grain. Furthermore, experiments demonstrate that solid NO can be formed by energetic processing of H_2O:N_2 or CO:N_2 ices (Kim et al. 2011; Zheng et al. 2011), which suggest that it could also be present in the H_2O-rich phase. Thus, NO could be contained both in the outer layer with CO and within the H_2O-rich mantle, and this could be included in gas/grains models. The present pure phase investigation can be viewed as a preliminary study in the case of interstellar NO as photodesorption yields are certainly different for more complex systems such as NO:CO layers and mixtures, and NO:H_2O layers and mixtures in relevant abundances. Indeed, NO dimerization could be hindered by other organizations in the case of CO:NO or NO:H_2O co-adsorption. Moreover, the effect of the molecular environment on desorption can drastically change the photodesorption yields. For instance, it has been shown that the photodesorption of some species co-adsorbed as mixes or layers in CO-rich ices is mainly due to the absorption of CO molecules via the indirect DIET mechanism. However, the efficiency of this process depends on the nature of the species: it is very efficient for N_2 (Bertin et al. 2013), becomes less effective for slightly more complex molecules such as CH_4 or CO_2 (Fillion et al. 2014; Dupuy et al. 2017), and finally is not observed in the case of CH_3OH (Bertin et al. 2016). We therefore expect that the photodesorption yield of NO will be different in the case of realistic mixtures in CO- or H_2O-rich ices.

4. Conclusions

We measured the NO photodesorption spectrum from pure NO ices and some of its features were assigned. Photodesorption of NO from pure NO ices is very efficient, of the same order of magnitude as photodesorption yields of CO from a pure CO ice. The possible mechanisms at the origin of the photodesorption, photochemistry, and/or indirect DIET were also discussed. The high photodesorption efficiency observed for the pure NO ice system encourages a more detailed laboratory study on NO in representative molecular mixtures which include CO- and H_2O-rich ice phases, and we suggest that it could be included in gas-grain models. More laboratory studies, modelling, and perhaps observations of NO ices are needed to fill the NO-man's-land.

Acknowledgements. We thank L. Pagani for fruitful discussions concerning NO abundances in dense cores. This work was supported by the Programme National "Physique et Chimie du Milieu Interstellaire" (PCMI) of CNRS/INSU with INC/INP co-funded by CEA and CNES, and by the European Organization for Nuclear Research (CERN) under the collaboration agreement KE3324/TE. We acknowledge SOLEIL for provision of synchrotron radiation facilities under the project 20150760 and we would like to thank Laurent Nahon and the DESIRS staff for assistance on the beamline. Financial support from the LabEx MiChem, part of the French state funds managed by the ANR within the investissements d'avenir program under reference ANR-11-10EX-0004-02 is acknowledged. Fundings by the Ile-de-France region DIM ACAV program is gratefully acknowledged.

References

Akyilmaz, M., Flower, D. R., Hily-Blant, P., Pineau des Forêts, G., & Walmsley, C. M. 2007, A&A, 462, 221
Andersson, S., Arasa, C., Yabushita, A., et al. 2011, Phys. Chem. Chem. Phys., 13, 15810
Bergin, E. A., & Tafalla, M. 2007, ARA&A, 45, 339
Bertin, M., Fayolle, E. C., Romanzin, C., et al. 2012, Phys. Chem. Chem. Phys., 14, 9929
Bertin, M., Fayolle, E. C., Romanzin, C., et al. 2013, ApJ, 779, 120
Bertin, M., Romanzin, C., Doronin, M., et al. 2016, ApJ, 817, L12
Bertolo, M., & Jacobi, K. 1990, Surface Sci., 226, 207
Boogert, A. A., Gerakines, P. A., & Whittet, D. C. 2015, ARA&A, 53, 541
Chang, W. F., Cooper, G., & Brion, C. E. 1993, Chem. Phys., 170, 111
Charnley, S. B., Rodgers, S. D., & Ehrenfreund, P. 2001, A&A, 378, 1024
Congiu, E., Fedoseev, G., Ioppolo, S., et al. 2012, ApJ, 750, L12
Cruz-Diaz, G. A., Martín-Doménech, R., Muñoz Caro, G. M., & Chen, Y.-J. 2016, A&A, 592, A68
Dominik, C., Ceccarelli, C., Hollenbach, D., & Kaufman, M. 2005, ApJ, 635, L85
Doronin, M., Bertin, M., Michaut, X., Philippe, L., & Fillion, J.-H. 2015, J. Chem. Phys., 143, 084703
Dulmage, W. J., Meyers, E. A., & Lipscomb, W. N. 1953, Acta Cryst., 6, 760
Dupuy, R., Bertin, M., Féraud, G., et al. 2017, A&A, 603, A61
Fayolle, E. C., Bertin, M., Romanzin, C., et al. 2011, ApJ, 739, L36
Fayolle, E. C., Bertin, M., Romanzin, C., et al. 2013, A&A, 556, A122
Fedoseev, G., Chuang, K.-J., van Dishoeck, E. F., Ioppolo, S., & Linnartz, H. 2016, MNRAS, 460, 4297
Fillion, J.-H., Fayolle, E. C., Michaut, X., et al. 2014, Faraday Discussions, 168, 533
Forte, E., & Van Den Bergh, H. 1978, Chem. Phys., 30, 325
Gerin, M., Viala, Y., Pauzat, F., & Ellinger, Y. 1992, A&A, 266, 463
Gredel, R., Lepp, S., & Dalgarno, A. 1987, ApJ, 323, L137
Heays, A. N., Bosman, A. D., & van Dishoeck, E. F. 2017, A&A, 602, A105
Herbst, E., & Klemperer, W. 1973, ApJ, 185, 505
Hily-Blant, P., Walmsley, M., Pineau des Forêts, G., & Flower, D. 2010, A&A, 513, A41
Hogerheijde, M. R., Bergin, E. A., Brinch, C., et al. 2011, Science, 334, 338
Jansen, D. J., Spaans, M., Hogerheijde, M. R., & van Dishoeck, E. F. 1995, A&A, 303, 541
Kim, Y. S., Zhang, F., & Kaiser, R. I. 2011, Phys. Chem. Chem. Phys., 13, 15766
Le Gal, R., Hily-Blant, P., Faure, A., et al. 2014, A&A, 562, A83
Levchenko, S. V., Reisler, H., Krylov, A. I., et al. 2006, J. Chem. Phys., 125, 084301
Lu, H.-C., Chen, H.-K., Cheng, B.-M., & Ogilvie, J. 2008, Spectrochim. Acta A, 71, 1485
Martín, S., Mauersberger, R., Martín-Pintado, J., García-Burillo, S., & Henkel, C. 2003, A&A, 411, L465
Martín-Doménech, R., Muñoz Caro, G. M., & Cruz-Díaz, G. A. 2016, A&A, 589, A107
Mathis, J. S., Mezger, P. G., & Panagia, N. 1983, A&A, 128, 212
Minissale, M., Fedoseev, G., Congiu, E., et al. 2014, Phys. Chem. Chem. Phys., 16, 8257
Muñoz Caro, G. M., Chen, Y.-J., Aparicio, S., et al. 2016, A&A, 589, A19
Nahon, L., de Oliveira, N., Garcia, G. A., et al. 2012, J. Synchrotron Rad., 19, 508
Öberg, K. I. 2016, Chem. Rev., 116, 9631
Öberg, K. I., van Dishoeck, E. F., & Linnartz, H. 2009, A&A, 496, 281
Öberg, K. I., Boogert, A. C. A., Pontoppidan, K. M., et al. 2011, ApJ, 740, 109
Pagani, L., Bourgoin, A., & Lique, F. 2012, A&A, 548, L4
Quintana-Lacaci, G., Agúndez, M., Cernicharo, J., et al. 2013, A&A, 560, L2
Ruaud, M., Wakelam, V., & Hersant, F. 2016, MNRAS, 459, 3756
Theulé, P., Duvernay, F., Danger, G., et al. 2013, Adv. Space Res., 52, 1567
Wade, E. A., Cline, J. I., Lorenz, K. T., Hayden, C., & Chandler, D. W. 2002, J. Chem. Phys., 116, 4755
Wallis, M. K., & Krishna Swamy, K. S. 1987, A&A, 187, 329
Willacy, K., & Langer, W. D. 2000, ApJ, 544, 903
Zheng, W., Kim, Y. S., & Kaiser, R. I. 2011, Phys. Chem. Chem. Phys., 13, 15749
Zimmermann, F. M., & Ho, W. 1995, Surface Sci. Rep., 22, 127
Ziurys, L. M., McGonagle, D., Minh, Y., & Irvine, W. M. 1991, ApJ, 373, 535

Paper II: The efficient photodesorption of nitric oxide (NO) ices: A laboratory astrophysics study

Paper III: X-ray photodesorption from water ice in protoplanetary disks and X-ray-dominated regions

LETTERS
https://doi.org/10.1038/s41550-018-0532-y

nature astronomy

X-ray photodesorption from water ice in protoplanetary disks and X-ray-dominated regions

R. Dupuy[1*], M. Bertin[1], G. Féraud[1], M. Hassenfratz[1], X. Michaut[1], T. Putaud[1], L. Philippe[1], P. Jeseck[1], M. Angelucci[2], R. Cimino[2], V. Baglin[3], C. Romanzin[4] and J.-H. Fillion[1]

Water is the main constituent of interstellar ices, and it plays a key role in the evolution of many regions of the interstellar medium, from molecular clouds to planet-forming disks[1]. In cold regions of the interstellar medium, water is expected to be completely frozen out onto the dust grains. Nonetheless, observations indicate the presence of cold water vapour, implying that non-thermal desorption mechanisms are at play. Photodesorption by ultraviolet photons has been proposed to explain these observations[2,3], with the support of extensive experimental and theoretical work on ice analogues[4–6]. In contrast, photodesorption by X-rays, another viable mechanism, has been little studied. The potential of this process to desorb key molecules such as water, intact rather than fragmented or ionized, remains unexplored. We experimentally investigated X-ray photodesorption from water ice, monitoring all desorbing species. We found that desorption of neutral water is efficient, while ion desorption is minor. We derived yields that can be implemented in astrochemical models. These results open up the possibility of taking into account the X-ray photodesorption process in the modelling of protoplanetary disks or X-ray-dominated regions.

Numerous studies have explored the effects of X-rays on the chemistry of various regions of the interstellar medium (ISM)[7–10], with a few taking into account solid-phase processes[11,12]. In the example of protoplanetary disks, as sketched in Fig. 1, the X-ray-dominated region corresponds to a thin layer. The extent of the X-ray layer will depend on the type of star, the degree of evolution of the disk (for example, dust settling) and the physical model of disk considered. In a T Tauri model[11], the limit between the ultraviolet (UV) and X-ray-dominated layers occurs around $z/R \approx 0.2$, where R is the midplane distance to the star and z is the vertical distance to the midplane, as indicated in Fig. 1. The location of ices is disk dependent as well, with the horizontal onset varying between < 1 AU and 10 AU. Beyond a few tens of astronomical units, dust temperatures are cold enough for water to freeze out throughout the disk, and the X-ray layer overlaps with the icy region (compare with Fig. 1). The region where X-rays are dominant can extend to the whole midplane if the disk is shielded from cosmic rays, as suggested by an earlier study[13].

The goal of this study is to provide experimental constraints on X-ray photodesorption, which allows modellers to assess the relevance of this process to the physics and chemistry of disks and other regions. Previous experimental studies have mainly focused on ion desorption[14–16], and only a few have attempted to derive quantitative desorption yields[17]. We used synchrotron radiation from the SEXTANTS beamline (SOLEIL facility) to irradiate amorphous solid water at either 15 K or 90 K in an ultra-high-vacuum chamber (see Methods). Our set-up allows us to monitor directly in the gas phase the desorption of neutral molecules, cations and anions through mass spectrometry. Measuring desorption in the gas phase allows us to unambiguously identify which species are desorbing, and prevents overestimation of the rates due to photochemistry into the ice[6]. We are thus able to obtain a complete picture of the desorbing species, within our limits of sensitivity. The photodesorption yields (Y^{inc}, number of species desorbed per incident photon) at 550 eV of the species observed are given in Table 1. One of our main findings is that the desorption of neutral species (H_2O, O_2 and H_2) is one to two orders of magnitude higher than the desorption of H^+, the most abundant ion. Therefore, the investigation of neutral desorption is crucial for a quantitative understanding of X-ray photodesorption. This letter will focus on neutral desorption, while more information about ion desorption can be found in the Supplementary Information.

Figure 2b shows the photodesorption yield of H_2O at 15 K and Fig. 2a the total electron yield (assumed to reflect the absorption of the ice; see Methods) as a function of photon energy between 520 eV and 600 eV. Detailed interpretations have been made of the X-ray absorption spectrum of ice between 530 eV and 550 eV (ref. [18]). The 561 eV feature is the first extended X-ray absorption fine-structure oscillation[19], and small features before 533 eV have been attributed to photoproducts in the ice[20]. The photodesorption yield of H_2O follows the total electron yield, which is evidence that photodesorption is indeed caused by excitation or ionization of the oxygen 1s electron of the ice bulk water molecules, and not by the substrate.

We now consider the more intrinsic quantity given by the number of molecules desorbed per absorbed photon (Y^{abs}). This can be derived when we know the absorption cross-section of water and the number of monolayers below the surface involved in the photodesorption process. The former requires us to approximate the unknown solid-phase water absorption to the gas-phase one. The latter requires consideration of the length scale of the various processes involved. A rough estimate is $Y^{abs} \approx 0.2$ H_2O molecules desorbed per absorbed photon for a thickness of 50 monolayers (see Methods).

Following a core electronic transition, energy is released through Auger decay, where most of the energy is carried away by an electron. In water, this electron has 500 eV of kinetic energy and will create multiple secondary valence ionization and excitation events on its track, leading to the desorption of molecules, usually called X-ray-induced electron-stimulated desorption. As most of the energy is transferred to the Auger electron, X-ray-induced

[1]LERMA, Sorbonne Université, Observatoire de Paris, Université PSL, CNRS, Paris, France. [2]Laboratori Nazionali di Frascati, INFN, Frascati, Italy. [3]CERN, Geneva, Switzerland. [4]Laboratoire de Chimie Physique, CNRS, Univ. Paris-Sud, Université Paris-Saclay, Orsay, France. *e-mail: remi.dupuy@obspm.fr

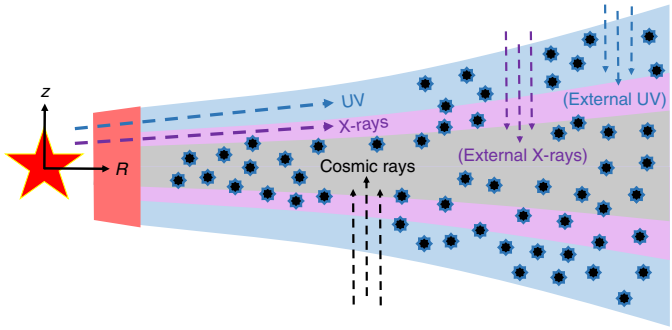

Fig. 1 | Schematic representation of a vertical slice of a protoplanetary disk. The various sources of irradiation in the ice-containing regions are shown. The UV, X-ray and cosmic ray dominated regions are shown in blue, violet and grey, respectively. On the left is the central star, with the red zone being a hot region of dust sublimation. Icy grains are symbolized by black and blue stars. The limits between the different regions (UV dominated, X-ray dominated or cosmic ray dominated, as well as the snow surface locating the onset of ices) are all disk dependent. The outer part of the disk can be illuminated by external UV photons from the interstellar radiation field, but also by external X-rays[49].

electron-stimulated desorption will usually dominate the desorption yield. The fact that the desorption yield of neutral molecules is much higher than that of ions is probably due in part to the inability of secondary electrons to produce ions with sufficient kinetic energy to desorb and overcome interactions specific to charged particles (stabilization by polar molecules, reneutralization and so on). The value we derived above for Y^{abs} is close to the yield derived for 87 eV electron-stimulated desorption, 0.5 molecules per electron[21], which is another indication that X-ray-induced electron-stimulated desorption dominates. The value is much higher than the one derived for UV photodesorption, ~10^{-2} molecules per absorbed photon[4]. However, it appears that this quantity scales roughly with the deposited energy, as X-ray photons carry about two orders of magnitude more energy than UV photons.

We also observed photodesorption of other neutral species, O_2 and H_2 (see Fig. 2c,d and Table 1), with a spectral behaviour similar to H_2O. The desorption of these species as well as others such as OH fragments has been studied in detail in UV irradiation experiments[22]. We did not observe the desorption of OH radicals, and considering the experimental noise on this channel, the estimated sensitivity limit was 10^{-3} molecules per incident photon. We did not observe desorption of HO_2 or H_2O_2 either. The desorption of H_2 and O_2 is an indicator of the chemistry occurring in the ice. This chemistry can also be probed in situ through the above-mentioned small features before 533 eV in the absorption spectrum (Supplementary Information). We can identify the presence of OH, O, HO_2, O_2 and H_2O_2 in the ice amounting to a few percent of the total content[20], with no evolution with the photon dose. All the data shown here thus correspond to a steady state, where formation and destruction of the species has reached an equilibrium. The photodesorption yield of ices that have been exposed to much lower photon doses and where this steady state has not been reached, as could be the case in the ISM, could be different for O_2 and H_2 because chemistry plays an important role. It should not differ much for water, because its desorption is presumably dominated by single-excitation processes (see also Methods).

The observed temperature effects for desorbing O_2 and H_2 (Table 1) are similar to those observed in the UV range[23] and are well explained by diffusion and thermal desorption processes. At 15 K, O_2 is not mobile, and thus its desorption yield is very low and confined to the molecules produced near the surface. At 90 K, O_2 can diffuse and thermally desorb once it is formed, and thus its desorption is increased by one order of magnitude. H_2 can diffuse and thermally desorb at both of these temperatures, but its diffusion and desorption are higher at 90 K. The enhancement of the thermal diffusion of radicals at 90 K, as seen in the absorption spectrum (Supplementary Information), can also contribute to the observed effects. A small temperature effect is also observed for H_2O desorption, as was found in the UV range[24]. This behaviour suggests that H_2O desorption is not linked, or only in a minor way, to diffusion processes and thermal desorption.

Our experimental data are limited to the 520–600 eV range, while X-ray spectra in the ISM typically span from 0.1 keV to at least 10 keV. Therefore, to be included in astrochemical models, the photodesorption yields need to be extrapolated to higher photon energies. Photodesorption of neutral molecules is proportional to absorption, and absorption is still dominated by oxygen 1*s* ionization from 600 eV up until 10 keV. The extrapolation can therefore be done using the absorption cross-section of water, once again using the gas-phase value (see Methods). The extrapolated yields from 150 eV to 10 keV are available in the Supplementary Information. The local average photodesorption yield can then be calculated by multiplying the energy-dependent photodesorption yields by the local X-ray spectrum, which gives the photodesorption yield per average incident photon (see Methods). The X-ray spectrum at a given location can vary a lot depending on the column density of gas traversed, as the softer X-rays are more attenuated. To illustrate this dependence, we took observation spectra from two different sources, TW Hydrae (TW Hya)[25] as an example of a young star

Table 1 | Photodesorption yields (Y^{inc}) at 550 eV for a compact amorphous solid water ice at 15 K or 90 K (desorbed species per incident photon)

	Neutral molecules			Cations			Anions	
	90 K	15 K		90 K	15 K		90 K	15 K
H_2O	3.8×10^{-3}	3.4×10^{-3}	H^+	1.0×10^{-4}	4.3×10^{-5}	H^-	1.3×10^{-5}	6.5×10^{-6}
H_2	8.9×10^{-3}	5.3×10^{-3}	H_2^+	5.0×10^{-7}	1.6×10^{-7}	H_2^-	3.0×10^{-10}	
O_2	2.5×10^{-3}	4.0×10^{-4}	H_3^+	2.5×10^{-9}		O^-	1.3×10^{-7}	2.3×10^{-8}
OH	$<1.0\times10^{-3}$	$<1.0\times10^{-3}$	O^+	3.6×10^{-8}	2.8×10^{-8}	OH^-	2.2×10^{-8}	6.4×10^{-9}
			OH^+	6.0×10^{-9}	4.6×10^{-9}	H_2O^-	3.0×10^{-10}	
			H_2O^+	3.0×10^{-9}	3.7×10^{-9}	O_2^-	8.0×10^{-10}	
			H_3O^+	1.2×10^{-8}	1.6×10^{-8}			
			O_2^+	2.9×10^{-8}				
			$(H_2O)_2H^+$	1.9×10^{-8}	2.4×10^{-8}			

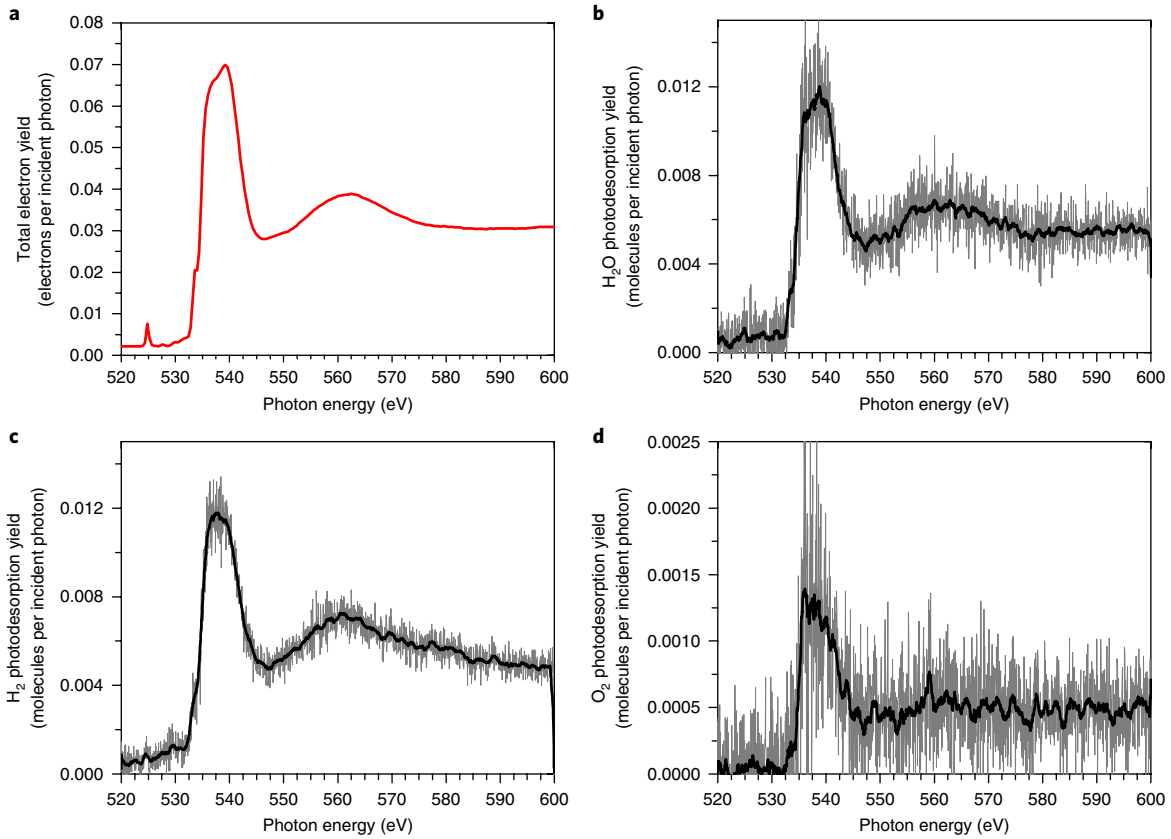

Fig. 2 | Photodesorption yields of the neutral species observed, as a function of photon energy. a–d, Total electron yield (**a**) in electrons per incident photon, and H_2O (**b**), H_2 (**c**) and O_2 (**d**) photodesorption yields in molecules per incident photon, as a function of photon energy, for a 100 ML compact amorphous solid water ice at 15 K. The grey traces are the raw data, and the black traces have been smoothed. The total electron yield is assumed to represent the absorption of the ice (see Methods).

that may illuminate a protoplanetary disk or a protostellar envelope, and Markarian 231 (MKN 231)[26] as an example of an ultra-luminous infrared galaxy with active galactic nuclei and starburst components, and we calculated the spectrum for different column densities traversed. Then, we calculated the photodesorption yield per average incident photon. The results are given in Table 2. Numbers vary from 2.5×10^{-3} to 6.6×10^{-6}, illustrating both the strong source and column density dependence of the efficiency of X-ray photodesorption. These numbers can be used as a rough approximation in models, or the photodesorption yield adequate to the modelled environment can be calculated using our extrapolated energy-resolved photodesorption yields (Supplementary Information).

UV photodesorption is important in the current understanding of gas-phase water in cold regions of the ISM[2,3], and the existing experimental constraints allow it to be taken into account in models. Our experimental results open up the possibility of taking into account the X-ray photodesorption process in regions of the ISM where ices and X-rays coexist. As mentioned above, one such region is the layer of protoplanetary disks where X-rays can dominate over UV photons and cosmic rays (Fig. 1). One key element of the understanding of planet formation is the determination of the water snow line, which requires accurate modelling of all processes affecting gas-phase and solid-phase water in disks. Taking one specific example with a model of a T Tauri star[11], the UV field is completely attenuated below $z/R\approx0.2$. The X-ray flux in this region varies between 10^{-6} erg s^{-1} cm^{-2} and 10^{-4} erg s^{-1} cm^{-2}, that is, 10^{3}–10^{5} photons s^{-1} cm^{-2}. Conversely, secondary UV photons produced by cosmic rays amount to ~10^{3} photons s^{-1} cm^{-2} (ref. [27]), while direct cosmic ray sputtering has about the same efficiency as photodesorption from these secondary UV photons[28]. If we consider that the efficiency of X-ray photodesorption is comparable to UV photodesorption (10^{-4}–10^{-3} H_2O molecules per incident photon), X-ray photodesorption is expected to play a role in this case. If we consider instead that cosmic rays are excluded from the midplane of the disk[13], then X-rays largely dominate. The relevance of X-ray photodesorption for a given disk, however, depends on many parameters, as discussed above: the type of star, the X-ray spectrum, the physical model considered and so on. The case of M dwarf stars could be particularly interesting because they feature weak UV and strong X-ray emission as well as extended regions of cold dust temperatures[29].

Table 2 | Average photodesorption yields of intact water (H_2O molecules per incident photon) for the X-ray spectra of different regions at different attenuations

	TW Hya (young star)	MKN 231 (ultra-luminous infrared galaxy)
Source spectrum	$2.3\pm1.2\times10^{-3}$	$1.0\pm0.5\times10^{-3}$
$n_H=10^{21}$ cm^2	$2.5\pm1.3\times10^{-3}$	$8.0\pm4.0\times10^{-4}$
$n_H=10^{22}$ cm^2	$1.2\pm0.6\times10^{-3}$	$1.8\pm0.9\times10^{-4}$
$n_H=10^{23}$ cm^2	$1.2\pm0.6\times10^{-4}$	$2.0\pm1.0\times10^{-5}$
$n_H=10^{24}$ cm^2	$1.2\pm0.6\times10^{-5}$	$6.6\pm3.3\times10^{-6}$

n_H is the column density of gas by which the source spectrum has been attenuated. Corresponding spectra are given in the Supplementary Information. The cumulative uncertainties of the various sources of errors are estimated to be ±50% s.d., as detailed in Methods. The yields used are those for compact amorphous solid water ice at 15 K.

Molecular clouds exposed to intense X-ray sources and modelled by so-called X-ray-dominated region codes are also of interest. They include the envelopes of young stellar objects[12] and molecular clouds close to active galactic nuclei[10] or strong supernovae shocks[9]. Because X-ray photons can penetrate deep into clouds and do not heat grains very efficiently, these regions can host ices. X-ray-dominated region codes could also include the X-ray photodesorption process, to assess its relevance to the physics and chemistry of these various environments.

Methods

Experimental set-up. Experiments were conducted in the SPICES 2 (Surface Processes and ICES 2) set-up, a recently upgraded version of the SPICES set-up. SPICES 2 is an ultra-high-vacuum chamber (base pressure ~2×10^{-10} mbar) equipped with a rotatable cryostat, at the tip of which is attached a sample holder. The temperature of the samples can be controlled with 0.1 K precision between 15 K and 300 K. The experiments were carried out on a copper substrate (polycrystalline oxygen-free high-conductivity copper), which was isolated electrically, but not thermally, from the sample holder by a Kapton foil. This allowed us to read the drain current of the substrate generated by the electrons escaping the surface following X-ray absorption, the so-called total electron yield. The number of escaping electrons is proportional to the number of absorbed photons, and thus the drain current is proportional to the absorption of the ice. The chamber is also equipped with a gas-dosing system, described below, and two quadrupole mass spectrometers (QMSs), one (Pfeiffer Vacuum) used for the detection of neutral species and the other (Hiden Analytical) for the detection of positive and negative ions.

The SEXTANTS beamline. The SPICES 2 set-up was brought to the SOLEIL synchrotron facility and connected to the SEXTANTS beamline[30]. For these experiments, we used photons in the 520–600 eV range. Settings were such that the resolution was $\Delta E = 150$ meV, where E is the photon energy, and the flux, as measured with a silicon photodiode, was approximately 1.4×10^{13} photons s^{-1}, with little variation except for a significant dip around 535 eV due to the oxygen 1*s* absorption of oxygen pollution on the optics of the beamline. The absorption spectra of ice that we obtained from our total electron yield measurements, when corrected from the photon flux, compare well with those found in the literature and obtained using many different techniques[18], which makes us confident that our spectra are not distorted by the structure of the flux. The unfocused beam was sent at a 45° incidence on the surface, which resulted in a spot of approximately 0.1 cm^2. All experiments were performed using the horizontal polarization setting, which with a 45° incidence, resulted in a 50% in-plane and 50% out-of-plane polarization at the surface.

Ice growth. Water (liquid chromatography standard, Fluka) was purified by a series of freeze–pump–thaw cycles, and the vapour pressure was let into a gas injection line. The ice was grown on the substrate by bringing a dosing tube 1 mm close to it and by injecting water vapour into the tube using a microleak valve. This allowed us to grow relatively thick ice (~100 equivalent bilayers) without increasing the pressure in the chamber to more than a few billionths of a millibar. The thickness of the ice can be calibrated by using the temperature-programmed desorption (TPD) technique[31]. All water ices were grown at 90 K, which resulted in a compact amorphous solid water structure. The irradiation experiments were subsequently performed either at 90 K or after cooling the ice to 15 K. The thickness of the ice ensures that the influence of the copper substrate on the desorption processes is negligible (see discussion of the length scales of the processes in 'Estimation of photodesorption yields per absorbed photon'), as confirmed by the fact that no important desorption signal was seen, apart from the resonances of water (oxygen adsorbed on copper would have been observed around 530 eV)[32]. As mentioned above, all of the spectra shown correspond to a steady state, that is, two consecutive scans gave the same results. This steady state was reached immediately in our experiments. From an estimate of the photon dose required to reach a steady state of the ice bulk chemistry (a few 10^{15} eV cm^{-2})[20], it should indeed be reached in just a few seconds. The erosion of the ice due to photodesorption during irradiation was also small (~2 ML h^{-1} at 600 eV). Consequently, the ice sample was renewed every few hours, which did not cause reproducibility issues. Pure water ice is resilient to X-ray irradiation because the modifications induced are small, a conclusion that was reached also for ion bombardment[28].

In the conditions of the ISM, the photon fluxes are much lower than the ones used in our experiments, which raises the question of whether our results can be extrapolated to these regions. Considering, for example, a flux of 100 photons s^{-1} cm^{-2}, the steady-state dose would be reached in about 1,200 yr, which is small compared with the lifetime of a protoplanetary disk. However, whether or not the steady-state dose will be reached will still depend on the location of the ice, while the fact that a realistic ice contains not just water but also other species will change the nature of the steady state. The yields of water and electrons, which are presumably dominated by single-excitation processes, should not be affected much by the irradiation history of the ice. However, it could be the case for the desorption of species such as O_2 and H_2, which are linked to chemistry that requires multiple excitation events.

Calibration of the photodesorption yields. The flux of molecules desorbed from the surface on irradiation is proportional to the signal current measured on the QMS, once it has been subtracted from the contribution of the background, that is, the signal current when the irradiation is off. To obtain the proportionality factor between molecule flux and signal current, we used the above-mentioned TPD technique. TPD allows us to determine when one monolayer of a given molecule has been deposited on the surface[31]. In the present case, this calibration was done on CO, where determination of the monolayer is unambiguous because the monolayer and the multilayer contributions appear at clearly distinct temperatures. The TPD behaviour of H_2O, however, is particularly complex and thus not very suited for this method: there is no clearly distinguishable monolayer peak, and the TPD follows a zero-order kinetic even in the submonolayer regime. However, once the proportionality factor for a given molecule is known, it can be deduced for other molecules by correcting for the molecule-dependent factors, as explained in earlier studies[33]. These factors are the differences in electron-impact ionization cross-sections (taken from the literature[34,35]), and the differences in transmission and detection efficiencies in the QMS, which depend on the mass of the molecule and have been calibrated for our QMS.

When a monolayer of CO is deposited, knowing the density of CO (ref. [36]) and the size of the surface (15 mm x 15 mm), we thus know the absolute number of molecules on the surface. During a TPD experiment, all of these molecules are released in the gas phase. Thus, the integrated signal of the TPD experiment, when subtracted from the background contribution, is proportional to the integrated flux of molecules, that is, the absolute number of molecules that were present on the surface. The ratio of these two known quantities gives us the proportionality factor for thermal desorption. We then assume that the proportionality for photodesorbed molecules is similar to that for thermally desorbed molecules. For example, this means that we must make the assumption that the angular and speed distribution of desorbed products are the same in both cases. This is reasonable in the case of neutral photodesorption from amorphous molecular solids, where we do not expect high-energy molecules or strong orientational effects. The validity of this method was tested against another calibration technique used in UV photodesorption experiments. In the UV range, the photodesorption of CO can be calibrated by monitoring CO loss in the ice using infrared spectroscopy[37] (such a technique cannot be used in irradiation experiments where chemistry occurs and molecule loss cannot be related simply to desorption). Both of these techniques gave similar results within the 50% estimated uncertainty for UV CO photodesorption.

We can estimate the uncertainty of this method, taking into account the uncertainty on the monolayer calibration (±20%), the flux (±10%), the electron-impact ionization cross-sections (±10%) and the apparatus function (±40%), which makes a total of ±50%. Because the uncertainty of the apparatus function for H_2 is larger and not easy to estimate, the H_2 absolute yields should be taken with caution.

Estimation of photodesorption yields per absorbed photon. The photodesorption yield per absorbed photon, Y^{abs}, is derived from the following formula[38]:

$$Y^{abs} = \frac{Y^{inc}}{1-e^{-\sigma N}}$$

where σ is the absorption cross-section and N is the column density of molecules that we consider to be involved in the photodesorption process. As far as we know, the absorption cross-sections of water ice in the soft X-ray range are not available in the literature. Only the gas-phase cross-sections are[39], and we thus assume that they can be used here. While the cross-sections have no reason to be similar between ice and gas in the edge region, off-resonance (at 600 eV), it is a reasonable assumption because the cross-section is then mostly the atomic oxygen 1*s* ionization cross-section and does not depend significantly on the molecule or its phase. The column density of molecules involved in the photodesorption process, that is, the number of monolayers below the surface that participate in desorption, has been well constrained in the case of UV photodesorption of CO (ref. [40]). Desorbed CO molecules come from the surface, and the excitations that lead to desorption are localized in the top three monolayers. The situation is more complex here because we need to consider primary X-ray excitations as well as secondary excitations that follow Auger decay processes, and the mechanisms through which these excitations lead to desorption. Let us review the various length scales involved. With an absorption cross-section of the order of 5×10^{-19} cm^2, our ice of 100 ML thickness will absorb only ~5% of the incident photons. The primary excitations can thus take place over the whole ice; however, only a fraction of them will lead to desorption, depending on their distance to the surface. The electron cloud created by an Auger electron in water has an approximate radius of 10 nm (ref. [41]), that is, ~30 ML, and thus, secondary excitations can be created near the surface from molecules 30 ML deep in the ice. Additionally, the desorption mechanisms that follow secondary excitations have their own length scales.

The possible mechanisms of desorption of H_2O that have been discussed for UV excitation include kick-out by hot H fragments, chemical recombination[42] and exciton-induced dipole reversal[43], to which we can add at least, due to the possibility of ionization, recombination of H_3O^+ ions with electrons and subsequent desorption of the H_2O product[44], and collision-induced desorption[45]. These processes involve the scales of hot H atom mean free path, fragment diffusion, exciton diffusion and proton diffusion along the H-bond network. These length scales are not well constrained. Molecular dynamics simulations yield a hot H atom mean free path of ~8 Å (ref. [42]), which is small enough to be neglected. The experimental findings of an earlier study[21] suggest a characteristic migration scale of excitons of ~25 ML. Taking into account the radius of the electron cloud and the migration scale of excitons, we thus consider that the first 50 ML are involved in X-ray photodesorption for water. Using this characteristic thickness, we derive a yield of ~0.2 H_2O molecules desorbed per absorbed photon at 600 eV and at 15 K. This should be considered as an order-of-magnitude estimate, considering the uncertainties on the length scales and absorption cross-sections mentioned above. Since the photodesorption yield is proportional to the absorption spectrum, and the absorption is weak ($\sigma N \ll 1$), this number is valid at all photon energies, as long as the main source of secondary electrons is the Auger electron. The photoelectron issued from ionization can also contribute when its kinetic energy (which is equal to the photon energy minus the core ionization potential) is high enough (> 150 eV) to create a significant number of secondary electrons, but low enough (< 1 keV) that it will interact with the ice before escaping. This can be estimated using, for example, the CASINO software[46]. Thus, we may expect an increase of a factor of at most two or three in the 700–1,500 eV photon energy region.

Estimation of average photodesorption yields for astrophysical models. The experimental photodesorption spectrum in the 520–600 eV range follows the absorption spectrum of the ice. Above 600 eV, the absorption is still dominated by oxygen 1*s* ionization, and therefore, the physical and chemical processes involved are the same. We can thus extrapolate the photodesorption yield above 600 eV if we know the absorption cross-section of water ice. As mentioned above, this is not the case, but it can be safely extrapolated from the gas-phase value off-resonance. Before the edge, we assume that the photodesorption yield is constant from 150 eV to 520 eV and equal to the value measured at 520 eV. Such an assumption is certainly wrong, because the absorption cross-section of H_2O is not constant in this region. However, in this region, we cannot make an extrapolation similar to the one described above, since the cross-section is dominated by the continuum of the ionization of the $2a_1$ molecular orbital of water and other higher-energy states, and those states are very different from the oxygen 1*s* core hole state: they do not lead to an Auger decay. Changing the value of the photodesorption yield below 520 eV leads to only negligible changes in the average value; therefore, this approximation, although crude, is not critical. The yields extrapolated from 150 eV to 10 keV are available in the Supplementary Information, along with the values of the absorption cross-section used.

The extrapolated photodesorption yields are then multiplied by a normalized X-ray spectrum. To illustrate the average yields obtained for various relevant regions at different attenuations, we retrieved observed X-ray spectra of TW Hya[25] and of the ultra-luminous infrared galaxy MKN 231[26]. TW Hya is intended to be representative of a young star, a source that can illuminate protoplanetary disks and protostellar envelopes, although the spectra of such stars can vary. The spectrum of MKN 231 does not correspond to a spectrum illuminating any specific molecular cloud; therefore, it should be taken only as an illustration of a harder and flatter X-ray spectrum than that of a young star. We then applied to each of these spectra an attenuation corresponding to various column densities of a gas and dust mix using the attenuation cross-section of the standard model of ref. [47]. The elemental abundances and dust parameters of this reference are taken for protoplanetary disks. We make the assumption that these numbers should not be too different for other types of molecular gas and dust environments. The spectra considered are given in the Supplementary Information.

The integral of the yield spectrum $Y^{\mathrm{inc}}(\lambda)$ (where λ is the wavelength) multiplied by the normalized flux spectrum $\phi(\lambda)$ gives the following average photodesorption yield[48]:

$$Y^{\mathrm{avg}} = \frac{\int Y^{\mathrm{inc}}(\lambda)\phi(\lambda)\mathrm{d}\lambda}{\int \phi(\lambda)\mathrm{d}\lambda}$$

The results for different sources and attenuations are given in Table 2. These numbers can be used in astrochemical models to treat X-ray photodesorption similarly to the way UV photodesorption is treated, using the following photodesorption rate k^{PD}_i for species *i*, in units of $\mathrm{cm}^{-3}\,\mathrm{s}^{-1}$:

$$k_i^{\mathrm{PD}} = \theta_i \sigma_{\mathrm{gr}} n_{\mathrm{gr}} Y_i^{\mathrm{avg}} F_{\mathrm{X}}$$

where θ_i is the surface coverage of species *i*, $\sigma_{\mathrm{gr}} n_{\mathrm{gr}}$ is the effective grain surface (σ_{gr} is the geometrical cross-section of the grain and n_{gr} is the grain density) and F_{X} is the integrated X-ray photon flux.

Data availability. The data that support the plots within this paper and other findings of this study are available from the corresponding author upon reasonable request.

Received: 27 October 2017; Accepted: 18 June 2018;
Published online: 16 July 2018

References

1. van Dishoeck, E. F., Bergin, E. A., Lis, D. C. & Lunine, J. I. in *Protostars and Planets VI* (eds Beuther, H. et al.) 835–858 (Univ. Arizona Press, Tucson, 2014).
2. Hogerheijde, M. R. et al. Detection of the water reservoir in a forming planetary system. *Science* **334**, 338–340 (2011).
3. Caselli, P. et al. First detection of water vapor in a pre-stellar core. *Astrophys. J. Lett.* **759**, L37 (2012).
4. Arasa, C., Koning, J., Kroes, G.-J., Walsh, C. & van Dishoeck, E. F. Photodesorption of H_2O, HDO, and D_2O ice and its impact on fractionation. *Astron. Astrophys.* **575**, A121 (2015).
5. Muñoz Caro, G. M. et al. Photodesorption and physical properties of CO ice as a function of temperature. *Astron. Astrophys.* **589**, A19 (2016).
6. Bertin, M. et al. UV photodesorption of methanol in pure and CO-rich ices: desorption rates of the intact molecules and the photofragments. *Astrophys. J. Lett.* **817**, L12 (2016).
7. Aikawa, Y. & Herbst, E. Molecular evolution in protoplanetary disks. Two-dimensional distributions and column densities of gaseous molecules. *Astron. Astrophys.* **351**, 233–246 (1999).
8. Walsh, C., Nomura, H., Millar, T. J. & Aikawa, Y. Chemical processes in protoplanetary disks. II. On the importance of photochemistry and X-ray ionization. *Astrophys. J.* **747**, 114 (2012).
9. Maloney, P. R., Hollenbach, D. J. & Tielens, A. G. G. M. X-ray-irradiated molecular gas. I. Physical processes and general results. *Astrophys. J.* **466**, 561–584 (1996).
10. Meijerink, R., Spaans, M. & Israel, F. P. Diagnostics of irradiated dense gas in galaxy nuclei. II. A grid of XDR and PDR models. *Astron. Astrophys.* **461**, 793–811 (2007).
11. Walsh, C., Millar, T. J. & Nomura, H. Chemical processes in protoplanetary disks. *Astrophys. J.* **722**, 1607–1623 (2010).
12. Stäuber, P., Jørgensen, J. K., van Dishoeck, E. F., Doty, S. D. & Benz, A. O. Water destruction by X-rays in young stellar objects. *Astron. Astrophys.* **453**, 555–565 (2006).
13. Cleeves, L. I., Bergin, E. A., Qi, C., Adams, F. C. & Öberg, K. I. Constraining the X-ray and cosmic-ray ionization chemistry of the TW Hya protoplanetary disk: evidence for a sub-interstellar cosmic-ray rate. *Astrophys. J.* **799**, 204 (2015).
14. Rosenberg, R. A.et al. K-shell excitation of D_2O and H_2O ice: photoion and photoelectron yields. *Phys. Rev. B* **28,** 3026–3030 1983).
15. Coulman, D. et al. Excitation, deexcitation, and fragmentation in the core region of condensed and adsorbed water. *J. Chem. Phys.* **93**, 58–75 (1990).
16. Mase, K., Nagasono, M., Tanaka, S.-i, Sekitani, T. & Nagaoka, S.-i Ion desorption from molecules condensed at low temperature: a study with electron-ion coincidence spectroscopy combined with synchrotron radiation (review). *Low Temp. Phys.* **29**, 243–258 (2003).
17. Pilling, S. & Andrade, D. P. P. in *X-Ray Spectroscopy* (ed. Sharma, S. K.) Ch. 10 (InTech, London, 2012); https://doi.org/10.5772/29591
18. Nilsson, A. et al. X-ray absorption spectroscopy and X-ray Raman scattering of water and ice; an experimental view. *J. Electron Spectrosc.* **177**, 99–129 (2010).
19. Parent, P., Laffon, C., Mangeney, C., Bournel, F. & Tronc, M. Structure of the water ice surface studied by X-ray absorption spectroscopy at the O K-edge. *J. Chem. Phys.* **117**, 10842–10851 (2002).
20. Laffon, C., Lacombe, S., Bournel, F. & Parent, P. Radiation effects in water ice: a near-edge X-ray absorption fine structure study. *J. Chem. Phys.* **125**, 204714 (2006).
21. Petrik, N. G. & Kimmel, G. A. Electron-stimulated sputtering of thin amorphous solid water films on Pt(111). *J. Chem. Phys.* **123**, 054702 (2005).
22. Yabushita, A., Hama, T. & Kawasaki, M. Photochemical reaction processes during vacuum-ultraviolet irradiation of water ice. *J. Photoch. Photobio. C* **16**, 46–61 (2013).
23. Cruz-Diaz, G. A., Martn-Doménech, R., Moreno, E., Muñoz Caro, G. M. & Chen, Y.-J. New measurements on water ice photodesorption and product formation under ultraviolet irradiation. *Mon. Not. R. Astron. Soc.* **474**, 3080–3089 (2018).
24. Arasa, C., Andersson, S., Cuppen, H. M., van Dishoeck, E. F. & Kroes, G.-J. Molecular dynamics simulations of the ice temperature dependence of water ice photodesorption. *J. Chem. Phys.* **132**, 184510 (2010).
25. Nomura, H., Aikawa, Y., Tsujimoto, M., Nakagawa, Y. & Millar, T. J. Molecular hydrogen emission from protoplanetary disks. II. Effects of X-ray irradiation and dust evolution. *Astrophys. J.* **661**, 334–353 (2007).

26. Braito, V. et al. The XMM-Newton and BeppoSAX view of the ultra luminous infrared galaxy MKN 231. *Astron. Astrophys.* **420**, 79–88 (2004).
27. Cecchi-Pestellini, C. & Aiello, S. Cosmic ray induced photons in dense interstellar clouds. *Mon. Not. R. Astron. Soc.* **258**, 125–133 (1992).
28. Dartois, E. et al. Heavy ion irradiation of crystalline water ice: cosmic ray amorphisation cross-section and sputtering yield. *Astron. Astrophys.* **576**, A125 (2015).
29. Walsh, C., Nomura, H. & van Dishoeck, E. The molecular composition of the planet-forming regions of protoplanetary disks across the luminosity regime. *Astron. Astrophys.* **582**, A88 (2015).
30. Sacchi, M. et al. The SEXTANTS beamline at SOLEIL: a new facility for elastic, inelastic and coherent scattering of soft X-rays. *J. Phys. Conf. Ser.* **425**, 072018 (2013).
31. Doronin, M., Bertin, M., Michaut, X., Philippe, L. & Fillion, J.-H. Adsorption energies and prefactor determination for CH_3OH adsorption on graphite. *J. Chem. Phys.* **143**, 084703 (2015).
32. Naumkin, A. V., Kraut-Vass, A., Gaarenstroom, S. W. & Powell, C. J. *NIST X-ray Photoelectron Spectroscopy Database* (National Institute of Standards and Technology, 2012); https://srdata.nist.gov/xps/
33. Dupuy, R. et al. Spectrally-resolved UV photodesorption of CH_4 in pure and layered ices. *Astron. Astrophys.* **603**, A61 (2017).
34. Orient, O. J. & Strivastava, S. K. Electron impact ionisation of H_2O, CO, CO_2 and CH_4. *J. Phys. B* **20**, 3923–3936 (1987).
35. Straub, H. C., Renault, P., Lindsay, B. G., Smith, K. A. & Stebbings, R. F. Absolute partial cross sections for electron-impact ionization of H_2, N_2, and O_2 from threshold to 1000 eV. *Phys. Rev. A* **54,** 2146–2153 (1996).
36. Vegard, I. Struktur und Leuchtfähigkeit von festem Kohlenoxyd. *Z. Phys. A Hadron Nucl.* **61**, 185–190 (1930).
37. Fayolle, E. C. et al. CO ice photodesorption: a wavelength-dependent study. *Astrophys. J. Lett.* **739**, L36 (2011).
38. Cruz-Diaz, G. A., Muñoz Caro, G. M., Chen, Y.-J. & Yih, T.-S. Vacuum-UV spectroscopy of interstellar ice analogs. I. Absorption cross-sections of polar-ice molecules. *Astron. Astrophys.* **562**, A119 (2014).
39. Berkowitz, J. *Atomic and Molecular Photoabsorption: Absolute Total Cross Sections* (Academic, London, 2002).
40. Bertin, M. et al. UV photodesorption of interstellar CO ice analogues: from subsurface excitation to surface desorption. *Phys. Chem. Chem. Phys.* **14,** 9929–9935 (2012).
41. Tîmneanu, N., Caleman, C., Hajdu, J. & van der Spoel, D. Auger electron cascades in water and ice. *Chem. Phys.* **299**, 277–283 (2004).
42. Andersson, S. & van Dishoeck, E. F. Photodesorption of water ice. *Astron. Astrophys.* **491**, 907–916 (2008).
43. DeSimone, A. J., Crowell, V. D., Sherrill, C. D. & Orlando, T. M. Mechanisms of H_2O desorption from amorphous solid water by 157-nm irradiation: an experimental and theoretical study. *J. Chem. Phys.* **139**, 164702 (2013).
44. Kimmel, G. A., Orlando, T. M., Vézina, C. & Sanche, L. Low-energy electron-stimulated production of molecular hydrogen from amorphous water ice. *J. Chem. Phys.* **101**, 3282–3286 (1994).
45. Redlich, B., Zacharias, H., Meijer, G. & von Helden, G. Resonant infrared laser-induced desorption of methane condensed on NaCl(100): isotope mixture experiments. *J. Chem. Phys.* **124**, 044704 (2006).
46. Hovington, P., Drouin, D. & Gauvin, R. CASINO: a new Monte Carlo code in C language for electron beam interaction—part I: description of the program. *Scanning* **19**, 1–14 (2006).
47. Bethell, T. J. & Bergin, E. A. Photoelectric cross-sections of gas and dust in protoplanetary disks. *Astrophys. J.* **740**, 7 (2011).
48. Dupuy, R. et al. The efficient photodesorption of nitric oxide (NO) ices: a laboratory astrophysics study. *Astron. Astrophys.* **606**, L9 (2017).
49. Rab, C. et al. X-ray radiative transfer in protoplanetary disks: the role of dust and X-ray background fields. *Astron. Astrophys.* **609**, A91 (2018).

Acknowledgements

We thank C. Walsh for insights on X-rays in protoplanetary disks, D. Lis for comments on the paper and P. Marie-Jeanne for technical support. We acknowledge SOLEIL for the provision of synchrotron radiation facilities under project 20161406, and we thank N. Jaouen and the SEXTANTS team for their help on the beamline. This work was supported by the Programme National 'Physique et Chimie du Milieu Interstellaire' (PCMI) of CNRS/INSU with INC/INP co-funded by CEA and CNES. Financial support from LabEx MiChem, part of the French state funds managed by the ANR within the *investissements d'avenir* programme under reference ANR-11-10EX-0004-02, and by the Ile-de-France region DIM ACAV programme, is gratefully acknowledged. This work was done in collaboration with and through financial support from the European Organization for Nuclear Research (CERN) under collaboration agreement KE3324/TE.

Author contributions

R.D. treated and analysed the data and wrote the manuscript. M.B., G.F., M.H. and J.-H.F. provided extensive input on the data analysis and the manuscript. J.-H.F., M.B., G.F. and R.D. initiated and supervised the project. J.-H.F., M.B. and P.J. designed the experimental set-up. G.F. contributed to the bibliographic work. All authors participated in the experimental runs at the SOLEIL synchrotron where the data were acquired.

Competing interests

The authors declare no competing interests.

Additional information

Supplementary information is available for this paper at https://doi.org/10.1038/s41550-018-0532-y.

Reprints and permissions information is available at www.nature.com/reprints.

Correspondence and requests for materials should be addressed to R.D.

Publisher's note: Springer Nature remains neutral with regard to jurisdictional claims in published maps and institutional affiliations.

Paper III: X-ray photodesorption from water ice in protoplanetary disks and X-ray-dominated regions

Paper IV: Desorption of neutrals, cations and anions from core-excited amorphous solid water

Desorption of neutrals, cations and anions from core-excited amorphous solid water

R. Dupuy,[1] G. Féraud,[1] M Bertin,[1] C. Romanzin,[2] L. Philippe,[1] T. Putaud,[1] X. Michaut,[1] R. Cimino,[3] V. Baglin,[4] and J.-H. Fillion[1]

[1)] *Sorbonne Université, Observatoire de Paris, Université PSL, CNRS, LERMA, F-75005, Paris, France*

[2)] *Laboratoire de Chimie Physique, CNRS, Univ. Paris-Sud, Université Paris-Saclay, 91405, Orsay, France*

[3)] *Laboratori Nazionali di Frascati (LNF)-INFN I-00044 Frascati*

[4)] *CERN, CH-1211 Geneva 23, Switzerland*

Core-excitation of water ice releases many different molecules and ions in the gas phase. Studying these desorbed species and the underlying mechanisms can provide useful information on the effects of X-ray irradiation in ice. We report a detailed study of the X-ray induced desorption of a number of neutral, cationic and anionic species from amorphous solid water. We discuss the desorption mechanisms, and the relative contributions of Auger and secondary electrons (X-ray induced Electron Stimulated Desorption) and initial excitation ("true" photon-stimulated desorption) as well as the role of photochemistry. Anions are shown to desorb not just through processes linked with secondary electrons but also through direct dissociation of the core-excited molecule. The desorption spectra of oxygen ions (O^+, OH^+, H_2O^+, O^-, OH^-) give a new perspective on their previously reported very low desorption yields for most types of irradiation of water, showing that they mostly originate from the dissociation of photoproducts such as H_2O_2.

I. INTRODUCTION

Water ice is of primary importance in numerous domains of science. It is ubiquitous on Earth but also in space, on various bodies of the solar system and on the dust grains of the interstellar medium, where it plays a primordial role in e.g. planet formation in protoplanetary disks[1,2]. The interaction of water ice with energetic radiation such as UV or X-rays interests different fields, such as planetary science[3] or astrochemistry: water frozen on interstellar dust grains can be released to the gas phase through a process called photodesorption, which has shown its importance in the field over the last decade[4–7]. Amorphous solid water is also often used as a model for liquid water to which a different variety of experimental techniques can be applied. It can therefore be used to study e.g. radiation effects in liquid water, which is relevant in many fields like biology or nuclear reactors[8,9], but also for understanding the structure of condensed water itself. Numerous studies have been dedicated to elucidating the structure of various forms of condensed phase water[10–12], especially liquid water, but the latter still eludes complete characterization. X-ray absorption spectroscopy of liquid and different forms of solid water have been a major element in the recent discoveries and controversies surrounding the structure of the different forms of condensed water[10].

In this context, having a more fundamental understanding of the various processes occurring during X-ray irradiation of water ice is important. One way of getting insights into the dissociation of molecules, photochemistry and energy relaxation pathways is to study under high vacuum conditions thin films of water ice and to investigate what is ejected in the gas phase. This gives information different and complementary to that obtained using techniques that probe the condensed phase. Previous studies of core excitation of water ice by X-rays have mostly investigated the desorption of the H^+ ion, which is by far the most abundant ion desorbed. The desorption of other fragments like O^+ or OH^+ is reported as being particularly low for not only X-ray core excitation[13] but also other types of irradiations such as electrons[14] or XUV photons[15].

Some studies have attempted to derive structural parameters of the ice from the desorption spectrum of H^+[16,17]. Another work[13] looked into the details of the dissociation dynamics by investigating specific features that appear in the H^+ desorption spectrum but not in the absorption of the ice, in particular the lowest energy peak of the spectrum, sometimes called the pre-edge, which is shifted and enhanced in the H^+ spectrum. This feature was interpreted as pertaining to surface molecules, and it was suggested that an ultrafast dissociation process (i.e. breaking of the O-H bond on the potential energy surface of the core hole state, before its decay) could be occurring. It was later found by Auger electron - ion coincidence (AEPICO)[18] and investigation of the desorption of neutral molecules[19], especially neutral H, and kinetic energy distributions[20], that no ultrafast dissocation took place, but still a "fast" desorption process was at play, with a significant elongation of the O-H bond during the core hole lifetime. This illustrates the importance of exploring the exact mechanisms of desorption in order to use it to derive information on the investigated system. Indeed, the pre-edge peak is a keystone of the current interpretation of X-ray absorption and desorption spectra of condensed water that are used to derive structural information[10].

One basic distinction that is usually made, in terms of desorption mechanisms for core excitations, is between desorption mediated by the Auger electron and

the subsequent secondary electrons created (which is usually termed X-ray induced Electron-Stimulated Desorption, XESD) from desorption mediated directly by the core excitation decay (as a result of the molecule being left in a highly excited state), which is sometimes called "true" photon-stimulated desorption (true PSD)[13]. Another point that can be discussed in this case is the role that photochemistry plays in the desorption phenomena. It is, for example, known that chemistry plays an important role in UV photodesorption of water ice[21].

Here, we investigated the spectrally-resolved desorption from core-excited water ice for not only H^+ but also most of the other species that could be detected in our set-up. The objective is to make a survey of the desorption of different species upon core-excitation. Desorption of neutral species, protonated clusters, and cation fragments other than H^+ are discussed and compared with results from other types of irradiation (electrons, UV photons and energetic ions) when such results exist in the literature. In each case, we attempt to discuss desorption mechanisms when possible and whether we can distinguish the contributions of XESD and true PSD. The desorption spectra of oxygen-bearing ions bring a new perspective to their low desorption yields. We also investigate the desorption of anions, which had not been hitherto reported for any type of irradiation of water ice to our knowledge, to the exception of low energy electrons, where the specific dissociative electron attachment (DEA) process can occur - which we show to not be the only process at play here.

II. METHODS

A. Experimental set-up

Experiments were performed in the SPICES 2 set-up. Some aspects of the experiments have already been detailed elsewhere[4]. Briefly, the set-up is an ultra-high vacuum chamber equipped with a closed-cycle helium cryostat, reaching a base temperature of 15 K at the sample holder and a base pressure of $\sim 1 \times 10^{-10}$ mbar at 15 K. The substrate used was a technical copper surface (polycrystalline OFHC copper), electrically insulated from the holder by a kapton foil. This allows to measure the sample current generated by X-ray absorption, when Auger and secondary electrons escape the surface of the ice. This total electron yield (TEY) is considered to represent the absorption of the ice. Water (liquid chromatography standard, Fluka, purified by freeze-pump-thaw cycles) vapour was injected through a dosing tube to grow a ~ 100 monolayers (ML) thick ice on the substrate at 90 K, to yield a compact amorphous solid water[22] (c-ASW). The thickness ensures a negligible substrate influence on desorption. Experiments were performed at either 90 K or 15 K. Cooling to 15 K is not expected to change the compact amorphous structure of the ice.

The set-up was installed on the SEXTANTS beamline of the SOLEIL synchrotron. During irradiation, the photon energy was scanned typically between 520 and 600 eV. The monochromatized beam had a resolution of 150 meV and a flux of 1.4×10^{13} photon.s^{-1} for the experiments on neutral molecules, and a resolution of 80 meV and flux of 2.8×10^{12} photon.s^{-1} for the experiments on ions, constant over the whole range except around 535 eV where a dip was present. The spot at the surface was approximately 0.1 cm^2 large. The beam was incident at 47° relative to the surface normal, and the polarization was set to horizontal so that at the surface the light had a half out-of-plane and half in-plane components. The absolute energy scale was set so that the pre-edge (thereafter peak 1) of bulk water ice absorption was at 535 eV, which is what is usually done in the literature[10,17]. We had not shifted the scale in our previous study[4], but it does not change any conclusions: it is only more convenient to compare the results of different papers. This re-calibration was cross-checked to be coherent with the position of the main resonance peak of solid CO near the O 1s edge, which was studied during these same experimental runs.

Neutral species desorption was detected using a quadrupole mass spectrometer (Pfeiffer Vacuum). Ion desorption was detected with another quadrupole mass spectrometer (EQS Hiden Analytical), which can detect both positive and negative ions. This QMS is equipped with a 45° deflector kinetic energy analyser[23]. It is important to note that kinetic energy filtering is not optional with such a device: all the spectra that we present are taken at a given kinetic energy, the center of the KE distribution unless stated otherwise. Because we have evidence that kinetic energy filtering can have an effect on the relative intensities of the spectral features for some ions (which will not be discussed further here), KE distributions at different fixed photon energies were measured and integrated to check that the KE-differentiated spectra we present are not distorted compared to the KE-integrated spectra.

B. Calibration of the photodesorption yields

We estimated the absolute photodesorption yields of the different species we observed. The derivation of absolute yields for neutral species were presented in detail previously[4]. For deriving the yields of ions, several steps are necessary. Since our QMS is equipped with a kinetic energy filter, we first integrated the kinetic energy distribution of each ion. The result is corrected by the photon flux at the relevant energy. Then in order to compare different ions between themselves, we estimated the relative detection efficiencies. The assumption is that the relative detection efficiency only depends on the mass of the ion. Estimations made with different gases with known cracking patterns and compared using a calibrated pressure gauge allowed to derive an apparatus function for the QMS, which roughly follows a $(m/z)^{-0.5}$ power law

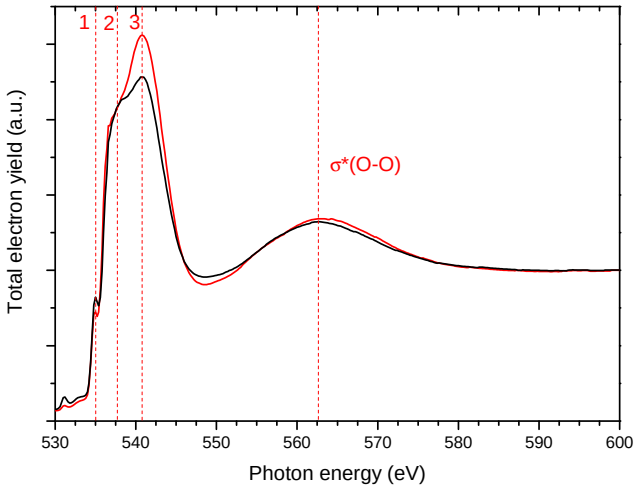

FIG. 1. Total electron yield (TEY) as a function of photon energy at 15 K (black trace) and 90 K (red trace) from c-ASW grown at 90 K. The curves have been normalized at 600 eV. The water features are indicated by vertical dashed red lines (see the text for attributions).

(except for the very light H^+ and H_2^+ ions, for which separate estimations of the apparatus function were made). The last step is to calibrate the absolute desorption yield of at least one ion. The solution we adopted for now was to scale our data with published desorption yield values of a given system. In this case we irradiated CO ice and scaled the data we obtained for the C^+ ion on the absolute values of Rosenberg et al.[24]. This yielded a detection efficiency for this ion of ∼2% with our QMS.

We are confident with the values given for neutral species, within the uncertainty of ±40% that we estimated[4]. The absolute values for cations (and anions) rely on the validity of the measurements of Rosenberg et al. The relative comparison of cations, however, is valid within the ±40% error of the apparatus function calibration. The inter-comparison of cations and anions, on the other hand, relies on the assumption that the detection efficiency still only depends on the mass, which given that other parameters of the QMS change may not be true. The calibration of anions should therefore be considered as an order of magnitude estimate.

III. RESULTS AND DISCUSSION

A. Ice absorption spectroscopy and structure

As explained in section II, the measured total electron yield (TEY), i.e. the number of electrons escaping the surface of the ice per incident photon, will be assimilated to the absorption of the ice. The dominant contribution to the TEY are the secondary electrons created by the Auger cascade. The probing depth of the technique, corresponding roughly to the radius of the electron cascade, is about 100 Å (∼ 30 ML)[25]. The contributions of the bulk of the ice are thus presumably dominant, although the surface roughness of amorphous ice may increase the surface contributions and make the estimation of probing depth more complicated. As stated before, contribution of the substrate to the TEY can be neglected given the thickness of the ice (100 ML). The total electron yield curves obtained in our experimental conditions at 15 and 90 K are presented in fig. 1.

Interpretation of the TEY spectra as well as the photodesorption spectra that will be presented later requires first a recall of the electronic structure of water and the extensive literature existing on the interpretation of X-ray absorption spectroscopy of condensed water. The free water molecule has three outer valence molecular orbitals $1b_1$, $3a_1$ and $1b_2$ and an inner valence orbital $2a_1$, as well as a core $1a_1$ orbital which is the almost unperturbed oxygen 1s orbital[26]. The $1b_2$ and $2a_1$ orbitals mostly constitute the O-H bonds, while the $1b_1$ and $3a_1$ make up the oxygen lone pairs. There are two empty molecular orbitals below the ionisation threshold of water, the $4a_1$ and $2b_2$ orbitals, respectively strongly and weakly antibonding. Above these orbitals lie higher Rydberg states. The absorption spectrum of gas phase water around the O 1s region exhibits four successive peaks before a ionization continuum[27], which are thus simply attributed to promotion of the 1s electron to, in order, the $4a_1$, $2b_2$, and Rydberg orbitals.

Upon condensation, according to absorption and photoelectron spectroscopy experiments[28], the valence electronic structure of water is not heavily modified. Shifts and broadening are observed for the filled orbitals. The $4a_1$ empty orbital is below the conduction band and in condensed phase language would correspond to a Frenkel exciton. The $2b_2$ orbital on the other hand overlaps with the ionisation threshold and constitutes a conduction band.

In condensed phase, all spectra of water in the core excitation region display three features with varying relative intensities, which we will simply call peak 1, 2 and 3 here for reasons explained below. These are seen on our TEY spectra (fig. 1) at 535, 537.5 and 541 eV respectively. The peak at 563 eV is the first EXAFS oscillation, which we label σ^*(O-O) to signify its inter-molecular resonance character. Most early works on water core excitation[16,17,29] attributed the first three features according to the gas phase features, with the first peak being inherited from the $4a_1$ free molecule orbital, the second from the $2b_2$ orbital, and the third corresponding to Rydberg orbitals that are heavily modified in condensed phase because of their spatial extension. This is in line with more recent work[30] interpreting the first peak as a localized state of core-excitonic nature, therefore little affected by hydrogen bonding and inheriting from the free molecule $4a_1$ orbital, while the third one corresponds to a state delocalized along the H-bond network, bearing no relation with the free molecule, but coherent with the solid state notion of a conduction band.

Another interpretation of the spectra has also been proposed. As mentioned in the introduction, X-ray absorption spectroscopy and related techniques have been used to fuel the debate regarding the structure of liquid water and other forms of condensed water. The interpretation takes into account the fact that in condensed phase, all water molecules are not necessarily equivalent. Even in the crystalline phases, the picture of a non-distorted, tetrahedrally bonded molecule does not hold due to the presence of the surface, various defects, grain boundaries and admixtures of amorphous ice in even the best crystalline samples. Calculations have shown the X-ray spectrum of water to be strongly dependent on the bonding of the molecule[31]. In particular, single H-bond donor molecules (i.e. with a free hydrogen) exhibit different features from fully coordinated molecules. These calculations in addition to considerable amounts of experimental data on various forms of condensed water (see refs[10,32] and references therein) lend credit to the following interpretation: peak 1 and 2 of the spectra, called pre- and main-edge in these references, gain intensity from weakly coordinated, and in particular single donor (SD) species, while peak 3 (called the post-edge) gains intensity from fully coordinated species. The key difference between this interpretation and the previous one is whether there can be a localized excitation contributing to the pre-edge feature for fully coordinated species in the ice. The transposition of gas-phase peak attributions to the condensed phase is therefore not so clear, which is why we adopted the labels peak 1, 2 and 3 for this paper.

We will use the second theory as a framework of interpretation of our data. The difference of our TEY spectra at 15 and 90 K can thus be interpreted as follow. We see that at 90 K, the post-edge (peak 3) is more intense and sharper than at 15 K, while the pre-edge (peak 1) is slightly decreased. We can conclude that at 90 K, more fully coordinated species with less distorted H-bond are probed. The ice is grown at 90 K, which yields a compact amorphous structure, and we do not expect cooling it from 90 to 15 K to change that structure. However we are never probing a pristine ice: the high photon flux used modifies the ice, as expected for any type of irradiation[33]. The irradiation should create defects and trapped species that change the local structure, affecting the hydrogen-bond network. The differences between the two temperatures therefore stem from the fact that at 90 K, the ice more easily regenerates itself, as defects and trapped species can diffuse and molecules can more easily rearrange themselves. This is why more fully-coordinated species with sharper features (peak 3) are observed at 90 K.

B. X-ray induced fragmentation and chemistry

Core excitation of a water molecule leads to Auger decay, which (i) leaves the molecule that absorbed the photon in a highly excited state, and (ii) releases an Auger electron. The highly excited states of a molecule that underwent Auger decay are typically doubly ionized (2h: two holes in valence orbitals) states after core ionization and singly ionized excited states (2h1e: two holes in valence orbitals and one electron in a previously empty orbital) after core excitation. These states lead to complex fragmentation patterns. The Auger electron, here with an energy of about 500 eV, will scatter in the ice creating secondary excitations and ionisations - according to simulations, about 25 in the case of water ice[25]. Although an energetic electron can create highly excited states in molecules as well, most of these secondary events will create "simple" states, i.e. singly ionised or excited molecules. Part of the focus of this paper, as mentioned in the introduction, will be to distinguish between desorption triggered by the Auger electron cascade (XESD) from desorption mediated directly by the core excitation decay (true PSD)[13].

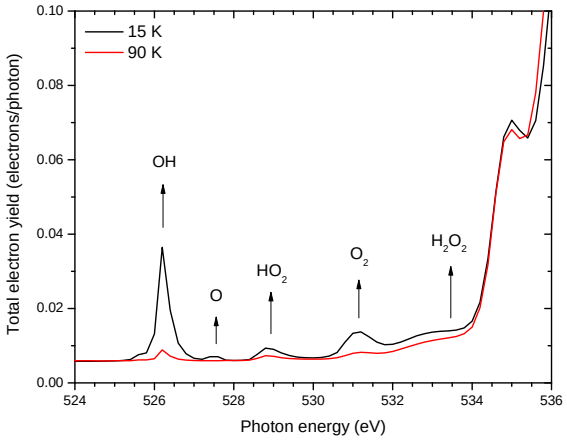

FIG. 2. Total electron yield (TEY) as a function of photon energy in the pre-edge region at 15 K (black trace) and 90 K (red trace) from a compact ASW ice grown at 90 K. Attribution of the peaks following Laffon et al.[34] are indicated.

The chemistry induced by X-rays, but also by energetic ions or electrons, sometimes termed radiolysis, is mostly driven by the cascade of secondary electrons and secondary excitations. The resulting outcome is qualitatively similar to photolysis chemistry, i.e. chemistry driven by UV photons (see Yabushita et al.[21] for a recent review of water photolysis). The driver of water chemistry is the dissociation of excited H_2O^* in OH + H, which is the main dissociation pathway, although direct production of O radicals is also possible. The radicals then react to form further products. In our experiment, some of the main elements of the water chemical network can be identified in situ in the X-ray absorption spectrum of the ice. Figure 2 shows the TEY between 524 and 536 eV at either 15 or 90 K. The observed peaks can be attributed to various species other than H_2O created by X-ray irradiation in the ice: we see the O, OH and

TABLE I. Photodesorption yields (molecules/photon) at 550 eV for c-ASW, at either 15 K or 90 K

	90 K	15 K		90 K	15 K		90 K	15 K
H_2O	3.8×10^{-3}	3.4×10^{-3}	H^+	1×10^{-4}	4.3×10^{-5}	H^-	1.3×10^{-5}	6.5×10^{-6}
H_2	8.9×10^{-3}	5.3×10^{-3}	H_2^+	5×10^{-7}	1.6×10^{-7}	H_2^-	3×10^{-10}	
O_2	6.3×10^{-3}	4×10^{-4}	H_3^+	2.5×10^{-9}		O^-	1.3×10^{-7}	2.3×10^{-8}
OH	$< 1 \times 10^{-3}$	$< 1 \times 10^{-3}$	O^+	3.6×10^{-8}	2.8×10^{-8}	OH^-	2.2×10^{-8}	6.4×10^{-9}
			OH^+	6×10^{-9}	4.6×10^{-9}	H_2O^-	3×10^{-10}	
			H_2O^+	3×10^{-9}	3.7×10^{-9}	O_2^-	8×10^{-10}	
			H_3O^+	1.2×10^{-8}	1.6×10^{-8}			
			O_2^+	2.9×10^{-8}				
			$(H_2O)_3H^+$	1.9×10^{-8}	2.4×10^{-8}			

HO_2 radicals as well as O_2 and H_2O_2. The intensity of these peaks (at a given temperature) do not change upon further irradiation of the ice, showing that we are probing a steady state. In this steady state, Laffon et al.[34] estimated from the peak intensities that these chemical products amount to no more than a few percent of the ice. Pure water ice shows a resiliency to irradiation, i.e. most of the photochemistry occurring leads back to H_2O as the end product. In photodesorption, two volatile products of the chemistry, H_2 and O_2 are also observed. The desorption of neutral species is discussed in more details in section C and in a previous publication[4]. Other elements that play a role in water photochemistry and cannot be probed here are the important atomic H, the solvated electron, and the presence of defects in the ice.

Temperature plays a major role in this chemistry, by activating or not the diffusion of radicals. We see in figure 2 that at 15 K, the OH radical is much more abundant than at 90 K, a temperature at which it can diffuse easily and react. At 90 K volatile species such as O_2 are also more depleted as they can diffuse to the surface and desorb. Part of these species stay trapped in the ice, which has important consequences for astrophysical applications, where the origin of trapped oxygen in ice has been a long-studied question that is not yet fully solved[35].

In addition to the radicals-fuelled chemistry, ionising radiation also opens the possibility of ion chemistry. Contrary to valence excitation, ionization of H_2O is not necessarily dissociative[36]. H_2O^+ ions will therefore be created along with protons and possibly other ions. The released electrons, once thermalized, can be trapped[37] or mobile[38] and are equivalent to the solvated electron in liquid water. Models of liquid water radiolysis[39] usually consider that charge or proton transfer processes rapidly make the end product of an ionisation event a hydronium (H_3O^+) ion and a solvated electron, regardless of the initial product of ionisation. Diffusion of these two species will subsequently lead to recombination and either water reformation or dissociation into radicals, leading back to radical chemistry. However, the fate of the various ions in solid water, where diffusion processes are not necessarily effective, is unclear. Presumably other ionic fragments than H_3O^+ are also created, although evidence of their presence inside the ice is scarce[35]. Our detection of various ions in desorption (see table I) suggest that they should also exist within the ice, although they may not be abundant or long-lived. For example, the observation of the desorption of protonated clusters $(H_2O)_nH^+$, detailed in section D, is an indirect evidence of structural rearrangements in the ice of water molecules around a proton, because of ion-dipole interactions. The desorption of anions, detailed in section F and G, shows that they should be present as well. The chemistry induced in water ice by low energy electrons, especially dissociative electron attachment (DEA) and the creation of anionic species, has been studied previously[40]. Desorption can thus provide some insights on the chemistry happening in the ice upon irradiation.

C. Desorption of neutral species

We observed the desorption of three neutral species (table I), H_2O, O_2 and H_2. Their photodesorption spectra are given in figure 3 at both 15 and 90 K. The desorption of neutral species has already been discussed in a previous article[4], therefore the results will only be briefly recalled here along with some new elements. Regarding the distinction between XESD and true PSD, we argued previously that neutral desorption is probably dominated by XESD. The fact that the photodesorption spectra follow the TEY is a first argument, although it is weak: while an XESD process necessarily follows the TEY (electrons created at different photon energies are undistinguishable and will lead to the same effects, therefore these effects should be proportional to the total number of electrons), it is not sufficient: it would also make sense for a true PSD process to follow the absorption spectrum. The argument becomes strong when it is reversed and there is a deviation of the photodesorption spectrum from the TEY, signing unambiguously a true PSD process, as we will see later for ion desorption.

Another interesting argument is the estimated photodesorption yield per absorbed photon[4] (instead of per incident photon) of H_2O, which is about 0.2 molecules/photon, which accounting for the uncertainty is close to the yield derived for electron-stimulated desorption[41]. To better understand the importance of this quantitative argument, we can first point out that XESD dominating for neutral desorption is sensible in the

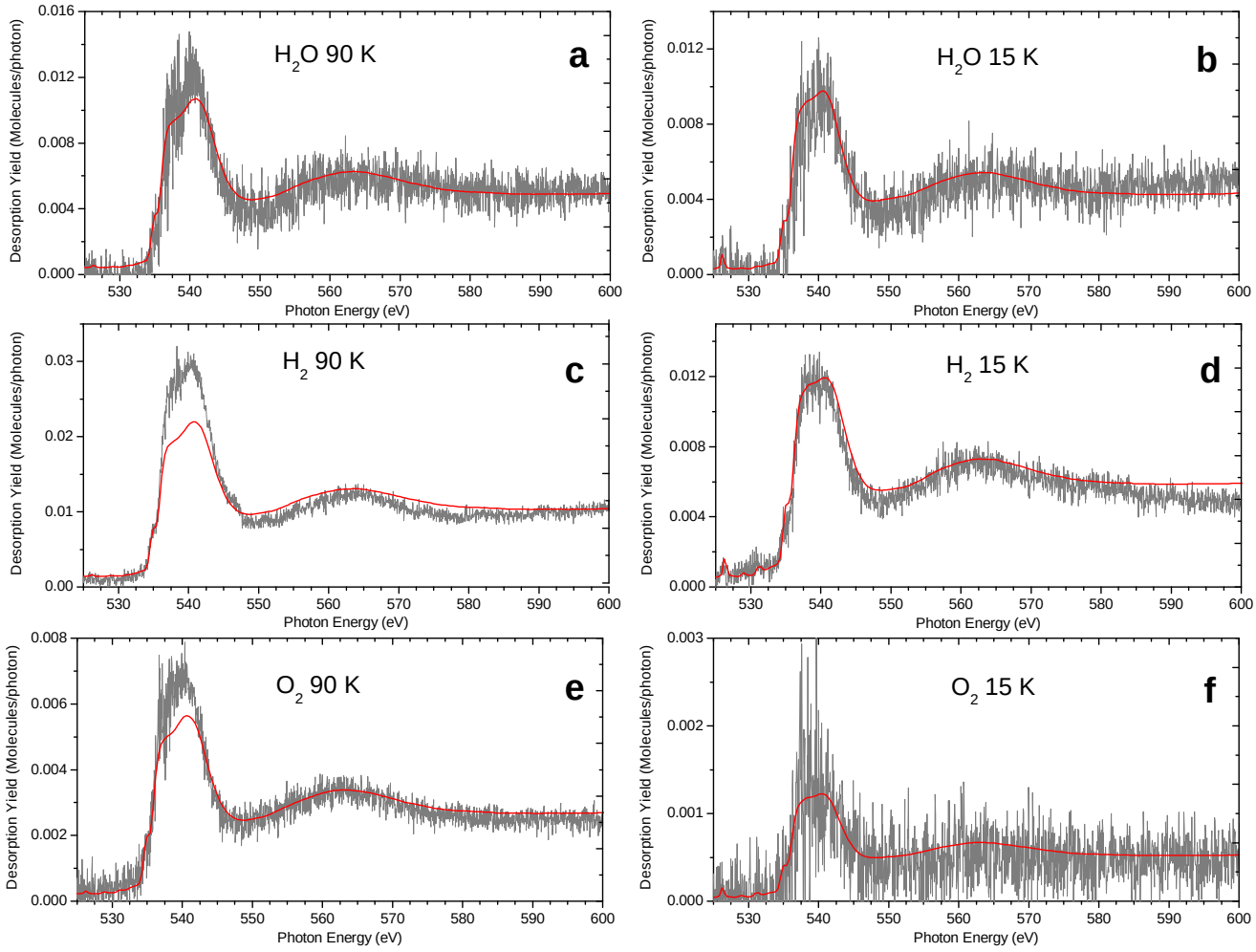

FIG. 3. Photodesorption spectra of neutral molecules, with the TEY (red line) shown for comparison, normalized so as to make the different features match best. a. H_2O at 90 K b. H_2O at 15 K c. H_2 at 90 K d. H_2 at 15 K e. O_2 at 90 K f. O_2 at 15 K

picture we have of how the energy of the initial photon is distributed in the ice. Most of the energy of the initial photon goes into the Auger electron and therefore into the secondary events, which suggests they should dominate desorption. Putting it in numerical terms, since there is one true PID event for 20-25 secondary events (single ionization + creation of a secondary electron that can cause one valence excitation), if all those events have similar partial cross sections for desorption (within an order of magnitude), then the secondary events will obviously dominate. For this to be true, the secondary events need to be energetically sufficient to lead to desorption. Desorption of neutral species has a threshold around 6 eV for electron irradiation[42]. The secondary electrons are therefore energetically able to desorb neutral species, and the single ionization events which dominate the inelastic scattering of the Auger electron can cause desorption of neutral species as well. The only way true PSD could dominate in such a case is if the true PSD process, involving the highly excited initial molecule, is much more efficient than these "simple" excitations to desorb molecules. However, the similarity between the X-ray photodesorption yield per absorbed photon and the electron-stimulated desorption yield does not lend credit to such a possibility. Thus, although a definitive proof is not accessible, we can state with some confidence that XESD dominates the desorption of neutral species.

Desorption of H_2 and O_2 was observed in irradiation by electrons, ions and UV photons before, and it is not surprising that we see these species during X-ray irradiation as well, considering the chemistry triggered by secondary electrons and excitations is expected to be similar. We could not measure desorption of OH radicals, however our sensitivity limit was rather high ($\sim 1 \times 10^{-3}$ molecule/photon). We did not look for H or O fragments, which were seen desorbing under UV irradiation[21], where H is in fact the most abundant desorbing species. Temperature effects on the desorption yields are much more important for the desorption of products of chemistry such as H_2 and O_2 than for H_2O

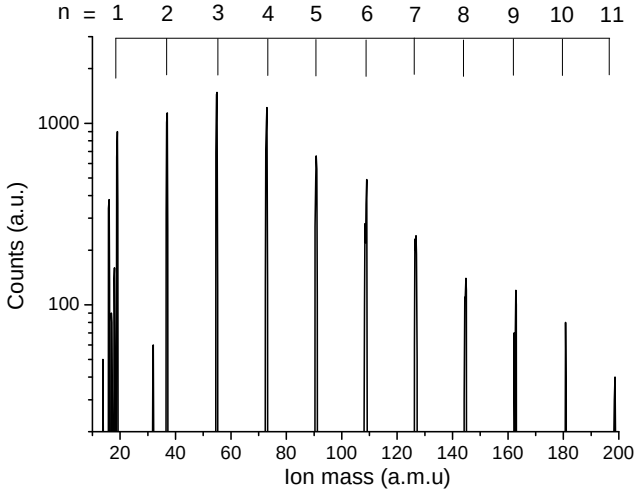

FIG. 4. Mass spectrum of the positive ions desorbing at 540 eV and at 15 K from c-ASW. The protonated clusters $(H_2O)_nH^+$ from n = 1 to 11 are indicated.

(fig. 3). Such effects have been studied in detail for other types or irradiation[35], and include different contributions. The activation of diffusion of some radicals promotes the creation of these species, and they can also overcome their own diffusion and desorption barriers when the temperature is high enough.

In the spectra of H_2 and O_2 desorption at 90 K, a relative increase of the features in the 535-540 eV region relative to the TEY is observed, but it does not seem to have a physical meaning and could instead come from background subtraction issues.

D. Desorption of protonated clusters

The desorption of protonated water clusters $(H_2O)_nH^+$ was observed up until n = 11 (m/z = 199), which is the limit of our mass spectrometer (m/z = 200). The mass spectrum is shown in figure 4. Desorption of protonated clusters from water ice by core-excitation was reported before[43]. It has also been observed and studied in the case of electron[14,44] and ion[45,46] irradiation, as well as in field-assisted photon-stimulated desorption[47] or electron and UV photon stimulated desorption from water adsorbed on rare-gas solids[48,49].

The formation of protonated clusters in ice exposed to dissociative ionisation is expected, as protons created by ionising dissociation can be stabilized in the form of hydronium (H_3O^+) ions, onto which a hydration shell can then form due to the strength of the ion-dipole interaction. Based on this microscopic representation, Floyd & Prince first suggested a model[44] to explain the observed size distribution of the desorbed clusters. The distribution of the intensities of the clusters, when corrected for the apparatus function of the QMS, peaks at n = 3 in our case, then decreases with increasing cluster size. This distribution reflects the balance of the energy required to break the hydrogen bonds and detach a cluster of size n, and the energy gained from the formation of the ion bonds to the cluster. The former energy increases linearly with n, while the latter decreases quickly beyond addition of the first few molecules. Christiansen et al.[45] instead use RRK theory to describe the mass distribution of their clusters. All studies do not present the same maxima for their distributions: while our distribution peaks at n = 3, these of Christiansen et al peak at n = 1, Herring-Captain et al. peak at n = 2, Rocker et al. at n = 2 and Floyd & Prince at n = 5. These differences could come from different experimental conditions (such as the use of a quadrupole mass spectrometer in our case instead of a TOF mass spectrometer, even though we have corrected our distribution for the apparatus function of the QMS), or from the fact that we use X-rays rather than electrons or ions. In the case of water adsorbed on rare gas films, the maximum varies from n = 1 to n = 3 depending on temperature and coverage[48], which confirms the role played by the experimental conditions in the maximum of the distribution.

According to the detailed study of Herring-Captain et al., the mechanism of desorption of cluster ions is distinct from the formation mechanism. The electron energy threshold they observed is above 70 eV, indicating that desorption of clusters requires a complex excitation, such as the formation of a two-hole $(2a_1)^{-2}$ state. The energy for desorption comes from the Coulomb repulsion between the two holes located on the same molecule, i.e. a Coulomb explosion. They argue that the excess energy of the formation of the cluster goes only into their internal modes, and not into translational motion, while no energy from the coulomb interaction is involved in forming the cluster. One of their main argument is the fact that the measured kinetic energy distribution of the clusters is the same for all values of n. We did observe this similarity of kinetic energy distributions as well (not shown). We have also observed a similar temperature effect to theirs: the desorption yield of clusters are slightly higher at 15 K than at 90 K (table I), contrary to all other ions.

The photodesorption spectra of all protonated clusters are similar. An example is shown in figure 5 for $(H_2O)_3H^+$. The spectrum follows the TEY, except for a deviation at high energies where a rising slope seems to be added to the TEY part. Considering the similarities between protonated cluster desorption in ESD and X-ray core excitation, we could argue that XESD dominates the desorption of clusters. However, the case is different from the desorption of neutrals, for which we claimed that XESD dominates. As mentioned previously, desorption of neutrals by electrons has a threshold of around 6 eV, corresponding to "simple" valence excitations or ionizations and easily attained by secondary electrons. On the other hand, clusters desorption has an energy threshold by ESD of as high as 70 eV, corresponding to highly ex-

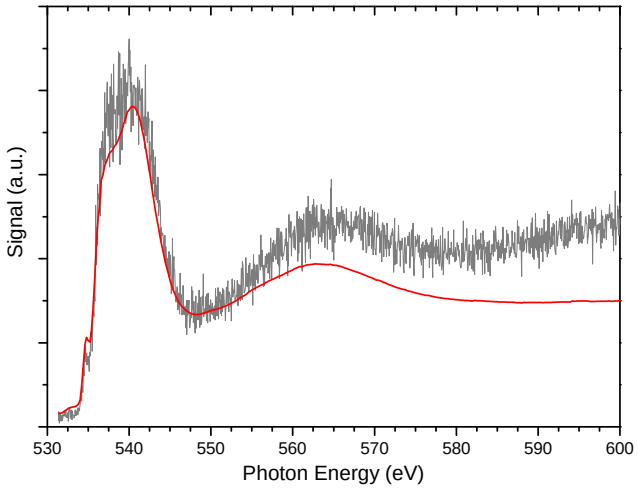

FIG. 5. Photodesorption spectrum of $(H_2O)_3H^+$ at 90 K from c-ASW. Indicated in red is the TEY for comparison, normalized so as to best make the different features match.

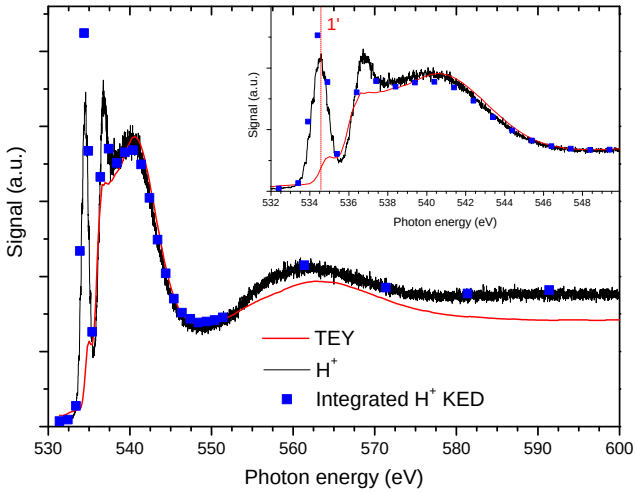

FIG. 6. Photodesorption spectrum of H^+ for a 90 K c-ASW. The black trace is the spectrum at a kinetic energy of 7 eV, while the dots correspond to the signal integrated over the whole kinetic energy distribution (KED), showing that the spectrum at 7 eV is not distorted compared to the integrated signal. Also shown is the TEY (red trace) for comparison, normalized so as to best make the features match. Inset: zoom into the 532-550 eV region, showing the difference between peak 1 and peak 1'.

cited "complex" states[14]. These cannot be reached by secondary electrons. The initial Auger electron can excite such states but not with a high probability. On the other hand, decay of the initially excited molecule naturally leads to this kind of highly excited state. Therefore in this case, there is no good argument favouring XESD, meaning true PSD should play an important role. This is also corroborated by the deviation from the TEY at high energy. It could be suggested that this deviation simply corresponds to a slowly increasing desorption probability following the increasing energy of the photoelectron from core ionisation. However, this is not coherent with the measured ESD threshold of cluster desorption at 70 eV[14]. Considering a ionization potential (IP) at 537 eV[50], the kinetic energy of the photoelectrons would reach 70 eV for a photon energy of 607 eV, which is above our photon energy range. This might instead be linked to multielectron excitations (i.e. excitation/ionisation of a valence electron alongside the core electron) embedded in the ionization continuum, that have a small excitation cross-section (and cannot be seen in the absorption spectrum) but yield final states with multiple holes that are (i) more likely to stay localized on a molecule and (ii) propitious to Coulomb explosion and cluster desorption.

E. Desorption of H^+

As mentioned in the introduction, the desorption of H^+ has been the most studied in water ice core excitation so far. Figure 6 shows the photodesorption spectrum of H^+ at the maximum of the kinetic energy distribution ($\sim$ 7 eV), along with points that correspond to the integrated kinetic energy distributions at various photon energies and a comparison with the TEY. We can see that the photodesorption spectrum shown here corresponds well to the result we obtain by integrating over the whole kinetic energy distribution. We have observed evidence that taking a spectrum at different kinetic energy settings can change the relative intensities of some features, which will not be discussed in this paper.

Here we see that the desorption spectrum deviates from the TEY for several features. A prominent feature of the spectrum is the red-shifted and much more intense peak at 534.4 eV. We will label it peak 1' here. This feature has been studied in detail[13], and as explained in the introduction the following conclusions were reached: (i) it originates from direct core dissociation of surface water molecules, those with a dangling H, and (ii) evidence suggests a fast dissociation mechanism, with significant nuclear motion already during the lifetime of the core hole. The surface origin of the feature is confirmed by surface-sentitive grazing incidence Auger electron spectroscopy[51]. The fast dissociation mechanism is further compounded by desorbing ion/Auger electron coincidence studies[52], which reveals what final states are involved in desorption.

We have measured the kinetic energy distribution of H^+ ions at various photon energies (fig. 7). Some rough measurements had already been presented by Coulman et al.[13], who had remarked that ions created at the pre-edge feature were slower than others. Here we see that H^+ at the main edge excitation or above ionisation at 600 eV have the same kinetic energy distribution, while it is very different for ions at peak 1' (534.4 eV). The kinetic energy distribution at peak 1' is narrower and has a maximum at lower kinetic energy. This difference is

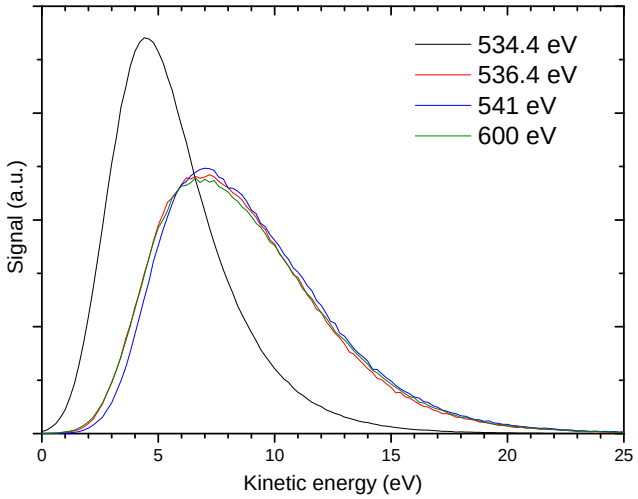

FIG. 7. Kinetic energy distributions of H^+ ions at different photon energies, for c-ASW at 90 K.

well explained considering the fast dissociation mechanism. When exciting peak 1', the O-H bond is significantly elongated during the lifetime of the core hole, and the kinetic energy acquired by the proton is thus governed by the shape of the repulsive potential curve of the core-excited state along this coordinate. For other photon energies, various final states (2h1e and 2h states involving different valence orbitals) are at the origin of the proton fragments and the kinetic energy reflects the variety of these states (see ref[36,53] for a detailed discussion of the kinetic energies for the different final states).

Another feature is visible on the spectrum at 536.8 eV that resembles peak 1', in the sense that it is a sharp peak more intense than in the TEY, although the increase is not as dramatic as in the case of peak 1'. This feature has been suggested to correspond to a surface feature as well[13]. It is however different from the previously discussed feature, as at this photon energy the kinetic energy distribution is similar to other photon energies (fig. 7). This peak has a polarization dependence orthogonal to peak 1' according to the detailed polarization dependence studies of Coulman et al.[13]. Coincidence studies around this energy show the expected results for regular Auger decay[18] (i.e. results similar to those obtained when probing "bulk" features), however the peak is not evident in their spectra, which might be due to the polarization they used. Still, the conclusion is that there is no evidence of fast dissociation associated with this feature, which is however a true PSD feature.

The H^+ spectrum also deviates from the TEY in the EXAFS region, from 550 eV and above. The EXAFS region, and the first EXAFS oscillation at around 560 eV, are characteristic of the O-O distance and arrangement inside the ice. Therefore it was previously suggested that the discrepancy between the H^+ and the TEY spectra could be attributed to a surface vs bulk behaviour as well[13,17], with the surface molecules having higher average O-O distances. The difference derived from an EXAFS analysis by Parent et al.[17] was rather small, 2.76 Å for the bulk vs 2.77 Å for the surface. On the other hand, Coulman et al.[13] had previously claimed that EXAFS analysis of the H^+ spectrum was not possible, due to the fact that in this region, contrary to peak 1', secondary electrons and bulk excitations still contribute significantly to the H^+ yield. The spectrum in this region is therefore more complicated to interpret. Aside from the peak shift, there is also an increase of the non-resonant continuum relative to the rest. It is worth noting that this increase is slightly different from the rise observed in the clusters spectra, but this does not preclude the possibility of a similar explanation: the role played by multi-electron excitations. Such states would indeed be expected to have higher proton fragment yields than double-ionized states, as they are more likely to stay localized on the molecule and lead to a Coulomb explosion. Multi-electron excitations have been shown to play an even more important role in desorption of ions after core ionization of adsorbed CO, for example[54].

True PSD and surface molecules therefore clearly play an important role in H^+ desorption. However, outside of peak 1' it is difficult to separate the possible contributions of true PSD and XESD. It is even less likely that H^+ desorption is a surface-only probe in the whole region of the spectrum.

F. Desorption of H^-

The desorption of anions in X-ray core excitation of condensed molecules has been observed before[55,56], showing such highly ionizing radiation can still yield negative ions. Anions in the present case can come from two distinct mechanisms, once again related to the distinction between XESD and true photodesorption. Electrons can mainly create anions by dissociative electron attachment (DEA) or by ion pair dissociation. Low energy electron stimulated desorption of anions from water ice, especially through the DEA process, has been studied extensively[57,58]. The DEA resonance of water around 7-9 eV corresponds well to the typical energy of secondary electrons, while the Auger electron and higher energy secondaries can cause ion pair dissociation from the neutral molecule. The other possibility for anion formation is direct dissociation of the core excited molecule in an anion fragment and highly charged cation fragments. Such dissociation pathways, although less likely than cation or cation-neutral dissociation, have been observed in the gas phase[59–61]. Their cross-section is typically 10^{-3}-10^{-4} lower than dissociation pathways involving only cations and neutrals[59].

Fig 8 shows the photodesorption spectrum of H^- at 90 K at the maximum of the kinetic energy distribution, along with a comparison with the TEY. The integrated KEDs for H^- show a good match with the displayed spectrum, confirming its shape. The photodes-

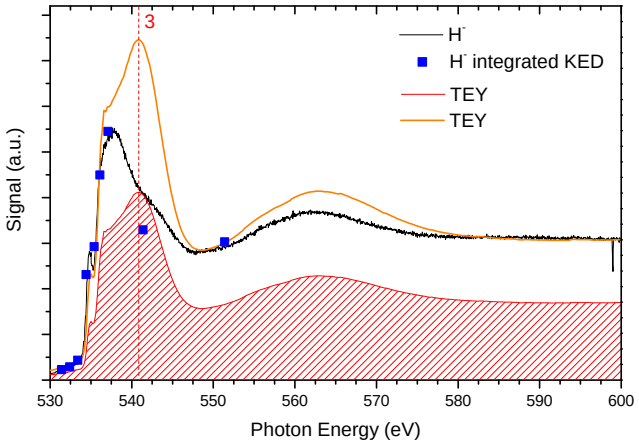

FIG. 8. Photodesorption spectrum of H^- at 90 K from c-ASW, at the maximum of the kinetic energy (black trace). The blue dots are the integrated H^- KED. The TEY is indicated as an orange trace (normalized at 600 eV) and as a hatched red area under the H^- desorption spectrum, representing the maximum contribution of XESD to H^- desorption (see the text).

orption spectrum differs markedly from the TEY around 541 eV, where the post-edge feature (peak 3) is strongly suppressed, and in the ionization continuum. The maximum contribution of XESD to the desorption of H^- can be estimated from these differences. Indeed, the contribution of the XESD in the spectrum has to follow the spectral shape of the TEY. This maximum contribution corresponds to the hatched TEY-shaped area in red under the H^- desorption spectrum. This hatched area is approximately 60% of the total area. Conversely, true photodesorption processes in this spectrum therefore account for at least 40% of the H^- desorption. This quantification is only indicative as it depends on the energy range considered, but what we can conclude is that there has to be a true PSD process with an efficiency at least comparable to XESD. Such a result is surprising considering the orders of magnitude difference of cross-sections for the dissociation pathways involving or not an anion, mentioned above. We find an estimated one order of magnitude difference between desorption of H^+ and H^- (assuming similar detection efficiencies for both ions). There is therefore a gap of at least two orders of magnitude with the gas phase results. One possibility is that the difference occurs at the desorption step, but it is difficult to see why H^- would have a much higher desorption probability than H^+ after formation. The more likely explanation is a condensed phase effect. All the possible rapid charge transfers to neighbouring molecules that can occur in the condensed phase seem to enhance significantly the probability of anion formation during core-excited/ionized water dissociation.

On the H^- desorption spectrum (fig. 8), intensity is missing on peak 3, which as mentioned previously is attributed to four-coordinated molecules and a delocalized excitation. A delocalized excitation means the final state after Auger decay will a be a 2h state, as the electron density is quickly delocalized over several molecules. We could expect a 2h state to be less likely to yield anions than a 2h1e state, but then the H^- signal in the ionization continuum would also be suppressed relative to the pre and main edge (peaks 1 and 2). This missing intensity may then rather be linked to the fact that mostly four-coordinated molecules are excited here, which for a reason yet to be found is less likely to yield anions. A similar explanation can also hold for the lessened EXAFS oscillation, i.e. a resonance also linked with the coordination shell of the molecules.

G. Desorption of oxygen-bearing ions

The desorption of fragment cations other than H^+ was previously observed[13] during core excitation with a much lower yield than for H^+ but no detailed studies were performed, and in particular no spectra were shown. The observation of low yields of oxygen-bearing fragments (O^+, OH^+, H_2O^+) desorbing from water ice is a common feature of not only soft X-ray irradiation[13], but also XUV irradiation[15] and medium energy (100-200 eV) electrons[14]. Studies of anion desorption by dissociative electron attachment (DEA) of low-energy (<20 eV) electrons on water ice also reported very low O^- and OH^- desorption signals[62]. Our estimated desorption yields for oxygen-bearing fragments are, similarly, much lower than H^+(table I). Several reasons can be invoked to explain these observations.

As the oxygen cation and anion fragments are readily observed in core dissociation of gas-phase water[59,60,64], we cannot ascribe the observed lower desorption of these fragments to a dissociation branching ratio that would favor neutral oxygen radicals instead of ions so heavily, especially in cases where multiple holes are involved. One important difference is the kinetic energy of the different fragments. In dissociation of an isolated water molecule into two fragments H and OH (regardless of their charge), momentum conservation implies that the H fragment takes away ∼94% of the kinetic energy, and little is left for the oxygen-bearing fragment. In the case of dissociation into three fragments, the symmetry of the molecule also plays a role: it has been observed in Coulomb explosion of molecules that the central atom has much less kinetic energy because the recoil energy of the peripheric fragments compensate[65]. Such would be the case for dissociation of H_2O in H + O + H. In a condensed medium there are also other channels for energy loss, as well as environment effects on the symmetry of the molecules, so that the theoretical kinetic energy partition in the isolated molecule is only an upper limit. The lower kinetic energy of the oxygen fragments would reduce their probability to overcome the desorption barrier.

Other explanations have been suggested to explain this low desorption yield: one explanation is based on

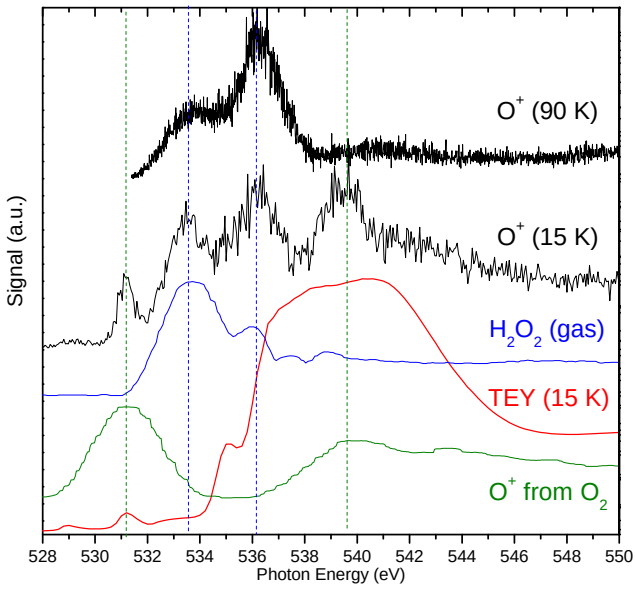

FIG. 9. Photodesorption spectra of O^+ at 90 and 15 K from c-ASW. The TEY is indicated (red trace) for comparison, along with the gas-phase absorption spectrum of H_2O_2 (blue trace), adapted from Ruhl et al.[63] and shifted to match the first H_2O_2 peak, and the O^+ desorption spectrum for O_2 ice (green trace) from Rosenberg et al.[24]

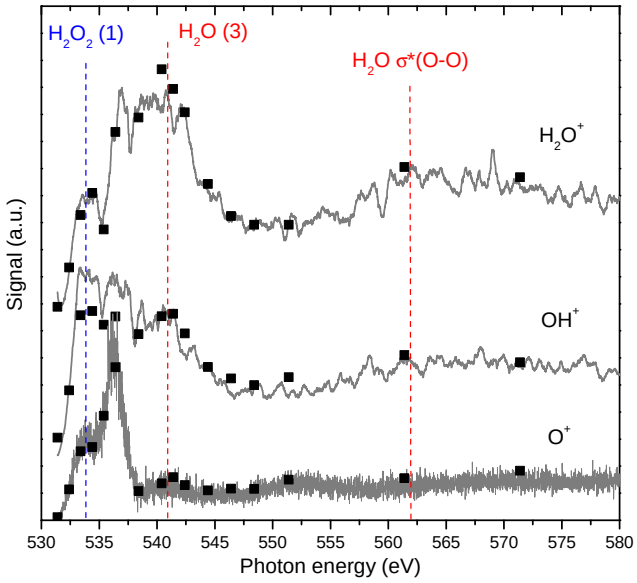

FIG. 10. Photodesorption spectra of O^+, OH^+ and H_2O^+ at 90 K from c-ASW. The spectra were taken at the maxima of the kinetic energy distributions of the ions. The spectra of OH^+ and H_2O^+ have been smoothed. Also indicated are the integrated kinetic energy distributions at various photon energies (black dots) to show that these spectra are indeed representative of the non-differentiated spectra. The attribution of the main features are given, indicating the molecule and peak attribution, using the same color code as in fig. 9. The curves have been arbitrarily scaled to have roughly the same size.

the assumption that the surface orientation of water molecules is always unfavourable to desorption of oxygen fragments[15]. Another stems from the fact that there is a competition between desorption of an ion and decay of the ionic state through reneutralization[36]. The H-bond network of ice facilitates rapid intermolecular charge transfer processes. This is in fact also linked with the previous argument on kinetic energies: fragments with lower kinetic energies will spend a longer time at or near the surface before escaping, which increases the likelihood of their reneutralization. Another possibility that would prevent desorption is if the cation is trapped. Once again, the trapping probability should be higher for slower ions, considering the time it would take for the structural rearrangement of surrounding dipoles that would stabilize the ion in the ice. Such a structural rearrangement certainly could not occur in the case of fast desorption of H^+, for example, which takes place on a timescale of a few tens of fs.

The desorption spectra of oxygen-bearing fragments provide useful information to discuss their low desorption efficiency. The desorption spectrum of O^+ in fig. 9 bears no resemblance to the TEY. Instead the spectrum at 90 K is dominated by two features which can be recognized as two peaks of the spectrum of H_2O_2. The first one is in fact visible in the TEY as mentioned in section B. The comparison to the gas phase H_2O_2 spectrum (O^+ yield[63], shifted to match the first peak) shown in the figure allows to attribute the second feature, which is not visible in the TEY where it would overlap with and be hidden by the water peaks. Looking at the desorption spectrum of O^+ at 15 K (fig. 9), two other features are observed which can be attributed to O_2 (the desorption of O^+ from O_2 ice from Rosenberg et al.[16] is shown as well for comparison). Once again the first O_2 feature is visible in the TEY, although weak, and we saw that it was more abundant in the ice at 15 K than at 90 K. This spectral information indicates that the desorption of O^+ is dominated by direct excitation and dissociation (therefore a true PSD process) of products of the photochemistry, which are present only at the few percent level in the ice. We cannot exclude that the concentration of photoproducts is higher at the surface than in the bulk, because diffusion of radicals, and the subsequent chemistry, can be different at the surface. Still, considering the relative abundances, the desorption of O^+ through excitation of these photoproducts must be much more efficient than through XESD or direct excitation of H_2O. This strong contribution of H_2O_2 is also seen in the desorption spectra of the other oxygen-bearing fragments, OH^+, H_2O^+ (fig. 10), O^- and OH^- (fig. 11).

These observations are coherent with the idea that kinetic energy partition during dissociation is important. Indeed, dissociation of H_2O_2 or O_2 instead of H_2O implies breaking (at least) an O-O bond, yielding fragments of similar masses and thus releasing more energy into

oxygen-bearing fragments. It would also at first weaken the explanation of a competition between desorption and decay of an ionic state, as there is no reason that an O^+ or OH^+ fragment from H_2O_2 would have a different decay probability than if they resulted from H_2O dissociation. However this is not completely ruled out because, as pointed out above the explanations can be complementary rather than contradictory: a higher kinetic energy for the fragment implies less time spent in the ice and thus a lower probability of decay. Another consideration is that we do not know the structural arrangement of photoproducts in the ice: if the connection of these species to the H-bonding network is poor, the lifetime of the ionic states could be longer and also favor desorption. Similarly if there are species with dangling OH or O pointing outwards at the surface desorption would be favored. The various factors explaining low desorption of O-bearing fragments from ice (kinetic energy partition from dissociation, reneutralization probability, structural arrangement...) are inter-connected, thus it is difficult to rule out one of them, but the present experimental observations are consistent with the general picture they form.

Comparisons of the spectra of the different fragments also show some interesting differences. In fig. 10, the spectra of O^+, OH^+ and H_2O^+ for a 90 K ice are plotted. The integrated kinetic energy distributions at different photon energies are plotted as well (black dots) to show that the displayed spectra are indeed representative of the non-differentiated spectra. We can see that the relative contributions to the desorption of H_2O_2 and H_2O (either XESD or true PSD), as indicated by the relative intensities of the first H_2O_2 peak and the H_2O peak 3 and σ^*(O-O), are different for the three ions. The spectrum of O^+ is devoid of any clear H_2O features. On the other hand, the H_2O peak 3 at 541 eV and the σ^*(O-O) at 562 eV are visible in the spectrum of OH^+, although strong contributions of H_2O_2 are still present. In the H_2O^+ spectrum, the H_2O contributions become stronger than the H_2O_2 contributions.

The difference between O^+ and OH^+ would be in line with the symmetry considerations mentioned above: in dissociation of H_2O in H + H + O^+ (regardless of the charge of the H fragments), not only is the kinetic energy taken away by the lighter H fragments, the central place of the O atom would also yield it even less kinetic energy than in the case of a dissociation in two fragments. This could explain the absence of any water-related feature in the O^+ spectrum. The case of H_2O^+ is different: H_2O^+ is the result of simple ionization of water, with no dissociation is involved. Simple ionization is unlikely to lead to H_2O^+ desorption, considering there should be a rather high desorption barrier due to the stability of the ion in a water matrix (and also the competition with formation of H_3O^+, presumably). A mechanism should therefore be invoked to explain the contribution of H_2O to the yield. One possibility is that the energy for desorption comes from Coulomb repulsion between two neighbour ionized

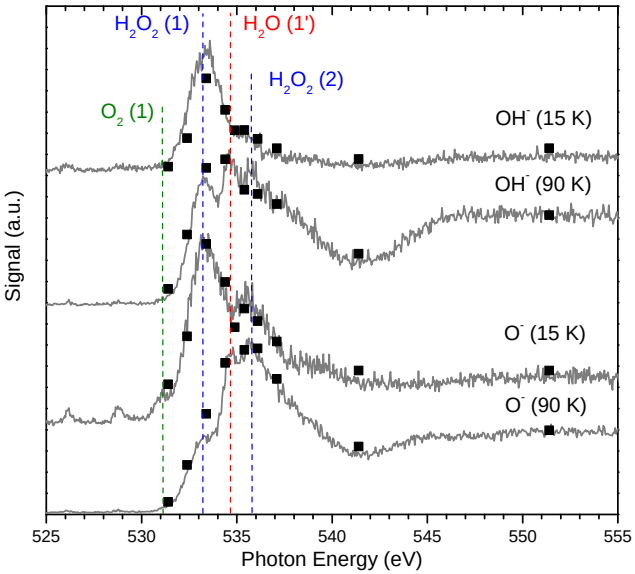

FIG. 11. Photodesorption spectra of O^- and OH^- at 90 K or 15 K from c-ASW. The spectra were taken at the maxima of the kinetic energy distributions of the ions. Also indicated are the integrated kinetic energy distributions at various photon energies (black dots) to show that the these spectra are indeed representative of the non-differentiated spectra. The attribution of some peaks are given, with the molecule and the number of the peak, using the same color code as in fig. 9. The curves have been arbitrarily scaled to have roughly the same size.

molecules. Such a situation can happen when a charge transfer or proton transfer occurs from a 2h final state, or when the core ionized state undergoes intermolecular coulombic decay (ICD), i.e. the Auger electron is directly ejected from a neighbour molecule of the core ionized one. If we consider such a mechanism to be at the origin of H_2O^+ desorption after H_2O excitation, it is more likely that true PSD will dominate over XESD, since double-ionization processes are not energetically possible for secondary electrons and not very likely for Auger electron scattering.

The desorption spectra of the anions O^- and OH^- are shown in the edge region in figure 11 (at 15 and 90 K) and extended up to 600 eV in figure 12 (at 90 K only). The H_2O_2 features are prominent in the edge region while the bulk water features such as peak 3 at 541 eV and the σ^*(O-O) resonance at 560 eV are completely absent, similar to O^+ (fig. 9), although the spectra are still different in the continuum region. However, surprisingly, a peak corresponding to peak 1' of water at 534.4 eV is observed, especially at 90 K (at 15 K it could be hidden by the H_2O_2 peaks). The presence of this peak in the absence of any other water feature is surprising and suggests that O^- and OH^- anions may be produced in the fast desorption process discussed for H^+. This is especially surprising in the case of OH^-, since formation of OH^- from water dissociation after core excitation

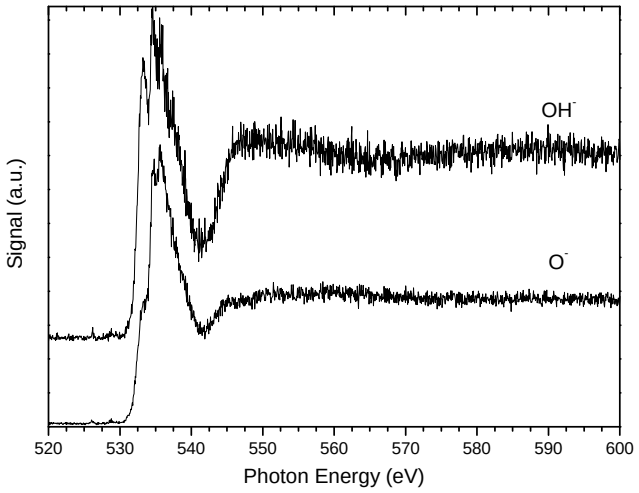

FIG. 12. Photodesorption spectra of O^- and OH^- at 90 K from c-ASW, from 520 to 600 eV. The spectra were taken at the maxima of the kinetic energy distributions of the ions. The curves have been arbitrarily scaled to have roughly the same size.

necessarily implies either charge transfer to neighbouring molecules or radiative, rather than Auger decay (1% of the events). More investigations would be required to see if this apparent feature can truly be attributed to H_2O. Another feature that is distinctive of these two ions is the ionization continuum (fig. 12, above ∼540 eV), for which we see a clear sigmoid shape with no EXAFS feature or shape resonance. A possible attribution of this feature is the ionization continuum of H_2O_2. However, the fact that it is not seen for O^+ raises doubt about this interpretation. The lack of resemblance with the TEY of these continuum features rules out an XESD contribution. A true PSD contribution from H_2O excitation is also unlikely, since no dissociation pathway starting from excited H_2O^{2+} (after core ionization and Auger decay) could yield O^- or OH^-. Such a true PSD process would only be possible, again, if transfer of a positive charge to a neighbouring molecule occurs, or after radiative decay.

IV. CONCLUSION

The objective of this study was to explore all the species that are released in the gas phase when core-exciting amorphous water ice, to attempt to distinguish different desorption mechanisms when possible, and to see what information can the desorption of some specific species tell us about dissociation, chemistry and relaxation following core-excitation. We have observed neutral species, cations and anions (summarized in table I), and the escaping electrons as well. We quantified the desorption of neutrals and the escaping electrons, and tentatively quantified the desorption of ions.

We conclude that XESD - desorption mediated by the Auger and secondary electrons - is dominant in neutral desorption. For ions, there is evidence that this is not the case at all photon energies and true PSD processes - desorption mediated directly by the core-excited/ionized molecule - contribute as well. XESD could play a role in the desorption of H^+ or protonated clusters, but it is much less clear than for neutrals. True PSD is at least as efficient as XESD in the case of H^- desorption, so that there must exist dissociation pathways of core-excited and even core-ionized H_2O that lead to anions, in addition to the processes induced by secondary electrons. These dissociation pathways are identified in the gas phase but are not very efficient, so the very clear signals we obtain for ion desorption are still somewhat surprising and suggest a strong condensed phase effect (due to the possibility of charge transfers) favouring anion formation. We have also shown that true PSD dominates completely O^+ desorption and always plays a major role in the desorption of other oxygen fragment ions (OH^+, H_2O^+, O^-, OH^-). An important conclusion for these oxygen fragments is that true PSD following core-excitation of water itself is not efficient: instead true PSD following core-excitation of radiolysis products and in particular H_2O_2 plays a very important role.

Now after this broad exploration, efforts should focus on the details of the desorption of specific species such as H^- or O^+, similarly to the work that has been done on H^+, to further understand the information they can yield on core-excitation of water ice, since clearly interesting elements remain to be uncovered.

ACKNOWLEDGMENTS

This work was done in collaboration and with financial support by the European Organization for Nuclear Research (CERN) under the collaboration agreement KE3324/TE. We acknowledge SOLEIL for provision of synchrotron radiation facilities under the projects 20161406 and 20181140 and we thank Nicolas Jaouen and the SEXTANTS team for their help on the beamline. This work was supported by the Programme National Physique et Chimie du Milieu Interstellaire (PCMI) of CNRS/INSU with INC/INP co-funded by CEA and CNES. Financial support from the LabEx MiChem, part of the French state funds managed by the ANR within the investissements d'avenir program under reference ANR-11-10EX-0004-02, and by the Ile-de-France region DIM ACAV program, is gratefully acknowledged.

[1] E. F. van Dishoeck, E. Herbst, and D. A. Neufeld, Chemical Reviews **113**, 9043 (2013).
[2] E. F. Van Dishoeck, E. A. Bergin, D. C. Lis, and J. I. Lunine, arXiv preprint arXiv:1401.8103 (2014).
[3] A. M. Grannas, A. E. Jones, J. Dibb, M. Ammann, C. Anastasio, H. J. Beine, M. Bergin, J. Bottenheim, C. S. Boxe, G. Carver, G. Chen, J. H. Crawford, F. Domine, M. M. Frey, M. I. Guzman, D. E. Heard, D. Helmig, M. R. Hoffmann, R. E. Honrath, L. G. Huey, M. Hutterli, H. W. Jacobi, P. Klan, B. Lefer, J. McConnell, J. Plane, R. Sander, J. Savarino, P. B. Shepson, W. R. Simpson,

J. R. Sodeau, R. Weller, E. W. Wolff, and T. Zhu, Atmos. Chem. Phys. , 45 (2007).
[4]R. Dupuy, M. Bertin, G. Féraud, M. Hassenfratz, X. Michaut, T. Putaud, L. Philippe, P. Jeseck, M. Angelucci, R. Cimino, V. Baglin, C. Romanzin, and J.-H. Fillion, Nature Astronomy **2**, 796 (2018).
[5]M. R. Hogerheijde, E. A. Bergin, C. Brinch, L. I. Cleeves, J. K. Fogel, G. A. Blake, C. Dominik, D. C. Lis, G. Melnick, D. Neufeld, *et al.*, Science **334**, 338 (2011).
[6]I. Kamp, W.-F. Thi, G. Meeus, P. Woitke, C. Pinte, R. Meijerink, M. Spaans, I. Pascucci, G. Aresu, and W. R. F. Dent, Astronomy & Astrophysics **559**, A24 (2013).
[7]E. Mitchell, U. Raut, D. Fulvio, M. Schaible, C. Dukes, and R. Baragiola, Planetary and Space Science **89**, 42 (2013).
[8]B. C. Garrett, D. A. Dixon, D. M. Camaioni, D. M. Chipman, M. A. Johnson, C. D. Jonah, G. A. Kimmel, J. H. Miller, T. N. Rescigno, P. J. Rossky, S. S. Xantheas, S. D. Colson, A. H. Laufer, D. Ray, P. F. Barbara, D. M. Bartels, K. H. Becker, K. H. Bowen, S. E. Bradforth, I. Carmichael, J. V. Coe, L. R. Corrales, J. P. Cowin, M. Dupuis, K. B. Eisenthal, J. A. Franz, M. S. Gutowski, K. D. Jordan, B. D. Kay, J. A. LaVerne, S. V. Lymar, T. E. Madey, C. W. McCurdy, D. Meisel, S. Mukamel, A. R. Nilsson, T. M. Orlando, N. G. Petrik, S. M. Pimblott, J. R. Rustad, G. K. Schenter, S. J. Singer, A. Tokmakoff, L.-S. Wang, and T. S. Zwier, Chemical Reviews **105**, 355 (2005).
[9]E. Alizadeh and L. Sanche, Chemical Reviews **112**, 5578 (2012).
[10]A. Nilsson, D. Nordlund, I. Waluyo, N. Huang, H. Ogasawara, S. Kaya, U. Bergmann, L.-å. Näslund, H. Öström, P. Wernet, K. Andersson, T. Schiros, and L. Pettersson, Journal of Electron Spectroscopy and Related Phenomena **177**, 99 (2010).
[11]T. Bartels-Rausch, V. Bergeron, J. H. E. Cartwright, R. Escribano, J. L. Finney, H. Grothe, P. J. Gutiérrez, J. Haapala, W. F. Kuhs, J. B. C. Pettersson, S. D. Price, C. I. Sainz-Díaz, D. J. Stokes, G. Strazzulla, E. S. Thomson, H. Trinks, and N. Uras-Aytemiz, Reviews of Modern Physics **84**, 885 (2012).
[12]J. C. Palmer, P. H. Poole, F. Sciortino, and P. G. Debenedetti, Chemical Reviews **118**, 9129 (2018).
[13]D. Coulman, A. Puschmann, U. Höfer, H.-P. Steinrück, W. Wurth, P. Feulner, and D. Menzel, The Journal of Chemical Physics **93**, 58 (1990).
[14]J. Herring-Captain, G. A. Grieves, A. Alexandrov, M. T. Sieger, H. Chen, and T. M. Orlando, Physical Review B **72** (2005), 10.1103/PhysRevB.72.035431.
[15]R. A. Rosenberg, V. Rehn, V. O. Jones, A. K. Green, C. C. Parks, G. Loubriel, and R. H. Stulen, Chemical Physics Letters **80**, 488 (1981).
[16]R. A. Rosenberg, P. R. LaRoe, V. Rehn, J. Stöhr, R. Jaeger, and C. C. Parks, Physical Review B **28**, 3026 (1983).
[17]P. Parent, C. Laffon, C. Mangeney, F. Bournel, and M. Tronc, The Journal of Chemical Physics **117**, 10842 (2002).
[18]K. Mase, M. Nagasono, S.-i. Tanaka, T. Sekitani, and S.-i. Nagaoka, Low Temperature Physics **29**, 243 (2003).
[19]R. Romberg, S. Frigo, A. Ogurtsov, P. Feulner, and D. Menzel, Surface Science **451**, 116 (2000).
[20]R. Weimar, R. Romberg, B. Naydenov, D. Menzel, and P. Feulner, Chemical Physics Letters **510**, 78 (2011).
[21]A. Yabushita, T. Hama, and M. Kawasaki, Journal of Photochemistry and Photobiology C: Photochemistry Reviews **16**, 46 (2013).
[22]G. A. Kimmel, K. P. Stevenson, Z. Dohnálek, R. S. Smith, and B. D. Kay, The Journal of Chemical Physics **114**, 5284 (2001).
[23]E. Hamers, W. van Sark, J. Bezemer, W. Goedheer, and W. van der Weg, International Journal of Mass Spectrometry and Ion Processes **173**, 91 (1998).
[24]R. A. Rosenberg, P. J. Love, P. R. LaRoe, V. Rehn, and C. C. Parks, Physical Review B **31**, 2634 (1985).
[25]N. Tıṁneanu, C. Caleman, J. Hajdu, and D. van der Spoel, Chemical Physics **299**, 277 (2004).
[26]W. L. Jorgensen and L. Salem, *The Organic Chemist's Book of Orbitals* (Academic Press, 1973).
[27]G. R. Wight and C. E. Brion, Journal of Electron Spectroscopy and Related Phenomena **4**, 25 (1974).
[28]K. Kobayashi, The Journal of Physical Chemistry **87**, 4317 (1983).
[29]M. Tronc and R. Azria, International Journal of Mass Spectrometry , 7 (2001).
[30]J. S. Tse, D. M. Shaw, D. D. Klug, S. Patchkovskii, G. Vankó, G. Monaco, and M. Krisch, Physical Review Letters **100** (2008), 10.1103/PhysRevLett.100.095502.
[31]M. Cavalleri, H. Ogasawara, L. Pettersson, and A. Nilsson, Chemical Physics Letters **364**, 363 (2002).
[32]J. A. Sellberg, S. Kaya, V. H. Segtnan, C. Chen, T. Tyliszczak, H. Ogasawara, D. Nordlund, L. G. M. Pettersson, and A. Nilsson, The Journal of Chemical Physics **141**, 034507 (2014).
[33]E. Dartois, B. Augé, H. Rothard, P. Boduch, R. Brunetto, M. Chabot, A. Domaracka, J.-J. Ding, O. Kamalou, X.-Y. Lv, E. F. da Silveira, J.-C. Thomas, T. Pino, C. Mejia, M. Godard, and A. de Barros, Nuclear Instruments and Methods in Physics Research Section B: Beam Interactions with Materials and Atoms **365**, 472 (2015).
[34]C. Laffon, S. Lacombe, F. Bournel, and P. Parent, The Journal of Chemical Physics **125**, 204714 (2006).
[35]R. E. Johnson, in *Physics and Chemistry at Low Temperatures* (2011) pp. 297–339.
[36]D. E. Ramaker, Chemical Physics **80**, 183 (1983).
[37]W. C. Simpson, T. M. Orlando, L. Parenteau, K. Nagesha, and L. Sanche, The Journal of Chemical Physics **108**, 5027 (1998).
[38]Q.-B. Lu and L. Sanche, Physical Review B **63** (2001).
[39]B. Gervais, M. Beuve, G. Olivera, and M. Galassi, Radiation Physics and Chemistry **75**, 493 (2006).
[40]X. Pan, A. D. Bass, J.-P. Jay-Gerin, and L. Sanche, Icarus **172**, 521 (2004).
[41]N. G. Petrik and G. A. Kimmel, The Journal of Chemical Physics **123**, 054702 (2005).
[42]G. A. Kimmel, T. M. Orlando, C. Vézina, and L. Sanche, The Journal of Chemical Physics **101**, 3282 (1994).
[43]G. Rocker, D. Coulman, P. Feulner, R. Scheuerer, Z. Lin, and D. Menzel, in *Desorption Induced by Electronic Transitions DIET IV*, Vol. 19, edited by G. Ertl, R. Gomer, H. K. V. Lotsch, G. Betz, and P. Varga (Springer Berlin Heidelberg, Berlin, Heidelberg, 1990) pp. 261–267.
[44]G. R. Floyd and R. H. Prince, Nature Physical Science **240**, 11 (1972).
[45]J. W. Christiansen, I. S. T. Tsong, and S. H. Lin, The Journal of Chemical Physics **86**, 4701 (1987).
[46]R. Martinez, A. N. Agnihotri, P. Boduch, A. Domaracka, D. Fulvio, G. Muniz, M. E. Palumbo, H. Rothard, and G. Strazzulla, J. Phys. Chem. A , 8 (2019).
[47]S. Jaenicke, A. Ciszewski, W. Drachsel, U. Weigmann, T. T. Tsong, J. R. Pitts, J. H. Block, and D. Menzel, Le Journal de Physique Colloques **47**, C7 (1986).
[48]R. Souda, Surface science **506**, L275 (2002).
[49]T. Tachibana, T. Miura, and I. Arakawa, Low Temperature Physics **32**, 1092 (2006).
[50]B. Baron and F. Williams, The Journal of Chemical Physics **64**, 3896 (1976).
[51]D. Nordlund, H. Ogasawara, P. Wernet, M. Nyberg, M. Odelius, L. Pettersson, and A. Nilsson, Chemical Physics Letters **395**, 161 (2004).
[52]K. Mase, M. Nagasono, S. Tanaka, T. Urisu, E. Ikenaga, T. Sekitani, and K. Tanaka, The Journal of Chemical Physics **108**, 6550 (1998).
[53]M. T. Sieger, W. C. Simpson, and T. M. Orlando, Physical Review B **56**, 4925 (1997).
[54]P. Feulner, R. Romberg, S. P. Frigo, R. Weimar, M. Gsell, A. Ogurtsov, and D. Menzel, Surface science **451**, 41 (2000).
[55]G. Dujardin, L. Hellner, B. J. Olsson, M. J. Besnard-Ramage, and A. Dadouch, Physical Review Letters **62**, 745 (1989).
[56]D. P. P. Andrade, M. L. M. Rocco, and H. M. Boechat-Roberty, Monthly Notices of the Royal Astronomical Society **409**, 1289

(2010).
[57] M. Tronc, R. Azria, Y. Le Coat, and E. Illenberger, The Journal of Physical Chemistry **100**, 14745 (1996).
[58] W. C. Simpson, L. Parenteau, R. S. Smith, L. Sanche, and T. M. Orlando, Surface science **390**, 86 (1997).
[59] W. C. Stolte, M. M. Sant'Anna, G. Öhrwall, I. Dominguez-Lopez, M. N. Piancastelli, and D. W. Lindle, Physical Review A **68** (2003), 10.1103/PhysRevA.68.022701.
[60] M. N. Piancastelli, R. Sankari, S. Sorensen, A. De Fanis, H. Yoshida, M. Kitajima, H. Tanaka, and K. Ueda, Physical Review A **71** (2005), 10.1103/PhysRevA.71.010703.
[61] C. Stråhlman, A. Kivimäki, R. Richter, and R. Sankari, The Journal of Physical Chemistry A **120**, 6389 (2016).
[62] X. Pan, H. Abdoul-Carime, P. Cloutier, A. D. Bass, and L. Sanche, Radiation Physics and Chemistry **72**, 193 (2005).
[63] E. Rühl and A. P. Hitchcock, Chemical physics **154**, 323 (1991).
[64] M. N. Piancastelli, A. Hempelmann, F. Heiser, O. Gessner, A. Rüdel, and U. Becker, Physical Review A **59**, 300 (1999).
[65] T. A. Carlson, in *Desorption Induced by Electronic Transitions DIET I*, Vol. 24, edited by V. I. Goldanskii, R. Gomer, F. P. Schäfer, J. P. Toennies, N. H. Tolk, M. M. Traum, J. C. Tully, and T. E. Madey (Springer Berlin Heidelberg, Berlin, Heidelberg, 1983) pp. 169–182.

Rémi DUPUY **10 Octobre 2019**

Sujet : Photon and electron induced desorption from molecular ices

Résumé : L'excitation électronique de molécules condensées sur des surfaces froides (10-100 K) peut mener à la désorption de certaines de ces molécules. Ce processus fondamental a des conséquences dans de nombreuses disciplines, dont deux ont guidé ce travail : l'astrochimie et la dynamique du vide dans les accélérateurs. La désorption induite par photons et électrons est étudiée pour des films amorphes de molécules condensées (glaces) telles que CO, H_2O, NO ou CH_4. Un objectif de cette thèse est la quantification de la désorption des différentes espèces, et d'explorer les paramètres pouvant affecter l'efficacité du processus. Le second objectif est de déterminer l'évolution et la relaxation des excitations électroniques initiales et par quel mécanisme cela mène à la désorption. La photodésorption est étudiée au LERMA en utilisant le rayonnement synchrotron dans la gamme du VUV (5-14 eV) et des X mous (520-600 eV). Cela permet d'obtenir une information spectrale cruciale pour la compréhension des mécanismes et pour l'implémentation dans les modèles. La désorption induite par les électrons est étudiée au CERN dans la gamme d'énergie 150-2000 eV. Les résultats obtenus étendent les données de photodésorption UV disponibles et permettent de déterminer la pertinence de la désorption par les électrons ou les rayons X pour l'astrochimie. Des progrès sont faits dans la compréhension des mécanismes, notamment sur le rôle du transport d'énergie ou de particules depuis l'intérieur de la glace vers la surface, ou sur la désorption indirecte. Un nouveau dispositif expérimental a aussi été mis en place au LERMA pour des expériences de désorption par laser et de spectroscopie laser, permettant d'obtenir l'énergie interne et cinétique des molécules désorbées.

Mots clés : Surfaces, Astrochimie, Vide, VUV, X mous, Electrons, Glaces moléculaires

Subject : Photon and electron induced desorption from molecular ices

Abstract: The deposition of energy in the form of electronic excitations in molecules condensed on cold surfaces (10-100 K) can lead to the desorption of some of these molecules. This basic surface science process has consequences in a variety of fields, two of which are of concern here: astrochemistry and vacuum dynamics. Photon and Electron-Induced desorption are studied in this manuscript for thin films of condensed molecules (ices), e.g. CO, H_2O, NO or CH_4. The first objective is to obtain a quantification of the desorption of the various desorbing species, and to look for the parameters that affect the efficiency of the process. The second objective is to understand the mechanisms of evolution and relaxation of the initial electronic excitations that lead to desorption. Photon-induced desorption is studied at LERMA using synchrotron radiation in the VUV range (5-14 eV) and soft X-ray range (520-600 eV). This allows to obtain spectrally-resolved information, which is crucial both for model implementation and fundamental understanding of the mechanisms. Electron-induced desorption is studied at CERN in the 150-2000 eV range. The results expand the available data on UV photodesorption and allow to determine the relevance of electron or X-ray desorption for astrochemistry. Progress has also been made on the understanding of mechanisms, particularly on the role of energy or particle transport from the bulk to the surface of the ice, on indirect desorption, or on the desorption of ions in the soft X-ray range. A new experimental set-up has also been developed at LERMA for laser desorption and laser spectroscopy experiments, allowing quantum-state and kinetic energy resolved measurements of desorbed molecules.

Keywords : Surface science, Astrochemistry, Vacuum dynamics, VUV, Soft X-rays, Electrons, Molecular ices, Non-thermal desorption